

The transit of an elastic capsule through a bifurcation

A thesis submitted to the School of Mathematics of the University of East
Anglia in partial fulfilment of the requirements for the degree of
Doctor of Philosophy

By Hugh Woolfenden
October 2010

© This copy of the thesis has been supplied on condition that anyone who consults it is understood to recognise that its copyright rests with the author and that no quotation from the thesis, nor any information derived therefrom, may be published without the author's prior, written consent.

© Copyright 2010
by
Hugh Woolfenden

Abstract

The motion of a rigid particle and a flexible fluid-filled capsule in a pressure-driven flow through a channel with a side branch is investigated. The fluid velocity profiles are assumed to adopt those of unidirectional Poiseuille flow far upstream and downstream in the main channel, and downstream in the side branch. The flow rates are prescribed, leaving the instantaneous pressure drop between the entrance and exits to be calculated as part of the solution. The rigid particle is assumed to be both force-free and torque-free. The membrane of the flexible capsule is treated as a thin two-dimensional elastic sheet which develops elastic tensions and bending moments according to simple constitutive laws. The problem is solved numerically using the boundary element method for Stokes flow. The computational novelty of the formulation is the inclusion of a notional boundary at the entrance to the side branch which avoids the need to collocate the channel ends.

An elastic capsule which is released in a straight channel flow quickly deforms from its resting configuration into a parachute-like shape after travelling a few capsule radii, but takes a much greater distance to attain a steady shape. Increasing the viscosity of the fluid inside the capsule increases the time taken to reach an almost identical steady-state shape. However, when the stiffness of the membrane is increased, the capsule deforms less and the steady-state shape is attained in a shorter time.

A capsule in a branching channel flow is drawn out of the main channel when the flow rate in the side branch is sufficiently strong. The deformation suffered by an elastic capsule depends on its size, its initial location and the width and angle of the branch channel. When the branch angle is acute or a right-angle, the capsule may become trapped on the downstream branch corner and experience relatively large membrane tensions, thus presenting the possibility of bursting. Obtuse-angled branchings decrease the possibility of a capsule becoming trapped on the corner, although the residence time in the vicinity of the corner increases significantly. A capsule may suffer considerable distortion as it negotiates the branching region, but the membrane tensions are less than those experienced by a trapped capsule. When a capsule is on a path which takes it close to the downstream corner of the branch entrance, the path taken depends on the properties of the elastic membrane. A capsule with a stiffer membrane is more likely to remain in the main channel. Although the results are for a two-dimensional branching, they are nonetheless consistent with experimental observations of plasma skimming.

Acknowledgements

First I would like to thank my supervisor Mark Blyth for securing the funding which enabled me to undertake this work, and for his unflagging patience, help and encouragement throughout the course of my studies.

I would like to thank my wife Emma for her support which enabled me to return to university and pursue a research degree. I would like also to thank my children, William and Tom, for their 'helpful' comments and patience while I wrote this thesis.

Finally I would like to thank EPSRC who supported this research under grant EP/E028241/1.

Contents

Abstract	v
Acknowledgements	vii
1 Introduction	1
1.1 Physical background	1
1.2 Literature review	3
1.3 Mathematical background	8
1.3.1 Stokes equation	8
1.3.2 Poiseuille flow	9
1.3.3 Two-dimensional boundary integral equations for Stokes flow . .	11
2 A conveyor belt, a straight channel and the boundary integral method	17
2.1 Problem statement	17
2.2 Numerical method	25
2.3 Validation	29
2.4 Results	31
2.5 Discussion	39
3 The motion of a rigid particle in a straight channel	41
3.1 Problem statement	41
3.2 Numerical method	53
3.3 Validation	58
3.4 Results	60
3.5 Discussion	68
4 The motion of a fluid drop or a flexible capsule in a straight channel	69
4.1 Problem statement	69
4.2 Constitutive equations for fluid drops and elastic capsules	76
4.3 Numerical method	79
4.4 Model validation and results	86
4.4.1 A fluid drop – results	87
4.4.2 An elastic capsule – results	98
4.5 Discussion	111

5	Stokes flow through a bifurcation	113
5.1	Problem statement	113
5.2	Numerical method	125
5.3	Validation	131
5.4	Results for a fluid-filled branching channel	133
5.5	The dividing streamline	146
5.6	Discussion	149
6	The motion of a rigid particle through a bifurcation	153
6.1	Problem statement	153
6.2	Numerical method	162
6.3	Validation	168
6.4	Deformation of the notional boundary	169
6.5	Results	176
6.6	Discussion	180
7	The motion of a flexible capsule through a bifurcation	183
7.1	Problem statement	183
7.2	Numerical method	194
7.3	Flow parameters	202
7.4	Validation	203
7.5	Results	204
7.6	Deformation of the notional boundary	218
7.7	Discussion	219
7.8	Further work	222
8	Conclusions	227
	Appendices	235

List of tables

5.1	Pressure drops between the entrance and exits of a branching channel for a range of branch widths, δ , branch angles, α , and flux ratios, Q	150
6.1	Particle velocity and exit pressures for different configurations of \mathcal{A} in a branching channel containing a particle with $\rho = 0.2$ positioned at three different locations.	172
E.1	Values of the stream-function parameter, γ , for various branch angles. . .	255

List of figures

1.3.1	Two-dimensional Poiseuille flow in a straight channel. The parabolic velocity profile is shown on the left.	10
2.1	Channel with a localised disturbance on the lower wall	18
2.2	Disturbance tractions for a variety of configurations on the upper and lower walls for $L = 2d$ and $U = 1$	30
2.3	Disturbance tractions on the upper and lower walls for $\beta = 2$ and $U = 1$.	31
2.4	Velocity and streamlines for $\beta = 2$ and $U = 1$ when the Poiseuille flow is absent	32
2.5	Velocities and streamlines when $F = 1$ and $\beta = 2$	34
2.6	Velocities and streamlines when $F = 6$ and $\beta = 2$	35
2.7	The normalised top-wall shear stress for $F = 1, 2.21$ and 6 and $\beta = 2$. . .	35
2.8	Velocities and streamlines when $F = -1$ and $\beta = 2$	36
2.9	Disturbance tractions, velocity profiles and streamlines for $F = 6$ and $\beta = 4$	37
2.10	Velocity profiles and streamlines for $F = 6$ and $\beta = 1$	38
2.11	Velocity profiles and streamlines for $F = 12$ and $\beta = 0.5$	39
3.1	A straight-walled channel containing a rigid neutrally-buoyant particle. .	42
3.2	Decay of the disturbance to the x -component of velocity along the centreline for $\rho = 0.5$ and $\sigma = 0$. The particle boundary is at $x/d = 5.5$. . .	59
3.3	Upper wall disturbance tractions, particle tractions, streamlines and pathlines for $\rho = 0.5$ and $\sigma = 0$	61
3.4	Tractions on the channel walls and the particle for $\rho = 0.5$ and $\sigma = 0.25$.	63
3.5	Pathlines in a section of the channel for $\rho = 0.5$ and $\sigma = 0.25$. The particle rotates anti-clockwise and the fluid in the eddies rotates clockwise. The frame of reference is moving with the particle. The arrows indicate the flow direction relative to the particle.	64
3.6	Pathlines in a section of the channel for $\rho = 0.7$ and $\sigma = 0.25$. The particle rotates anti-clockwise and the fluid in the eddies rotates clockwise. The frame of reference is moving with the particle. The arrows indicate the flow direction relative to the particle.	65
3.7	Disturbance pressure vs. ρ for offsets $\sigma = 0$ (—), 0.25 (---) and 0.5 (···). .	65
3.8	Disturbance pressure vs. σ for two particles with $\rho = 0.25$ (—) and 0.5 (---).	66
3.9	Variation of the particle's translational velocity with respect to ρ and σ . .	66

3.10	Variation of the dimensionless particle angular velocity with respect to ρ and σ	67
4.1	A straight-walled channel containing a neutrally-buoyant capsule which encapsulates a fluid of viscosity $\lambda\mu$	70
4.2	Elastic capsule with unit normal \mathbf{n} , unit tangent \mathbf{t} , in-plane tension τ and transverse shear tension q . The arc-length is s and its direction is indicated by the arrow.	78
4.3	Disturbance tractions on the top wall and the centreline velocity for a steady drop with $\lambda = 1$, $\rho = 0.5$, $\sigma = 0$ and $C_a = 1$	89
4.4	Steady shape, disturbance pressure, boundary velocities and interfacial traction jump for a steady fluid drop with $\lambda = 1$, $\rho = 0.5$, $\sigma = 0$, $C_a = 1$	90
4.5	Streamlines and pathlines for a steady fluid drop $\lambda = 1$, $\rho = 0.5$, $\sigma = 0$, $C_a = 1$	92
4.6	Top wall disturbance tractions, steady shape, disturbance pressure and drop boundary velocities for a steady fluid drop with $\lambda = 1$, $\rho = 0.75$, $\sigma = 0$, $C_a = 1$	93
4.7	Pathlines for a steady fluid drop $\lambda = 1$, $\rho = 0.75$, $\sigma = 0$ and $C_a = 1$. The frame of reference is moving with the drop centroid.	93
4.8	Steady drop shape, disturbance pressure and pathlines for a fluid drop with $\lambda = 1$, $\rho = 0.5$, $\sigma = 0$ and $C_a = 0.5$	94
4.9	Steady drop shape, disturbance pressure and pathlines for a fluid drop with $\lambda = 1$, $\rho = 0.5$, $\sigma = 0$ and $C_a = 2$	95
4.10	Evolution of the drop centroid, disturbance pressure and the boundary velocity for a fluid drop with $\lambda = 1$, $\rho = 0.5$, $\sigma = 0.25$ and $C_a = 1$	96
4.11	Pathlines around the fluid drop with $\lambda = 1$, $\rho = 0.5$, $\sigma = 0.25$ and $C_a = 1$ at $t = 11.14 d/U_0$. The centroid is displayed as a dot at $(6, 0.125)$ and the frame of reference is moving axially with the drop centroid. Arc-length is measured anti-clockwise from zero at the rightmost point of the drop.	96
4.12	Disturbance pressure for drops with $\rho = 0.5$, $\sigma = 0$ and $C_a = 1$. The viscosity ratios are $\lambda = 1$ (–), $\lambda = 2$ (– –) and $\lambda = 5$ (· · ·).	97
4.13	Centroid paths for fluid drops with $\lambda = 10$, $\rho = 0.25$, $C_a = 1$ and $\sigma = -0.05, -0.35, -0.5$ and -0.65	98
4.14	Evolution of the drop shape for $\lambda = 10$, $\rho = 0.25$, $\sigma = -0.65$ and $C_a = 1$. The drops from left to right are for $tU_0/d = 0, 4, 8, 12, 17, 21, 25$ and 28.8 . The abscissa label is intentionally omitted, however the marks indicate the x -coordinate of the drop centroid.	98
4.15	Deformation of an elastic capsule with $M = 0$ in a shear flow for $\Omega = 0.0125, 0.125$ and 1.2 . For comparison against Figure 2 in Breyiannis and Pozrikidis (2000).	100
4.16	Capsule shape, disturbance pressure, wall disturbance traction, centreline velocity and interfacial tractions for an elastic capsule with $\lambda = 1$, $\rho = 0.5$, $\sigma = 0$, $W = 1$ and $M = 0$	101

4.17	Capsule shape, disturbance pressure, wall disturbance traction and centreline velocity for an elastic capsule with $\lambda = 1$, $\rho = 0.5$, $\sigma = 0$, $W = 1$ and $M = 0.001$	102
4.18	The membrane tensions and the bending moment versus arc-length, for the steady-state capsule shown in figure 4.17 (a). Arc-length is measured anti-clockwise from zero at the front of the capsule. The trailing tips are at $s = 1.55d$ and $s = 3.08d$ respectively.	103
4.19	Capsule shape, disturbance pressure, wall disturbance traction and centreline velocity for an elastic capsule with $\lambda = 1$, $\rho = 0.5$, $\sigma = 0$, $W = 5$ and $M = 0.001$	104
4.20	Capsule shape, disturbance pressure, wall disturbance traction and centreline velocity for an elastic capsule with $\lambda = 5$, $\rho = 0.5$, $\sigma = 0$, $W = 1$ and $M = 0.001$	105
4.21	Centroid trajectories and capsule shapes for $\lambda = 1$, $\rho = 0.5$, $W = 1$ and $M = 10^{-3}$	107
4.22	Wall disturbance traction, centreline velocity and the pathlines at $t = 2.08 d/U_0$ for an elastic capsule with $\lambda = 1$, $\rho = 0.5$, $\sigma = 0.3$, $W = 1$ and $M = 0.001$	109
4.23	Capsule shape, disturbance pressure, wall disturbance traction and centreline velocity for an elastic capsule with $\lambda = 1$, $\rho = 0.75$, $\sigma = 0$, $W = 1$ and $M = 0.001$	110
4.24	Capsule shape, disturbance pressure, wall disturbance traction and centreline velocity for an elastic capsule with $\lambda = 1$, $\rho = 1.1$, $\sigma = 0$, $W = 1$, $M = 0.001$ and an elliptical initial shape.	111
5.1	A straight-walled channel with a branch which contains a fluid of viscosity μ	114
5.2	Streamlines, wall tractions and centreline velocities for a branching channel with $\delta = 1$, $\alpha = \pi/2$ and $Q = 0.5$	135
5.3	Streamlines, wall tractions and centreline velocities for a branching channel with $\delta = 1$, $\alpha = \pi/2$ and $Q = 0.1$	137
5.4	Streamlines, wall tractions and centreline velocities for a branching channel with $\delta = 1$, $\alpha = \pi/2$ and $Q = 0.9$	138
5.5	Streamlines, wall tractions and centreline velocities for a branching channel with $\delta = 1$, $\alpha = \pi/4$ and $Q = 0.5$	140
5.6	Streamlines, wall tractions and centreline velocities for a branching channel with $\delta = 1$, $\alpha = \pi/4$ and $Q = 0.1$	141
5.7	Streamlines, wall tractions and centreline velocities for a branching channel with $\delta = 1$, $\alpha = \pi/4$ and $Q = 0.9$	142
5.8	Streamlines, wall tractions and centreline velocities for a branching channel with $\delta = 1$, $\alpha = 3\pi/4$ and $Q = 0.5$	143
5.9	Streamlines, wall tractions and centreline velocities for a branching channel with $\delta = 1$, $\alpha = 3\pi/4$ and $Q = 0.1$	144

5.10	Streamlines, wall tractions and centreline velocities for a branching channel with $\delta = 1$, $\alpha = 3\pi/4$ and $Q = 0.9$	145
5.11	Streamlines, wall tractions and centreline velocities for a branching channel with $\delta = 0.5$, $\alpha = \pi/2$ and $Q = 0.5$	146
5.12	Streamlines, wall tractions and centreline velocities for a branching channel with $\delta = 2$, $\alpha = \pi/2$ and $Q = 0.5$	147
5.13	Distance of point where $\tau = 0$ from the right-hand corner of the branch entrance.	149
6.1	A straight-walled channel with a branch which contains a fluid of viscosity μ	154
6.2	Velocity profiles in a channel with $D = d$, $\alpha = \pi/2$ and $Q = 0.5$	170
6.3	Section of the flow domain showing the notional boundary configurations for a particle of radius $\rho = 0.2$ and centroid at $\mathbf{x}_c/d = (6.65, -0.795)$	173
6.4	Section of the flow domain showing the notional boundary configurations for a particle of radius $\rho = 0.2$ and centroid at $\mathbf{x}_c/d = (6.65, -1)$	174
6.5	Section of the flow domain showing the notional boundary configurations for a particle of radius $\rho = 0.2$ and centroid at $\mathbf{x}_c/d = (6.65, -1.205)$	174
6.6	Dividing boundary configurations during particle migration into the branch channel.	175
6.7	A portion of the flow domain showing the centroid trajectories for a rigid particle with $\rho = 0.5$, $\alpha = \pi/2$ initially located at $\mathbf{x}_c/d = (2, 0)$ for $Q = 0.1, 0.5$ and 0.9	177
6.8	Normalised pressures for a rigid particle with $\rho = 0.5$, $\alpha = \pi/2$ initially located at $\mathbf{x}_c/d = (2, 0)$ for $Q = 0.1, 0.5$ and 0.9	179
6.9	Magnitude of the translational velocity and the rotational velocity for a particle with $\rho = 0.5$, $\alpha = \pi/2$ and initially located at $\mathbf{x}_c/d = (2, 0)$ for $Q = 0.1, 0.5$ and 0.9	180
7.1	A straight-walled branching channel which contains a fluid of viscosity μ and a deformable capsule containing a fluid of viscosity $\lambda\mu$	184
7.2	Capsule journeys when $\lambda = 1$, $\rho = 0.5$, $W = 1$, $\alpha = \pi/2$ and $Q = 0.9$. At $t = 0$ the capsule centroid is at $\mathbf{x}_c/d = (2, 0)$	205
7.3	Capsule journeys, membrane tensions and bending moments when $\lambda = 1$, $\rho = 0.5$, $W = 1$, $\alpha = \pi/2$ and $Q = 0.1$. At $t = 0$ the capsule centroid is at $\mathbf{x}_c/d = (2, 0)$. In (c) and (d) arc-length is measured anti-clockwise from zero at the lowermost point on the capsule as it appears in the final shape in figure 7.3 (b).	206
7.4	The membrane tensions and the bending moment versus arc-length, for the steady-state shape of a capsule in a straight channel with $\lambda = 1$, $\rho = 0.5$, $W = 1$ and $M = 0.001$. The capsule shape is shown in figure 4.17 (a).	207
7.5	Evolution of the final capsule shape from figure 7.3 (b) when $t = 13.06 d^2/Q_1$. Capsule shapes shown in (a), (b), (c) and (d) at $(Q_1/d^2)t = 0, 3.7, 9.0$ and 37.1 respectively. The final shape is the steady-state shape.	207

7.6	Normalised pressures \hat{p}_2 (–) and \hat{p}_3 (---) against time for $\lambda = 1$, $\rho = 0.5$, $W = 1$, $M = 10^{-3}$, $\alpha = \pi/2$ and $Q = 0.1$. The capsule journey is shown in figure 7.3 (b).	208
7.7	Capsule journeys and membrane tensions when $\lambda = 1$, $\rho = 0.5$, $W = 1$, $\alpha = \pi/2$ and $Q = 0.5$. At $t = 0$ the capsule centroid is at $\mathbf{x}_c/d = (2, 0)$	209
7.8	Capsule journeys for $\lambda = 1$, $\rho = 0.5$, $W = 5$, $M = 0.001$ and $\alpha = \pi/2$. At $t = 0$ the capsule centroid is at $\mathbf{x}_c/d = (2, 0)$	210
7.9	Capsule journeys for $\lambda = 5$, $a = 0.5d$, $W = 1$ and $M = 10^{-3}$	210
7.10	Capsule journeys when $\lambda = 1$, $\rho = 0.75$, $W = 1$, $M = 10^{-3}$ and $\alpha = \pi/2$. At $t = 0$ the capsule centroid is at $\mathbf{x}_c/d = (2, 0)$	211
7.11	Capsule journeys when $\lambda = 1$, $M = 10^{-3}$, $\alpha = \pi/2$ and $Q = 0.1$. At $t = 0$ the capsule centroid is at $\mathbf{x}_c/d = (2, 0)$	211
7.12	Centroid paths for capsules with $\lambda = 1$, $\rho = 0.5$, $W = 1$, $M = 0.001$ and $\alpha = \pi/2$. In both figures trajectories terminating in a dot correspond to capsules which become trapped at the corner.	212
7.13	Capsule journey when $\lambda = 1$, $\rho = 0.5$, $W = 1$ and $M = 10^{-3}$	214
7.14	Centroid paths for capsules with $\lambda = 1$, $\rho = 0.5$, $W = 1$, $M = 0.001$ and $Q = 0.5$. Capsule centroid at $t = 0$ is $\mathbf{x}_c = (2d, y_c)$ where y_c/d varies from -0.4 to 0.4 in steps of 0.1 . Trajectories terminating in a dot correspond to capsules which become trapped at the corner.	215
7.15	Capsule journeys when $\lambda = 1$, $\rho = 0.5$, $M = 0.001$, $\alpha = 3\pi/4$ and $Q = 0.5$. The capsule centroid is initially located at $(2, 0.13)d$	215
7.16	Membrane tensions and bending moment for the final capsule shown in 7.15 (a) at $t = 25.88 d^2/Q_1$. Arc-lengths at the trailing and leading tips are $s/d = 0.80$ and $s/d = 3.23$ respectively, and is measured in an anti-clockwise direction.	216
7.17	Capsule journeys when $\lambda = 1$, $\rho = 0.5$, $M = 0.001$, $\alpha = 3\pi/4$, $\delta = 1/2$ and $Q = 2/3$. The capsule centroid is initially located at $(2, 0)d$	218
7.18	Configurations of the deformed notional boundary.	220
D.1	Two-dimensional fluid-filled branching channel. The arrows indicate the prevailing flow direction and the walls are numbered 1–5.	247
D.2	Streamlines for $Q = 0.5$ in a section of the branching channel computed by the finite difference method.	250
E.1	Local geometry at the right-hand corner of the branch entrance of the branching channel, with plane polar coordinates r and θ	252
E.2	Streamlines close to a corner for $\alpha = 0.57\pi$ and $\gamma = 2$. The stress on the walls is well-defined in this case. When the constant A is positive in equation (E.16) the streamlines enter from the top-left.	256
E.3	Streamlines close to a corner for $\alpha = 3\pi/4$ and $\gamma = 1.67358343$. The stress is singular at the corner.	256
E.4	Streamlines close to a corner with $\alpha = \pi/2$ for the two values of γ . The stress is singular at the corner in both cases.	257

E.5 Streamlines close to a corner with $\alpha = \pi/4$ for the two values of γ . The stress is singular at the corner in both cases. 257

Chapter 1

Introduction

In this introductory chapter we will motivate our research by providing the physical and mathematical background to the motion of a particle in a channel which we will investigate in subsequent chapters.

1.1 Physical background

There are many examples of small particles moving within a fluid which is also in motion. If we limit our attention to the motion of particles in pipes, then one of the most well known examples is the circulation of blood around the cardiovascular system. During the journey of oxygenated blood through the systemic circulation, blood travels from the heart into the aorta and on into the arteries, then into smaller vessels called arterioles and then into the capillaries which are the smallest blood vessels. Oxygen-depleted blood is returned from the capillaries via venules and the veins to the heart where it is pumped to the lungs in order to release carbon dioxide and receive oxygen. Blood consists of platelets, white blood cells and red blood cells which are all suspended in plasma. In a healthy cubic millimetre of human blood there will be approximately 5 million red blood cells, 7500 white blood cells and 0.5 million platelets. While the red blood cells account for around 45% of blood volume the combined volume of white blood cells and platelets is around 1%. Further detail on the constituents of blood and blood flow may be found in Caro et al. (1978). Therefore the mechanical properties of blood are dominated by the behaviour of the red blood cells due to their high concentration. In vessels such as the aorta and large arteries, blood flow may be treated homogeneously because the cells are much smaller than the vessel through which they travel. However in the smaller blood vessels, such as capillaries, the size of the red blood cells is of the same order as the vessel and so blood must be treated heterogeneously and the particulate nature must be taken into account. To put this into perspective, a typical human red blood cell whose undeformed shape is a biconcave disk, has a thickness of $2\mu\text{m}$ and a maximum diameter of $8\mu\text{m}$ which is larger than the minimum diameter of a capillary, which can be as low as $5\mu\text{m}$. To pass through capillaries of this size red blood cells undergo considerable deformation, and either adopt a shape which is similar to a parachute or they fold along a

diameter of the cell. The red blood cells are therefore extremely flexible. There are several different types of white blood cells and they are all roughly spherical, with the diameter of the largest type around $21\mu\text{m}$ in humans. Platelets are smaller than red blood cells and are irregularly shaped with a volume which is about $1/10\text{th}$ that of a red blood cell.

The properties of blood flow have been widely studied in many disciplines, including medicine, physiology and mathematics. The first published results which quantitatively described the flow of blood were by Jean Louis Marie Poiseuille in 1840 where he experimentally derived his law ¹ in a circular pipe. The law relates the volumetric flow rate, Q , along the pipe to the applied pressure difference, Δp , the diameter, D , and the vessel length L and was originally stated as

$$Q = K \frac{\Delta p D^4}{L} \quad (1.1.1)$$

where K was an experimentally derived constant which depended on the temperature and the liquid. Later it was found that $K = \pi/128\mu$ where μ is the fluid's viscosity. A history of Poiseuille's law is given in Suter and Skalak (1993). We can see that the flux is proportional to the pressure drop and to the fourth power of the pipe diameter. Consequently to maintain a specific flow rate along a pipe the applied pressure difference must be quadrupled if the cross-sectional area is halved. The Hagen-Poiseuille law may be applied successfully to the flow of blood through the smaller vessels, and more generally to any non-turbulent fluid flow along a pipe of constant circular cross-section.

There are numerous other examples of particles moving along channels in nature as well as technology. For example the flow of particles into the air pathways of the lungs is of particular interest in the design of medicines. Fluidisation chambers are used in the petrochemical industry as well as other industries (Davidson et al. 1985). An example is the fluid catalytic cracking process which is used to break apart the heavier petroleum compounds to extract petroleum spirit. The resulting fluid may then be easily extracted along pipes. The flow of immiscible fluids through a porous media is of interest to many disciplines, including petroleum engineers and geophysicists (e.g. Gunstensen and Rothman 1993). The coating of paper and the manufacture of ink involves the flow of emulsions or colloids through pipes (e.g. Jensen et al. 2006). An in-depth knowledge of the fluid mechanics are required in the design and construction of microfluidic devices (e.g. Roberts and Olbricht 2006) which could for example be used to sort cells, or some other chemical investigation.

To determine the governing forces in a specific flow a measure which is of interest to engineers and mathematicians is the Reynolds number, which may be thought of as the ratio of inertial forces to viscous forces. A high Reynolds number indicates that inertia dominates the fluid motion, and a low Reynolds number means that viscosity dominates. If U is the typical fluid velocity and L is the typical length (e.g. the tube diameter) then

¹Called the Hagen-Poiseuille law to recognise its independent discovery by Gotthilf Hagen.

the Reynolds number, Re , is defined by

$$Re = \frac{\rho U L}{\mu} \quad (1.1.2)$$

where μ is the fluid's viscosity and ρ is its density. In the cardiovascular system the Reynolds number is greater in the larger blood vessels, i.e. it is high in the aorta, and low in the capillaries ($Re = 0.0003$ (Popel and Johnson 2005)). It must also be said that the viscosity of whole blood varies from vessel to vessel in the cardiovascular system. This variation is called the Fahraeus-Lindqvist effect and is observed in vessels with a diameter of less than about 1 mm. There are several factors which cause the decrease in viscosity but the main physical reason for the effect is due to the red blood cells migrating towards the vessel centreline. A cell-free layer near the wall is created which then reduces the flow resistance and therefore the apparent viscosity. For a fuller description of the effect see chapter 4 in Pozrikidis (2003) and the references therein. Throughout this work we are interested in regimes where the Reynolds number is small such that viscous forces dominate the mechanics of the fluid and particle motion. Furthermore we are interested in cells which may contain a fluid of generally different viscosity to the surrounding fluid. For example a red blood cell contains haemoglobin which is 4–5 times as viscous as the surrounding plasma (Caro et al. 1978, p. 161).

In this work we will use the term particle to refer to a rigid cell of constant shape, the term drop to refer to an immiscible liquid suspended in an ambient fluid and the term capsule to refer to a thin, flexible walled cell which contains a secondary fluid. We will use the term cell as a collective term for a rigid particle of constant shape, a fluid drop and an elastic capsule. Although there is a small difference between the density of blood plasma and blood cells (e.g. Benson 1999), the effect will be negligible in the microcirculation due to the small size of the cells and vessels. For the cells considered herein we will therefore assume that the ambient fluid and the encapsulated fluid have the same constant density and that the cell is inertia-free thus rendering the cell neutrally buoyant.

1.2 Literature review

The motion of fluid drops, particles and elastic capules is a rich and intensively studied area of hydrodynamics. The behaviour of each type of cell has been investigated in unbounded flows as well as above plane walls and in channels and tubes. While some studies concentrate on a single cell, others investigate the behaviour of aggregates or suspensions of many cells. The field has been studied experimentally and theoretically with both disciplines employing a wide variety of investigative tools. Here we will provide a brief review of the literature regarding the motion of cell through channels and tubes.

The placement of a cell in an unbounded flow allows the analysis to concentrate on the dynamics of the cell and its motion. Investigations into the nature of the deformation could lead to predictions on the conditions which would cause the cell to break up. Barthès-Biesel (1980) used asymptotic expansions to investigate the small deformations

of a spherical capsule in a shear flow. She found that increasing the viscosity of the encapsulated fluid increased the capsule's inclination to the incident streamlines of the background shear flow. The assumption of a small deformation was relaxed by Zahalak et al. (1987) in their two-dimensional work on an inextensible capsule in an unbounded shear flow using a series solution and conformal transformations. They found that the capsule reaches an equilibrium state in which the normal component of the membrane's velocity is zero while the tangential component is non-zero so that the cell boundary exhibits a tank-treading motion. Furthermore, they showed how the shear rate of the background flow and the fluid viscosities affect the velocity field, membrane deformation and tension. In a later work, Rao et al. (1994) studied an elastic capsule in an unbounded two-dimensional shear flow and concentrated on how the viscosity ratio affected the apparent viscosity of the whole fluid. They found that the apparent viscosity was inversely proportional to the encapsulated fluid's viscosity. Zhou and Pozrikidis (1995) considered a cell with an incompressible membrane with a variety of undeformed shapes in a two-dimensional shear flow, and a spheroidal cell in a three-dimensional shear flow. They found that the deformed steady cell shape depended on the undeformed shape and that there were qualitative and quantitative similarities between the deformation of the two and three-dimensional cells. Ramanujan and Pozrikidis (1998) studied the deformation of a cell with an elastic membrane in a three-dimensional shear flow. They found that the viscosity ratio did not profoundly affect the equilibrium shape of the cell.

In the above cited works, the cell membrane does not resist bending. The inclusion of a bending stiffness was made in Pozrikidis (2001) in order to study its effect on the cell's deformation in a three-dimensional shear flow and for an arbitrary viscosity ratio. He found that the bending resistance restricted the cell's deformation and prevented the cell from developing regions of relatively high curvature. However the time-integration method was shown to be sensitive to the size of the time-step, with a smaller time-step required when bending resistance was taken into account.

The fluid was unbounded in the previous studies. However in many applications of practical interest the cell travels along a channel or pipe. Rigid particles in an elastic tube were studied by Lighthill (1968) who used lubrication theory to show the existence of a thin lubricating layer ($0.2\mu\text{m}$) in the case of tightly fitting pellets. Later, Tözere and Skalak (1978) presented a significantly more accurate method of calculating the pressure drop across a tightly fitting pellet which was duly endorsed by Lighthill. Brenner (1970) derived analytic expressions for the additional pressure drop due to a rigid neutrally-buoyant particle moving in a tube where the background flow was Poiseuille. He considered a sphere in a circular pipe as well as non-circular pipes and ellipsoidal particles. The motion of fluid drops and bubbles of constant surface tension was investigated in Brenner (1971) where expressions for the pressure drop were derived. Sugihara-Seki (1993) studied the motion of an inertia-free elliptical cylinder in a channel with a background Poiseuille flow. The finite-element method was used to calculate the velocity of the particle and the fluid. He calculated the particle trajectories for a range of particle sizes and displacements from the centreline. In Sugihara-Seki (1996) the numerical

model was updated to model the motion of an ellipsoid in a circular tube. Prolate and oblate spheroids were shown to exhibit differing behaviour depending on several factors including the particle-tube size ratio and centreline offset.

Quéguiner and Barthès-Biesel (1997) developed a numerical axisymmetric model for an elastic cell which encapsulated a fluid of the same viscosity as the ambient fluid. The cell travelled from a hyperbolic entrance area into a circular tube where it was allowed to reach an equilibrium state. The deformation was then also studied as the cell moved out of the tube into a hyperbolic exit area. They showed that steady-state deformed shape was similar to that seen in experiments (e.g. Secomb et al. 2007). The length of the tube required to reach the steady shape displayed a strong dependence on the cell size and membrane behaviour. Mortazavi and Tryggvason (2000) studied the motion of an immiscible fluid drop of a generally different viscosity and density in a two-dimensional channel using the finite-difference method for Reynolds numbers of 0.25 and above. They showed that the drops migrate across streamlines with the motion directed towards an equilibrium position at the centreline or at a point closer to the wall which for a specific Reynolds number depended on the viscosity ratio and density ratio.

Staben et al. (2003) used the boundary integral method to investigate the motion of a rigid spherical particle in a Poiseuille flow between two plane walls, and where the particle was close to one or both of the walls. The formulation allowed the authors to avoid meshing the channel walls which facilitated the accurate computation of the particle motion even when the particle-wall separation was less than 1% of the particle radius. They showed that larger particles translated slower along the channel. They also calculated the rotational velocity and showed how it increased as the particle was moved away from the centreline. However at a point close to the wall the rotational velocity began to decrease due to the proximity of the walls. Pozrikidis (2005b) computed the motion of a rigid spherical particle and the induced additional pressure drop in a tube using the boundary integral method, and where the background flow was assumed to be Poiseuille. The results were found to be consistent with previous asymptotic solutions. The rigid particle was replaced by an elastic cell in Pozrikidis (2005c). The cell did not resist bending and contained a fluid with viscosity equal to that of the ambient fluid. The concentrically positioned cell was found to develop a shape resembling a parachute. An eccentrically positioned cell was found to migrate towards the centreline while developing a shape resembling a slipper. Both shapes are observed in experiments on the flow of red blood cells in capillaries (e.g. Secomb et al. 2007).

Pipes and channels with a branch or even multiple branchings have been studied both experimentally and theoretically. Pries et al. (1986) studied the flow of blood cells in a section of the rat mesentery experimentally. They found that the more peripheral vessels received a lower proportion of the red blood cells. Yan et al. (1991) studied the three-dimensional motion of a rigid spheres moving from a large tube into a smaller circular side pore. However comparisons with the fluid-skimming phenomenon (e.g. Krogh 1922) observed in capillaries revealed differences which were attributed to the rigid nature of the particles in the study. Kiani and Cokelet (1994) calculated the additional pressure drop

at a single bifurcation using a large-scale experimental apparatus consisting of circular tubes containing glycerol and flexible disks to model the blood plasma and red blood cells respectively. They found that the pressure drop was significantly higher across the bifurcation when the disks were introduced into the system. A theoretical study by El-Kareh and Secomb (2000) considered the motion of rigid spherical caps in the flow between parallel plates with a cylinder joining the plates to simulate a bifurcation. They concluded that red blood cells will only follow fluid streamlines if the cells approach the bifurcation with random orientations with respect to the streamlines of the background flow. Manga (2006) studied the effect of a symmetric branching on the flow of one or more fluid drops in two dimensions using the boundary integral method. He found that the drops were more likely to enter the branch with the higher flow rate when the viscosity ratio decreases, the capillary number increases or the drop size increases.

Roberts and Olbricht (2006) studied experimentally the motion of rigid disks in branching channels of square and rectangular cross-section. They limited their study to two specific bifurcation geometries. They found that under certain flow conditions the particles could be segregated from the suspending fluid. Secomb et al. (2007) studied the motion of red blood cells through a single bifurcation in a microvessel of a rat's mesentery. They then went on to perform a numerical study of their observed results by loading a two-dimensional rendering of the blood vessel into a finite-element software package together with a visco-elastic model capsule. The mechanical properties of the capsule were set from experimental calculations. They found that their numerical model accurately predicted their observed results regarding capsule shape and lateral migration in the channel. In their treatment only a specific channel geometry was considered and the additional pressure drop across the particle was not computed. The work of Barber et al. (2008) followed on from Secomb et al. (2007). Barber et al. (2008) computed the partitioning and deformation at a rounded capillary bifurcation using a visco-elastic capsule and the finite-element method. They found that the numerical predictions of their two-dimensional model were consistent with the experimental results. However the evolution of the additional pressure drop due to the capsule was not included in their analysis.

In the majority of the above works the cell is treated in isolation. The motion and behaviour of multiple cells in a suspension has been studied by many authors, with applications including various industrial and natural processes, as previously mentioned. Batchelor (1970) derived an analytic formula for the bulk stress of a suspension in an unbounded flow by averaging over the system. Zhou and Pozrikidis (1993, 1994) studied the motion of a suspension of fluid drops in a two-dimensional channel flow using the boundary integral method. A single file of drops was considered in Zhou and Pozrikidis (1993) where the motion was driven by a shear flow and shear-thinning of the suspension was evident in all simulations. A Poiseuille flow was used for the background flow in Zhou and Pozrikidis (1994) where the drops were found to migrate towards the centreline, forming either a single row or multiple rows. Numerical simulations were carried out by Loewenberg and Hinch (1996) who studied the motion of a three-dimensional periodic array of up to twelve drops in an unbounded shear flow. Their results revealed a complex

rheology in the suspension with the emphasis on drops which encapsulated a fluid with viscosity equal to that of the ambient fluid, although some steady-state comparisons are made for drops with viscosity ratios in the range zero to five. Secomb and Hsu (1996) studied the axisymmetric motion of elastic fluid-filled capsules in a tube where lubrication theory was employed to describe the motion of the surrounding plasma. They showed that the resistance to cell motion was higher in a tube of varying cross-section than in a tube of uniform cross-section, thereby demonstrating that the deformation suffered by a red blood cell may contribute significantly to the flow resistance in capillaries.

Coulliette and Pozrikidis (1998) conducted a three-dimensional analysis of an array of fluid drops in a circular pipe with a background Poiseuille flow, and where the ambient and encapsulated fluids' viscosities were assumed to be equal. They found that drops migrated towards the centreline. They calculated the apparent viscosity of the suspension by averaging over the system and found that the apparent viscosity was higher for a non-axisymmetric file of drops than for an axisymmetric one. Breyiannis and Pozrikidis (2000) investigated the motion of up to 50 elastic cells in a periodic domain in a two-dimensional shear flow where the viscosity of the encapsulated fluid was assumed to be equal to that of the ambient fluid. They found that a solitary test cell reached an equilibrium state for all values of the imposed shear rate of the background flow and that the rheological properties of the suspension was somewhere between that of a suspension of fluid drops and rigid particles, due to cell deformability and the tank-treading ability of the cell membrane. Secomb et al. (2001) studied numerically the effect of an endothelial surface layer (ESL) on the motion of red blood cells in a capillary. Their elastic cell also included resistance to bending and the parameter values of the cell were taken from human red blood cells. They showed that the ESL causes the red cell shape and its velocity to more closely match experimental results. Pozrikidis (2005a) examined the axisymmetric motion of a file of elastic cells in a Poiseuille flow in a tube using the boundary integral method. The cell resisted bending and the viscosity ratio was set to unity. The results showed the significance of capillary size and cell spacing on the discharge haematocrit and apparent viscosity of the whole fluid.

We can therefore see that theoretical studies have tended to concentrate on the motion of elastic capsules in unbounded domains, straight channels and tubes, whereas motion of capsules at bifurcations has received less attention. In some applications bifurcations may closely follow each other. In capillary networks, for example, the blood vessels undergo numerous branchings (Popel and Johnson 2005), and the distribution of cells throughout the network is known to be non-uniform, with cells at flow junctions tending to favour the branch with the higher flow rate (Fung 1973). Indeed Pozrikidis (2009) performed simulations in a tree-like capillary network where a probability function was used to decide on the direction of the cell at a branching. In microfluidic channels, branchings may be engineered to selectively control the distribution of cells (Roberts and Olbricht 2006). In order to more fully understand the mechanical factors which affect capsule motion at a junction we require a numerical model which not only takes into account the properties of the membrane but also the flow conditions and the branch geometry. Our aim

therefore is to construct a numerical model which accurately reflects the complex interaction between the fluid flow, the deforming capsule boundary and the channel geometry at a bifurcation.

1.3 Mathematical background

In this section we provide the details of the mathematical tools which we will use to study the motion of a particle or capsule in a straight and a branching channel flow. We will describe the equations of Poiseuille flow for the unidirectional flow of fluid in a straight channel and the boundary integral method which we will later use to derive the governing equations in the regimes of interest. We will start by describing the Stokes equations which govern the flow of fluids in the limit of vanishing Reynolds number.

1.3.1 Stokes equation

Throughout this thesis we are concerned with the flow of Newtonian fluids of constant density which have a small Reynolds number. A Newtonian fluid is one in which the relationship between the fluid stress, $\boldsymbol{\sigma}$, and the rate of strain is linear and is described mathematically by

$$\sigma_{ij} = -p \delta_{ij} + \mu \left(\frac{\partial u_i}{\partial x_j} + \frac{\partial u_j}{\partial x_i} \right), \quad (1.3.1)$$

where p is the pressure, δ_{ij} is the Kronecker delta which equals 1 when $i = j$ and 0 otherwise, \mathbf{u} is the velocity, and $i, j = x, y$ in two-dimensions. For example, in the cardiovascular system both the haemoglobin encapsulated by a red blood cell and the plasma may be treated as Newtonian fluids (Halpern and Secomb 2006). When the density is constant the conservation of mass gives

$$\nabla \cdot \mathbf{u} = 0 \quad (1.3.2)$$

which is called the incompressibility condition, or the continuity equation. The cornerstone of fluid mechanics is the Navier-Stokes equation,

$$\rho \left(\frac{\partial \mathbf{u}}{\partial t} + (\mathbf{u} \cdot \nabla) \mathbf{u} \right) = -\nabla p + \mu \nabla^2 \mathbf{u}, \quad (1.3.3)$$

which relates the velocity and its derivatives to the spatial derivative of the pressure. By an appropriate scaling of the pressure, velocity and length the Navier-Stokes equation becomes the Stokes equation (e.g. Pozrikidis 1992),

$$-\nabla p + \mu \nabla^2 \mathbf{u} = \mathbf{0} \quad (1.3.4)$$

in the limit $Re \rightarrow 0$, and where we assume the flow to be steady (i.e. to be independent of time) and unaffected by a body force. Care must be exercised when assuming the flow to be steady, especially in regimes like the cardiovascular system where the flow of blood

is pulsatile and therefore unsteady. In the larger blood vessels the pulsatile nature cannot be omitted, however in the capillaries the pulse has a negligible effect (p.291 Fung 1997) and so the flow there may be treated as steady.

Since we have assumed that all considered fluids have the same constant density there will be no buoyancy effect. If we were to include a body force such as gravity we could modify the pressure accordingly since gravity is a conservative field. However we consider very small length scales and so we neglect gravity. One may restate equation (1.3.4) as

$$\nabla \cdot \boldsymbol{\sigma} = \mathbf{0} \quad (1.3.5)$$

using equations (1.3.1) and (1.3.2). With reference to the normal vector, \mathbf{n} , the traction,

$$\mathbf{f} = \boldsymbol{\sigma} \cdot \mathbf{n}, \quad (1.3.6)$$

may be used to calculate the force on an element of fluid from the normal component of the stress tensor. In index notation we have

$$f_i = \sigma_{ij} n_j = -p n_i + \mu \left(\frac{\partial u_i}{\partial x_j} + \frac{\partial u_j}{\partial x_i} \right) n_j. \quad (1.3.7)$$

When the velocity vanishes on a surface due to the no-slip and no-penetration conditions, the pressure on that surface may be obtained from the traction by taking the scalar product with the normal to get

$$p = -\mathbf{f} \cdot \mathbf{n}. \quad (1.3.8)$$

When we examine the motion of a particle or a capule in a channel flow we will treat the flow as being composed of a background and a disturbance flow. The natural choice for the background flow in a channel is the Poiseuille flow which satisfies both the Stokes equation and the Navier-Stokes equations exactly. The mathematical details of which are described in the next section. If we represent the Poiseuille stress by $\boldsymbol{\sigma}^P$ and the disturbance stress by $\boldsymbol{\sigma}^D$ then the total stress $\boldsymbol{\sigma}$ is given by

$$\boldsymbol{\sigma} = \boldsymbol{\sigma}^P + \boldsymbol{\sigma}^D, \quad (1.3.9)$$

which also satisfies the Stokes equation (1.3.5) provided $\nabla \cdot \boldsymbol{\sigma}^D = \mathbf{0}$. We will use this idea to separate the background flow from the disturbance flow throughout this thesis.

1.3.2 Poiseuille flow

Let us consider a two-dimensional channel of width, $2d$, which contains an incompressible viscous fluid. When a constant pressure gradient is applied across two end-points of the channel the resultant fluid motion is called Poiseuille flow, after the aforementioned Jean Louis Marie Poiseuille. The velocity is observed to be steady, unidirectional and oriented in the axial direction. The geometry is illustrated in figure 1.3.1. Writing the velocity as,

$$\mathbf{u}^P = u^P(x, y) \mathbf{i} \quad (1.3.10)$$

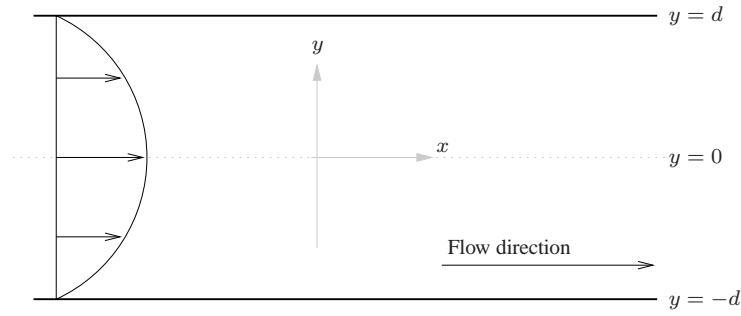


Figure 1.3.1 : Two-dimensional Poiseuille flow in a straight channel. The parabolic velocity profile is shown on the left.

where \mathbf{i} is the unit vector in the axial (or x) direction. We can show that the continuity equation (1.3.2) is satisfied only when the velocity is purely a function of y . Therefore the left-hand side of the Navier-Stokes equation (1.3.3) is zero and so Poiseuille flow automatically satisfies the Stokes equation (1.3.4). Expanding equation (1.3.4) shows that the pressure is purely a function of x . Let us set the pressure gradient,

$$\frac{dp^P}{dx} = -G \quad (1.3.11)$$

where G is a positive constant. The Poiseuille pressure is given by

$$p^P(x) = -Gx \quad (1.3.12)$$

where we have chosen the pressure to be zero at $x = 0$. We impose the no-slip and no-penetration condition,

$$\mathbf{u}^P = \mathbf{0} \quad (1.3.13)$$

on the walls, and solve equation (1.3.4) for the velocity to obtain

$$\mathbf{u}^P = u^P(y) \mathbf{i} = U_0 \left(1 - \frac{y^2}{d^2}\right) \mathbf{i} \quad (1.3.14)$$

where

$$U_0 = \frac{Gd^2}{2\mu}, \quad (1.3.15)$$

is the centreline velocity. The parabolic profile is shown on the left-hand side in figure 1.3.1. The streamwise flux rate, Q , may be found by integrating the velocity between $y = -d$ and $y = d$ to get

$$Q = \frac{2Gd^3}{3\mu} = \frac{4}{3}dU_0. \quad (1.3.16)$$

By substituting the Poiseuille pressure and velocity into equation (1.3.1) we find the Poiseuille stress tensor is given by

$$\sigma_{ij}^P = \begin{bmatrix} \sigma_{xx} & \sigma_{xy} \\ \sigma_{yx} & \sigma_{yy} \end{bmatrix} = \begin{bmatrix} -p^P & \mu \frac{\partial u^P}{\partial y} \\ \mu \frac{\partial u^P}{\partial y} & -p^P \end{bmatrix} = G \begin{bmatrix} x & -y \\ -y & x \end{bmatrix}, \quad (1.3.17)$$

and the Poiseuille traction is given by

$$f_i^P = \sigma_{ij}^P n_j = G \begin{bmatrix} x & -y \\ -y & x \end{bmatrix} \cdot \begin{bmatrix} n_x \\ n_y \end{bmatrix}, \quad (1.3.18)$$

where $\mathbf{n} = (n_x, n_y)$.

1.3.3 Two-dimensional boundary integral equations for Stokes flow

To derive the two-dimensional boundary integral equations for Stokes flow we bring together the Green's functions for Stokes flow and the reciprocal relation of Lorentz. See Kuiken (1996) for an accessible review of the work of Lorentz. To start our discussion we will outline the derivation of the reciprocal relation.

Let us define two incompressible flows so that the viscosity, velocity and stress is $(\mu_1, \mathbf{u}_1, \boldsymbol{\sigma}_1)$ in flow 1 and $(\mu_2, \mathbf{u}_2, \boldsymbol{\sigma}_2)$ in flow 2. To proceed, let us construct $\mu_1 \mathbf{u}_1 \cdot \boldsymbol{\sigma}_2 - \mu_2 \mathbf{u}_2 \cdot \boldsymbol{\sigma}_1$ and take its divergence to obtain

$$\frac{\partial}{\partial x_j} \left(\mu_1 u_{1,i} \sigma_{2,ij} - \mu_2 u_{2,i} \sigma_{1,ij} \right) = \mu_1 u_{1,i} \left(\frac{\partial \sigma_{2,ij}}{\partial x_j} \right) - \mu_2 u_{2,i} \left(\frac{\partial \sigma_{1,ij}}{\partial x_j} \right) \quad (1.3.19)$$

in index notation, and where the additional terms from performing the differentiation disappear either due to incompressibility or cancellation. If both flows also satisfy the Stokes equation (1.3.5) over some region Γ then the right-hand side of equation (1.3.19) will be zero and we have

$$\nabla \cdot (\mu_1 \mathbf{u}_1 \cdot \boldsymbol{\sigma}_2 - \mu_2 \mathbf{u}_2 \cdot \boldsymbol{\sigma}_1) = 0 \quad (1.3.20)$$

in vector notation. Next we integrate equation (1.3.20) over Γ and apply the divergence theorem to get

$$\int_{\partial\Gamma} \mu_1 \mathbf{u}_1 \cdot \mathbf{f}_2 \, ds(\mathbf{x}) = \int_{\partial\Gamma} \mu_2 \mathbf{u}_2 \cdot \mathbf{f}_1 \, ds(\mathbf{x}), \quad (1.3.21)$$

where $\partial\Gamma$ is the piecewise continuous boundary of the domain Γ , $\mathbf{f}_1 = \boldsymbol{\sigma}_1 \cdot \mathbf{n}$ is the traction of flow 1, $\mathbf{f}_2 = \boldsymbol{\sigma}_2 \cdot \mathbf{n}$ is the traction in flow 2, \mathbf{n} is the unit normal vector pointing out of Γ and s is the arc-length along $\partial\Gamma$. When the viscosities are equal we have $\mu_1 = \mu_2$ and equations (1.3.20) and (1.3.21) become

$$\nabla \cdot (\mathbf{u}_1 \cdot \boldsymbol{\sigma}_2 - \mathbf{u}_2 \cdot \boldsymbol{\sigma}_1) = 0, \quad (1.3.22)$$

in vector notation, and

$$\int_{\partial\Gamma} \mathbf{u}_1 \cdot \mathbf{f}_2 \, ds(\mathbf{x}) = \int_{\partial\Gamma} \mathbf{u}_2 \cdot \mathbf{f}_1 \, ds(\mathbf{x}) \quad (1.3.23)$$

respectively. Equations (1.3.21) and (1.3.23) are known as the Lorentz reciprocal relations for Stokes flow. The reciprocal relations give us the ability to compute information about a particular flow by using another flow, e.g. one could compute the force on a particle by eliminating the disturbance velocity caused by the particle in favour of the known

background flow.

The Green's functions for Stokes flow are solutions to the singularly forced Stokes equation,

$$-\nabla p' + \mu \nabla^2 \mathbf{u}' = \nabla \cdot \boldsymbol{\sigma}' = -\mathbf{b}' \delta(\mathbf{x} - \mathbf{x}_0), \quad (1.3.24)$$

where \mathbf{b}' is the strength of a point force located at \mathbf{x}_0 and $\delta(\mathbf{x} - \mathbf{x}_0)$ is the two-dimensional Dirac delta function which is zero everywhere except \mathbf{x}_0 where its value tends to infinity and whose integral over all space equals 1. If we introduce the Green's function $\mathbf{G}(\mathbf{x}, \mathbf{x}_0)$ then the velocity, pressure and stress fields which satisfy equation (1.3.24) are given by

$$u'_i(\mathbf{x}) = \frac{1}{4\pi\mu} G_{ij}(\mathbf{x}, \mathbf{x}_0) b_j, \quad (1.3.25)$$

$$p'(\mathbf{x}) = \frac{1}{4\pi} P_j(\mathbf{x}, \mathbf{x}_0) b_j, \quad (1.3.26)$$

$$\sigma'_{ik}(\mathbf{x}) = \frac{1}{4\pi} T_{ijk}(\mathbf{x}, \mathbf{x}_0) b_j, \quad (1.3.27)$$

where $\mathbf{P}(\mathbf{x}, \mathbf{x}_0)$ and $\mathbf{T}(\mathbf{x}, \mathbf{x}_0)$ are the pressure vector and the stress tensor associated with the Green's function. We call \mathbf{x}_0 the pole or the singular point. The stress tensor is defined in relation to the pressure vector and the Green's function as

$$T_{ijk}(\mathbf{x}, \mathbf{x}_0) = -\delta_{ik} P_j(\mathbf{x}, \mathbf{x}_0) + \frac{\partial}{\partial x_k} (G_{ij}(\mathbf{x}, \mathbf{x}_0)) + \frac{\partial}{\partial x_i} (G_{kj}(\mathbf{x}, \mathbf{x}_0)), \quad (1.3.28)$$

from which we can see that the stress tensor is symmetric, i.e. $T_{ijk}(\mathbf{x}, \mathbf{x}_0) = T_{kji}(\mathbf{x}, \mathbf{x}_0)$. The simplest Green's function is the free-space Green's function although the choice of Green's function may be dependent on the geometry under consideration and the boundary conditions. Throughout this thesis we will elect to use the two-dimensional free-space Green's function which is defined by

$$G_{ij}(\mathbf{x}, \mathbf{x}_0) = -\delta_{ij} \ln |\mathbf{x} - \mathbf{x}_0| + \frac{\hat{x}_i \hat{x}_j}{|\mathbf{x} - \mathbf{x}_0|^2}, \quad (1.3.29)$$

where $\hat{x}_i = x_i - x_{0,i}$, and its associated stress tensor is

$$T_{ijk}(\mathbf{x}, \mathbf{x}_0) = -4 \frac{\hat{x}_i \hat{x}_j \hat{x}_k}{|\mathbf{x} - \mathbf{x}_0|^4}. \quad (1.3.30)$$

A derivation of equations (1.3.29) and (1.3.30) may be found in Pozrikidis (1992). Using equations (1.3.24)–(1.3.28) and the properties of the Dirac delta function we may prove

the following integral identities for Stokes flow,

$$\int_{\partial\Gamma} T_{ijk}(\mathbf{x}, \mathbf{x}_0) n_i(\mathbf{x}) \, ds(\mathbf{x}) = \begin{bmatrix} 4\pi \\ 2\pi \\ 0 \end{bmatrix} \delta_{jk} \quad (1.3.31)$$

$$\epsilon_{ilm} \int_{\partial\Gamma} x_l T_{mjk}(\mathbf{x}, \mathbf{x}_0) n_k(\mathbf{x}) \, ds(\mathbf{x}), = \begin{bmatrix} 4\pi \\ 2\pi \\ 0 \end{bmatrix} \epsilon_{ilj} x_{0,l}, \quad (1.3.32)$$

where the 4π value is taken when \mathbf{x}_0 lies inside Γ , the 2π value is taken when \mathbf{x}_0 lies on $\partial\Gamma$ and the identity equals zero when \mathbf{x}_0 lies outside Γ , and where \mathbf{n} is the unit normal vector directed into Γ and ϵ_{ilm} is the alternating tensor defined by

$$\epsilon_{ilm} = \begin{cases} 1 & \text{when 'ilm' form a cyclic permutation, e.g. 123,} \\ -1 & \text{when 'ilm' form an anti-cyclic permutation, e.g. 321,} \\ 0 & \text{when any of } i, l \text{ or } m \text{ are equal.} \end{cases} \quad (1.3.33)$$

We obtain one final identity by substituting equation (1.3.25) into the continuity equation (1.3.2), integrating over Γ and applying the divergence theorem to get

$$\int_{\partial\Gamma} G_{ij}(\mathbf{x}, \mathbf{x}_0) n_i(\mathbf{x}) \, ds(\mathbf{x}) = 0, \quad (1.3.34)$$

for \mathbf{x}_0 inside Γ , outside Γ or on the boundary $\partial\Gamma$. Equation (1.3.34) is the integral analogue of the continuity equation. We are now in a position to provide a sketch of the derivation of the boundary integral equations for Stokes flow. A full derivation may be found in chapter 2 of Pozrikidis (1992). In equation (1.3.22) we set flow 1 to be the solution to the singularly forced Stokes equation and flow 2 to be a solution to Stokes equation. We substitute equations (1.3.25) and (1.3.27) into equation (1.3.22) and adopt index notation to get

$$\frac{\partial}{\partial x_k} (G_{ij} \sigma_{ik} - \mu u_i T_{ijk}) = 4\pi\mu u_j \delta(\mathbf{x} - \mathbf{x}_0), \quad (1.3.35)$$

where we have cancelled the common factor, b_j , and dropped the 2 subscript from flow 2. When \mathbf{x}_0 lies outside Γ the left-hand side of equation (1.3.35) is regular throughout Γ and so we can integrate over Γ and apply the divergence theorem to get

$$\int_{\partial\Gamma} (-G_{ij} \sigma_{ik} + \mu u_i T_{ijk}) n_k \, ds(\mathbf{x}) = 0, \quad (1.3.36)$$

where we have defined \mathbf{n} to point into Γ . This is the boundary integral equation which is valid when \mathbf{x}_0 lies outside of the flow domain Γ .

When \mathbf{x}_0 lies inside Γ the left-hand side of equation (1.3.35) is singular at \mathbf{x}_0 and so we define a small circle around \mathbf{x}_0 with domain Γ_0 and boundary $\partial\Gamma_0$. Integrating

equation (1.3.35) over the reduced area $\Gamma - \Gamma_0$ and applying the divergence theorem we obtain

$$\int_{\partial\Gamma, \partial\Gamma_0} (-G_{ij} \sigma_{ik} + \mu u_i T_{ijk}) n_k \, ds(\mathbf{x}) = 0, \quad (1.3.37)$$

since \mathbf{x}_0 lies outside the reduced area. Calculation of the integral over $\partial\Gamma_0$ as the radius of Γ_0 tends to zero yields the result,

$$\int_{\partial\Gamma} (-G_{ij} \sigma_{ik} + \mu u_i T_{ijk}) n_k \, ds(\mathbf{x}) = 4\pi\mu u_j(\mathbf{x}_0), \quad (1.3.38)$$

for \mathbf{x}_0 inside Γ . Finally when \mathbf{x}_0 lies on the boundary of Γ we find

$$-\int_{\partial\Gamma} G_{ij} \sigma_{ik} n_k \, ds(\mathbf{x}) + \mu \int_{\partial\Gamma}^{PV} u_i T_{ijk} n_k \, ds(\mathbf{x}) = 2\pi\mu u_j(\mathbf{x}_0), \quad (1.3.39)$$

where PV indicates a principal value integral. The requirement to take the principal value of the integral comes from the discontinuous behaviour of the integral over the stress tensor which jumps in value by $4\pi\mu \mathbf{u}$ as \mathbf{x}_0 crosses the domain boundary. Equations (1.3.36)–(1.3.39) may be summarised as

$$\begin{aligned} \chi u_j(\mathbf{x}_0) = & -\frac{1}{4\pi\mu} \int_{\partial\Gamma} f_i(\mathbf{x}) G_{ij}(\mathbf{x}, \mathbf{x}_0) \, ds(\mathbf{x}) \\ & + \frac{1}{4\pi} \int_{\partial\Gamma} u_i(\mathbf{x}) T_{ijk}(\mathbf{x}, \mathbf{x}_0) n_k(\mathbf{x}) \, ds(\mathbf{x}), \end{aligned} \quad (1.3.40)$$

where $\chi = 0$ when \mathbf{x}_0 lies outside Γ , $\chi = 1/2$ when \mathbf{x}_0 lies on $\partial\Gamma$ and $\chi = 1$ when \mathbf{x}_0 lies inside Γ , and remembering to take the principal value of the second integral when \mathbf{x}_0 lies on $\partial\Gamma$. In the literature the first integral is called the single layer potential and the second is called the double layer potential.

To compute the velocity field in a Stokes flow using the boundary integral method we start by applying equation (1.3.40) to the flow and place \mathbf{x}_0 on the boundaries of the flow domain. We use the boundary element method (Pozrikidis 2002a) to discretise the boundaries into small elements and the equations into their discrete analogues. By assigning unknown tractions and velocities to the boundary elements we can construct a system of algebraic equations from which the *a priori* unknown boundary values may be computed. The velocity field throughout the flow domain is then be computed from the discrete version of equation (1.3.40) using the calculated values of the unknown boundary tractions and velocities. We will explain this process fully and carefully in each chapter.

Our investigation begins in the next chapter with an examination of the motion of a fluid in a straight two-dimensional channel with rigid walls which is subject to a disturbance caused by the motion of a small ‘conveyor’ belt on one of the channel walls. This

example provides an introduction to the boundary integral and boundary element methods and their application to a simple flow in a channel. In chapter 2 and all subsequent chapters we will assume that the flow in the channel is pressure-driven with a prescribed flow rate and is governed by the equations of Stokes flow.

In chapter 3 we introduce a rigid particle into the straight channel before replacing the rigid particle with a fluid-filled elastic capsule in chapter 4. We will assume that the fluid inside the capsule is also governed by the Stokes equations and that the capsule membrane obeys simple constitutive laws which describe the in-plane and transverse membrane tensions. We calculate the limiting or steady shape of the capsule in chapter 4 together with the additional pressure drop due to the capsule.

We remove the capsule and add a daughter channel to the straight channel in chapter 5 and examine its effect upon the fluid flow while maintaining a prescribed flow rates which we vary to increase or decrease the proportion of fluid which enters the branch channel. In chapter 6 we study the motion of a rigid particle in a branching channel flow.

In chapter 7 we replace the rigid particle with a fluid-filled elastic capsule and investigate its motion through a bifurcation. Our aim in chapter 7 is to compute the trajectory of a capsule started from an arbitrary position upstream of the branch, and to calculate the pressure drop across the branch both in the presence and in the absence of the capsule. Of particular interest is the deformation experienced by the capsule in the neighbourhood of the branch entrance, and the conditions under which the capsule is drawn into the branch. We also examine the effect of the channel geometry, the capsule's elastic properties, the ratio of the encapsulated fluid to the ambient fluid, the capsule size and the flow conditions. Also of interest is the magnitude of the stress experienced by the capsule under deformation, particularly in the case when the capsule becomes trapped at the sharp corners at the branch entrance. In this case, the portion of the membrane closest to the sharp corner is placed under a high level of stress, which may ultimately cause the capsule to burst. We will show that as we add a branch channel and a flexible capsule the increasingly diverse parameter space will be easily incorporated via the boundary integral and boundary element formulation. Our results are discussed in chapter 8.

Chapter 2

A conveyor belt, a straight channel and the boundary integral method

In this chapter we demonstrate the application of the boundary integral method to a simple channel flow containing a disturbance caused by a conveyor belt on a portion of one of the walls. This problem provides an insight into the effect of a disturbance to the channel flow which will be of benefit in subsequent chapters. In chapter 3 we will change the source of the disturbance from a conveyor belt to a rigid particle moving with the flow. Much of the analysis contained in this chapter is directly applicable to the mathematical model of a channel containing a particle. A free-boundary is substituted for the rigid particle in chapter 4, where we examine the motion of a fluid drop and an elastic capsule in a straight channel. In chapters 5 onwards we extend the analysis by adding a branch channel to the main channel and examining the disturbance caused by the branch entrance and the capsule.

Although we use an isolated conveyor belt here to demonstrate the application of the boundary integral and element methods, a parallel may be drawn between the problem studied in this chapter and the mechanism by which large plant cells induce cytoplasmic streaming (e.g. Verchot-Lubicz and Goldstein 2009). In large tubular plant cells, streaming is induced by molecular motors arranged along helical cytoskeletal filaments. Therefore the cell walls in a plant cell could be viewed as a continuous conveyor belt which moves with a suitable velocity distribution.

2.1 Problem statement

Let us consider the motion of a fluid with viscosity μ in an infinite straight-walled channel of width $2d$. The flow is disturbed by a portion of one of the walls which behaves like a conveyor belt. The flow geometry which is sketched in figure 2.1, comprises the channel, \mathcal{C} , and the conveyor belt, \mathcal{A} , which is centred on the lower wall of the channel. The unit vectors in the x and y directions are \mathbf{i} and \mathbf{j} respectively. We introduce the disturbance by setting the velocity to be $\mathbf{u} = U \mathbf{i}$ on \mathcal{A} where U is a constant. Far upstream and downstream of the disturbance, the flow in the channel is described by the classical

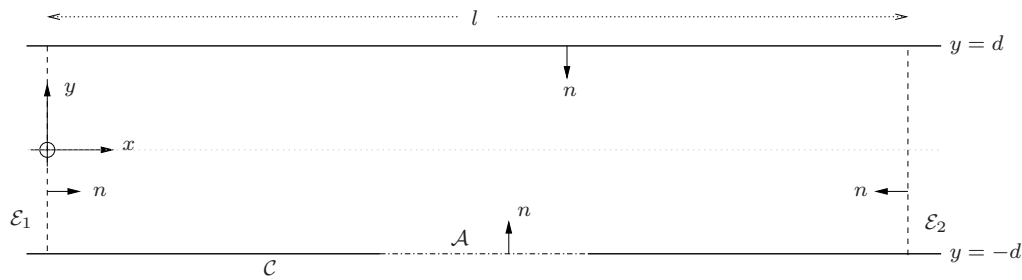


Figure 2.1 : Channel with a localised disturbance on the lower wall

unidirectional Poiseuille solution with flux Q and velocity \mathbf{u}^P , defined by

$$\mathbf{u}^P = U_0 \left(1 - \frac{y^2}{d^2}\right) \mathbf{i} \quad (2.1)$$

where U_0 is the centreline speed of the Poiseuille flow and is related to the flux, Q , by

$$Q = \frac{4}{3} d U_0. \quad (2.2)$$

Our aim is to compute the velocity field throughout the flow domain. We assume that the Reynolds number of the flow is very small, and that the main flow in the channel may be described using the linear equations of Stokes flow (1.3.4).

In preparation for the numerical method, we truncate the channel and designate the channel entry, located at $x = 0$, as \mathcal{E}_1 , and the exit, located at $x = l$, as \mathcal{E}_2 . We note that \mathcal{E}_1 and \mathcal{E}_2 are the entrance and exit to the computational domain and are not the inflow and outflow of the channel, where end effects would be encountered. The unit normal vectors, \mathbf{n} , on all boundaries point into the fluid as shown in figure 2.1. The region \mathcal{A} has length L and lies between $x = l/2 - L/2$ and $x = l/2 + L/2$. The motion of \mathcal{A} disturbs the oncoming Poiseuille flow, but at the caps \mathcal{E}_1 and \mathcal{E}_2 , we assume that the disturbance has decayed and the flow has settled to Poiseuille flow.

We decompose the velocity field, \mathbf{u} , the stress field, $\boldsymbol{\sigma}$, and the traction field, \mathbf{f} , into background Poiseuille and disturbance components, indicated by the superscripts P and D respectively, so that

$$\mathbf{u} = \mathbf{u}^P + \mathbf{u}^D, \quad (2.3)$$

$$\boldsymbol{\sigma} = \boldsymbol{\sigma}^P + \boldsymbol{\sigma}^D, \quad (2.4)$$

$$\mathbf{f} = \mathbf{f}^P + \mathbf{f}^D \quad (2.5)$$

and where the traction, $\mathbf{f} = \boldsymbol{\sigma} \cdot \mathbf{n}$. On \mathcal{C} we have

$$\mathbf{u} = \mathbf{u}^P = \mathbf{u}^D = \mathbf{0} \quad (2.6)$$

due to the no-slip and no-penetration conditions, and

$$\mathbf{u} = \mathbf{u}^D = U \mathbf{i}, \quad \mathbf{u}^P = \mathbf{0} \quad (2.7)$$

on the disturbance region, \mathcal{A} .

Previous studies on two-dimensional channel flow by Gaver and Kute (1998) and Cortez (2002) show that the disturbance velocity decays upstream and downstream from the disturbance. Gaver and Kute (1998) studied a straight-walled channel with a semi-circular protrusion on one wall. The flow is driven by a constant pressure drop across the entrance and exit. When the protuberance is small the disturbance decays rapidly with distance from the centre of the bump. In section 4.3 of Cortez (2002) the same geometry is examined, albeit with a slightly longer channel. The pressure drop is again prescribed and the disturbance velocity due to the obstruction is assumed to have decayed so that the velocity profile at the entrance and exit is Poiseuille. The results from this example in Cortez (2002) are nearly identical to the pertinent case in Gaver and Kute (1998). We will therefore assume that the disturbance velocity field due to the conveyor belt decays rapidly as we move away from it and that the velocity at the entrance and exit is Poiseuille. We will however make sure the numerical solution satisfies this assumption in section 2.3. We therefore set

$$\mathbf{u}^D = \mathbf{0} \quad (2.8)$$

at \mathcal{E}_1 and \mathcal{E}_2 . As a consequence of the rapid decay of the disturbance velocity and hence its derivatives, we may write the disturbance traction,

$$f_i^D = -p^D n_i + \mu \left(\frac{\partial u_i^D}{\partial x_j} + \frac{\partial u_j^D}{\partial x_i} \right) n_j, \quad (2.9)$$

as

$$f_i^D \approx -p^D n_i \quad (2.10)$$

to leading order, where $p^D(\mathbf{x})$ is the disturbance pressure and the index $i = 1, 2$. Substituting the stress tensor definition (1.3.1) into the Stokes equation, $\nabla \cdot \boldsymbol{\sigma}^D = 0$, we find that the y -component gives

$$0 = -\frac{\partial p^D}{\partial y} + \mu \frac{\partial^2 u_y^D}{\partial x_i^2} \approx -\frac{\partial p^D}{\partial y} \quad (2.11)$$

as we move away from the source of the disturbance due to the rapid decay of the disturbance velocity. Therefore at the caps the disturbance pressure will be constant. By setting the disturbance pressures at \mathcal{E}_1 and \mathcal{E}_2 to π_1 and π_2 respectively, we may write the disturbance traction at \mathcal{E}_1 as

$$\mathbf{f}^D = -\pi_1 \mathbf{n}, \quad (2.12)$$

and

$$\mathbf{f}^D = -\pi_2 \mathbf{n} \quad (2.13)$$

at \mathcal{E}_2 . Since we are interested in the additional pressure drop between \mathcal{E}_1 and \mathcal{E}_2 we set $\pi_1 = 0$ without loss of generality. The disturbance pressure drop, Δp^D , between \mathcal{E}_1 and \mathcal{E}_2 is given by

$$\Delta p^D = p^D(\mathcal{E}_1) - p^D(\mathcal{E}_2) = -\pi_2. \quad (2.14)$$

The Poiseuille pressure, $p^P(x)$, is a known function defined by

$$p^P(x) = G(l - x) \quad (2.15)$$

where $G = 2\mu U_0/d^2$ is a positive constant, and $-G$ is the imposed constant pressure gradient between the entrance and exit. We have defined p^P so that it is zero at \mathcal{E}_2 . The total pressures at the caps are

$$p(\mathcal{E}_1) = p^P(\mathcal{E}_1) + p^D(\mathcal{E}_1) = p^P(\mathcal{E}_1) = Gl, \quad (2.16)$$

$$p(\mathcal{E}_2) = p^P(\mathcal{E}_2) + p^D(\mathcal{E}_2) = p^D(\mathcal{E}_2) = \pi_2, \quad (2.17)$$

and so the total pressure at \mathcal{E}_1 is given by the Poiseuille pressure and the total pressure at \mathcal{E}_2 equals the disturbance pressure. The total pressure drop between the entrance and exit, Δp , is given by

$$\Delta p = p(\mathcal{E}_1) - p(\mathcal{E}_2) = Gl - \pi_2. \quad (2.18)$$

We may now derive an equation for π_2 by applying Lorentz's reciprocal relation (1.3.22) to the Poiseuille and disturbance flows in the channel, to give

$$\nabla \cdot (\mathbf{u}^D \cdot \boldsymbol{\sigma}^P - \mathbf{u}^P \cdot \boldsymbol{\sigma}^D) = 0. \quad (2.19)$$

Let us integrate (2.19) around the flow domain to get

$$\int_{\partial\Gamma} \mathbf{u}^D \cdot \mathbf{f}^P \, ds(\mathbf{x}) = \int_{\partial\Gamma} \mathbf{u}^P \cdot \mathbf{f}^D \, ds(\mathbf{x}), \quad (2.20)$$

where s is the boundary arc-length, $\partial\Gamma = \mathcal{E}_1 \cup \mathcal{C} \cup \mathcal{A} \cup \mathcal{E}_2$ is the piecewise-continuous closed boundary of the flow domain Γ , and the divergence theorem has been used to convert the area integrals into line integrals. Expansion of the integral on the left-hand side of (2.20) gives

$$\begin{aligned} \int_{\partial\Gamma} \mathbf{u}^D \cdot \mathbf{f}^P \, ds(\mathbf{x}) &= \int_{\mathcal{E}_1, \mathcal{E}_2, \mathcal{C}} \mathbf{u}^D \cdot \mathbf{f}^P \, ds(\mathbf{x}) + \int_{\mathcal{A}} \mathbf{u}^D \cdot \mathbf{f}^P \, ds(\mathbf{x}) \\ &= U \int_{\mathcal{A}} \mathbf{i} \cdot \mathbf{f}^P \, ds(\mathbf{x}) \end{aligned} \quad (2.21)$$

since the disturbance velocity at the caps and on the walls is zero. The integrand may be

simplified using the definition of the traction and the stress tensor to get

$$\mathbf{i} \cdot \mathbf{f}^P = f_x^P = \sigma_{xj}^P n_j = \sigma_{xy}^P = \mu \frac{\partial u^P}{\partial y} \quad (2.22)$$

since $\mathbf{n} = \mathbf{j}$ on \mathcal{A} and where u^P is the x -component of the Poiseuille velocity which is defined in equation (2.1). Hence we have

$$\mathbf{i} \cdot \mathbf{f}^P = -\frac{2\mu U_0}{d^2} y = \frac{2\mu U_0}{d} \quad (2.23)$$

since $y = -d$ on \mathcal{A} . Substitution into (2.21) yields

$$\int_{\partial\Gamma} \mathbf{u}^D \cdot \mathbf{f}^P \, ds(\mathbf{x}) = \frac{2\mu U U_0}{d} \int_{\mathcal{A}} ds(\mathbf{x}) = \frac{2\mu L U U_0}{d}. \quad (2.24)$$

We now substitute (2.24) back into (2.20) and expand the integral on the right-hand side to obtain

$$\begin{aligned} \frac{2\mu L U U_0}{d} &= \int_{\mathcal{A}, \mathcal{C}, \mathcal{E}_1} \mathbf{u}^P \cdot \mathbf{f}^D \, ds(\mathbf{x}) + \int_{\mathcal{E}_2} \mathbf{u}^P \cdot \mathbf{f}^D \, ds(\mathbf{x}) \\ &= -\pi_2 \int_{\mathcal{E}_2} \mathbf{u}^P \cdot \mathbf{n} \, ds(\mathbf{x}) \end{aligned} \quad (2.25)$$

since the Poiseuille velocity is zero on \mathcal{A} and \mathcal{C} and the disturbance pressure is zero at \mathcal{E}_1 . The integral on the right-hand side is the flux, Q , which is defined by

$$Q = \int_{\mathcal{E}_1} \mathbf{n} \cdot \mathbf{u}^P \, ds(\mathbf{x}) = - \int_{\mathcal{E}_2} \mathbf{n} \cdot \mathbf{u}^P \, ds(\mathbf{x}), \quad (2.26)$$

and so we can rearrange (2.25) to get

$$\pi_2 = \frac{2\mu L U}{d} \left(\frac{U_0}{Q} \right) = \frac{3\mu L U}{2d^2}, \quad (2.27)$$

where equation (2.2) has been used to eliminate U_0/Q . Equation (2.27) provides us with a simple formula for calculating the disturbance pressure at \mathcal{E}_2 and hence the total pressure drop,

$$\Delta p = \frac{\mu}{2d^2} (4lU_0 - 3LU). \quad (2.28)$$

We can derive an alternative expression for the disturbance pressure by integrating the Stokes equation for the disturbance stress, $\nabla \cdot \boldsymbol{\sigma}^D = 0$, over the flow domain. Application

of the divergence theorem and the boundary conditions provides the equations,

$$\pi_2 = -\frac{1}{2d} \int_{\mathcal{A}, \mathcal{C}} \mathbf{i} \cdot \mathbf{f}^D \, ds(\mathbf{x}) \quad \text{and} \quad (2.29)$$

$$0 = \int_{\mathcal{A}, \mathcal{C}} \mathbf{j} \cdot \mathbf{f}^D \, ds(\mathbf{x}). \quad (2.30)$$

Equation (2.27) is favoured over (2.29) because π_2 may be calculated exactly using L , U , μ and d . We can only evaluate equation (2.29) exactly if we know the disturbance tractions at every point on \mathcal{A} and \mathcal{C} . However, as we will see in the next section, the method of solution will only provide discrete values of the disturbance tractions and so equation (2.29) would only provide an approximation.

It is interesting to note from (2.27) that the sign of π_2 depends solely on the sign of U . When U is in the positive x direction, π_2 is positive and the total pressure drop in equation (2.18) is reduced. The disturbance flow caused by the motion of \mathcal{A} could therefore be interpreted as helping the flow because a lower pressure drop is required to maintain the flow. When U is negative, the disturbance could be seen to impede the flow because a larger pressure difference is needed to maintain the same flow rate.

Now that we have a formula for the disturbance pressure drop, we move onto our next goal of deriving an integral equation which governs the disturbance velocity in the channel. We apply the boundary integral equation (1.3.40) to the disturbance flow with the pole, \mathbf{x}_0 , in the fluid to get

$$4\pi\mu u_j^D(\mathbf{x}_0) = - \int_{\partial\Gamma} f_i^D G_{ij} \, ds(\mathbf{x}) + \mu \int_{\partial\Gamma} u_i^D T_{ijk} n_k \, ds(\mathbf{x}), \quad (2.31)$$

where G_{ij} and T_{ijk} are the free-space Green's function and its associated stress tensor defined in equations (1.3.29) and (1.3.30). Knowledge of the disturbance tractions and velocities on the boundaries coupled with equation (2.31) would allow the disturbance velocity to be calculated at any point in the flow domain. To obtain the boundary values of \mathbf{f}^D and \mathbf{u}^D we start by writing down the boundary integral equation for \mathbf{x}_0 on the domain boundary,

$$2\pi\mu u_j^D(\mathbf{x}_0) = - \int_{\partial\Gamma} f_i^D G_{ij} \, ds(\mathbf{x}) + \mu \int_{\partial\Gamma}^{PV} u_i^D T_{ijk} n_k \, ds(\mathbf{x}), \quad (2.32)$$

using (1.3.40) and where PV indicates a principal value integral. We simplify (2.32) by applying the boundary conditions given in equations (2.6), (2.7), (2.8), (2.13) together

with the zero disturbance pressure on \mathcal{E}_1 to get

$$2\pi\mu u_j^D(\mathbf{x}_0) = - \int_{\mathcal{A},\mathcal{C}} f_i^D G_{ij} \, ds(\mathbf{x}) + \pi_2 \int_{\mathcal{E}_2} n_i G_{ij} \, ds(\mathbf{x}) + \mu U \int_{\mathcal{A}}^{PV} T_{xjk} n_k \, ds(\mathbf{x}), \quad (2.33)$$

where the principal value of the double-layer potential integral in (2.33) need only be evaluated when the pole is located on \mathcal{A} . The only unknown quantities in equation (2.33) are the disturbance tractions on \mathcal{A} and \mathcal{C} . The formula for the disturbance pressure at \mathcal{E}_2 means that we do not need to find the tractions there, moreover we do not need to evaluate (2.33) with the pole on either \mathcal{E}_1 or \mathcal{E}_2 . Pozrikidis (2005c) notes that evaluation of the boundary integral equation for flow in a pipe suffers from numerical sensitivities when the pole is located on the entrance or exit. This issue is neatly side-stepped by adapting the derivation of the disturbance pressure equation given in Pozrikidis (2005b) to our geometry.

It is worth noting that we could choose a Green's function which would be zero on the channel walls, thereby removing the single-layer potential integral over \mathcal{C} in (2.33). However, the Green's function for a straight channel is computationally intensive to calculate relative to the Stokeslet. In future models, we will add a branch to the channel which would invalidate the use of the straight channel Green's function. Modifications could theoretically be made to the Green's function, but we would need to exercise care in order to avoid singularities occurring within the flow domain. At the expense of computing the integral over \mathcal{C} , the two-dimensional Stokeslet is used.

It is enlightening to non-dimensionalise equation (2.33) using U , d and $\mu U/d$ as the velocity, length and traction scales to get

$$2\pi u_j^D(\mathbf{x}_0) = - \int_{\mathcal{A},\mathcal{C}} f_i^D G_{ij} \, ds(\mathbf{x}) + \pi_2 \int_{\mathcal{E}_2} n_i G_{ij} \, ds(\mathbf{x}) + \int_{\mathcal{A}}^{PV} T_{xjk} n_k \, ds(\mathbf{x}) \quad (2.34)$$

where all quantities are dimensionless. From this equation we can see that the dimensionless disturbance tractions are invariant to the belt speed but depend on the size of the belt via the integrals over \mathcal{A} . Therefore it is only necessary to find the dimensionless disturbance tractions, for a given L , and scale them according to the belt speed, U . However, we will calculate the total velocity by adding the Poiseuille velocity to the disturbance velocity and so our problem contains two velocity scales, U_0 and U . We will choose to use U_0 as our scale and so we will continue with the dimensional equation (2.33).

To obtain the solution we employ the boundary element method (Pozrikidis 2002a) and discretise the boundary into straight elements. The accuracy of our numerical scheme is therefore equal to the level of discretisation, i.e. if each element is of length h then the solution is $O(h)$ accurate. On each element of \mathcal{A} and \mathcal{C} we set the disturbance traction to

a constant 2-vector. When \mathbf{x}_0 is placed on \mathcal{A} , equation (2.33) becomes

$$2\pi\mu U \delta_{jx} = - \int_{\mathcal{A}, \mathcal{C}} f_i^D G_{ij} \, ds(\mathbf{x}) + \pi_2 \int_{\mathcal{E}_2} n_i G_{ij} \, ds(\mathbf{x}) + \mu U \int_{\mathcal{A}}^{PV} T_{xjk} n_k \, ds(\mathbf{x}) \quad (2.35)$$

and when \mathbf{x}_0 is on \mathcal{C} we have

$$0 = - \int_{\mathcal{A}, \mathcal{C}} f_i^D G_{ij} \, ds(\mathbf{x}) + \pi_2 \int_{\mathcal{E}_2} n_i G_{ij} \, ds(\mathbf{x}) + \mu U \int_{\mathcal{A}} T_{xjk} n_k \, ds(\mathbf{x}). \quad (2.36)$$

Now let us focus our attention on the integrand of the double-layer potential integral in equation (2.35). The stress tensor is singular when $\mathbf{x} = \mathbf{x}_0$ but as $\mathbf{x} \rightarrow \mathbf{x}_0$ along \mathcal{A} we have

$$T_{xjk} n_k = -4 \frac{\hat{x} \hat{x}_j \hat{x}_k}{r^4} n_k = -4 \frac{\hat{x} \hat{x}_j}{r^4} \hat{x}_k n_k = 0 \quad (2.37)$$

since \hat{x}_k and n_k are orthogonal. Therefore the double-layer potential in (2.35) is zero and so the equation reduces to

$$2\pi\mu U \delta_{jx} = - \int_{\mathcal{A}, \mathcal{C}} f_i^D G_{ij} \, ds(\mathbf{x}) + \pi_2 \int_{\mathcal{E}_2} n_i G_{ij} \, ds(\mathbf{x}) \quad (2.38)$$

when \mathbf{x}_0 lies on \mathcal{A} . We can simplify (2.36) when \mathbf{x}_0 lies on the lower wall because $\hat{y} = y - y_0 = 0$ and so the stress tensor is zero. Equation (2.36) becomes

$$0 = - \int_{\mathcal{A}, \mathcal{C}} f_i^D G_{ij} \, ds(\mathbf{x}) + \pi_2 \int_{\mathcal{E}_2} n_i G_{ij} \, ds(\mathbf{x}) \quad (2.39)$$

when \mathbf{x}_0 is positioned on the lower wall of \mathcal{C} .

Evaluation of (2.38) with \mathbf{x}_0 at the mid-point of each boundary element of \mathcal{A} provides a sufficient number of equations for the unknown tractions on \mathcal{A} . We have the same sufficiency on \mathcal{C} by equation (2.36). Therefore the number of unknowns equals the number of equations and so our system is complete. Once the solution is known we may calculate the velocity at any point in the flow domain using

$$u_j(\mathbf{x}_0) = u_j^P(\mathbf{x}_0) + \frac{1}{4\pi\mu} \left(- \int_{\mathcal{A}, \mathcal{C}} f_i^D G_{ij} \, ds(\mathbf{x}) + \pi_2 \int_{\mathcal{E}_2} n_i G_{ij} \, ds(\mathbf{x}) + \mu U \int_{\mathcal{A}} T_{xjy} \, ds(\mathbf{x}) \right) \quad (2.40)$$

which we obtained from equation (2.31) by applying the boundary conditions and adding the Poiseuille velocity, \mathbf{u}^P .

2.2 Numerical method

Our aim is to write the governing boundary integral equations in the form of the linear system,

$$\mathbf{A} \cdot \mathbf{x} = \mathbf{b}, \quad (2.41)$$

where \mathbf{A} is a square matrix of ‘influence’ coefficients, \mathbf{x} is the column vector of unknown tractions on \mathcal{A} and \mathcal{C} , and \mathbf{b} is a column vector of known values. Let us begin by separating the unknown tractions from the known values in equation (2.38) to get

$$\int_{\mathcal{A}, \mathcal{C}} f_i^D G_{ij} \, ds(\mathbf{x}) = \pi_2 \int_{\mathcal{E}_2} n_i G_{ij} \, ds(\mathbf{x}) - 2\pi\mu U \delta_{jx} \quad (2.42)$$

for \mathbf{x}_0 on \mathcal{A} , and in equation (2.36) to get

$$\int_{\mathcal{A}, \mathcal{C}} f_i^D G_{ij} \, ds(\mathbf{x}) = \pi_2 \int_{\mathcal{E}_2} n_i G_{ij} \, ds(\mathbf{x}) + \mu U H(\mathbf{x}_0) \int_{\mathcal{A}} T_{xjy} \, ds(\mathbf{x}) \quad (2.43)$$

when \mathbf{x}_0 is on \mathcal{C} , and where $H(\mathbf{x}_0) = 0$ when \mathbf{x}_0 is on the lower wall of \mathcal{C} and $H(\mathbf{x}_0) = 1$ when it is on the top wall. The right-hand sides of (2.42) and (2.43) are known functions of \mathbf{x}_0 . We may calculate $\int_{\mathcal{E}_2} n_i G_{ij} \, ds(\mathbf{x})$ analytically for \mathbf{x}_0 away from \mathcal{E}_2 , to get

$$\int_{\mathcal{E}_2} n_i G_{ix} \, ds(\mathbf{x}) = - \int_{\mathcal{E}_2} G_{xx} \, ds(\mathbf{x}) = \frac{1}{2} \left(d \ln(r_1 r_2) + y_0 \ln \left(\frac{r_2}{r_1} \right) - 4d \right) \quad (2.44)$$

$$\int_{\mathcal{E}_2} n_i G_{iy} \, ds(\mathbf{x}) = - \int_{\mathcal{E}_2} G_{xy} \, ds(\mathbf{x}) = \frac{\hat{x}}{2} \ln \left(\frac{r_2}{r_1} \right) \quad (2.45)$$

since $\mathbf{n} = -\mathbf{i}$ on \mathcal{E}_2 , and where $\hat{x} = l - x_0$, $r_1 = \hat{x}^2 + (d - y_0)^2$ and $r_2 = \hat{x}^2 + (d + y_0)^2$. The integral of T_{xjy} over \mathcal{A} is

$$\int_{\mathcal{A}} T_{xxy} \, ds(\mathbf{x}) = 2 \left(\arctan(\hat{a}) - \arctan(\hat{b}) - \frac{\hat{a}}{1 + \hat{a}^2} + \frac{\hat{b}}{1 + \hat{b}^2} \right), \quad (2.46)$$

$$\int_{\mathcal{A}} T_{xyy} \, ds(\mathbf{x}) = 2 \left(\frac{1}{1 + \hat{b}^2} - \frac{1}{1 + \hat{a}^2} \right), \quad (2.47)$$

where $\hat{a} = (l/2 - L/2 - x_0)/\hat{y}$, $\hat{b} = (l/2 + L/2 - x_0)/\hat{y}$ and $\hat{y} = -(d + y_0)$. We now have formulae for the right-hand sides of equations (2.42) and (2.43).

Let us define

$$I_{\mathcal{A},j}^S(\mathbf{x}_0) = \int_{\mathcal{A}} f_i^D G_{ij} \, ds(\mathbf{x}), \quad (2.48)$$

$$I_{\mathcal{C},j}^S(\mathbf{x}_0) = \int_{\mathcal{C}} f_i^D G_{ij} \, ds(\mathbf{x}), \quad (2.49)$$

$$k_{\mathcal{A},j}(\mathbf{x}_0) = \pi_2 \int_{\mathcal{E}_2} n_i G_{ij} \, ds(\mathbf{x}) - 2\pi\mu U \delta_{jx}, \text{ and} \quad (2.50)$$

$$k_{\mathcal{C},j}(\mathbf{x}_0) = \pi_2 \int_{\mathcal{E}_2} n_i G_{ij} \, ds(\mathbf{x}) + \mu U H(\mathbf{x}_0) \int_{\mathcal{A}} T_{xjy} \, ds(\mathbf{x}) \quad (2.51)$$

where the S superscript is shorthand for single-layer potential, and where $k_{\mathcal{A},j}(\mathbf{x}_0)$ and $k_{\mathcal{C},j}(\mathbf{x}_0)$ are the right-hand sides of equations (2.42) and (2.43) respectively. The governing equations (2.42) and (2.43) may be concisely written as

$$I_{\mathcal{A},j}^S(\mathbf{x}_0) + I_{\mathcal{C},j}^S(\mathbf{x}_0) = k_{\mathcal{A},j}(\mathbf{x}_0), \quad (2.52)$$

and

$$I_{\mathcal{A},j}^S(\mathbf{x}_0) + I_{\mathcal{C},j}^S(\mathbf{x}_0) = k_{\mathcal{C},j}(\mathbf{x}_0). \quad (2.53)$$

To apply the boundary element method we discretise \mathcal{A} into $N_{\mathcal{A}}$ equally-sized straight elements and \mathcal{C} into $N_{\mathcal{C}}$ equally-sized straight elements. On the r^{th} boundary element, E_r , we label the disturbance traction f_r^D and discretise $I_{\mathcal{A}}^S$ and $I_{\mathcal{C}}^S$ so that the integral over the boundary is approximated by a sum of integrals over the boundary elements. The discretised equations are

$$I_{\mathcal{A},j}^S(\mathbf{x}_0) = \int_{\mathcal{A}} f_i^D G_{ij} \, ds(\mathbf{x}) \approx \sum_{r=1}^{N_{\mathcal{A}}} f_{i,r}^D \tilde{G}_{ij,r}, \quad (2.54)$$

where

$$\tilde{G}_{ij,r}(\mathbf{x}_0) = \int_{E_r} G_{ij}(\mathbf{x}, \mathbf{x}_0) \, ds(\mathbf{x}), \quad (2.55)$$

and

$$I_{\mathcal{C},j}^S(\mathbf{x}_0) = \int_{\mathcal{C}} f_i^D G_{ij} \, ds(\mathbf{x}) \approx \sum_{r=1}^{N_{\mathcal{C}}} f_{i,r}^D \tilde{G}_{ij,r}. \quad (2.56)$$

When \mathbf{x}_0 lies on the r^{th} element, $G_{ij}(\mathbf{x}, \mathbf{x}_0)$ will have a logarithmic singularity but $\tilde{G}_{ij,r}(\mathbf{x}_0)$ remains integrable. Details of the numerical integration scheme may be found in Appendix A and Pozrikidis (1998). For the numerical integration, we typically used 20

base-points in the numerical scheme. Expanding (2.54) gives

$$\begin{aligned} I_{\mathcal{A},j}^S(\mathbf{x}_0) &= \left(\tilde{G}_{xj,1} f_{x,1}^D + \tilde{G}_{yj,1} f_{y,1}^D + \dots + \tilde{G}_{xj,N_{\mathcal{A}}} f_{x,N_{\mathcal{A}}}^D + \tilde{G}_{yj,N_{\mathcal{A}}} f_{y,N_{\mathcal{A}}}^D \right) \\ &= \begin{bmatrix} \tilde{G}_{xj,1} & \tilde{G}_{yj,1} & \dots & \tilde{G}_{xj,N_{\mathcal{A}}} & \tilde{G}_{yj,N_{\mathcal{A}}} \end{bmatrix} \begin{bmatrix} f_{x,1}^D & f_{y,1}^D & \dots & f_{x,N_{\mathcal{A}}}^D & f_{y,N_{\mathcal{A}}}^D \end{bmatrix}^T \\ &= \mathbf{I}_{\mathcal{A},j}^G(\mathbf{x}_0) \cdot \mathbf{F}_{\mathcal{A}}, \end{aligned} \quad (2.57)$$

where the T superscript means transpose, and we have defined the $1 \times 2N_{\mathcal{A}}$ ‘influence’ row-vector $\mathbf{I}_{\mathcal{A},j}^G(\mathbf{x}_0)$ to be,

$$\mathbf{I}_{\mathcal{A},j}^G(\mathbf{x}_0) = \begin{bmatrix} \tilde{G}_{xj,1} & \tilde{G}_{yj,1} & \dots & \tilde{G}_{xj,N_{\mathcal{A}}} & \tilde{G}_{yj,N_{\mathcal{A}}} \end{bmatrix}, \quad (2.58)$$

and the column-vector $\mathbf{F}_{\mathcal{A}}$ to be,

$$\mathbf{F}_{\mathcal{A}} = \begin{bmatrix} f_{x,1}^D & f_{y,1}^D & \dots & f_{x,N_{\mathcal{A}}}^D & f_{y,N_{\mathcal{A}}}^D \end{bmatrix}^T, \quad (2.59)$$

which represents the disturbance tractions on the elements of \mathcal{A} . Expanding (2.56) gives

$$\begin{aligned} I_{\mathcal{C},j}^S(\mathbf{x}_0) &= \left(\tilde{G}_{xj,1} f_{x,1}^D + \tilde{G}_{yj,1} f_{y,1}^D + \dots + \tilde{G}_{xj,N_{\mathcal{C}}} f_{x,N_{\mathcal{C}}}^D + \tilde{G}_{yj,N_{\mathcal{C}}} f_{y,N_{\mathcal{C}}}^D \right) \\ &= \begin{bmatrix} \tilde{G}_{xj,1} & \tilde{G}_{yj,1} & \dots & \tilde{G}_{xj,N_{\mathcal{C}}} & \tilde{G}_{yj,N_{\mathcal{C}}} \end{bmatrix} \begin{bmatrix} f_{x,1}^D & f_{y,1}^D & \dots & f_{x,N_{\mathcal{C}}}^D & f_{y,N_{\mathcal{C}}}^D \end{bmatrix}^T \\ &= \mathbf{I}_{\mathcal{C},j}^G(\mathbf{x}_0) \cdot \mathbf{F}_{\mathcal{C}}, \end{aligned} \quad (2.60)$$

where $\mathbf{I}_{\mathcal{C},j}^G$ is the $1 \times 2N_{\mathcal{C}}$ ‘influence’ row-vector,

$$\mathbf{I}_{\mathcal{C},j}^G(\mathbf{x}_0) = \begin{bmatrix} \tilde{G}_{xj,1} & \tilde{G}_{yj,1} & \dots & \tilde{G}_{xj,N_{\mathcal{C}}} & \tilde{G}_{yj,N_{\mathcal{C}}} \end{bmatrix}, \quad (2.61)$$

and the column-vector, $\mathbf{F}_{\mathcal{C}}$, is

$$\mathbf{F}_{\mathcal{C}} = \begin{bmatrix} f_{x,1}^D & f_{y,1}^D & \dots & f_{x,N_{\mathcal{C}}}^D & f_{y,N_{\mathcal{C}}}^D \end{bmatrix}^T, \quad (2.62)$$

which represents the disturbance tractions on \mathcal{C} . We may therefore write the x and y components of the discretised version of (2.52) more compactly as

$$\begin{bmatrix} \mathbf{I}_{\mathcal{A},x}^G(\mathbf{x}_0) & \mathbf{I}_{\mathcal{C},x}^G(\mathbf{x}_0) \\ \mathbf{I}_{\mathcal{A},y}^G(\mathbf{x}_0) & \mathbf{I}_{\mathcal{C},y}^G(\mathbf{x}_0) \end{bmatrix} \begin{bmatrix} \mathbf{F}_{\mathcal{A}} \\ \mathbf{F}_{\mathcal{C}} \end{bmatrix} = \begin{bmatrix} k_{\mathcal{A},x}(\mathbf{x}_0) \\ k_{\mathcal{A},y}(\mathbf{x}_0) \end{bmatrix}, \quad (2.63)$$

which is for \mathbf{x}_0 on \mathcal{A} . The discretised version of (2.53) is

$$\begin{bmatrix} \mathbf{I}_{\mathcal{A},x}^G(\mathbf{x}_0) & \mathbf{I}_{\mathcal{C},x}^G(\mathbf{x}_0) \\ \mathbf{I}_{\mathcal{A},y}^G(\mathbf{x}_0) & \mathbf{I}_{\mathcal{C},y}^G(\mathbf{x}_0) \end{bmatrix} \begin{bmatrix} \mathbf{F}_{\mathcal{A}} \\ \mathbf{F}_{\mathcal{C}} \end{bmatrix} = \begin{bmatrix} k_{\mathcal{C},x}(\mathbf{x}_0) \\ k_{\mathcal{C},y}(\mathbf{x}_0) \end{bmatrix}. \quad (2.64)$$

where \mathbf{x}_0 is on \mathcal{C} . As we move \mathbf{x}_0 over \mathcal{A} we re-evaluate (2.63) and generate $N_{\mathcal{A}}$ pairs of

equations which may be expressed as the matrix/vector product,

$$\begin{bmatrix} \mathcal{A}_{\mathcal{A}} & \mathcal{A}_{\mathcal{C}} \end{bmatrix} \begin{bmatrix} \mathbf{F}_{\mathcal{A}} \\ \mathbf{F}_{\mathcal{C}} \end{bmatrix} = \mathbf{K}_{\mathcal{A}}, \quad (2.65)$$

where

$$\mathcal{A}_{\mathcal{A}} = \begin{bmatrix} \mathbf{I}_{\mathcal{A},x}^G(\mathbf{x}_0^{(1)}) \\ \mathbf{I}_{\mathcal{A},y}^G(\mathbf{x}_0^{(1)}) \\ \vdots \\ \mathbf{I}_{\mathcal{A},x}^G(\mathbf{x}_0^{(N_{\mathcal{A}})}) \\ \mathbf{I}_{\mathcal{A},y}^G(\mathbf{x}_0^{(N_{\mathcal{A}})}) \end{bmatrix}, \quad \mathcal{A}_{\mathcal{C}} = \begin{bmatrix} \mathbf{I}_{\mathcal{C},x}^G(\mathbf{x}_0^{(1)}) \\ \mathbf{I}_{\mathcal{C},y}^G(\mathbf{x}_0^{(1)}) \\ \vdots \\ \mathbf{I}_{\mathcal{C},x}^G(\mathbf{x}_0^{(N_{\mathcal{A}})}) \\ \mathbf{I}_{\mathcal{C},y}^G(\mathbf{x}_0^{(N_{\mathcal{A}})}) \end{bmatrix}, \quad \mathbf{K}_{\mathcal{A}} = \begin{bmatrix} k_{\mathcal{A},x}(\mathbf{x}_0^{(1)}) \\ k_{\mathcal{A},y}(\mathbf{x}_0^{(1)}) \\ \vdots \\ k_{\mathcal{A},x}(\mathbf{x}_0^{(N_{\mathcal{A}})}) \\ k_{\mathcal{A},y}(\mathbf{x}_0^{(N_{\mathcal{A}})}) \end{bmatrix}, \quad (2.66)$$

and $\mathbf{x}_0^{(1)} \dots \mathbf{x}_0^{(N_{\mathcal{A}})}$ are the boundary element mid-points of \mathcal{A} . The matrix $\mathcal{A}_{\mathcal{A}}$ has size $2N_{\mathcal{A}} \times 2N_{\mathcal{A}}$ and represents the influence of \mathcal{A} on itself. $\mathcal{A}_{\mathcal{C}}$ represents the effect of \mathcal{A} on \mathcal{C} and has size $2N_{\mathcal{A}} \times 2N_{\mathcal{C}}$. $\mathbf{K}_{\mathcal{A}}$ is a column vector containing $2N_{\mathcal{A}}$ elements. We follow the same procedure for equation (2.64), and move \mathbf{x}_0 over the $N_{\mathcal{C}}$ elements of \mathcal{C} to get

$$\begin{bmatrix} \mathcal{C}_{\mathcal{A}} & \mathcal{C}_{\mathcal{C}} \end{bmatrix} \begin{bmatrix} \mathbf{F}_{\mathcal{A}} \\ \mathbf{F}_{\mathcal{C}} \end{bmatrix} = \mathbf{K}_{\mathcal{C}}, \quad (2.67)$$

where

$$\mathcal{C}_{\mathcal{A}} = \begin{bmatrix} \mathbf{I}_{\mathcal{A},x}^G(\mathbf{x}_0^{(1)}) \\ \mathbf{I}_{\mathcal{A},y}^G(\mathbf{x}_0^{(1)}) \\ \vdots \\ \mathbf{I}_{\mathcal{A},x}^G(\mathbf{x}_0^{(N_{\mathcal{C}})}) \\ \mathbf{I}_{\mathcal{A},y}^G(\mathbf{x}_0^{(N_{\mathcal{C}})}) \end{bmatrix}, \quad \mathcal{C}_{\mathcal{C}} = \begin{bmatrix} \mathbf{I}_{\mathcal{C},x}^G(\mathbf{x}_0^{(1)}) \\ \mathbf{I}_{\mathcal{C},y}^G(\mathbf{x}_0^{(1)}) \\ \vdots \\ \mathbf{I}_{\mathcal{C},x}^G(\mathbf{x}_0^{(N_{\mathcal{C}})}) \\ \mathbf{I}_{\mathcal{C},y}^G(\mathbf{x}_0^{(N_{\mathcal{C}})}) \end{bmatrix}, \quad \mathbf{K}_{\mathcal{C}} = \begin{bmatrix} k_{\mathcal{C},x}(\mathbf{x}_0^{(1)}) \\ k_{\mathcal{C},y}(\mathbf{x}_0^{(1)}) \\ \vdots \\ k_{\mathcal{C},x}(\mathbf{x}_0^{(N_{\mathcal{C}})}) \\ k_{\mathcal{C},y}(\mathbf{x}_0^{(N_{\mathcal{C}})}) \end{bmatrix}, \quad (2.68)$$

which have dimensions $2N_{\mathcal{C}} \times 2N_{\mathcal{A}}$, $2N_{\mathcal{C}} \times 2N_{\mathcal{C}}$ and $2N_{\mathcal{C}} \times 1$ respectively. The points $\mathbf{x}_0^{(1)} \dots \mathbf{x}_0^{(N_{\mathcal{C}})}$ are the boundary element mid-points of \mathcal{C} . $\mathcal{C}_{\mathcal{A}}$ represents the effect of \mathcal{C} on \mathcal{A} and $\mathcal{C}_{\mathcal{C}}$ describes the effect of \mathcal{C} on itself. We can combine equations (2.65) and (2.67) to get

$$\begin{bmatrix} \mathcal{A}_{\mathcal{A}} & \mathcal{A}_{\mathcal{C}} \\ \mathcal{C}_{\mathcal{A}} & \mathcal{C}_{\mathcal{C}} \end{bmatrix} \begin{bmatrix} \mathbf{F}_{\mathcal{A}} \\ \mathbf{F}_{\mathcal{C}} \end{bmatrix} = \begin{bmatrix} \mathbf{K}_{\mathcal{A}} \\ \mathbf{K}_{\mathcal{C}} \end{bmatrix} \quad (2.69)$$

which matches the form of our linear system in (2.41) and has dimension $2N_{\mathcal{A}} + 2N_{\mathcal{C}}$. The solution of (2.69) provides the disturbance tractions on \mathcal{A} and \mathcal{C} . In our simulations we took $N_{\mathcal{A}} = 200$ and $N_{\mathcal{C}} = 800$.

We are now able to construct our linear system and solve it using a standard numerical method. We found it practical to use Gaussian elimination to find the disturbance tractions. The values of the disturbance tractions may then be used in (2.31) to obtain the disturbance velocity at any point in the flow. To calculate the streamlines of the flow, we

start at a specified point and integrate the equation

$$\frac{d\mathbf{x}}{ds} = \mathbf{u}(\mathbf{x}), \quad (2.70)$$

where \mathbf{x} is the position vector of the point, s is the arc-length along the streamline, and the velocity on the right-hand side of (2.70) is computed from (2.40). We used the adaptive stepping Runga-Kutta-Fehlberg method of orders 2 and 3 (e.g. Atkinson 1978) to integrate equation (2.70).

2.3 Validation

When checking the numerical solution we set the conveyor belt length, $L = 2d$, and truncated the channel so that $l = 12d$, which was found to be sufficient for the disturbance to decay. The geometry discretisation was verified using the discretised analogues of the integral identities for Stokes flow,

$$S_j^{(1)}(\mathbf{x}_0) = \int_{\partial\Gamma} n_i G_{ij} ds(\mathbf{x}) = 0, \quad (2.71)$$

$$S_{ij}^{(2)}(\mathbf{x}_0) = \frac{1}{4\pi\mu} \int_{\partial\Gamma} T_{ijk} n_k ds(\mathbf{x}) = \begin{cases} 0 & \text{when } \mathbf{x}_0 \text{ is outside } \Gamma \\ \frac{1}{2}\delta_{ij} & \text{when } \mathbf{x}_0 \text{ lies on } \partial\Gamma \\ \delta_{ij} & \text{when } \mathbf{x}_0 \text{ lies inside } \Gamma \end{cases} \quad (2.72)$$

with \mathbf{x}_0 at the mid-point of each boundary element, and at several points inside and outside the flow domain. Both of the integral identities were satisfied such that $|S_j^{(1)}(\mathbf{x}_0)| < 10^{-9}$ and $|S_{ij}^{(2)}(\mathbf{x}_0) - 1/2 k \delta_{ij}| < 10^{-9}$ for all tested values of \mathbf{x}_0 , and where $k = 0, 1, 2$ when \mathbf{x}_0 lies outside, on and inside the boundary.

In our formulation of the governing equations, we assumed that the disturbance velocity decayed rapidly to zero as we approached the caps. To check this assumption we removed the Poiseuille flow and set the belt speed, $U = 1$, and the belt length $L/d = 2$. The maximum values of the x and y components of the disturbance velocity at the caps were 0.02% of the belt speed. The error was the same when we introduced the Poiseuille flow and set $U_0 = U$.

To validate the accuracy of the computed disturbance tractions we compared the traction distributions over the top and bottom walls when the number of boundary elements and the channel length were increased. The tractions are displayed for the simulations in figure 2.2. The channel in each simulation has been centred so that \mathcal{E}_1 lies at $x = -l/2$ and \mathcal{E}_2 lies at $l/2$. Our reference configuration has a channel length of $l = 12d$ with 200 boundary elements on \mathcal{A} and 800 elements on \mathcal{C} . To test the effect of adding more boundary elements we doubled the number of elements such that \mathcal{A} was discretised into 400 elements and \mathcal{C} into 1600 elements. The only observable difference can be seen in figure 2.2 (c) where the spike in the value of the traction has a magnitude which is double that seen in the reference case. Since the x component of the traction represents the wall

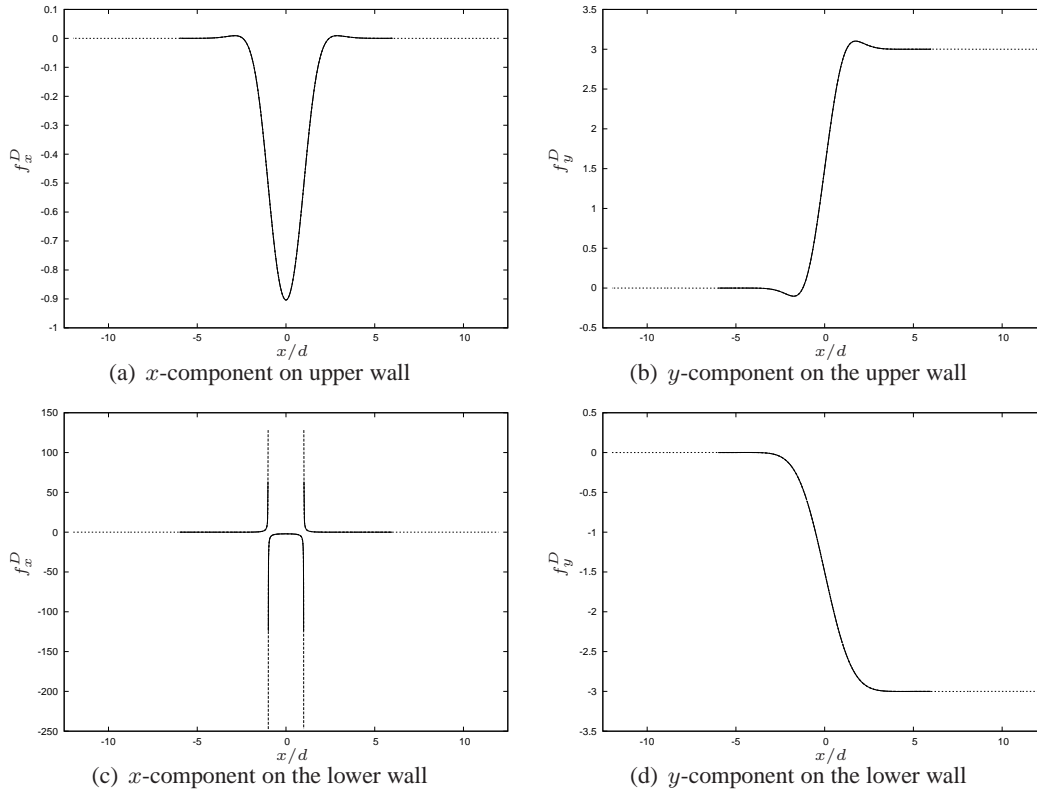


Figure 2.2 : Disturbance tractions for a variety of configurations on the upper and lower walls plotted against a rebased x coordinate for $L = 2d$ and $U = 1$. Reference configuration (—) is for $l = 12d$ and $N = 1000$, (---) is for $l = 12d$ and $N = 2000$ and (···) is for $l = 24d$ and $N = 1800$. The conveyor belt lies between $x/d = -1$ and 1 .

shear stress, we expect the traction to be singular at the point where the lower wall meets the conveyor belt because the velocity on the wall jumps from zero to U . Increasing the number of boundary elements leads to an increased resolution of the singularity. To test the effect of the channel length, we doubled the length so that $l = 24d$ and preserved the element length on the channel walls with respect to the reference configuration and maintained the length of \mathcal{A} . The total number of elements in this configuration is $N = 1800$. The traction profiles, as depicted in figure 2.2, demonstrate the excellent agreement between the solutions. The absolute value in the difference between the solutions is less than $0.001 \mu U/d$.

Finally, as a check on the disturbance tractions, we calculated the approximate value of the disturbance pressure using equation (2.29). The error in the approximate value was 0.02%. When the number of boundary elements was doubled the error was halved, showing that the error is due to the discretisation. The y -component of the disturbance tractions was checked using equation (2.30). The equation was satisfied to within a numerical tolerance of 10^{-10} .

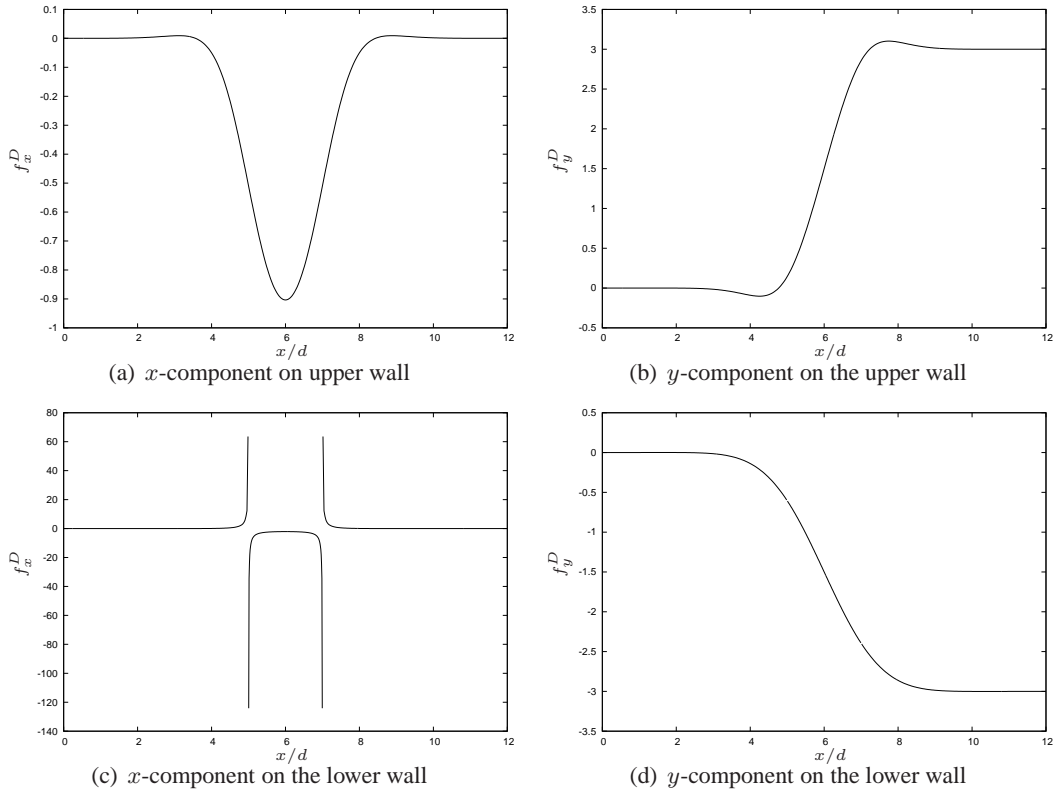


Figure 2.3 : Disturbance tractions on the upper and lower walls plotted against the x coordinate for $\beta = 2$ and $U = 1$. The conveyor belt lies between $x/d = 5$ and 7 .

2.4 Results

All of the results to be presented in this section were computed with the channel length, $l = 12d$. In the first case we discuss the effect of the belt in isolation and define the dimensionless belt size, β , to be

$$\beta = \frac{L}{d}, \quad (2.73)$$

which we will set to 2 initially. We remove the Poiseuille flow and set the belt speed, $U = 1$, and look at the effect of the belt. For these parameters the disturbance pressure, $\pi_2 = 3\mu U/d$ and the pressure drop between the entrance and exit is $-\pi_2$. Figure 2.3 shows the variation in the disturbance tractions over the walls and the belt. We expect the y -component of the disturbance traction to decay to zero at the entrance because we have set the disturbance pressure to zero there. We can see from figures (b) and (d) that this decay condition is satisfied. Towards the entrance the traction values decay to no more than $0.002\mu U/d$. Both components of the traction reach their steady value at a distance of approximately a quarter of the channel length from the channel centre. As we approach the exit we expect the normal component of the disturbance traction to tend to the disturbance pressure which takes the value $3\mu U/d$. Figures (b) and (d) show that the normal component of the disturbance traction tends to this value on the top and bottom walls, where the sign change is due to the direction of the normal vector. The discontinuity in the x -component of the traction in figure 2.3 (c) at the points where \mathcal{A} and \mathcal{C} meet is to be

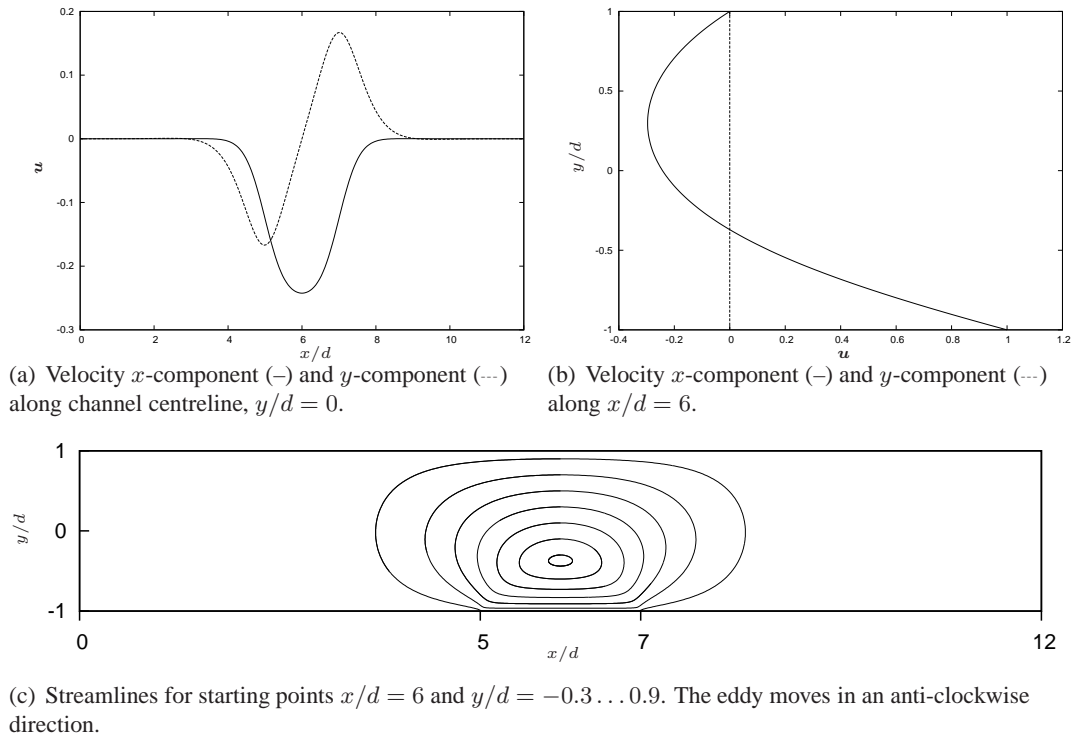


Figure 2.4 : Velocities and streamlines for $\beta = 2$ and $U = 1$ when the Poiseuille flow is absent. The conveyor belt lies between $x/d = 5$ and 7 .

expected, since the velocity is also discontinuous at these points. The numerical method performs no special treatment of the traction discontinuity at these points. This concludes the discussion on the disturbance tractions since we are able to obtain the disturbance tractions for other belt speeds by scaling by U , as noted earlier. A change in the belt size would require the disturbance tractions to be recomputed.

In figure 2.4 we show the velocity and streamlines for the case just discussed, where $\beta = 2$ and $U = 1$. The velocity profile along the centreline is shown in figure 2.4 (a). The velocity decays rapidly as we move away from the belt and reaches its steady values at around $x/d = 2$ and $x/d = 10$. At the caps, the x and y components of velocity are no more than 0.02% of U . If the conveyor belt were absent the velocities would be $\mathbf{u} = \mathbf{0}$. In figure 2.4 (b) we can see how the velocity varies on the channel mid-point line, $x/d = 6$. The y -component is zero for all values of y , which shows that all movement is in the x -direction. The x -component of velocity has both positive and negative regions, indicating that the fluid close to \mathcal{A} is moving in the positive x -direction and the fluid above $y/d \approx -0.37$ is moving in the opposite direction. The sign change in the velocity suggests that a region of circulating region of fluid is present with its centre closer to the bottom wall. The magnitude of velocity is greatest on \mathcal{A} and the fluid close to \mathcal{A} flows faster than fluid elsewhere on the mid-point line. The fluid flows with greater speed when $-1 < y/d < -0.615$ than in any other region on the mid-point line. In figure 2.4 (c) we plot the streamlines for the flow using $x/d = 6$ and $y/d = -0.3 \dots 0.9$ as the starting

points, where y/d is incremented in steps of 0.2. The fluid in the eddy moves in an anti-clockwise direction. When we change the direction of the conveyor belt the fluid inside the eddy moves in the opposite direction. It is interesting to note that even though the pressure drop between the entrance and exit is non-zero, there is no induced transfer of fluid. Since there is no flux between the entrance and exit there must be zero flux across every cross-section of the channel. Thus on every cross-section which intersects the eddy we would expect the fluid flux moving in the positive x -direction to exactly balance the flux moving in the negative x -direction. This is particularly interesting in light of the fact that the pressure drop between the entrance and exit equals $-\pi_2$ which is non-zero. In a channel with a quiescent fluid, this pressure drop would normally induce a Poiseuille flow in the negative x -direction. However, the presence of the eddy exactly balances the pressure drop thus ensuring zero flux at the caps.

When the Poiseuille flow is present, the dynamics are governed by the prescribed flux and the speed and size of the conveyor belt. Dimensional analysis reveals the importance of the previously mentioned dimensionless belt size and the relative importance of the belt speed to the centreline speed of the Poiseuille flow,

$$F = \frac{U}{U_0}. \quad (2.74)$$

In the following results we maintain the size of the belt and vary F . Later we will change the size of the belt and examine the effect upon the flow.

In the next set of results we set the centreline speed of the Poiseuille flow equal to the speed of the conveyor belt and maintain the size of the belt, so that $F = 1$ and $\beta = 2$. The centreline velocity is shown in figure 2.5 (a) where we can see that the velocity profiles are equivalent to those in figure 2.4 (a), albeit with a shift in the x -component due to the non-zero Poiseuille velocity. We can see that the x -component decays to its Poiseuille value at a distance of around $4d$ from the caps. The y -component does not decay quite so rapidly, but has decayed to zero a further distance d toward either cap. The channel mid-point line velocity is plotted in figure 2.5 (b). The y -component is zero showing that the movement is solely in the x -direction and the x -component smoothly falls from its conveyor belt speed of U on \mathcal{A} to its no-slip value of zero on the top wall as we move from the lower wall to the upper one. The streamlines are shown in figure 2.5 (c) for the starting positions, $x/d = 0$ and $y/d = -0.9 \dots 0.9$ where y/d was increased in steps of 0.2. We can see that all of the streamlines are drawn towards the conveyor belt with the greatest deflection being experienced by those which start closer to the lower wall. When a streamline starts close to the lower wall it turns very sharply close to the meeting points of \mathcal{A} and \mathcal{C} . Although all the streamlines start at $x = 0$ they do not terminate at the same value of x . The last point of each streamline in the figure is the last valid point recorded by the adaptive time-stepping Runge-Kutta-Fehlberg method.

The next set of results are for the same sized belt and with $F = 6$ and $\beta = 2$. The centreline and mid-point line velocity profiles together with the streamlines are shown in figure 2.6. The profiles of the velocity along the centreline are equivalent to those in

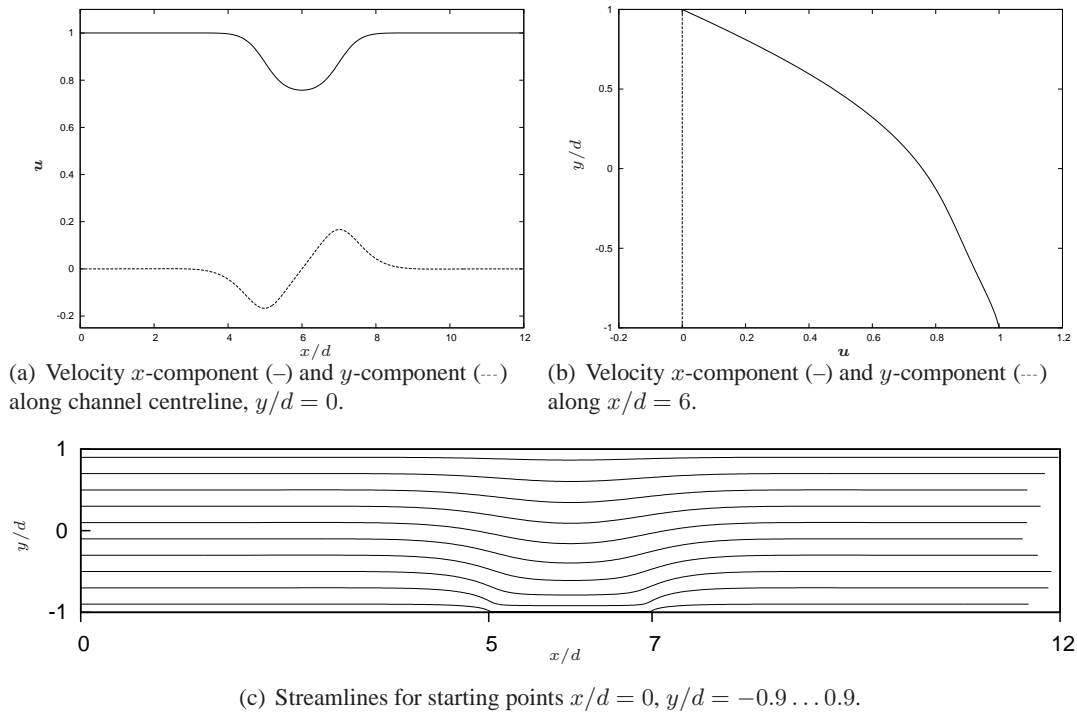


Figure 2.5 : Velocity and streamlines when $F = 1$ and $\beta = 2$. The conveyor belt lies between $x/d = 5$ and 7 .

figure 2.4 with the disturbance velocity scaled by F . In figure 2.6 (b) the x -component of velocity is negative when $y/d > -0.165$ which means that the fluid above this value moves in the negative x -direction while the fluid below moves in the opposite direction. The streamlines are shown in figure 2.6 (c) for the starting points $x/d = 0$ and $y/d = -0.9 \dots 0.9$, where y/d has been incremented in steps of 0.2 . The figure shows the eddy streamlines which move in an anti-clockwise direction and were started from $x/d = 6$ with $y/d = -0.1 \dots 0.9$, where y/d value was incremented in steps of 0.2 . The streamlines which move from entrance to exit become very tightly grouped in the region close to \mathcal{A} . We found stagnation points on the top wall close to $x/d = 4.7$ and 7.3 . The x -component of velocity to the left and right of these points are of opposite sign.

We have seen that as the conveyor belt speed is increased above the Poiseuille centreline speed a symmetric eddy is created above \mathcal{A} . Although the eddy centre in the previous case is closer to the lower wall, we found that when an eddy first appears it is closer to the top wall. Therefore there is a critical value of F , for a fixed β , which identifies the transition point between a flow without an eddy and one with an eddy. We investigated the behaviour of the x -component of the disturbance traction on the top wall as a possible explanation for eddy formation. There are two reasons for this; the eddy and f_x^D are both symmetrical about $x/d = 6$, and f_x^D is a component of the shear stress on the wall, which we would expect to change sign when there is a sudden flow reversal. The shear wall stress, τ , on the top wall is given by $\tau = \sigma_{xy}^P + \sigma_{xy}^D = -f_x^P - f_x^D$, where $f_x^P = 2\mu U_0/d$. We normalise τ by dividing by the wall stress due to the Poiseuille flow, as if the disturbance were not present, to get $\hat{\tau} = -\tau/f_x^P = 1 + f_x^D/f_x^P$. The normalised

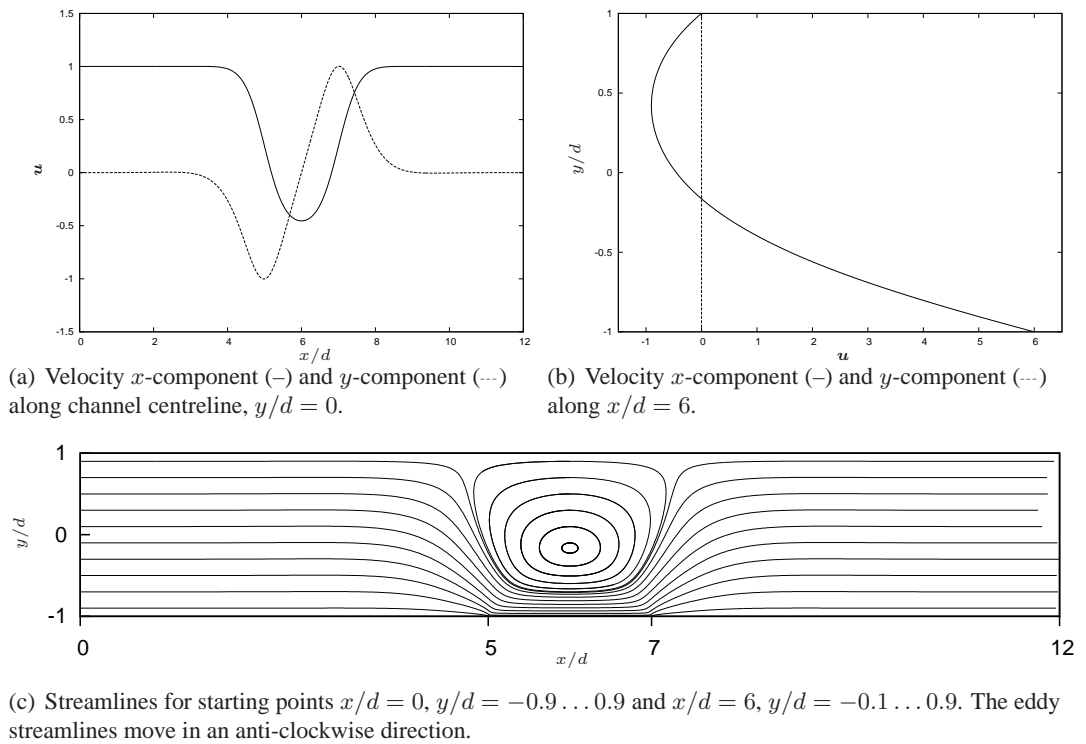


Figure 2.6 : Velocities and streamlines when when $F = 6$ and $\beta = 2$. The conveyor belt lies between $x/d = 5$ and 7 .

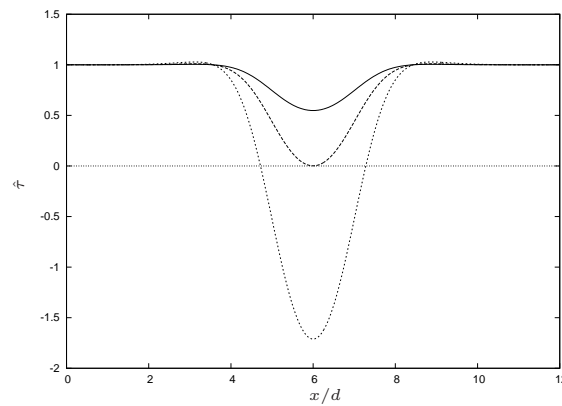


Figure 2.7 : The normalised top-wall shear stress, $\hat{\tau}$, for $F = 1, 2.21$ and 6 and $\beta = 2$. The solid line is $F = 1$, the dashed line is $F = 2.21$ and the dotted line is $F = 6$. The conveyor belt lies between $x/d = 5$ and 7 .

top-wall shear stress for three values of F is shown in figure 2.7. We have seen that an eddy does not occur for $F = 1$ and figure 2.7 shows us that the shear wall stress does not change sign along the top wall. We found the critical value of F by substituting the minimum value of $f_x^D (= -0.904 \mu U/d)$ into the expression for τ and setting it equal to zero, which gives $F = 2.21$. Increasing F to the critical value makes the shear wall stress zero at $x/d = 6$ and the eddy forms for $F \geq 2.21$. Setting $F = 6$ makes $\hat{\tau}$ zero at $x/d = 4.72$ and 7.28 . We can see from figure 2.6 (c) that this region is where the streamlines, which start from the entrance and close to the top wall, meet the eddy streamlines. These

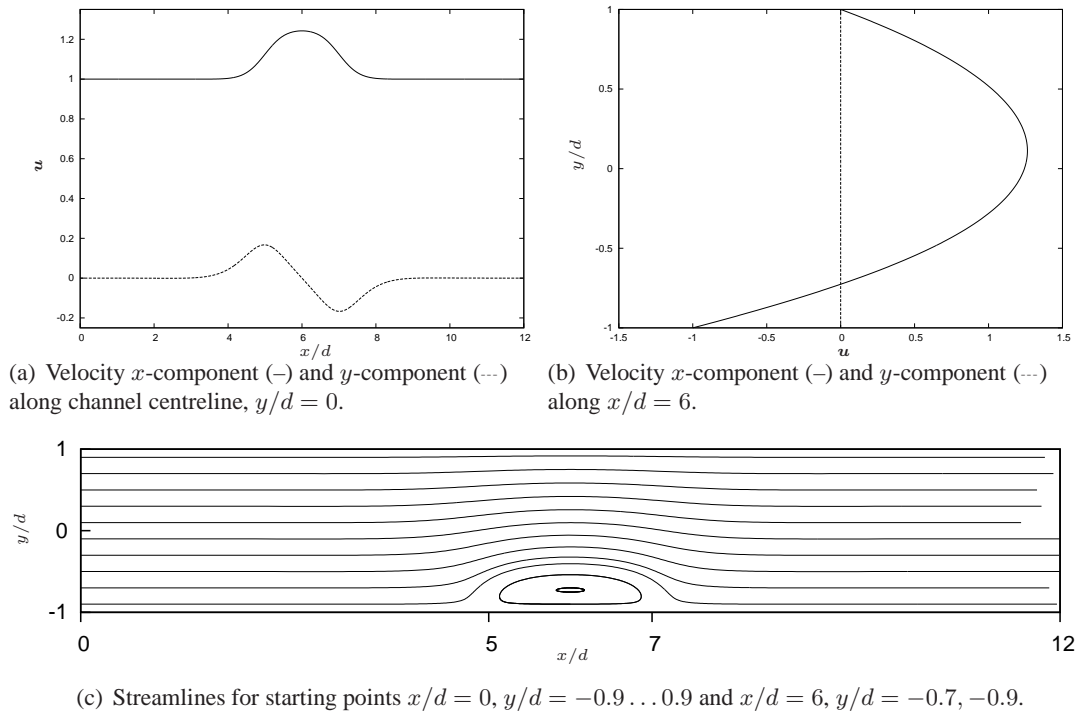


Figure 2.8 : Velocities and streamlines when $F = -1$ and $\beta = 2$. The conveyor belt lies between $x/d = 5$ and 7 .

points also correspond to the locations of the stagnation points noted earlier. To create a small eddy we set $F = 2.24$. The centre of the eddy is located at $y/d \approx 0.97$ and it has height $0.028d$ and width $0.153d$, where height and width are measured in the x and y directions respectively. As F is increased beyond 2.21 the eddy increases in size and its centre moves towards the lower wall.

So far we have had the conveyor belt moving in the positive x -direction. For the next set of results we reverse the direction of the belt such that $F = -1$. The velocity profiles and the streamlines are shown in figure 2.8. The profiles along the centreline are again equivalent to those in 2.5 with the disturbance velocity negated due to the velocity scaling. The mid-point line profiles indicate the presence of an eddy which is shown in the streamline figure 2.8 (c). The streamlines were started from $x/d = 0, y/d = -0.9 \dots 0.9$ incremented in steps of 0.2 , and $x/d = 6, y/d = -0.7$ and -0.9 . An eddy is created close to \mathcal{A} for all negative F .

In this set of results we increase the size of the belt so that $\beta = 4$ and set $F = 6$. Since we have changed the size of the belt, we checked the decay of the disturbance velocity and the disturbance pressure. We found the maximum error in the disturbance velocity at the caps to be 0.03% of U_0 . The approximate value of the disturbance pressure calculated from equation (2.29) differed from the exact value by 0.003% . In figure 2.9 we show the disturbance tractions on the top wall, the velocity profiles along the centreline and mid-line, and the streamlines. The disturbance tractions on the top wall are shown in figures 2.9 (a) and 2.9 (b). We can see that the profile is blunted for the x -component and the turning points are moved towards the caps for the y -component. The disturbance

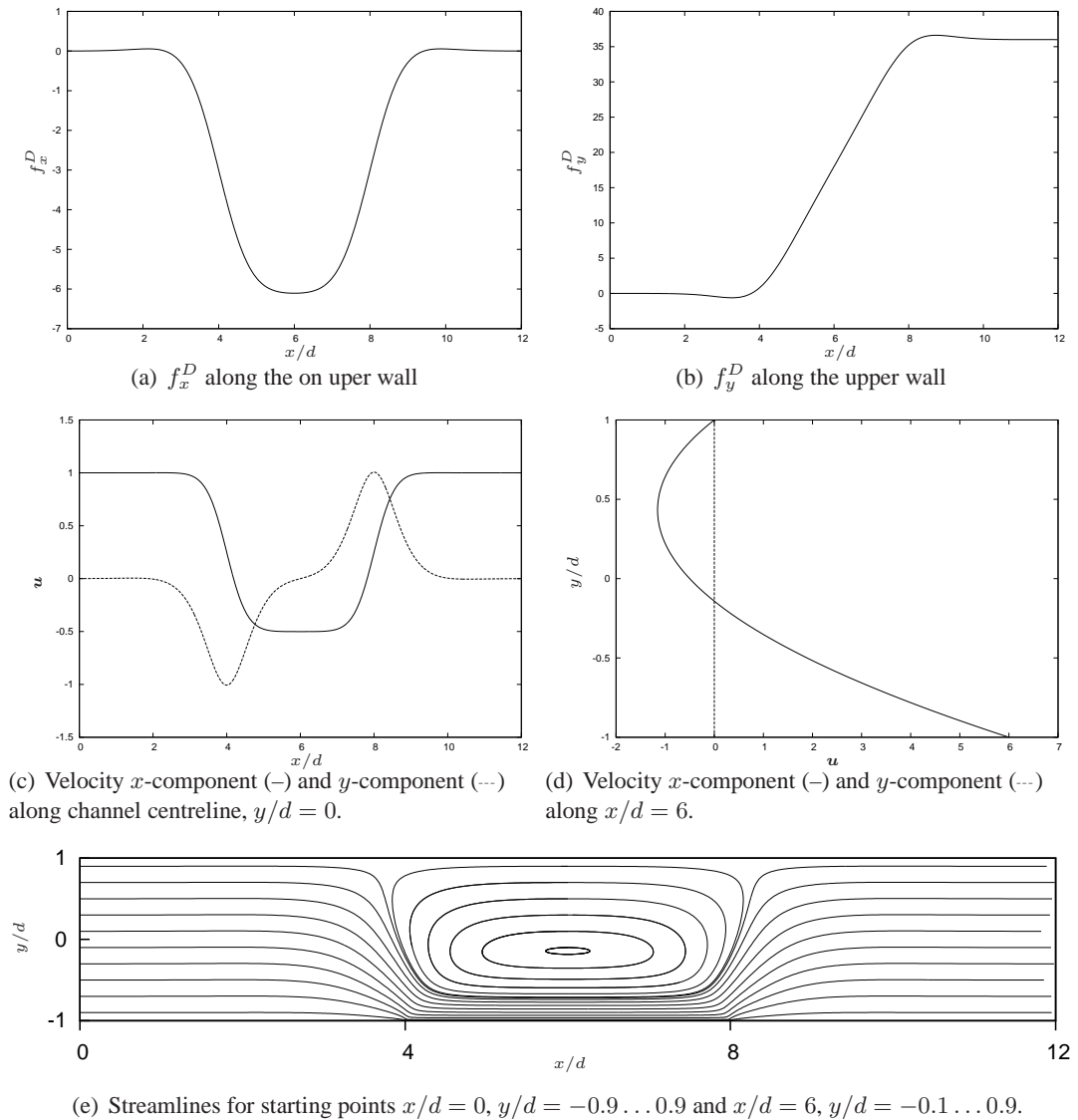


Figure 2.9 : Disturbance tractions, velocity profiles and streamlines for $F = 6$ and $\beta = 4$. The conveyor belt lies between $x/d = 4$ and 8 .

tractions on the lower wall are not materially different from those shown in figure 2.3. An interesting feature of the centreline velocity profile, shown in figure 2.9 (c), is the plateau region in the x -component above the belt. The mid-line plot in figure 2.9 (d) shows that the x -component of velocity changes sign and so an eddy will be present. From the velocity profiles we expect the eddy to be wider, measured in the x -direction, because the x -component of velocity reaches a steady value above the belt. Confirmation is shown in figure 2.9 (e) which shows the flow streamlines, plotted for starting positions $x/d = 0, y/d = -0.9 \dots 0.9$ and $x/d = 6, y = -0.1 \dots 0.9$, where y/d is incremented in steps of 0.2 in both cases.

In the penultimate set of results we reduce the size of the conveyor belt so that $\beta = 1$ and $F = 6$. Since we have again changed the size of the belt, we checked the decay of the disturbance velocity and the disturbance pressure. We found the maximum error

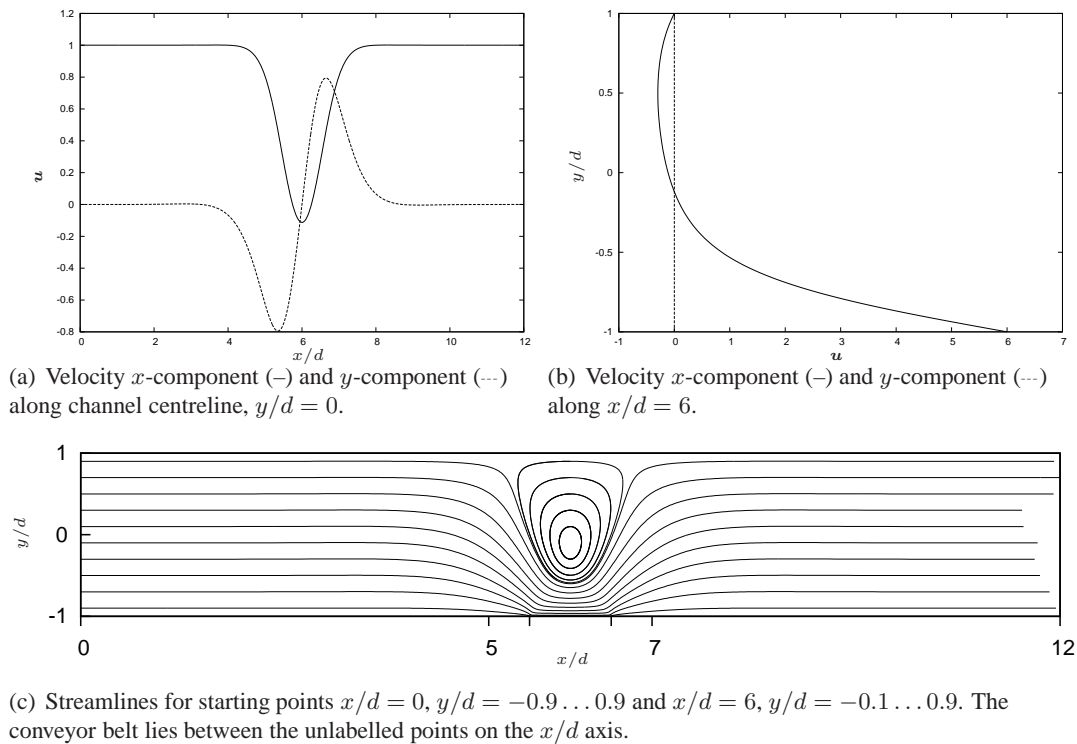


Figure 2.10 : Velocity profiles and streamlines for $F = 6$ and $\beta = 1$. The conveyor belt lies between $x/d = 5.5$ and 6.5 .

in the disturbance velocity at the caps to be 0.1% of U_0 . The approximate value of the disturbance pressure calculated from equation (2.29) differed from the exact value by 0.05% . In figure 2.10 we show the centreline velocity profiles, the mid-line velocity profiles and the streamlines. The disturbance tractions were not materially different from those shown in figure 2.3 and so are not plotted. From the centreline velocity profile, shown in figure 2.10 (a), we can see that the velocity is almost zero at $(6, 0)$. The mid-line plot in figure 2.10 (b) shows that an eddy is present because the x -component of velocity changes sign at $y/d = -0.12$. The streamlines are shown in figure 2.10 (c) and were started from $x/d = 0, y/d = -0.9 \dots 0.9$ and $x/d = 6, y/d = 0.1 \dots 0.9$, where y/d is incremented in steps of 0.2 in both cases. The eddy shape is noticeably more triangular than in the previous results.

Finally, we reduce the belt length such that $\beta = 0.5$ and set $F = 12$. For this value of β we checked the disturbance velocity decay and the disturbance pressure. We found the maximum error in the disturbance velocity at the caps to be 0.4% of U_0 . Once again we use equation (2.29) to calculate the approximate value of the disturbance pressure. The approximate value differed from the exact value by 0.08% . In figure 2.11 we show the centreline velocity profiles, the mid-line velocity profiles and the streamlines. The disturbance tractions were not materially different from those shown in figure 2.3 and so are not plotted. The results are similar to the previous set for $F = 6$ and $\beta = 1$. However when $\beta = 1/2$ an eddy is not present for $F = 6$ and so we increased F to 12 . The velocity profile on the mid-line, shown in figure 2.11 (b), shows that the fluid moves

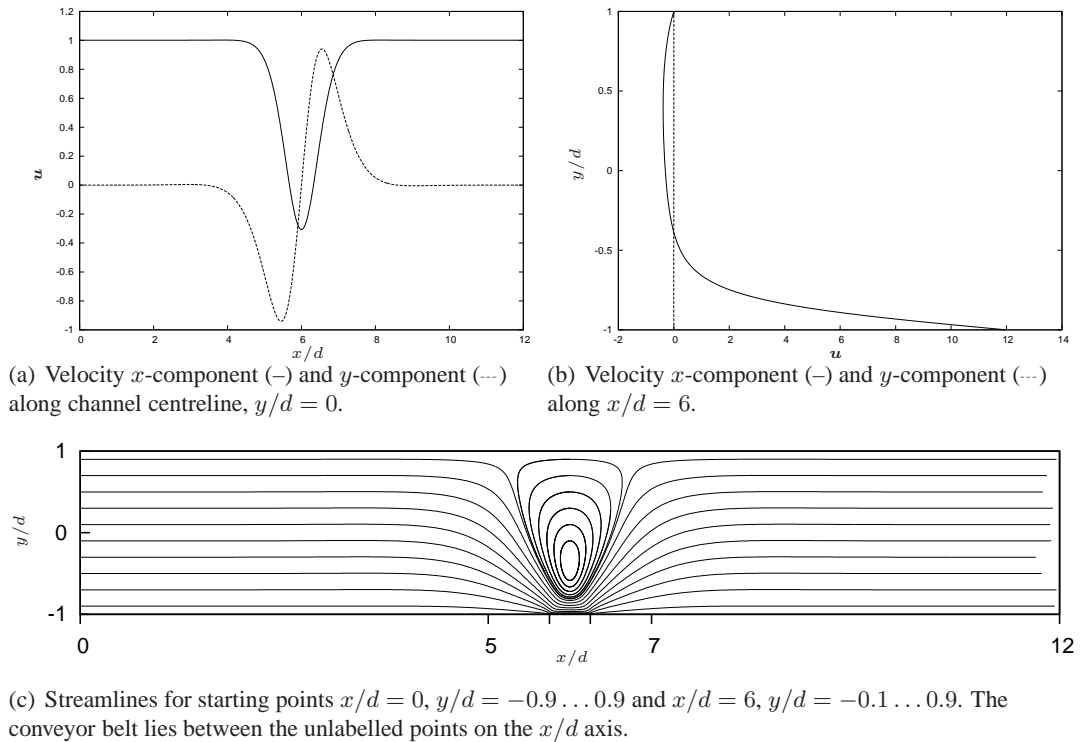


Figure 2.11 : Velocity profiles and streamlines for $F = 12$ and $\beta = 0.5$. The conveyor belt lies between $x/d = 5.75$ and 6.25 .

relatively slowly above the eddy centre. The streamlines in figure 2.11 (c) again show an eddy with a ‘rounded’ triangular shape. The streamlines were started from $x/d = 0, y/d = -0.9 \dots 0.9$ and $x/d = 6, y = -0.1 \dots 0.9$, where y/d is incremented in steps of 0.2 in both cases.

2.5 Discussion

We derived boundary integral equations which govern the velocity field inside a channel containing a disturbance caused by a conveyor belt on one of the walls. An exact expression for the disturbance pressure at the channel exit was derived using the Lorentz reciprocal relation, wherein the disturbance flow was related to the Poiseuille flow. We discretised the geometry and equations using the boundary element method. We constructed a linear system from the discretised equations and found its solution by a standard numerical method.

If the Poiseuille flow was absent then the conveyor belt created an eddy in the fluid. When the Poiseuille flow was present and the conveyor belt speed was in the same direction and sufficiently small then the fluid experienced a pull towards the conveyor belt. The pull towards the conveyor belt increased when the conveyor belt speed was increased. At a critical value of the conveyor belt speed an eddy formed close to the top wall. As the conveyor belt speed was increased past this critical value the eddy increased in size and its centre moved further towards the lower wall. When the conveyor belt speed was in

the same direction as the Poiseuille flow the pressure drop between the entrance and exit decreased. However even when the pressure drop is zero, the presence of the conveyor belt and the induced eddy maintain the flux rate at the exit.

Changing the size of the belt affects the shape and size of the eddy. When the belt size is increased the eddy becomes wider and the fluid closest to the belt moves almost parallel to it. A smaller belt induces an eddy which does not exhibit this property. Instead the eddy adopts a 'rounded' triangular shape. When the conveyor belt moved in the opposite direction to the Poiseuille flow, an eddy was immediately created close to the conveyor belt. The fluid which was not caught in the eddy was diverted away from the conveyor belt. Interesting further work on this problem could involve a parameter study whereby the speed and size of the conveyor belt could be related to the eddy size.

This concludes the chapter on the conveyor belt problem. In the next chapter we will consider a straight channel containing a disturbance caused by the presence of a capsule.

Chapter 3

The motion of a rigid particle in a straight channel

In the previous chapter we studied the disturbance flow due to the motion of a conveyor belt on one of the walls in a two-dimensional channel flow. In this chapter we remove the conveyor belt and introduce a rigid neutrally-buoyant particle to the flow. The particle is free to move with the flow and we assume that the flow exerts no force or torque on the particle. We model the disturbance caused by the particle using the boundary integral method and derive the equations which govern the motion of the fluid and the particle. We derive the discrete analogues of the governing equations using the boundary element method and write the equations in the form of a linear matrix system. We solve the linear system by a standard numerical method, and compare the solution to known results where applicable. The mathematical treatment of this problem will provide a guide to the next chapter, where we will substitute the particle's rigid boundary with a flexible one, and allow it to contain a secondary fluid.

3.1 Problem statement

Let us consider the motion of a fluid with viscosity μ in an infinite straight-walled channel of width $2d$. A disturbance to the pressure-driven flow is caused by the presence of a rigid particle of a prescribed shape. We assume that the particle is neutrally-buoyant and that the flow exerts zero force and torque on the particle so that the particle has zero inertia and moves freely with the flow. The geometry is shown in figure 3.1 and comprises the channel walls, \mathcal{C} , and the particle, \mathcal{P} . Far upstream and downstream of the disturbance caused by the particle, the flow in the channel is described by classical unidirectional Poiseuille flow, which is characterised by the prescribed flux, Q . The Poiseuille velocity, \mathbf{u}^P , is defined by

$$\mathbf{u}^P = U_0 \left(1 - \frac{y^2}{d^2}\right) \mathbf{i} = u^P \mathbf{i} \quad (3.1)$$

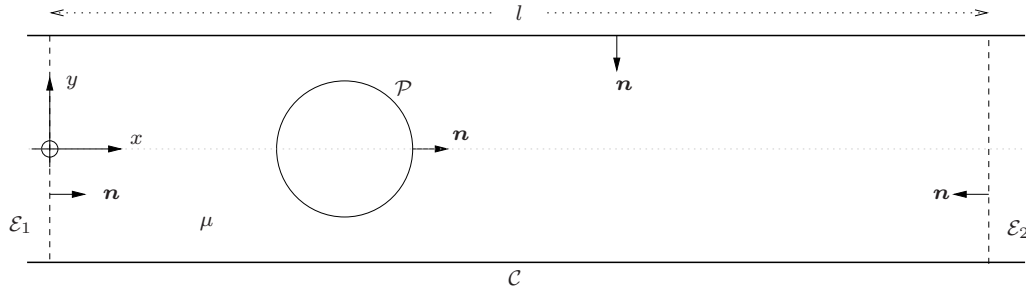


Figure 3.1 : A straight-walled channel containing a rigid neutrally-buoyant particle.

where U_0 is the speed on the centreline and $u^P = U_0(1 - y^2/d^2)$ is the x -component of the Poiseuille velocity. The flux and the centreline speed are related by

$$Q = \frac{4}{3} d U_0. \quad (3.2)$$

Our aim is to compute the velocity field throughout the flow domain, the translational and rotational velocities of the particle and the additional pressure drop between the entrance and exit due to the presence of the particle. We assume that the Reynolds number of the flow is very small so that the flow in the channel may be described using the linear equations of Stokes flow given in equation (1.3.4).

In preparation for the numerical method, we truncate the channel and label the entrance, located at $x = 0$, as \mathcal{E}_1 and the exit, located at $x = l$, as \mathcal{E}_2 . We note that \mathcal{E}_1 and \mathcal{E}_2 are the entrance and exit to the computational domain and are not the inflow and outflow of the channel, where end effects would be encountered. The unit normal vectors, \mathbf{n} , on all boundaries point into the fluid as shown in figure 3.1. The particle disturbs the Poiseuille flow, but at \mathcal{E}_1 and \mathcal{E}_2 , we assume that the disturbance has decayed and the flow has settled to Poiseuille flow.

We decompose the velocity field, \mathbf{u} , the stress field, $\boldsymbol{\sigma}$, and the traction field, \mathbf{f} , into background Poiseuille and disturbance components, which we indicate by the superscripts P and D respectively, so that

$$\mathbf{u} = \mathbf{u}^P + \mathbf{u}^D, \quad (3.3)$$

$$\boldsymbol{\sigma} = \boldsymbol{\sigma}^P + \boldsymbol{\sigma}^D, \quad (3.4)$$

$$\mathbf{f} = \mathbf{f}^P + \mathbf{f}^D \quad (3.5)$$

and where the traction, $\mathbf{f} = \boldsymbol{\sigma} \cdot \mathbf{n}$. On \mathcal{C} we have

$$\mathbf{u} = \mathbf{u}^P = \mathbf{u}^D = \mathbf{0} \quad (3.6)$$

due to the no-slip and no-penetration conditions, and on \mathcal{P} we have

$$\mathbf{u} = \mathbf{V} + \boldsymbol{\Omega} \wedge (\mathbf{x} - \mathbf{x}_c) \quad (3.7)$$

where $\mathbf{V} = (V_x, V_y)$ is the translational velocity, $\boldsymbol{\Omega}$ is the rotational velocity, \mathbf{x} is a point

on the particle boundary and \mathbf{x}_c is the particle's centroid, calculated by

$$\mathbf{x}_c = \frac{1}{S_{\mathcal{P}}} \int_{\mathcal{P}} \mathbf{x} \, ds(\mathbf{x}), \quad (3.8)$$

where $S_{\mathcal{P}}$ is the length of the particle perimeter. When the particle rotates in the xy -plane, the rotational velocity is given by $\boldsymbol{\Omega} = \Omega \mathbf{k}$, where Ω is the angular velocity and \mathbf{k} is the unit vector which points out of the paper towards the reader. When Ω is positive the particle rotates in an anti-clockwise direction.

In the previous chapter we assumed that the disturbance velocity decayed rapidly as we moved away from the source of the disturbance. We justified this assumption on the basis of studies of Gaver and Kute (1998) and Cortez (2002) regarding the effects of a small obstruction in a channel. We calculated the disturbance velocity at the entrance and exit to the computational domain and found an excellent agreement between the numerical results and our assumptions. Now that the source of our disturbance is allowed to flow with the fluid we must examine our assumption. Naturally we expect the disturbance flow caused by the particle to decay as we move away from the particle. However we require the decay to be sufficiently rapid so that our assumption of Poiseuille flow at \mathcal{E}_1 and \mathcal{E}_2 is justified. Sugihara-Seki (1993) studied the motion of a rigid ellipse in a two-dimensional channel flow. The velocity decay was assumed, and computed, to be sufficiently rapid for a shorter computational domain than the one considered in this chapter. Therefore from our results in the previous chapter, the results of Gaver and Kute (1998), Cortez (2002) on the decay of a disturbance in a channel and the results of Sugihara-Seki (1993) regarding the decay of an ellipse in a channel flow, we assume that the disturbance velocity decays sufficiently rapidly as we approach the ends. In summary, the disturbance velocity and disturbance traction satisfy

$$\mathbf{u}^D = \mathbf{0}, \quad (3.9)$$

$$\mathbf{f}^D = -p^D \mathbf{n} \quad (3.10)$$

at \mathcal{E}_1 and \mathcal{E}_2 where p^D is the disturbance pressure due to the particle. We take p^D to be constant at the ends and set $p^D = 0$ at \mathcal{E}_1 without loss of generality. At \mathcal{E}_2 we have

$$\mathbf{f}^D = -\pi_2 \mathbf{n} \quad (3.11)$$

where $\pi_2 = p^D(\mathcal{E}_2)$ is the disturbance pressure at the exit. The disturbance pressure drop between the entrance and exit due to the particle is therefore given by

$$\Delta p^D = p^D(\mathcal{E}_1) - p^D(\mathcal{E}_2) = -\pi_2. \quad (3.12)$$

The Poiseuille pressure in the channel is given by

$$p^P = G(l - x) \quad (3.13)$$

where $G = 2\mu U_0/d^2$ is a positive constant, and $-G$ is the imposed constant pressure gradient between the entrance and the exit. The Poiseuille pressure varies linearly along the x -axis of the channel and is zero at \mathcal{E}_2 where $x = l$. Therefore the total pressure drop, Δp , between the entrance and exit is

$$\begin{aligned}\Delta p &= p(\mathcal{E}_1) - p(\mathcal{E}_2) = p^P(\mathcal{E}_1) + p^D(\mathcal{E}_1) - (p^P(\mathcal{E}_2) + p^D(\mathcal{E}_2)) \\ &= Gl - \pi_2.\end{aligned}\quad (3.14)$$

We may now derive an equation for π_2 by applying Lorentz's reciprocal relation (1.3.22) to the Poiseuille and disturbance flows in the channel, to give

$$\nabla \cdot (\mathbf{u}^D \cdot \boldsymbol{\sigma}^P - \mathbf{u}^P \cdot \boldsymbol{\sigma}^D) = 0. \quad (3.15)$$

Integration of (3.15) over the flow domain, Γ , gives

$$\int_{\partial\Gamma} \mathbf{u}^D \cdot \mathbf{f}^P \, ds(\mathbf{x}) = \int_{\partial\Gamma} \mathbf{u}^P \cdot \mathbf{f}^D \, ds(\mathbf{x}), \quad (3.16)$$

where s is the boundary arc-length, $\partial\Gamma = \mathcal{E}_1 \cup \mathcal{C} \cup \mathcal{P} \cup \mathcal{E}_2$ is the piecewise-continuous closed boundary of Γ , and the divergence theorem has been used to convert the area integrals into line integrals. Expansion of the integral on the left-hand side of equation (3.16) gives

$$\begin{aligned}\int_{\partial\Gamma} \mathbf{u}^D \cdot \mathbf{f}^P \, ds(\mathbf{x}) &= \int_{\mathcal{E}_1, \mathcal{E}_2, \mathcal{C}} \mathbf{u}^D \cdot \mathbf{f}^P \, ds(\mathbf{x}) + \int_{\mathcal{P}} \mathbf{u}^D \cdot \mathbf{f}^P \, ds(\mathbf{x}) \\ &= \int_{\mathcal{P}} \mathbf{u}^D \cdot \mathbf{f}^P \, ds(\mathbf{x})\end{aligned}\quad (3.17)$$

since the disturbance velocity at \mathcal{E}_1 , \mathcal{E}_2 and on the walls is zero. The right-hand side of (3.16) simplifies to

$$\begin{aligned}\int_{\partial\Gamma} \mathbf{u}^P \cdot \mathbf{f}^D \, ds(\mathbf{x}) &= \int_{\mathcal{E}_1, \mathcal{C}} \mathbf{u}^P \cdot \mathbf{f}^D \, ds(\mathbf{x}) + \int_{\mathcal{E}_2, \mathcal{P}} \mathbf{u}^P \cdot \mathbf{f}^D \, ds(\mathbf{x}) \\ &= \int_{\mathcal{E}_2, \mathcal{P}} \mathbf{u}^P \cdot \mathbf{f}^D \, ds(\mathbf{x})\end{aligned}\quad (3.18)$$

because the velocity is zero on the walls and $\mathbf{f}^D = \mathbf{0}$ at \mathcal{E}_1 . Substitution into (3.16) gives

$$\begin{aligned} \int_{\mathcal{P}} \mathbf{u}^D \cdot \mathbf{f}^P \, ds(\mathbf{x}) &= \int_{\mathcal{E}_2, \mathcal{P}} \mathbf{u}^P \cdot \mathbf{f}^D \, ds(\mathbf{x}) \\ &= -\pi_2 \int_{\mathcal{E}_2} \mathbf{u}^P \cdot \mathbf{n} \, ds(\mathbf{x}) + \int_{\mathcal{P}} \mathbf{u}^P \cdot \mathbf{f}^D \, ds(\mathbf{x}) \\ &= \pi_2 Q + \int_{\mathcal{P}} \mathbf{u}^P \cdot \mathbf{f}^D \, ds(\mathbf{x}) \end{aligned} \quad (3.19)$$

since the flux at \mathcal{E}_2 is defined by

$$Q = \int_{\mathcal{E}_2} \mathbf{u}^P \, ds(\mathbf{x}) = - \int_{\mathcal{E}_2} \mathbf{u}^P \cdot \mathbf{n} \, ds(\mathbf{x}). \quad (3.20)$$

Rearranging (3.19) gives

$$\pi_2 = \frac{1}{Q} \int_{\mathcal{P}} (\mathbf{u}^D \cdot \mathbf{f}^P - \mathbf{u}^P \cdot \mathbf{f}^D) \, ds(\mathbf{x}), \quad (3.21)$$

where the unknown quantities are the disturbance tractions and velocities on \mathcal{P} . However, equation (3.7) provides a boundary condition for the total velocity, \mathbf{u} , on the particle's boundary and so we eliminate the disturbance quantities using the decompositions in equations (3.3) and (3.5). Equation (3.21) becomes

$$\begin{aligned} \pi_2 &= \frac{1}{Q} \int_{\mathcal{P}} ((\mathbf{u} - \mathbf{u}^P) \cdot \mathbf{f}^P - \mathbf{u}^P \cdot (\mathbf{f} - \mathbf{f}^P)) \, ds(\mathbf{x}) \\ &= \frac{1}{Q} \int_{\mathcal{P}} (\mathbf{u} \cdot \mathbf{f}^P - \mathbf{u}^P \cdot \mathbf{f}) \, ds(\mathbf{x}). \end{aligned} \quad (3.22)$$

We may simplify this equation further by writing the total velocity in the integrand's first term in terms of the particle's translational and rotational velocities, to get

$$\begin{aligned} \int_{\mathcal{P}} \mathbf{u} \cdot \mathbf{f}^P \, ds(\mathbf{x}) &= \int_{\mathcal{P}} (\mathbf{V} + \boldsymbol{\Omega} \wedge (\mathbf{x} - \mathbf{x}_c)) \cdot \mathbf{f}^P \, ds(\mathbf{x}) \\ &= \mathbf{V} \cdot \int_{\mathcal{P}} \mathbf{f}^P \, ds(\mathbf{x}) + \boldsymbol{\Omega} \cdot \int_{\mathcal{P}} (\mathbf{x} - \mathbf{x}_c) \wedge \mathbf{f}^P \, ds(\mathbf{x}), \end{aligned} \quad (3.23)$$

where \mathbf{V} and $\boldsymbol{\Omega}$ may be brought in front of the integral sign because they are instantaneously constant on the particle's perimeter, and where the triple product, $\boldsymbol{\Omega} \wedge (\mathbf{x} - \mathbf{x}_c) \cdot \mathbf{f}^P$, has been rewritten using the identity, $(\mathbf{a} \wedge \mathbf{b}) \cdot \mathbf{c} \equiv \mathbf{a} \cdot (\mathbf{b} \wedge \mathbf{c})$. Now let us define the

Poiseuille force and torque vectors,

$$\mathbf{F}^P = \int_{\mathcal{P}} \mathbf{f}^P \, ds(\mathbf{x}), \quad (3.24)$$

$$\mathbf{T}^P = \int_{\mathcal{P}} (\mathbf{x} - \mathbf{x}_c) \wedge \mathbf{f}^P \, ds(\mathbf{x}), \quad (3.25)$$

where \mathbf{F}^P corresponds to the force exerted on the particle by the Poiseuille flow, and \mathbf{T}^P corresponds to the torque. More specifically \mathbf{F}^P and \mathbf{T}^P are the force and torque exerted on a contour in the flow which is identical to the particle's boundary because they depend solely on the background Poiseuille flow. We may write equation (3.23) as

$$\int_{\mathcal{P}} \mathbf{u} \cdot \mathbf{f}^P \, ds(\mathbf{x}) = \mathbf{V} \cdot \mathbf{F}^P + \boldsymbol{\Omega} \cdot \mathbf{T}^P. \quad (3.26)$$

Application of the divergence theorem to \mathbf{F}^P gives

$$\mathbf{F}^P = \int_{\mathcal{P}} \boldsymbol{\sigma}^P \cdot \mathbf{n} \, ds(\mathbf{x}) = \iint_{\mathcal{P}} \nabla \cdot \boldsymbol{\sigma}^P \, dA(\mathbf{x}) = \mathbf{0} \quad (3.27)$$

since $\boldsymbol{\sigma}^P$ satisfies the Stokes equation, $\nabla \cdot \boldsymbol{\sigma}^P = \mathbf{0}$. Similarly for the Poiseuille torque, in index notation, we have

$$T_i^P = \int_{\mathcal{P}} \epsilon_{ijk} (x_j - x_{c,j}) \sigma_{kl}^P n_l \, ds(\mathbf{x}), \quad (3.28)$$

where ϵ_{ijk} is the alternating tensor defined in equation (1.3.33). We use the divergence theorem to transform (3.28) from a line integral to

$$\begin{aligned} T_i^P &= \iint_{\mathcal{P}} \frac{\partial}{\partial x_l} (\epsilon_{ijk} (x_j - x_{c,j}) \sigma_{kl}^P) \, dA(\mathbf{x}) \\ &= \epsilon_{ijk} \iint_{\mathcal{P}} \sigma_{kj}^P + (x_j - x_{c,j}) \frac{\partial}{\partial x_l} (\sigma_{kl}^P) \, dA(\mathbf{x}) \\ &= \epsilon_{ijk} \iint_{\mathcal{P}} (x_j - x_{c,j}) \frac{\partial}{\partial x_l} (\sigma_{kl}^P) \, dA(\mathbf{x}) \end{aligned} \quad (3.29)$$

where A is the area bounded by \mathcal{P} and where $\epsilon_{ijk} \sigma_{kj}^P = 0$ due to the anti-symmetry of the alternating tensor, $\epsilon_{ijk} = -\epsilon_{ikj}$, and the symmetry of the stress tensor, $\sigma_{ij} = \sigma_{ji}$. Reverting to vector notation we have

$$\mathbf{T}^P = \iint_{\mathcal{P}} (\mathbf{x} - \mathbf{x}_c) \wedge (\nabla \cdot \boldsymbol{\sigma}^P) \, dA(\mathbf{x}) = \mathbf{0}, \quad (3.30)$$

since $\nabla \cdot \boldsymbol{\sigma}^P = \mathbf{0}$, and so both the Poiseuille force and traction on the particle contour are

zero. Substituting (3.27) and (3.30) into (3.26) gives

$$\int_{\mathcal{P}} \mathbf{u} \cdot \mathbf{f}^P \, ds(\mathbf{x}) = 0 \quad (3.31)$$

which simplifies equation (3.22) to

$$\pi_2 = -\frac{1}{Q} \int_{\mathcal{P}} \mathbf{u}^P \cdot \mathbf{f} \, ds(\mathbf{x}), \quad (3.32)$$

which is our equation for the disturbance pressure. Therefore the disturbance pressure at \mathcal{E}_2 is expressed in terms of the prescribed flux, Q , the known Poiseuille velocity, \mathbf{u}^P , and the unknown tractions on the perimeter of the particle. It is interesting to note that the disturbance pressure may only be calculated from equation (3.32) when we know the tractions on the particle's boundary, which is in contrast to the explicit disturbance pressure formula given in equation (2.27) of the previous chapter. Since the Poiseuille velocity is unidirectional only the x -components of \mathbf{f} will affect π_2 . We may also define the force, \mathbf{F} , and the torque, \mathbf{T} , on the particle due to the total flow which are both zero because we have assumed the particle is force and torque free. Therefore,

$$\mathbf{F} = \int_{\mathcal{P}} \mathbf{f} \, ds(\mathbf{x}) = \mathbf{0}, \quad (3.33)$$

$$\mathbf{T} = \int_{\mathcal{P}} (\mathbf{x} - \mathbf{x}_c) \wedge \mathbf{f} \, ds(\mathbf{x}) = \mathbf{0}, \quad (3.34)$$

and the force and torque on the particle due to the disturbance flow are given by

$$\mathbf{F}^D = \int_{\mathcal{P}} \mathbf{f}^D \, ds(\mathbf{x}) = \mathbf{0}, \quad (3.35)$$

$$\mathbf{T}^D = \int_{\mathcal{P}} (\mathbf{x} - \mathbf{x}_c) \wedge \mathbf{f}^D \, ds(\mathbf{x}) = \mathbf{0}, \quad (3.36)$$

which are both zero because $\mathbf{F} = \mathbf{F}^P + \mathbf{F}^D$ and $\mathbf{T} = \mathbf{T}^P + \mathbf{T}^D$.

In the previous chapter we derived an alternative expression for the disturbance pressure by integrating the Stokes equation for the disturbance stress. Integrating $\nabla \cdot \boldsymbol{\sigma}^D = \mathbf{0}$ over the flow domain and applying the Divergence theorem gives

$$\begin{aligned} \pi_2 \mathbf{i} &= -\frac{1}{2d} \int_{c, \mathcal{P}} \mathbf{f}^D \, ds(\mathbf{x}) \\ &= -\frac{1}{2d} \left(\int_c \mathbf{f}^D \, ds(\mathbf{x}) + \mathbf{F}^D \right) \\ &= -\frac{1}{2d} \int_c \mathbf{f}^D \, ds(\mathbf{x}), \end{aligned} \quad (3.37)$$

which in component form gives

$$\pi_2 = -\frac{1}{2d} \int_C \mathbf{i} \cdot \mathbf{f}^D \, ds(\mathbf{x}), \quad (3.38)$$

$$0 = \int_C \mathbf{j} \cdot \mathbf{f}^D \, ds(\mathbf{x}). \quad (3.39)$$

Equation (3.38) expresses π_2 in terms of the disturbance tractions over the channel walls as opposed to equation (3.32), which expresses π_2 in terms of the total traction over the particle. We choose to calculate π_2 using (3.32) and use equation (3.38) as a means of checking the disturbance pressure. We use equation (3.39) to check the y -components of the disturbance tractions.

Now that we have a formula for the disturbance pressure, we move onto our next goal of deriving an integral equation which governs the disturbance velocity in the channel. We apply the boundary integral equation (1.3.40) to the disturbance flow with the pole, \mathbf{x}_0 , located in the fluid to get

$$4\pi\mu u_j^D(\mathbf{x}_0) = - \int_{\partial\Gamma} f_i^D G_{ij} \, ds(\mathbf{x}) + \mu \int_{\partial\Gamma} u_i^D T_{ijk} n_k \, ds(\mathbf{x}), \quad (3.40)$$

where G_{ij} is the free-space Green's function and T_{ijk} is its associated stress tensor. The velocity can be calculated at any point in the flow given the disturbance tractions and velocities on the boundaries. We simplify (3.40) by applying the boundary conditions given in equations (3.6), (3.9), (3.11) together with the zero disturbance pressure on \mathcal{E}_1 to get

$$4\pi\mu u_j^D(\mathbf{x}_0) = \pi_2 \int_{\mathcal{E}_2} n_i G_{ij} \, ds(\mathbf{x}) - \int_{C, \mathcal{P}} f_i^D G_{ij} \, ds(\mathbf{x}) + \mu \int_{\mathcal{P}} u_i^D T_{ijk} n_k \, ds(\mathbf{x}). \quad (3.41)$$

Once again we would like to eliminate \mathbf{u}^D from the equation in favour of the total velocity because the boundary condition on \mathcal{P} is written in terms of \mathbf{u} . By considering only the boundary of the particle and the Poiseuille flow, we can write

$$0 = - \int_{\mathcal{P}} f_i^P G_{ij} \, ds(\mathbf{x}) + \mu \int_{\mathcal{P}} u_i^P T_{ijk} n_k \, ds(\mathbf{x}), \quad (3.42)$$

for \mathbf{x}_0 in the fluid and where the left-hand side is zero because \mathbf{x}_0 lies outside of \mathcal{P} . Since \mathbf{x}_0 lies in the fluid in both equations (3.41) and (3.42) we may add them to get

$$\begin{aligned} 4\pi\mu u_j^D(\mathbf{x}_0) &= \pi_2 \int_{\mathcal{E}_2} n_i G_{ij} \, ds(\mathbf{x}) - \int_C f_i^D G_{ij} \, ds(\mathbf{x}) \\ &\quad - \int_{\mathcal{P}} f_i G_{ij} \, ds(\mathbf{x}) + \mu \int_{\mathcal{P}} u_i T_{ijk} n_k \, ds(\mathbf{x}), \end{aligned} \quad (3.43)$$

where we have fulfilled our aim of eliminating the disturbance velocity on the particle boundary in favour of the total velocity. Re-expressing the double-layer potential in terms of the translational and rotational velocities gives

$$\begin{aligned} \int_{\mathcal{P}} u_i T_{ijk} n_k \, ds(\mathbf{x}) &= \int_{\mathcal{P}} (V_i + \epsilon_{ilm} \Omega_l (x_m - x_{c,m})) T_{ijk} n_k \, ds(\mathbf{x}) \\ &= (V_i - \epsilon_{ilm} \Omega_l x_{c,m}) \int_{\mathcal{P}} T_{ijk} n_k \, ds(\mathbf{x}) \\ &\quad + \epsilon_{ilm} \Omega_l \int_{\mathcal{P}} x_m T_{ijk} n_k \, ds(\mathbf{x}), \end{aligned} \quad (3.44)$$

which may be evaluated using the stress tensor identities (Pozrikidis 1992, p59)

$$\int_{\mathcal{P}} T_{ijk} n_k \, ds(\mathbf{x}) = 0, \quad (3.45)$$

$$\epsilon_{lmi} \int_{\mathcal{P}} x_m T_{ijk} n_k \, ds(\mathbf{x}) = 0, \quad (3.46)$$

which are valid when \mathbf{x}_0 lies outside the domain of \mathcal{P} , and so

$$\int_{\mathcal{P}} u_i T_{ijk} n_k \, ds(\mathbf{x}) = 0. \quad (3.47)$$

The boundary integral equation (3.43) therefore reduces to

$$u_j^D(\mathbf{x}_0) = \frac{1}{4\pi\mu} \left(\pi_2 \int_{\mathcal{E}_2} n_i G_{ij} \, ds(\mathbf{x}) - \int_{\mathcal{C}} f_i^D G_{ij} \, ds(\mathbf{x}) - \int_{\mathcal{P}} f_i G_{ij} \, ds(\mathbf{x}) \right). \quad (3.48)$$

The total velocity, \mathbf{u} , is found by adding the Poiseuille velocity. The unknown quantities in (3.48) are the disturbance tractions on the channel walls, the tractions on the particle and the disturbance pressure at the exit. The particle velocities are unknown but only enter the problem via the boundary condition on \mathcal{P} . The equation for the disturbance pressure means that we do not have to evaluate (3.48) at a point on \mathcal{E}_2 in order to obtain an extra equation for π_2 . Pozrikidis (2005b) notes the presence of numerical sensitivities in the boundary integral equation when \mathbf{x}_0 lies on \mathcal{E}_1 or \mathcal{E}_2 . We have side-stepped this issue by proceeding in line with Brenner (1971) and Pozrikidis (2005b) and derived an equation for the disturbance pressure using the Lorentz reciprocal relation.

There is a problem in equation (3.48) regarding the uniqueness of the solution. The equation does not permit a unique solution because an arbitrary multiple of the normal vector may be added to the particle's traction. Letting χ be an arbitrary constant and

mapping $\mathbf{f} \rightarrow \mathbf{f} + \chi \mathbf{n}$ in the integral over \mathcal{P} gives

$$\begin{aligned} \int_{\mathcal{P}} f_i G_{ij} \, ds(\mathbf{x}) &\rightarrow \int_{\mathcal{P}} (f_i + \chi n_i) G_{ij} \, ds(\mathbf{x}) \\ &= \int_{\mathcal{P}} f_i G_{ij} \, ds(\mathbf{x}) + \chi \int_{\mathcal{P}} n_i G_{ij} \, ds(\mathbf{x}) \\ &= \int_{\mathcal{P}} f_i G_{ij} \, ds(\mathbf{x}), \end{aligned} \quad (3.49)$$

since $\int_{\mathcal{P}} n_i G_{ij} \, ds(\mathbf{x}) = 0$ is one of the integral identities of Stokes flow. To render the solution unique and thus regularise equation (3.48) we add a ‘deflation’ term to the equation. The deflation term is a function of \mathbf{x}_0 , the particle shape and its tractions, and is defined to be

$$D_j(\mathbf{x}_0) = n_j(\mathbf{x}_0) \int_{\mathcal{P}} n_i f_i \, ds(\mathbf{x}), \quad (3.50)$$

which is not invariant under the mapping given above. We can show that the deflation term is zero. Thus addition of \mathbf{D} to equation (3.48) preserves the solution and ensures its uniqueness. Details on the deflation term can be found in Appendix B and Pozrikidis (1992).

In order to use (3.48) we need to find the disturbance pressure, π_2 , the disturbance tractions on \mathcal{C} and the tractions on \mathcal{P} . To calculate the disturbance tractions we require a boundary integral equation which is valid on the boundaries of the flow domain. Since the double-layer potential is absent from (3.48) the equation is continuous as the pole approaches the boundary of the flow domain. This would not be the case if the double-layer potential were present. Therefore equation (3.48) is valid when \mathbf{x}_0 lies on the boundary and is

$$0 = \pi_2 \int_{\mathcal{E}_2} n_i G_{ij} \, ds(\mathbf{x}) - \int_{\mathcal{C}} f_i^D G_{ij} \, ds(\mathbf{x}) - \int_{\mathcal{P}} f_i G_{ij} \, ds(\mathbf{x}) \quad (3.51)$$

when \mathbf{x}_0 lies on the channel walls since $\mathbf{u}^D = \mathbf{0}$ on \mathcal{C} , and

$$4\pi\mu u_j^D(\mathbf{x}_0) = \pi_2 \int_{\mathcal{E}_2} n_i G_{ij} \, ds(\mathbf{x}) - \int_{\mathcal{C}} f_i^D G_{ij} \, ds(\mathbf{x}) - \int_{\mathcal{P}} f_i G_{ij} \, ds(\mathbf{x}) \quad (3.52)$$

when \mathbf{x}_0 lies on the particle perimeter. To bring the unknown translational and angular velocities into equation (3.52) we substitute $\mathbf{u}^D = \mathbf{u} - \mathbf{u}^P$ into the equation and write the total velocity in terms of \mathbf{V} and $\mathbf{\Omega}$.

Before moving on we will confirm the validity of equations (3.51) and (3.52) by deriving them directly from the form of the general boundary integral equation applicable

when \mathbf{x}_0 lies on the domain boundary. When \mathbf{x}_0 lies on \mathcal{C} , equation (1.3.40) gives

$$\pi_2 \int_{\mathcal{E}_2} n_i G_{ij} \, ds(\mathbf{x}) - \int_{\mathcal{C}, \mathcal{P}} f_i^D G_{ij} \, ds(\mathbf{x}) + \mu \int_{\mathcal{P}} u_i^D T_{ijk} n_k \, ds(\mathbf{x}) = 2\pi\mu u_j^D(\mathbf{x}_0) = 0 \quad (3.53)$$

after applying the boundary conditions. Application of equation (1.3.40) to the Poiseuille flow and the particle gives

$$0 = - \int_{\mathcal{P}} f_i^P G_{ij} \, ds(\mathbf{x}) + \mu \int_{\mathcal{P}} u_i^P T_{ijk} n_k \, ds(\mathbf{x}) \quad (3.54)$$

where the left-hand side is zero because \mathbf{x}_0 lies outside of \mathcal{P} . Addition of equations (3.53) and (3.54) and elimination of the double-layer potential by equation (3.47) gives

$$0 = \pi_2 \int_{\mathcal{E}_2} n_i G_{ij} \, ds(\mathbf{x}) - \int_{\mathcal{C}} f_i^D G_{ij} \, ds(\mathbf{x}) - \int_{\mathcal{P}} f_i G_{ij} \, ds(\mathbf{x}) \quad (3.55)$$

which is identical to (3.51). Therefore we have verified that equation (3.51) is valid when \mathbf{x}_0 lies on the channel walls. When \mathbf{x}_0 lies on \mathcal{P} we obtain

$$2\pi\mu u_j^D(\mathbf{x}_0) = \pi_2 \int_{\mathcal{E}_2} n_i G_{ij} \, ds(\mathbf{x}) - \int_{\mathcal{C}, \mathcal{P}} f_i^D G_{ij} \, ds(\mathbf{x}) + \mu \int_{\mathcal{P}}^{PV} u_i^D T_{ijk} n_k \, ds(\mathbf{x}), \quad (3.56)$$

by considering the disturbance flow in the whole flow domain, and

$$-2\pi\mu u_j^P(\mathbf{x}_0) = - \int_{\mathcal{P}} f_i^P G_{ij} \, ds(\mathbf{x}) + \mu \int_{\mathcal{P}}^{PV} u_i^P T_{ijk} n_k \, ds(\mathbf{x}) \quad (3.57)$$

for the Poiseuille flow over the particle's domain, and where the minus sign on the left-hand side appears because the normal vector is directed out of \mathcal{P} . When we add equations (3.56) and (3.57) we cannot eliminate the double-layer potential because it takes its principal value, and so we get

$$\begin{aligned} 2\pi\mu (u_j^D(\mathbf{x}_0) - u_j^P(\mathbf{x}_0)) &= \pi_2 \int_{\mathcal{E}_2} n_i G_{ij} \, ds(\mathbf{x}) - \int_{\mathcal{C}} f_i^D G_{ij} \, ds(\mathbf{x}) \\ &\quad - \int_{\mathcal{P}} f_i G_{ij} \, ds(\mathbf{x}) + \mu \int_{\mathcal{P}}^{PV} u_i T_{ijk} n_k \, ds(\mathbf{x}). \end{aligned} \quad (3.58)$$

We can evaluate the double-layer potential by using the aforementioned stress tensor identities which take the values

$$\int_{\mathcal{P}} T_{ijk} n_k \, ds(\mathbf{x}) = -2\pi \delta_{ij}, \quad (3.59)$$

$$\epsilon_{lmi} \int_{\mathcal{P}} x_m T_{ijk} n_k \, ds(\mathbf{x}) = -2\pi \epsilon_{lmj} x_{0,m}, \quad (3.60)$$

when \mathbf{x}_0 lies on the boundary and where the signs on the right-hand side are due to the direction of the normal vector on \mathcal{P} . Therefore the double-layer potential is

$$\begin{aligned} \int_{\mathcal{P}}^{PV} u_i T_{ijk} n_k \, ds(\mathbf{x}) &= (V_i - \epsilon_{ilm} \Omega_l x_{c,m}) \int_{\mathcal{P}}^{PV} T_{ijk} n_k \, ds(\mathbf{x}) \\ &\quad + \epsilon_{ilm} \Omega_l \int_{\mathcal{P}}^{PV} x_m T_{ijk} n_k \, ds(\mathbf{x}) \\ &= -2\pi (V_j - \epsilon_{jlm} \Omega_l x_{c,m} + \epsilon_{jlm} \Omega_l x_{0,m}) \\ &= -2\pi u_j(\mathbf{x}_0) \end{aligned} \quad (3.61)$$

which upon substitution into (3.58) gives

$$4\pi\mu u_j^D(\mathbf{x}_0) = \pi_2 \int_{\mathcal{E}_2} n_i G_{ij} \, ds(\mathbf{x}) - \int_{\mathcal{C}} f_i^D G_{ij} \, ds(\mathbf{x}) - \int_{\mathcal{P}} f_i G_{ij} \, ds(\mathbf{x}) \quad (3.62)$$

which is identical to equation (3.52). We have now verified that equation (3.52) is valid when \mathbf{x}_0 lies on the particle perimeter.

We use the boundary element method (Pozrikidis 2002a) to obtain a linear system which represents the governing equations. The boundaries are discretised into elements upon which we evaluate the pertinent boundary integral equation. Evaluation of (3.51) with \mathbf{x}_0 on each of \mathcal{C} 's boundary elements will provide a sufficient number of equations for the unknown disturbance tractions on the walls. We have the same sufficiency on \mathcal{P} by equation (3.52), and equation (3.32) provides for π_2 . However we require three more equations to complement the unknown translational and angular velocities of the particle. Inclusion of the force equation (3.33) provides two equations and the z -component of the torque equation (3.34) provides the final equation. Therefore the number of unknowns equals the number of equations and so our system is complete. Once the disturbance pressure and the unknown tractions are known we may calculate the velocity at any point in the flow domain using

$$u_j(\mathbf{x}_0) = u_j^P(\mathbf{x}_0) + \frac{1}{4\pi\mu} \left(\pi_2 \int_{\mathcal{E}_2} n_i G_{ij} \, ds(\mathbf{x}) - \int_{\mathcal{C}} f_i^D G_{ij} \, ds(\mathbf{x}) - \int_{\mathcal{P}} f_i G_{ij} \, ds(\mathbf{x}) \right), \quad (3.63)$$

where we have added the Poiseuille velocity to get the total velocity on the left-hand side. To ascertain the important parameters in equations (3.32) and (3.63) we render them dimensionless by scaling distances by d , velocities by U_0 , and tractions and pressures by $\mu U_0/d$, to get

$$\hat{\pi}_2 = -\frac{3}{4} \int_{\mathcal{P}} \hat{\mathbf{u}}^P \cdot \hat{\mathbf{f}} \, d\hat{s} \quad (3.64)$$

for the disturbance pressure, where a circumflex indicates a dimensionless quantity, and

$$\hat{u}_j(\mathbf{x}_0) = \hat{u}_j^P(\mathbf{x}_0) + \frac{1}{4\pi} \left(\hat{\pi}_2 \int_{\mathcal{E}_2} n_i G_{ij} \, d\hat{s} - \int_{\mathcal{C}} \hat{f}_i^D G_{ij} \, d\hat{s} - \int_{\mathcal{P}} \hat{f}_i G_{ij} \, d\hat{s} \right) \quad (3.65)$$

for the boundary integral equation. Therefore it is clear that the flow is solely dependent on the shape, size and location of the particle via the integrals over \mathcal{P} . We have now fulfilled our aim of deriving the boundary integral equation for a channel containing a rigid particle.

3.2 Numerical method

As in the previous chapter we will discretise the boundary integral equations using the boundary element method and form the equations into the linear matrix system,

$$\mathbf{A} \cdot \mathbf{x} = \mathbf{b}, \quad (3.66)$$

where \mathbf{A} is the square ‘influence’ matrix, \mathbf{x} is the vector of unknown tractions, the disturbance pressure and the particle velocities and \mathbf{b} is the vector of known values. To apply the boundary element method we discretise the channel walls into $N_{\mathcal{C}}$ equally-sized straight elements. We may discretise \mathcal{P} into straight lines, circular arcs or cubic splines (e.g. Pozrikidis 2002a). Here, for simplicity, we choose to use straight boundary elements for the particle and discretise the perimeter into $N_{\mathcal{P}}$ equally-sized straight elements. The numerical scheme is therefore $O(h)$ accurate where h is the element length. On each of the elements we set the unknown traction to a constant 2-vector. We label the disturbance traction on the r^{th} element of \mathcal{C} as \mathbf{f}_r^D and the traction of the r^{th} element of \mathcal{P} as \mathbf{f}_r . The vector of unknowns is

$$\mathbf{x} = \left[\mathbf{F}_{\mathcal{C}}^D \quad \mathbf{F}_{\mathcal{P}} \quad \pi_2 \quad \mathbf{V} \quad \Omega \right]^T \quad (3.67)$$

where $\mathbf{F}_{\mathcal{C}}^D$ is a vector containing the $2N_{\mathcal{C}}$ components of the disturbance tractions of \mathcal{C} , $\mathbf{F}_{\mathcal{P}}$ is a vector which holds the $2N_{\mathcal{P}}$ components of the tractions of \mathcal{P} , \mathbf{V} is the 2-vector representing the particle’s translational velocity and the superscript T means transpose.

The vectors \mathbf{F}_C^D , \mathbf{F}_P and \mathbf{V} are defined to be

$$\mathbf{F}_C^D = \begin{bmatrix} f_{x,1}^D & f_{y,1}^D & \cdots & f_{x,N_C}^D & f_{y,N_C}^D \end{bmatrix}, \quad (3.68)$$

$$\mathbf{F}_P = \begin{bmatrix} f_{x,1} & f_{y,1} & \cdots & f_{x,N_P} & f_{y,N_P} \end{bmatrix}, \quad (3.69)$$

$$\mathbf{V} = \begin{bmatrix} V_x & V_y \end{bmatrix}. \quad (3.70)$$

We will now derive the discretised analogues of the governing equations. The equation for the disturbance pressure (3.32) is approximated by

$$\begin{aligned} 0 &= Q \pi_2 + \int_{\mathcal{P}} \mathbf{u}^P \cdot \mathbf{f} \, ds(\mathbf{x}) \\ &\approx Q \pi_2 + \sum_{r=1}^{N_P} u^P(\mathbf{x}_{m,r}) f_{x,r} l_r, \end{aligned} \quad (3.71)$$

where u^P is the x -component of the Poiseuille velocity, $\mathbf{x}_{m,r} = (x_{m,r}, y_{m,r})$ is the mid-point of the r^{th} element and l_r is the element length. By defining,

$$\mathbf{W}_P = \begin{bmatrix} u^P(\mathbf{x}_{m,1}) l_1 & 0 & \cdots & u^P(\mathbf{x}_{m,N_P}) l_{N_P} & 0 \end{bmatrix}, \quad (3.72)$$

we may write (3.71) as the product of two vectors,

$$\begin{bmatrix} \mathbf{0} & \mathbf{W}_P & Q & \mathbf{0} & 0 \end{bmatrix} \cdot \mathbf{x} = 0. \quad (3.73)$$

The discretisation of the force equation (3.33) is

$$F_i = \sum_{r=1}^{N_P} \int_{E_r} f_{i,r} \, ds(\mathbf{x}) \approx \sum_{r=1}^{N_P} f_{i,r} l_r = 0 \quad (3.74)$$

which by defining

$$\mathbf{L}_P = \begin{bmatrix} l_1 & 0 & \cdots & l_{N_P} & 0 \\ 0 & l_1 & \cdots & 0 & l_{N_P} \end{bmatrix} \quad (3.75)$$

may be written as

$$\begin{bmatrix} \mathbf{0} & \mathbf{L}_P & \mathbf{0} & \mathbf{0} & 0 \end{bmatrix} \cdot \mathbf{x} = 0. \quad (3.76)$$

Similarly for the z -component of the torque equation (3.34) we have

$$\epsilon_{zjk} \int_{\mathcal{P}} (x_j - x_{c,j}) f_k \, ds(\mathbf{x}) = 0 \quad (3.77)$$

which we can represent as

$$\begin{bmatrix} \mathbf{0} & \mathbf{T}_P & \mathbf{0} & \mathbf{0} & 0 \end{bmatrix} \cdot \mathbf{x} = 0 \quad (3.78)$$

where the row vector,

$$\mathbf{T}_{\mathcal{P}} = \begin{bmatrix} -(y_{m,1} - y_c)l_1 & (x_{m,1} - x_c)l_1 & \cdots & -(y_{m,N_{\mathcal{P}}} - y_c)l_{N_{\mathcal{P}}} & (x_{m,N_{\mathcal{P}}} - x_c)l_{N_{\mathcal{P}}} \end{bmatrix}, \quad (3.79)$$

and where the particle centre, $\mathbf{x}_c = (x_c, y_c)$. To complete the construction of the linear system we will discretise the boundary integral equations using the procedure detailed in section 2.2 of the previous chapter. First we will place the pole, \mathbf{x}_0 , on the channel walls and write equation (3.51) as

$$\int_{\mathcal{C}} f_i^D G_{ij} \, ds(\mathbf{x}) + \int_{\mathcal{P}} f_i G_{ij} \, ds(\mathbf{x}) + n_j(\mathbf{x}_0) \int_{\mathcal{P}} n_i f_i \, ds(\mathbf{x}) - \pi_2 \int_{\mathcal{E}_2} n_i G_{ij} \, ds(\mathbf{x}) = 0, \quad (3.80)$$

where we have also included the deflation term (3.50). Taking the equation term by term, we discretise the integral over \mathcal{C} to get

$$\int_{\mathcal{C}} f_i^D G_{ij} \, ds(\mathbf{x}) \approx \sum_{r=1}^{N_{\mathcal{C}}} f_{i,r}^D \tilde{G}_{ij,r} = I_{\mathcal{C},j}^G(\mathbf{x}_0) \cdot [F_{\mathcal{C}}^D]^T \quad (3.81)$$

where $\tilde{G}_{ij,r}$ contains the integrated Green's function and is defined by equation (2.55), and $I_{\mathcal{C},j}^G(\mathbf{x}_0)$ is defined by (2.61), which is

$$\mathbf{I}_{\mathcal{C},j}^G(\mathbf{x}_0) = \begin{bmatrix} \tilde{G}_{xj,1} & \tilde{G}_{yj,1} & \cdots & \tilde{G}_{xj,N_{\mathcal{C}}} & \tilde{G}_{yj,N_{\mathcal{C}}} \end{bmatrix}. \quad (3.82)$$

The calculation of $\tilde{G}_{ij,r}$ was carried out by numerically integrating the Green's function using Gauss-Legendre quadrature, details of which may be found in Appendix A and Pozrikidis (1998). We typically used 20 base-points in the quadrature. For the integrals over \mathcal{P} we have

$$\int_{\mathcal{P}} f_i G_{ij} \, ds(\mathbf{x}) + n_j(\mathbf{x}_0) \int_{\mathcal{P}} n_i f_i \, ds(\mathbf{x}) \approx \sum_{r=1}^{N_{\mathcal{P}}} f_{i,r} \tilde{G}_{ij,r} + n_j(\mathbf{x}_0) \sum_{r=1}^{N_{\mathcal{P}}} n_{i,r} f_{i,r} l_r = I_{\mathcal{P},j}^G(\mathbf{x}_0) \cdot [F_{\mathcal{P}}]^T \quad (3.83)$$

where we have included the deflation term defined in equation (3.50), and $I_{\mathcal{P},j}^G(\mathbf{x}_0)$ is defined to be

$$\mathbf{I}_{\mathcal{P},j}^G(\mathbf{x}_0) = \begin{bmatrix} \tilde{G}_{xj,1} & \tilde{G}_{yj,1} & \cdots & \tilde{G}_{xj,N_{\mathcal{P}}} & \tilde{G}_{yj,N_{\mathcal{P}}} \end{bmatrix} + n_j(\mathbf{x}_0) \begin{bmatrix} n_{x,1}l_1 & n_{y,1}l_1 & \cdots & n_{x,N_{\mathcal{P}}}l_{N_{\mathcal{P}}} & n_{y,N_{\mathcal{P}}}l_{N_{\mathcal{P}}} \end{bmatrix}, \quad (3.84)$$

and where $\mathbf{n}_r = (n_{x,r}, n_{y,r})$ is the unit normal vector on the r^{th} element of \mathcal{P} .

The integral over \mathcal{E}_2 can be calculated exactly using the formulae given in equations (2.44) and (2.45) of the previous chapter. Putting equations (3.81) and (3.83) together and

defining,

$$I_{\mathcal{E}_2,j}^G = \int_{\mathcal{E}_2} n_i G_{ij} \, ds(\mathbf{x}), \quad (3.85)$$

we can represent the boundary integral equation (3.80) as

$$\begin{bmatrix} \mathbf{I}_{\mathcal{C},j}^G & \mathbf{I}_{\mathcal{P},j}^G & -I_{\mathcal{E}_2,j}^G & \mathbf{0} & 0 \end{bmatrix} \cdot \mathbf{x} = 0. \quad (3.86)$$

Re-evaluation of this equation with \mathbf{x}_0 equal to the mid-point of each of the channel walls' boundary elements creates $N_{\mathcal{C}}$ pairs of equations which are assembled into the matrix,

$$\begin{bmatrix} \mathcal{C}_{\mathcal{C}} & \mathcal{C}_{\mathcal{P}} & \mathcal{C}_{\mathcal{E}_2} & \mathbf{0} & 0 \end{bmatrix} \cdot \mathbf{x} = \mathbf{0}, \quad (3.87)$$

where each of $\mathcal{C}_{\mathcal{C}}$, $\mathcal{C}_{\mathcal{P}}$ and $\mathcal{C}_{\mathcal{E}_2}$ consist of the $N_{\mathcal{C}}$ pairs of $\mathbf{I}_{\mathcal{C},j}^G(\mathbf{x}_0)$, $\mathbf{I}_{\mathcal{P},j}^G(\mathbf{x}_0)$ and $-I_{\mathcal{E}_2,j}^G(\mathbf{x}_0)$ respectively. The matrix labels are in the form A_B in order to clearly identify A as the boundary on which the pole lies, and B as the boundary over which we are integrating. So for example, the matrix $\mathcal{C}_{\mathcal{P}}$ has the pole on \mathcal{C} and it corresponds to the integral over \mathcal{P} . The boundary integral equation for \mathbf{x}_0 on the particle boundary is

$$\int_{\mathcal{C}} f_i^D G_{ij} \, ds(\mathbf{x}) + \int_{\mathcal{P}} f_i G_{ij} \, ds(\mathbf{x}) - \pi_2 \int_{\mathcal{E}_2} n_i G_{ij} \, ds(\mathbf{x}) + 4\pi\mu u_j(\mathbf{x}_0) = 4\pi\mu u_j^P(\mathbf{x}_0). \quad (3.88)$$

We have already discussed the discretisation of the integrals in this equation. It remains to discretise the total velocity on the left-hand side and write down the components of the Poiseuille velocity on the right-hand side. By writing the total velocity in terms of the unknown translational and angular velocities, and using $\boldsymbol{\Omega} = \Omega \mathbf{k}$, we get

$$u_j(\mathbf{x}_0) = V_j + \epsilon_{jkl} \Omega_k (x_{0,l} - x_{c,l}) = V_j + \epsilon_{zlj} \Omega (x_{0,l} - x_{c,l}), \quad (3.89)$$

which we can write in matrix form as

$$u_j(\mathbf{x}_0) = \begin{bmatrix} \delta_{jx} & \delta_{jy} & \epsilon_{zlj} (x_{0,l} - x_{c,l}) \end{bmatrix} \cdot \begin{bmatrix} V_x & V_y & \Omega \end{bmatrix}^T. \quad (3.90)$$

By defining,

$$\mathbf{I}_{u,j} = 4\pi\mu \begin{bmatrix} \delta_{jx} & \delta_{jy} \end{bmatrix}, \quad (3.91)$$

$$I_{\Omega,j}(\mathbf{x}_0) = 4\pi\mu \epsilon_{zlj} (x_{0,l} - x_{c,l}), \quad (3.92)$$

we we can write the discretised version of equation (3.88) as

$$\begin{bmatrix} \mathbf{I}_{\mathcal{C},j}^G & \mathbf{I}_{\mathcal{P},j}^G & -I_{\mathcal{E}_2,j}^G & \mathbf{I}_{u,j} & I_{\Omega,j}(\mathbf{x}_0) \end{bmatrix} \cdot \mathbf{x} = 4\pi\mu u_j^P(\mathbf{x}_0) \quad (3.93)$$

Re-evaluation of this equation with \mathbf{x}_0 at the mid-point of each of the particle's boundary

elements creates $N_{\mathcal{P}}$ pairs of equations which we assemble into the matrix,

$$\begin{bmatrix} \mathcal{P}_{\mathcal{C}} & \mathcal{P}_{\mathcal{P}} & \mathcal{P}_{\mathcal{E}_2} & \mathcal{P}_u & \mathcal{P}_{\Omega} \end{bmatrix} \cdot \mathbf{x} = \mathbf{b}_{\mathcal{P}}, \quad (3.94)$$

where each of $\mathcal{P}_{\mathcal{C}}$, $\mathcal{P}_{\mathcal{P}}$, $\mathcal{P}_{\mathcal{E}_2}$, \mathcal{P}_u and \mathcal{P}_{Ω} consist of the $N_{\mathcal{P}}$ pairs of $\mathbf{I}_{\mathcal{C},j}^G(\mathbf{x}_0)$, $\mathbf{I}_{\mathcal{P},j}^G(\mathbf{x}_0)$, $-\mathbf{I}_{\mathcal{E}_2,j}^G(\mathbf{x}_0)$, $\mathbf{I}_{u,j}$ and $\mathbf{I}_{\Omega,j}(\mathbf{x}_0)$ respectively, and $\mathbf{b}_{\mathcal{P}}$ is the vector containing the $N_{\mathcal{P}}$ pairs of components of the Poiseuille velocity for the different values of \mathbf{x}_0 on the particle's boundary elements.

We have now completed the discretisation of the boundary integral equations, the disturbance pressure equation and the force and torque equations. We assemble the master linear system from equations (3.73), (3.76), (3.78), (3.87) and (3.94) to get

$$\begin{bmatrix} \mathcal{C}_{\mathcal{C}} & \mathcal{C}_{\mathcal{P}} & \mathcal{C}_{\mathcal{E}_2} & \mathbf{0} & \mathbf{0} \\ \mathcal{P}_{\mathcal{C}} & \mathcal{P}_{\mathcal{P}} & \mathcal{P}_{\mathcal{E}_2} & \mathcal{P}_u & \mathcal{P}_{\Omega} \\ \mathbf{0} & \mathbf{W}_{\mathcal{P}} & Q & \mathbf{0} & \mathbf{0} \\ \mathbf{0} & \mathbf{L}_{\mathcal{P}} & \mathbf{0} & \mathbf{0} & \mathbf{0} \\ \mathbf{0} & \mathbf{T}_{\mathcal{P}} & 0 & \mathbf{0} & \mathbf{0} \end{bmatrix} \cdot \mathbf{x} = \begin{bmatrix} \mathbf{0} \\ \mathbf{b}_{\mathcal{P}} \\ 0 \\ \mathbf{0} \\ 0 \end{bmatrix} \quad (3.95)$$

which is in our desired form. The rows and columns of the 'influence' matrix in (3.95) may contain one or more rows and columns. For example, $\mathcal{C}_{\mathcal{C}}$ is a matrix with dimensions $2N_{\mathcal{C}} \times 2N_{\mathcal{C}}$, where the rows correspond to the x and y components of the pertinent boundary integral equation with \mathbf{x}_0 placed on an element of \mathcal{C} . The size of the 'influence' matrix is $(2N_{\mathcal{C}} + 2N_{\mathcal{P}} + 4) \times (2N_{\mathcal{C}} + 2N_{\mathcal{P}} + 4)$. In our simulations we took $N_{\mathcal{C}} = 800$ and $N_{\mathcal{P}} = 316$. We increased $N_{\mathcal{P}}$ for larger particles to maintain the element length, and decreased $N_{\mathcal{P}}$ for smaller particles. Our formulation caters for an arbitrary shaped particle but in the simulations we restrict our attention to a circular particle of radius a .

One of the features of Stokes flow is its reversibility, i.e. the Stokes equation is invariant to a transformation whereby the pressure and velocity fields are negated. Therefore fluid particles in a Stokes flow will eventually regain their original position if the flow is reversed. More details may be found in Acheson (1990). Let us consider a circular particle translating along the channel and suppose the particle is also moving towards one of the channel walls. Now reverse the flow by negating the pressure and velocity fields. Due to reversibility the particle will start to return to its original position. Therefore the particle will start to move away from the wall it was travelling towards and back to its original location. However the velocity shear from the incident flow across the particle before and after the flow reversal are equal but opposite, implying that in one case the particle moves towards a region of higher shear and in the other case towards a region of lower shear. We have a contradiction and so the particle cannot move towards either channel wall. Therefore the particle must remain at its initial axial location and $V_y = 0$. For a geometrical argument see Cox and Mason (1971). Furthermore, by symmetry a circular particle will have constant V_x and Ω .

Now we can build the linear system and solve it using a standard method. We found it practical to use Gaussian elimination to find the tractions, disturbance pressure and the

particle velocities. The solution was then used in equation (3.63) to find the velocity at any point in the flow domain.

We calculated the flow streamlines by integrating the equation

$$\frac{d\mathbf{x}}{ds} = \mathbf{u}(\mathbf{x}) \quad (3.96)$$

along the streamline, where \mathbf{x} is the position vector of a point on the streamline, s measures the arc-length along the streamline and the velocity on the right-hand side is computed from equation (3.63). We also calculated the streamlines relative to a frame of reference fixed on the particle, which we will call pathlines to distinguish them from the streamlines. To calculate the pathlines, we integrated the kinematic equation,

$$\frac{d\mathbf{x}'}{dt} = \mathbf{u}(\mathbf{x}') - V_x \mathbf{i}, \quad (3.97)$$

where \mathbf{x}' is the position vector of a point moving with the frame of reference, \mathbf{u} is again calculated from equation (3.63), and V_x is the x -component of the particle's translational velocity. We used the adaptive time-stepping Runge-Kutta-Fehlberg method (e.g. Atkinson 1978) to integrate (3.97).

3.3 Validation

For all validation checks and results we truncated the channel so that $l = 12d$. We found this truncation length sufficient for the disturbance flow to decay as per our initial assumptions. For this channel length, the Poiseuille pressure drop is $24\mu U_0/d$ between the entrance and the exit. Dimensional analysis shows the importance of the dimensionless particle radius ρ , and the centreline offset, σ , which are defined to be

$$\rho = \frac{a}{d}, \quad (3.98)$$

$$\sigma = \frac{y_c}{d}. \quad (3.99)$$

We placed the particle at the mid-point of the channel, $x/d = 6$, and varied the offset from the centreline, σ , and its dimensionless radius, ρ .

As a check on the numerical implementation, we confirmed that the discretised form of the integral identities (1.3.34) and (1.3.31) were satisfied to within an acceptable tolerance. We checked the validity of both identities by setting \mathbf{x}_0 to the mid-point of every boundary element and to several points inside and outside of the flow domain. Equation (1.3.34) was satisfied to within a numerical tolerance of $10^{-9}d$ and (1.3.31) was satisfied to within 10^{-9} . We also checked that the discretised value of the integral in the deflation term was effectively zero for a range of ρ and σ .

For each simulation, we checked that the x -components of the disturbance tractions on the walls decayed to zero as we approached the entrance and the exit. The x -components of the disturbance tractions on the elements close to \mathcal{E}_1 and \mathcal{E}_2 were typically $10^{-5}\mu U_0/d$.

We expect the y -component of the disturbance pressure to tend to zero at the entrance whereas we found that $f_y^D \approx 10^{-5} \mu U_0/d$. At the exit, the y -component of the disturbance traction should tend to the disturbance pressure. We found the difference between π_2 and f_y^D at this point to be no more than 0.001%. For all of the simulations the disturbance velocity decayed as we approach \mathcal{E}_1 and \mathcal{E}_2 with the disturbance velocity components no more than $10^{-6} U_0$ at the entrance or exit. Figure 3.2 shows the decay of the x -component of the velocity along the channel centreline between \mathcal{E}_1 and the particle, which lies on the centreline with $\rho = 0.5$ and its centre at $(6d, 0)$. At $x/d = 5.5$ the velocity equals the particle's translational velocity, $V_x = 0.888$. We can see that the ve-

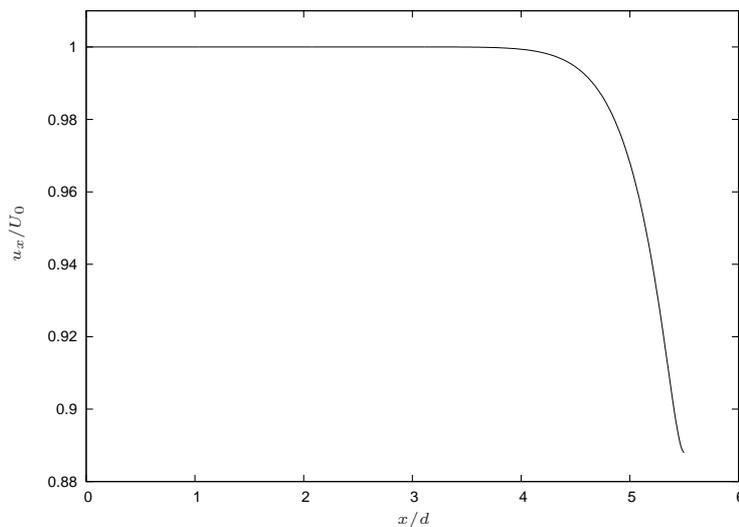


Figure 3.2 : Decay of the disturbance to the x -component of velocity along the centreline for $\rho = 0.5$ and $\sigma = 0$. The particle boundary is at $x/d = 5.5$.

locity rapidly attains its Poiseuille centreline speed as we move away from the particle, where the disturbance is at its maximum. As we move away from the particle along the centreline the disturbance velocity decays to 0.5% of its peak value at $x/d = 4$ and 0.02% at $x/d = 3.5$, which represent 3 and 4 radii from the particle boundary respectively. We performed the same check for a range of values of ρ and σ with very similar results for the disturbance velocity decay.

To validate the numerical solution we used the configuration described above as our reference configuration. Firstly we computed the solution for a longer channel with $l = 24d$ while preserving the element length, with respect to the reference configuration. To test the effect of the number of boundary elements we took the reference configuration and doubled the number of elements on each of the boundaries. In all cases we found that the tractions in the solution vector differed by less than $0.002 \mu U_0/d$ from the values obtained for the reference configuration.

As a final check on the equations which are used to construct the linear system, we calculated the force and torque using (3.74) and (3.77). Both quantities were effectively zero as the force is approximately $10^{-14} \mu U_0$ and the torque is approximately $10^{-14} \mu U_0 d$.

To verify the disturbance tractions on \mathcal{C} we calculated the disturbance pressure from

equation (3.38) which uses the disturbance tractions on the wall. For a range of radii, the difference between the two independently calculated values of π_2 was no more than 0.0001%. The y -components of the disturbance tractions were verified by equation (3.39), which was satisfied to within a numerical tolerance of $10^{-10} \mu U_0/d$.

The only remaining quantities in the solution vector which require checking are the particle velocities. We expect the particle to ‘slip’ in the fluid relative to the Poiseuille velocity calculated at the particle’s centre. For a range of ρ and σ we found V_x was less than the Poiseuille velocity calculated at $y = y_c$. Due to the reversibility of Stokes flow we expect $V_y = 0$ and we find that this condition is met to a very fine degree of accuracy in our numerical solution. When we reduce the particle radius to zero the particle tends to a fluid element and thus it will not cause a disturbance flow. Therefore we expect the translational velocity of the particle to equal the Poiseuille velocity calculated at the particle centre in the limit of vanishing particle radius. Furthermore the angular velocity may be checked against the local vorticity since we expect the angular velocity to equal half the vorticity of the Poiseuille flow. Therefore we expect

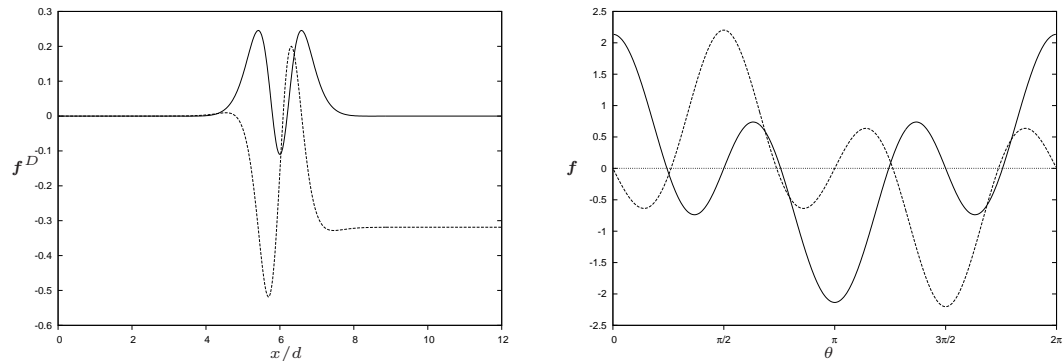
$$\Omega \approx \frac{1}{2} |\nabla \wedge \mathbf{u}^P| = \frac{1}{2} \left| -\frac{2 U_0}{d^2} y \mathbf{k} \right| = \frac{U_0}{d^2} y. \quad (3.100)$$

We set $\rho = 0.01$ and computed \mathbf{V} and Ω for σ between 0 and 0.9. For $y_c/d \leq 0.7$ the error in V_x with respect to the computed Poiseuille velocity was less than 0.04%, and the error in Ω was less than 0.05%, with respect to equation (3.100). For larger σ the error increased. For example, the error is 0.5% when $\sigma = 0.9$ for both V_x and Ω .

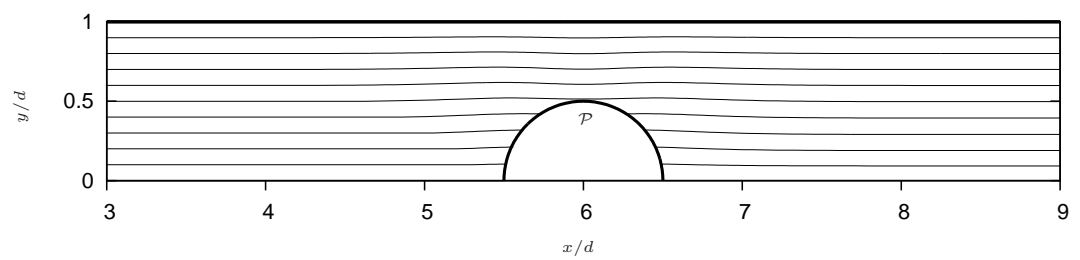
We have checked the geometry and the numerical solution to the discretised boundary integral equations and found that the computed values show excellent agreement with the theoretical predictions.

3.4 Results

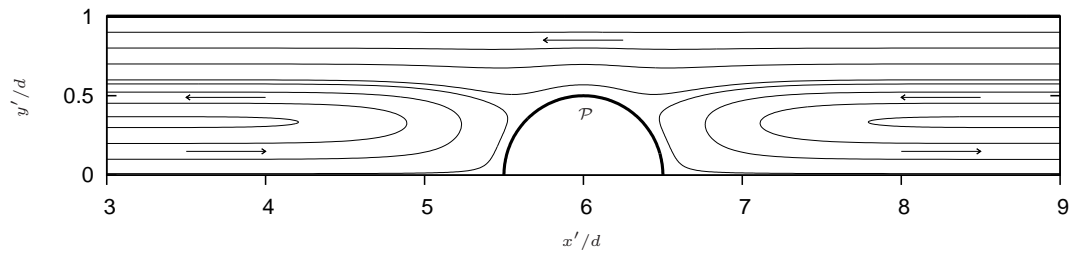
In all results we truncate the channel length so that $l = 12d$. In the first set of results we set $\rho = 0.5$ and place the particle on the centreline so that $\sigma = 0$. The disturbance tractions on the upper wall and the particle tractions are shown in figure 3.3. The lower wall disturbance tractions are not shown because the x -component is identical to that on the upper wall and the y -component is equal to the negated disturbance traction on the upper wall, due to the opposite direction of the normal vector. The decay of the disturbance traction to a steady value is evident as we move away from the particle. The x -component decays to zero at the entrance and exit. The y -component decays to zero at the entrance but tends to the negated value of the disturbance pressure at the exit due to the direction of the normal vector on the upper wall. For these parameter values $V_x = 0.888 U_0$ and $\pi_2 = -0.319 \mu U_0/d$. The values of V_y and Ω are effectively zero. Therefore the particle’s presence increases the pressure drop by only 1.3%. The normal and tangential components of the particle tractions are shown in figure 3.3 (b). The normal component of the particle traction, $\mathbf{f} \cdot \mathbf{n}$, is symmetric about $\theta = \pi$ which implies $\mathbf{f} \cdot \mathbf{n}$ is equal for



(a) The x (—) and y (---) components of the disturbance traction on the upper channel wall vs. x/d . (b) The normal (—) and tangential (---) components of the particle traction vs. θ which is zero at the right-most point of the particle.



(c) Instantaneous streamlines in a section of the upper half-channel.



(d) Pathlines in a section of the upper half-channel. The frame of reference is moving with the particle. The arrows indicate the flow direction relative to the particle.

Figure 3.3 : Upper wall disturbance tractions, particle tractions, streamlines and pathlines for $\rho = 0.5$ and $\sigma = 0$.

equal values of x/d . We expect this behaviour due to the symmetry of the flow geometry in this case. The particle's tangent vector is directed in an anti-clockwise direction. The tangential component, $\mathbf{f} \cdot \mathbf{t}$, on the upper half-perimeter is symmetric about $\theta = \pi/2$ and symmetric on the lower half-perimeter about $\theta = 3\pi/2$. It is interesting to note that there are six points on the particle perimeter where the tangential components of the traction change sign. As we saw in the previous chapter, when the tangential component of the traction changed sign there was a stagnation point and a sudden flow reversal on either side of the point. These points lie at approximately $\theta = n\pi/4$ where $n = 0, 1, 3, 4, 5$ and 7 . Figure 3.3 (c) shows the instantaneous streamlines in a truncated portion of the upper half-channel. Only the upper half is shown because the flow is symmetrical about $y/d = 0$. The streamlines only deviate from lines parallel to the y -axis close to the particle. The pathlines shown in figure 3.3 (d), for the same channel region, show the flow behaviour relative to the particle. The frame of reference moves with the particle's

constant translational velocity. The arrows in the figure indicate the direction of the flow relative to the particle. There are stagnation points at $\theta = 0$ and $\theta = \pi$. The streamline which starts at $y/d = 0$ on \mathcal{E}_1 terminates at a stagnation point on the particle boundary, corresponding to $\theta = \pi$. The fluid close to the centreline moves towards the particle when $x/d < 5.5$ in the region indicated by the bottom-left arrow. When the streamline approaches the particle it moves away from the centreline and into a region of slower moving fluid, where it travels back towards the entrance, relative to the particle. The fluid close to the exit may be divided into three regions; the first region is close to the wall and is not significantly affected by the particle's presence, the second, which at the exit lies in the range $0.33 < |y/d| < 0.57$, moves closer to the particle where the fluid moves towards the centreline and into the third region, which moves faster than the particle. The location of the stagnation points on the particle's upper half-perimeter can be inferred from figure 3.3 (d). For example, for the pathlines starting at the exit, and with y/d between 0.57 and 0.6, there will be a pathline which stagnates on the particle's boundary because the pathlines diverge, with one passing over the top of the particle and the other moving towards the centreline before travelling to the exit. Therefore stagnation points occur at all the points where the tangential component of the particle traction are zero. Increasing the size of the particle while keeping $\sigma = 0$ does not materially change the behaviour of the flow. For example, when $\rho = 0.9$ the disturbance pressure, $\pi_2 = -7.778 \mu U_0/d$, and $V_x = 0.712 U_0$. The disturbance pressure represents a 32.4% rise in the Poiseuille pressure drop.

In the next set of results we set $\rho = 0.5$ and $\sigma = 0.25$. For these parameters the particle translates with $V_x = 0.816 U_0$ and rotates with $\Omega = 0.210 U_0/d$ which is anti-clockwise. The translational velocity is smaller than when the particle was positioned on the centreline. The disturbance pressure drop is $0.993 \mu U_0/d$, which represents an increase to the Poiseuille pressure drop of 4.1%, and is higher than for the same sized particle located on the centreline. At first sight this may seem counter-intuitive because an off-centre particle induces a greater disturbance pressure. However we will see that when we break the flow symmetry, by placing the particle away from the centreline, we cause a significant increase in the maximum value of the boundary tractions. Since the disturbance pressure is calculated from the boundary tractions the disturbance pressure increases. In figures 3.4 (a) and 3.4 (b) we show the distribution of the disturbance tractions on both walls, where we have used the same scale on the traction axis to demonstrate the difference in magnitude. All components at the entrance are zero and the y -component tends to the disturbance pressure, $\pi_2 = -0.993 \mu U_0/d$, at the exit. The opposite sign of f_y^D on the lower wall is due to the normal vector which is oriented in the opposite direction. Comparison of the disturbance tractions on the upper wall, depicted in figures 3.3 (a) and 3.4 (a), shows that the profiles are very similar but the latter demonstrates a significant amplification. The x component of the disturbance traction on the lower wall does not change significantly while the y -component increases in the right-hand half of the channel and does not exhibit the peaked profile of the top wall. The maximum values of the x and y components of f^D on the top wall are approximately 6 and 8 times larger when

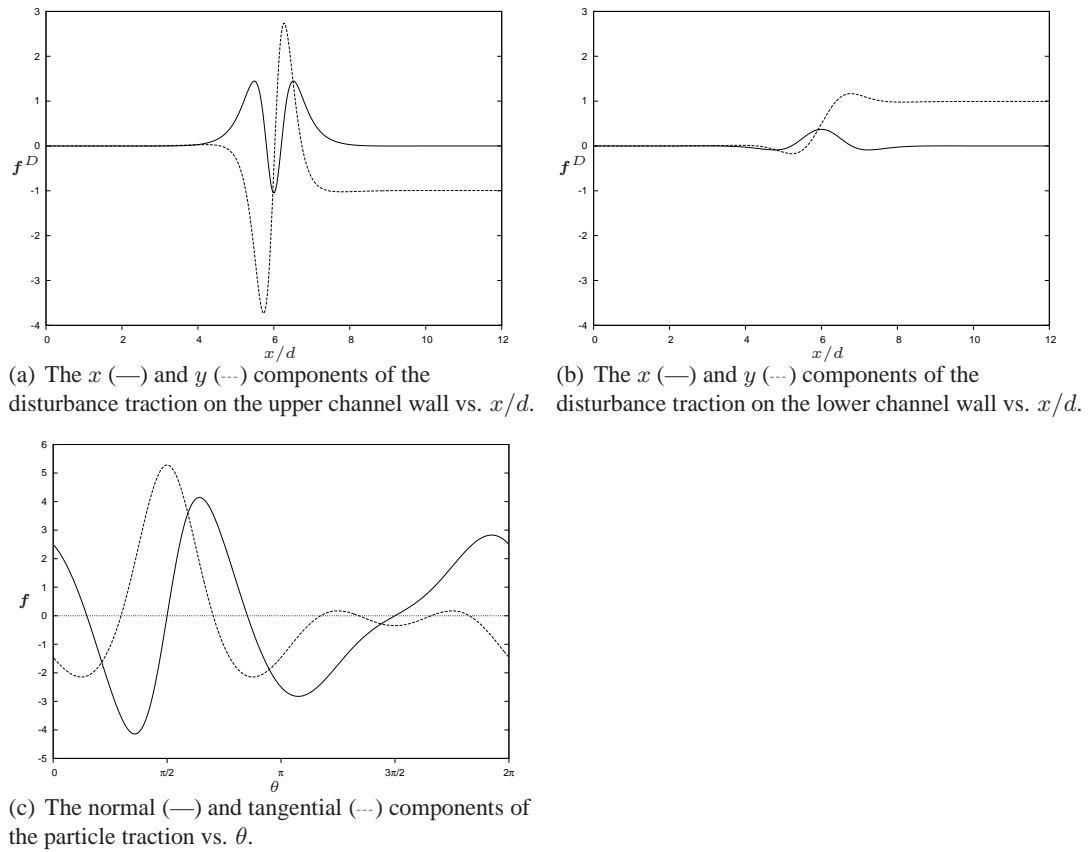


Figure 3.4 : Tractions on the channel walls and the particle for $\rho = 0.5$ and $\sigma = 0.25$.

$\sigma = 0.25$ than when $\sigma = 0$. From equation (3.37) we can see that f_x^D directly affects the disturbance pressure, and so π_2 will increase. The particle tractions are shown in figure 3.4 (c) where we can see that the normal component's symmetry about $\theta = \pi$ has disappeared. The tangential component of the particle traction has preserved its symmetry, whereby $\mathbf{f} \cdot \mathbf{t}$ is symmetric about $\theta = \pi/2$ on the upper half-perimeter, and symmetric about $\theta = 3\pi/2$ on the lower half-perimeter. The normal and tangential components of the tractions are approximately 2–3 times greater than for the centred particle. The tangential component of the particle traction is zero for six values of θ with two on the top half-perimeter and four on the lower. Previously we saw that stagnation points occurred at these points. However the particle is now rotating and so stagnation points will not occur on its boundary. The pathlines for the flow are plotted in figure 3.5 where the arrows show the direction of the fluid relative to the particle. The flow in the upper half-channel is similar in behaviour to that in the previous set of results where $\sigma = 0$. The lower half-channel now exhibits two interesting features. The first is the presence of eddies which lie upstream and downstream of the particle and below the channel's centreline. In both eddies the fluid rotates in a clockwise direction. The second feature relates to the behaviour of the velocity on the segment of the mid-line, $x/d = 6$, below the particle, particularly around $y/d = -0.479$. Fluid below this value is moving slower in the x -direction than the particle and so will move towards the entrance, relative to the particle.

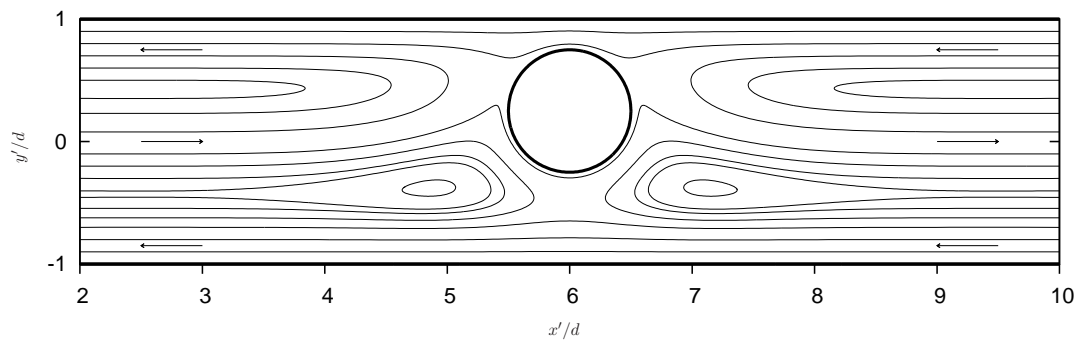


Figure 3.5 : Pathlines in a section of the channel for $\rho = 0.5$ and $\sigma = 0.25$. The particle rotates anti-clockwise and the fluid in the eddies rotates clockwise. The frame of reference is moving with the particle. The arrows indicate the flow direction relative to the particle.

Fluid above this critical point will continue to the exit in the same way as the streamline which skirts the underside of the particle in the figure. Since the y -component of velocity is zero on the mid-line, the point $(6, -0.479)d$ is a saddle-like critical point in the flow. Eddies similar to the ones seen here were studied and photographed by Hasimoto and Sano (1980), who also examined the flow around two stationary cylinders.

Although it is not evident from figure 3.5, there is a small region close to the particle in which pathlines orbit the particle in an anti-clockwise direction. Jeffrey and Onishi (1981) show a circulating region of fluid around their rotating cylinder above a plane wall. In figure 3.5, pathlines started from $(6d, qd)$ where $-0.284 \leq q/d < -0.25$ move anti-clockwise around the particle demonstrating the presence of a ‘captured’ layer of thickness $0.034d$. The key differences between this set of results and the previous one is the presence of eddies, the increased disturbance pressure, the increased boundary tractions and the presence of pathlines circulating around the particle. We conclude that the increased disturbance pressure drop is due to the off-centre location of the particle which causes a significant increase to the boundary tractions, especially in the region of the wall closest to the particle.

For the next set of results we maintain $\sigma = 0.25$ and increase the particle size to $\rho = 0.7$ so that the gap between the top of the particle and the top wall reduces to $0.05d$. The disturbance pressure $\pi_2 = -7.454 \mu U_0/d$, which represents a 31% rise to the Poiseuille pressure drop. The particle’s velocities are $V_x = 0.706 U_0$ and $\Omega = 0.167 U_0/d$. When a particle of this size is located on the centreline, $\pi_2 = -1.506 \mu U_0/d$. The pathlines for the flow are shown in figure 3.6 where again we can see that eddies are present in the flow, and are about the same size as in figure 3.5. The particle has a layer of fluid which circulates around its perimeter, although the thickness of the ‘captured’ layer has reduced to $0.011d$.

So far we have discussed the flow for specific values of ρ and σ . Now we look at how the pressure and particle velocities vary with ρ and σ . In figure 3.7 we show how the disturbance pressure varies with ρ for a centred particle and for two particles with $\sigma = 0.25$ and 0.5 . In figure 3.7 (a) we can see that the behaviour is qualitatively similar for all three values of σ . For small ρ the disturbance pressure increases at a very low

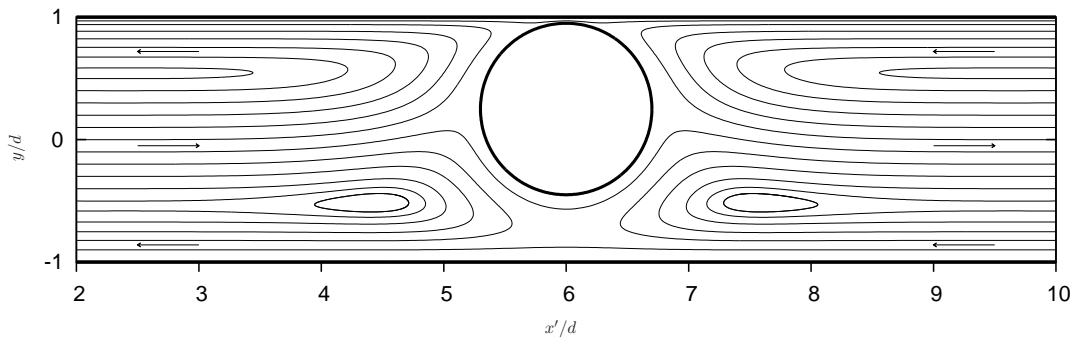


Figure 3.6 : Pathlines in a section of the channel for $\rho = 0.7$ and $\sigma = 0.25$. The particle rotates anti-clockwise and the fluid in the eddies rotates clockwise. The frame of reference is moving with the particle. The arrows indicate the flow direction relative to the particle.

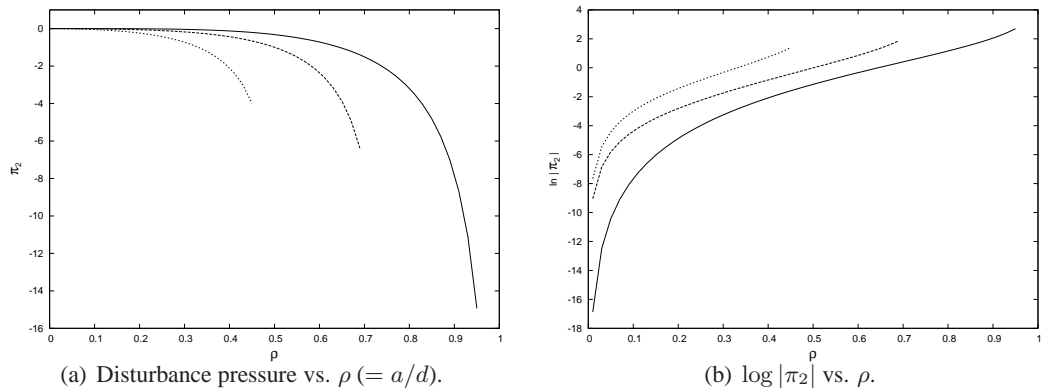


Figure 3.7 : Disturbance pressure vs. ρ for offsets $\sigma = 0$ (—), 0.25 (---) and 0.5 (···).

rate. For larger ρ the disturbance pressure increases rapidly. We can see from the plot of $\log |\pi_2|$ against ρ in figure 3.7 (b) that the pressure increases almost exponentially for larger values of ρ since the curves have become nearly straight. It is interesting to note that for a given ρ , the disturbance pressure increases with the offset from the centreline. The kinks for small ρ in figure 3.7 (b) are due to the constant increment size in ρ used in the calculation of the pressure. A smaller increment would provide a smoother curve. For example, when $\rho = 0.41$ the disturbance pressures are $-0.138 \mu U_0/d$, $-0.469 \mu U_0/d$ and $-2.357 \mu U_0/d$ for the particles with $\sigma = 0, 0.25$ and 0.5 respectively. Therefore we can see that as σ increases, and the gap between the top of the particle and wall reduces, the disturbance pressure increases significantly.

In figure 3.8 we plot the disturbance pressure against σ for a particle with $\rho = 0.25$ and a particle with $\rho = 0.5$. Figure 3.8 (a) shows how π_2 varies with respect to σ . The larger particle induces a greater disturbance pressure for the same value of σ . In figure 3.8 (b) we plot the logarithm of the disturbance pressure against σ for the two particles. Since both curves are approximately straight lines, we conclude that the disturbance pressure depends almost exponentially on σ .

Next we examine the effect of ρ and σ on the particle's velocity. In figure 3.9 (a) we plot the translational velocity, V_x/U_0 , against ρ . When ρ is small, the particle's velocity is approximately equal to the Poiseuille velocity calculated at the particle centre. As ρ

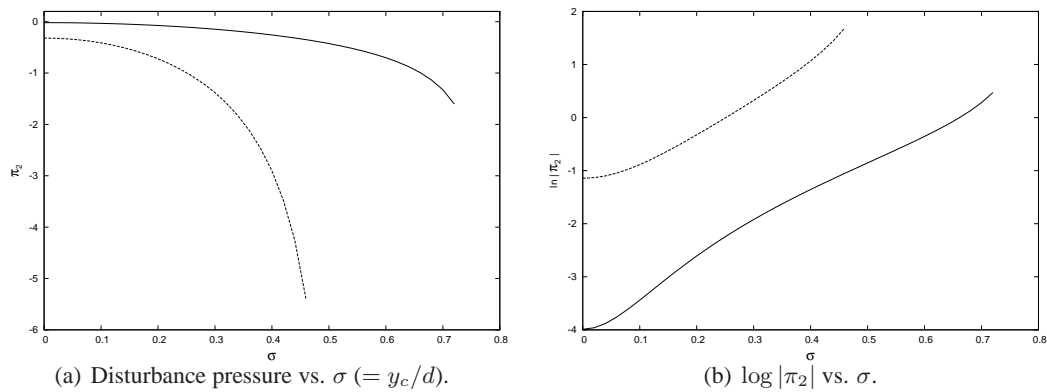


Figure 3.8 : Disturbance pressure vs. σ for two particles with $\rho = 0.25$ (—) and 0.5 (---).

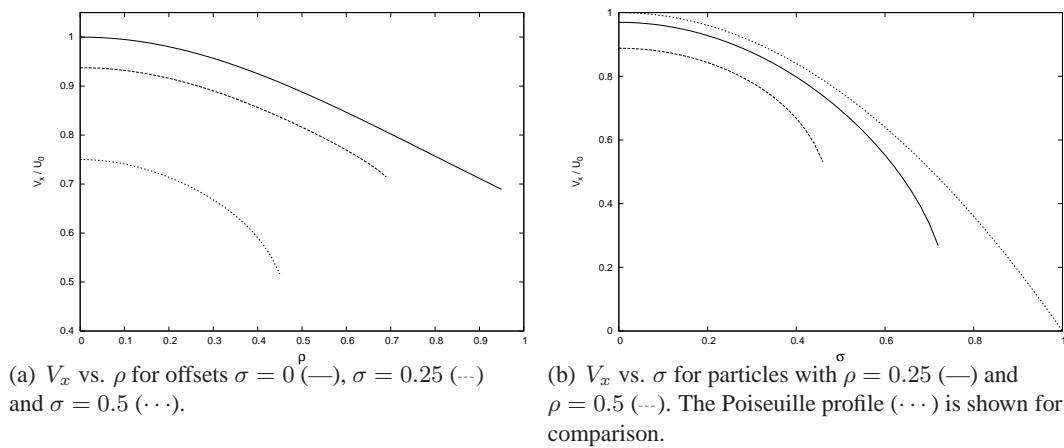


Figure 3.9 : Variation of the particle's translational velocity with respect to ρ and σ .

increases the particle's velocity decreases almost linearly with ρ and the particle 'slips' relative to the Poiseuille velocity calculated at particle centre. The results for the $\sigma = 0$ case show an excellent agreement with the equivalent results in figure 3 of Sugihara-Seki (1993), which were calculated using the finite element method. The particle with $\sigma = 0.25$ initially translates at the Poiseuille velocity. The particle's velocity decreases as the particle size increases but does not strongly exhibit a linear dependence on ρ . When σ is increased to 0.5 the particle's velocity starts at the Poiseuille velocity. As ρ increases the particle's velocity decreases at an increasing rate, and does not display a linear relationship between V_x and the particle size. In summary, the difference between U_0 and the particle's velocity is significantly greater when ρ is large or when the particle is close to the channel wall. This effect is due to the stress exerted on the particle by the fluid in the narrow gap between the particle boundary and the wall as described by Staben et al. (2003) who used the boundary integral method to analyse the motion of a sphere in a Poiseuille flow between two plane walls. Figure 3.9 (b) shows the relationship between the particle's translational velocity and σ for two particles with $\rho = 0.25$ and 0.5 . A portion of the Poiseuille velocity profile is also shown to aid comparison. For small σ , both particles show similar behaviour to the Poiseuille velocity profile. As the distance from

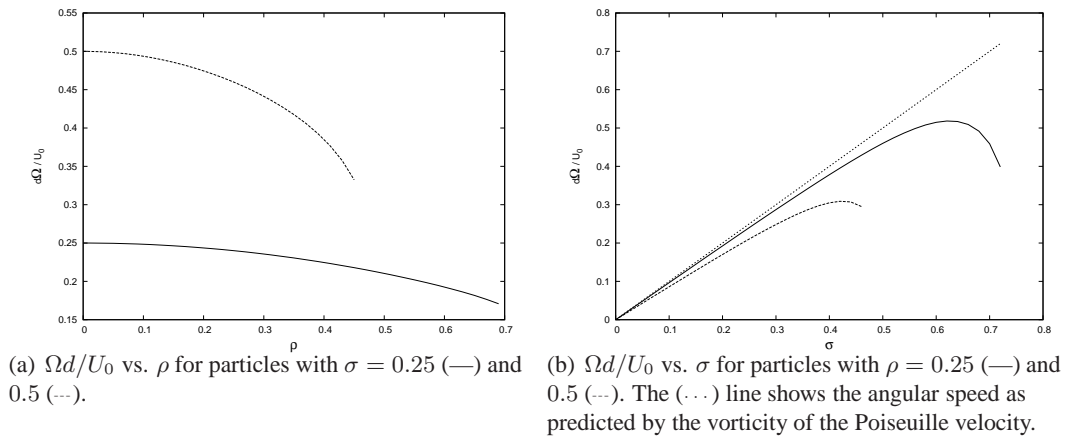


Figure 3.10 : Variation of the dimensionless particle angular velocity with respect to ρ and σ .

the centreline increases the particle velocity decreases at a faster rate than the Poiseuille velocity.

Finally we look at the angular velocity Ω and its dependence on ρ and σ . Figure 3.10 (a) shows $\Omega d/U_0$ plotted against ρ for two particles with $\sigma = 0.25$ and 0.5 . For small ρ the angular velocity is approximately equal to that predicted by the vorticity of the Poiseuille velocity. As the particle increases in size the angular velocity decreases at an increasing rate. We also note that a centred particle has $\Omega = 0$ for all ρ . In figure 3.10 (b) we plot $\Omega d/U_0$ against σ for two particles with $\rho = 0.25$ and 0.5 . The straight line is the angular velocity calculated from the vorticity of the Poiseuille velocity. The smaller particle deviates slightly from the straight line until $\sigma \approx 0.5$. After which it attains a maximum of $\Omega = 0.518 U_0/d$ at $\sigma = 0.62$ before decreasing rapidly as the gap between the particle and the wall reduces in size. The gap width is $0.13 d$ for $\sigma = 0.62$ and $\rho = 0.25$. If Ω were dependent on the difference between the Poiseuille velocities at the top and bottom of the particle then we would expect the maximum value of Ω to occur at around $\sigma = 0.75$ for a particle with $\rho = 0.25$. However, we can see that the proximity of the upper wall and the flow in the gap start to play a significant role when $\sigma > 0.62$. The particle's angular speed starts to decrease rapidly. The particle with $\rho = 0.5$ shows behaviour similar in nature to the smaller particle. A maximum angular speed is attained at around $\sigma = 0.41$, corresponding to a gap width of $0.09 d$. As the gap width becomes even smaller the angular speed reduces. A comparison can be made between the results presented in figure 3.10 (b) and those shown in figure 5 of Staben et al. (2003), who study the motion of a solid sphere in a Poiseuille flow in an infinite channel between two plane parallel walls. The three-dimensional results of Staben et al. (2003) exhibit the same qualitative behaviour such that the angular speed of the particle increases with the offset from the centreline before reaching a maximum and decreasing as the gap between the plane wall and the particle becomes small. The explanation put forward by Staben et al. (2003) for the retardation lies in the competition between the incident velocity gradient which causes the rotation and the hydrodynamic interactions and shear stresses which oppose the rotation.

3.5 Discussion

In this chapter we have considered a pressure-driven channel flow which contains a rigid neutrally buoyant particle. We formulated the problem using the boundary integral method and found its solution numerically using the boundary element method. The solution provides the tractions on the particle boundary, the disturbance tractions on the channel walls and the pressure drop across the particle.

We found that in all cases the disturbance tractions decayed to their expected values as we approached the entrance or exit. The disturbance velocity decayed rapidly as we moved away from the particle, and we found that the disturbance velocity due to the particle decayed to less than 1% of its maximum value at a distance of three particle radii from the centre. When the particle lay with its centre on the channel centreline, six stagnation points are present on the particle's boundary. When the particle was moved away from the centreline the stagnation points disappeared and the particle was surrounded by a thin region of circulating fluid, similar to that found by Jeffrey and Onishi (1981) on their work regarding a rotating cylinder above a plane wall.

For all particle positions we found that the translational velocity is less than the centreline Poiseuille velocity demonstrating that the particle 'slips' relative to the background Poiseuille flow. When the particle radius is small, the particle's velocity is approximately equal to the Poiseuille velocity calculated at the particle centre. For a centred circular particle, we demonstrated an excellent agreement with the results of Sugihara-Seki (1993) (figure 3) regarding the relationship between the particle velocity and particle size. The difference between the Poiseuille velocity and the particle's velocity increases as the gap between one or both of the walls and the particle becomes small. This effect is due to the stress exerted on the particle by the fluid in the narrow gap between the particle boundary and the wall as described by Staben et al. (2003) in their work on a sphere in a channel flow between plane walls. We also confirmed that the y -component of the translational velocity was zero, which we expect due to the reversibility of Stokes flow, i.e. the particle does not move closer to either wall as it translates. We found that a centred particle did not rotate and small particles rotated with a speed equal to that predicted by the vorticity of the Poiseuille velocity. As the particle is moved away from the centreline the angular speed increases to a maximum at which point the flow in the narrow gap slows the particle's rotation and the angular speed decreases.

We found that the pressure drop across the particle increased when we fixed the centroid and increased the particle radius, and when we fixed the radius and moved the capsule further from the centreline. When we moved the particle away from the channel centreline two eddies were formed in the fluid in front of and behind the particle. Eddies similar to the ones seen here were studied and photographed by Hasimoto and Sano (1980). When the gap between the particle and one or both of the walls is small, we found that the pressure drop between the ends of the computational domain increases exponentially as the gap width decreases.

Chapter 4

The motion of a fluid drop or a flexible capsule in a straight channel

In the previous chapter we studied the disturbance caused by a rigid particle in a channel flow. Now we replace the rigid particle with a flexible one, with the aim of modelling the motion of a fluid drop or a fluid-filled elastic capsule in a straight channel. We maintain our assumption that the capsule is neutrally buoyant and that the flow imparts no force or torque on the capsule. We model the disturbance caused by the particle using the boundary integral method and derive the boundary integral equations which govern the motion of the fluid and the capsule. We will formulate the constitutive equations, applicable to fluid drops and elastic capsules, which govern the behaviour of the flexible boundary. The mathematical treatment in this chapter will help us in later chapters where we will add an additional channel which will branch off from the main channel. We will solve the boundary integral equations numerically by application of the boundary element method and compare our solution to known results where applicable.

4.1 Problem statement

Following our work in the previous chapter, we consider the motion of a fluid with viscosity μ in an infinite straight-walled channel of width $2d$. A disturbance to the flow is caused by the presence of a deformable capsule which moves with the flow. We assume that the capsule is neutrally buoyant and that the flow does not impart a force or a torque on the capsule. The capsule contains a fluid with viscosity $\lambda\mu$ so that when $\lambda > 1$ the encapsulated fluid is more viscous than the ambient fluid and vice versa. The fluid viscosities are identical when $\lambda = 1$. Since we omit the body force due to gravity from the Stokes equation the fluid density does not play a role in the flow behaviour. The channel geometry is displayed in figure 4.1, where we label the channel walls, \mathcal{C} , and the capsule, \mathcal{P} . Far upstream and downstream of the disturbance caused by the capsule, the flow in the channel is described by classical unidirectional Poiseuille flow, which is characterised by

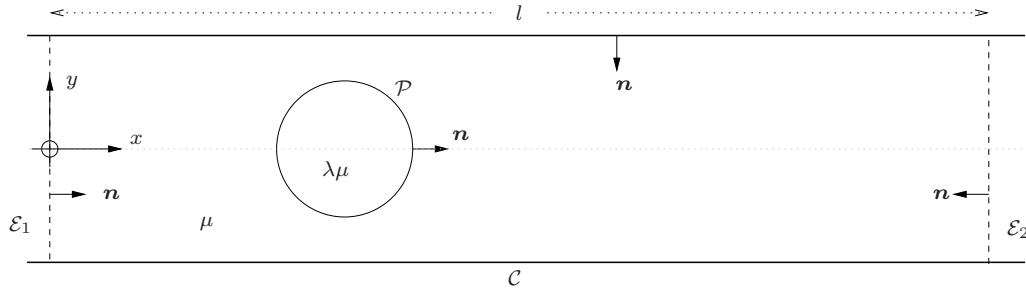


Figure 4.1 : A straight-walled channel containing a neutrally-buoyant capsule which encapsulates a fluid of viscosity $\lambda\mu$.

the prescribed flux, Q . The equations describing the Poiseuille flow are

$$\mathbf{u}^P = u^P \mathbf{i}, \quad (4.1)$$

$$u^P = U_0 \left(1 - \frac{y^2}{d^2} \right), \quad (4.2)$$

$$Q = \frac{4}{3} d U_0, \quad (4.3)$$

and

$$\mathbf{f}_i^P = -p^P n_i + \mu \left(\frac{\partial u_i^P}{\partial x_j} + \frac{\partial u_j^P}{\partial x_i} \right) n_j, \quad (4.4)$$

where U_0 is the Poiseuille centreline speed, \mathbf{f}^P is the Poiseuille traction, p^P is the Poiseuille pressure and \mathbf{n} is the unit normal vector. In preparation for the numerical method, we truncate the channel and label the entrance to the computational domain as \mathcal{E}_1 , and the exit to the domain as \mathcal{E}_2 . The entrance and exit are located at $x = 0$ and $x = l$ respectively. The unit normal vectors, \mathbf{n} , on all boundaries point into the ambient fluid which we will label fluid 1. The fluid inside the capsule will be labelled fluid 2. The capsule's presence disturbs the Poiseuille flow, but at \mathcal{E}_1 and \mathcal{E}_2 , we assume that the disturbance has decayed and the flow has settled to Poiseuille flow. In the previous chapter we justified this assumption for a rigid particle with reference to the work of Sugihara-Seki (1993), Gaver and Kute (1998), Cortez (2002) and showed that the velocity decay is indeed rapid as we move away from the source of the disturbance. The two-dimensional study of fluid drops in a channel by Mortazavi and Tryggvason (2000) demonstrated that the velocity decay was sufficiently rapid for a range of Reynolds numbers. The authors justified their assumption regarding the decay of the disturbance velocity with reference to the work of Liron and Mochon (1976), Liron and Shahar (1978) who studied the disturbance due to a three-dimensional Stokeslet in the flow between two plates and in a pipe, and found that the disturbance velocity decayed exponentially. Therefore we will follow the lead of Mortazavi and Tryggvason (2000) together with the results of our previous chapters and maintain that the disturbance velocity decays as we move away from the capsule, and is negligible at the entrance and exit to our computational domain. We will verify this assumption when we validate the numerical solution.

We assume that the Reynolds number of the flow is very small so that the flow in

the channel may be described using the linear equations of Stokes flow given in equation (1.3.4). Our aim is to compute the velocity field throughout the flow domain, the additional pressure drop between the entrance and exit due to the capsule and the motion of the capsule's boundary. From the work of previous authors (e.g. Mortazavi and Tryggvason 2000) we know that a capsule with a flexible boundary will migrate towards the channel centreline for moderate λ . When λ is small, Mortazavi and Tryggvason (2000) found that a fluid drop migrated towards a point between the channel centreline and the nearest wall. Although this lateral migration may seem contrary to the reversibility of Stokes flow, the capsule's deformation allows such a migration to occur. Therefore we would also like to examine the capsule's behaviour when its starting position is away from the centreline, and for a range of λ .

We decompose the velocity field, \mathbf{u} , the stress field, $\boldsymbol{\sigma}$, and the traction field, \mathbf{f} , into Poiseuille and disturbance components in the usual way, such that

$$\mathbf{u} = \mathbf{u}^P + \mathbf{u}^D, \quad (4.5)$$

$$\boldsymbol{\sigma} = \boldsymbol{\sigma}^P + \boldsymbol{\sigma}^D, \quad (4.6)$$

$$\mathbf{f} = \mathbf{f}^P + \mathbf{f}^D, \quad (4.7)$$

where the P and D superscripts indicate the Poiseuille and disturbance components respectively. Our boundary conditions are

$$\mathbf{u} = \mathbf{u}^P = \mathbf{u}^D = \mathbf{0} \quad (4.8)$$

on \mathcal{C} due to no-slip and no-penetration, and

$$\mathbf{u}^D = \mathbf{0}, \quad (4.9)$$

$$\mathbf{f}^D = -p^D \mathbf{n}, \quad (4.10)$$

at \mathcal{E}_1 and \mathcal{E}_2 , where p^D is the disturbance pressure which is constant over the entrance or exit. We assume that no fluid passes across the capsule boundary and that the velocity on both sides of the boundary is equal, so that on \mathcal{P} we have

$$\mathbf{u}^{(1)} = \mathbf{u}^{(2)}, \quad (4.11)$$

where the superscript indicates the fluid to which the velocity applies, i.e. $\mathbf{u}^{(2)}$ is the velocity of fluid 2 inside the capsule. We also introduce the interfacial traction jump, $\Delta\mathbf{f}$, which is defined by

$$\Delta\mathbf{f} = (\boldsymbol{\sigma}^{(1)} - \boldsymbol{\sigma}^{(2)}) \cdot \mathbf{n} = \mathbf{f}^{(1)} - \mathbf{f}^{(2)}, \quad (4.12)$$

where the superscripts indicate to which fluid the traction applies. We will see later that we can calculate the interfacial traction jump from a suitable constitutive equation. For example, $\Delta\mathbf{f}$ may be calculated from the Young-Laplace equation when the capsule is a drop of an immiscible liquid. Therefore in the derivation of our equation we will seek

to eliminate disturbance velocities and tractions on the capsule boundary in favour of the total velocities and tractions.

Since we are interested in the additional pressure drop between the entrance and exit due to the capsule, we set $p^D(\mathcal{E}_1) = 0$ without loss of generality and let $p^D(\mathcal{E}_2) = \pi_2$. Therefore the disturbance traction at \mathcal{E}_2 is given by

$$\mathbf{f}^D = -\pi_2 \mathbf{n}, \quad (4.13)$$

and the disturbance pressure drop between the entrance and the exit is

$$\Delta p^D = p^D(\mathcal{E}_1) - p^D(\mathcal{E}_2) = -\pi_2. \quad (4.14)$$

Therefore we expect π_2 to be negative because the capsule's presence will increase the total pressure drop. The Poiseuille pressure in the channel is given by

$$p^P = G(l - x) \quad (4.15)$$

where $G = 2\mu U_0/d^2$ is a positive constant, $-G$ is the imposed constant pressure gradient between the entrance and the exit, and we have chosen the Poiseuille pressure to be zero at \mathcal{E}_2 . Therefore the total pressure drop, Δp , between the entrance and exit is

$$\begin{aligned} \Delta p &= p(\mathcal{E}_1) - p(\mathcal{E}_2) = p^P(\mathcal{E}_1) + p^D(\mathcal{E}_1) - (p^P(\mathcal{E}_2) + p^D(\mathcal{E}_2)) \\ &= Gl - \pi_2. \end{aligned} \quad (4.16)$$

To obtain an equation for the disturbance pressure we apply Lorentz's reciprocal relation (1.3.22) to the Poiseuille and disturbance flows. We will use equation (3.22) (on page 45) from the previous chapter as our starting point, which we rewrite here as

$$Q\pi_2 = \int_{\mathcal{P}} \left(\mathbf{u}^{(1)} \cdot \mathbf{f}^P - \mathbf{u}^P \cdot \mathbf{f}^{(1)} \right) ds(\mathbf{x}), \quad (4.17)$$

and where we have added the (1) superscript to indicate that the velocity and traction apply to fluid 1. Next we apply the Lorentz reciprocal relation to the Poiseuille flow and the capsule's internal flow in order to introduce the interfacial traction, $\Delta \mathbf{f}$, to our equation. Since the viscosity of the Poiseuille flow and the internal flow are different we use the Lorentz reciprocal relation applicable to two fluids which have different viscosities, to get

$$\nabla \cdot \left(\mu \mathbf{u}^P \cdot \mathbf{f}^{(2)} - \lambda \mu \mathbf{u}^{(2)} \cdot \mathbf{f}^P \right) = 0, \quad (4.18)$$

which we divide by μ , integrate over \mathcal{P} and add to (4.17) to get

$$\pi_2 = -\frac{1}{Q} \left(\int_{\mathcal{P}} \mathbf{u}^P \cdot \Delta \mathbf{f} ds(\mathbf{x}) + (\lambda - 1) \int_{\mathcal{P}} \mathbf{u}^{(1)} \cdot \mathbf{f}^P ds(\mathbf{x}) \right), \quad (4.19)$$

where we have also used equation (4.11). Therefore the disturbance pressure is dependent on the capsule's shape and the velocity of the capsule's perimeter. The interfacial tractions will be obtained from a constitutive equation, and the Poiseuille velocity and traction values may be calculated from equations (4.1) and (4.4). It is interesting to note that when $\lambda = 1$ the velocities on \mathcal{P} are not included in the equation and the disturbance pressure may be calculated directly given the capsule shape and the interfacial traction.

We obtain an alternative expression for π_2 from the Stokes equation for the total stress in the ambient fluid, $\nabla \cdot \boldsymbol{\sigma}^{(1)} = \mathbf{0}$. We integrate around the flow boundary and apply the divergence theorem to get

$$\begin{aligned} \mathbf{0} &= \int_{\partial\Gamma} \mathbf{f}^{(1)} \, ds(\mathbf{x}) \\ &= \int_{\mathcal{E}_1} \mathbf{f}^P \, ds(\mathbf{x}) + 2d\pi_2 \mathbf{i} + \int_{\mathcal{E}_2} \mathbf{f}^P \, ds(\mathbf{x}) + \int_{\mathcal{C}} \mathbf{f}^{(1)} \, ds(\mathbf{x}) + \int_{\mathcal{P}} \mathbf{f}^{(1)} \, ds(\mathbf{x}), \end{aligned} \quad (4.20)$$

where we have applied the boundary conditions. Integrating $\nabla \cdot \boldsymbol{\sigma}^{(2)} = \mathbf{0}$ over \mathcal{P} gives

$$\int_{\mathcal{P}} \mathbf{f}^{(2)} \, ds(\mathbf{x}) = \mathbf{0} \quad (4.21)$$

which we subtract from equation (4.20) to get

$$\mathbf{0} = \int_{\mathcal{E}_1} \mathbf{f}^P \, ds(\mathbf{x}) + 2d\pi_2 \mathbf{i} + \int_{\mathcal{E}_2} \mathbf{f}^P \, ds(\mathbf{x}) + \int_{\mathcal{C}} \mathbf{f}^{(1)} \, ds(\mathbf{x}) + \int_{\mathcal{P}} \Delta \mathbf{f} \, ds(\mathbf{x}). \quad (4.22)$$

We can substitute the Poiseuille traction and the stress tensor into the cap integrals in (4.22) to get

$$\begin{aligned} \int_{\mathcal{E}_1} f_i^P \, ds(\mathbf{x}) + \int_{\mathcal{E}_2} f_i^P \, ds(\mathbf{x}) &= \int_{\mathcal{E}_1} \sigma_{ix}^P \, ds(\mathbf{x}) - \int_{\mathcal{E}_2} \sigma_{ix}^P \, ds(\mathbf{x}) \\ &= -2dGl \delta_{ix}, \end{aligned} \quad (4.23)$$

since $\sigma_{xx} = -p^P(x)$ and $\sigma_{yx} = \mu \frac{\partial u^P}{\partial y}$. After substitution of (4.23) into (4.22) the x and y components are given by

$$\pi_2 = Gl - \frac{1}{2d} \left(\int_{\mathcal{C}} \mathbf{f}^{(1)} \cdot \mathbf{i} \, ds(\mathbf{x}) + \int_{\mathcal{P}} \Delta \mathbf{f} \cdot \mathbf{i} \, ds(\mathbf{x}) \right), \quad (4.24)$$

$$0 = \int_{\mathcal{C}} \mathbf{f}^{(1)} \cdot \mathbf{j} \, ds(\mathbf{x}) + \int_{\mathcal{P}} \Delta \mathbf{f} \cdot \mathbf{j} \, ds(\mathbf{x}). \quad (4.25)$$

The total tractions, $\mathbf{f}^{(1)}$, on the walls consists of the known Poiseuille tractions and the unknown disturbance tractions. The unknowns in equation (4.24) are the disturbance tractions on the walls and the capsule shape, which is in contrast to equation (4.19) which

requires the velocities on the capsule boundary and its shape. When $\lambda = 1$, π_2 can be calculated directly using equation (4.19). However, we are unable to calculate π_2 directly using equation (4.24) under any circumstances. Equation (4.25) therefore provides a method of checking the disturbance tractions on the walls.

Now that we have a formula for the disturbance pressure, we will focus on deriving a boundary integral equation which governs the disturbance velocity in the channel. When the pole, \mathbf{x}_0 , lies in fluid 1 the disturbance velocity satisfies equation (3.43), which we rewrite as

$$4\pi\mu u_j^D(\mathbf{x}_0) = \pi_2 \int_{\mathcal{E}_2} n_i G_{ij} \, ds(\mathbf{x}) - \int_{\mathcal{C}} f_i^D G_{ij} \, ds(\mathbf{x}) - \int_{\mathcal{P}} f_i^{(1)} G_{ij} \, ds(\mathbf{x}) + \mu \int_{\mathcal{P}} u_i^{(1)} T_{ijk} n_k \, ds(\mathbf{x}), \quad (4.26)$$

where we have added the superscript (1) to the traction and the velocity in the capsule integrals to indicate that the traction and velocity apply to fluid 1. Application of the general boundary integral equation (1.3.40) to the flow inside the particle gives

$$0 = - \int_{\mathcal{P}} f_i^{(2)} G_{ij} \, ds(\mathbf{x}) + \lambda\mu \int_{\mathcal{P}} u_i^{(2)} T_{ijk} n_k \, ds(\mathbf{x}), \quad (4.27)$$

where the left-hand side is zero because \mathbf{x}_0 lies outside of the domain of \mathcal{P} . We subtract (4.27) from (4.26) to get

$$u_j^D(\mathbf{x}_0) = \frac{1}{4\pi\mu} \left(\pi_2 \int_{\mathcal{E}_2} n_i G_{ij} \, ds(\mathbf{x}) - \int_{\mathcal{C}} f_i^D G_{ij} \, ds(\mathbf{x}) - \int_{\mathcal{P}} \Delta f_i G_{ij} \, ds(\mathbf{x}) + \mu(1 - \lambda) \int_{\mathcal{P}} u_i^{(1)} T_{ijk} n_k \, ds(\mathbf{x}) \right), \quad (4.28)$$

which may be used to calculate the disturbance velocity at any point in fluid 1 given the disturbance pressure, the disturbance tractions on the channel walls, the interfacial tractions on the capsule boundary and the velocity field on the capsule boundary. When the viscosity ratio is unity the integral involving the capsule velocities disappears from the equation. In the previous section we had to add a ‘deflation’ term to the boundary integral equation because the equation did not admit a unique solution. We do not have the same problem with equation (4.28) because $\Delta \mathbf{f}$ will be known and hence the integral, $\int_{\mathcal{P}} \Delta f_i G_{ij} \, ds(\mathbf{x})$, can be computed. However the boundary integral equation does become ill-conditioned in the limits $\lambda \rightarrow 0$ and $\lambda \rightarrow \infty$, which correspond to a bubble and a rigid particle respectively. The integral equation may be regularised by adding the deflation term given in Zhou and Pozrikidis (1993), Staben et al. (2003) who studied the motion of a drop in a two-dimensional channel and a particle in a channel between plane walls respectively. Here we limit the range of λ so that we do not encounter problems.

The total velocity at a point in the fluid is computed by adding the Poiseuille velocity to the disturbance velocity obtained from equation (4.28).

Before we can use (4.28) we need to find the disturbance pressure, π_2 , the disturbance tractions on \mathcal{C} and the velocities of \mathcal{P} . Therefore we would like to place the pole on the channel walls and the capsule boundary and evaluate the boundary integral equation. When \mathbf{x}_0 lies on the channel walls equation (4.28) reduces to

$$0 = \pi_2 \int_{\mathcal{E}_2} n_i G_{ij} \, ds(\mathbf{x}) - \int_{\mathcal{C}} f_i^D G_{ij} \, ds(\mathbf{x}) - \int_{\mathcal{P}} \Delta f_i G_{ij} \, ds(\mathbf{x}) + \mu(1 - \lambda) \int_{\mathcal{P}} u_i^{(1)} T_{ijk} n_k \, ds(\mathbf{x}), \quad (4.29)$$

where the left-hand side is zero because $\mathbf{u}^D = \mathbf{0}$ on the channel walls and although the double-layer potential is present it is not discontinuous when \mathbf{x}_0 lies on \mathcal{C} . When the pole lies on the capsule's boundary the double-layer potential is

$$\int_{\mathcal{P}} u_i^{(1)} T_{ijk} n_k \, ds(\mathbf{x}) = 2\pi u_j^{(1)}(\mathbf{x}_0) + \int_{\mathcal{P}}^{PV} u_i^{(1)} T_{ijk} n_k \, ds(\mathbf{x}), \quad (4.30)$$

by equation (2.6.25) in Pozrikidis (1992), and where PV indicates the principal value of the integral. Substitution into (4.28) yields

$$2\pi\mu(1 + \lambda)u_j^{(1)}(\mathbf{x}_0) = 4\pi\mu u_j^P(\mathbf{x}_0) + \pi_2 \int_{\mathcal{E}_2} n_i G_{ij} \, ds(\mathbf{x}) - \int_{\mathcal{C}} f_i^D G_{ij} \, ds(\mathbf{x}) - \int_{\mathcal{P}} \Delta f_i G_{ij} \, ds(\mathbf{x}) + \mu(1 - \lambda) \int_{\mathcal{P}}^{PV} u_i^{(1)} T_{ijk} n_k \, ds(\mathbf{x}), \quad (4.31)$$

which is valid when \mathbf{x}_0 lies on the capsule boundary and where we have expressed the left-hand side in terms of the total velocity.

Now that we have derived the equation for π_2 and the boundary integral equations which are valid when \mathbf{x}_0 lies on \mathcal{C} and \mathcal{P} , we find the solution by writing the equations as a linear system and solving it by standard means. To construct the linear system we employ the boundary element method (Pozrikidis 2002a) whereby we discretise the channel walls and the capsule boundary into elements. We evaluate (4.29) with the pole, \mathbf{x}_0 , on each of the boundary elements of \mathcal{C} to obtain a sufficient number of equations for the unknown disturbance tractions on the channel walls. We have the same sufficiency on the capsule boundary by evaluating equation (4.31) with \mathbf{x}_0 on each of the boundary elements of \mathcal{P} . The remaining unknown quantity is π_2 for which we have equation (4.19). Therefore we have the same number of unknowns as equations and so our system is complete. When the solution to the linear system is available, we may calculate the velocity at any point in

the flow domain using,

$$u_j^{(1)}(\mathbf{x}_0) = u_j^P(\mathbf{x}_0) + \frac{1}{4\pi\mu} \left(\pi_2 \int_{\mathcal{E}_2} n_i G_{ij} \, ds(\mathbf{x}) - \int_{\mathcal{C}} f_i^D G_{ij} \, ds(\mathbf{x}) - \int_{\mathcal{P}} \Delta f_i G_{ij} \, ds(\mathbf{x}) + \mu(1-\lambda) \int_{\mathcal{P}} u_i^{(1)} T_{ijk} n_k \, ds(\mathbf{x}) \right), \quad (4.32)$$

where we have added equation (4.26) to the Poiseuille velocity to get the total velocity. We non-dimensionalise equations (4.19) and (4.32) to obtain the important parameters. We scale distances by d , velocities by U_0 , and tractions and pressures by $\mu U_0/d$, and identify dimensionless quantities with a circumflex. The disturbance pressure equation (4.19) becomes

$$\hat{\pi}_2 = -\frac{3}{4} \left(\int_{\mathcal{P}} \hat{\mathbf{u}}^P \cdot \Delta \hat{\mathbf{f}} \, d\hat{s} + (\lambda - 1) \int_{\mathcal{P}} \hat{\mathbf{u}}^{(1)} \cdot \hat{\mathbf{f}}^P \, d\hat{s} \right), \quad (4.33)$$

and equation (4.32) becomes

$$\hat{u}_j^{(1)}(\mathbf{x}_0) = \hat{u}_j^P(\mathbf{x}_0) + \frac{1}{4\pi} \left(\hat{\pi}_2 \int_{\mathcal{E}_2} n_i G_{ij} \, d\hat{s} - \int_{\mathcal{C}} \hat{f}_i^D G_{ij} \, d\hat{s} - \int_{\mathcal{P}} \Delta \hat{f}_i G_{ij} \, d\hat{s} + (1-\lambda) \int_{\mathcal{P}} \hat{u}_i^{(1)} \hat{T}_{ijk} n_k \, d\hat{s} \right). \quad (4.34)$$

Therefore it is clear that the flow is dependent on the shape, size and location of the particle via the integrals over \mathcal{P} together with the ratio of the fluid viscosities and the physical properties of the capsule boundary. We have completed the derivation of our governing equations, however to proceed we require a method of calculating the interfacial traction jump, $\Delta \mathbf{f}$. In the next section we demonstrate how to calculate $\Delta \mathbf{f}$.

4.2 Constitutive equations for fluid drops and elastic capsules

We will consider capsules of two fundamentally different types. First we will look at fluid drops with constant surface tension before examining the behaviour of a fluid encapsulated by an infinitely thin flexible membrane. To calculate the jump in the interfacial traction for a fluid drop, we use the Young-Laplace equation (e.g. Batchelor 1967, p.69),

$$\Delta \mathbf{f}(s) = \gamma \kappa(s) \mathbf{n}(s) \quad (4.35)$$

where γ is the constant surface tension, κ is the local curvature, \mathbf{n} is the unit normal vector pointing into fluid 1, and where we have included the arguments for clarity. The arc-length, s , increases as we move anti-clockwise around the capsule. Taking the definition

of the curvature from (Stoker 1969, Eq 2.17), we have

$$\kappa(s) \mathbf{n} = -\frac{d\mathbf{t}}{ds}, \quad (4.36)$$

where \mathbf{t} is the unit tangent vector oriented in the direction of increasing s , and where we have used the minus sign to make the definition geometrically consistent. Equivalently we may write,

$$\kappa(s) = -\mathbf{n} \cdot \frac{d\mathbf{t}}{ds} = \frac{d\mathbf{n}}{ds} \cdot \mathbf{t}. \quad (4.37)$$

For instance, a circle of radius r will have curvature, $\kappa = 1/r$. On the circle we have $\mathbf{n} = \hat{\mathbf{r}}$, $\mathbf{t} = \hat{\boldsymbol{\theta}}$ and $s = r\theta$, where $\hat{\mathbf{r}}$ and $\hat{\boldsymbol{\theta}}$ are the orthogonal unit vectors in the radial and θ directions respectively. Substitution into (4.37) gives

$$\kappa = -\hat{\mathbf{r}} \cdot \left(\frac{1}{r} \frac{d\hat{\boldsymbol{\theta}}}{d\theta} \right) = -\frac{1}{r} \hat{\mathbf{r}} \cdot (-\hat{\mathbf{r}}) = \frac{1}{r} \quad (4.38)$$

since $\frac{d\hat{\boldsymbol{\theta}}}{d\theta} = -\hat{\mathbf{r}}$. To ensure that equation (4.35) is consistent with our definition of curvature we form $\mathbf{n} \cdot \Delta \mathbf{f}$, to get

$$\gamma \kappa = \mathbf{n} \cdot \Delta \mathbf{f} = \mathbf{n} \cdot (\boldsymbol{\sigma}^{(1)} - \boldsymbol{\sigma}^{(2)}) \cdot \mathbf{n}. \quad (4.39)$$

To expand the right-hand side we use

$$n_i \sigma_{ij}^{(1)} n_j = -p^{(1)} + 2\mu n_i e_{ij}^{(1)} n_j, \quad (4.40)$$

$$n_i \sigma_{ij}^{(2)} n_j = -p^{(2)} + 2\lambda\mu n_i e_{ij}^{(2)} n_j, \quad (4.41)$$

where $e_{ij}^{(a)} = \frac{1}{2} \left(\frac{\partial u_i^{(a)}}{\partial x_j} + \frac{\partial u_j^{(a)}}{\partial x_i} \right)$ is the rate of strain tensor for fluid $a = 1, 2$. On the perimeter of the fluid drop $e_{ij}^{(1)} = e_{ij}^{(2)}$ since $\mathbf{u}^{(1)} = \mathbf{u}^{(2)}$. Therefore we may write

$$\gamma \kappa = p^{(2)} - p^{(1)} + 2(1 - \lambda)\mu n_i e_{ij}^{(1)} n_j. \quad (4.42)$$

Since we are interested only in checking the sign of the curvature we consider a bubble in air so that $\lambda = 1$, and

$$p^{(2)} = p^{(1)} + \gamma \kappa, \quad (4.43)$$

where $p^{(1)}$ is the air pressure and $p^{(2)}$ is the pressure inside the bubble. Since $p^{(2)} > p^{(1)}$ and the surface tension, γ , will be a positive constant we require the curvature to be positive, which is consistent with our definition in equation (4.37). In summary, to calculate $\Delta \mathbf{f}$ for a fluid drop we specify the surface tension and compute the normal vector and the curvature, κ .

We compute the interfacial traction jump for an elastic capsule according to an assumed equilibrium balance between the elastic forces developing within the two-dimensional

elastic membrane and the hydrodynamic load on the capsule. The capsule is shown in figure 4.2. The capsule membrane is treated as being comprised of a thin incompressible

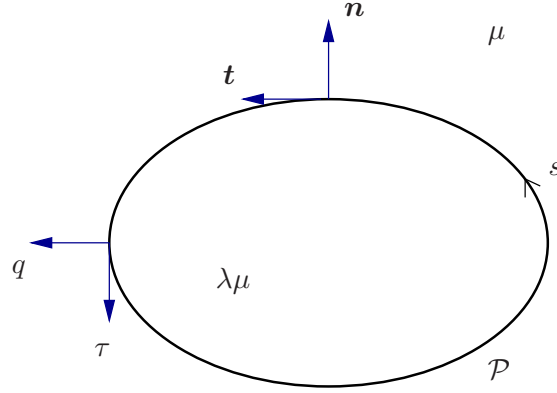


Figure 4.2 : Elastic capsule with unit normal \mathbf{n} , unit tangent \mathbf{t} , in-plane tension τ and transverse shear tension q . The arc-length is s and its direction is indicated by the arrow.

elastic material (e.g. Barthès-Biesel 1980). To establish formulae for the traction jump, we first define the membrane tension vector,

$$\mathbf{T} \equiv q \mathbf{n} + \tau \mathbf{t}, \quad (4.44)$$

where τ is the in-plane tension and q is the transverse shear tension which incorporates the effects of bending resistance. Next, we consider a force balance over an infinitesimal section of the membrane to obtain

$$\frac{d\mathbf{T}}{ds} + \Delta\mathbf{f} = \mathbf{0}, \quad (4.45)$$

which expresses the equilibrium balance between the elastic stress and the hydrodynamic load on the capsule membrane. Differentiating the tension in equation (4.44) with respect to s gives

$$\frac{d\mathbf{T}}{ds} = \frac{dq}{ds} \mathbf{n} + q \frac{d\mathbf{n}}{ds} + \frac{d\tau}{ds} \mathbf{t} - \kappa \tau \mathbf{n} \quad (4.46)$$

by the chain rule and equation (4.36). Taking the scalar product with \mathbf{n} gives

$$\frac{d\mathbf{T}}{ds} \cdot \mathbf{n} = \frac{dq}{ds} - \kappa \tau \quad (4.47)$$

since $\mathbf{n} \cdot \mathbf{t} = \frac{d\mathbf{n}}{ds} \cdot \mathbf{n} = 0$. The tangential component of the tension is given by

$$\frac{d\mathbf{T}}{ds} \cdot \mathbf{t} = q \frac{d\mathbf{n}}{ds} \cdot \mathbf{t} + \frac{d\tau}{ds} = \kappa q + \frac{d\tau}{ds} \quad (4.48)$$

using equation (4.37). Therefore the normal and tangential components of equation (4.45) give us

$$\Delta\mathbf{f} \cdot \mathbf{t} = - \left(\frac{d\tau}{ds} + \kappa q \right) \quad (4.49)$$

and

$$\Delta \mathbf{f} \cdot \mathbf{n} = - \left(\frac{dq}{ds} - \kappa \tau \right), \quad (4.50)$$

for the components of the hydrodynamic load. For simplicity we adopt a linear elastic model for the in-plane elastic tension, and assume that it may be expressed as a linear function of the membrane strain. Following Breyiannis and Pozrikidis (2000) we write

$$\tau = k (e - 1), \quad (4.51)$$

where k is the membrane stiffness and $e - 1$ is the membrane strain with the extension,

$$e = \frac{\partial s}{\partial s_R} \quad (4.52)$$

where $s(t)$ is arc-length along the deforming membrane boundary and s_R is arc-length in the unstressed membrane. Although the simple relationship (4.51) is strictly only true for small deformations, it still captures qualitatively the inclination for a deformed capsule to return to its unstressed configuration. In the unstressed state, $s = s_R$, and so the in-plane tension will be zero. A moment balance over an infinitesimal section of the membrane yields

$$q = \frac{dm}{ds}, \quad (4.53)$$

where m is membrane bending moment. Following Pozrikidis (2002b), we assume a linear constitutive relationship between the bending moment and the membrane curvature to get

$$m = E_B (\kappa - \kappa_R), \quad (4.54)$$

where E_B is the bending modulus and κ_R is the curvature of the unstressed membrane. The physical properties of the capsule boundary are the membrane stiffness, k , and the bending modulus, E_B . We set $E_B = 0$ to model a membrane which does not resist bending, which is equivalent to setting $q = 0$. From inspection of (4.49) and (4.50), we can see that we need to compute κ , q , $\frac{dq}{ds}$, τ and $\frac{d\tau}{ds}$ in order to calculate $\Delta \mathbf{f}$. The computation of q and $\frac{dq}{ds}$ is equivalent to calculating the first and second derivative of the curvature. For simplicity, we will assume that the shape of an unstressed elastic capsule will be a circle. Therefore the reference curvature, κ_R , is constant and does not affect the calculations.

Now that we have the governing integral equations and a method of calculating the interfacial traction jump we have completed our derivation of the equations and so we are in a position to proceed to the numerical method.

4.3 Numerical method

Now that we have the governing equations we wish to write them in the form of a linear system,

$$\mathbf{A} \cdot \mathbf{x} = \mathbf{b}, \quad (4.55)$$

as we have explained in the previous section and chapter. To start the boundary element method, we discretise the geometry into boundary elements. We divide the channel walls into N_C equally-sized straight elements upon each of which we set the unknown disturbance traction to a constant vector. On the r^{th} wall element the disturbance traction is \mathbf{f}_r^D . We continue to use straight-line boundary elements on the capsule as we did in the previous section and discretise the capsule into N_P boundary elements. Since we will evaluate the boundary integral equation at the element mid-point, \mathbf{x}_m , we will set the velocity to be $\mathbf{u}_r^{(1)}$ at the mid-point of the r^{th} element. The vector of unknowns is therefore given by

$$\mathbf{x} = \left[\mathbf{F}_C^D \quad \mathbf{U}_P^{(1)} \quad \pi_2 \right]^T, \quad (4.56)$$

where T means transpose, and \mathbf{F}_C^D is a vector storing the disturbance tractions on the walls and $\mathbf{U}_P^{(1)}$ is the vector of capsule velocities. The vectors \mathbf{F}_C^D and $\mathbf{U}_P^{(1)}$ are,

$$\mathbf{F}_C^D = \left[f_{x,1}^D \quad f_{y,1}^D \quad \dots \quad f_{x,N_C}^D \quad f_{y,N_C}^D \right], \quad (4.57)$$

$$\mathbf{U}_P^{(1)} = \left[u_{x,1}^{(1)} \quad u_{y,1}^{(1)} \quad \dots \quad u_{x,N_P}^{(1)} \quad u_{y,N_P}^{(1)} \right]. \quad (4.58)$$

The evaluation of the disturbance pressure equation and the boundary integral equation involves the computation of $\Delta \mathbf{f}$ which in turn requires the value of the curvature, κ , and possibly its derivatives. Since the curvature is zero on a straight line we require a method of calculating κ on a boundary element. Therefore we will introduce a periodic cubic spline (e.g. Pozrikidis 2002a, §3) to represent the capsule's boundary, and from this spline we will calculate the necessary derivatives. In order to create the periodic cubic spline we must introduce a monotonically increasing parameter for the spline. We choose, for simplicity, the cumulative straight line distance along the straight elements which we will label β . We compute β at each node by traversing the capsule's boundary elements, and use β_r to indicate the value of β at the r^{th} node. The length of the r^{th} element is l_r and is computed by $l_r = \beta_{r+1} - \beta_r$. By periodicity, the start point of the first element will have $\beta = 0$ and $\beta = \beta_T$ where β_T is the total polygonal arc-length of the boundary. We construct the (β, \mathbf{x}) spline using the value of β at each of the boundary's nodes. The spline provides an approximation to the capsule's true boundary and also the first and second derivatives of \mathbf{x} with respect to β . The curvature may then be calculated using the formula

$$\kappa(\beta) = \frac{x' y'' - x'' y'}{\left((x')^2 + (y')^2 \right)^{\frac{3}{2}}}, \quad (4.59)$$

where the primes denotes differentiation with respect to β . However the inherent problem with a cubic spline is that the first derivative is quadratic in β and the second is linear in β . Furthermore the second derivative is continuous but not differentiable at a boundary node. To smooth the derivatives we use the first derivative from the (β, \mathbf{x}) spline to construct a (β, \mathbf{x}') spline, which in turn is used to construct a spline for the second derivative. These latter two splines are then used to calculate the curvature by equation (4.59). The calculated value of κ for each value of β is used to construct a (β, κ) spline. When

we consider an elastic capsule that resists bending we also require the derivatives of the curvature. We therefore apply the same process and construct the (β, κ') spline from the curvature spline, and the spline for the second derivative from the spline for the first derivative. The Δf calculation requires the values of $\frac{d\kappa}{ds}$ and $\frac{d^2\kappa}{ds^2}$, which we calculate from the splines using the chain rule, to get

$$\frac{d\kappa}{ds} = \frac{\kappa'}{s'}, \quad (4.60)$$

$$\frac{d^2\kappa}{ds^2} = \frac{\kappa''}{(s')^2} - \frac{s'' \kappa'}{(s')^3}, \quad (4.61)$$

where $s' = \sqrt{(x')^2 + (y')^2}$ and $s'' = (x'x'' + y'y'')/s'$. To validate the calculation of the curvature and its derivatives we considered the unit circle and ellipses of various aspect ratios but with an area equal to π . The curvature of a circle is equal to the reciprocal of its radius and the derivatives are zero. The values obtained from the cubic spline calculations were within 10^{-7} of their expected values (where the value has been non-dimensionalised by multiplication of the appropriate power of the radius). The curvature of an ellipse defined by $(x/a)^2 + (y/b)^2 = 1$ is given by

$$\kappa = ab \left(\left(\frac{a}{b} \right)^2 y^2 + \left(\frac{b}{a} \right)^2 x^2 \right)^{-\frac{3}{2}}. \quad (4.62)$$

The curvature derivatives may be obtained by differentiating this expression. The error in the calculations increased for the ellipses but lay within 10^{-4} for all tested aspect ratios. Once again the values were appropriately non-dimensionalised.

An elastic capsule also requires the value of the in-plane tension, τ , and its first derivative in the computation of Δf . We approximate τ , given in equation (4.51), using the lengths of the boundary elements in their rest and stressed states. The value of τ on the r^{th} element is approximated by

$$\tau = k \left(\frac{\partial s}{\partial s_R} - 1 \right) \approx k \left(\frac{l_r}{l_{r,0}} - 1 \right), \quad (4.63)$$

where l_r is the element length and $l_{r,0}$ is the length of the unstressed element. We construct a (β, τ) periodic cubic spline using the value of β at the element mid-point and the value of τ computed from equation (4.63)

We now proceed to the discretisation of the equations, starting with the pressure equation (4.19), which we write as

$$Q \pi_2 + (\lambda - 1) \int_{\mathcal{P}} \mathbf{u}^{(1)} \cdot \mathbf{f}^P \, ds(\mathbf{x}) = - \int_{\mathcal{P}} \mathbf{u}^P \cdot \Delta \mathbf{f} \, ds(\mathbf{x}). \quad (4.64)$$

We approximate the integrals as sums over the boundary elements such that the integral

on the left-hand side is

$$\begin{aligned} (\lambda - 1) \int_{\mathcal{P}} \mathbf{u}^{(1)} \cdot \mathbf{f}^P \, ds(\mathbf{x}) &\approx (\lambda - 1) \sum_{r=1}^{N_{\mathcal{P}}} \mathbf{u}_r^{(1)} \cdot \mathbf{f}_r^P(\mathbf{x}_{m,r}) l_r \\ &= \mathbf{\Pi}_{\mathcal{P}} \cdot \mathbf{U}_{\mathcal{P}}^{(1)} \end{aligned} \quad (4.65)$$

where $\mathbf{f}_r^P(\mathbf{x}_{m,r})$ is the Poiseuille traction computed at the element mid-point, and

$$\mathbf{\Pi}_{\mathcal{P}} = (\lambda - 1) \begin{bmatrix} f_{x,1}^P l_1 & f_{y,1}^P l_1 & \cdots & f_{x,N_{\mathcal{P}}}^P l_{N_{\mathcal{P}}} & f_{y,N_{\mathcal{P}}}^P l_{N_{\mathcal{P}}} \end{bmatrix}. \quad (4.66)$$

The integral on the right-hand side of (4.64) is

$$\int_{\mathcal{P}} \mathbf{u}^P \cdot \Delta \mathbf{f} \, ds(\mathbf{x}) \approx \sum_{r=1}^{N_{\mathcal{P}}} \mathbf{u}^P(\mathbf{x}_{m,r}) \cdot \Delta \mathbf{f}(\mathbf{x}_{m,r}) l_r = \Pi_{\Delta} \quad (4.67)$$

so that we may write equation (4.64) as the matrix/vector product,

$$\begin{bmatrix} \mathbf{0} & \mathbf{\Pi}_{\mathcal{P}} & Q \end{bmatrix} \cdot \mathbf{x} = -\Pi_{\Delta}. \quad (4.68)$$

Next we discretise the boundary integral equation which is valid when \mathbf{x}_0 lies on the walls of the channel. We separate the unknown and the known quantities in equation (4.29) to get

$$\begin{aligned} \int_{\mathcal{C}} f_i^D G_{ij} \, ds(\mathbf{x}) - \pi_2 \int_{\mathcal{E}_2} n_i G_{ij} \, ds(\mathbf{x}) + \mu(\lambda - 1) \int_{\mathcal{P}} u_i^{(1)} T_{ijk} n_k \, ds(\mathbf{x}) \\ = - \int_{\mathcal{P}} \Delta f_i G_{ij} \, ds(\mathbf{x}). \end{aligned} \quad (4.69)$$

The first term on the left-hand side is approximated by

$$\int_{\mathcal{C}} f_i^D G_{ij} \, ds(\mathbf{x}) \approx \mathbf{I}_{\mathcal{C},j}^G(\mathbf{x}_0) \cdot [\mathbf{F}_{\mathcal{C}}^D]^T \quad (4.70)$$

where

$$\mathbf{I}_{\mathcal{C},j}^G(\mathbf{x}_0) = \begin{bmatrix} \tilde{G}_{xj,1} & \tilde{G}_{yj,1} & \cdots & \tilde{G}_{xj,N_{\mathcal{C}}} & \tilde{G}_{yj,N_{\mathcal{C}}} \end{bmatrix}, \quad (4.71)$$

and $\tilde{G}_{ij,r}$ is defined by equation (2.55). The integral over \mathcal{E}_2 is labelled

$$I_{\mathcal{E}_2,j}^G(\mathbf{x}_0) = \int_{\mathcal{E}_2} n_i G_{ij}(\mathbf{x}, \mathbf{x}_0) \, ds(\mathbf{x}) \quad (4.72)$$

and can be computed exactly from equations (2.44) and (2.45). We denote the integral of

the stress tensor over the r^{th} element, E_r , by

$$\tilde{T}_{ij,r}(\mathbf{x}_0) = \int_{E_r} T_{ijk}(\mathbf{x}, \mathbf{x}_0) n_k \, ds(\mathbf{x}), \quad (4.73)$$

which is zero when \mathbf{x}_0 lies on the element for the reasons given in section 2.1 on page 24. Using (4.73) we can approximate the capsule integral on the left-hand side of equation (4.69) to get

$$\int_{\mathcal{P}} u_i^{(1)} T_{ijk} n_k \, ds(\mathbf{x}) \approx \sum_{r=1}^{N_{\mathcal{P}}} u_{r,i}^{(1)} \tilde{T}_{ij,r}(\mathbf{x}_0) = \mathbf{I}_{\mathcal{P},j}^T(\mathbf{x}_0) \cdot [\mathbf{U}_{\mathcal{P}}^{(1)}]^T \quad (4.74)$$

where

$$\mathbf{I}_{\mathcal{P},j}^T(\mathbf{x}_0) = \left[\tilde{T}_{xj,1}(\mathbf{x}_0) \quad \tilde{T}_{yj,1}(\mathbf{x}_0) \quad \cdots \quad \tilde{T}_{xj,N_{\mathcal{P}}}(\mathbf{x}_0) \quad \tilde{T}_{yj,N_{\mathcal{P}}}(\mathbf{x}_0) \right]. \quad (4.75)$$

The integral on the right-hand side of (4.69) is

$$\int_{\mathcal{P}} \Delta f_i G_{ij}(\mathbf{x}, \mathbf{x}_0) \, ds(\mathbf{x}) \approx \sum_{r=1}^{N_{\mathcal{P}}} \Delta f_i(\mathbf{x}_{m,r}) \tilde{G}_{ij,r}(\mathbf{x}_0) = \Pi_{G,j}(\mathbf{x}_0) \quad (4.76)$$

so that we may write the discretised analogue of equation (4.69) as

$$\left[\mathbf{I}_{\mathcal{C},j}^G(\mathbf{x}_0) \quad \mu(\lambda - 1) \mathbf{I}_{\mathcal{P},j}^T(\mathbf{x}_0) \quad -\mathbf{I}_{\mathcal{E}_2,j}^G(\mathbf{x}_0) \right] \cdot \mathbf{x} = -\Pi_{G,j}(\mathbf{x}_0). \quad (4.77)$$

Re-evaluation of this equation with \mathbf{x}_0 at the mid-point of each of the channel walls' boundary elements creates $N_{\mathcal{C}}$ pairs of equations which are assembled into the matrix,

$$\left[\mathbf{C}_{\mathcal{C}} \quad \mathbf{C}_{\mathcal{P}} \quad \mathbf{C}_{\mathcal{E}_2} \right] \cdot \mathbf{x} = \mathbf{b}_{\mathcal{C}} \quad (4.78)$$

where each of $\mathbf{C}_{\mathcal{C}}$, $\mathbf{C}_{\mathcal{P}}$, $\mathbf{C}_{\mathcal{E}_2}$ and $\mathbf{b}_{\mathcal{C}}$ consist of the $N_{\mathcal{C}}$ pairs of $\mathbf{I}_{\mathcal{C},j}^G(\mathbf{x}_0)$, $\mu(\lambda - 1) \mathbf{I}_{\mathcal{P},j}^T(\mathbf{x}_0)$, $-\mathbf{I}_{\mathcal{E}_2,j}^G(\mathbf{x}_0)$ and $-\Pi_{G,j}(\mathbf{x}_0)$ respectively. Finally we discretise the boundary integral equation (4.31) which is valid when \mathbf{x}_0 lies on the capsule boundary. We rewrite the equation as

$$\begin{aligned} \int_{\mathcal{C}} f_i^D G_{ij} \, ds(\mathbf{x}) - \pi_2 \int_{\mathcal{E}_2} n_i G_{ij} \, ds(\mathbf{x}) + \mu(\lambda - 1) \int_{\mathcal{P}} u_i^{(1)} T_{ijk} n_k \, ds(\mathbf{x}) \\ + 2\pi\mu(1 + \lambda)u_j^{(1)}(\mathbf{x}_0) = 4\pi\mu u_j^P(\mathbf{x}_0) - \int_{\mathcal{P}} \Delta f_i G_{ij} \, ds(\mathbf{x}). \end{aligned} \quad (4.79)$$

We use $\mathbf{x}_0^{(r)}$ to indicate the mid-point of the r^{th} element and define

$$\mathcal{P}_{u,j}(\mathbf{x}_0^{(r)}) = \left[\delta_{r1} \delta_{xj} \quad \delta_{r1} \delta_{yj} \quad \cdots \quad \delta_{rN_{\mathcal{P}}} \delta_{xj} \quad \delta_{rN_{\mathcal{P}}} \delta_{yj} \right], \quad (4.80)$$

which enables us to write equation (4.79) in the form

$$\begin{aligned} \left[\mathbf{I}_{\mathcal{C},j}^G(\mathbf{x}_0^{(r)}) - \mu(\lambda - 1) \mathbf{I}_{\mathcal{P},j}^{T,PV}(\mathbf{x}_0^{(r)}) + 2\pi\mu(1 + \lambda) \mathcal{P}_{u,j}(\mathbf{x}_0^{(r)}) - I_{\mathcal{E}_2,j}^G(\mathbf{x}_0^{(r)}) \right] \cdot \mathbf{x} \\ = 4\pi\mu u_j^P(\mathbf{x}_0^{(r)}) - \Pi_{G,j}(\mathbf{x}_0^{(r)}). \end{aligned} \quad (4.81)$$

Re-evaluation of this equation with \mathbf{x}_0 at the mid-point of each of the capsule's boundary elements creates $N_{\mathcal{P}}$ pairs of equations which are assembled into the matrix,

$$\begin{bmatrix} \mathcal{P}_{\mathcal{C}} & \mathcal{P}_{\mathcal{P}} & \mathcal{P}_{\mathcal{E}_2} \end{bmatrix} \cdot \mathbf{x} = \mathbf{b}_{\mathcal{P}} \quad (4.82)$$

where each of $\mathcal{P}_{\mathcal{C}}$, $\mathcal{P}_{\mathcal{P}}$, $\mathcal{P}_{\mathcal{E}_2}$ and $\mathbf{b}_{\mathcal{P}}$ consist of the $2N_{\mathcal{P}}$ equations generated from equation (4.81).

We have now completed the discretisation of the disturbance pressure equations and the boundary integral equations which govern the flow. We assemble the master linear system from equations (4.68), (4.78) and (4.82) to get

$$\begin{bmatrix} \mathcal{C}_{\mathcal{C}} & \mathcal{C}_{\mathcal{P}} & \mathcal{C}_{\mathcal{E}_2} \\ \mathcal{P}_{\mathcal{C}} & \mathcal{P}_{\mathcal{P}} & \mathcal{P}_{\mathcal{E}_2} \\ \mathbf{0} & \mathbf{\Pi}_{\mathcal{P}} & Q \end{bmatrix} \cdot \mathbf{x} = \begin{bmatrix} \mathbf{b}_{\mathcal{C}} \\ \mathbf{b}_{\mathcal{P}} \\ -\mathbf{\Pi}_{\Delta} \end{bmatrix}. \quad (4.83)$$

The submatrices in the first column of equation (4.83) have $2N_{\mathcal{C}}$ columns, the submatrices in the second column have $2N_{\mathcal{P}}$ columns and the final column has one. The rows of equation (4.83) each have $2N_{\mathcal{C}}$, $2N_{\mathcal{P}}$ and 1 row(s) respectively. Therefore the influence matrix has size $(2N_{\mathcal{C}} + 2N_{\mathcal{P}} + 1) \times (2N_{\mathcal{C}} + 2N_{\mathcal{P}} + 1)$. In our simulations we set $N_{\mathcal{C}} = 800$ for the channel walls, and $N_{\mathcal{P}} = 316$ for a capsule of initial radius 0.5. We increased $N_{\mathcal{P}}$ for larger particles to maintain the element length, and decreased $N_{\mathcal{P}}$ for smaller particles. The initial capsule shape was usually circular but the formulation caters for an arbitrary initial shape. In the absence of external forces the fluid drop will adopt a circular shape. The elastic capsule has a circle as its unstressed shape.

Now we can build the linear system and solve it using a standard method. We found it practical to use the Generalised Minimal Residuals (GMRES) (e.g. Trefethen and Bau 1997, Saad 2003) to find the disturbance tractions, the disturbance pressure and the capsule element mid-point velocities. The iterative scheme typically converged in under 200 iterations for the discretisation configuration given above. We therefore found it unnecessary to precondition the matrix. We computed the capsule node velocities from the mid-point velocities via a periodic cubic spline. We use an iterative solver in favour of Gaussian elimination because it is an order of magnitude faster and we will be using the solution to move the capsule. Once the capsule nodes have been moved the master linear system is rebuilt and resolved. To move the capsule we integrated the kinematic equation,

$$\frac{d\mathbf{x}_r}{dt} = \mathbf{u}(\mathbf{x}_r), \quad (4.84)$$

where \mathbf{x}_r is the position vector of the r^{th} capsule node and the values of $\mathbf{u}(\mathbf{x}_r)$ are obtained from the velocity cubic spline, which was constructed using the element mid-point velocities. It should be noted that we have a choice in the way we move the capsule boundary. We chose to use equation (4.84) which in effect uses the local fluid velocity. As an alternative, we could have used the normal component of velocity to move each node. We used the adaptive time-stepping Runga-Kutta-Fehlberg method (e.g. Atkinson 1978) to integrate (4.84). For the time integration we took an initial time step of $dt = 0.01 d/U_0$ for a fluid drop and $dt = 0.005 d/U_0$ for an elastic capsule which does not resist bending. A particularly small time step was found to be required when bending moments are taken into account in the membrane, $E_B \neq 0$, in line with the observations of Pozrikidis (2001). Therefore we took the initial time step to be $dt = 0.0005 d/U_0$ for an elastic capsule which resists bending. To avoid a situation where the capsule would move close to the exit, after each iteration of the numerical scheme we moved the capsule such that the x -component of its centroid was positioned at $x/d = l/2$. We exit the numerical scheme if the capsule attains a steady shape, where we define a steady shape to be one where the y 's component of the centroid's velocity and the normal component of the boundary node velocities, with respect to the velocity of the capsule centroid, are all less than than $0.0001 U_0$. We computed the instantaneous streamlines by integrating the equation

$$\frac{d\mathbf{x}}{ds} = \mathbf{u}(\mathbf{x}) \quad (4.85)$$

along the streamline, where \mathbf{x} is the position vector of a point on the streamline, s measures the arc-length along the streamline and the velocity on the right-hand side is computed from equation (4.32). We also calculated the streamlines relative to a frame of reference fixed at the capsule's centroid, which we will call pathlines to distinguish them from the streamlines. To calculate the pathlines, we integrated the kinematic equation,

$$\frac{d\mathbf{x}'}{dt} = \mathbf{u}(\mathbf{x}') - V_x \mathbf{i}, \quad (4.86)$$

where \mathbf{x}' is the position vector of a point moving with the frame of reference, \mathbf{u} is again calculated from equation (4.32), and V_x is the x -component of the velocity of the capsule's centroid.

The discretisation which leads to the linear system in equation (4.83) was formulated for a general capsule. However when $\lambda = 1$, considerable simplifications can be made. The disturbance pressure equation becomes,

$$\pi_2 = -\frac{1}{Q} \int_{\mathcal{P}} \mathbf{u}^P \cdot \Delta \mathbf{f} \, ds(\mathbf{x}), \quad (4.87)$$

which can be computed directly for a given capsule shape. When \mathbf{x}_0 lies on \mathcal{C} , equation

(4.29) simplifies to

$$\int_{\mathcal{C}} f_i^D G_{ij} \, ds(\mathbf{x}) = \pi_2 \int_{\mathcal{E}_2} n_i G_{ij} \, ds(\mathbf{x}) - \int_{\mathcal{P}} \Delta f_i G_{ij} \, ds(\mathbf{x}), \quad (4.88)$$

which means that the linear system reduces to,

$$\mathcal{C}_C \cdot \mathbf{F}_C^D = \mathbf{b}_C, \quad (4.89)$$

and the left-hand side is independent of the capsule. Therefore, the inverse of the \mathcal{C}_C matrix is computed and the wall disturbance tractions are found directly, and the iterative method is not required. As the capsule's shape evolves the right-hand side of equation (4.89) is recomputed and the solution found by

$$\mathbf{F}_C^D = (\mathcal{C}_C)^{-1} \cdot \mathbf{b}_C. \quad (4.90)$$

The capsule node velocities, or any other point in the flow, may then be found by

$$u_j^{(1)}(\mathbf{x}_0) = u_j^P(\mathbf{x}_0) + \frac{1}{4\pi\mu} \left(\pi_2 \int_{\mathcal{E}_2} n_i G_{ij} \, ds(\mathbf{x}) - \int_{\mathcal{C}} f_i^D G_{ij} \, ds(\mathbf{x}) - \int_{\mathcal{P}} \Delta f_i G_{ij} \, ds(\mathbf{x}) \right), \quad (4.91)$$

and the capsule nodes are updated using equation (4.84).

We have now finished describing the numerical method. We will first consider a fluid drop and validate the numerical model before moving on to the results. An elastic capsule is considered in section 4.4.2.

4.4 Model validation and results

For all results we truncated the channel so that $l = 12d$. We found this truncation length sufficient for the disturbance flow to decay as we approach the entrance or exit to the computational domain. The Poiseuille pressure drop between the entrance and exit for a channel of length $l = 12d$ is $24\mu U_0/d$.

The dynamics depend on the viscosity ratio, λ , the initial dimensionless particle radius, ρ , and the initial centreline offset, σ , which are defined by

$$\rho = \frac{a}{d}, \quad \sigma = \frac{y_c}{d}, \quad (4.92)$$

where a is the radius of the unstressed circular shape, $\mathbf{x}_c = (x_c, y_c)$ is the capsule centroid calculated using equation (3.8). We placed the drop or capsule centroid at the mid-point of the channel, such that $x_c/d = 6$, and varied λ , ρ and σ . As in previous chapters, we checked the numerical implementation by confirming that the discretised form of the

integral identities for Stokes flow given in equations (1.3.34) and (1.3.31) were satisfied to within an acceptable tolerance. We checked the validity of both identities by setting \mathbf{x}_0 to the mid-point of every boundary element and to several points inside and outside of the flow domain.

To validate the numerical solution we used a channel with $l = 12d$ and a capsule with $\rho = 0.5$ and $\sigma = 0$ as our reference configuration. The boundary velocities were included in the solution by setting $\lambda = 2$. Firstly we computed the solution for a longer channel with $l = 24d$, then we reset the channel length and doubled the number of elements on each boundary with respect to the reference configuration. In all cases we found that the tractions in the solution vector differed by less than $0.001 \mu U_0/d$ from the values obtained for the reference configuration, and the nodal velocities by less than $0.0005 U_0$.

We will present results for a fluid drop before moving on to an elastic capsule in 4.4.2.

4.4.1 A fluid drop – results

In addition to λ , ρ , and σ the dynamics of a fluid drop also depend on the Capillary number, C_a , which we define as

$$C_a = \frac{\mu U_0}{\gamma}, \quad (4.93)$$

where U_0 is the centreline velocity of the undisturbed Poiseuille flow and γ is the constant surface tension. The capillary number represents the relative effect of viscous forces to surface tension.

To further validate the numerics for a fluid drop, we compared the steady shape for the reference configuration described above with the steady shape when the number of boundary elements was doubled. In both simulations we set $\lambda = 1$ and $C_a = 1$. There were negligible differences between the two shapes. For instance, the difference in the position of the nodes between the two configurations was less than $0.0001d$. Also the evolution of the pressure for the two configurations typically differed by less than $0.0001 \mu U_0/d$ for a given time.

We placed a circular drop in the flow and computed the disturbance pressure and the wall tractions for $\lambda = 1$. At $t = 0$ we expect the disturbance pressure to be zero because the drop is in its unstressed state and so the pressure equation reduces to

$$\pi_2 = -\frac{1}{Q} \int_{\mathcal{P}} \mathbf{u}^P \cdot \Delta \mathbf{f} \, ds(\mathbf{x}) = -\frac{\gamma \kappa}{Q} \int_{\mathcal{P}} \mathbf{u}^P \cdot \mathbf{n} \, ds(\mathbf{x}), \quad (4.94)$$

which is zero when \mathcal{P} is a circle. We also expect the disturbance tractions on the channel walls to vanish since from equation (4.29) we have

$$\int_{\mathcal{C}} f_i^D G_{ij} \, ds(\mathbf{x}) \approx - \int_{\mathcal{P}} \Delta f_i G_{ij} \, ds(\mathbf{x}) = -\gamma \kappa \int_{\mathcal{P}} n_i G_{ij} \, ds(\mathbf{x}) = 0, \quad (4.95)$$

by equation (1.3.34). In our computations we found $\pi_2 \approx 10^{-14} \mu U_0/d$ and $|\mathbf{f}^D| \approx 10^{-12} \mu U_0/d$ for a range of ρ , σ and C_a . Under these conditions the disturbance velocity

is negligible. When $\lambda \neq 1$ the disturbance pressure will be non-zero for a circular capsule because an additional integral over the capsule is included in the calculation.

For each simulation, we will check that the velocity decays as we move away from the drop and is negligible at the entrance and exit, and that the disturbance tractions decay to zero at the entrance. At the exit we will check that f_x^D decays to zero at the exit and f_y^D tends to the disturbance pressure. We will also check that the capsule's area is preserved since it should remain constant due to the incompressibility of the capsule fluid. If numerical error leads to the area error increasing above 0.1% then we perform an isotropic expansion or deflation of the shape by dividing each node vector (from the centroid) by a factor equal to the original radius divided by the current equivalent radius, $\sqrt{A/\pi}$, where A is the current area, which is in line with Zhou and Pozrikidis (1993). To compute the area we apply the divergence theorem with the vector field equal to the position vector, $\mathbf{x} = x\mathbf{i} + y\mathbf{j}$. Since $\nabla \cdot \mathbf{x} = 2$, we have

$$\int_{\mathcal{P}} \mathbf{x} \cdot \mathbf{n} \, ds(\mathbf{x}) = \iint_{D_{\mathcal{P}}} \nabla \cdot \mathbf{x} \, dA(\mathbf{x}) = 2 A_{\mathcal{P}}, \quad (4.96)$$

where $D_{\mathcal{P}}$ is the capsule domain and $A_{\mathcal{P}}$ is the capsule area, and so

$$A_{\mathcal{P}} = \frac{1}{2} \int_{\mathcal{P}} \mathbf{x} \cdot \mathbf{n} \, ds(\mathbf{x}), \quad (4.97)$$

where we can compute \mathbf{x} on the capsule boundary using the (β, \mathbf{x}) spline, and $\mathbf{n} = (x', y')/s'$, where the prime denotes differentiation with respect to β . Our final check regards the drop's interfacial tractions. Application of equation (4.36) gives

$$\int_{\mathcal{P}} \kappa \mathbf{n} \, ds(\mathbf{x}) = - \int_{\mathcal{P}} \frac{dt}{ds} \, ds(\mathbf{x}) = - \int_{\mathcal{P}} dt = 0 \quad (4.98)$$

by periodicity. Therefore, for a fluid drop, we have

$$\int_{\mathcal{P}} \Delta \mathbf{f} \, ds(\mathbf{x}) = 0, \quad (4.99)$$

which is used at each time step in the numerical integration to check the computed values of the interfacial traction jump. We found that for all simulations $|\int_{\mathcal{P}} \kappa \mathbf{n} \, ds(\mathbf{x})| < 10^{-4}$. During the course of the simulation the boundary elements may lengthen or shorten. If the lengths of one or more element became less or more than a threshold value, the boundary was discretised with points located regularly with respect to β . The boundary was then smoothed using the 5-point formula of Longuet-Higgins and Cokelet (1976).

We start our results with an initially circular drop which has $\lambda = 1$, $\rho = 0.5$, $\sigma = 0$ and $C_a = 1$. At $t = 0$ the disturbance pressure and tractions are negligible, as expected. Therefore the disturbance to the flow, in terms of the velocity and wall tractions, is also negligible. As the simulation progresses the circular shape deforms due to the incident

velocity profile and at $t = 9.12 d/U_0$, the drop attains a steady shape. When the drop attains a steady shape, the disturbance pressure is $-0.099 \mu U_0/d$, the centroid velocity is $0.935 U_0 \mathbf{i}$ and it has travelled a distance of 17 drop radii along the channel. To compare the results for a fluid drop with those for a rigid particle we set the initial shape of the rigid particle to be the shape of the steady drop and computed the disturbance pressure and translational velocity. The disturbance pressure is $-0.287 \mu U_0/d$ for the rigid particle which is almost three times greater than for a fluid drop. The rigid particle translates with velocity $0.895 U_0 \mathbf{i}$ which is 96% of the drop's velocity. It is interesting to note that while the particle and drop velocities do not differ greatly, the disturbance pressure is significantly higher for a rigid particle. Next we checked the value of the disturbance pressure against that predicted by equation (4.24), and found that it differed by less than 0.02% from $-0.099 \mu U_0/d$. We can see from the decay of the disturbance traction shown in figure 4.3 (a) that the x -component decays to zero, and the y -component decays to zero at the entrance and to the value of the disturbance pressure at the exit. The x -component of the fluid velocity along the channel centreline, $y/d = 0$, is plotted in figure 4.3 (b). The gap in the profile corresponds to the drop, where the velocity was not calculated. Both parts of the curve terminate at $u_x^{(1)} = 0.935 U_0$, but close to the left-hand side of the drop the x -component of velocity decreases further before returning to $0.935 U_0$ at the drop boundary. Points close to the drop suffer the greatest disturbance from the Poiseuille centreline velocity, but upstream and downstream, the disturbance has decayed to less than 1% after 4 drop radii from the drop centroid. The steady shape is shown

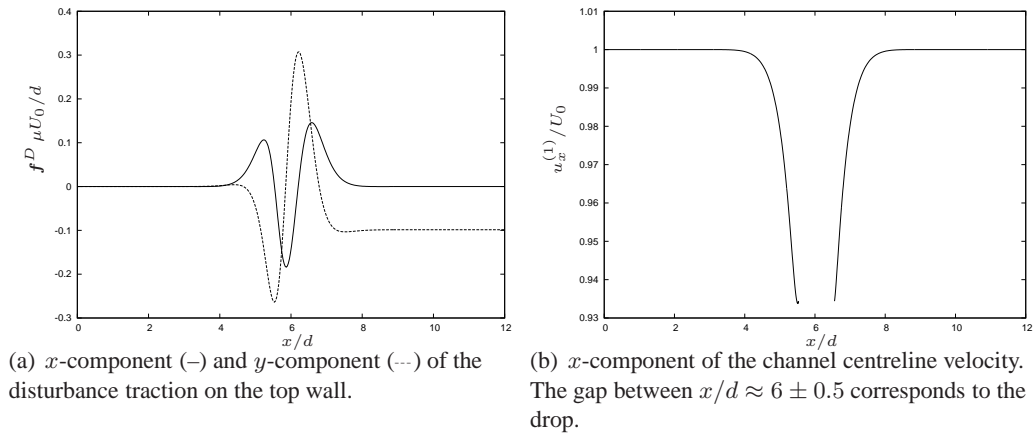


Figure 4.3 : Disturbance tractions on the top wall and the centreline velocity for a steady drop with $\lambda = 1$, $\rho = 0.5$, $\sigma = 0$ and $C_a = 1$.

in figure 4.4 (a) where we can see that the rear of the drop becomes flattened and the shape resembles a rounded triangle. The disturbance pressure is displayed in figure 4.4 (b), where we define the normalised disturbance pressure $\hat{\pi}_2$ by $\hat{\pi}_2 = \pi_2 d/\mu U_0$. In the figure we can see that the pressure increases in magnitude from zero to a maximum value of $\hat{\pi}_2 = -0.104$ at $t = 2.65 d/U_0$ before tending to $\hat{\pi}_2 = -0.099$. The evolution of the disturbance pressure is characterised by the initial rapid change as the circular drop responds to the incident flow, and a second phase in which the drop settles to its steady

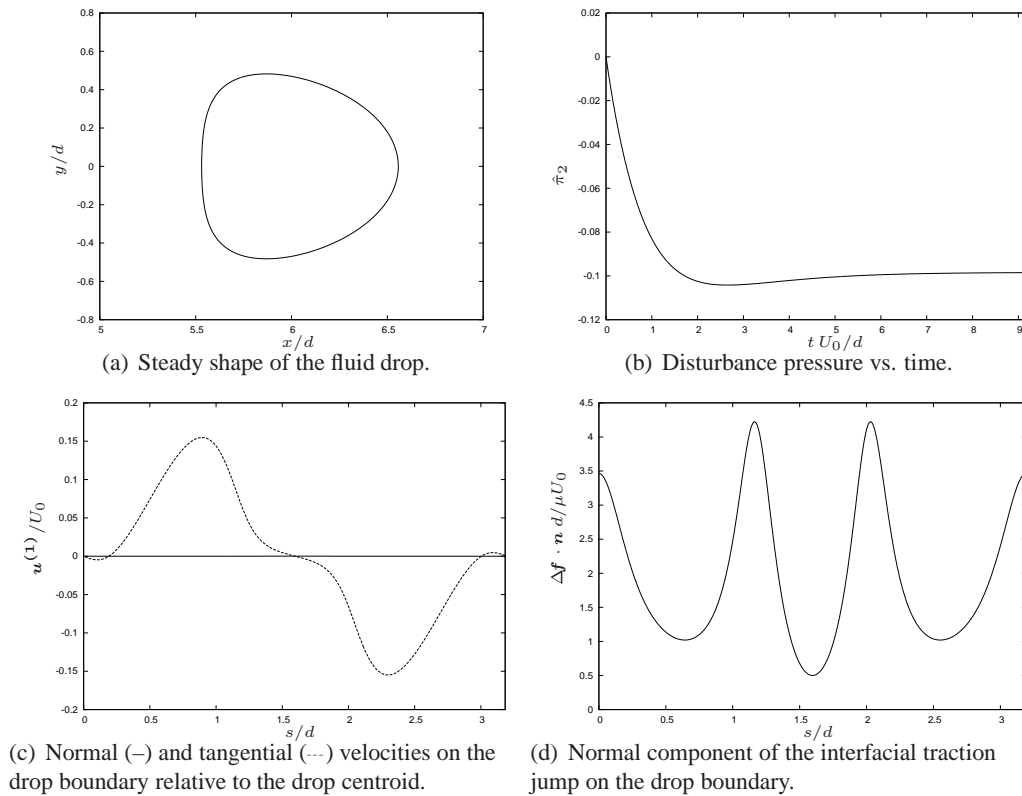


Figure 4.4 : Steady shape, disturbance pressure, boundary velocities and interfacial traction jump for a steady fluid drop with $\lambda = 1$, $\rho = 0.5$, $\sigma = 0$, $C_a = 1$.

shape. In figure 4.4 (c) we plot the normal and tangential velocities, with respect to the drop centroid, as a function of arc-length, s . We measure s anti-clockwise from zero at the right-most point on the drop, and the total arc-length of the drop is $S_T = 3.19 d$. The normal component is effectively zero, which is implied by our criteria for a steady shape. The tangential component reveals some interesting features of the drop's boundary velocities. For positive s close to zero the tangential velocity is negative which indicates the velocity is directed towards the point with $s = 0$. The tangential velocity is zero at $s = 0.19 d$. For $s \in (0.19 d, S_T/2)$ the tangential velocity is positive and therefore in the same direction as increasing s , and a maximum value of the tangential velocity is attained at $s = 0.9 d$. The tangential velocity is zero at $s = S_T/2$. The story is reversed on the lower half of the drop. For $s \in (S_T/2, 3.00 d)$ the velocity is towards the rear of the drop, and in the region $(3.00 d, S_T)$ the velocity is towards the point with $s = 0$ or equivalently $s = S_T$. These zeroes in the tangential velocity imply that there are four stagnation points on the drop boundary at $s/d = 0, 0.19, 1.60$ and 3.00 . In figure 4.4 (d) we show the normal component of the interfacial traction jump, $\Delta \mathbf{f}$, which equals $\gamma \kappa$. Since the surface tension is constant, the figure shows how the curvature varies with arc-length around the drop. There are three peaks in the curvature which correspond to the three 'corners' of the rounded triangle. On the rear of the drop, the curvature drops to a minimum of 0.5 which would be the curvature of a circle of radius 2. Finally for this drop, we plot the instantaneous streamlines in figure 4.5 (a) and the pathlines in figure 4.5 (b),

where the former is from a frame of reference fixed to the walls and the latter for a frame of reference moving with the constant translational velocity of the centroid. The pathlines close to the left-hand side of the steady drop are shown in figure 4.5 (c) where we can see the presence of a point at $(5.48, 0)d$ which moves with the same velocity as the drop. Fluid on the centreline with $x/d < 5.48$, and fluid in the gap between $x/d = 5.48$ and the drop moves towards the point $(5.48, 0)d$. The pathlines which enter the figure from the top-right move towards the centreline before turning sharply and moving upwards and to the left. The pathlines then move towards the entrance as they move away from the drop.

In our next set of results we increase the drop radius such that $\rho = 0.75$, and maintain the values of the remaining parameters. The drop attains a steady shape at $t = 17.58 d/U_0$ which is almost twice as long as for the drop with $\rho = 0.5$ considered above. The disturbance pressure and translational velocity for the steady drop are $-0.266 \mu U_0/d$ and $0.899 U_0 \hat{i}$ respectively. Using equation (4.24), we computed a value for the disturbance pressure which differed by only 0.02%. Compared to the drop with $\rho = 0.5$, the disturbance pressure has increased by a factor of about 2.7 while the velocity has only decreased by 3.8%. Figure 4.6 (a) shows the x and y components of the disturbance tractions on the top wall. We can see that the x -component decays to zero at the entrance and exit, the y -component decays to zero at the entrance and to the value of the disturbance pressure at the exit. The magnitude of the maximum disturbance traction has increased significantly compared to the previous case when $\rho = 0.5$. We computed the centreline velocity and found the disturbance velocity close to the drop decays to 1% of its maximum value at a distance of 3.2 drop radii, upstream and downstream, from the drop centroid. This distance is only slightly greater than for the drop with $\rho = 0.5$ which demonstrates the rapid decay of the disturbance velocity as we move away from the drop. The steady drop shape is shown in figure 4.6 (b) where this time the shape resembles a bullet, and a slight dimple may be seen at the rear of the drop. The drop has travelled 20.8 drop radii (or equivalently $15.6 d$) along the channel when it reaches its steady shape. The evolution of the disturbance pressure is shown in figure 4.6 (c). The behaviour is qualitatively similar to the $\rho = 0.5$ case but this time the disturbance pressure overshoots the steady value considerably before settling to the steady value. Figure 4.6 (d) shows the normal and tangential velocities, with respect to the drop centroid, as a function of arc-length, s . Again $s = 0$ at the right-most point of the drop. The total arc-length of the drop is $S_T = 5.10 d$ and again the normal component is zero since the drop is steady. The tangential component exhibits the same qualitative behaviour as for the drop with $\rho = 0.5$, but now the magnitude of the maximum velocity is greater. We show the pathlines in figure 4.7 where the frame of reference is moving with the constant translational velocity of the drop centroid. The pathlines are similar in nature to those shown previously in figure 4.5 (b).

Next we decrease the capillary number and place a drop on the centreline such that, $\lambda = 1$, $\rho = 0.5$, $\sigma = 0$ and $C_a = 0.5$. A decrease in the capillary number corresponds to an increase in the effect of surface tension relative to the viscous forces on the drop. The drop attained a steady shape at $t = 4.35 d/U_0$ with respect to an increased nodal velocity tolerance of $0.0007 U_0$. The steady drop's velocity is $0.931 \hat{i}$. The steady shape is shown

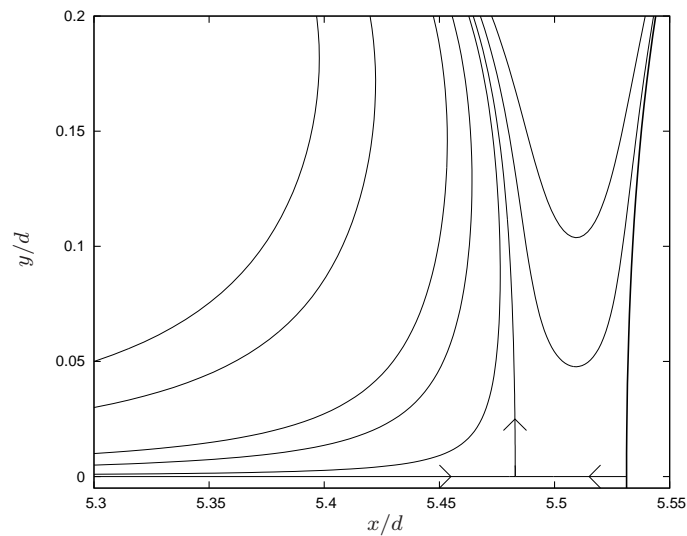
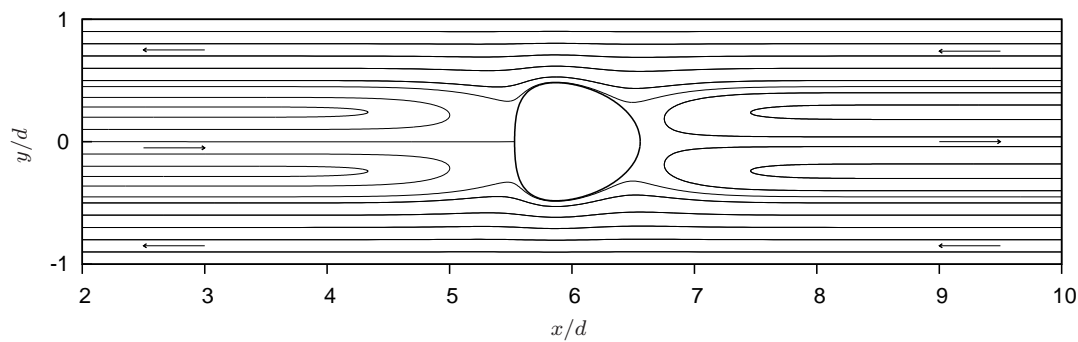
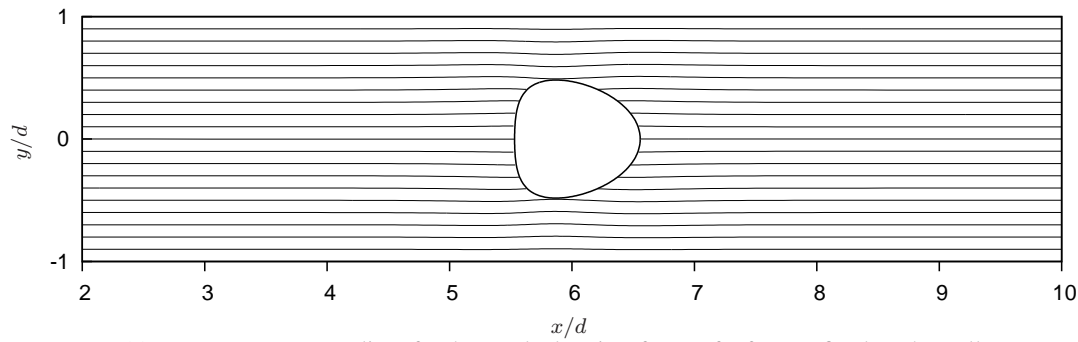


Figure 4.5 : Streamlines and pathlines for a steady fluid drop $\lambda = 1$, $\rho = 0.5$, $\sigma = 0$, $C_a = 1$.

in figure 4.8 (a). We can see that the shape is noticeably less deformed than the shape in figure 4.4 (a) where $C_a = 1$ and the remaining parameters are identical. The disturbance pressure settles to $-0.108 \mu U_0/d$ which is slightly higher than the disturbance pressure when $C_a = 1$. The evolution of the disturbance pressure is shown in figure 4.8 (b). We can see from the figure that the disturbance pressure does not overshoot the steady value during the initial period of deformation. The pathlines are shown in figure 4.8 (c) where

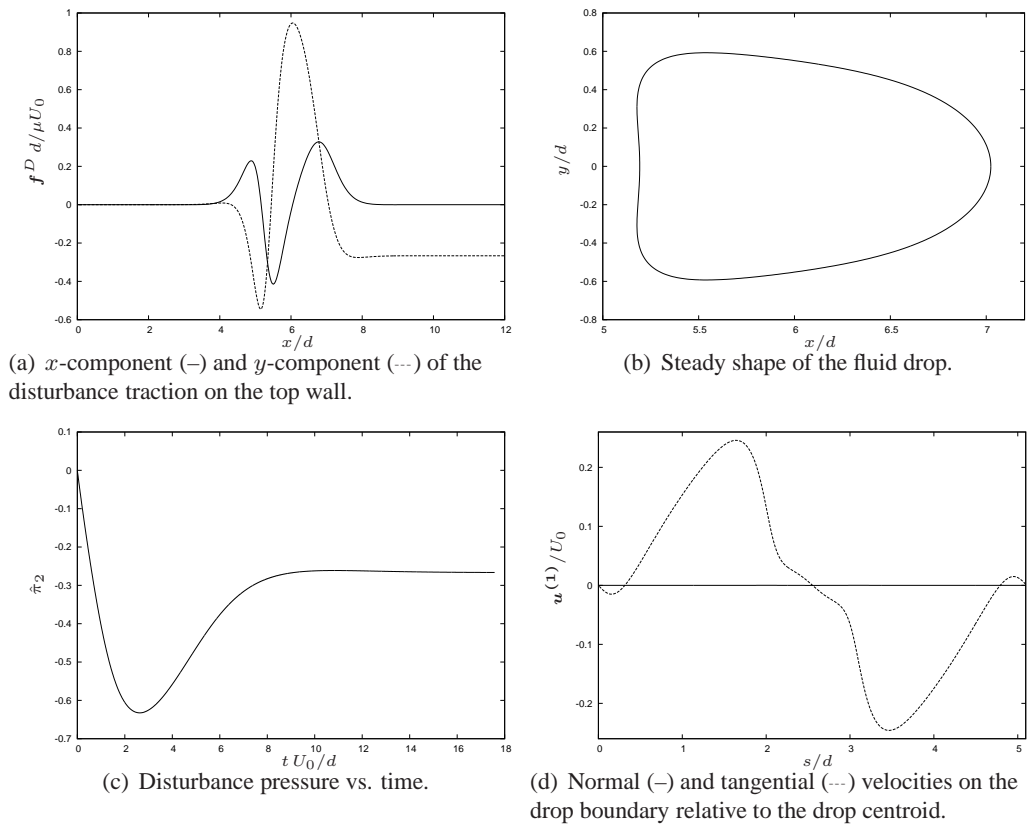


Figure 4.6 : Top wall disturbance tractions, steady shape, disturbance pressure and drop boundary velocities for a steady fluid drop with $\lambda = 1$, $\rho = 0.75$, $\sigma = 0$, $C_a = 1$.

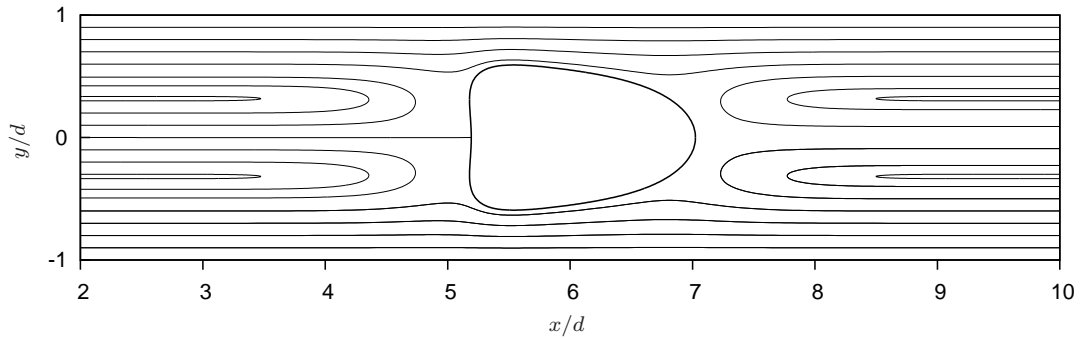


Figure 4.7 : Pathlines for a steady fluid drop $\lambda = 1$, $\rho = 0.75$, $\sigma = 0$ and $C_a = 1$. The frame of reference is moving with the drop centroid.

the behaviour is similar to previous simulations.

In our next set of results we increase the capillary number in order to observe the effect of a lower surface tension. The simulation parameters are $\lambda = 1$, $\rho = 0.5$, $\sigma = 0$ and $C_a = 2$. The shape becomes steady at $t = 19.28 d/U_0$ with respect to an increased velocity tolerance of $0.002 U_0$. The drop shape is shown in figure 4.9 (a) where we can see a well developed dimple at the rear of the drop, and the shape is deformed more than the simulation in which $C_a = 1$. The evolution of the disturbance pressure is shown in figure 4.9 (b) where we see that the disturbance pressure drops to around $-0.102 \mu U_0/d$ before settling to $-0.079 \mu U_0/d$. The pathlines relative to the moving drop are shown in

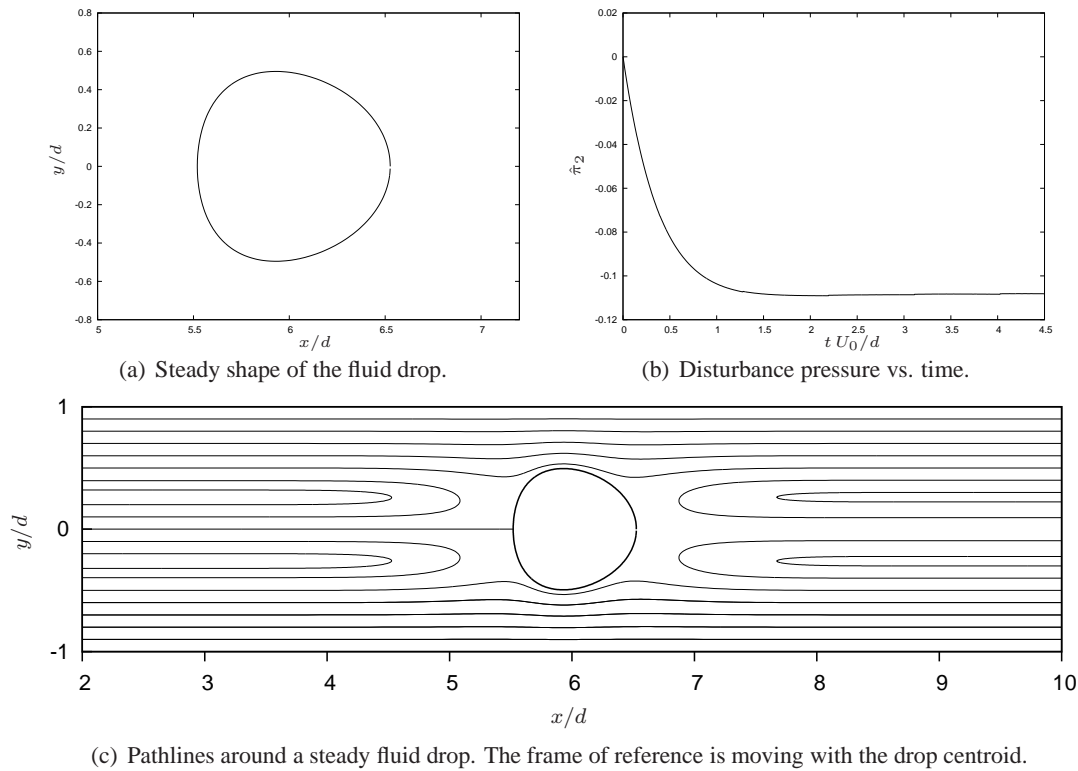


Figure 4.8 : Steady drop shape, disturbance pressure and pathlines for a fluid drop with $\lambda = 1$, $\rho = 0.5$, $\sigma = 0$ and $C_a = 0.5$.

figure 4.9 (c).

Next we offset the drop from the centreline and set $\lambda = 1$, $\rho = 0.5$, $\sigma = 0.25$ and $C_a = 1$. The drop moves towards the centreline as the simulation progresses. When $t = 11.14 d/U_0$ the drop's centroid lies at $(6, 0.125)$ which is half way to the centreline, and the centroid is within $0.001 d$ when $t > 102.8 d/U_0$. The migration of the drop towards the centreline is much swifter initially, reflecting the fact that the velocity gradient across the drop (in the y -direction) is greatest when the drop is offset from the centreline. The centroid's y -component is plotted against time in figure 4.10 (a). We see that drop moves slightly closer to the top wall at the start of the simulation during a period of initialisation. As time progresses the distance between the centreline and the centroid reduces exponentially, with $y_c/d \approx \sigma \exp^{-0.06 t}$. The disturbance pressure is shown in figure 4.10 (b), where we see a large change initially before the pressure settles to $-0.099 \mu U_0/d$, which is slightly different to the case for a centred drop. The discrepancy is due to the fact the drop does not quite reach the centreline and its boundary remains slightly unsymmetric. We computed the normal and tangential components of velocity on the drop's perimeter, relative to the drop's centroid, when $t = 11.14 d/U_0$, and they are shown in figure 4.10 (c) where the arc-length, s , is measured anti-clockwise from zero at the right-most point of the drop. The centroid's velocity at this juncture is $(0.928, -0.009)U_0$. The normal component, although small, is non-zero indicating the drop shape is still evolving. The tangential component is zero at four points around the boundary; $s/d = 0.19, 1.18, 1.82$ and 2.55 , thus indicating the presence of four stagnation points on the boundary. The

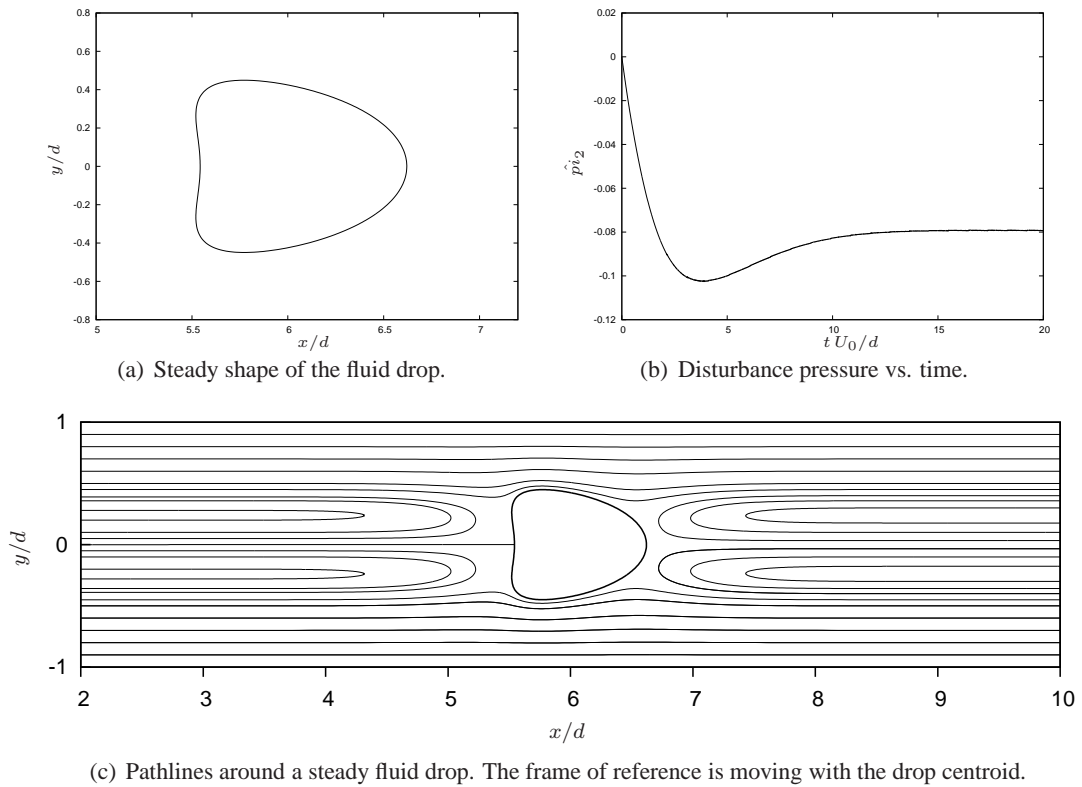


Figure 4.9 : Steady drop shape, disturbance pressure and pathlines for a fluid drop with $\lambda = 1$, $\rho = 0.5$, $\sigma = 0$ and $C_a = 2$.

tangential component has a maximum at $s/d \approx 1$ which corresponds to the portion of the drop closest to the top wall. We computed the pathlines for the drop when its centroid is located at $(6, 0.125)$ and they are shown in figure 4.11. We can see the change in the drop shape, with the region closest to the top wall suffering the most deformation. Two eddies are present, one upstream and one downstream from the drop, in a similar fashion to the case of an off-centre rigid particle discussed in the previous chapter. However, in this case the eddies are considerably different in size. The fluid in both eddies moves in a clockwise direction. The pathlines which are closest to the channel walls suffer little deflection from their original paths, but the pathlines which pass close to the drop are deflected around the drop. The most deflection is suffered by the pathline which passes around the top of the drop and then circumnavigates the downstream eddy before continuing its journey to the exit. The figure also shows a pathline which terminates close to the right-most point of the drop, corresponding to the stagnation point at $s/d = 0.19$.

We ran simulations for drops with $\lambda = 2$ and 5 , and with $\rho = 0.5$, $\sigma = 0$ and $C_a = 1$. The eventual drop shape was not materially different to the $\lambda = 1$ case shown in figure 4.4 (a), however as the viscosity ratio increases it takes longer for the drop to attain the shape. The disturbance pressure induced by the drop is considerably higher when $\lambda > 1$. When $\lambda = 1$ the disturbance pressure tends to $-0.099 \mu U_0/d$ which increases to $-0.171 \mu U_0/d$ when $\lambda = 2$, and to $-0.232 \mu U_0/d$ when $\lambda = 5$. For comparison purposes, the disturbance pressure for a rigid particle with the same shape is $-0.287 \mu U_0/d$. Therefore as the

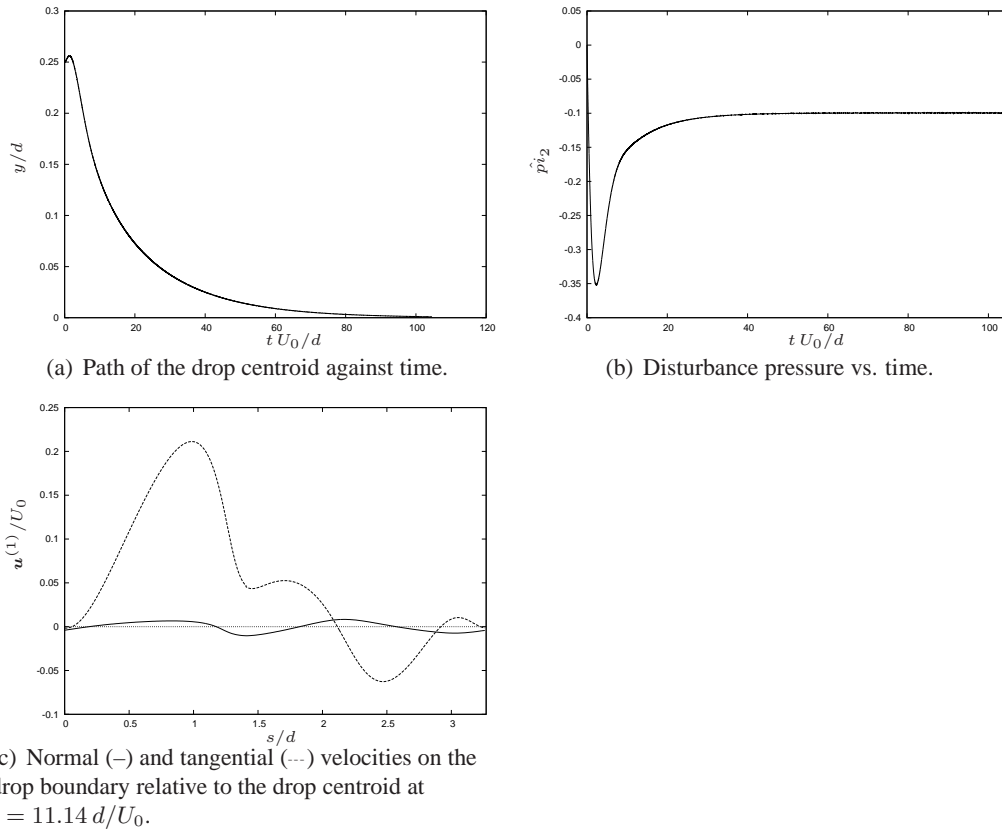


Figure 4.10 : Evolution of the drop centroid, disturbance pressure and the boundary velocity for a fluid drop with $\lambda = 1$, $\rho = 0.5$, $\sigma = 0.25$ and $C_a = 1$.

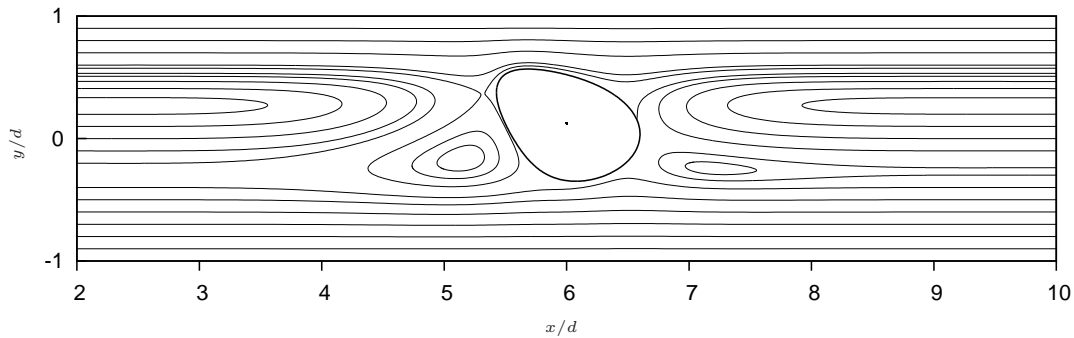


Figure 4.11 : Pathlines around the fluid drop with $\lambda = 1$, $\rho = 0.5$, $\sigma = 0.25$ and $C_a = 1$ at $t = 11.14 d/U_0$. The centroid is displayed as a dot at $(6, 0.125)$ and the frame of reference is moving axially with the drop centroid. Arc-length is measured anti-clockwise from zero at the rightmost point of the drop.

viscosity ratio increases, the disturbance pressure tends to the rigid particle disturbance pressure, which we expect since the limit, $\lambda \rightarrow \infty$, corresponds to the drop becoming a rigid particle. The drop centroid velocities are $0.920 U_0 \mathbf{i}$ and $0.907 U_0 \mathbf{i}$ for the drops with $\lambda = 2$ and 5 respectively. Both drops move more slowly than the $\lambda = 1$ drop, which translates with velocity $0.935 U_0 \mathbf{i}$. As λ increases further we would expect the velocity to tend to the rigid particle's translational velocity of $0.895 U_0 \mathbf{i}$. In figure 4.12 we compare the evolution of the disturbance pressures for $\lambda = 1, 2$ and 5 . At the start of each

simulation we see that the disturbance pressure increases in magnitude, although the rate at which it changes decreases as the viscosity ratio increases. As the viscosity ratio increases the difference between the initial value of the disturbance pressure and its steady value becomes smaller.

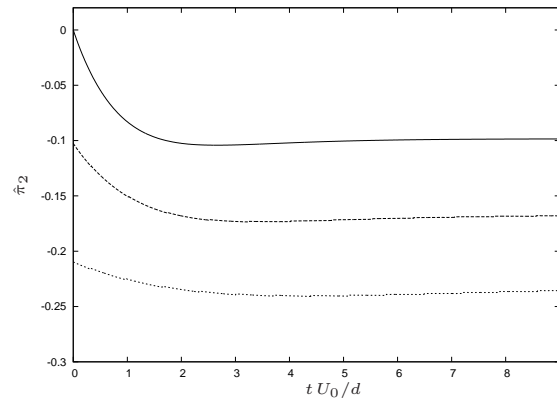


Figure 4.12 : Disturbance pressure for drops with $\rho = 0.5$, $\sigma = 0$ and $C_a = 1$. The viscosity ratios are $\lambda = 1$ (—), $\lambda = 2$ (---) and $\lambda = 5$ (···).

Finally we attempted to replicate the results in figure 14 of Zhou and Pozrikidis (1994) who considered the two-dimensional pressure-driven flow of liquid drops in a channel using the boundary integral method. The parameters for the simulations were $\lambda = 10$, $\rho = 0.25$ and $C_a = 1$. The evolution of drops released with their dimensionless offsets at $\sigma = -0.05$, -0.35 , -0.5 and -0.65 were computed. The centroid paths are displayed in figure 4.13 and the evolving drop shape for the $\sigma = -0.65$ case is shown in figure 4.14, where these figures are the analogues of Figures 14(a) and 14(e) in Zhou and Pozrikidis (1994). The centroids displayed in figure 4.13 do not meander like the centroids in Zhou and Pozrikidis (1994). We find that the drop with $\sigma = -0.05$ does not deviate, whereas Zhou and Pozrikidis (1994) found that it moved away from the centreline. The other drops all move towards the centreline, whereas Zhou and Pozrikidis (1994) found their drops tended to congregate in the region $-0.55 < y/d < -0.4$. The evolution of the drop shape for $\sigma = -0.65$ is shown in figure 4.14 and we can see that the initial deformation is the greatest before the drop regains a more circular shape as it travels towards the centreline. The drop shapes in Zhou and Pozrikidis (1994) exhibit greater deformation for longer. There are several possible reasons for the differences. In Zhou and Pozrikidis (1994) the boundary integral equation was deflated and a periodic straight channel Green's function was used. Additionally an adaptive method regarding the distribution of the drop's marker points was adopted whereby a node would either be added or eliminated depending on the size of its neighbouring boundary elements (more details on the adaptive boundary element method may be found in Pozrikidis (1992)). However, it should be noted that in experiments with fluid drop in tubes at low Reynolds numbers (e.g. Hiller and Kowalewski 1986), the fluid drops do not exhibit the oscillatory behaviour shown in figure 14 of Zhou and Pozrikidis (1994). Indeed, the paths of the drop centroids in figure 14 of Hiller and Kowalewski (1986) demonstrate a smooth transition towards the equilibrium position, as

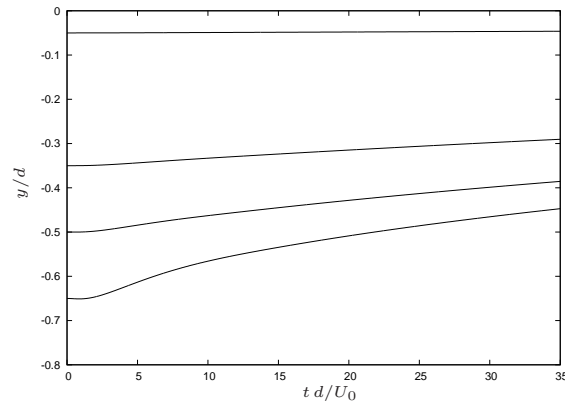


Figure 4.13 : Centroid paths for fluid drops with $\lambda = 10$, $\rho = 0.25$, $C_a = 1$ and $\sigma = -0.05$, -0.35 , -0.5 and -0.65 .

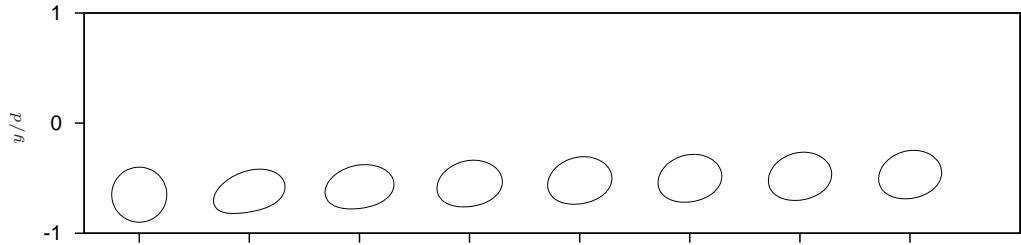


Figure 4.14 : Evolution of the drop shape for $\lambda = 10$, $\rho = 0.25$, $\sigma = -0.65$ and $C_a = 1$. The drops from left to right are for $t U_0/d = 0, 4, 8, 12, 17, 21, 25$ and 28.8 . The abscissa label is intentionally omitted, however the marks indicate the x -coordinate of the drop centroid.

shown for our two-dimensional model in figure 4.13.

4.4.2 An elastic capsule – results

The dynamics of the elastic capsule depend on the viscosity ratio, λ , the capsule radius to channel height ratio, $\rho = a/d$, the initial centreline offset, $\sigma = y_c/d$, and the two dimensionless parameters,

$$M = \frac{E_b}{\mu Q d}, \quad W = \frac{k d}{\mu Q}, \quad (4.100)$$

where E_b is the bending modulus of the elastic membrane and k is the membrane stiffness. The M parameter describes the relative importance of bending moments in the elastic capsule membrane and W describes the relative importance of the membrane stiffness. We set $M = 0$ to model a capsule which does not resist bending and $M = 0.001$ for a capsule which does. The model was sensitive to the size of M with larger values causing instabilities to develop in the numerics. The small value of M is of a similar order to the analogous three-dimensional quantity used in Pozrikidis (2001). The unstressed capsule shape is a circle, and in most of our presented results the capsule will also start each simulation as a circle. When the capsule is unstressed the interfacial traction jump, Δf , will be zero. Therefore when the capsule starts as a circle and $\lambda = 1$, the disturbance

pressure, π_2 , will be zero by equation (4.19) and the disturbance tractions on the walls will be zero by equation (4.29). In our computations we found $\pi_2 \approx 10^{-19} \mu U_0/d$ and $|\mathbf{f}^D| \approx 10^{-15} \mu U_0/d$ for a range of λ , ρ , σ , W and M . Under these conditions the disturbance velocity is negligible. As the numerical simulation progresses, the capsule will deform and its motion will be computed by (4.84). After each iteration of the numerical scheme we will store the distance moved and re-centre the capsule such that the x -component of its centroid lies at the mid-point of the channel, $x/d = l/2$, thus keeping it away from \mathcal{E}_1 and \mathcal{E}_2 and avoiding the requirement to discretise further portions of the channel walls. For each simulation, we checked that the velocity decays as we move away from the capsule and is negligible at the entrance and exit, and that the disturbance tractions decay to zero at the entrance. At the exit we will check that the x -component of the disturbance traction decays to zero and the y -component tends to the disturbance pressure. We will also check that the capsule's area is preserved since it should remain constant due to the incompressibility of the capsule fluid. If numerical error leads to the area error increasing above 0.5% then we perform an isotropic expansion or deflation of the shape as described in the previous section.

To further confirm the numerical code for the elastic capsule with no resistance to bending, we placed the capsule in a simple shear flow and computed the deformation and the steady capsule shape. We compared our results with those given in figure 2 of Breyiannis and Pozrikidis (2000) for $\Omega = 0.0125, 0.125$ and 1.2 , where the authors define

$$\Omega = \frac{\mu \hat{k} a}{k}, \quad (4.101)$$

where \hat{k} is the shear rate, a is the equivalent radius of the capsule and k is the membrane stiffness. We computed the evolution of the Taylor deformation parameter,

$$D = \frac{L - B}{L + B}, \quad (4.102)$$

where L is the length of the capsule and B is the breadth. Our computations shown in figure 4.15 demonstrate a good qualitative agreement with Figure 2(a) in Breyiannis and Pozrikidis (2000). As our final validation of the numerics for an elastic drop, we compared the steady shape for a reference configuration with the steady capsule shape when the number of boundary elements on each boundary was doubled. In both simulations we set $\lambda = 1$, $M = 0.001$ and $W = 1$. There were negligible differences between the two steady shapes.

In our first set of results, we consider an initially circular elastic capsule which does not resist bending. The simulation parameters are $\lambda = 1$, $\rho = 0.5$, $\sigma = 0$, $M = 0$ and $W = 1$. The capsule is released into the flow at $t = 0$ and we allow the capsule to deform. The capsule shape at $t = 13.5 d/U_0$ is shown in figure 4.16 (a), at which point the error in the capsule area has increased by 0.2% from its initial value. The convex front and concave rear is consistent with shapes of vesicles which have been observed in capillary tubes (Secomb et al. 2007). The disturbance pressure at this point in time is $-0.4245 \mu U_0/d$

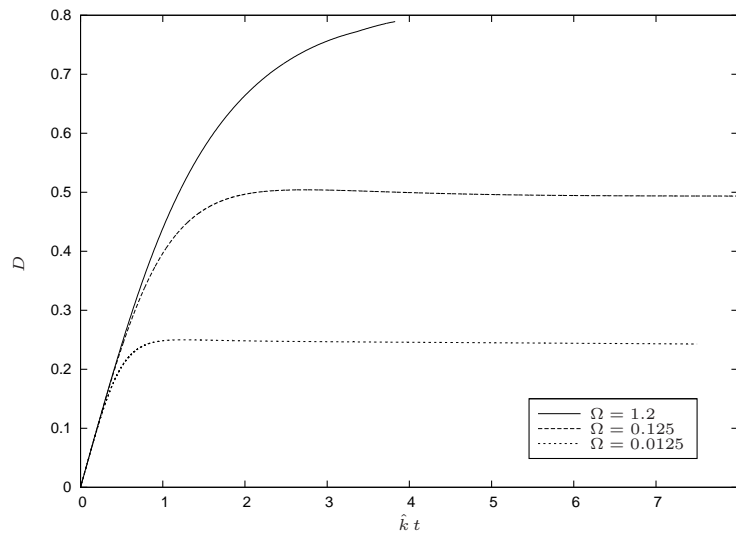


Figure 4.15 : Deformation of an elastic capsule with $M = 0$ in a shear flow for $\Omega = 0.0125$, 0.125 and 1.2 . For comparison against Figure 2 in Breyiannis and Pozrikidis (2000).

which has an error of 0.83% compared with the value predicted by equation (4.24). The evolution of the disturbance pressure is shown in figure 4.16 (b) where we can see the magnitude gradually increasing. We can see that after about $t = 4d/U_0$ ripples appear in the pressure profile. This may be attributed to the onset of numerical issues which later caused us to terminate the simulation due to loss of accuracy. As the simulation proceeds beyond the instant shown in figure 4.16 (a), the two trailing tips of the capsule become increasingly slender and the smooth capsule boundary becomes crinkled. Our failure to compute a steady shape is due to problems resolving the regions of very high curvature at the capsule tips, and not due to the lack of existence of such a shape. Indeed steady shapes for elastic capsules, in the absence of bending moments, have been computed in two and three-dimensional shear flows by Breyiannis and Pozrikidis (2000) and Ramanujan and Pozrikidis (1998) respectively. Furthermore the authors found that the elastic capsule attained a steady shape irrespective of the rate of the incident shear flow. The disturbance tractions on the top wall are shown in figure 4.16 (c) where we can see that the tractions decay to zero at the entrance, and the x -component decays to zero at the exit while the y -component tends to the value of the disturbance pressure. Figure 4.16 (d) shows the velocity along the centreline, $y/d = 0$, which decays rapidly as we move away upstream or downstream from the capsule. The gap at around $x/d \approx 6$ corresponds to the capsule, inside which the velocity was not calculated. It is interesting to note that the velocity slightly upstream from the capsule is slower than the velocity slightly downstream. This is to be expected since the capsule has not attained a steady shape. The disturbance velocity has decayed to 1% of its maximum value at $x/d = 4.03$ downstream, and $x/d = 8.11$ upstream, which are both approximately 4 capsule radii from the capsule's centroid. At \mathcal{E}_1 and \mathcal{E}_2 , where we expect the velocity to be purely Poiseuille, we find that the error in the velocity is no more than 0.07% .

In the hope of computing a steady state in which the capsule has ceased to deform, we

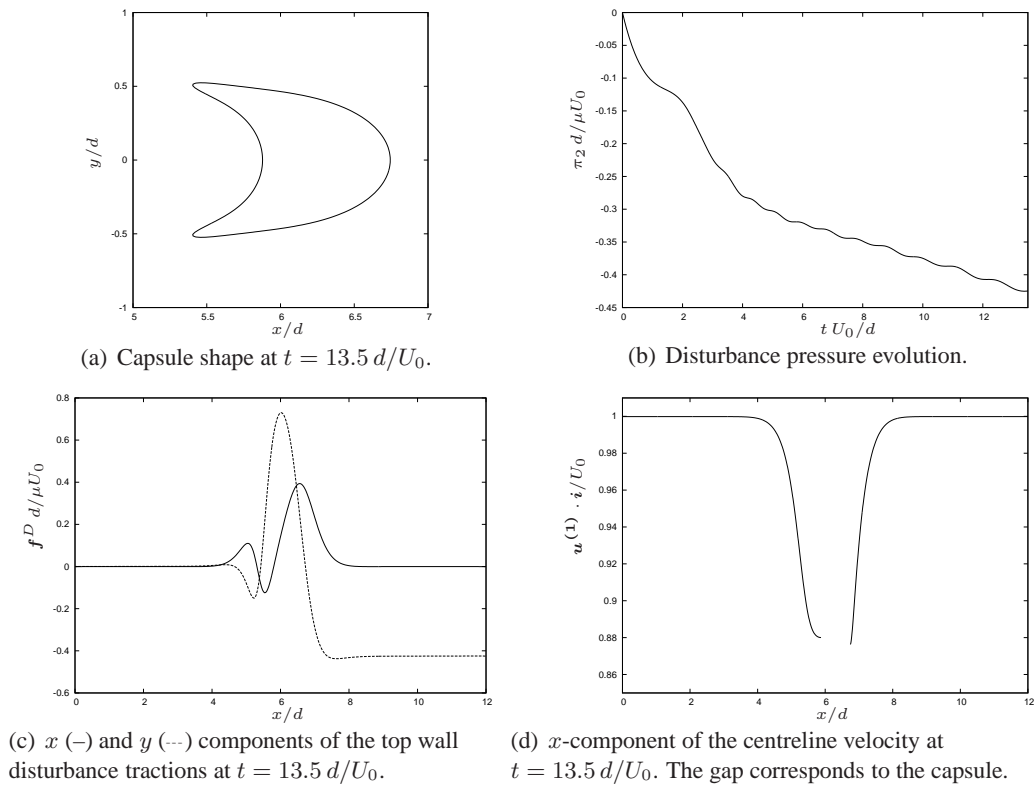


Figure 4.16 : Capsule shape, disturbance pressure, wall disturbance traction, centreline velocity and interfacial tractions for an elastic capsule with $\lambda = 1$, $\rho = 0.5$, $\sigma = 0$, $W = 1$ and $M = 0$.

repeated the calculation with the same parameter values except $M = 0.001$, which corresponds to the introduction of bending resistance. In the presence of bending moments, we find that the capsule does eventually attain a steady state. The capsule rapidly develops its concave rear shape after travelling a distance of about three capsule radii.

The steady state is reached at $t \approx 47.2 d/U_0$ by which point the centroid of the capsule has travelled an approximate distance of $82 a$ along the channel centreline. The steady capsule configuration is shown in figure 4.17 (a) and its velocity is $0.864 U_0 \mathbf{i}$. It is interesting to note that the steady deformed shape of the capsule is qualitatively consistent with the three-dimensional cell shapes computed by Quéguiner and Barthès-Biesel (1997), Pozrikidis (2005a) and Pozrikidis (2005c) in cylindrical tube flow. The capsule's resistance to bending forces is clearly seen in the shape of the trailing tips which are now much more rounded than in the $M = 0$ case shown in figure 4.16 (a). The shape of the capsule perimeters close to $y/d = 0$ show little difference between the $M = 0$ and $M = 0.001$ cases. The evolution of the disturbance pressure is shown in figure 4.17 (b) where we can see the pressure increasing in magnitude before tending to $-0.570 \mu U_0 / d$. In this case the error in the disturbance pressure with respect to the value obtained from equation (4.24) reduces to 0.09% which is better than the previous result for the case $M = 0$. Figure 4.17 (c) shows the disturbance tractions on the top wall, which we compare with figure 4.16 (c). The profile in both figures is the same however the steady shape for $M = 0.001$ induces disturbance tractions which are greater in magnitude. Figure

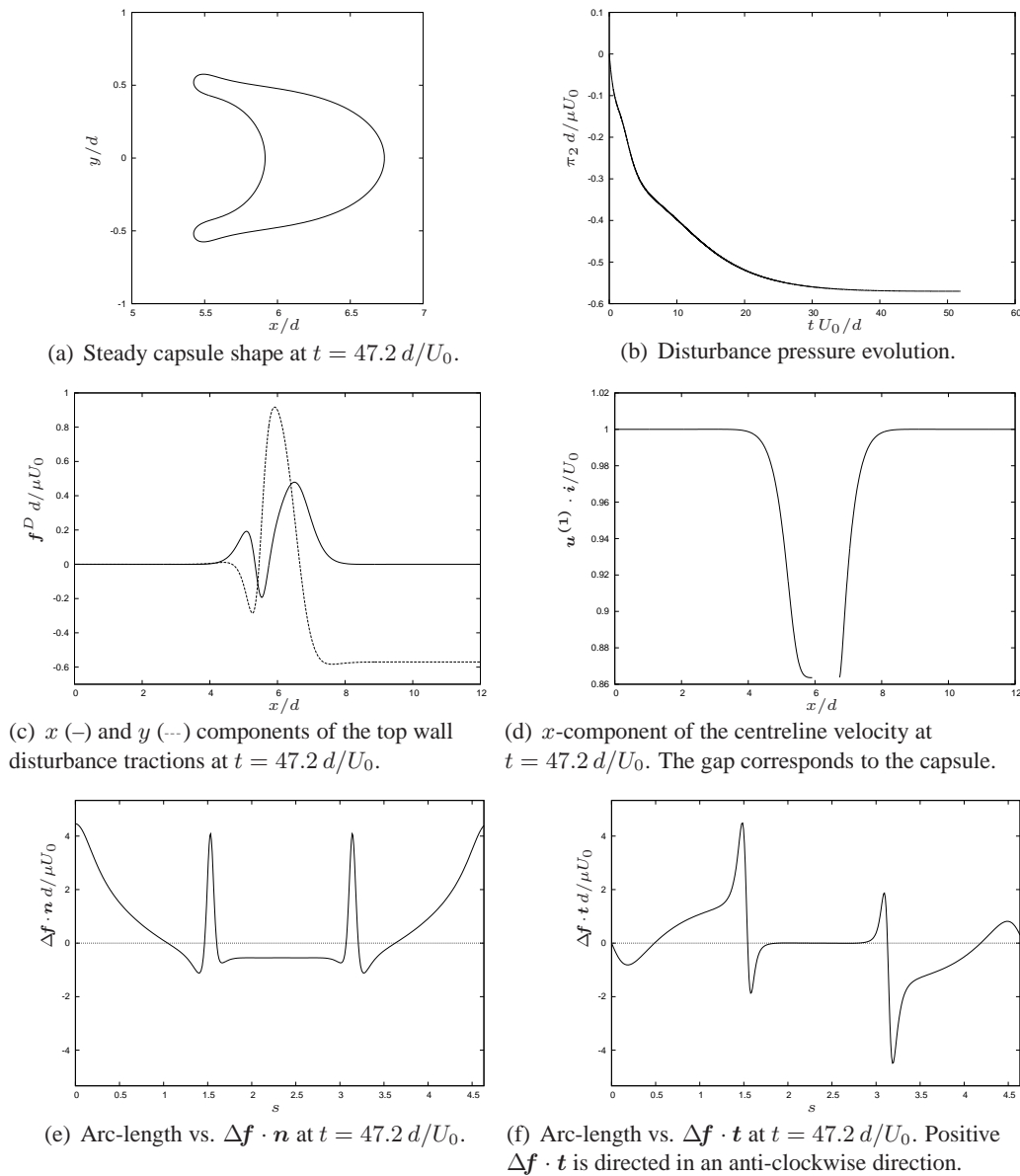


Figure 4.17 : Capsule shape, disturbance pressure, wall disturbance traction and centreline velocity for an elastic capsule with $\lambda = 1$, $\rho = 0.5$, $\sigma = 0$, $W = 1$ and $M = 0.001$.

4.17 (c) also confirms the decay of the disturbance traction to their appropriate values at the entrance and exit of the computational domain. A rigid particle with the same shape as in figure 4.17 (a) induces a disturbance pressure of $-0.569 \mu U_0/d$ and translates with velocity $0.864 U_0 \hat{i}$, both of which are almost identical to their elastic capsule counterparts. The x -component of the centreline velocity is displayed in figure 4.17 (d) which tells a story similar to that in figure 4.16 (d), albeit with a slightly larger disturbance to the velocity. Again, once we have moved roughly four capsule radii from the centroid the disturbance velocity has decayed to 1% of its maximum value. By the time we have reached the ends, where the velocity is assumed to be Poiseuille, the error in the velocity is no more than 0.01%. The normal and tangential components of the interfacial traction, $\Delta \mathbf{f}$, are plotted against arc-length around the capsule's perimeter in figures 4.17 (e) and

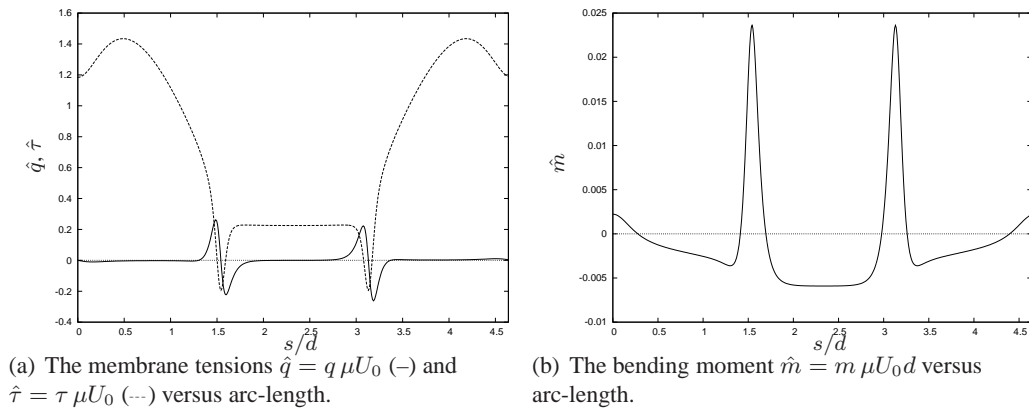


Figure 4.18 : The membrane tensions and the bending moment versus arc-length, for the steady-state capsule shown in figure 4.17 (a). Arc-length is measured anti-clockwise from zero at the front of the capsule. The trailing tips are at $s = 1.55d$ and $s = 3.08d$ respectively.

4.17 (f). Arc-length is measured anti-clockwise from zero at the rightmost point on the capsule's perimeter. At the start of the simulation the total arc-length of the capsule in its undeformed state is πd . At $t = 47.2 d/U_0$ the total arc-length of the deformed capsule is $4.63 d$, which represents an extension of 47%. Although this may be outside the limit of linear elasticity, and indeed the physical capabilities of many materials, we will continue to use our linear relationship between the in-plane tension and the stretch. However we note that a comparison of the results presented here with those for different elasticity laws would be interesting further work. The normal component of the fluid loading on the capsule membrane attains its maximum values at the points of greatest curvature, namely at the front of the capsule and at the trailing edges. The tangential component of the fluid loading goes through both positive and negative values, indicating that some parts of the capsule wall receive a compressive force while others experience an extensional force. These forces are most intensive at the trailing tips of the capsule, corresponding to the arc-lengths $1.55 d$ and $3.08 d$. In figure 4.18 (a) we show the in-plane tension, τ , and the transverse tension, q , plotted against arc-length for the steady-state shape in figure 4.17 (a). The in-plane tension, τ , graphed in figure 4.18 (a) achieves its maxima at $s = 0.48 d$ and $s = 4.15 d$; the local membrane extension is then greatest at these points according to equation (4.51). The membrane is in extension around most of the perimeter, where τ is positive, and is in compression in a region around the trailing tips where τ is negative. The bending moment, m , is plotted against arc-length in figure 4.18 (b). This graph is notable for the two spikes which occur at the trailing tips, where $s = 1.55 d$ and $s = 3.08 d$. A similar qualitative spike-like behaviour in the bending moment profile was encountered by Pozrikidis (2005a) in his axisymmetric calculations of red blood cells moving in a tube flow (see his figure 9b).

In the next set of results we increase the membrane stiffness such that $W = 5$ and set the remaining parameters to $\lambda = 1$, $\rho = 0.5$, $\sigma = 0$ and $M = 0.001$. The steady state is reached at $t \approx 12.3 d/U_0$ when the capsule has travelled approximately $22 a$ along the channel centreline. The steady shape is shown in figure 4.19 (a) and its velocity is

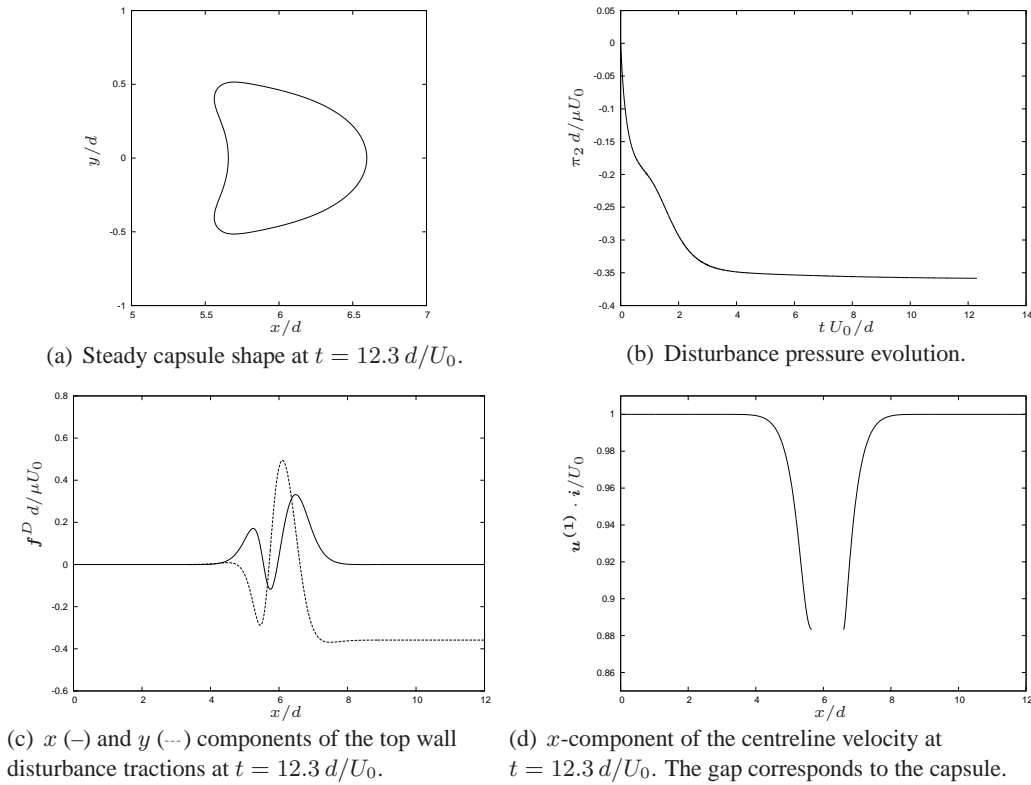


Figure 4.19 : Capsule shape, disturbance pressure, wall disturbance traction and centreline velocity for an elastic capsule with $\lambda = 1$, $\rho = 0.5$, $\sigma = 0$, $W = 5$ and $M = 0.001$.

$0.883 U_0 \hat{i}$. The evolution of the disturbance pressure is shown in figure 4.19 (b) where we can see the pressure increasing in magnitude before tending to $-0.358 \mu U_0 / d$. In this case the error in the disturbance pressure with respect to the value obtained from equation (4.24) is 0.03%. Comparing the results for the $W = 1$ and the $W = 5$ cases we see that the capsule with $W = 5$ attains its steady shape approximately four times quicker, translates slightly faster, has less deformed trailing tips and induces a slightly lower disturbance pressure. Figure 4.19 (c) shows the disturbance tractions on the top wall, which we compare with those in figure 4.17 (c). The profile in both figures is the same however the capsule with $W = 5$ induces disturbance tractions which are smaller in magnitude than those shown in figure 4.17 (c). Figure 4.19 (c) also confirms the decay of the disturbance traction to their appropriate values at the entrance and exit of the computational domain. The x -component of the centreline velocity is displayed in figure 4.19 (d) which tells a story similar to that in figure 4.17 (d), albeit with a smaller disturbance to the velocity. Again, once we have moved roughly four capsule radii from the centroid the disturbance velocity has decayed to 1% of its maximum value. By the time we have reached the ends, where the velocity is assumed to be Poiseuille, the error in the velocity is no more than 0.001%.

In the next set of results we increase the viscosity ratio to $\lambda = 5$ and set the remaining parameters to $\rho = 0.5$, $\sigma = 0$, $W = 1$ and $M = 0.001$. We terminated the simulation at $t = 88.6 d/U_0$ when the magnitude of the capsule's velocity normal to the boundary was

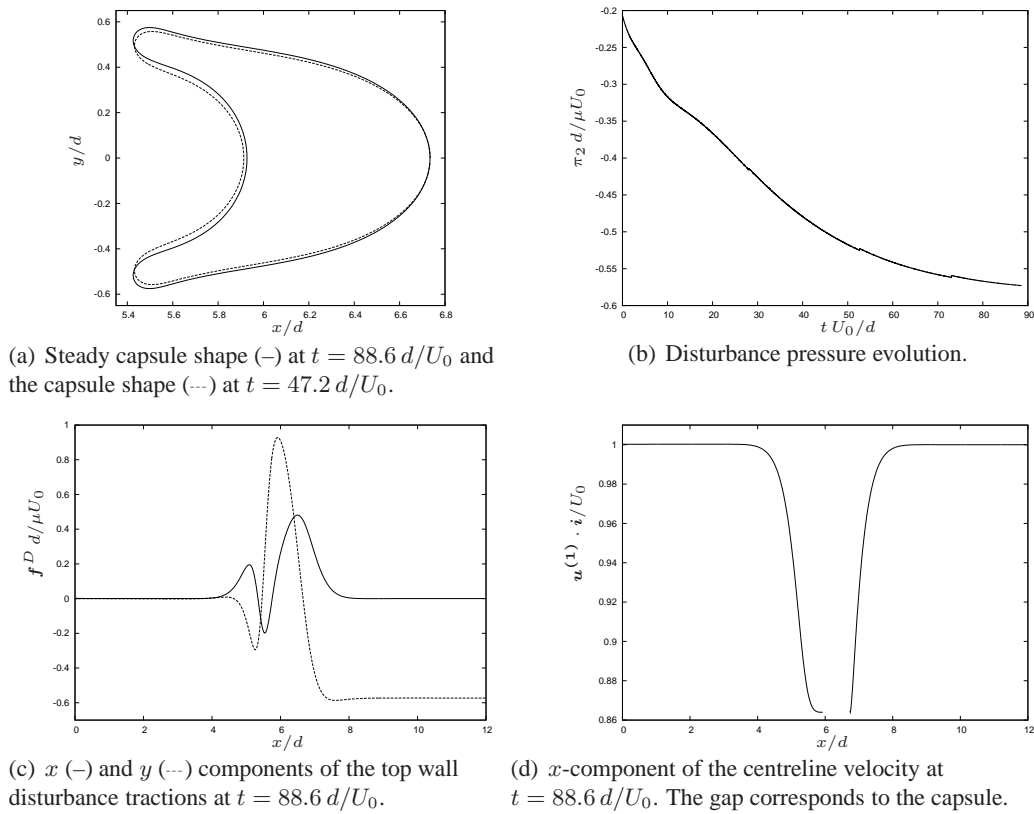
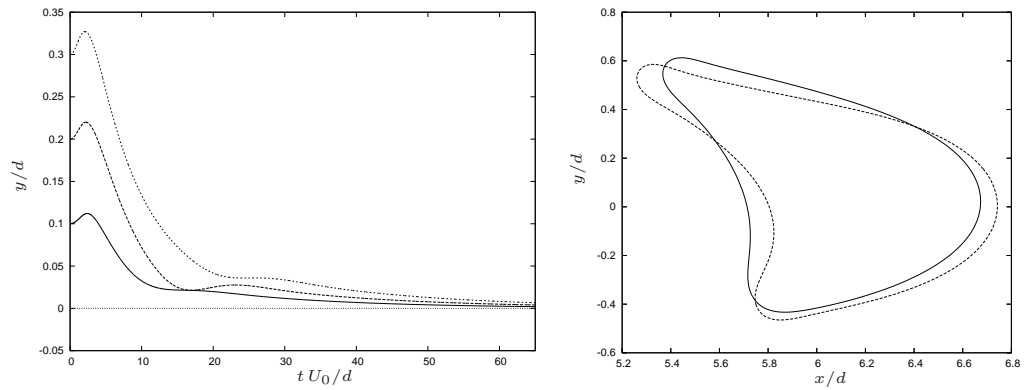


Figure 4.20 : Capsule shape, disturbance pressure, wall disturbance traction and centreline velocity for an elastic capsule with $\lambda = 5$, $\rho = 0.5$, $\sigma = 0$, $W = 1$ and $M = 0.001$.

less than $0.0003 U_0$. The capsule is not steady with respect to our nodal velocity criteria although the nodal velocities are small. The discrepancy may be due to the calculation of the nodal velocities from the mid-point velocities using a cubic spline, which is required when $\lambda \neq 1$. The capsule shape at $t = 88.6 d/U_0$ is shown as the solid lined shape in figure 4.20 (a) where it had travelled the equivalent of 155 capsule radii, its velocity was $0.864 U_0$ and the disturbance pressure was $-0.573 \mu U_0/d$, which are almost equal to the computed values for the $\lambda = 1$ case. The capsule's shape is almost identical to the steady shape for $\lambda = 1$, although in this case the shape here is achieved in twice the length of time. The dashed-line shape in figure 4.20 (a) is the shape at $t = 47.2 d/U_0$ which is the time at which the $\lambda = 1$ capsule attains a steady shape. Although there is little difference between the shapes, the $\lambda = 5$ shape does deform more slowly, and it takes an additional time of $41.39 d/U_0$ to deform to the solid-lined shape. The evolution of the disturbance pressure is shown in figure 4.20 (b) where we can see the pressure increasing in magnitude before tending to $-0.573 \mu U_0/d$. In this case the error in the disturbance pressure with respect to the value obtained from equation (4.24) is 0.14%. Figure 4.20 (c) shows the disturbance tractions on the top wall, which are almost identical to the profile shown in figure 4.17 (c) for $\lambda = 1$, which is expected since the $\lambda = 5$ shape has almost attained the same shape. Figure 4.20 (c) confirms the decay of the disturbance traction to their appropriate values at the entrance and exit of the computational domain. The x -component of the centreline velocity is displayed in figure 4.20 (d) which displays the

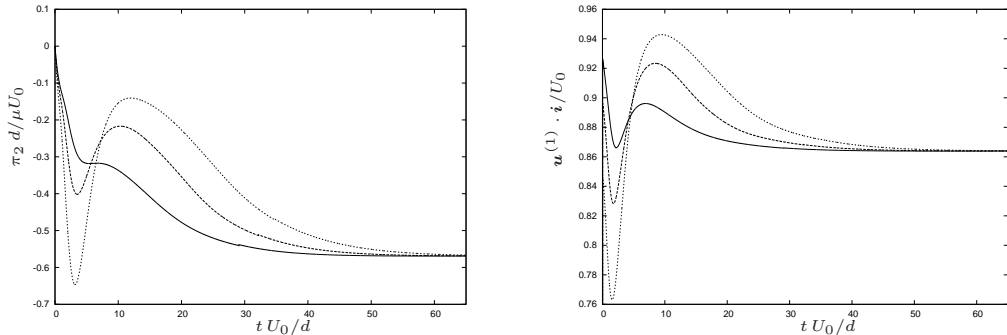
same profile as figure 4.17 (d). Again, once we have moved roughly four capsule radii from the centroid the disturbance velocity has decayed to 1% of its maximum value. By the time we have reached the ends, where the velocity is assumed to be Poiseuille, the error in the velocity is no more than 0.02%.

In the previous chapter we verified that a rigid particle carried by a flow parallel to a solid wall remains at a fixed distance from the wall in accordance with the reversibility of Stokes flow. In the previous section we showed that a fluid drop migrates away from the wall in a channel flow due to the flexibility of its boundary. Experiments conducted by Secomb et al. (2007) and previous three-dimensional calculations (Pozrikidis 2005c) have shown that a deformable capsule will tend to migrate away from a solid boundary. Accordingly we expect that a capsule released away from the channel centreline will migrate towards the centreline over time. We performed three simulations for capsules with $\lambda = 1$, $\rho = 0.5$, $W = 1$, $M = 0.001$ and set σ to 0.1, 0.2 and 0.3. In each simulation the capsule starts in its circular stress-free shape. In figure 4.21 (a) we see the trajectories of the capsule centroids. As can be seen, the long-term behaviour of the capsules is a gradual drift toward the channel centreline. In the early stages of each simulation, however, the capsule moves upwards towards the channel wall located at $y = d$. The same qualitative behaviour is observed in figure 6 of Pozrikidis (2005c) for the motion of an initially spherical elastic particle in a cylindrical tube. Capsules with their centroids placed further from the centreline show a more pronounced initial deviation toward the upper wall before migrating towards the centreline. The capsule with $\sigma = 0.2$ moves towards the top wall at $t \approx 20 d/U_0$ as well as in the initial period of the simulation. However the other two simulations do not exhibit this behaviour, although their migration towards the centreline is arrested for a short period at $t \approx 15 d/U_0$ for the $\sigma = 0.1$ drop and $t \approx 25 d/U_0$ for the $\sigma = 0.3$ drop. In the latter stages of the simulation the y -offset is decreasing exponentially slowly as time increases, e.g. $y \approx e^{-0.04t}$ for the capsule released from $\sigma = 0.1$. Since the capsules did not quite reach the centreline in the simulations we stopped at $t = 65 d/U_0$. Figure 4.21 (b) displays the computed shapes at two different times for the capsule released at $\sigma = 0.1$. When $t = 2.39 d/U_0$ the capsule centroid is at its closest to the upper wall, and at $t = 3.96 d/U_0$ the centroid has returned to $y = 0.1 d$ on its journey towards the centreline. The capsule profiles qualitatively resemble those found by Secomb et al. (2007) for particles released away from the line of symmetry. As might be expected, when the capsule is above the channel centreline the upper of the two trailing tips deforms the most and tends to elongate more than the lower trailing tip. The width, measured in the y -direction between the top and bottom of the capsule, increases beyond that of the initial shape. In a separate simulation with the same parameter values, the limiting capsule shape shown in figure 4.17 (a) was released with its centroid at $\sigma = 0.1$. This time we observed a slightly smaller initial movement towards the upper wall before the capsule drifted towards the centreline. We show the evolution of the disturbance pressure in figure 4.21 (c), where we can see an initial rapid increase in the magnitude of the pressure before it tends back towards zero in the $\sigma = 0.2$ and 0.3 cases, and remains relatively constant for a short period in the $\sigma = 0.1$ case. As time



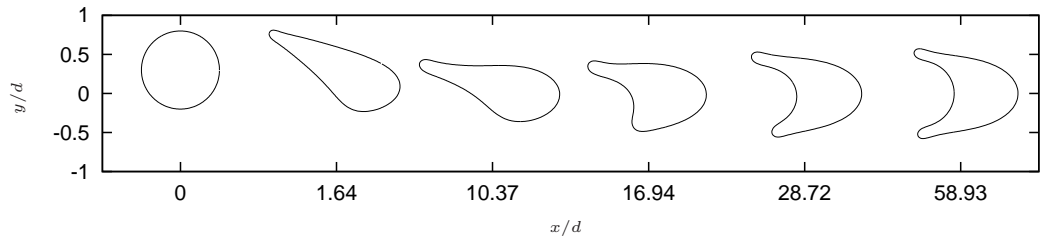
(a) Centroid trajectories for circular capsules initially positioned at $\sigma = 0.1$ (—), 0.2 (---) and 0.3 (···).

(b) Capsule shapes for the simulation started with $\sigma = 0.1$ at $t = 2.39 d/U_0$ (—) when the centroid is closest to the top wall and at $t = 3.96 d/U_0$ (---) when it returns to $y/d = 0.1$.



(c) Disturbance pressure evolution for the capsules started from $\sigma = 0.1$ (—), 0.2 (---) and 0.3 (···).

(d) Centroid velocity evolution for the capsules started from $\sigma = 0.1$ (—), 0.2 (---) and 0.3 (···).



(e) Deformation of the $\sigma = 0.3$ capsule at $tU_0/d = 0, 2.08, 11.70, 18.79, 32.06$ and 66.93 . The values on the x/d axis are the distances that the centroid has travelled since $t = 0$.

Figure 4.21 : Centroid trajectories and capsule shapes for $\lambda = 1, \rho = 0.5, W = 1$ and $M = 10^{-3}$.

progresses the disturbance pressure in all cases tends to $-0.567 \mu U_0/d$ which is close to the $0.570 \mu U_0/d$ value computed in the $\sigma = 0$ case earlier. The difference is due to the fact that the simulations for $\sigma \neq 0$ do not quite reach a steady state within $t = 65 d/U_0$. The x -component of velocity for the capsule's centroid is plotted in figure 4.21 (d), from which we can see a dramatic decrease in the velocity at the start of the simulation before the velocity increases and then settles to $0.864 U_0$ at $t = 65 d/U_0$, which equals the value for the steady capsule with $\sigma = 0$. In figure 4.21 (e) we show the evolution of the shape for the capsule released from $\sigma = 0.3$, where we have chosen this case to demonstrate the significant deformation which is experienced by a capsule when it is further from the centreline. The capsule shape at $x/d = 1.64$, when $t = 2.77 d/U_0$, is comparable with

the solid-lined shape in figure 4.21 (b) because they both represent the capsule's closest approach to the top wall. The capsule shape in the $\sigma = 0.1$ simulation has developed a parachute shape by $t = 2.39 d/U_0$, whereas the capsule in the $\sigma = 0.3$ simulation does not develop the parachute shape until slightly before $t = 18.79 d/U_0$, which is almost eight times as long. As time progresses the lower tip extends and the upper tip contracts as the particle shape settles to the limiting configuration depicted in figure 4.17 (a).

We will briefly look at the $\sigma = 0.3$ simulation in isolation. Figure 4.22 shows the top wall disturbance tractions and the centreline velocity for the capsule with $\sigma = 0.3$ at $t = 2.08 d/U_0$, at which time the capsule is at its closest to the top wall and the disturbance pressure is at its maximum value. The centroid's velocity at this moment is $(0.774, 10^{-5}) U_0$. and the disturbance pressure is $-0.517 \mu U_0/d$, which differs from the value obtained from equation (4.24) by 0.03%. The disturbance tractions on the top wall are shown in figure 4.22 (a) for the $t = 2.08 d/U_0$ capsule shape shown in figure 4.21 (e). Since the capsule is closer to the top wall the induced disturbance tractions are of generally greater magnitude than the disturbance tractions for a steady centred capsule shown in figure 4.17 (c). There is a sharp peak in both the x and y component of the disturbance tractions in figure 4.22 (a) at $x/d = 5.1$ which is above the capsule's top trailing edge. Figure 4.22 (a) also confirms the decay of the disturbance traction to their appropriate values at the entrance and exit of the computational domain. The x -component of the centreline velocity for the $t = 2.08 d/U_0$ capsule shape in figure 4.21 (e) is displayed in figure 4.22 (b) which shows the disturbance decays rapidly as we move away from the capsule, and has a small oscillation close to the downstream edge of the capsule. We can see from the pathlines shown in figure 4.22 (c) that two eddies are present, with the downstream one of greater size. The fluid in the eddies moves in a clockwise direction. Since the motion of the fluid is relative to the capsule, the fluid close to the centreline is moving from left to right, and the fluid closer to the walls is moving from right to left. The disturbance velocity has decayed to 1% of its maximum value when $x/d = 3.69$ and $x/d = 8.19$ which represent 4.62 and 4.38 capsule radii from the capsule centroid respectively. By the time we have reached the ends, where the velocity is assumed to be Poiseuille, the magnitude of the disturbance velocity is less than $10^{-6} U_0$.

So far we have considered capsules with $\rho = 0.5$. Now let us increase the capsule radius so that $\rho = 0.75$ and with $\lambda = 1$, $\sigma = 0$, $W = 1$ and $M = 0.001$. We terminated the simulation at $t = 66.0 d/U_0$ when the capsule shape was almost steady, meaning that the absolute value of the normal components of velocity on the capsule boundary were less than $0.001 U_0$. The capsule shape is shown in figure 4.23 (a) and its velocity is $0.799 U_0 \hat{i}$. The capsule had travelled an approximate distance of $71 a$ along the channel centreline at $t = 66.0 d/U_0$. The evolution of the disturbance pressure is shown in figure 4.23 (b) where we can see the pressure increasing in magnitude to around $-2.5 \mu U_0/d$. In this case the error in the disturbance pressure with respect to the value obtained from equation (4.24) is 0.02%. Figure 4.23 (c) shows the disturbance tractions on the top wall, which decay rapidly to their appropriate values at the entrance and exit of the computational domain. The profile of the disturbance tractions for $\rho = 0.75$ is similar to the profile

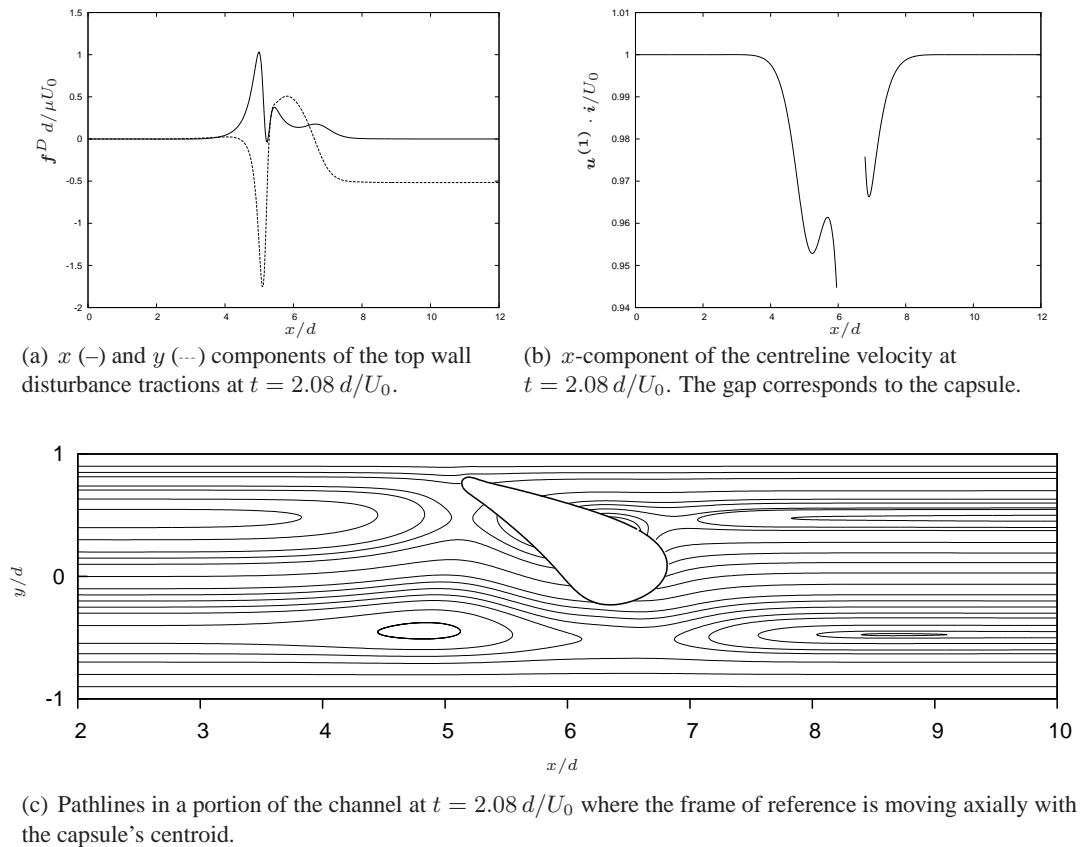


Figure 4.22 : Wall disturbance traction, centreline velocity and the pathlines at $t = 2.08 d/U_0$ for an elastic capsule with $\lambda = 1$, $\rho = 0.5$, $\sigma = 0.3$, $W = 1$ and $M = 0.001$.

when $\rho = 0.5$, although the sharp peak at $x/d = 5.9$ for the smaller capsule has now been replaced by a flattened region where the peak value of the disturbance traction has more than doubled. The x -component of the centreline velocity is displayed in figure 4.23 (d) which also shows a rapid decay in the disturbance velocity as we move away from the capsule even for this large capsule. The disturbance velocity has decayed to 1% of its maximum value at $x/d = 3.39$ and $x/d = 8.80$ which correspond to 3.48 and 3.73 capsule radii respectively. By the time we have reached the ends, where the velocity is assumed to be Poiseuille, the disturbance velocity is less than $10^{-5} U_0$.

Finally we will consider an oversize capsule with $\rho = 1.1$ which in its unstressed state would not fit into the channel. The remaining parameters are $\lambda = 1$, $\sigma = 0$, $W = 1$ and $M = 0.001$. Before releasing the capsule, we deform the circular boundary into an elliptical one such that the axis in the x -direction is $1.5125 d$ and the axis in the y -direction is $0.8 d$. Since we have seen that the capsule quickly adopts a shape which is essentially similar in nature to its steady shape, we stop the simulation at $t = 20 d/U_0$ to observe the shape, the disturbance tractions and the centreline velocity. The velocity of the capsule centroid is $0.811 U_0 i$ and the capsule shape is shown in figure 4.24 (a) where we can see the elongated trailing tips. At this moment the capsule has moved about 14 capsule radii along the channel and the disturbance pressure drop is $3.021 \mu U_0/d$ which equates to about one eighth of the Poiseuille pressure drop. The error in the disturbance

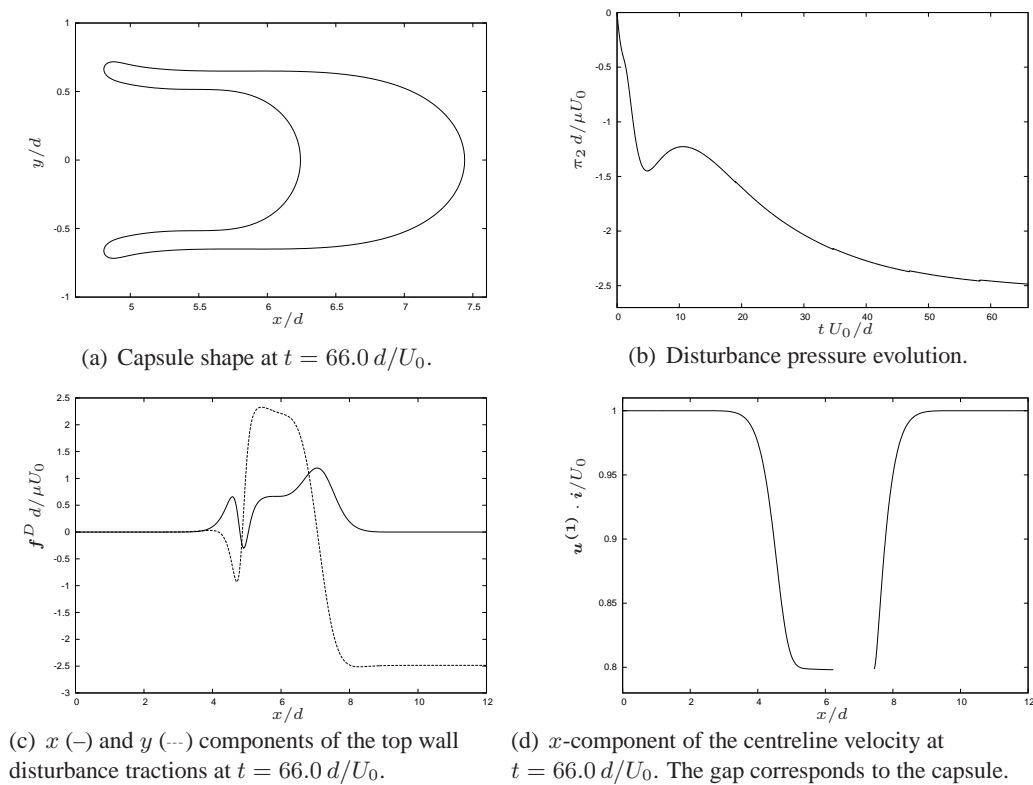


Figure 4.23 : Capsule shape, disturbance pressure, wall disturbance traction and centreline velocity for an elastic capsule with $\lambda = 1$, $\rho = 0.75$, $\sigma = 0$, $W = 1$ and $M = 0.001$.

pressure with respect to that computed from equation (4.24) is 0.04%. The evolution of the disturbance pressure is shown in figure 4.24 (b) where we can see the magnitude of the disturbance pressure increasing until it reaches a relative plateau between $t = 8 d/U_0$ and $t = 15 d/U_0$, after which the disturbance pressure continues to increase in magnitude. Figure 4.24 (c) shows the disturbance tractions on the top wall, which confirms the decay of the disturbance traction to their appropriate values at the entrance and exit of the computational domain. The x -component of the centreline velocity is displayed in figure 4.24 (d) which show that the decay of the disturbance velocity remains rapid even for an oversize capsule. The disturbance velocity has decayed to 1% of its maximum value at $x/d = 2.57$ and $x/d = 10.06$, which are 3.1 and 3.7 initial capsule radii from the capsule centroid respectively. By the time we have reached the ends, where the velocity is assumed to be Poiseuille, the disturbance velocity is no more than $10^{-4} U_0$. Although the velocity and traction decay to their expected values as we move towards the channel ends the pressure continues to change. This indicates that the numerical model is suffering from a loss in precision. The reasons for this could be the proximity of the capsule to the ends or the regions of high curvature on the trailing tips.

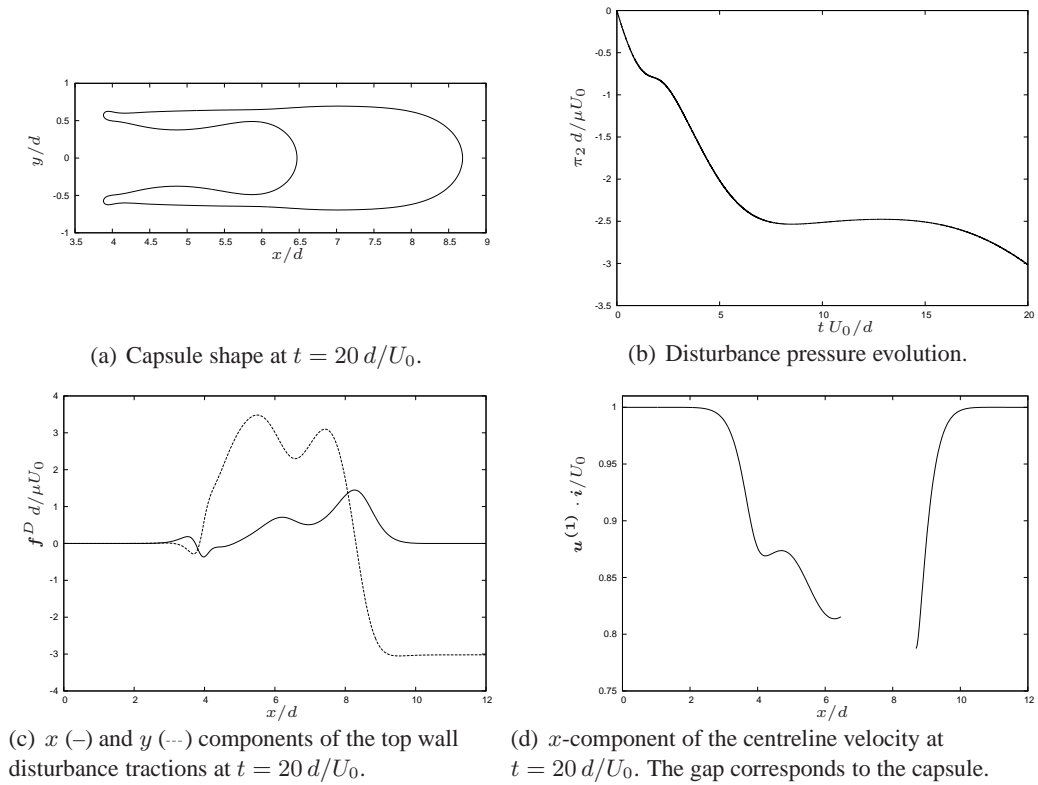


Figure 4.24 : Capsule shape, disturbance pressure, wall disturbance traction and centreline velocity for an elastic capsule with $\lambda = 1$, $\rho = 1.1$, $\sigma = 0$, $W = 1$, $M = 0.001$ and an elliptical initial shape.

4.5 Discussion

In this chapter we have considered a pressure-driven channel flow which contains a fluid drop or an elastic capsule. We formulated the problem using the boundary integral method and found its solution numerically using the boundary element method. The solution provides the velocities on the capsule boundary, the disturbance tractions on the channel walls and the pressure drop across the particle.

In summary we have found that an elastic capsule which resists bending will attain a steady shape, but a capsule which does not suffers numerical sensitivities which result in the failure of the numerical method due to a lack of resolution in regions of high curvature. A higher value of the membrane stiffness results in a capsule which reaches its steady shape quicker, translates faster and induces a lower disturbance pressure drop due to the fact that the capsule deforms less. A comparison between capsules which only differ by their viscosity ratios shows that there is little difference between the eventual shape of the deformed capsule boundary but a higher value of the viscosity ratio leads to a higher characteristic time of deformation. We can rearrange the expression for M in equation (4.100) to show

$$t \sim \frac{\mu d^3}{E_B}, \quad (4.103)$$

from which we can see that the characteristic time depends linearly on the viscosity. This

observation and the findings herein are in accord with the three-dimensional work of Quéguiner and Barthès-Biesel (1997) who studied the axisymmetric motion of a capsule into a circular pore using the boundary integral method. Quéguiner and Barthès-Biesel (1997) limit their study to capsules with $\lambda = 1$ on the basis that the viscosity ratio only affects the transient phase of the capsule motion and not its eventual equilibrium shape.

We found that capsules which start away from the centreline will gradually drift towards it, although this migration becomes exponentially slow. We found that larger capsules tend to a steady shape with elongated trailing tips, induce a greater disturbance pressure and translate slower than smaller capsules along the channel. Finally we found that in all cases the disturbance velocity decayed rapidly and it had reduced to 1% of its maximum value at a typical distance of four capsule radii from the capsule's centroid, and at the ends the disturbance velocity was negligible.

Chapter 5

Stokes flow through a bifurcation

In the previous two chapters we studied the motion of a rigid particle, a fluid drop and an elastic capsule in a straight two-dimensional channel. In this chapter we add a side-branch to the main channel and examine the motion of the fluid through the bifurcation. Upstream and downstream of the branch entrance we assume the flow is described by unidirectional Poiseuille flow. We derive the equations which govern the motion of the fluid in the main channel and in the branch, and we calculate the disturbance caused by the branch using the boundary integral method. By deriving the discrete analogues to the governing equations we utilise the boundary element method in order to write the equations as a linear matrix system, which we solve by standard methods. In the next chapter we will introduce a force-free torque-free neutrally-buoyant rigid particle to the flow which will draw extensively on the models derived here and in chapter 3.

5.1 Problem statement

Let us consider the motion of a fluid with viscosity μ in an infinite straight-walled channel of width, $2d$, which is attached to a semi-infinite straight-walled channel of width, $2D$. A disturbance to the upstream and downstream flows is caused by the branch entrance, or bifurcation, where the fluid either carries on along the main channel or moves into the branch channel. The geometry of the branching channel is shown in figure 5.1 and comprises the walls of the main channel, \mathcal{C} , the walls of the branch channel, \mathcal{B} , and a notional dividing boundary, \mathcal{A} , which we introduce in order to treat the channels separately. Far upstream and downstream in the main channel and the branch channel, the disturbance caused by the branch entrance is assumed to have decayed so that the flow in the channel is described by classical unidirectional Poiseuille flow. In preparation for the numerical method, we truncate the infinite main channel and the semi-infinite branch channel and label the entrance to the main channel as \mathcal{E}_1 , the exit to the main channel as \mathcal{E}_2 and the exit to the branch channel as \mathcal{E}_3 . The ends \mathcal{E}_1 and \mathcal{E}_2 are located at $x = 0$ and $x = l$ respectively. In the branch we define local coordinates (X, Y) , which are positioned as indicated in the figure. The branch joins onto the main channel such that the centreline of the branch channel meets \mathcal{A} at the point $(l/2, -d)$, and meets the lower wall

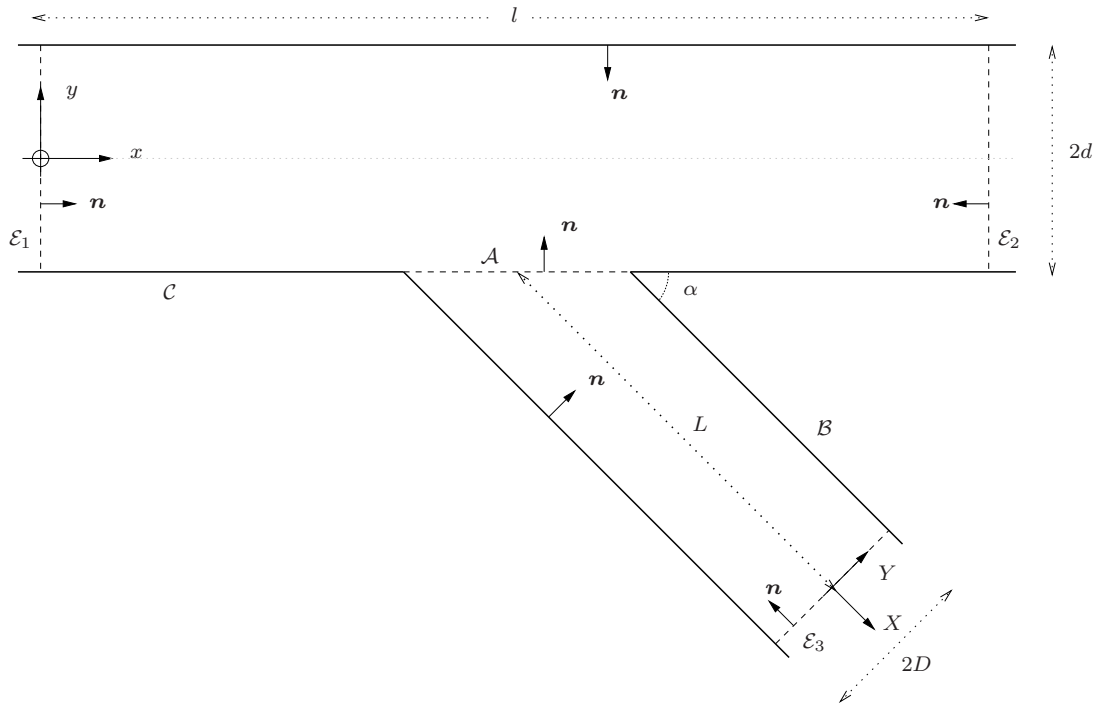


Figure 5.1 : A straight-walled channel with a branch which contains a fluid of viscosity μ .

at the points $(l/2 - D \operatorname{cosec} \alpha, -d)$ and $(l/2 + D \operatorname{cosec} \alpha, -d)$. The exit to the branch channel, \mathcal{E}_3 , lies at $X = 0$. The unit normal vectors, \mathbf{n} , on all boundaries point into the fluid as shown in figure 5.1. We choose to direct the unit normal vector on \mathcal{A} into the fluid of the main channel. To define the mapping between points relative to the two coordinate systems, we label the origin on \mathcal{E}_1 as \mathbf{O}_1 and the origin on \mathcal{E}_3 as \mathbf{O}_3 , where $\mathbf{O}_3 = (l/2 + L \cos \alpha, -d - L \sin \alpha)$ relative to \mathbf{O}_1 . If a point relative to \mathbf{O}_1 is labelled \mathbf{p}_1 then relative to \mathbf{O}_3 it is given by

$$\mathbf{p}_3 = \mathbf{R} \cdot (\mathbf{p}_1 - \mathbf{O}_3), \quad (5.1)$$

where \mathbf{p}_3 is the point relative to \mathbf{O}_3 and \mathbf{R} is the rotation matrix given by

$$\mathbf{R} = \begin{bmatrix} \cos \alpha & -\sin \alpha \\ \sin \alpha & \cos \alpha \end{bmatrix}. \quad (5.2)$$

The unit normals in the X and Y directions are,

$$\mathbf{i}' = \cos \alpha \mathbf{i} - \sin \alpha \mathbf{j}, \quad \mathbf{j}' = \sin \alpha \mathbf{i} + \cos \alpha \mathbf{j}, \quad (5.3)$$

in terms of \mathbf{i} , \mathbf{j} and α , which were calculated using the inverse of \mathbf{R} .

The branch entrance disturbs the flow but at \mathcal{E}_1 , \mathcal{E}_2 and \mathcal{E}_3 we assume that the disturbance has decayed and the flow has settled to Poiseuille flow, characterised by the streamwise flux rate at the pertinent entrance or exit. At \mathcal{E}_i we label the flux, Q_i , where $i = 1, 2$ and 3 refer to the entrance, the exit of the main channel and the exit of the branch

channel respectively. We have

$$Q_1 = Q_2 + Q_3 \quad (5.4)$$

for the fluxes where all Q_i are positive. Therefore the Poiseuille velocity at \mathcal{E}_1 is

$$\mathbf{u}^{P_1} = U_0^{P_1} \left(1 - \frac{y^2}{d^2}\right) \mathbf{i} = u^{P_1} \mathbf{i}, \quad (5.5)$$

and at \mathcal{E}_2 it is

$$\mathbf{u}^{P_2} = U_0^{P_2} \left(1 - \frac{y^2}{d^2}\right) \mathbf{i} = u^{P_2} \mathbf{i}, \quad (5.6)$$

where $U_0^{P_i}$ are the centreline velocities of the Poiseuille velocity defined with reference to \mathcal{E}_i . At \mathcal{E}_3 we have

$$\mathbf{u}^{P_3} = U_0^{P_3} \left(1 - \frac{Y^2}{D^2}\right) \mathbf{i}' = u^{P_3} \mathbf{i}', \quad (5.7)$$

where $U_0^{P_3}$ is the centreline Poiseuille velocity at \mathcal{E}_3 . The $U_0^{P_i}$ are related to the fluxes, Q_i , by

$$Q_i = \frac{4}{3} d_i U_0^{P_i}, \quad (5.8)$$

with $d_1 = d_2 = d$ and $d_3 = D$. Application of equation (5.8) at the exits in conjunction with equation (5.4) yields the following relationships between the centreline speeds at the exits and the entrance,

$$U_0^{P_2} = Q U_0^{P_1}, \quad (5.9)$$

$$U_0^{P_3} = \left(\frac{1-Q}{\delta}\right) U_0^{P_1}, \quad (5.10)$$

where Q is the flux ratio in the main channel, and δ is the channel width ratio, which are defined by

$$Q = \frac{Q_2}{Q_1} \quad \text{and} \quad \delta = \frac{D}{d}. \quad (5.11)$$

Our aim is to compute the velocity field throughout the flow domain and the additional pressure drop at both exits due to disturbance caused by the branch entrance. We assume that the Reynolds number of the flow is very small so that the flow in the channels may be described using the linear equations of Stokes flow given in equation (1.3.4). We decompose the velocity field, \mathbf{u} , the stress field, $\boldsymbol{\sigma}$, and the traction field, \mathbf{f} , into background Poiseuille and disturbance components, which we indicate by the superscripts P_i and D_i respectively, and where the i indicates to which of \mathcal{E}_i the quantity applies. In the main channel we have,

$$\mathbf{u} = \mathbf{u}^{P_1} + \mathbf{u}^{D_1} = \mathbf{u}^{P_2} + \mathbf{u}^{D_2}, \quad (5.12)$$

$$\boldsymbol{\sigma} = \boldsymbol{\sigma}^{P_1} + \boldsymbol{\sigma}^{D_1} = \boldsymbol{\sigma}^{P_2} + \boldsymbol{\sigma}^{D_2}, \quad (5.13)$$

$$\mathbf{f} = \mathbf{f}^{P_1} + \mathbf{f}^{D_1} = \mathbf{f}^{P_2} + \mathbf{f}^{D_2}, \quad (5.14)$$

where the P_1 and D_1 quantities are defined with reference to bE_1 and the P_2 and D_2

quantities are defined with reference to \mathcal{E}_2 . In the branch channel we have,

$$\mathbf{u} = \mathbf{u}^{P_3} + \mathbf{u}^{D_3}, \quad (5.15)$$

$$\boldsymbol{\sigma} = \boldsymbol{\sigma}^{P_3} + \boldsymbol{\sigma}^{D_3}, \quad (5.16)$$

$$\mathbf{f} = \mathbf{f}^{P_3} + \mathbf{f}^{D_3}, \quad (5.17)$$

where the P_3 and D_3 quantities are defined with reference to \mathcal{E}_3 . On the main channel walls, \mathcal{C} , we have

$$\mathbf{u} = \mathbf{u}^{P_1} = \mathbf{u}^{D_1} = \mathbf{u}^{P_2} = \mathbf{u}^{D_2} = \mathbf{0}, \quad (5.18)$$

and on the walls of the branch channel, we have

$$\mathbf{u} = \mathbf{u}^{P_3} = \mathbf{u}^{D_3} = \mathbf{0}, \quad (5.19)$$

by no-slip and no-penetration. We will seek a solution which has unidirectional Poiseuille flow as its entrance and exit flows. Therefore we will assume the disturbance velocity decays so that

$$\mathbf{u}^{D_1} \rightarrow \mathbf{0}, \quad \mathbf{u}^{D_2} \rightarrow \mathbf{0}, \quad \mathbf{u}^{D_3} \rightarrow \mathbf{0}, \quad (5.20)$$

as we approach the ends \mathcal{E}_1 , \mathcal{E}_2 and \mathcal{E}_3 respectively. We also assume that the spatial derivatives of the disturbance velocity decay along with the disturbance velocity which allows us to write the disturbance traction at the ends as

$$\mathbf{f}^{D_1} = -p^{D_1} \mathbf{n}, \quad \mathbf{f}^{D_2} = -p^{D_2} \mathbf{n}, \quad \mathbf{f}^{D_3} = -p^{D_3} \mathbf{n}, \quad (5.21)$$

as we approach \mathcal{E}_1 , \mathcal{E}_2 and \mathcal{E}_3 respectively, and where the p^{D_r} ($r = 1, 2$ or 3) are the disturbance pressures. The total pressure, p , is obtained by adding the disturbance and Poiseuille pressures with matching indices, e.g. $p = p^{P_1} + p^{D_1}$. At each of the ends the disturbance pressure in equation (5.21) is constant and since we are interested in the additional disturbance pressure drop between the entrance and the exits, we set $p^{D_1} = 0$ at \mathcal{E}_1 without loss of generality. For brevity we label the exit disturbance pressures as $p^{D_2} = \pi_2$ at \mathcal{E}_2 and $p^{D_3} = \pi_3$ at \mathcal{E}_3 , so that the disturbance tractions may be expressed as

$$\mathbf{f}^{D_1} = \mathbf{0} \text{ at } \mathcal{E}_1, \quad (5.22)$$

$$\mathbf{f}^{D_2} = -\pi_2 \mathbf{n} \text{ at } \mathcal{E}_2, \quad (5.23)$$

$$\mathbf{f}^{D_3} = -\pi_3 \mathbf{n} \text{ at } \mathcal{E}_3. \quad (5.24)$$

The Poiseuille pressures in the main channel are given by

$$p^{P_1}(x) = -G_1 x, \quad (5.25)$$

$$p^{P_2}(x) = -G_2 x \quad (5.26)$$

where $p^{P_1}(x)$ is the Poiseuille pressure due to the entrance Poiseuille flow with pressure gradient $-G_1$, and $p^{P_2}(x)$ is the Poiseuille pressure due to the Poiseuille flow which

exits the main channel which has pressure gradient, $-G_2$. The pressure gradients may be expressed in terms of the centreline velocity or the flux by,

$$G_1 = \frac{2\mu U_0^{P_1}}{d^2} = \frac{3\mu Q_1}{2d^3} \quad (5.27)$$

$$G_2 = Q G_1. \quad (5.28)$$

We have defined the Poiseuille pressures such that $p^{P_1} = p^{P_2} = 0$ at \mathcal{E}_1 . The Poiseuille pressure drops between \mathcal{E}_1 and \mathcal{E}_2 for the two main channel Poiseuille flows are

$$\Delta p^{P_1} = p^{P_1}(\mathcal{E}_1) - p^{P_1}(\mathcal{E}_2) = G_1 l, \quad (5.29)$$

$$\Delta p^{P_2} = p^{P_2}(\mathcal{E}_1) - p^{P_2}(\mathcal{E}_2) = G_2 l. \quad (5.30)$$

In the branch channel the Poiseuille pressure is

$$p^{P_3}(X) = -G_3 X \quad (5.31)$$

where $G_3 = 2\mu U_0^{P_3}/D^2 = 3\mu Q_3/2D^3$, and $-G_3$ is the pressure gradient which when applied to the branch channel results in the flux Q_3 at \mathcal{E}_3 . We may now write the pressure difference between the entrance and the exit of the main channel, Δp_2 , as

$$\begin{aligned} \Delta p_2 &= p(\mathcal{E}_1) - p(\mathcal{E}_2) \\ &= (p^{P_1}(\mathcal{E}_1) + p^{D_1}(\mathcal{E}_1)) - (p^{P_2}(\mathcal{E}_2) + p^{D_2}(\mathcal{E}_2)) \\ &= G_2 l - \pi_2 \end{aligned} \quad (5.32)$$

by equations (5.25) and (5.26), and between the entrance of the main channel and the exit of the branch channel, Δp_3 , as

$$\begin{aligned} \Delta p_3 &= p(\mathcal{E}_1) - p(\mathcal{E}_3) \\ &= (p^{P_1}(\mathcal{E}_1) + p^{D_1}(\mathcal{E}_1)) - (p^{P_3}(\mathcal{E}_3) + p^{D_3}(\mathcal{E}_3)) \\ &= -\pi_3 \end{aligned} \quad (5.33)$$

by equations (5.25) and (5.31). The total pressures at the exits are

$$p(\mathcal{E}_2) = \pi_2 - G_2 l, \quad \text{and} \quad p(\mathcal{E}_3) = \pi_3. \quad (5.34)$$

So far we have discussed the boundary conditions on the channel walls and at the entrance and exits. The only remaining boundary is the notional boundary, \mathcal{A} , on which we impose continuity of velocity and traction, so that

$$\mathbf{u} = \mathbf{u}^{P_1} + \mathbf{u}^{D_1} = \mathbf{u}^{P_2} + \mathbf{u}^{D_2} = \mathbf{u}^{P_3} + \mathbf{u}^{D_3} \quad (5.35)$$

$$\mathbf{f} = \mathbf{f}^{P_1} + \mathbf{f}^{D_1} = \mathbf{f}^{P_2} + \mathbf{f}^{D_2} = \mathbf{f}^{P_3} + \mathbf{f}^{D_3}. \quad (5.36)$$

Since the traction is defined with reference to the unit normal vector, $\mathbf{f} = \boldsymbol{\sigma} \cdot \mathbf{n}$, we define

the tractions in equation (5.36) with respect to the same unit normal vector which points into the main channel.

We have introduced unknown disturbance tractions on the notional boundary and on the walls of the channels, unknown pressures at the exits and unknown velocities on the notional boundary. The disturbance tractions and velocities are defined with reference to \mathcal{E}_1 , \mathcal{E}_2 or \mathcal{E}_3 . Therefore during the forthcoming derivation of the equations we will need to choose which quantities to keep and which to eliminate. In the main channel we have the disturbance pressure, π_2 , and the disturbance tractions, \mathbf{f}^{D_1} , on the walls. In the branch channel we have the disturbance pressure, π_3 , and \mathbf{f}^{D_3} on the walls. On the notional boundary we are free to choose any one of the disturbance quantities since we can eliminate the other ones by the continuity of velocity and traction stated in equations (5.35) and (5.36). On \mathcal{A} we will choose to favour the disturbance tractions and velocities, \mathbf{f}^{D_1} and \mathbf{u}^{D_1} , for consistency with the main channel, where we use \mathbf{f}^{D_1} .

We are now in a position to derive equations for the disturbance pressure and velocity in the channels. Let us start with the main channel and use the reciprocal relation of Lorentz given in equation (1.3.22) to derive an equation for the disturbance pressure at \mathcal{E}_2 . We apply the formula to the pair of flows $(\mathbf{u}^{P_1}, \boldsymbol{\sigma}^{P_1})$ and $(\mathbf{u}^{D_1}, \boldsymbol{\sigma}^{D_1})$ to get

$$\nabla \cdot (\mathbf{u}^{P_1} \cdot \boldsymbol{\sigma}^{D_1} - \mathbf{u}^{D_1} \cdot \boldsymbol{\sigma}^{P_1}) = 0, \quad (5.37)$$

which we integrate over the main channel's flow domain and apply the divergence theorem to get

$$\int_{\partial\Gamma_1} \mathbf{u}^{P_1} \cdot \mathbf{f}^{D_1} \, ds(\mathbf{x}) = \int_{\partial\Gamma_1} \mathbf{u}^{D_1} \cdot \mathbf{f}^{P_1} \, ds(\mathbf{x}), \quad (5.38)$$

where $\partial\Gamma_1 = \mathcal{E}_1 \cup \mathcal{E}_2 \cup \mathcal{A} \cup \mathcal{C}$, which can be simplified to

$$\int_{\mathcal{E}_2} (\mathbf{u}^{P_1} \cdot \mathbf{f}^{D_1} - \mathbf{u}^{D_1} \cdot \mathbf{f}^{P_1}) \, ds(\mathbf{x}) = \int_{\mathcal{A}} (\mathbf{u}^{D_1} \cdot \mathbf{f}^{P_1} - \mathbf{u}^{P_1} \cdot \mathbf{f}^{D_1}) \, ds(\mathbf{x}), \quad (5.39)$$

by the boundary conditions given in equations (5.20) and (5.21) together with the no-slip and no-penetration conditions on the walls. Although the Poiseuille velocity, \mathbf{u}^{P_1} , is zero on the notional boundary, as it is displayed in figure 5.1, we retain the term because in later chapters we will deform \mathcal{A} and so the velocity may be non-zero. Using the decompositions of velocity and traction in equations (5.12) and (5.14), and by applying the boundary conditions (5.20) and (5.21) we have

$$\mathbf{u}^{D_1} = \mathbf{u}^{P_2} - \mathbf{u}^{P_1}, \quad (5.40)$$

$$\mathbf{f}^{D_1} = \mathbf{f}^{P_2} - \mathbf{f}^{P_1} - \pi_2 \mathbf{n}, \quad (5.41)$$

which we substitute into the left-hand side of equation (5.39) to get

$$\int_{\mathcal{E}_2} (\mathbf{u}^{P_1} \cdot \mathbf{f}^{D_1} - \mathbf{u}^{D_1} \cdot \mathbf{f}^{P_1}) \, ds(\mathbf{x}) = Q_1 \pi_2 + \int_{\mathcal{E}_2} (\mathbf{u}^{P_1} \cdot \mathbf{f}^{P_2} - \mathbf{u}^{P_2} \cdot \mathbf{f}^{P_1}) \, ds(\mathbf{x}), \quad (5.42)$$

where we have used the definition of the flux, $Q_1 = - \int_{\mathcal{E}_2} \mathbf{u}^{P_1} \cdot \mathbf{n} \, ds(\mathbf{x})$. By equation (5.9) and the definition of the traction and pressure in the main channel we find

$$\mathbf{u}^{P_2} = Q \mathbf{u}^{P_1}, \quad \text{and} \quad \mathbf{f}^{P_2} = Q \mathbf{f}^{P_1}, \quad (5.43)$$

so that

$$\int_{\mathcal{E}_2} (\mathbf{u}^{P_1} \cdot \mathbf{f}^{P_2} - \mathbf{u}^{P_2} \cdot \mathbf{f}^{P_1}) \, ds(\mathbf{x}) = 0 \quad (5.44)$$

and equation (5.42) simplifies to

$$\int_{\mathcal{E}_2} (\mathbf{u}^{P_1} \cdot \mathbf{f}^{D_1} - \mathbf{u}^{D_1} \cdot \mathbf{f}^{P_1}) \, ds(\mathbf{x}) = Q_1 \pi_2. \quad (5.45)$$

Substitution of equation (5.45) into equation (5.39) gives

$$\pi_2 = \frac{1}{Q_1} \int_{\mathcal{A}} (\mathbf{u}^{D_1} \cdot \mathbf{f}^{P_1} - \mathbf{u}^{P_1} \cdot \mathbf{f}^{D_1}) \, ds(\mathbf{x}) \quad (5.46)$$

for the disturbance pressure at \mathcal{E}_2 . Using equation (5.46) we can find the disturbance pressure at \mathcal{E}_2 given the disturbance velocities and tractions on the notional boundary. Integration of the Stokes equation, $\nabla \cdot \boldsymbol{\sigma}^{D_1} = \mathbf{0}$, for the disturbance in the main channel yields the following equations

$$\pi_2 = (Q - 1) G_1 l - \frac{1}{2d} \int_{\mathcal{A}, \mathcal{C}} f_x^{D_1} \, ds(\mathbf{x}), \quad \text{and} \quad (5.47)$$

$$0 = \frac{1}{2d} \int_{\mathcal{A}, \mathcal{C}} f_y^{D_1} \, ds(\mathbf{x}), \quad (5.48)$$

which are useful for checking the disturbance pressure at \mathcal{E}_2 and the disturbance tractions on \mathcal{A} and \mathcal{C} in the numerical solution and where $\mathbf{f}^{D_1} = (f_x^{D_1}, f_y^{D_1})$.

Now let us derive an equation for the disturbance pressure at \mathcal{E}_3 by applying the Lorentz reciprocal relation to the $(\mathbf{u}^{P_3}, \boldsymbol{\sigma}^{P_3})$ and $(\mathbf{u}^{D_3}, \boldsymbol{\sigma}^{D_3})$ flows in the branch channel, to get

$$\nabla \cdot (\mathbf{u}^{P_3} \cdot \boldsymbol{\sigma}^{D_3} - \mathbf{u}^{D_3} \cdot \boldsymbol{\sigma}^{P_3}) = 0. \quad (5.49)$$

We integrate the equation over the flow domain of the branch channel and apply the divergence theorem to get

$$\int_{\partial\Gamma_2} \mathbf{u}^{P_3} \cdot \mathbf{f}^{D_3} \, ds(\mathbf{x}) = \int_{\partial\Gamma_2} \mathbf{u}^{D_3} \cdot \mathbf{f}^{P_3} \, ds(\mathbf{x}), \quad (5.50)$$

where $\partial\Gamma_2 = \mathcal{A} \cup \mathcal{B} \cup \mathcal{E}_3$. By the requirements of the divergence theorem, the unit normal vectors all point out of the flow domain. In previous applications of the Lorentz reciprocal relation we have implicitly negated the normal vectors in order for them to point into the flow domain. However, in this case we will only negate the normal vector on \mathcal{B} and \mathcal{E}_3

since we want the normal on \mathcal{A} to point into the main channel. Expanding equation (5.50) gives

$$\int_{\mathcal{A}} (\mathbf{u}^{P_3} \cdot \mathbf{f}^{D_3} - \mathbf{u}^{D_3} \cdot \mathbf{f}^{P_3}) \, ds(\mathbf{x}) = \int_{\mathcal{B}, \mathcal{E}_3} (\mathbf{u}^{P_3} \cdot \mathbf{f}^{D_3} - \mathbf{u}^{D_3} \cdot \mathbf{f}^{P_3}) \, ds(\mathbf{x}), \quad (5.51)$$

where we have amended the direction of the normal vector as stated. Application of the boundary conditions in equations (5.18) and (5.20) enable us to simplify equation (5.51) to

$$\int_{\mathcal{E}_3} \mathbf{u}^{P_3} \cdot \mathbf{f}^{D_3} \, ds(\mathbf{x}) = \int_{\mathcal{A}} (\mathbf{u}^{P_3} \cdot \mathbf{f}^{D_3} - \mathbf{u}^{D_3} \cdot \mathbf{f}^{P_3}) \, ds(\mathbf{x}), \quad (5.52)$$

where the normal vector on \mathcal{A} points into the main channel and the normal on \mathcal{E}_2 points into the branch channel. The left-hand side is simplified further using equation (5.21) and $Q_3 = - \int_{\mathcal{E}_3} \mathbf{u}^{P_3} \cdot \mathbf{n} \, ds(\mathbf{x})$ to get

$$\int_{\mathcal{E}_3} \mathbf{u}^{P_3} \cdot \mathbf{f}^{D_3} \, ds(\mathbf{x}) = -\pi_3 \int_{\mathcal{E}_3} \mathbf{u}^{P_3} \cdot \mathbf{n} \, ds(\mathbf{x}) = Q_3 \pi_3 \quad (5.53)$$

which allows us to write equation (5.52) as

$$\pi_3 = \frac{1}{Q_3} \int_{\mathcal{A}} (\mathbf{u}^{P_3} \cdot \mathbf{f}^{D_3} - \mathbf{u}^{D_3} \cdot \mathbf{f}^{P_3}) \, ds(\mathbf{x}), \quad (5.54)$$

which provides an equation for the disturbance pressure at \mathcal{E}_3 in terms of the disturbance velocities and tractions on the notional boundary, \mathcal{A} . However we would like to express equation (5.54) in terms of the unknown disturbance velocities and tractions, \mathbf{u}^{D_1} and \mathbf{f}^{D_1} . Using the continuity of velocity and traction on \mathcal{A} given in the equations (5.35) and (5.36), we can rewrite (5.54) as

$$\pi_3 = \frac{1}{Q_3} \left(\int_{\mathcal{A}} (\mathbf{u}^{P_3} \cdot \mathbf{f}^{D_1} - \mathbf{u}^{D_1} \cdot \mathbf{f}^{P_3}) \, ds(\mathbf{x}) + \psi \right), \quad (5.55)$$

where

$$\psi = \int_{\mathcal{A}} (\mathbf{u}^{P_3} \cdot \mathbf{f}^{P_1} - \mathbf{u}^{P_1} \cdot \mathbf{f}^{P_3}) \, ds(\mathbf{x}), \quad (5.56)$$

which only contains known Poiseuille velocities and tractions, and when \mathcal{A} is straight is given by

$$\psi = \frac{4}{3} \mu (1 - Q) (2 \cot \alpha - l/d) (U_0^{P_1})^2. \quad (5.57)$$

Integrating the Stokes equation for the disturbance in the branch, $\nabla \cdot \boldsymbol{\sigma}^{D_3} = \mathbf{0}$, yields

$$\pi_3 = \frac{1}{2D} \mathbf{i}' \cdot \left(\int_{\mathcal{A}} (\mathbf{f}^{P_1} - \mathbf{f}^{P_3}) \, ds(\mathbf{x}) + \int_{\mathcal{A}} \mathbf{f}^{D_1} \, ds(\mathbf{x}) - \int_{\mathcal{B}} \mathbf{f}^{D_3} \, ds(\mathbf{x}) \right), \quad (5.58)$$

$$0 = \frac{1}{2D} \mathbf{j}' \cdot \left(\int_{\mathcal{A}} (\mathbf{f}^{P_1} - \mathbf{f}^{P_3}) \, ds(\mathbf{x}) + \int_{\mathcal{A}} \mathbf{f}^{D_1} \, ds(\mathbf{x}) - \int_{\mathcal{B}} \mathbf{f}^{D_3} \, ds(\mathbf{x}) \right), \quad (5.59)$$

which we can use to check the disturbance pressure at \mathcal{E}_3 and the disturbance tractions on \mathcal{A} and \mathcal{B} , and where \mathbf{i}' and \mathbf{j}' are defined in equation (5.3). When \mathcal{A} is straight the x and y components of the first integral over \mathcal{A} are given by,

$$\int_{\mathcal{A}} (\mathbf{f}^{P_1} - \mathbf{f}^{P_3}) \, ds(\mathbf{x}) = 2\mu U_0^{P_1} \operatorname{cosec} \alpha \left(\frac{2D}{d}, \frac{lD}{d^2} + \frac{2Ld(1-Q)}{D^2} \right). \quad (5.60)$$

Now that we have equations for the disturbance pressures we move on to the derivation of the boundary integral equations starting with the main channel. We apply the boundary integral equation (1.3.40) to the $(\mathbf{u}^{D_1}, \boldsymbol{\sigma}^{D_1})$ disturbance flow in the main channel to get

$$u_j^{D_1}(\mathbf{x}_0) = -\frac{1}{4\pi\mu} \int_{\partial\Gamma_1} f_j^{D_1} G_{ij} \, ds(\mathbf{x}) + \frac{1}{4\pi} \int_{\partial\Gamma_1} u_i^{D_1} T_{ijk} n_k \, ds(\mathbf{x}), \quad (5.61)$$

for \mathbf{x}_0 in the fluid of the main channel and where G_{ij} is the free-space Green's function and T_{ijk} is its associated stress tensor. Once \mathbf{u}^{D_1} and \mathbf{f}^{D_1} are known on the boundaries we may calculate the disturbance velocity anywhere in the fluid in the main channel using equation (5.61). We expand the single-layer potential to get

$$\begin{aligned} I_j^{S,\partial\Gamma_1}(\mathbf{x}_0) &\equiv \int_{\partial\Gamma_1} f_i^{D_1} G_{ij} \, ds(\mathbf{x}) = \int_{\mathcal{A}, \mathcal{E}_1, \mathcal{E}_2, \mathcal{C}} f_i^{D_1} G_{ij} \, ds(\mathbf{x}) \\ &= \int_{\mathcal{A}, \mathcal{C}} f_i^{D_1} G_{ij} \, ds(\mathbf{x}) - \pi_2 \int_{\mathcal{E}_2} n_i G_{ij} \, ds(\mathbf{x}) + (Q-1) \int_{\mathcal{E}_2} f_i^{P_1} G_{ij} \, ds(\mathbf{x}), \end{aligned} \quad (5.62)$$

where we have used equations (5.22), (5.41) and (5.43). The double-layer potential is expanded to give

$$\begin{aligned} I_j^{D,\partial\Gamma_1}(\mathbf{x}_0) &\equiv \int_{\partial\Gamma_1} u_i^{D_1} T_{ijk} n_k \, ds(\mathbf{x}) = \int_{\mathcal{A}, \mathcal{E}_1, \mathcal{E}_2, \mathcal{C}} u_i^{D_1} T_{ijk} n_k \, ds(\mathbf{x}) \\ &= \int_{\mathcal{A}} u_i^{D_1} T_{ijk} n_k \, ds(\mathbf{x}) + (Q-1) \int_{\mathcal{E}_2} u_i^{P_1} T_{ijk} n_k \, ds(\mathbf{x}), \end{aligned} \quad (5.63)$$

where we have used the boundary conditions given in equations (5.18), (5.20) and (5.40).

Substituting equations (5.62) and (5.63) into (5.61) gives

$$4\pi\mu u_j^{D1}(\mathbf{x}_0) = - \int_{\mathcal{A},\mathcal{C}} f_i^{D1} G_{ij} \, ds(\mathbf{x}) + \pi_2 \int_{\mathcal{E}_2} n_i G_{ij} \, ds(\mathbf{x}) \\ + \mu \int_{\mathcal{A}} u_i^{D1} T_{ijk} n_k \, ds(\mathbf{x}) + I_j(\mathbf{x}_0), \quad (5.64)$$

where $I(\mathbf{x}_0)$ is defined by

$$I_j(\mathbf{x}_0) = (1 - Q) \int_{\mathcal{E}_2} \left(f_i^{P1} G_{ij} - \mu u_i^{P1} T_{ijk} n_k \right) \, ds(\mathbf{x}), \quad (5.65)$$

which is a known function of \mathbf{u}^{P1} and \mathbf{f}^{P1} and its calculation is described in Appendix C. The integral over \mathcal{E}_2 in equation (5.64) may be evaluated exactly using equations (2.44) and (2.45). We can find the total velocity in the main channel, \mathbf{u} , by calculating \mathbf{u}^{D1} from equation (5.64) and adding the Poiseuille velocity, \mathbf{u}^{P1} . The unknown quantities in equation (5.64) are the disturbance tractions on the channel walls and the notional boundary, the disturbance velocities on the notional boundary and π_2 . Equation (5.46) for the disturbance pressure, π_2 , means that we do not have to evaluate the boundary integral equation with the pole on \mathcal{E}_2 . We have proceeded in this manner to avoid just such an evaluation which suffers from numerical sensitivities as documented by Pozrikidis (2005b).

In order to find the disturbance tractions and velocities on the boundaries we require the boundary integral equations which are valid when \mathbf{x}_0 lies on the walls and on \mathcal{A} . Since the discontinuous double-layer potential over the channel walls does not appear in (5.64) we are able to write

$$0 = - \int_{\mathcal{A},\mathcal{C}} f_i^{D1} G_{ij} \, ds(\mathbf{x}) + \pi_2 \int_{\mathcal{E}_2} n_i G_{ij} \, ds(\mathbf{x}) + \mu \int_{\mathcal{A}} u_i^{D1} T_{ijk} n_k \, ds(\mathbf{x}) + I_j(\mathbf{x}_0), \quad (5.66)$$

when \mathbf{x}_0 lies on \mathcal{C} since $\mathbf{u}^{D1} = \mathbf{0}$ on \mathcal{C} . When we place the pole on \mathcal{A} the double-layer potential is

$$\int_{\mathcal{A}} u_i^{D1} T_{ijk} n_k \, ds(\mathbf{x}) = 2\pi u_i^{D1} + \int_{\mathcal{A}}^{PV} u_i^{D1} T_{ijk} n_k \, ds(\mathbf{x}) \quad (5.67)$$

where PV indicates that the integral takes its principal value, which upon substitution

into (5.64) leads to

$$2\pi\mu u_i^{D1}(\mathbf{x}_0) = - \int_{\mathcal{A}, \mathcal{C}} f_i^{D1} G_{ij} \, ds(\mathbf{x}) + \pi_2 \int_{\mathcal{E}_2} n_i G_{ij} \, ds(\mathbf{x}) + \mu \int_{\mathcal{A}}^{PV} u_i^{D1} T_{ijk} n_k \, ds(\mathbf{x}) + I_j(\mathbf{x}_0), \quad (5.68)$$

which is valid when \mathbf{x}_0 lies on \mathcal{A} .

Now that we have considered the main channel, we derive a boundary integral equation which is valid for the $(\mathbf{u}^{D3}, \boldsymbol{\sigma}^{D3})$ flow in the branch channel. Using equation (1.3.40) we write

$$u_j^{D3}(\mathbf{x}_0) = -\frac{1}{4\pi\mu} \int_{\partial\Gamma_2} f_{\mathcal{B},j}^{D3} G_{ij} \, ds(\mathbf{x}) + \frac{1}{4\pi} \int_{\partial\Gamma_2} u_i^{D3} T_{ijk} n_{\mathcal{B},k} \, ds(\mathbf{x}), \quad (5.69)$$

which is valid for \mathbf{x}_0 in the fluid of the branch channel and where the subscript \mathcal{B} indicates that the unit normal vector points into the fluid of the branch channel. Knowledge of \mathbf{u}^{D3} and $\mathbf{f}_{\mathcal{B}}^{D3}$ on the boundaries would enable us to calculate the disturbance velocity at any point in the branch channel using equation (5.69). Since there is no ambiguity about the direction of the normal vectors on \mathcal{B} and \mathcal{E}_3 we omit the subscript from the disturbance traction and the normal vector on these boundaries. However, on \mathcal{A} the normal vector points into the main channel. Therefore we will replace $\mathbf{n}_{\mathcal{B}}$ with $-\mathbf{n}$ and $\mathbf{f}_{\mathcal{B}}^{D3}$ with $-\mathbf{f}^{D3}$ in the integrals over \mathcal{A} in equation (5.69). Expanding the single-layer potential yields

$$\begin{aligned} I_j^{S,\partial\Gamma_2}(\mathbf{x}_0) &\equiv \int_{\partial\Gamma_2} f_{\mathcal{B},i}^{D3} G_{ij} \, ds(\mathbf{x}) = - \int_{\mathcal{A}} f_i^{D3} G_{ij} \, ds(\mathbf{x}) + \int_{\mathcal{B}, \mathcal{E}_3} f_i^{D3} G_{ij} \, ds(\mathbf{x}) \\ &= - \int_{\mathcal{A}} f_i^{D1} G_{ij} \, ds(\mathbf{x}) - \int_{\mathcal{A}} (f_i^{P1} - f_i^{P3}) G_{ij} \, ds(\mathbf{x}) \\ &\quad + \int_{\mathcal{B}} f_i^{D3} G_{ij} \, ds(\mathbf{x}) - \pi_3 \int_{\mathcal{E}_3} n_i G_{ij} \, ds(\mathbf{x}) \end{aligned} \quad (5.70)$$

where we have used equations (5.24) and (5.36). The double-layer potential is expanded to give

$$\begin{aligned} I_j^{D,\partial\Gamma_2}(\mathbf{x}_0) &\equiv \int_{\partial\Gamma_2} u_i^{D3} T_{ijk} n_{\mathcal{B},k} \, ds(\mathbf{x}) = \int_{\mathcal{A}, \mathcal{B}, \mathcal{E}_3} u_i^{D3} T_{ijk} n_{\mathcal{B},k} \, ds(\mathbf{x}) \\ &= - \int_{\mathcal{A}} u_i^{D3} T_{ijk} n_k \, ds(\mathbf{x}) \\ &= - \int_{\mathcal{A}} u_i^{D1} T_{ijk} n_k \, ds(\mathbf{x}) + \int_{\mathcal{A}} (u_i^{P3} - u_i^{P1}) T_{ijk} n_k \, ds(\mathbf{x}) \end{aligned} \quad (5.71)$$

where we have used the boundary conditions given in equations (5.19), (5.20) and (5.35).

Substituting equations (5.70) and (5.71) into (5.69) gives

$$4\pi\mu u_j^{D3}(\mathbf{x}_0) = \int_{\mathcal{A}} f_i^{D1} G_{ij} \, ds(\mathbf{x}) - \int_{\mathcal{B}} f_i^{D3} G_{ij} \, ds(\mathbf{x}) + \pi_3 \int_{\mathcal{E}_3} n_i G_{ij} \, ds(\mathbf{x}) - \mu \int_{\mathcal{A}} u_i^{D1} T_{ijk} n_k \, ds(\mathbf{x}) + K_j(\mathbf{x}_0), \quad (5.72)$$

where $\mathbf{K}(\mathbf{x}_0)$ is defined by

$$K_j(\mathbf{x}_0) = \int_{\mathcal{A}} \left((f_i^{P1} - f_i^{P3}) G_{ij} + \mu (u_i^{P3} - u_i^{P1}) T_{ijk} n_k \right) ds(\mathbf{x}). \quad (5.73)$$

The unknown quantities in equation (5.72) are the disturbance tractions on the channel walls, π_3 and the disturbance tractions and velocities on the notional boundary. The $\int_{\mathcal{E}_3} n_i G_{ij} \, ds(\mathbf{x})$ integral may be calculated exactly using equations (2.44) and (2.45), but where the integration is performed relative to the coordinate system with its origin on \mathcal{E}_3 , and the result transformed accordingly. Equation (5.55) for the disturbance pressure, π_3 , means that we do not have to evaluate the boundary integral equation with the pole on \mathcal{E}_3 . We can find the total velocity in the branch channel, \mathbf{u} , by calculating \mathbf{u}^{D3} from equation (5.72) and adding the Poiseuille velocity, \mathbf{u}^{P3} .

To calculate the unknown quantities on the boundaries we require the boundary integral equations which are valid when \mathbf{x}_0 lies on the notional boundary, \mathcal{A} , and the channel walls, \mathcal{B} . Since the discontinuous double-layer potential only pertains to the notional boundary, we can write,

$$0 = \int_{\mathcal{A}} f_i^{D1} G_{ij} \, ds(\mathbf{x}) - \int_{\mathcal{B}} f_i^{D1} G_{ij} \, ds(\mathbf{x}) + \pi_3 \int_{\mathcal{E}_3} n_i G_{ij} \, ds(\mathbf{x}) - \mu \int_{\mathcal{A}} u_i^{D1} T_{ijk} n_k \, ds(\mathbf{x}) + K_j(\mathbf{x}_0), \quad (5.74)$$

when \mathbf{x}_0 lies on \mathcal{B} because $\mathbf{u}^{D3}(\mathbf{x}_0) = \mathbf{0}$ on the walls. When the pole lies on \mathcal{A} the double-layer potential involving \mathbf{u}^{D1} in equation (5.72) and the double-layer potential in equation (5.73) are both discontinuous, which leads to

$$2\pi\mu \left(u_j^{D1}(\mathbf{x}_0) + u_j^{P1}(\mathbf{x}_0) - u_j^{P3}(\mathbf{x}_0) \right) = \int_{\mathcal{A}} f_i^{D1} G_{ij} \, ds(\mathbf{x}) - \int_{\mathcal{B}} f_i^{D1} G_{ij} \, ds(\mathbf{x}) + \pi_3 \int_{\mathcal{E}_3} n_i G_{ij} \, ds(\mathbf{x}) - \mu \int_{\mathcal{A}}^{PV} u_i^{D1} T_{ijk} n_k \, ds(\mathbf{x}) + K_j^{PV}(\mathbf{x}_0), \quad (5.75)$$

where we have expressed the left-hand side in terms of \mathbf{u}^{D1} using equation (5.35), and

where

$$K_j^{PV}(\mathbf{x}_0) = \int_{\mathcal{A}} \left(f_i^{P_1} - f_i^{P_3} \right) G_{ij} \, ds(\mathbf{x}) + \mu \int_{\mathcal{A}}^{PV} \left(u_i^{P_3} - u_i^{P_1} \right) T_{ijk} n_k \, ds(\mathbf{x}). \quad (5.76)$$

We use the boundary element method (e.g. Pozrikidis 2002a) to discretise the geometry and the governing equations. The boundaries are discretised into elements upon which we evaluate the boundary integral equations. We obtain a sufficient number of equations for the unknown tractions on \mathcal{C} by evaluating equation (5.66) on each boundary element. We have the same sufficiency on \mathcal{B} using equation (5.74). Evaluation of the equations (5.68) and (5.75) on \mathcal{A} provides a sufficient number of equations for the disturbance tractions and velocities on the notional boundary, \mathcal{A} . The disturbance pressure equations (5.46) and (5.55) provide the two equations for the disturbance pressures. Therefore we have the same number of equations as unknowns and so our system of equations is complete. We have completed our derivation of the governing equations for the flow through a bifurcation and now we move on to describe how the boundary element method is applied in order to find the numerical solution.

5.2 Numerical method

As in previous chapters our aim is to discretise the governing equations using the boundary element method and form the equations into the linear matrix system,

$$\mathbf{A} \cdot \mathbf{x} = \mathbf{b}, \quad (5.77)$$

where \mathbf{A} is the influence matrix containing the coefficients of the unknown disturbance pressures, tractions and velocities stored in the column-vector, \mathbf{x} , and \mathbf{b} is a column-vector containing known values. To apply the boundary element method we discretise the main channel walls, the branch channel walls and the notional boundary into $N_{\mathcal{C}}$, $N_{\mathcal{B}}$ and $N_{\mathcal{A}}$ equally-sized straight elements respectively. On each of the elements we set the unknown traction to a constant 2-vector, which we label $\mathbf{f}_r^{D_1}$ on the r^{th} element of \mathcal{C} , $\mathbf{f}_r^{D_3}$ on the r^{th} element of \mathcal{B} and $\mathbf{f}_r^{D_1}$ on the r^{th} element of \mathcal{A} . Additionally we set the disturbance velocity to $\mathbf{u}_r^{D_1}$ on the r^{th} element of \mathcal{A} . Therefore the vector of unknowns is defined by

$$\mathbf{x} = \left[\mathbf{F}_{\mathcal{C}}^D \quad \mathbf{F}_{\mathcal{A}}^D \quad \mathbf{F}_{\mathcal{B}}^D \quad \mathbf{U}_{\mathcal{A}}^D \quad \pi_2 \quad \pi_3 \right]^T \quad (5.78)$$

where $\mathbf{F}_{\mathcal{C}}^D$ is a vector containing the $2N_{\mathcal{C}}$ components of the disturbance tractions of \mathcal{C} , $\mathbf{F}_{\mathcal{A}}^D$ is a vector which holds the $2N_{\mathcal{A}}$ components of the disturbance traction on \mathcal{A} , $\mathbf{F}_{\mathcal{B}}^D$ is a vector holding the $2N_{\mathcal{B}}$ components of the disturbance tractions on \mathcal{B} , $\mathbf{U}_{\mathcal{A}}^D$ is the $2N_{\mathcal{A}}$ vector which stores the components of the disturbance velocities on \mathcal{A} , and the final two elements are the disturbance pressures at \mathcal{E}_2 and \mathcal{E}_3 respectively. The vectors $\mathbf{F}_{\mathcal{C}}^D$, $\mathbf{F}_{\mathcal{A}}^D$,

\mathbf{F}_B^D and \mathbf{U}_A^D are defined to be

$$\mathbf{F}_C^D = \begin{bmatrix} f_{x,1}^{D_1} & f_{y,1}^{D_1} & \cdots & f_{x,N_C}^{D_1} & f_{y,N_C}^{D_1} \end{bmatrix}, \quad (5.79)$$

$$\mathbf{F}_A^D = \begin{bmatrix} f_{x,1}^{D_1} & f_{y,1}^{D_1} & \cdots & f_{x,N_A}^{D_1} & f_{y,N_A}^{D_1} \end{bmatrix}, \quad (5.80)$$

$$\mathbf{F}_B^D = \begin{bmatrix} f_{x,1}^{D_3} & f_{y,1}^{D_3} & \cdots & f_{x,N_B}^{D_3} & f_{y,N_B}^{D_3} \end{bmatrix}, \quad (5.81)$$

and

$$\mathbf{U}_A^D = \begin{bmatrix} u_{x,1}^{D_1} & u_{y,1}^{D_1} & \cdots & u_{x,N_A}^{D_1} & u_{y,N_A}^{D_1} \end{bmatrix}. \quad (5.82)$$

We will now start on the discretisation of the governing equations starting with the equations for the disturbance pressures. Equation (5.46) for the disturbance pressure, π_2 , is approximated by

$$\begin{aligned} 0 &= Q_1 \pi_2 + \int_A (\mathbf{u}^{P_1} \cdot \mathbf{f}^{D_1} - \mathbf{u}^{D_1} \cdot \mathbf{f}^{P_1}) \, ds(\mathbf{x}) \\ &\approx Q_1 \pi_2 + \sum_{r=1}^{N_A} (\mathbf{u}^{P_1}(\mathbf{x}_{m,r}) \cdot \mathbf{f}_r^{D_1} - \mathbf{f}^{P_1}(\mathbf{x}_{m,r}) \cdot \mathbf{u}_r^{D_1}) l_r, \end{aligned} \quad (5.83)$$

where $\mathbf{x}_{m,r}$ is the mid-point of the r^{th} element and l_r is its length. By defining

$$\mathbf{U}_A^{P_1} = \begin{bmatrix} \mathbf{u}^{P_1}(\mathbf{x}_{m,1}) l_1 & \cdots & \mathbf{u}^{P_1}(\mathbf{x}_{m,N_A}) l_{N_A} \end{bmatrix}, \quad (5.84)$$

$$\mathbf{F}_A^{P_1} = \begin{bmatrix} \mathbf{f}^{P_1}(\mathbf{x}_{m,1}) l_1 & \cdots & \mathbf{f}^{P_1}(\mathbf{x}_{m,N_A}) l_{N_A} \end{bmatrix}, \quad (5.85)$$

we may write equation (5.83) as

$$Q_1 \pi_2 + \mathbf{U}_A^{P_1} \cdot \mathbf{F}_A^D - \mathbf{F}_A^{P_1} \cdot \mathbf{U}_A^D = 0, \quad (5.86)$$

which in terms of the vector of unknowns, \mathbf{x} , is

$$\begin{bmatrix} 0 & \mathbf{U}_A^{P_1} & \mathbf{0} & -\mathbf{F}_A^{P_1} & Q_1 & 0 \end{bmatrix} \cdot \mathbf{x} = 0. \quad (5.87)$$

Similarly for the π_3 equation (5.55), we have

$$\begin{aligned} \psi &= Q_3 \pi_3 + \int_A (\mathbf{u}^{D_1} \cdot \mathbf{f}^{P_3} - \mathbf{u}^{P_3} \cdot \mathbf{f}^{D_1}) \, ds(\mathbf{x}) \\ &\approx Q_3 \pi_3 + \sum_{r=1}^{N_A} (\mathbf{f}^{P_3}(\mathbf{x}_{m,r}) \cdot \mathbf{u}_r^{D_1} - \mathbf{u}^{P_3}(\mathbf{x}_{m,r}) \cdot \mathbf{f}_r^{D_1}) l_r, \end{aligned} \quad (5.88)$$

which we can write as

$$\begin{bmatrix} 0 & -\mathbf{U}_A^{P_3} & \mathbf{0} & -\mathbf{F}_A^{P_3} & 0 & Q_3 \end{bmatrix} \cdot \mathbf{x} = \psi, \quad (5.89)$$

by defining

$$\mathbf{U}_{\mathcal{A}}^{P_3} = \left[\mathbf{u}^{P_3}(\mathbf{x}_{m,1}) l_1 \quad \cdots \quad \mathbf{u}^{P_3}(\mathbf{x}_{m,N_{\mathcal{A}}}) l_{N_{\mathcal{A}}} \right], \quad (5.90)$$

$$\mathbf{F}_{\mathcal{A}}^{P_3} = \left[\mathbf{f}^{P_3}(\mathbf{x}_{m,1}) l_1 \quad \cdots \quad \mathbf{f}^{P_3}(\mathbf{x}_{m,N_{\mathcal{A}}}) l_{N_{\mathcal{A}}} \right], \quad (5.91)$$

and where ψ is evaluated using equation (5.57) for a straight \mathcal{A} . Before considering the boundary integral equations, we will summarise our previous notation in order for us to concisely discretise the boundary integral equations for \mathbf{x}_0 located on the boundaries \mathcal{A} , \mathcal{B} and \mathcal{C} . On a boundary ϕ , which has N_{ϕ} elements labelled $El_1 \dots El_{N_{\phi}}$, we define the vectors,

$$\mathbf{I}_{\phi,j}^G(\mathbf{x}_0) = \left[\tilde{G}_{xj,1}(\mathbf{x}_0) \quad \tilde{G}_{yj,1}(\mathbf{x}_0) \quad \cdots \quad \tilde{G}_{xj,N_{\phi}}(\mathbf{x}_0) \quad \tilde{G}_{yj,N_{\phi}}(\mathbf{x}_0) \right], \quad (5.92)$$

$$\mathbf{I}_{\phi,j}^T(\mathbf{x}_0) = \left[\tilde{T}_{xj,1}(\mathbf{x}_0) \quad \tilde{T}_{yj,1}(\mathbf{x}_0) \quad \cdots \quad \tilde{T}_{xj,N_{\phi}}(\mathbf{x}_0) \quad \tilde{T}_{yj,N_{\phi}}(\mathbf{x}_0) \right], \quad (5.93)$$

where $\tilde{G}_{ij,r}$ and $\tilde{T}_{ij,r}$ are the integrals over the r^{th} element of the Green's function and the stress tensor respectively, and are defined by

$$\tilde{G}_{ij,r}(\mathbf{x}_0) = \int_{El_r} G_{ij}(\mathbf{x}, \mathbf{x}_0) \, ds(\mathbf{x}), \quad (5.94)$$

$$\tilde{T}_{ij,r}(\mathbf{x}_0) = \int_{El_r} T_{ijk}(\mathbf{x}, \mathbf{x}_0) n_k \, ds(\mathbf{x}). \quad (5.95)$$

When \mathbf{x}_0 lies on El_r the Green's function is weakly singular but integrable. The stress tensor is also singular when \mathbf{x}_0 lies on El_r and so we replace $\tilde{T}_{ij,r}(\mathbf{x}_0)$ with the principal value integral,

$$\tilde{T}_{ij,r}^{PV}(\mathbf{x}_0) = \int_{El_r}^{PV} T_{ijk}(\mathbf{x}, \mathbf{x}_0) n_k \, ds(\mathbf{x}), \quad (5.96)$$

in the r^{th} pair of elements of $\mathbf{I}_{\phi,j}^T(\mathbf{x}_0)$ and denote the vector by $\mathbf{I}_{\phi,j}^{T,PV}(\mathbf{x}_0)$. It is important to note that the value of the jump in the discontinuous double-layer potential will already have been included in the governing boundary integral equation. We have shown in equation (2.37) that when El_r is straight, $\tilde{T}_{ij,r}^{PV}(\mathbf{x}_0) = 0$. Proceeding to the boundary integral

equations, we write equations (5.66), (5.68), (5.74) and (5.75) as

$$\int_{\mathcal{A}, \mathcal{C}} f_i^{D1} G_{ij} \, ds(\mathbf{x}) - \pi_2 \int_{\mathcal{E}_2} n_i G_{ij} \, ds(\mathbf{x}) - \mu \int_{\mathcal{A}} u_i^{D1} T_{ijk} n_k \, ds(\mathbf{x}) = I_j(\mathbf{x}_0), \quad (5.97)$$

$$\int_{\mathcal{A}, \mathcal{C}} f_i^{D1} G_{ij} \, ds(\mathbf{x}) - \pi_2 \int_{\mathcal{E}_2} n_i G_{ij} \, ds(\mathbf{x}) - \mu \int_{\mathcal{A}}^{PV} u_i^{D1} T_{ijk} n_k \, ds(\mathbf{x}) + 2\pi\mu u_i^{D1}(\mathbf{x}_0) = I_j(\mathbf{x}_0), \quad (5.98)$$

$$\int_{\mathcal{B}} f_i^{D3} G_{ij} \, ds(\mathbf{x}) - \int_{\mathcal{A}} f_i^{D1} G_{ij} \, ds(\mathbf{x}) - \pi_3 \int_{\mathcal{E}_3} n_i G_{ij} \, ds(\mathbf{x}) + \mu \int_{\mathcal{A}} u_i^{D1} T_{ijk} n_k \, ds(\mathbf{x}) = K_j(\mathbf{x}_0), \quad (5.99)$$

$$\int_{\mathcal{B}} f_i^{D3} G_{ij} \, ds(\mathbf{x}) - \int_{\mathcal{A}} f_i^{D1} G_{ij} \, ds(\mathbf{x}) - \pi_3 \int_{\mathcal{E}_3} n_i G_{ij} \, ds(\mathbf{x}) + 2\pi\mu u_j^{D1}(\mathbf{x}_0) + \mu \int_{\mathcal{A}}^{PV} u_i^{D1} T_{ijk} n_k \, ds(\mathbf{x}) = K_j^{PV}(\mathbf{x}_0) + 2\pi\mu \left(u_j^{P3}(\mathbf{x}_0) - u_j^{P1}(\mathbf{x}_0) \right), \quad (5.100)$$

where (5.97) is valid for \mathbf{x}_0 on \mathcal{C} , (5.99) is valid for \mathbf{x}_0 on \mathcal{B} , and both of (5.98) and (5.100) are for \mathbf{x}_0 located on \mathcal{A} . The integrals of the disturbance tractions over \mathcal{A} , \mathcal{B} and \mathcal{C} are approximated by

$$\int_{\mathcal{A}} f_i^{D1} G_{ij} \, ds(\mathbf{x}) \approx \sum_{r=1}^{N_A} \tilde{G}_{ij,r}(\mathbf{x}_0) f_{i,r}^{D1} = \mathbf{I}_{\mathcal{A},j}^G(\mathbf{x}_0) \cdot \mathbf{F}_{\mathcal{A}}^D, \quad (5.101)$$

$$\int_{\mathcal{B}} f_i^{D3} G_{ij} \, ds(\mathbf{x}) \approx \sum_{r=1}^{N_B} \tilde{G}_{ij,r}(\mathbf{x}_0) f_{i,r}^{D3} = \mathbf{I}_{\mathcal{B},j}^G(\mathbf{x}_0) \cdot \mathbf{F}_{\mathcal{B}}^D, \quad (5.102)$$

$$\int_{\mathcal{C}} f_i^{D1} G_{ij} \, ds(\mathbf{x}) \approx \sum_{r=1}^{N_C} \tilde{G}_{ij,r}(\mathbf{x}_0) f_{i,r}^{D1} = \mathbf{I}_{\mathcal{C},j}^G(\mathbf{x}_0) \cdot \mathbf{F}_{\mathcal{A}}^D. \quad (5.103)$$

We label the integral over \mathcal{E}_2 as $I_{\mathcal{E}_2,j}^G(\mathbf{x}_0) = \int_{\mathcal{E}_2} n_i G_{ij} \, ds(\mathbf{x})$, which can be calculated exactly using equations (2.44) and (2.45). We may also use these equations to calculate the integral over \mathcal{E}_3 , which we label $I_{\mathcal{E}_3,j}^G(\mathbf{x}_0)$, by using the mapping given in equation (5.1). The integrals of the disturbance velocity over \mathcal{A} are approximated by

$$\int_{\mathcal{A}} u_i^{D1} T_{ijk} n_k \, ds(\mathbf{x}) \approx \sum_{r=1}^{N_A} \tilde{T}_{ij,r}(\mathbf{x}_0) u_{i,r}^{D1} = \mathbf{I}_{\mathcal{A},j}^T(\mathbf{x}_0) \cdot \mathbf{U}_{\mathcal{A}}^D, \quad (5.104)$$

$$\int_{\mathcal{A}}^{PV} u_i^{D1} T_{ijk} n_k \, ds(\mathbf{x}) \approx \sum_{r=1}^{N_A} \tilde{T}_{ij,r}^{PV}(\mathbf{x}_0) u_{i,r}^{D1} = \mathbf{I}_{\mathcal{A},j}^{T,PV}(\mathbf{x}_0) \cdot \mathbf{U}_{\mathcal{A}}^D. \quad (5.105)$$

Finally we approximate $\mathbf{I}(\mathbf{x}_0)$, defined in equation (5.65), $\mathbf{K}(\mathbf{x}_0)$, defined in equation (5.73) and $\mathbf{K}^{PV}(\mathbf{x}_0)$ using

$$I_j(\mathbf{x}_0) \approx (1 - Q) \sum_{r=1}^{N_{\mathcal{E}_2}} \left(f_i^{P_1}(\mathbf{x}_{m,r}) \tilde{G}_{ij,r} + \mu u^{P_1}(\mathbf{x}_{m,r}) \tilde{T}_{xj,r} \right), \quad (5.106)$$

$$K_j(\mathbf{x}_0) \approx \sum_{r=1}^{N_{\mathcal{A}}} \left(\left(f_i^{P_1}(\mathbf{x}_{m,r}) - f_i^{P_3}(\mathbf{x}_{m,r}) \right) \tilde{G}_{ij,r} + \mu \left(u_i^{P_3}(\mathbf{x}_{m,r}) - u_i^{P_1}(\mathbf{x}_{m,r}) \right) \tilde{T}_{ij,r} n_k \right), \quad (5.107)$$

$$K_j^{PV}(\mathbf{x}_0) \approx \sum_{r=1}^{N_{\mathcal{A}}} \left(\left(f_i^{P_1}(\mathbf{x}_{m,r}) - f_i^{P_3}(\mathbf{x}_{m,r}) \right) \tilde{G}_{ij,r} + \mu \left(u_i^{P_3}(\mathbf{x}_{m,r}) - u_i^{P_1}(\mathbf{x}_{m,r}) \right) \tilde{T}_{ij,r}^{PV} n_k \right). \quad (5.108)$$

We are now able to write the discretised form of equation (5.97) as

$$\begin{bmatrix} \mathbf{I}_{\mathcal{C},j}^G(\mathbf{x}_0) & \mathbf{I}_{\mathcal{A},j}^G(\mathbf{x}_0) & \mathbf{0} & -\mu \mathbf{I}_{\mathcal{A},j}^T(\mathbf{x}_0) & -\mathbf{I}_{\mathcal{E}_2,j}^G(\mathbf{x}_0) & \mathbf{0} \end{bmatrix} \cdot \mathbf{x} = I_j(\mathbf{x}_0), \quad (5.109)$$

where \mathbf{x}_0 lies on \mathcal{C} . Repeated evaluation of this equation with \mathbf{x}_0 placed at the mid-point of each of \mathcal{C} 's boundary elements creates $N_{\mathcal{C}}$ pairs of equations which are assembled into the matrix,

$$\begin{bmatrix} \mathcal{C}_{\mathcal{C}} & \mathcal{C}_{\mathcal{A}} & \mathbf{0} & \mathcal{C}_{\mathcal{A}}^T & \mathcal{C}_{\mathcal{E}_2} & \mathbf{0} \end{bmatrix} \cdot \mathbf{x} = \mathcal{C}_I, \quad (5.110)$$

where each of $\mathcal{C}_{\mathcal{C}}$, $\mathcal{C}_{\mathcal{A}}$, $\mathcal{C}_{\mathcal{A}}^T$, $\mathcal{C}_{\mathcal{E}_2}$ and \mathcal{C}_I consist of the $N_{\mathcal{C}}$ pairs of $\mathbf{I}_{\mathcal{C},j}^G(\mathbf{x}_0)$, $\mathbf{I}_{\mathcal{A},j}^G(\mathbf{x}_0)$, $-\mu \mathbf{I}_{\mathcal{A},j}^T(\mathbf{x}_0)$, $-\mathbf{I}_{\mathcal{E}_2,j}^G(\mathbf{x}_0)$ and $I_j(\mathbf{x}_0)$ respectively. The discretised analogue of equation (5.98) is

$$\begin{bmatrix} \mathbf{I}_{\mathcal{C},j}^G(\mathbf{x}_0) & \mathbf{I}_{\mathcal{A},j}^G(\mathbf{x}_0) & \mathbf{0} & -\mu \mathbf{I}_{\mathcal{A},j}^{T,PV}(\mathbf{x}_0) & -\mathbf{I}_{\mathcal{E}_2,j}^G(\mathbf{x}_0) & \mathbf{0} \end{bmatrix} \cdot \mathbf{x} + 2\pi\mu u_j^{D_1}(\mathbf{x}_0) = I_j(\mathbf{x}_0), \quad (5.111)$$

where \mathbf{x}_0 is on \mathcal{A} . Repeated evaluation of this equation with \mathbf{x}_0 placed at the mid-point of each of \mathcal{A} 's elements creates $N_{\mathcal{A}}$ pairs of equations which are assembled into the matrix,

$$\begin{bmatrix} \mathcal{A}_{\mathcal{C}} & \mathcal{A}_{\mathcal{A}}^m & \mathbf{0} & \mathcal{A}_{\mathcal{A}}^{m,T} & \mathcal{A}_{\mathcal{E}_2} & \mathbf{0} \end{bmatrix} \cdot \mathbf{x} = \mathcal{A}_I, \quad (5.112)$$

where each of $\mathcal{A}_{\mathcal{C}}$, $\mathcal{A}_{\mathcal{A}}^m$, $\mathcal{A}_{\mathcal{E}_2}$ and \mathcal{A}_I consist of the $N_{\mathcal{A}}$ pairs of $\mathbf{I}_{\mathcal{C},j}^G(\mathbf{x}_0)$, $\mathbf{I}_{\mathcal{A},j}^G(\mathbf{x}_0)$, $-\mathbf{I}_{\mathcal{E}_2,j}^G(\mathbf{x}_0)$ and $I_j(\mathbf{x}_0)$ respectively. The $\mathcal{A}_{\mathcal{A}}^{m,T}$ submatrix consists of the $N_{\mathcal{A}}$ pairs of $-\mu \mathbf{I}_{\mathcal{A},j}^{T,PV}(\mathbf{x}_0)$. To clarify the structure of the matrix we define,

$$\tilde{\mathcal{A}}_{\mathcal{A}}^T = \begin{bmatrix} \mathbf{0} & \mathbf{T}_{1,2} & \cdots & \mathbf{T}_{1,N_{\mathcal{A}}-1} & \mathbf{T}_{1,N_{\mathcal{A}}} \\ \mathbf{T}_{2,2} & \mathbf{0} & \cdots & \mathbf{T}_{2,N_{\mathcal{A}}-1} & \mathbf{T}_{2,N_{\mathcal{A}}} \\ \vdots & \vdots & \ddots & \vdots & \vdots \\ \mathbf{T}_{N_{\mathcal{A}}-1,2} & \mathbf{T}_{N_{\mathcal{A}}-1,2} & \cdots & \mathbf{0} & \mathbf{T}_{N_{\mathcal{A}}-1,N_{\mathcal{A}}} \\ \mathbf{T}_{N_{\mathcal{A}},1} & \mathbf{T}_{N_{\mathcal{A}},2} & \cdots & \mathbf{T}_{N_{\mathcal{A}}-1,N_{\mathcal{A}}-1} & \mathbf{0} \end{bmatrix} \quad (5.113)$$

where each entry is itself a 2×2 matrix, and

$$\mathbf{T}_{p,q} = \begin{bmatrix} \tilde{T}_{xx,q}(\mathbf{x}_0^{(p)}) & \tilde{T}_{yx,q}(\mathbf{x}_0^{(p)}) \\ \tilde{T}_{xy,q}(\mathbf{x}_0^{(p)}) & \tilde{T}_{yy,q}(\mathbf{x}_0^{(p)}) \end{bmatrix} \quad (5.114)$$

when $p \neq q$, and $\mathbf{T}_{p,q} = \mathbf{0}$ when $p = q$ because $\tilde{T}_{yx,p}^{PV}(\mathbf{x}_0^{(p)}) = 0$ on a straight element. The indices p and q refer to the element on which \mathbf{x}_0 is located and the element over which we evaluate $\tilde{T}_{ij,q}$ respectively. Therefore we can write

$$\mathcal{A}_A^{m,T} = -\mu \tilde{\mathcal{A}}_A^T + 2\pi\mu \mathbf{I}_{2N_A}, \quad (5.115)$$

where the second term on the right-hand side accounts for the $2\pi\mu u_j^{D1}(\mathbf{x}_0)$ term in equation (5.98) and \mathbf{I}_{2N_A} is the identity matrix of size $2N_A \times 2N_A$.

The discretised form of equation (5.99) when \mathbf{x}_0 lies on \mathcal{B} is

$$\begin{bmatrix} 0 & -I_{\mathcal{A},j}^G(\mathbf{x}_0) & I_{\mathcal{B},j}^G(\mathbf{x}_0) & \mu I_{\mathcal{A},j}^T(\mathbf{x}_0) & 0 & -I_{\mathcal{E}_3,j}^G(\mathbf{x}_0) \end{bmatrix} \cdot \mathbf{x} = K_j(\mathbf{x}_0). \quad (5.116)$$

When we place \mathbf{x}_0 at the mid-point of each of the boundary elements of \mathcal{B} we generate N_B pairs of equations which we write as

$$\begin{bmatrix} \mathbf{0} & \mathcal{B}_A & \mathcal{B}_B & \mathcal{B}_A^T & \mathbf{0} & \mathcal{B}_{\mathcal{E}_3} \end{bmatrix} \cdot \mathbf{x} = \mathcal{B}_K, \quad (5.117)$$

where each of \mathcal{B}_A , \mathcal{B}_B , \mathcal{B}_A^T , $\mathcal{B}_{\mathcal{E}_3}$ and \mathcal{B}_K consist of the N_B pairs of $-I_{\mathcal{A},j}^G(\mathbf{x}_0)$, $I_{\mathcal{B},j}^G(\mathbf{x}_0)$, $\mu I_{\mathcal{A},j}^T(\mathbf{x}_0)$, $-I_{\mathcal{E}_3,j}^G(\mathbf{x}_0)$ and $K_j(\mathbf{x}_0)$ respectively. The discretised version of equation (5.100) is

$$\begin{bmatrix} 0 & -I_{\mathcal{A},j}^G(\mathbf{x}_0) & I_{\mathcal{B},j}^G(\mathbf{x}_0) & \mu I_{\mathcal{A},j}^{T,PV}(\mathbf{x}_0) & 0 & -I_{\mathcal{E}_3,j}^G(\mathbf{x}_0) \end{bmatrix} \cdot \mathbf{x} \\ + 2\pi\mu u_j^{D1}(\mathbf{x}_0) = K_j^{PV}(\mathbf{x}_0) + 2\pi\mu \left(u_j^{P3}(\mathbf{x}_0) - u_j^{P1}(\mathbf{x}_0) \right), \quad (5.118)$$

where \mathbf{x}_0 is on \mathcal{A} . Repeated evaluation of this equation with \mathbf{x}_0 placed at the mid-point of each of \mathcal{A} 's elements creates N_A pairs of equations which are assembled into the matrix,

$$\begin{bmatrix} \mathbf{0} & \mathcal{A}_A^b & \mathcal{A}_B & \mathcal{A}_A^{b,T} & \mathbf{0} & \mathcal{A}_{\mathcal{E}_3} \end{bmatrix} \cdot \mathbf{x} = \mathcal{A}_K, \quad (5.119)$$

where each of \mathcal{A}_A^b , \mathcal{A}_B and $\mathcal{A}_{\mathcal{E}_3}$ consist of the N_A pairs of $-I_{\mathcal{A},j}^G(\mathbf{x}_0)$, $I_{\mathcal{B},j}^G(\mathbf{x}_0)$ and $-I_{\mathcal{E}_3,j}^G(\mathbf{x}_0)$ respectively. The $\mathcal{A}_A^{b,T}$ submatrix is

$$\mathcal{A}_A^{b,T} = \mu \tilde{\mathcal{A}}_A^T + 2\pi\mu \mathbf{I}_{2N_A}, \quad (5.120)$$

and each pair of rows of \mathcal{A}_K corresponds to the right-hand side of (5.118).

Assembling equations (5.87), (5.89), (5.110), (5.112), (5.117) and (5.119) into one

matrix system gives

$$\begin{bmatrix} \mathcal{C}_C & \mathcal{C}_A & 0 & \mathcal{C}_A^T & \mathcal{C}_{\mathcal{E}_2} & 0 \\ \mathcal{A}_C & \mathcal{A}_A^m & 0 & \mathcal{A}_A^{m,T} & \mathcal{A}_{\mathcal{E}_2} & 0 \\ 0 & \mathcal{B}_A & \mathcal{B}_B & \mathcal{B}_A^T & 0 & \mathcal{B}_{\mathcal{E}_3} \\ 0 & \mathcal{A}_A^b & \mathcal{A}_B & \mathcal{A}_A^{b,T} & 0 & \mathcal{A}_{\mathcal{E}_3} \\ 0 & U_A^{P_1} & 0 & -F_A^{P_1} & Q_1 & 0 \\ 0 & -U_A^{P_3} & 0 & -F_A^{P_3} & 0 & Q_3 \end{bmatrix} \cdot \mathbf{x} = \begin{bmatrix} \mathcal{C}_I \\ \mathcal{A}_I \\ \mathcal{B}_K \\ \mathcal{A}_K \\ 0 \\ \psi \end{bmatrix} \quad (5.121)$$

which is in our desired form. The ‘influence’ matrix elements of our master linear system (5.121) are mostly submatrices as we have seen. The first and second rows correspond to the boundary integral equations valid in the main channel and where the first row corresponds to \mathbf{x}_0 on the walls of the channel and the second to \mathbf{x}_0 lying on the notional boundary, \mathcal{A} . The third and fourth rows correspond to the boundary integral equations valid in the branch channel and where the third row corresponds to \mathbf{x}_0 on the walls of the channel and the fourth to \mathbf{x}_0 lying on the notional boundary, \mathcal{A} . The fifth and sixth rows correspond to the pressure equations for π_2 and π_3 respectively. The size of the ‘influence’ matrix is $(4N_A + 2N_B + 2N_C + 2) \times (4N_A + 2N_B + 2N_C + 2)$. In our simulations we took $N_A = 200$, $N_B = 400$ and $N_C = 800$.

Once the master linear system is built we solve it using a standard method. Since our ‘influence’ matrix is considerably larger than in previous chapters we favoured the GMRES (e.g. Saad 2003) iterative solver over Gaussian elimination due to speed considerations. We can then calculate the disturbance velocity at a point using either equation (5.64) or (5.72) depending on the location of the point. Addition of the pertinent Poiseuille velocity provides the total velocity at the point. We calculated the flow streamlines by integrating the equation

$$\frac{d\mathbf{x}}{ds} = \mathbf{u}(\mathbf{x}) \quad (5.122)$$

along the streamline, where \mathbf{x} is the position vector of a point on the streamline and s measures the arc-length along the streamline. We used the adaptive stepping Runge-Kutta-Fehlberg method (e.g. Atkinson 1978) to integrate (5.122).

5.3 Validation

We truncated the channels so that $l = 12d$ and $L = l/2$. We found this truncation length sufficient for the disturbance velocity to decay as we approach the ends of the computational domain, as per our initial assumptions. The important parameters are the ratio of channel heights, $\delta = D/d$, the branch angle, α and the flux ratio, Q . As a check on the numerical implementation, we confirmed that the discretised form of the integral identities (1.3.34) and (1.3.31) were satisfied to within an acceptable tolerance. In each set of presented results we will check that the velocity field in the channel tends to the applicable Poiseuille flow as we approach the ends. For each set of parameters we will show the profile of the velocity along the centreline of the main channel and branch

channel. From these plots we will see the disturbance component of the velocity decay rapidly as we move away from the branch entrance. As we move towards the entrance or exits the profiles will show the velocity tending to the appropriate centreline Poiseuille velocity. In all calculations, we found that the streamwise velocity in the channels was well within 1% of its predicted value at an axial distance of $3d$ from the branch entrance. The y -component in the main channel and the Y -component in the branch channel, which should tend to zero, were all less than $0.005 U_0^{P_1}$ at a distance of $3d$ from the branch entrance. However, in the one case where we considered $\delta > 1$, so that the branch was wider than the main channel, the velocity disturbance had decayed to the stated tolerances at the distance, $5d$, which is somewhat closer to \mathcal{E}_3 . Although the velocity has decayed satisfactorily at this distance, the end \mathcal{E}_3 is only a further distance d , which lends weight to an argument for a longer branch channel when $\delta > 1$ to allow for the slower decay of the disturbance velocity.

In the main channel we checked the total traction and we display the profile on the top wall for the first three simulations. The profile is somewhat different to the disturbance tractions that we have seen in previous chapters because we display the total traction and not the disturbance traction. The reason for the change lies in the choice we must make between the disturbance tractions, \mathbf{f}^{D_1} and \mathbf{f}^{D_2} , where the former decays to zero at \mathcal{E}_1 and the latter which decays to $-\pi_2 \mathbf{n}$ at \mathcal{E}_2 . Therefore plotting the total traction against x/d allows us to see the traction attain a linear profile as we approach the ends, together with the traction disturbance close to the branch entrance. In all discussions regarding the pressures and tractions we render the quantity dimensionless by dividing by $\mu U_0^{P_1}/d$ and indicate a dimensionless quantity by a circumflex, e.g. $\mathbf{f} = \hat{\mathbf{f}} \mu U_0^{P_1}/d$. Since we have

$$\hat{\mathbf{f}} = \hat{\mathbf{f}}^{P_1} + \hat{\mathbf{f}}^{D_1} = \hat{\mathbf{f}}^{P_2} + \hat{\mathbf{f}}^{D_2}, \quad (5.123)$$

we calculate

$$\hat{\mathbf{f}} = \hat{\mathbf{f}}^{P_1} + \hat{\mathbf{f}}^{D_1} = 2(1, -x/d) + \hat{\mathbf{f}}^{D_1} \quad (5.124)$$

or equivalently

$$\hat{\mathbf{f}} = \hat{\mathbf{f}}^{P_2} + \hat{\mathbf{f}}^{D_2} = 2Q(1, -x/d) + \hat{\mathbf{f}}^{D_2}, \quad (5.125)$$

on the top wall, and where we have used the definition of the stress tensor to calculate the traction together with the Poiseuille pressures given in equations (5.25) and (5.26). On the top wall at the entrance, \mathcal{E}_1 , we have

$$\hat{\mathbf{f}} = (2, 0) \quad (5.126)$$

since $\hat{\mathbf{f}}^{D_1} = \mathbf{0}$, and

$$\hat{\mathbf{f}} = (2Q, -2Ql/d + \hat{\pi}_2) = (2Q, -24Q + \hat{\pi}_2) \quad (5.127)$$

on the top wall at the exit, \mathcal{E}_2 . Therefore we expect the x -component of the dimensionless traction to tend to 2 at \mathcal{E}_1 and $2Q$ at \mathcal{E}_2 . The y -component of the traction will vary linearly

with x along the channel wall, from zero at \mathcal{E}_1 to $-2Ql + \hat{\pi}_2$ at \mathcal{E}_2 . We only have the one disturbance traction, $\hat{\mathbf{f}}^{P_3}$, in the branch channel. In our results we show the profile of $\hat{\mathbf{f}}^{P_3}$ along the right-hand wall, $Y = D$, where we expect the X -component to tend to zero as we approach \mathcal{E}_3 and the Y -component to tend to the disturbance pressure, $\hat{\pi}_3$.

To validate the numerical solution we used a configuration with $l = 12d$, $L = l/2$, $\alpha = \pi/2$ and $D = d$ as our reference configuration. Firstly we doubled the number of elements on each boundary in the reference configuration and found that the total pressure at the exits differed by less than 0.1%. With regards to the boundary tractions, we found the largest discrepancy occurred on the elements neighbouring the corners of the entrance to the branch channel where the stress is formally infinite (see Appendix E for details). Away from the corners, we found that the absolute errors in the boundary tractions and velocities were less than $0.01 \mu U_0^{P_1}/d$ and $0.005 U_0^{P_1}$ respectively. Next we computed the solution for a longer channel with $l = 24d$ and $L = 12d$ while preserving the element length with respect to the reference configuration. We found that the pressures at the exits differed by less than 0.4% with respect to the reference configuration, and where the additional Poiseuille pressure drops at both ends due to the extra channel length has been taken into account. We found that the maximum absolute error in the velocities and the tangential component of the tractions remained less than $0.002 U_0^{P_1}$ and $0.005 \mu U_0^{P_1}/d$ respectively. The maximum absolute error in the normal component of the boundary tractions remained less than $0.05 \mu U_0^{P_1}/d$.

To provide additional confirmation on the validity of the velocity field we compared the boundary integral calculation to a finite-difference calculation for a configuration with $\alpha = \pi/2$ and various values of the flux ratio, Q . The details of the finite-difference calculation are given in Appendix D. The differences between the boundary integral and the finite-difference models' velocity fields were negligible, except for regions close to the entrance and exits. The maximum discrepancy in the velocity between the two calculations was $0.05 U_0^{P_1}$ which only occurred in the regions within a distance of d from the ends of the computational domain, probably due to end effects. Increasing the resolution reduced the error but did not remove the issue. Use of an appropriate forward or backward difference formula in areas close to the ends may remove or ameliorate this error. At the ends, we found that the velocity obtained by the boundary integral method was in much better agreement with the unidirectional Poiseuille velocity than the velocity calculated by the finite-difference method. Therefore we found that the boundary integral method provides a more accurate method of calculating the velocity field throughout the entire flow domain.

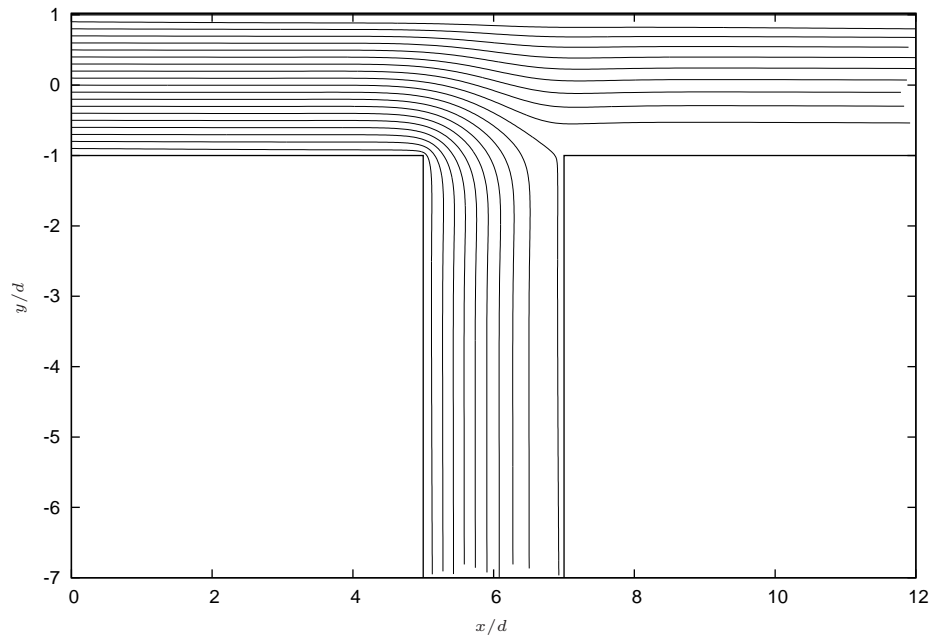
5.4 Results for a fluid-filled branching channel

In our first set of results we set $Q = 0.5$, $\delta = 1$ and $\alpha = \pi/2$. In figure 5.2 we show the streamlines, wall tractions and centreline velocity profiles for the branching channel. The streamlines for the flow are shown in figure 5.2 (a). Occasionally the streamlines computed using the numerical integration scheme terminate before the exit due to the

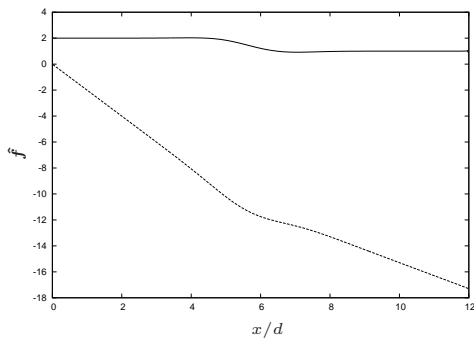
adaptive stepping method employed to calculate the streamline. When the next point lies outside the flow domain the streamline figure shows the last calculated point which lies within the flow domain. The streamline which starts from $(0, 0)$ is the dividing streamline when $Q = 0.5$, i.e. the streamlines which start below this point on \mathcal{E}_1 will travel into the branch channel and those which start above the point will remain in the main channel. In the finite-difference calculation the dividing streamline corresponds to $\psi = 0.5$, where ψ is the stream-function, and it terminated on the right-hand corner of the branch entrance. As we can see from figure 5.2 (a), the dividing streamline does indeed split the flow, however due to a slight inaccuracy in the calculation the streamline does not terminate on the corner. Doubling the number of boundary elements causes the streamline started from $(0, 0)$ to move $0.03d$ closer to the right-hand wall of the branch channel whereas the remaining streamlines trace the same paths to within $0.007d$. We found that a streamline started from $(0, 0.0034)d$ does indeed terminate on the right-hand corner.

At \mathcal{E}_2 and \mathcal{E}_3 the pressures are $-17.294 \mu U_0^{P_1}/d$ and $-18.227 \mu U_0^{P_1}/d$ respectively. Figure 5.2 (b) shows the total traction on the top wall of the main channel. Equations (5.126) and (5.127) show that the total dimensionless traction at $x/d = 0$ should be $(2, 0)$ and equal to $(1, -17.294)$ at \mathcal{E}_2 , which are in good agreement with the curves in the figure. We found that the value of the wall traction on the two or three boundary elements adjacent to the end suffered from a numerical sensitivity. For example, on the wall at \mathcal{E}_1 the error in the x -component was 0.8% and the absolute error in the y -component was $0.009 \mu U_0^{P_1}/d$. On the next boundary element away from \mathcal{E}_1 the error was halved. We also found that when the number of boundary elements was increased, the error reduced and the disturbance pressures changed very slightly. For example, doubling the number of boundary elements changed the disturbance pressures by less than 0.06% . The region in which the traction adjusts to its upstream or downstream profile is short compared to the length of the channel, showing that the disturbance caused by the branch entrance decays rapidly as we move away from it. In figure 5.2 (c) we plot the disturbance traction \mathbf{f}^{P_3} on the right-hand wall of the branch channel, where $x = l/2 + D$. We expect the x and y components of \mathbf{f}^{D_3} to tend to π_3 and zero respectively as we move towards \mathcal{E}_3 at $y/d = -7$. Both components of \mathbf{f}^{D_3} decay rapidly to their expected values as we move away from the branch entrance at $y/d = -1$ and move towards \mathcal{E}_3 . The values of π_2 and π_3 differed from the values obtained from equations (5.47) and (5.58) by 0.03% , and the check on the y -component found an absolute error of less than $0.001 \mu U_0^{P_1}/d$.

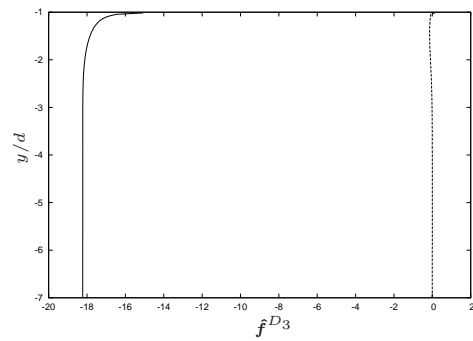
Figures 5.2 (d) and 5.2 (e) show the centreline velocities in the main and the branch channels. In the main channel we can see that as we move away from the branch entrance and approach \mathcal{E}_1 the disturbance to the velocity decays rapidly. The velocity tends to $U_0^{P_1} \mathbf{i}$ as we approach \mathcal{E}_1 and $0.5 U_0^{P_1} \mathbf{i}$ as we approach \mathcal{E}_2 . In figure 5.2 (e) we show the velocity along the centreline of the branch channel and up to the top wall of the main channel. Again we can see that as we move away from the branch entrance the velocity decays rapidly to $-0.5 U_0^{P_1} \mathbf{j}$, or equivalently $0.5 U_0^{P_1} \mathbf{i}'$. At the ends, the error in the velocity on the channel centreline was 0.10% at \mathcal{E}_1 , 0.07% at \mathcal{E}_2 and 0.23% at \mathcal{E}_3 . When we doubled the number of elements we halved the velocity error. In the regions at the channel ends



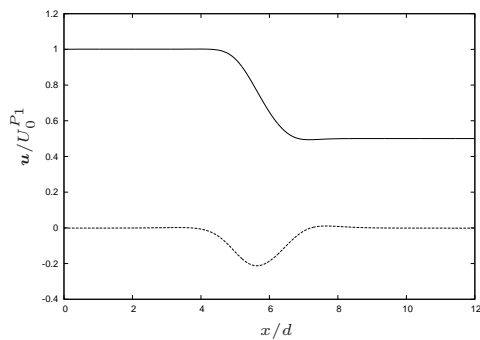
(a) Streamlines for an empty branching channel with $\delta = 1$, $\alpha = \pi/2$ and $Q = 0.5$.



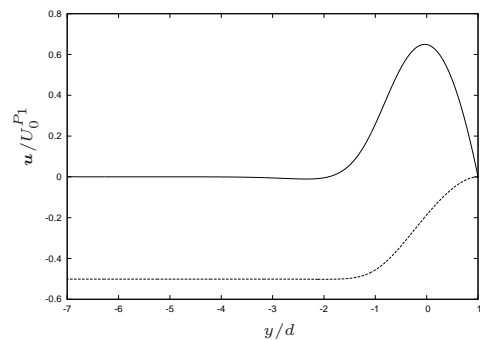
(b) x (—) and y (---) components of the traction on the top wall of the main channel.



(c) x (—) and y (---) components of the disturbance traction on the right-hand wall of the branch channel.



(d) x (—) and y (---) components of the velocity along the centreline of the main channel.



(e) x (—) and y (---) components of the velocity along the centreline of the branch channel.

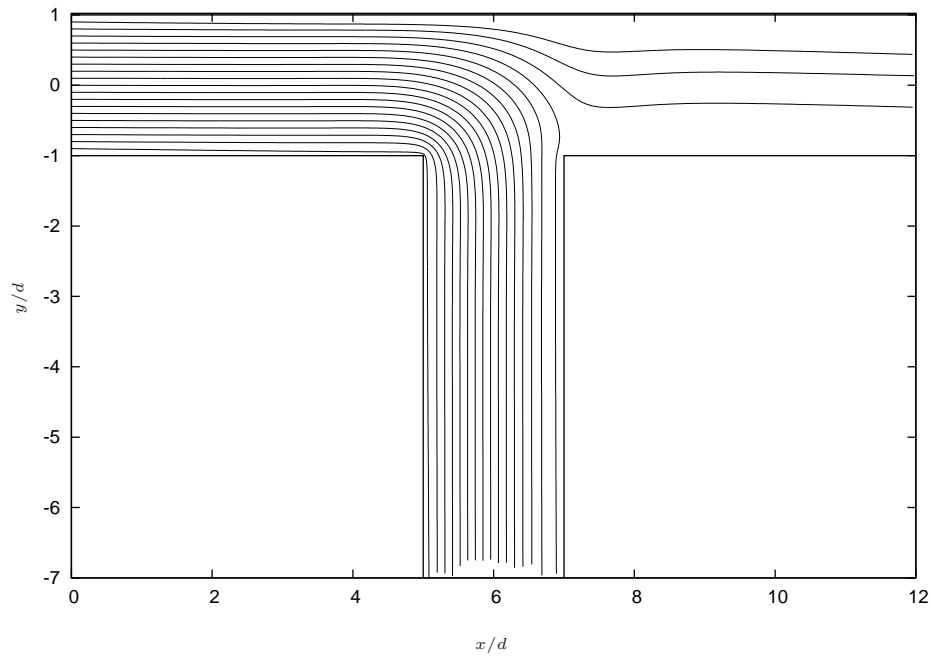
Figure 5.2 : Streamlines, wall tractions and centreline velocities for a branching channel with $\delta = 1$, $\alpha = \pi/2$ and $Q = 0.5$.

which are very close to the channel walls the error increases, but the magnitude of the velocity is small compared to that on the centreline and therefore has little effect upon the flow.

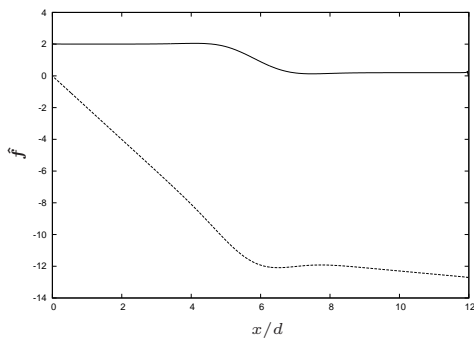
In the next set of results we keep $\delta = 1$ and $\alpha = \pi/2$ and reduce Q to 0.1 thereby decreasing the amount of fluid which travels to \mathcal{E}_2 with a concomitant increase in the amount of fluid travelling to \mathcal{E}_3 . We plot the streamlines in figure 5.3 (a) where we can see the majority of the streamlines entering the branch channel. The pressures at \mathcal{E}_2 and \mathcal{E}_3 are $-12.697 \mu U_0^{P_1}/d$ and $-23.592 \mu U_0^{P_1}/d$ respectively. The change in flux has increased the pressure at the end to which the majority of the fluid travels, when compared with the previous simulation. Figure 5.3 (b) shows the total traction on the top wall of the main channel. Equations (5.126) and (5.127) show that $\hat{\mathbf{f}}$ at $x/d = 0$ should be $(2, 0)$ and equal to $(0.2, -12.6969)$ at \mathcal{E}_2 , which are in good agreement with the curves in the figure. The error in the traction is similar to the previous simulation. Once again the region in which the traction adjusts to its downstream and upstream values is short compared with the channel length. The change in the x -component occurs between $x/d = 4$ and 8, and the change in the y -component occurs between $x/d = 4$ and 8.5. In figure 5.3 (c) we plot the disturbance traction \mathbf{f}^{P_3} on the right-hand wall of the branch channel. We expect the x and y components of \mathbf{f}^{D_3} to tend to π_3 and zero respectively as we move towards \mathcal{E}_3 . Both components of \mathbf{f}^{D_3} decay rapidly to their expected values as we move away from the branch entrance at $y/d = -1$ and move towards \mathcal{E}_3 . The values of π_2 and π_3 differed from the values obtained from equations (5.47) and (5.58) by 0.03% and 0.04% respectively, and the check on the y -component found an absolute error of less than $0.001 \mu U_0^{P_1}/d$.

Figures 5.3 (d) and 5.3 (e) show the centreline velocities in the main and the branch channels. In the main channel we can see that the disturbance to the velocity occurs between $x/d = 4$ and 8, and as we move away from this region the disturbance to the velocity decays rapidly. The velocity tends to $U_0^{P_1} \mathbf{i}$ as we approach \mathcal{E}_1 and $0.1 U_0^{P_1} \mathbf{i}$ as we approach \mathcal{E}_2 . In figure 5.3 (e) we show the velocity along the centreline of the branch channel and up to the top wall of the main channel. Again we can see that as we move away from the branch entrance the velocity decays rapidly to $-0.9 U_0^{P_1} \mathbf{j}$. The error in the centreline velocity was 0.17% at \mathcal{E}_1 , 0.43% at \mathcal{E}_2 and 0.22% at \mathcal{E}_3 .

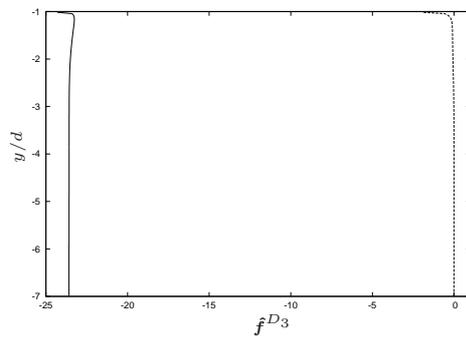
In the next set of results we set $Q = 0.9$ so that 90% of the fluid travels to \mathcal{E}_2 . We maintain the values of $\delta = 1$ and $\alpha = \pi/2$. The flow streamlines are plotted in figure 5.4 (a) where we can see the majority of the streamlines travelling the exit of the main channel. It is interesting to see that one streamline travels into the branch channel close to the right-hand corner before re-entering the main channel and travelling to \mathcal{E}_2 . The pressures at \mathcal{E}_2 and \mathcal{E}_3 are $-21.891 \mu U_0^{P_1}/d$ and $-12.862 \mu U_0^{P_1}/d$ respectively. Once more we see that the change in Q results in a higher pressure at the end receiving the majority of the fluid. Figure 5.4 (b) shows the total traction on the top wall of the main channel. Equations (5.126) and (5.127) show that $\hat{\mathbf{f}}$ at $x/d = 0$ should be $(2, 0)$ and equal to $(1.8, -21.8909)$ at \mathcal{E}_2 , which agrees with the figure. The error in the traction is again similar to the previous simulation. The change in the x -component of \mathbf{f} occurs between



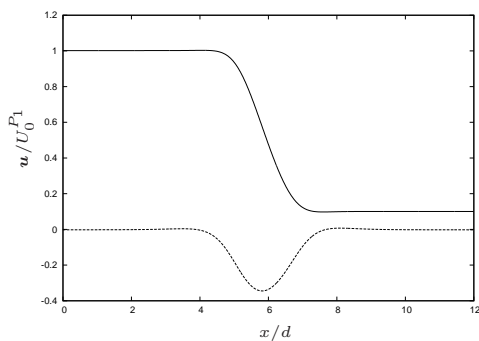
(a) Streamlines for an empty branching channel with $\delta = 1$, $\alpha = \pi/2$ and $Q = 0.1$.



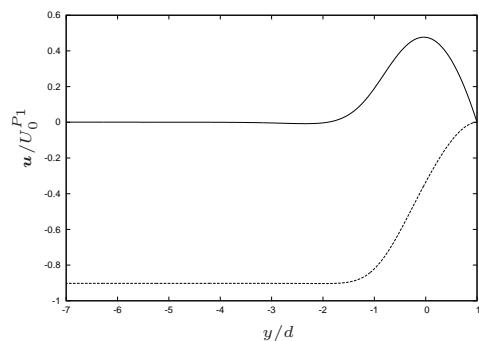
(b) x (—) and y (---) components of the traction on the top wall of the main channel.



(c) x (—) and y (---) components of the disturbance traction on the right-hand wall of the branch channel.

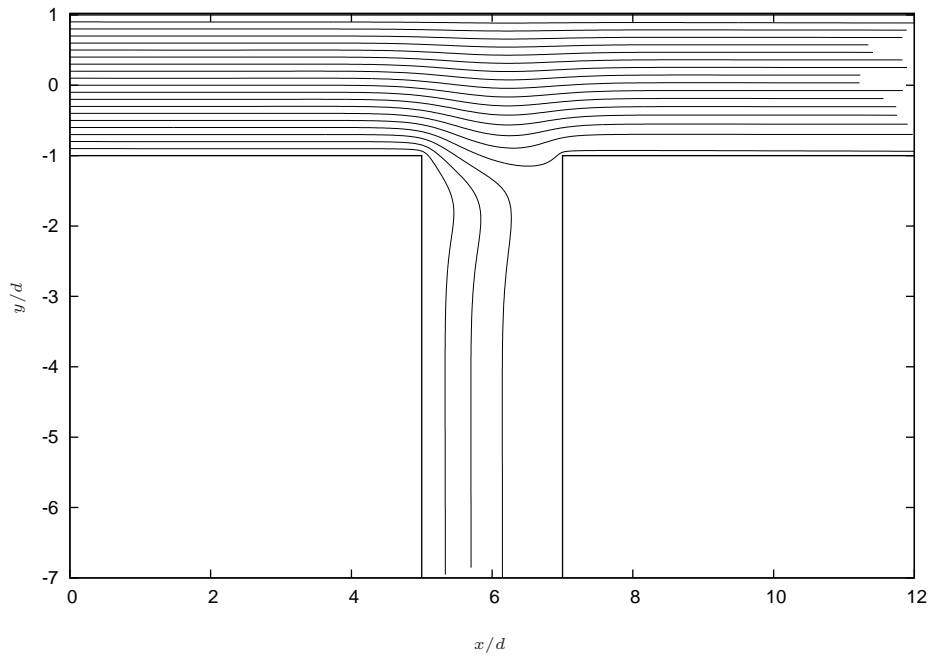


(d) x (—) and y (---) components of the velocity along the centreline of the main channel.

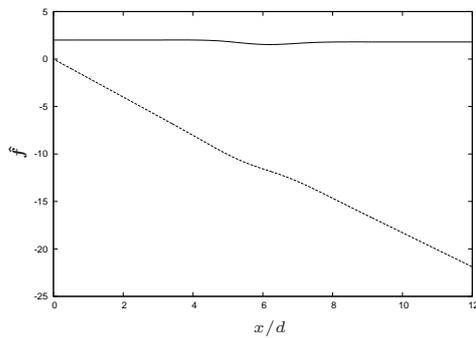


(e) x (—) and y (---) components of the velocity along the centreline of the branch channel.

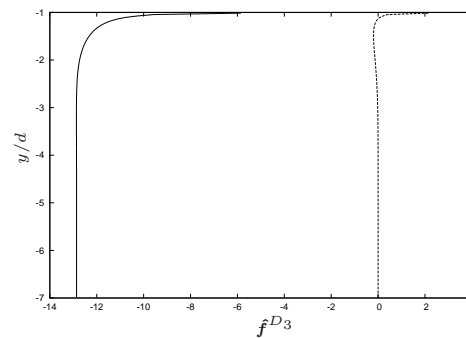
Figure 5.3 : Streamlines, wall tractions and centreline velocities for a branching channel with $\delta = 1$, $\alpha = \pi/2$ and $Q = 0.1$.



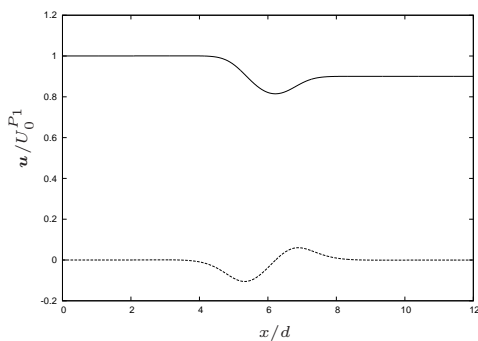
(a) Streamlines for an empty branching channel with $\delta = 1$, $\alpha = \pi/2$ and $Q = 0.9$.



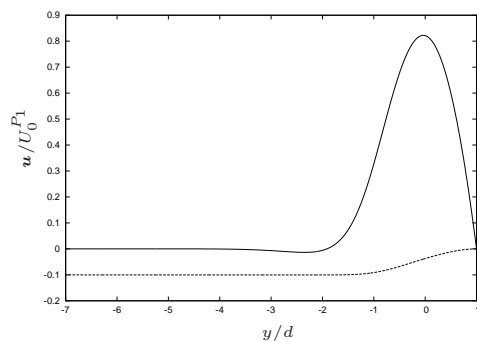
(b) x (–) and y (---) components of the traction on the top wall of the main channel.



(c) x (–) and y (---) components of the disturbance traction on the right-hand wall of the branch channel.



(d) x (–) and y (---) components of the velocity along the centreline of the main channel.



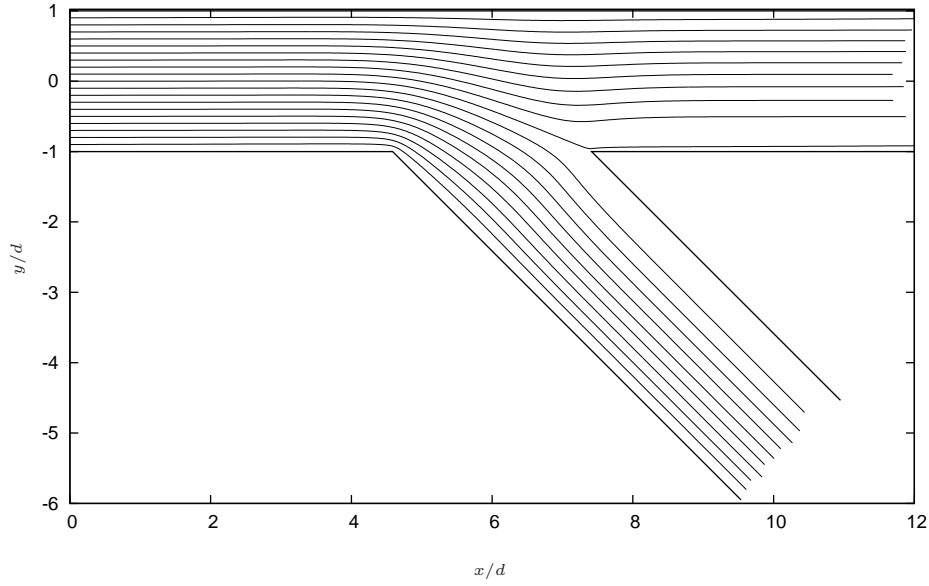
(e) x (–) and y (---) components of the velocity along the centreline of the branch channel.

Figure 5.4 : Streamlines, wall tractions and centreline velocities for a branching channel with $\delta = 1$, $\alpha = \pi/2$ and $Q = 0.9$.

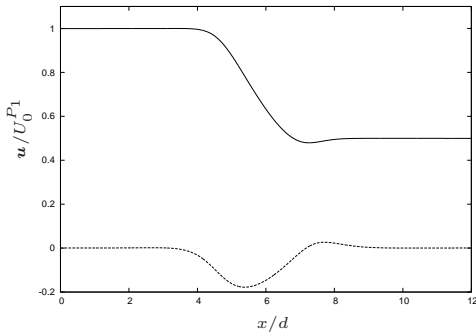
$x/d = 4$ and 8 , and the change in the y -component occurs between $x/d = 3$ and 9 . In figure 5.4 (c) we plot the disturbance traction \mathbf{f}^{D_3} on the right-hand wall of the branch channel. We expect the x and y components of \mathbf{f}^{D_3} to tend to π_3 and zero respectively as we move towards \mathcal{E}_3 . Both components of \mathbf{f}^{D_3} decay rapidly to their expected values as we move away from the branch entrance at $y/d = -1$ and move towards \mathcal{E}_3 . The values of π_2 and π_3 differed from the values obtained from equations (5.47) and (5.58) by 0.13% and 0.01% respectively, and the check on the y -component found an absolute error of less than $0.002 \mu U_0^{P_1}/d$. Figures 5.4 (d) and 5.4 (e) show the centreline velocities in the main and the branch channels. In the main channel we can see that the disturbance to the velocity again occurs between $x/d = 4$ and 8 , and the disturbance to the velocity decays rapidly as we move away from this region. The velocity tends to $U_0^{P_1} \mathbf{i}$ as we approach \mathcal{E}_1 and $0.9 U_0^{P_1} \mathbf{i}$ as we approach \mathcal{E}_2 . In figure 5.4 (e) we show the velocity along the centreline of the branch channel and up to the top wall of the main channel. We can see that as we move away from the branch entrance the velocity decays rapidly to $-0.1 U_0^{P_1} \mathbf{j}$. The error in the centreline velocity was 0.04% at \mathcal{E}_1 , 0.03% at \mathcal{E}_2 and 0.23% at \mathcal{E}_3 .

Now we set the flux ratio equal to 0.5 but change the branch angle so that $\alpha = \pi/4$ and maintain $\delta = 1$. The flow streamlines are plotted in figure 5.5 (a). When $\alpha = \pi/2$ the dividing streamline started from $(0, 0)$. Now that the branch angle has changed to $\pi/4$ we do not know whether the dividing streamline will terminate on the right-hand corner of the branch entrance. We can see from the figure that the streamline started from $(0, 0)$ terminates at \mathcal{E}_2 . In the next section we will explore more fully the dependence between the branch angle and the location at which the dividing streamline terminates. The pressures at \mathcal{E}_2 and \mathcal{E}_3 are $-16.474 \mu U_0^{P_1}/d$ and $-16.921 \mu U_0^{P_1}/d$ respectively, which represent a 4.7% and a 7.1% reduction compared to the same case with $\alpha = \pi/2$. Figures 5.5 (b) and 5.5 (c) show the centreline velocities in the main and the branch channels. In the main channel we can see that the disturbance to the velocity occurs between $x/d = 3$ and 9 , and the disturbance to the velocity decays rapidly as we move away from this region. The velocity tends to $U_0^{P_1} \mathbf{i}$ as we approach \mathcal{E}_1 and $0.5 U_0^{P_1} \mathbf{i}$ as we approach \mathcal{E}_2 . In figure 5.5 (c) we show the (X, Y) components of the velocity along the centreline of the branch channel and up to the top wall of the main channel. The velocity tends to the Poiseuille velocity $0.5 U_0^{P_1} \mathbf{i}'$ as we get close to \mathcal{E}_3 . The error in the centreline velocity was 0.06% at \mathcal{E}_1 , 0.09% at \mathcal{E}_2 and 0.10% at \mathcal{E}_3 .

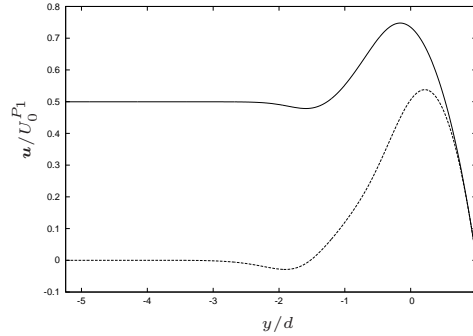
Now we decrease Q thus sending more fluid to \mathcal{E}_3 . The simulation parameters are $\delta = 1$, $\alpha = \pi/4$ and $Q = 0.1$. The flow streamlines are plotted in figure 5.6 (a) where we can see the majority entering the branch channel, as expected. The pressures at \mathcal{E}_2 and \mathcal{E}_3 are $-11.951 \mu U_0^{P_1}/d$ and $-21.830 \mu U_0^{P_1}/d$ respectively, where the pressure has increased at the end which receives the most fluid. Figures 5.6 (b) and 5.6 (c) show the centreline velocities in the main and the branch channels. In the main channel we can see that the disturbance to the velocity occurs between $x/d = 3$ and 9 , and the disturbance to the velocity decays rapidly as we move away from this region. The velocity tends to $U_0^{P_1} \mathbf{i}$ as we approach \mathcal{E}_1 and $0.1 U_0^{P_1} \mathbf{i}$ as we approach \mathcal{E}_2 . In figure 5.6 (c) we show the (X, Y) components of the velocity along the centreline of the branch channel and up to



(a) Streamlines for an empty branching channel with $\delta = 1$, $\alpha = \pi/4$ and $Q = 0.5$.



(b) x (—) and y (---) components of the velocity along the centreline of the main channel.

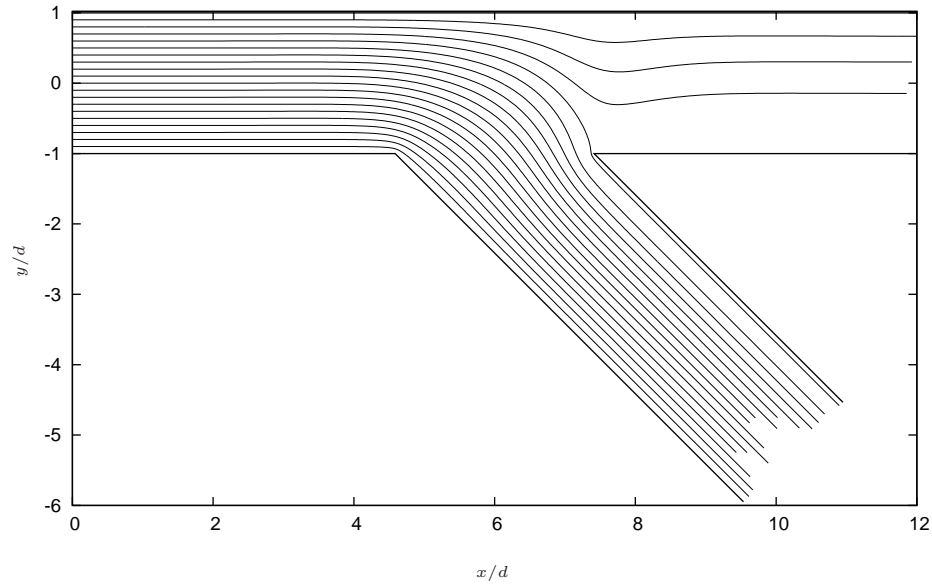


(c) X (---) and Y (—) components of the velocity along the centreline of the branch channel.

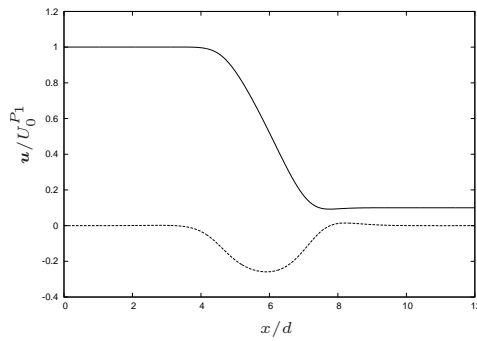
Figure 5.5 : Streamlines, wall tractions and centreline velocities for a branching channel with $\delta = 1$, $\alpha = \pi/4$ and $Q = 0.5$.

the top wall of the main channel. The velocity tends to the Poiseuille velocity $0.9 U_0^{P_1} \mathbf{i}'$ as we get close to \mathcal{E}_3 , where the disturbance effect of the branch entrance has disappeared by $y/d = -3$. The error in the centreline velocity was 0.05% at \mathcal{E}_1 , 0.08% at \mathcal{E}_2 and 0.04% at \mathcal{E}_3 .

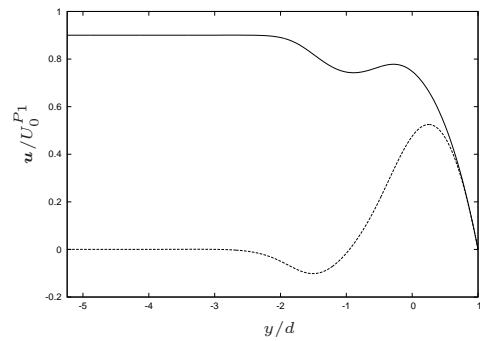
Now we increase Q thus sending more fluid to \mathcal{E}_2 . The simulation parameters are $\delta = 1$, $\alpha = \pi/4$ and $Q = 0.9$. The flow streamlines are plotted in figure 5.7 (a) where we can see the majority travelling to \mathcal{E}_2 , as expected. The pressures at \mathcal{E}_2 and \mathcal{E}_3 are $-20.997 \mu U_0^{P_1} / d$ and $-12.012 \mu U_0^{P_1} / d$ respectively, where the pressure has increased at the end which receives the most fluid, relative to the simulation with $\delta = 1$, $\alpha = \pi/4$ and $Q = 0.5$. Figures 5.7 (b) and 5.7 (c) show the centreline velocities in the main and the branch channels. In the main channel we can see that the disturbance to the velocity occurs between $x/d = 3$ and 9, and the disturbance to the velocity decays rapidly as we move away from this region. The velocity tends to $U_0^{P_1} \mathbf{i}$ as we approach \mathcal{E}_1 and $0.9 U_0^{P_1} \mathbf{i}$ as we



(a) Streamlines for an empty branching channel with $\delta = 1$, $\alpha = \pi/4$ and $Q = 0.1$.



(b) x (—) and y (---) components of the velocity along the centreline of the main channel.

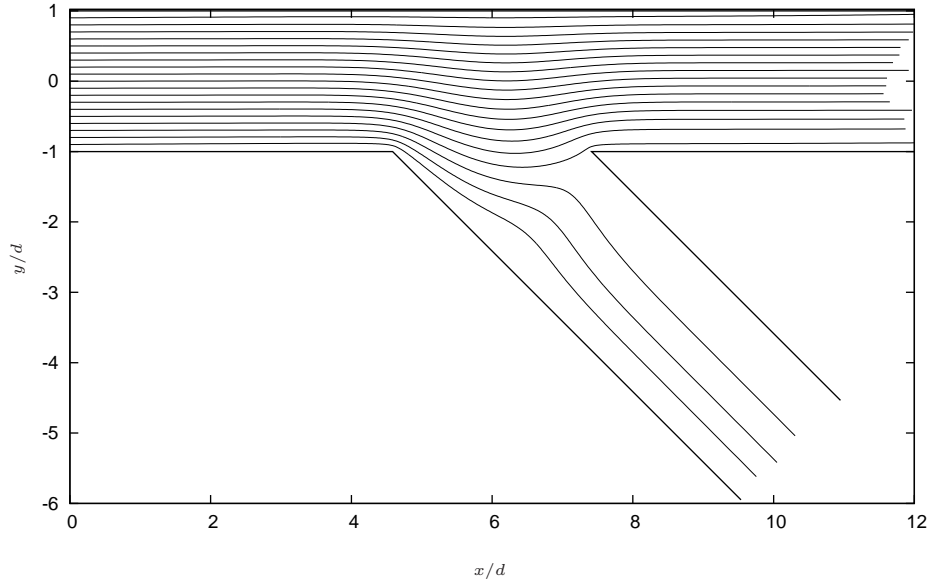


(c) X (---) and Y (—) components of the velocity along the centreline of the branch channel.

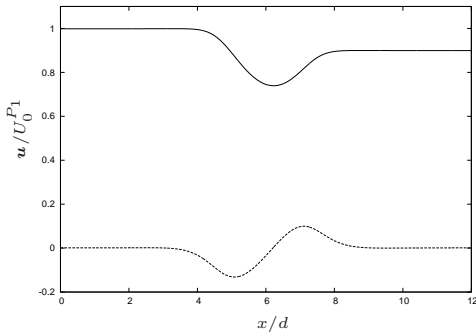
Figure 5.6 : Streamlines, wall tractions and centreline velocities for a branching channel with $\delta = 1$, $\alpha = \pi/4$ and $Q = 0.1$.

approach \mathcal{E}_2 . In figure 5.7 (c) we show the (X, Y) components of the velocity along the centreline of the branch channel and up to the top wall of the main channel. The velocity tends to the Poiseuille velocity $0.1 U_0^{P1} \hat{i}'$ as we get close to \mathcal{E}_3 , where the disturbance effect of the branch entrance has disappeared by $y/d = -3$. The error in the centreline velocity was 0.17% at \mathcal{E}_1 , 0.11% at \mathcal{E}_2 and 1.27% at \mathcal{E}_3 . We found that the error was consistently the highest at the end receiving the least fluid, i.e. when Q was high and \mathcal{E}_3 receives the least fluid the error will be the highest there. This factor is partly due to the lowering of the exit Poiseuille velocity on which the error value is based.

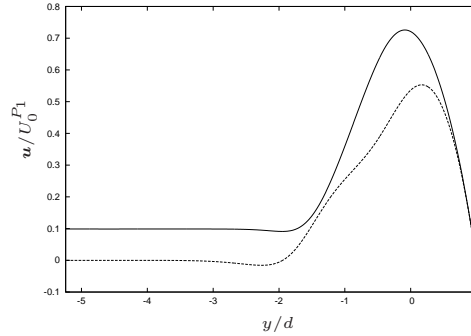
Now we set $Q = 0.5$, $\delta = 1$ and change the branch angle to $3\pi/4$. The flow streamlines are plotted in figure 5.8 (a). The pressures at \mathcal{E}_2 and \mathcal{E}_3 are $-16.752 \mu U_0^{P1}/d$ and $-17.480 \mu U_0^{P1}/d$ respectively. Figures 5.8 (b) and 5.8 (c) show the centreline velocities in the main and the branch channels. In the main channel we can see that the disturbance to the velocity occurs between $x/d = 3$ and 9, and the disturbance to the velocity decays



(a) Streamlines for an empty branching channel with $\delta = 1$, $\alpha = \pi/4$ and $Q = 0.9$.



(b) x (—) and y (---) components of the velocity along the centreline of the main channel.

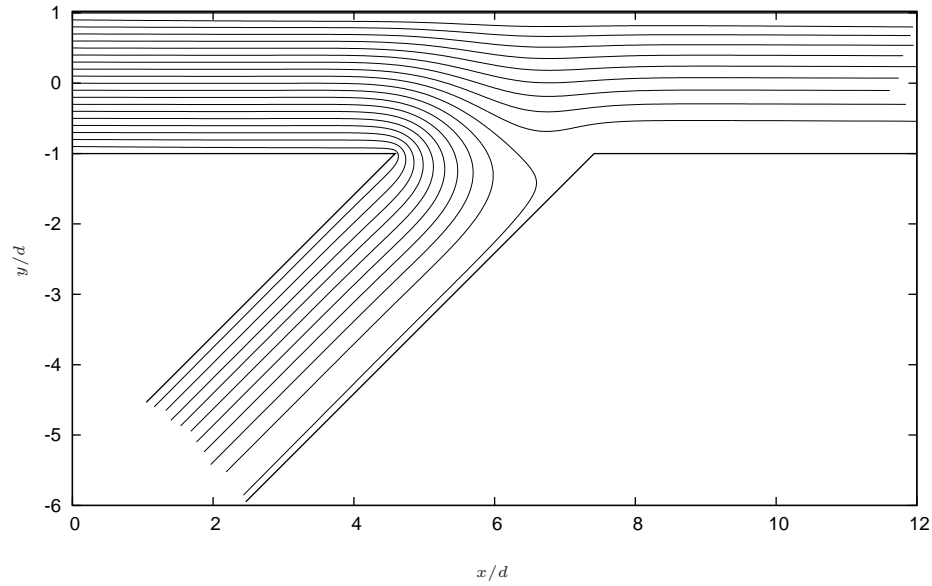


(c) X (---) and Y (—) components of the velocity along the centreline of the branch channel.

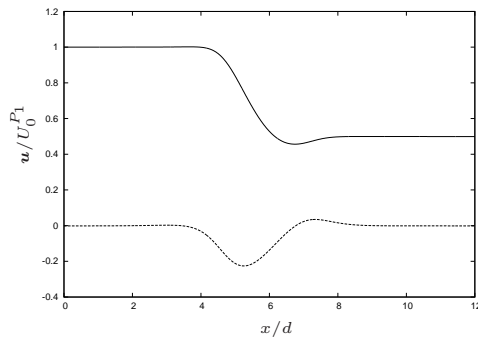
Figure 5.7 : Streamlines, wall tractions and centreline velocities for a branching channel with $\delta = 1$, $\alpha = \pi/4$ and $Q = 0.9$.

rapidly as we move away from this region. The velocity tends to $U_0^{P_1} \mathbf{i}$ as we approach \mathcal{E}_1 and $0.5 U_0^{P_1} \mathbf{i}$ as we approach \mathcal{E}_2 . In figure 5.8 (c) we show the (X, Y) components of the velocity along the centreline of the branch channel and up to the top wall of the main channel. The velocity tends to the Poiseuille velocity $0.5 U_0^{P_1} \mathbf{i}'$ as we get close to \mathcal{E}_3 , where the disturbance effect of the branch entrance has disappeared by $y/d = -3$. The error in the centreline velocity was 0.01% at \mathcal{E}_1 , 0.22% at \mathcal{E}_2 and 0.24% at \mathcal{E}_3 .

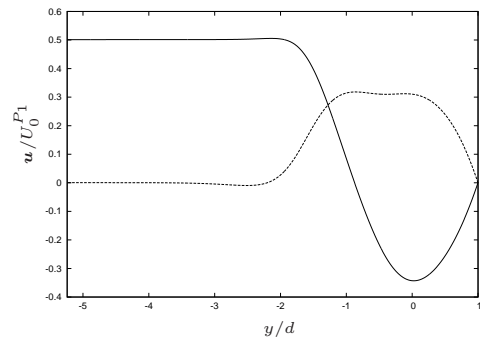
Now we decrease Q to 0.1 thus sending more fluid to \mathcal{E}_3 . The simulation parameters are $\delta = 1$, $\alpha = 3\pi/4$ and $Q = 0.1$. The flow streamlines are plotted in figure 5.9 (a) where most of the streamlines travel into the branch channel. The pressures at \mathcal{E}_2 and \mathcal{E}_3 are $-12.427 \mu U_0^{P_1} / d$ and $-22.377 \mu U_0^{P_1} / d$ respectively. Figures 5.9 (b) and 5.9 (c) show the centreline velocities in the main and the branch channels. In the main channel we can see that the disturbance to the velocity occurs between $x/d = 3$ and 8, and the disturbance to the velocity decays rapidly as we move away from this region. The velocity tends to



(a) Streamlines for an empty branching channel with $\delta = 1$, $\alpha = 3\pi/4$ and $Q = 0.5$.



(b) x (–) and y (---) components of the velocity along the centreline of the main channel.

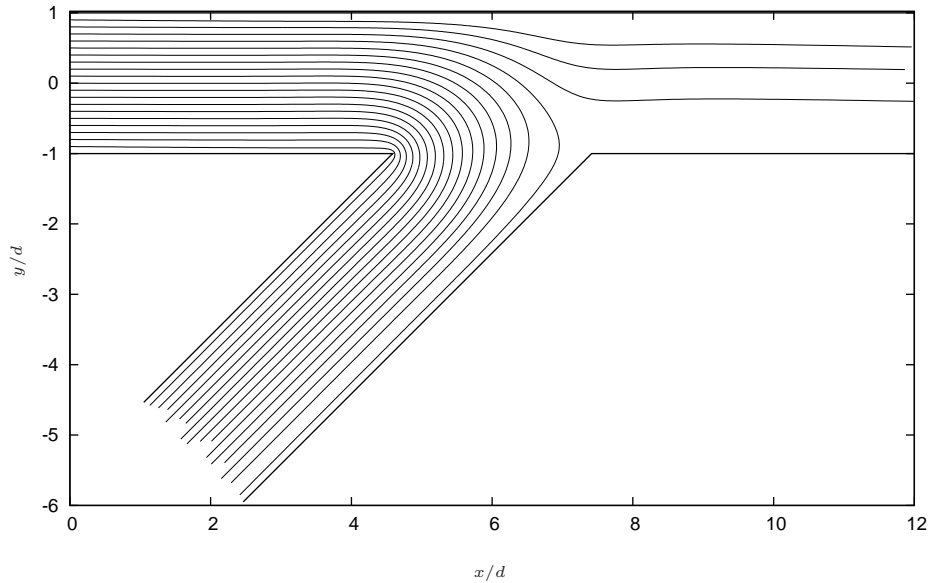


(c) X (---) and Y (–) components of the velocity along the centreline of the branch channel.

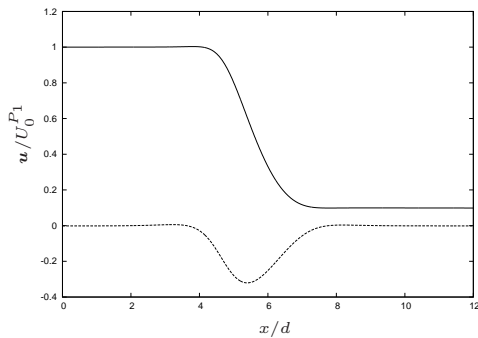
Figure 5.8 : Streamlines, wall tractions and centreline velocities for a branching channel with $\delta = 1$, $\alpha = 3\pi/4$ and $Q = 0.5$.

$U_0^{P1} \mathbf{i}$ as we approach \mathcal{E}_1 and $0.1 U_0^{P1} \mathbf{i}$ as we approach \mathcal{E}_2 . In figure 5.9 (c) we show the (X, Y) components of the velocity along the centreline of the branch channel and up to the top wall of the main channel. The velocity tends to the Poiseuille velocity $0.9 U_0^{P1} \mathbf{i}'$ as we get close to \mathcal{E}_3 , where the disturbance effect of the branch entrance has disappeared by $y/d = -3$. The error in the centreline velocity was 0.01% at \mathcal{E}_1 , 1.27% at \mathcal{E}_2 and 0.14% at \mathcal{E}_3 .

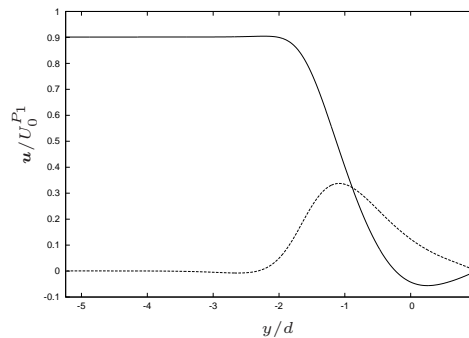
Now we increase Q to 0.9 thus sending more fluid to \mathcal{E}_2 . The simulation parameters are $\delta = 1$, $\alpha = 3\pi/4$ and $Q = 0.9$. The flow streamlines are plotted in figure 5.10 (a) where most of the streamlines travel to the exit of the main channel. The streamline which passes very close to the right-hand side of the branch entrance terminates on the wall in the main channel at $(7.6, -1)d$. The pressures at \mathcal{E}_2 and \mathcal{E}_3 are $-21.076 \mu U_0^{P1} / d$ and $-12.583 \mu U_0^{P1} / d$ respectively. Figures 5.10 (b) and 5.10 (c) show the centreline velocities in the main and the branch channels. In the main channel we can see that the



(a) Streamlines for an empty branching channel with $\delta = 1$, $\alpha = 3\pi/4$ and $Q = 0.1$.



(b) x (–) and y (---) components of the velocity along the centreline of the main channel.

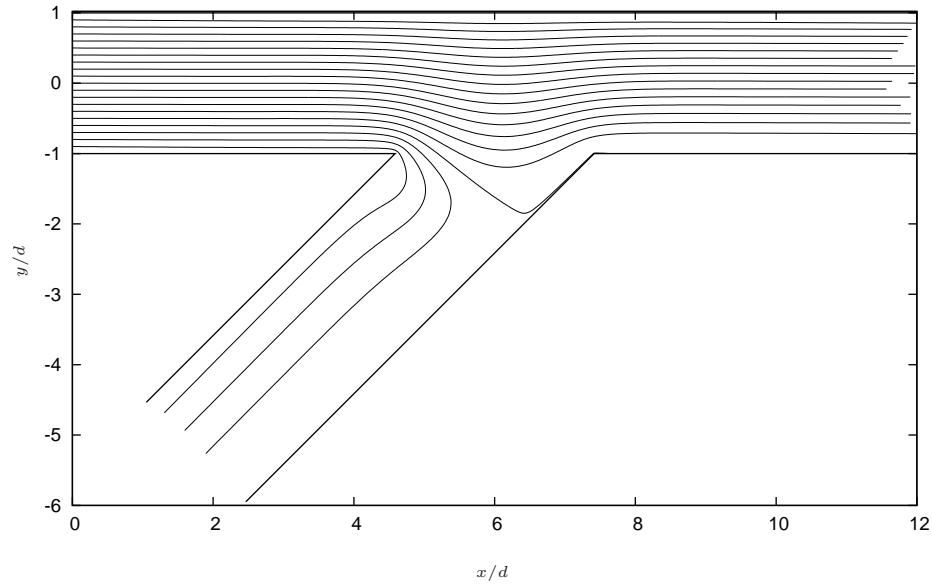


(c) X (---) and Y (–) components of the velocity along the centreline of the branch channel.

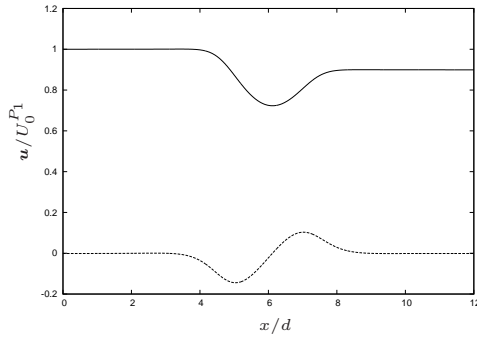
Figure 5.9 : Streamlines, wall tractions and centreline velocities for a branching channel with $\delta = 1$, $\alpha = 3\pi/4$ and $Q = 0.1$.

disturbance to the velocity occurs between $x/d = 3$ and 9 , and the disturbance to the velocity decays rapidly as we move away from this region. The velocity tends to $U_0^{P_1} \mathbf{i}$ as we approach \mathcal{E}_1 and $0.9 U_0^{P_1} \mathbf{i}$ as we approach \mathcal{E}_2 . In figure 5.6 (c) we show the (X, Y) components of the velocity along the centreline of the branch channel. The velocity tends to the Poiseuille velocity $0.1 U_0^{P_1} \mathbf{i}'$ as we get close to \mathcal{E}_3 , where the disturbance effect of the branch entrance has disappeared by $y/d = -3.5$. The error in the centreline velocity was 0.003% at \mathcal{E}_1 , 0.11% at \mathcal{E}_2 and 1.12% at \mathcal{E}_3 .

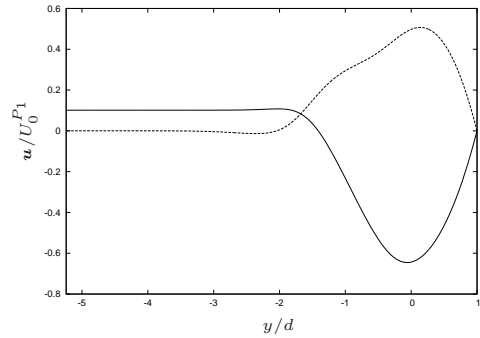
In the next set of results we set $\alpha = \pi/2$, $Q = 0.5$ and reduce the width of the branch such that $\delta = 0.5$. The streamlines for the flow are shown in figure 5.11 (a). At \mathcal{E}_2 and \mathcal{E}_3 the pressures are $-17.822 \mu U_0^{P_1} / d$ and $-63.000 \mu U_0^{P_1} / d$ respectively, where the difference in magnitude is due to the narrowing of the branch channel. The Poiseuille pressure drop between $y/d = -1$ and $y/d = -7$ increases from $6 \mu U_0^{P_1} / d$ to $48 \mu U_0^{P_1} / d$ when D is reduced from d to $d/2$. Figures 5.11 (b) and 5.11 (c) show the centreline velocities



(a) Streamlines for an empty branching channel with $\delta = 1$, $\alpha = 3\pi/4$ and $Q = 0.9$.



(b) x (–) and y (---) components of the velocity along the centreline of the main channel.

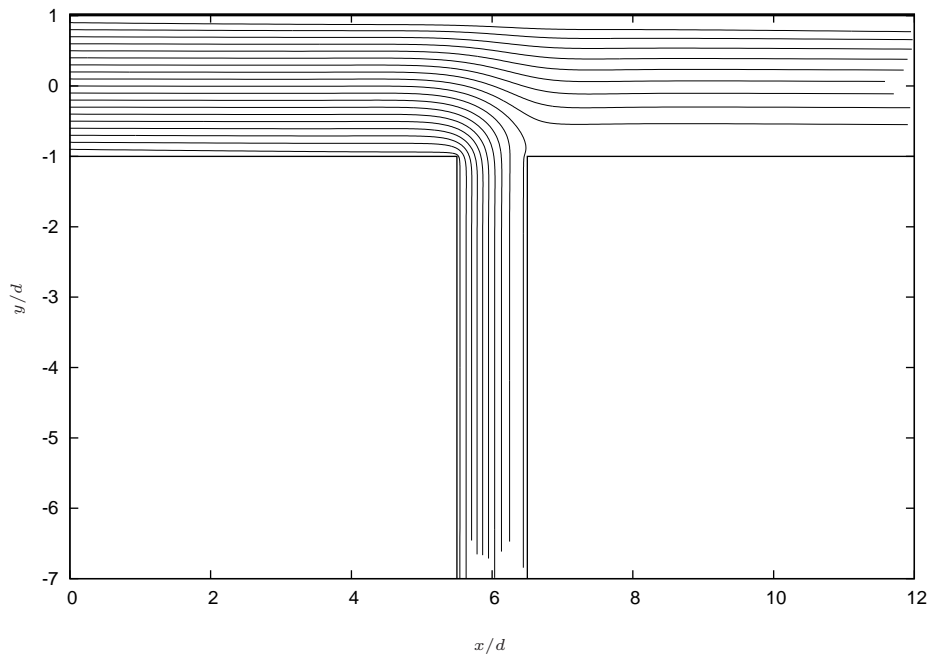


(c) X (---) and Y (–) components of the velocity along the centreline of the branch channel.

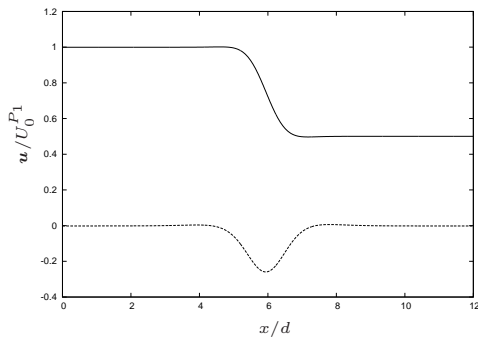
Figure 5.10 : Streamlines, wall tractions and centreline velocities for a branching channel with $\delta = 1$, $\alpha = 3\pi/4$ and $Q = 0.9$.

in the main and the branch channels. In the main channel we can see that as we move away from the branch entrance and approach \mathcal{E}_1 the disturbance to the velocity decays rapidly. The velocity tends to $U_0^{P_1} \mathbf{i}$ as we approach \mathcal{E}_1 and $0.5 U_0^{P_1} \mathbf{i}$ as we approach \mathcal{E}_2 . In figure 5.11 (c) we show the velocity along the centreline of the branch channel. We can see that as we move away from the branch entrance the velocity decays rapidly to $-\frac{1-Q}{\delta} U_0^{P_1} \mathbf{j} = -U_0^{P_1} \mathbf{j}$. At the ends, the error in the velocity on the channel centreline was 0.05% at \mathcal{E}_1 , 0.10% at \mathcal{E}_2 and 0.06% at \mathcal{E}_3 .

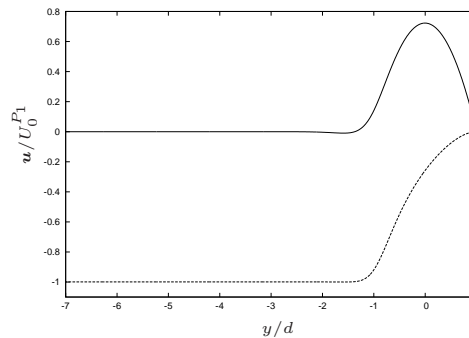
In the final set of results we set $\alpha = \pi/2$, $Q = 0.5$ and increase the width of the branch such that $\delta = 2$. The streamlines for the flow are shown in figure 5.12 (a). At \mathcal{E}_2 and \mathcal{E}_3 the pressures are $-15.201 \mu U_0^{P_1} / d$ and $-10.932 \mu U_0^{P_1} / d$ respectively. Figures 5.12 (b) and 5.12 (c) show the centreline velocities in the main channel and the branch channel. In the main channel we can see that as we move away from the branch entrance and approach \mathcal{E}_1 the disturbance to the velocity decays rapidly. The velocity tends to



(a) Streamlines for an empty branching channel with $\delta = 0.5$, $\alpha = \pi/2$ and $Q = 0.5$.



(b) x (–) and y (---) components of the velocity along the centreline of the main channel.



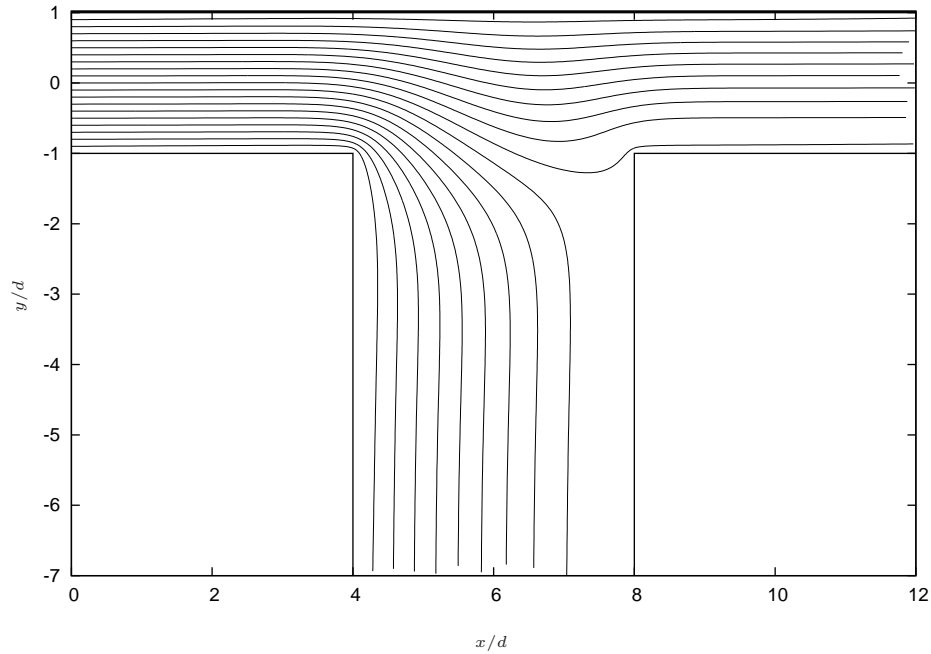
(c) x (–) and y (---) components of the velocity along the centreline of the branch channel.

Figure 5.11 : Streamlines, wall tractions and centreline velocities for a branching channel with $\delta = 0.5$, $\alpha = \pi/2$ and $Q = 0.5$.

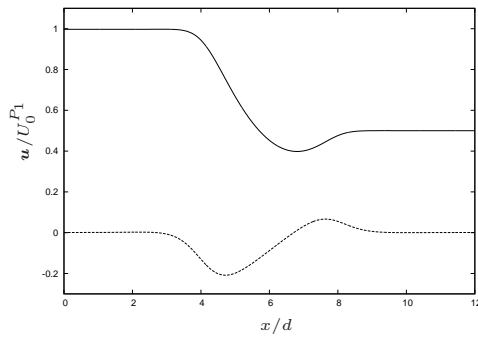
$U_0^{P1} \mathbf{i}$ as we approach \mathcal{E}_1 and $0.5 U_0^{P1} \mathbf{i}$ as we approach \mathcal{E}_2 . In figure 5.12 (c) we show the velocity along the centreline of the branch channel and up to the top wall of the main channel. We can see that as we move away from the branch entrance the velocity decays rapidly to $-\frac{1-Q}{\delta} U_0^{P1} \mathbf{j} = -0.25 U_0^{P1} \mathbf{j}$. At the ends, the error in the velocity on the channel centreline was 0.28% at \mathcal{E}_1 , 0.002% at \mathcal{E}_2 and 0.73% at \mathcal{E}_3 .

5.5 The dividing streamline

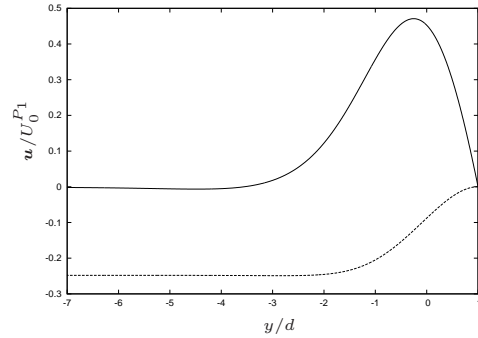
In a branching channel we use the flux ratio, Q , to define the proportion of the fluid at \mathcal{E}_1 which travels to the exit of the main channel at \mathcal{E}_2 . The remaining fluid travels to the exit of the branch channel at \mathcal{E}_3 . As we have shown, the flow streamlines may be plotted to gain insight into the direction in which the fluid travels at a particular location. In each flow there is a dividing streamline which terminates at some point on either the right-hand



(a) Streamlines for an empty branching channel with $\delta = 2$, $\alpha = \pi/2$ and $Q = 0.5$.



(b) x (–) and y (–) components of the velocity along the centreline of the main channel.



(c) x (–) and y (–) components of the velocity along the centreline of the branch channel.

Figure 5.12 : Streamlines, wall tractions and centreline velocities for a branching channel with $\delta = 2$, $\alpha = \pi/2$ and $Q = 0.5$.

wall of the branch channel, the right-hand corner of the branch entrance or at some point on the lower right-hand portion of the wall in the main channel. Let us define the starting point of the dividing streamline to be $(0, y_{DS})d$. Therefore a fluid element which starts its journey at $(0, y)d$ with $y > y_{DS}$ will remain above the dividing streamline and travel to \mathcal{E}_2 , whereas a fluid element started from $(0, y)d$ with $y < y_{DS}$ will travel to \mathcal{E}_3 . To calculate y_{DS} for a given value of the flux ratio we integrate the Poiseuille velocity at \mathcal{E}_1 from $y_{DS}d$ to d to get the following cubic polynomial,

$$y_{DS}^3 - 3y_{DS} + 2(1 - 2Q) = 0. \quad (5.128)$$

When $Q = 0.5$ we expect $y_{DS} = 0$. Substitution of $Q = 0.5$ into the cubic polynomial gives $(y_{DS}^2 - 3)y_{DS} = 0$, which has $y_{DS} = 0$ as its only root in the range $y_{DS} \in [-1, 1]$. To calculate the termination point of the dividing streamline we examine the wall shear

stress, τ , on the channel walls close to the right-hand corner of the branch entrance. On the bottom-right hand portion of wall in the main channel, the wall shear stress is given by

$$\tau = \mu \frac{\partial u}{\partial y} = \mathbf{f} \cdot \mathbf{i} = 2\mu U_0^{P1}/d + f_x^{D1}, \quad (5.129)$$

where f_x^{D1} is obtained from the solution vector to the linear system, and on the right-hand wall of the branch channel by

$$\tau = \mu \frac{\partial u}{\partial Y} = \mathbf{f} \cdot (-\mathbf{i}') = -2\mu U_0^{P3}/D + (-f_x^{D3} \cos \alpha + f_y^{D3} \sin \alpha), \quad (5.130)$$

where \mathbf{f}^{D3} is also obtained from the solution to the linear system. We take the termination point of the dividing streamline to be the location at which τ is zero, if there is such a point. When $\tau \neq 0$ on the channel walls we assume the dividing streamline terminates on the right-hand corner of the branch entrance where the stress is formally infinite, which is shown in Appendix E. Since the disturbance tractions are constant over a boundary element we find the two neighbouring elements between which τ changes sign, and use linear interpolation to obtain the coordinates of the point at which $\tau = 0$. The element length close to the corner was about $0.01 d$ for all calculations. Therefore the error bounds in the calculation of the termination point is accurate to within $\pm 0.01 d$. The termination point is therefore sensitive to the size of the boundary elements close to the right-hand corner of the branch entrance. We use s_{DS} to indicate the distance of the point where $\tau = 0$ to the right-hand corner of the branch entrance. When s_{DS} is negative the point is on the wall in the branch channel and a positive value indicates that the point is on the wall in the main channel. In figure 5.13 we plot the distance s_{DS} against the branch angle α for the three flux ratios, $Q = 0.1$, $Q = 0.5$ and $Q = 0.9$. The points at which s_{DS} was calculated are indicated by the points on the curves. When $Q = 0.1$ we can see from the figure s_{DS} is positive for acute and obtuse angles which demonstrates that the termination point of the dividing streamline is on the bottom-right wall of the main channel. When we increase α beyond 0.7π the termination point of the dividing streamline moves onto the wall of the branch channel. For $Q = 0.5$ and $Q = 0.9$ the termination point of the dividing streamline is always either at the corner or at a point on the wall in the branch channel. As the branch angle becomes more obtuse the value of s_{DS} becomes increasingly negative. Therefore the termination point of the dividing streamline moves away from the corner as the branch angle is increased and along the wall of the branch channel. The value of s_{DS} for the three values of Q and $\alpha = \pi/2$ were independently verified using a finite-difference calculation with a grid size of $\Delta x/d = \Delta y/d = 1/64$ with good agreement.

We are now in a position to interpret the dividing streamline in the streamline plots of the previous section for $\delta = 1$. In figure 5.2 (a) where $\alpha = \pi/2$ and $Q = 0.5$ the dividing streamline starts from $(0, 0)d$ and should terminate on the right-hand corner of the branch entrance. As noted earlier, we had to start the streamline at $(0, 0.0034)d$ for it to terminate on the corner, which represents an acceptable level of numerical error. In figure 5.3 (a) where $\alpha = \pi/2$ and $Q = 0.1$ the dividing streamline starts from $(0, 0.6084)d$

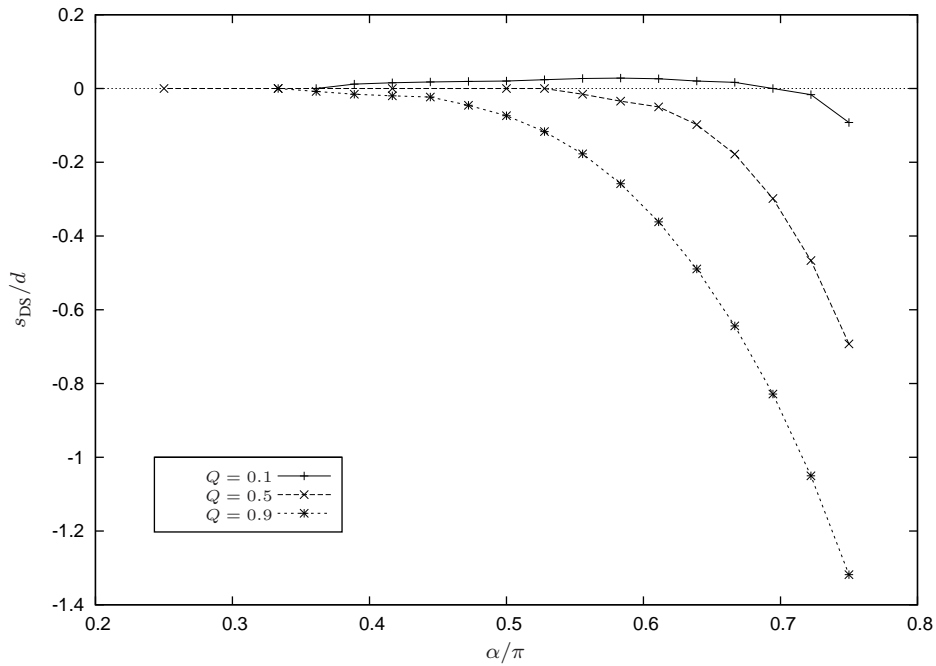


Figure 5.13 : Distance of point where $\tau = 0$ from the right-hand corner of the branch entrance.

and terminates on the main channel wall at $s_{DS} = 0.02d$. When $Q = 0.9$ the dividing streamline for figure 5.4 (a) where $\alpha = \pi/2$ and $Q = 0.9$ the dividing streamline starts from $(0, -0.6084)d$ and terminates on the branch channel wall at a distance $-0.07d$ from the corner. The dividing streamline's termination point for figures 5.5 (a)–5.10 (a) may be predicted with reference to the curves in figure 5.13.

5.6 Discussion

In this chapter we have considered a pressure-driven flow in a channel with a side branch. We prescribed the flux rates at the entrance and exits. We formulated the problem using the boundary integral method and found its solution numerically using the boundary element method. The solution provides the disturbance tractions on the channel walls and the pressure drops between the entrance and both exits.

We summarise the pressure drops for the simulations in table 5.1. The table displays the parameter values from each simulation together with the pressure drop, Δp_2 , between the entrance and \mathcal{E}_2 , and the pressure drop, Δp_3 , between the entrance and \mathcal{E}_3 . The pressure drops are defined in equations (5.32) and (5.33). The ratio of the Poiseuille pressure drop, Δp^{P_2} , to the total pressure drop in the main channel is displayed in the last column. A comparison is not made for the branch channel because the flow is not purely Poiseuille at its entrance. For reference, from equation (5.26) we have $\Delta p^{P_2} = 24 Q \mu U_0^{P_1} / d$ for a channel with $l = 12d$. The units for the pressure drops are $\mu U_0^{P_1} / d$. We can see from the table that for a fixed value of the flux ratio, Q , the pressure drop is greatest when $\alpha = \pi/2$ and the least when $\alpha = \pi/4$. The pressure drops for $\alpha \neq \pi/2$ are between 2% and 8% less than the pressure drop for $\alpha = \pi/2$. For constant α , the pressure drop is greatest between

δ	α	Q	Δp_2	Δp_3	$\Delta p^{P_2} / \Delta p_2$
1	$\pi/4$	0.1	11.951	21.830	20%
1	$\pi/2$	0.1	12.697	23.592	19%
1	$3\pi/4$	0.1	12.427	22.377	19%
1	$\pi/4$	0.5	16.474	16.921	73%
0.5	$\pi/2$	0.5	17.822	63.000	67%
1	$\pi/2$	0.5	17.294	18.227	69%
2	$\pi/2$	0.5	15.201	10.932	79%
1	$3\pi/4$	0.5	16.752	17.480	72%
1	$\pi/4$	0.9	20.997	12.012	97%
1	$\pi/2$	0.9	21.891	12.862	99%
1	$3\pi/4$	0.9	21.076	12.583	102%

Table 5.1 : Pressure drops between the entrance and exits of a branching channel for a range of branch widths, δ , branch angles, α , and flux ratios, Q .

the entrance and the exit to which the majority of the fluid flows. Specifically, the pressure drop Δp_2 decreases by 26% when the flux ratio is reduced from 0.5 to 0.1, and increases by the same percentage when it is increased from 0.5 to 0.9. Conversely, Δp_3 increases by 28% when the flux ratio is reduced from 0.5 to 0.1, and decreases by the same proportion when Q is raised from 0.5 to 0.9. Maintaining the branch angle and the flux ratio but reducing the width of the branch channel has little effect on the pressure drop between the entrance and \mathcal{E}_2 , but nearly quadruples the pressure drop between the entrance and \mathcal{E}_3 . Increasing the width of the branch channel so that it is greater than the width of the main channel causes a reduction in both pressure drops, with the decrease in Δp_3 significantly greater. The pressure ratio in the final column of the table shows that the Poiseuille pressure drop constitutes only around 20% of the total pressure drop when $Q = 0.1$ for all branch angles. The ratio increases to between 67% and 79% when $Q = 0.5$, showing that the pressure drop is dominated by the Poiseuille flow. When $Q = 0.9$ the disturbance pressure drop is a very small proportion (around 3%) of the total pressure drop. The value of 102% for $\alpha = 3\pi/4$ is due to a small negative disturbance pressure drop in the main channel, thereby lowering the pressure drop required in the main channel to maintain the flux rate at \mathcal{E}_2 . With regards to the disturbance caused by the branch entrance, we have seen from the simulations that the disturbance to the velocity decays rapidly as we move away from the branch entrance. As previously mentioned, the velocity is within 1% of its appropriate Poiseuille value at a distance of $3d$ from the branch entrance, which provides evidence that our initial assumption on the decay of the disturbance velocity is valid. However when considering a branch channel which is wider than the main channel, we should make the branch channel longer than the current truncation length, $L = l/2$, to allow for the slower decay rate of the disturbance velocity.

Finally we note that the termination point of the dividing streamline is dependent on the flux ratio, Q , and the branch angle, α . When the flux ratio is small so that most of the fluid enters the branch the dividing streamline terminates on the bottom-right hand

wall of the main channel at a point within $0.03d$ from the corner for a wide range of branch angles. When the flux ratio is increased so that the majority of fluid continues along the main channel we found that the dividing streamline terminated on the right-hand wall of the branch channel for acute and obtuse branch angles. As the branch angle becomes more obtuse the termination point moves further from the corner and into the branch channel, e.g. the dividing streamline terminates at a point a distance d from the corner when $Q = 0.1$ and $\alpha = 0.71\pi$.

Chapter 6

The motion of a rigid particle through a bifurcation

In this chapter we introduce a neutrally-buoyant rigid particle into the branching channel studied in the previous chapter. The mathematical model draws on the analysis of a rigid particle in a straight channel contained in chapter 3. The particle is free to move with the flow and we assume that the flow exerts no force or torque upon the particle. We derive the equations which govern the motion of the fluid and the particle in the main channel and in the branch, and we calculate the disturbance caused by the branch using the boundary integral method. The governing equations describe the velocity field throughout the flow domain together with the pressures at the exits to the computational domain. Application of the boundary element method to the governing equations yields a set of discretised equations which may be written as a linear matrix system and solved by standard methods.

6.1 Problem statement

We consider the motion of a fluid with viscosity μ in an infinite straight-walled channel of width $2d$. A branch channel of width $2D$ is attached to the lower wall of the channel at an angle α . When $\alpha = \pi/2$ the branch channel is perpendicular to the main channel. A disturbance to the upstream and downstream flows is caused by the branch entrance and by the presence of a rigid particle of a fixed shape, which moves with the flow. We assume that the particle is neutrally buoyant and that the flow exerts no force or torque on the particle. The geometry is shown in figure 6.1 and comprises the walls of the main channel, \mathcal{C} , the walls of the branch channel, \mathcal{B} , the particle \mathcal{P} and a notional boundary, \mathcal{A} , which we introduce to treat the main and branch channels separately. All unit normal vectors, \boldsymbol{n} , point into the fluid. On the notional boundary the unit normal vector points into the fluid of the main channel. We assume that the disturbance caused by the particle and the branch entrance decays upstream and downstream from the source of the disturbance so that the flow far from the disturbance is described by classical unidirectional Poiseuille flow. Since we will require a channel of finite length in the numerical method, we truncate the channels so that the main channel has length l and the branch channel has length L ,

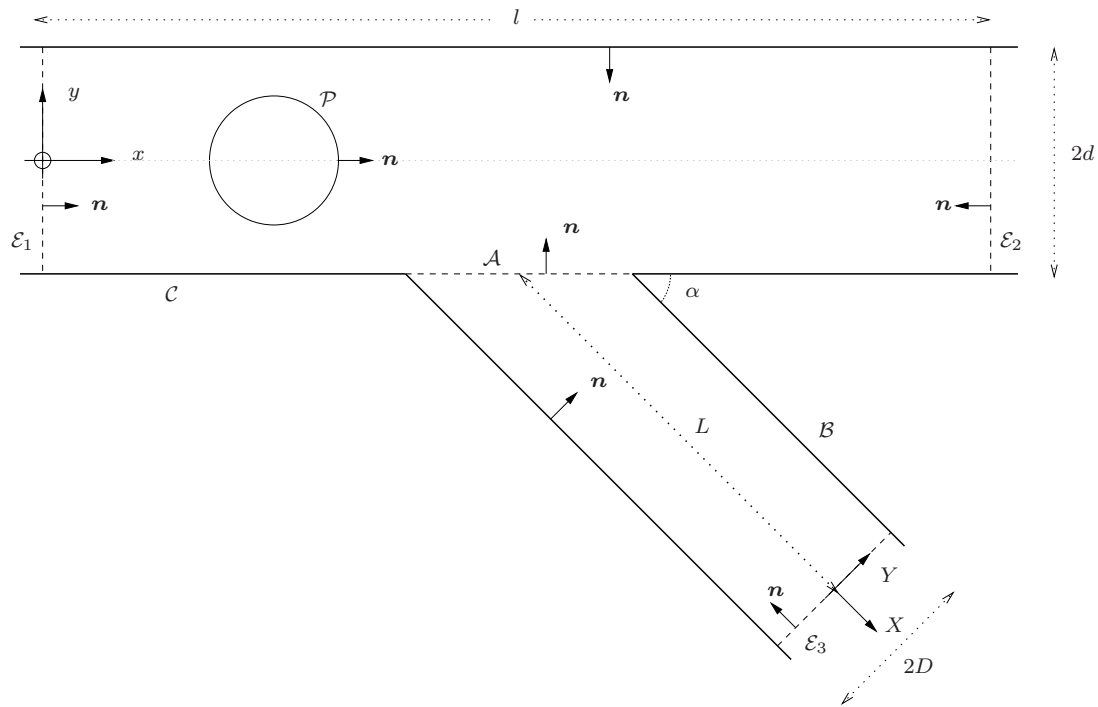


Figure 6.1 : A straight-walled channel with a branch which contains a fluid of viscosity μ .

as measured along their centrelines and illustrated in figure 6.1. We position the branch channel so that its centreline intersects the mid-point of the lower wall of the main channel, $(l/2, -d)$. We label the entrance of the main channel as \mathcal{E}_1 , the exit of the main channel as \mathcal{E}_2 and the exit of the branch channel as \mathcal{E}_3 . The entrance and exit in the main channel are located at $x = 0$ and $x = l$ respectively. In the branch channel we introduce local coordinates, (X, Y) , which have their origin on the centreline at \mathcal{E}_3 as indicated in figure 6.1. The mappings between the (x, y) coordinates of the main channel and the (X, Y) coordinates of the branch channel are given in equation (5.1) of the previous chapter. The unit vectors in the main channel are i and j , which are mapped to their branch channel equivalents i' and j' using equation (5.3). The particle and the branch entrance disturb the flow but at \mathcal{E}_1 , \mathcal{E}_2 and \mathcal{E}_3 we assume that the disturbance has decayed and the flow has settled to Poiseuille flow, characterised by the streamwise flux rate at the pertinent entrance or exit. As in the previous chapter we label the flux rate at each of \mathcal{E}_1 , \mathcal{E}_2 and \mathcal{E}_3 as Q_1 , Q_2 and Q_3 respectively. The equations for the fluxes and the Poiseuille velocities are given in equations (5.4)–(5.11) of the previous chapter.

Our aim is to compute the velocity field throughout the flow domain and the additional pressure drop at both exits due to disturbance caused by the branch entrance and the particle. We assume that the Reynolds number of the flow is very small so that the flow in the channels may be described using the linear equations of Stokes flow given in equation (1.3.4). We decompose the velocity field, \mathbf{u} , the stress field, $\boldsymbol{\sigma}$, and the traction field, \mathbf{f} , into background Poiseuille and disturbance components, which we identify using the

superscripts P and D respectively. The decompositions in the main channel are given by,

$$\mathbf{u} = \mathbf{u}^{P_1} + \mathbf{u}^{D_1} = \mathbf{u}^{P_2} + \mathbf{u}^{D_2}, \quad (6.1)$$

$$\boldsymbol{\sigma} = \boldsymbol{\sigma}^{P_1} + \boldsymbol{\sigma}^{D_1} = \boldsymbol{\sigma}^{P_2} + \boldsymbol{\sigma}^{D_2}, \quad (6.2)$$

$$\mathbf{f} = \mathbf{f}^{P_1} + \mathbf{f}^{D_1} = \mathbf{f}^{P_2} + \mathbf{f}^{D_2}, \quad (6.3)$$

where the quantities with the P_1 and D_1 superscripts are defined with reference to \mathcal{E}_1 , and the quantities with the P_2 and D_2 superscripts are defined with reference to \mathcal{E}_2 . The velocity, stress and traction decompositions in the branch channel are

$$\mathbf{u} = \mathbf{u}^{P_3} + \mathbf{u}^{D_3}, \quad (6.4)$$

$$\boldsymbol{\sigma} = \boldsymbol{\sigma}^{P_3} + \boldsymbol{\sigma}^{D_3}, \quad (6.5)$$

$$\mathbf{f} = \mathbf{f}^{P_3} + \mathbf{f}^{D_3}, \quad (6.6)$$

which are all defined with reference to \mathcal{E}_3 . On the notional boundary, \mathcal{A} , which separates the channels we impose continuity of the velocity, stress and traction fields such that

$$\mathbf{u} = \mathbf{u}^{P_1} + \mathbf{u}^{D_1} = \mathbf{u}^{P_2} + \mathbf{u}^{D_2} = \mathbf{u}^{P_3} + \mathbf{u}^{D_3} \quad (6.7)$$

$$\boldsymbol{\sigma} = \boldsymbol{\sigma}^{P_1} + \boldsymbol{\sigma}^{D_1} = \boldsymbol{\sigma}^{P_2} + \boldsymbol{\sigma}^{D_2} = \boldsymbol{\sigma}^{P_3} + \boldsymbol{\sigma}^{D_3}, \quad (6.8)$$

$$\mathbf{f} = \mathbf{f}^{P_1} + \mathbf{f}^{D_1} = \mathbf{f}^{P_2} + \mathbf{f}^{D_2} = \mathbf{f}^{P_3} + \mathbf{f}^{D_3}, \quad (6.9)$$

where we define all tractions with reference to a unit normal vector which points into the main channel. On the channel walls we have $\mathbf{u} = \mathbf{0}$ by no-slip and no-penetration, which implies

$$\mathbf{u}^{P_1} = \mathbf{u}^{D_1} = \mathbf{u}^{P_2} = \mathbf{u}^{D_2} = \mathbf{0} \quad (6.10)$$

on the walls of the main channel, and

$$\mathbf{u}^{P_3} = \mathbf{u}^{D_3} = \mathbf{0}, \quad (6.11)$$

on the walls of the branch channel. In the previous chapter regarding a fluid-filled branching channel we assumed and demonstrated that the disturbance velocities,

$$\mathbf{u}^{D_1} \rightarrow \mathbf{0}, \quad \mathbf{u}^{D_2} \rightarrow \mathbf{0}, \quad \mathbf{u}^{D_3} \rightarrow \mathbf{0}, \quad (6.12)$$

as we approach the ends, \mathcal{E}_1 , \mathcal{E}_2 and \mathcal{E}_3 respectively. In this chapter we have introduced a rigid particle whose effect on a straight channel flow we investigated in chapter 3. We found that the disturbance velocity due to the rigid particle in a straight channel decayed to less than 1% of its maximum value at a distance of 3 particle radii from the centroid. In light of this evidence and on previously cited works regarding flows in channels, we are justified in assuming the validity of equation (6.12). Following the same argument as

given in the derivation of equations (5.21)–(5.24), we assume

$$\mathbf{f}^{D_1} = \mathbf{0} \text{ at } \mathcal{E}_1, \quad (6.13)$$

$$\mathbf{f}^{D_2} = -\pi_2 \mathbf{n} \text{ at } \mathcal{E}_2, \quad (6.14)$$

$$\mathbf{f}^{D_3} = -\pi_3 \mathbf{n} \text{ at } \mathcal{E}_3, \quad (6.15)$$

where we have taken the disturbance pressure at \mathcal{E}_1 , \mathcal{E}_2 and \mathcal{E}_3 to be zero, π_2 and π_3 respectively. The Poiseuille pressures in the main channel are given by

$$p^{P_1}(x) = -G_1 x \quad (6.16)$$

$$p^{P_2}(x) = -G_2 x \quad (6.17)$$

where $p^{P_1}(x)$ is the Poiseuille pressure due to the entrance Poiseuille flow with pressure gradient $-G_1$, and $p^{P_2}(x)$ is the Poiseuille pressure due to the Poiseuille flow which exits the main channel which has pressure gradient, $-G_2$. The pressure gradients may be expressed in terms of the centreline velocity or the flux by,

$$G_1 = \frac{2\mu U_0^{P_1}}{d^2} = \frac{3\mu Q_1}{2d^3} \quad (6.18)$$

$$G_2 = Q G_1. \quad (6.19)$$

We have defined the Poiseuille pressures such that $p^{P_1} = p^{P_2} = 0$ at \mathcal{E}_1 . In the branch channel the Poiseuille pressure is

$$p^{P_3}(X) = -G_3 X \quad (6.20)$$

where $G_3 = 2\mu U_0^{P_3}/D^2 = 3\mu Q_3/2D^3$, and $-G_3$ is the pressure gradient which when applied to the branch channel results in the flux at \mathcal{E}_3 equalling Q_3 . We may now write the pressure difference between the entrance and the exit of the main channel, Δp_2 , as

$$\begin{aligned} \Delta p_2 &= p(\mathcal{E}_1) - p(\mathcal{E}_2) \\ &= (p^{P_1}(\mathcal{E}_1) + p^{D_1}(\mathcal{E}_1)) - (p^{P_2}(\mathcal{E}_2) + p^{D_2}(\mathcal{E}_2)) \\ &= G_2 l - \pi_2 \end{aligned} \quad (6.21)$$

by equations (6.16) and (6.17), and between the entrance and the exit of the branch channel, Δp_3 , as

$$\begin{aligned} \Delta p_3 &= p(\mathcal{E}_1) - p(\mathcal{E}_3) \\ &= (p^{P_1}(\mathcal{E}_1) + p^{D_1}(\mathcal{E}_1)) - (p^{P_3}(\mathcal{E}_3) + p^{D_3}(\mathcal{E}_3)) \\ &= -\pi_3 \end{aligned} \quad (6.22)$$

by equations (6.16) and (6.20). The total pressures at the exits are

$$p(\mathcal{E}_2) = \pi_2 - G_2 l, \quad \text{and} \quad p(\mathcal{E}_3) = \pi_3. \quad (6.23)$$

The final boundary condition regards the particle which translates with velocity, $\mathbf{V} = (V_x, V_y)$, and rotates with velocity, $\mathbf{\Omega} = \Omega \mathbf{k}$, where \mathbf{k} is the unit vector pointing out of the paper towards the reader. Therefore on \mathcal{P} we have,

$$\mathbf{u}(\mathbf{x}) = \mathbf{V} + \mathbf{\Omega} \wedge (\mathbf{x} - \mathbf{x}_c), \quad (6.24)$$

where \mathbf{x} is a point on \mathcal{P} and \mathbf{x}_c is the centroid of the particle calculated using equation (3.8) (on page 43).

In our discussion of the boundary conditions we have introduced unknown disturbance tractions, velocities and pressures. All quantities are defined with reference to \mathcal{E}_1 , \mathcal{E}_2 or \mathcal{E}_3 . Therefore during the forthcoming derivation of the equations we will need to choose which quantities to keep and which to eliminate. In the main channel we have the disturbance pressure, π_2 , and the disturbance tractions, \mathbf{f}^{D_1} , on the channel walls. In the branch channel we have π_3 and the \mathbf{f}^{D_3} on the channel walls. On the notional boundary we choose \mathbf{f}^{D_1} and \mathbf{u}^{D_1} , for consistency with the main channel.

To derive equations for the disturbance pressures π_2 and π_3 we bring together the analysis given in chapter 3 when discussing a rigid particle in a straight channel, and the derivation of the disturbance pressures equations for a branching channel given in the previous chapter. Firstly we will consider the main channel when it contains the particle, and apply the Lorentz reciprocal relation (1.3.22) to the pair of flows, $(\mathbf{u}^{P_1}, \boldsymbol{\sigma}^{P_1})$ and $(\mathbf{u}^{D_1}, \boldsymbol{\sigma}^{D_1})$, to get

$$\nabla \cdot (\mathbf{u}^{P_1} \cdot \boldsymbol{\sigma}^{D_1} - \mathbf{u}^{D_1} \cdot \boldsymbol{\sigma}^{P_1}) = 0, \quad (6.25)$$

which we integrate over the main channel's flow domain and apply the divergence theorem to get

$$\int_{\partial\Gamma_1} \mathbf{u}^{P_1} \cdot \mathbf{f}^{D_1} \, ds(\mathbf{x}) = \int_{\partial\Gamma_1} \mathbf{u}^{D_1} \cdot \mathbf{f}^{P_1} \, ds(\mathbf{x}), \quad (6.26)$$

where $\partial\Gamma_1 = \mathcal{E}_1 \cup \mathcal{E}_2 \cup \mathcal{A} \cup \mathcal{C} \cup \mathcal{P}$, which can be simplified to

$$\int_{\mathcal{E}_2} (\mathbf{u}^{P_1} \cdot \mathbf{f}^{D_1} - \mathbf{u}^{D_1} \cdot \mathbf{f}^{P_1}) \, ds(\mathbf{x}) = \int_{\mathcal{A}, \mathcal{P}} (\mathbf{u}^{D_1} \cdot \mathbf{f}^{P_1} - \mathbf{u}^{P_1} \cdot \mathbf{f}^{D_1}) \, ds(\mathbf{x}), \quad (6.27)$$

using equations (6.10) and (6.12). The left-hand side simplifies to $Q_1 \pi_2$ by equation

(5.45) from the previous chapter, and the integral over \mathcal{P} simplifies to

$$\begin{aligned} \int_{\mathcal{P}} (\mathbf{u}^{D_1} \cdot \mathbf{f}^{P_1} - \mathbf{u}^{P_1} \cdot \mathbf{f}^{D_1}) \, ds(\mathbf{x}) &= \int_{\mathcal{P}} ((\mathbf{u} - \mathbf{u}^{P_1}) \cdot \mathbf{f}^{P_1} - \mathbf{u}^{P_1} \cdot (\mathbf{f} - \mathbf{f}^{P_1})) \, ds(\mathbf{x}) \\ &= \int_{\mathcal{P}} (\mathbf{u} \cdot \mathbf{f}^{P_1} - \mathbf{u}^{P_1} \cdot \mathbf{f}) \, ds(\mathbf{x}) \\ &= - \int_{\mathcal{P}} \mathbf{u}^{P_1} \cdot \mathbf{f} \, ds(\mathbf{x}), \end{aligned} \quad (6.28)$$

using equations (6.1) and (6.3), and where $\int_{\mathcal{P}} \mathbf{u} \cdot \mathbf{f}^{P_1} \, ds(\mathbf{x}) = 0$ was shown in equation (3.31) of chapter 3. Therefore we can simplify equation (6.27) to get,

$$\pi_2 = \frac{1}{Q_1} \left(\int_{\mathcal{A}} (\mathbf{u}^{D_1} \cdot \mathbf{f}^{P_1} - \mathbf{u}^{P_1} \cdot \mathbf{f}^{D_1}) \, ds(\mathbf{x}) - \int_{\mathcal{P}} \mathbf{u}^{P_1} \cdot \mathbf{f} \, ds(\mathbf{x}) \right), \quad (6.29)$$

for the disturbance pressure at \mathcal{E}_2 . If the particle were in the branch channel the integral over \mathcal{P} would be omitted from equation (6.29). To obtain an equation for π_3 when the particle is in the branch channel, we include the particle boundary in equation (5.50) and obtain

$$\int_{\mathcal{E}_3} (\mathbf{u}^{P_3} \cdot \mathbf{f}^{D_3} - \mathbf{u}^{D_3} \cdot \mathbf{f}^{P_3}) \, ds(\mathbf{x}) = \int_{\mathcal{A}, \mathcal{P}} (\mathbf{u}^{P_3} \cdot \mathbf{f}^{D_3} - \mathbf{u}^{D_3} \cdot \mathbf{f}^{P_3}) \, ds(\mathbf{x}). \quad (6.30)$$

The left-hand side is simplified using boundary conditions (6.12) and (6.15), to get

$$\int_{\mathcal{E}_3} (\mathbf{u}^{P_3} \cdot \mathbf{f}^{D_3} - \mathbf{u}^{D_3} \cdot \mathbf{f}^{P_3}) \, ds(\mathbf{x}) = Q_3 \pi_3, \quad (6.31)$$

and where we have used $Q_3 = - \int_{\mathcal{E}_3} \mathbf{n} \cdot \mathbf{u}^{P_3} \, ds(\mathbf{x})$. The integral over \mathcal{P} may be re-expressed in the same way as equation (6.28) by changing the index 1 to 3, to obtain

$$\int_{\mathcal{P}} (\mathbf{u}^{P_3} \cdot \mathbf{f}^{D_3} - \mathbf{u}^{D_3} \cdot \mathbf{f}^{P_3}) \, ds(\mathbf{x}) = - \int_{\mathcal{P}} \mathbf{u}^{P_3} \cdot \mathbf{f} \, ds(\mathbf{x}). \quad (6.32)$$

Substitution of equations (6.31) and (6.32) into (6.30) and elimination of \mathbf{u}^{D_3} and \mathbf{f}^{D_3} on \mathcal{A} in favour of \mathbf{u}^{D_1} and \mathbf{f}^{D_1} gives

$$\pi_3 = \frac{1}{Q_3} \left(\int_{\mathcal{A}} (\mathbf{u}^{P_3} \cdot \mathbf{f}^{D_1} - \mathbf{u}^{D_1} \cdot \mathbf{f}^{P_3}) \, ds(\mathbf{x}) + \psi - \int_{\mathcal{P}} \mathbf{u}^{P_3} \cdot \mathbf{f} \, ds(\mathbf{x}) \right), \quad (6.33)$$

where ψ is defined by equation (5.56). When the particle is in the main channel the integral over \mathcal{P} is omitted from equation (6.33). To write the disturbance pressure equations

concisely we introduce a function, $\mathcal{H}_{\mathcal{P}}$, which is defined by

$$\mathcal{H}_{\mathcal{P}} = \begin{cases} 0 & \text{when the particle is in the branch channel,} \\ 1 & \text{when the particle is in the main channel,} \end{cases} \quad (6.34)$$

so that,

$$\pi_2 = \frac{1}{Q_1} \left(\int_{\mathcal{A}} (\mathbf{u}^{D_1} \cdot \mathbf{f}^{P_1} - \mathbf{u}^{P_1} \cdot \mathbf{f}^{D_1}) \, ds(\mathbf{x}) - \mathcal{H}_{\mathcal{P}} \int_{\mathcal{P}} \mathbf{u}^{P_1} \cdot \mathbf{f} \, ds(\mathbf{x}) \right), \quad (6.35)$$

$$\pi_3 = \frac{1}{Q_3} \left(\int_{\mathcal{A}} (\mathbf{u}^{P_3} \cdot \mathbf{f}^{D_1} - \mathbf{u}^{D_1} \cdot \mathbf{f}^{P_3}) \, ds(\mathbf{x}) + \psi - (1 - \mathcal{H}_{\mathcal{P}}) \int_{\mathcal{P}} \mathbf{u}^{P_3} \cdot \mathbf{f} \, ds(\mathbf{x}) \right), \quad (6.36)$$

for the disturbance pressures at the exits. When the line $y = -d$ bisects the particle it is between channels. In this situation the notional boundary \mathcal{A} will be deformed around the particle so that it lies wholly within the main or branch channel. The unknowns in equations (6.35) and (6.36) are the disturbance pressures, the disturbance velocities and tractions on \mathcal{A} and the tractions on the particle boundary.

We start the derivation of the boundary integral equation for the main channel using equation (5.64) and include the particle boundary, to get

$$4\pi\mu u_j^{D_1}(\mathbf{x}_0) = - \int_{\mathcal{A}, \mathcal{C}, \mathcal{P}} f_i^{D_1} G_{ij} \, ds(\mathbf{x}) + \pi_2 \int_{\mathcal{E}_2} n_i G_{ij} \, ds(\mathbf{x}) + \mu \int_{\mathcal{A}, \mathcal{P}} u_i^{D_1} T_{ijk} n_k \, ds(\mathbf{x}) + I_j(\mathbf{x}_0), \quad (6.37)$$

for \mathbf{x}_0 in the fluid of the main channel, and where $I(\mathbf{x}_0)$ is defined by equation (5.65). Application of the boundary integral equation (1.3.40) to the $(\mathbf{u}^{P_1}, \boldsymbol{\sigma}^{P_1})$ flow over the particle gives,

$$0 = - \int_{\mathcal{P}} f_i^{P_1} G_{ij} \, ds(\mathbf{x}) + \mu \int_{\mathcal{P}} u_i^{P_1} T_{ijk} n_k \, ds(\mathbf{x}), \quad (6.38)$$

for \mathbf{x}_0 in the fluid of the main channel. Adding this equation to (6.37) gives

$$4\pi\mu u_j^{D_1}(\mathbf{x}_0) = - \int_{\mathcal{A}, \mathcal{C}} f_i^{D_1} G_{ij} \, ds(\mathbf{x}) - \int_{\mathcal{P}} f_i G_{ij} \, ds(\mathbf{x}) + \pi_2 \int_{\mathcal{E}_2} n_i G_{ij} \, ds(\mathbf{x}) + \mu \int_{\mathcal{A}} u_i^{D_1} T_{ijk} n_k \, ds(\mathbf{x}) + I_j(\mathbf{x}_0) + \mu \int_{\mathcal{P}} u_i T_{ijk} n_k \, ds(\mathbf{x}), \quad (6.39)$$

and we have shown that the double-layer potential integral over a rigid particle is zero in

(3.47). Therefore we may write equation (6.39) as

$$u_j^{D1}(\mathbf{x}_0) = \frac{1}{4\pi\mu} \left(- \int_{\mathcal{A}, \mathcal{C}} f_i^{D1} G_{ij} \, ds(\mathbf{x}) - \mathcal{H}_{\mathcal{P}} \int_{\mathcal{P}} f_i G_{ij} \, ds(\mathbf{x}) \right. \\ \left. + \pi_2 \int_{\mathcal{E}_2} n_i G_{ij} \, ds(\mathbf{x}) + \mu \int_{\mathcal{A}} u_i^{D1} T_{ijk} n_k \, ds(\mathbf{x}) + I_j(\mathbf{x}_0) \right), \quad (6.40)$$

which is valid for \mathbf{x}_0 in the fluid of the main channel. When the particle is in the branch channel the particle integral is omitted. Equation (6.40) is also valid on the walls of the channel and the particle boundary because the discontinuous double-layer potential is not evaluated over either \mathcal{C} or \mathcal{P} . When the particle is in the main channel and the pole, \mathbf{x}_0 , is placed on \mathcal{P} we use $\mathbf{u}^{D1}(\mathbf{x}_0) = \mathbf{u}(\mathbf{x}_0) - \mathbf{u}^{P1}(\mathbf{x}_0)$, to replace the left-hand side of equation (6.40), and use equation (6.24) to write \mathbf{u} in terms of the translational and rotational velocities. When \mathbf{x}_0 lies on the notional boundary, \mathcal{A} , we obtain

$$u_j^{D1}(\mathbf{x}_0) = \frac{1}{2\pi\mu} \left(- \int_{\mathcal{A}, \mathcal{C}} f_i^{D1} G_{ij} \, ds(\mathbf{x}) - \mathcal{H}_{\mathcal{P}} \int_{\mathcal{P}} f_i G_{ij} \, ds(\mathbf{x}) \right. \\ \left. + \pi_2 \int_{\mathcal{E}_2} n_i G_{ij} \, ds(\mathbf{x}) + \mu \int_{\mathcal{A}}^{PV} u_i^{D1} T_{ijk} n_k \, ds(\mathbf{x}) + I_j(\mathbf{x}_0) \right), \quad (6.41)$$

by the same process as given in the derivation of equation (5.68). The derivation of the boundary integral equation applicable to the branch channel proceeds in much the same way as the main channel. We start by including the particle boundary in the branch channel boundary integral equation (5.72), to get

$$4\pi\mu u_j^{D3}(\mathbf{x}_0) = \int_{\mathcal{A}} f_i^{D1} G_{ij} \, ds(\mathbf{x}) - \int_{\mathcal{B}, \mathcal{P}} f_i^{D3} G_{ij} \, ds(\mathbf{x}) + \pi_3 \int_{\mathcal{E}_3} n_i G_{ij} \, ds(\mathbf{x}) \\ - \mu \int_{\mathcal{A}} u_i^{D1} T_{ijk} n_k \, ds(\mathbf{x}) + \mu \int_{\mathcal{P}} u_i^{D3} T_{ijk} n_k \, ds(\mathbf{x}) + K_j(\mathbf{x}_0), \quad (6.42)$$

for \mathbf{x}_0 located in the fluid of the branch channel, and where $\mathbf{K}(\mathbf{x}_0)$ is defined by (5.73). This time we apply the boundary integral equation (1.3.40) to the $(\mathbf{u}^{P3}, \boldsymbol{\sigma}^{P3})$ flow over the particle, and get

$$0 = - \int_{\mathcal{P}} f_i^{P3} G_{ij} \, ds(\mathbf{x}) + \mu \int_{\mathcal{P}} u_i^{P3} T_{ijk} n_k \, ds(\mathbf{x}), \quad (6.43)$$

for \mathbf{x}_0 in the fluid of the branch channel, which we add to equation (6.42) to obtain

$$4\pi\mu u_j^{D3}(\mathbf{x}_0) = \int_{\mathcal{A}} f_i^{D1} G_{ij} \, ds(\mathbf{x}) - \int_{\mathcal{B}} f_i^{D3} G_{ij} \, ds(\mathbf{x}) - \int_{\mathcal{P}} f_i G_{ij} \, ds(\mathbf{x}) + \pi_3 \int_{\mathcal{E}_3} n_i G_{ij} \, ds(\mathbf{x}) \\ - \mu \int_{\mathcal{A}} u_i^{D1} T_{ijk} n_k \, ds(\mathbf{x}) + \mu \int_{\mathcal{P}} u_i T_{ijk} n_k \, ds(\mathbf{x}) + K_j(\mathbf{x}_0), \quad (6.44)$$

and we have shown that the double-layer potential integral over a rigid particle is zero in (3.47). Therefore we may write equation (6.44) as

$$u_j^{D3}(\mathbf{x}_0) = \frac{1}{4\pi\mu} \left(\int_{\mathcal{A}} f_i^{D1} G_{ij} \, ds(\mathbf{x}) - \int_{\mathcal{B}} f_i^{D3} G_{ij} \, ds(\mathbf{x}) - (1 - \mathcal{H}_{\mathcal{P}}) \int_{\mathcal{P}} f_i G_{ij} \, ds(\mathbf{x}) \right. \\ \left. + \pi_3 \int_{\mathcal{E}_3} n_i G_{ij} \, ds(\mathbf{x}) - \mu \int_{\mathcal{A}} u_i^{D1} T_{ijk} n_k \, ds(\mathbf{x}) + K_j(\mathbf{x}_0) \right), \quad (6.45)$$

Since the discontinuous double-layer potential is only present for the notional boundary, equation (6.45) is also valid when \mathbf{x}_0 lies on the walls of the branch channel and on the particle boundary. When \mathbf{x}_0 lies on \mathcal{B} the left-hand side is zero by no-slip, and when \mathbf{x}_0 lies on \mathcal{P} we write $\mathbf{u}^{D3}(\mathbf{x}_0) = \mathbf{u}(\mathbf{x}_0) - \mathbf{u}^{P3}(\mathbf{x}_0)$. When the pole lies on \mathcal{A} we follow the same process as given in the derivation of equation (5.75), to get

$$u_j^{D3}(\mathbf{x}_0) = \frac{1}{2\pi\mu} \left(\int_{\mathcal{A}} f_i^{D1} G_{ij} \, ds(\mathbf{x}) - \int_{\mathcal{B}} f_i^{D3} G_{ij} \, ds(\mathbf{x}) - (1 - \mathcal{H}_{\mathcal{P}}) \int_{\mathcal{P}} f_i G_{ij} \, ds(\mathbf{x}) \right. \\ \left. + \pi_3 \int_{\mathcal{E}_3} n_i G_{ij} \, ds(\mathbf{x}) - \mu \int_{\mathcal{A}}^{PV} u_i^{D1} T_{ijk} n_k \, ds(\mathbf{x}) + K_j^{PV}(\mathbf{x}_0) \right). \quad (6.46)$$

We now have equations for the disturbance pressures and boundary integral equations for the main and branch channels. However, there is a problem regarding the uniqueness of the solution as discussed in chapter 3 (page 50). To render the solution unique we add a deflation term, which can be shown to be zero, to the integral over \mathcal{P} . The deflation term is

$$D_j(\mathbf{x}_0) = n_j(\mathbf{x}_0) \int_{\mathcal{P}} n_i f_i \, ds(\mathbf{x}), \quad (6.47)$$

which we add to the boundary integral equations whenever the integral over \mathcal{P} is present. More details on the deflation term may be found in Appendix B and Pozrikidis (2005b). To obtain a linear system which represents the governing equations we employ the boundary element method (e.g. Pozrikidis 2002a). We discretise the boundaries into elements upon which we evaluate the boundary integral equations. We obtain a sufficient number of equations for the unknown tractions on \mathcal{C} and \mathcal{B} by evaluating equations (6.40) and (6.45) with \mathbf{x}_0 on each element of the respective boundary. Evaluation of the equations (6.41) and (6.46) with \mathbf{x}_0 on \mathcal{A} provides a sufficient number of equations for the disturbance

tractions and velocities on the notional boundary. Depending on whether the particle is in the main channel or the branch channel, we evaluate either equation (6.40) or (6.45) with \mathbf{x}_0 on each boundary element of the particle to obtain equations for the particle tractions. We have two equations for the disturbance pressures at the exits, namely equations (6.35) and (6.36). However, we still have the unknown rotational velocity and the two components of the unknown translational velocity. Since we have assumed that the particle is force and torque free, we include equations (3.33) and (3.34) which state this assumption mathematically. Therefore we have the same number of equations as unknowns and so our system is complete. We have completed our derivation of the governing equations for the flow of a particle through a bifurcation and now we move on to describe how the boundary element method is applied in order to find the numerical solution.

6.2 Numerical method

In section 5.2 of the previous chapter we discretised the governing equations for a branching channel into the linear matrix form,

$$\mathbf{A} \cdot \mathbf{x} = \mathbf{b}, \quad (6.48)$$

where \mathbf{A} is the influence matrix, \mathbf{x} is the column-vector of unknown pressures, tractions and velocities, and \mathbf{b} is a column-vector containing known values. As before, we discretise the main channel walls, the branch channel walls and the notional boundary into N_C , N_B and N_A equally-sized straight elements respectively. We also discretise the particle into N_P equally-sized straight elements. On each element we set the unknown disturbance traction to a constant 2-vector, which we label $\mathbf{f}_r^{D_1}$ on the r^{th} element of \mathcal{A} and \mathcal{C} , $\mathbf{f}_r^{D_3}$ on the r^{th} element of \mathcal{B} and \mathbf{f}_r on the r^{th} element of \mathcal{P} . We also set the disturbance velocity to $\mathbf{u}_r^{D_1}$ on the r^{th} element of \mathcal{A} . The vector of unknowns is defined by

$$\mathbf{x} = \left[\mathbf{F}_C^D \quad \mathbf{F}_A^D \quad \mathbf{F}_B^D \quad \mathbf{U}_A^D \quad \pi_2 \quad \pi_3 \quad \mathbf{F}_P \quad \mathbf{V} \quad \Omega \right]^T \quad (6.49)$$

where the vectors \mathbf{F}_C^D , \mathbf{F}_A^D , \mathbf{F}_B^D and \mathbf{U}_A^D are defined in section 5.2, \mathbf{F}_P is defined by

$$\mathbf{F}_P = \left[f_{x,1} \quad f_{y,1} \quad \cdots \quad f_{x,N_P} \quad f_{y,N_P} \right], \quad (6.50)$$

and where \mathbf{V} and Ω are the translational and rotational velocities. To discretise the disturbance pressure equations, we write the equations as

$$Q_1 \pi_2 + \int_{\mathcal{A}} (\mathbf{u}^{P_1} \cdot \mathbf{f}^{D_1} - \mathbf{u}^{D_1} \cdot \mathbf{f}^{P_1}) ds(\mathbf{x}) + \mathcal{H}_P \int_{\mathcal{P}} \mathbf{u}^{P_1} \cdot \mathbf{f} ds(\mathbf{x}) = 0, \quad (6.51)$$

$$Q_3 \pi_3 + \int_{\mathcal{A}} (\mathbf{u}^{D_1} \cdot \mathbf{f}^{P_3} - \mathbf{u}^{P_3} \cdot \mathbf{f}^{D_1}) ds(\mathbf{x}) + (1 - \mathcal{H}_P) \int_{\mathcal{P}} \mathbf{u}^{P_3} \cdot \mathbf{f} ds(\mathbf{x}) = \psi. \quad (6.52)$$

We need only concentrate on the particle integral because the remaining terms have been discretised in equations (5.87) and (5.89). The integral over the particle in equation (6.51) is approximated by

$$\int_{\mathcal{P}} \mathbf{u}^{P_1} \cdot \mathbf{f} \, ds(\mathbf{x}) \approx \sum_{r=1}^{N_{\mathcal{P}}} \mathbf{u}^{P_1}(\mathbf{x}_{m,r}) \cdot \mathbf{f}_r l_r, \quad (6.53)$$

where $\mathbf{x}_{m,r}$ is the mid-point of the r^{th} element and l_r is its length. By defining

$$\mathbf{U}_{\mathcal{P}}^{P_1} = \left[\mathbf{u}^{P_1}(\mathbf{x}_{m,1}) l_1 \quad \cdots \quad \mathbf{u}^{P_1}(\mathbf{x}_{m,N_{\mathcal{P}}}) l_{N_{\mathcal{P}}} \right], \quad (6.54)$$

we may write

$$\int_{\mathcal{P}} \mathbf{u}^{P_1} \cdot \mathbf{f} \, ds(\mathbf{x}) \approx \mathbf{U}_{\mathcal{P}}^{P_1} \cdot \mathbf{F}_{\mathcal{P}}, \quad (6.55)$$

and so equation (6.51) can be expressed in the form,

$$\left[\mathbf{0} \quad \mathbf{U}_{\mathcal{A}}^{P_1} \quad \mathbf{0} \quad -\mathbf{F}_{\mathcal{A}}^{P_1} \quad Q_1 \quad 0 \quad \mathcal{H}_{\mathcal{P}} \mathbf{U}_{\mathcal{P}}^{P_1} \quad \mathbf{0} \quad 0 \right] \cdot \mathbf{x} = 0, \quad (6.56)$$

where $\mathbf{U}_{\mathcal{A}}^{P_1}$ and $\mathbf{F}_{\mathcal{A}}^{P_1}$ are defined by equations (5.84) and (5.85). To discretise the equation for π_3 we define

$$\mathbf{U}_{\mathcal{P}}^{P_3} = \left[\mathbf{u}^{P_3}(\mathbf{x}_{m,1}) l_1 \quad \cdots \quad \mathbf{u}^{P_3}(\mathbf{x}_{m,N_{\mathcal{P}}}) l_{N_{\mathcal{P}}} \right], \quad (6.57)$$

so that equation (6.52) may be written as

$$\left[\mathbf{0} \quad -\mathbf{U}_{\mathcal{A}}^{P_3} \quad \mathbf{0} \quad -\mathbf{F}_{\mathcal{A}}^{P_3} \quad 0 \quad Q_3 \quad (1 - \mathcal{H}_{\mathcal{P}}) \mathbf{U}_{\mathcal{P}}^{P_3} \quad \mathbf{0} \quad 0 \right] \cdot \mathbf{x} = \psi, \quad (6.58)$$

where $\mathbf{U}_{\mathcal{A}}^{P_3}$ and $\mathbf{F}_{\mathcal{A}}^{P_3}$ are defined by equations (5.90) and (5.91), and where ψ may be calculated exactly from equation (5.57) when \mathcal{A} is straight. However, the \mathcal{A} boundary may now be deformed to facilitate the passage of the particle into the branch channel. When this occurs we approximate ψ using

$$\psi \approx \sum_{r=1}^{N_{\mathcal{A}}} \left(\mathbf{u}^{P_3}(\mathbf{x}_{m,r}) \cdot \mathbf{f}^{P_1}(\mathbf{x}_{m,r}) - \mathbf{u}^{P_1}(\mathbf{x}_{m,r}) \cdot \mathbf{f}^{P_3}(\mathbf{x}_{m,r}) \right) l_r. \quad (6.59)$$

To discretise the boundary integral equations, we start with the main channel and write equation (6.40) as

$$\begin{aligned} \int_{\mathcal{A}, \mathcal{C}} f_i^{D_1} G_{ij} \, ds(\mathbf{x}) + \mathcal{H}_{\mathcal{P}} \int_{\mathcal{P}} f_i G_{ij} \, ds(\mathbf{x}) - \pi_2 \int_{\mathcal{E}_2} n_i G_{ij} \, ds(\mathbf{x}) \\ - \mu \int_{\mathcal{A}} u_i^{D_1} T_{ijk} n_k \, ds(\mathbf{x}) = I_j(\mathbf{x}_0), \end{aligned} \quad (6.60)$$

which is valid for \mathbf{x}_0 on \mathcal{C} , since $\mathbf{u}^{D1} = \mathbf{0}$. The only term which we have not previously discretised is the single-layer potential over \mathcal{P} , which we approximate by

$$\int_{\mathcal{P}} f_i G_{ij} \, ds(\mathbf{x}) \approx \mathbf{I}_{\mathcal{P},j}^G(\mathbf{x}_0) \cdot \mathbf{F}^P, \quad (6.61)$$

where

$$\mathbf{I}_{\mathcal{P},j}^G(\mathbf{x}_0) = \left[\tilde{G}_{xj,1}(\mathbf{x}_0) \quad \tilde{G}_{yj,1}(\mathbf{x}_0) \quad \cdots \quad \tilde{G}_{xj,N_{\mathcal{P}}}(\mathbf{x}_0) \quad \tilde{G}_{yj,N_{\mathcal{P}}}(\mathbf{x}_0) \right] \quad (6.62)$$

and $\tilde{G}_{ij,r}$ is the integral of the Green's function over the r^{th} element, El_r , and is defined by

$$\tilde{G}_{ij,r}(\mathbf{x}_0) = \int_{El_r} G_{ij}(\mathbf{x}, \mathbf{x}_0) \, ds(\mathbf{x}). \quad (6.63)$$

Therefore we can write equation (6.60) in the matrix form,

$$\left[\mathbf{I}_{\mathcal{C},j}^G(\mathbf{x}_0) \quad \mathbf{I}_{\mathcal{A},j}^G(\mathbf{x}_0) \quad \mathbf{0} \quad -\mu \mathbf{I}_{\mathcal{A},j}^T(\mathbf{x}_0) \quad -\mathbf{I}_{\mathcal{E}_2,j}^G(\mathbf{x}_0) \quad \mathbf{0} \quad \mathcal{H}_{\mathcal{P}} \mathbf{I}_{\mathcal{P},j}^G(\mathbf{x}_0) \quad \mathbf{0} \quad \mathbf{0} \right] \cdot \mathbf{x} = I_j(\mathbf{x}_0), \quad (6.64)$$

by augmenting equation (5.109) with $\mathcal{H}_{\mathcal{P}} \mathbf{I}_{\mathcal{P},j}^G(\mathbf{x}_0)$. When we repeatedly evaluate (6.64) with \mathbf{x}_0 placed at the mid-point of each of \mathcal{C} 's boundary elements, we obtain

$$\left[\mathcal{C}_{\mathcal{C}} \quad \mathcal{C}_{\mathcal{A}} \quad \mathbf{0} \quad \mathcal{C}_{\mathcal{A}}^T \quad \mathcal{C}_{\mathcal{E}_2} \quad \mathbf{0} \quad \mathcal{H}_{\mathcal{P}} \mathcal{C}_{\mathcal{P}} \quad \mathbf{0} \quad \mathbf{0} \right] \cdot \mathbf{x} = \mathcal{C}_I, \quad (6.65)$$

where $\mathcal{C}_{\mathcal{P}}$ corresponds to the $N_{\mathcal{C}}$ pairs of $\mathbf{I}_{\mathcal{P},j}^G(\mathbf{x}_0)$, and the remaining terms are defined in the derivation of equation (5.109). By following the same process with \mathbf{x}_0 placed on the walls of \mathcal{B} and the notional boundary, \mathcal{A} , we obtain

$$\left[\begin{array}{ccccccccc} \mathcal{C}_{\mathcal{C}} & \mathcal{C}_{\mathcal{A}} & \mathbf{0} & \mathcal{C}_{\mathcal{A}}^T & \mathcal{C}_{\mathcal{E}_2} & \mathbf{0} & \mathcal{H}_{\mathcal{P}} \mathcal{C}_{\mathcal{P}} & \mathbf{0} & \mathbf{0} \\ \mathcal{A}_{\mathcal{C}} & \mathcal{A}_{\mathcal{A}}^m & \mathbf{0} & \mathcal{A}_{\mathcal{A}}^{m,T} & \mathcal{A}_{\mathcal{E}_2} & \mathbf{0} & \mathcal{H}_{\mathcal{P}} \mathcal{A}_{\mathcal{P}}^m & \mathbf{0} & \mathbf{0} \\ \mathbf{0} & \mathcal{B}_{\mathcal{A}} & \mathcal{B}_{\mathcal{B}} & \mathcal{B}_{\mathcal{A}}^T & \mathbf{0} & \mathcal{B}_{\mathcal{E}_3} & (1 - \mathcal{H}_{\mathcal{P}}) \mathcal{B}_{\mathcal{P}} & \mathbf{0} & \mathbf{0} \\ \mathbf{0} & \mathcal{A}_{\mathcal{A}}^b & \mathcal{A}_{\mathcal{B}} & \mathcal{A}_{\mathcal{A}}^{b,T} & \mathbf{0} & \mathcal{A}_{\mathcal{E}_3} & (1 - \mathcal{H}_{\mathcal{P}}) \mathcal{A}_{\mathcal{P}}^b & \mathbf{0} & \mathbf{0} \\ \mathbf{0} & \mathbf{U}_{\mathcal{A}}^{P1} & \mathbf{0} & -\mathbf{F}_{\mathcal{A}}^{P1} & Q_1 & \mathbf{0} & \mathcal{H}_{\mathcal{P}} \mathbf{U}_{\mathcal{P}}^{P1} & \mathbf{0} & \mathbf{0} \\ \mathbf{0} & -\mathbf{U}_{\mathcal{A}}^{P3} & \mathbf{0} & -\mathbf{F}_{\mathcal{A}}^{P3} & \mathbf{0} & Q_3 & (1 - \mathcal{H}_{\mathcal{P}}) \mathbf{U}_{\mathcal{P}}^{P3} & \mathbf{0} & \mathbf{0} \end{array} \right] \cdot \mathbf{x} = \left[\begin{array}{c} \mathcal{C}_I \\ \mathcal{A}_I \\ \mathcal{B}_K \\ \mathcal{A}_K \\ 0 \\ \psi \end{array} \right], \quad (6.66)$$

where $\mathcal{A}_{\mathcal{P}}^m$ and $\mathcal{A}_{\mathcal{P}}^b$ correspond to the $N_{\mathcal{A}}$ pairs of $\mathbf{I}_{\mathcal{P},j}^G(\mathbf{x}_0)$ with \mathbf{x}_0 on \mathcal{A} , $\mathcal{B}_{\mathcal{P}}$ corresponds to the $N_{\mathcal{B}}$ pairs of $\mathbf{I}_{\mathcal{P},j}^G(\mathbf{x}_0)$ with \mathbf{x}_0 on \mathcal{B} , and the remaining terms are all defined in section 5.2 of the previous chapter. When \mathbf{x}_0 lies on the particle boundary and the particle is in the main channel we write the boundary integral equation (6.40) as

$$\int_{\mathcal{A},\mathcal{C}} f_i^{D1} G_{ij} \, ds(\mathbf{x}) - \mu \int_{\mathcal{A}} u_i^{D1} T_{ijk} n_k \, ds(\mathbf{x}) - \pi_2 \int_{\mathcal{E}_2} n_i G_{ij} \, ds(\mathbf{x}) + \int_{\mathcal{P}} f_i G_{ij} \, ds(\mathbf{x}) + 4\pi\mu u_j(\mathbf{x}_0) = I_j(\mathbf{x}_0) + 4\pi\mu u_j^{P1}(\mathbf{x}_0), \quad (6.67)$$

which by writing $\mathbf{u}(\mathbf{x}_0) = \mathbf{V} + \Omega \mathbf{k} \wedge (\mathbf{x}_0 - \mathbf{x}_c)$, we discretise to

$$\begin{aligned} \left[\mathbf{I}_{\mathcal{C},j}^G(\mathbf{x}_0) \quad \mathbf{I}_{\mathcal{A},j}^G(\mathbf{x}_0) \quad \mathbf{0} \quad -\mu \mathbf{I}_{\mathcal{A},j}^T(\mathbf{x}_0) \quad -I_{\mathcal{E}_2,j}^G(\mathbf{x}_0) \quad 0 \quad \mathbf{I}_{\mathcal{P},j}^G(\mathbf{x}_0) \quad \mathbf{I}_{u,j} \quad I_{\Omega,j}(\mathbf{x}_0) \right] \cdot \mathbf{x} \\ = I_j(\mathbf{x}_0) + 4\pi\mu u_j^{P_1}(\mathbf{x}_0), \end{aligned} \quad (6.68)$$

where $\mathbf{I}_{u,j}$ and $I_{\Omega,j}(\mathbf{x}_0)$ are defined by

$$\mathbf{I}_{u,j} = 4\pi\mu \begin{bmatrix} \delta_{jx} & \delta_{jy} \end{bmatrix}, \quad (6.69)$$

$$I_{\Omega,j}(\mathbf{x}_0) = 4\pi\mu \epsilon_{zlj} (x_{0,l} - x_{c,l}). \quad (6.70)$$

Evaluation of (6.68) on each boundary element of \mathcal{P} leads to $N_{\mathcal{P}}$ pairs of equations which we write as

$$\left[\mathcal{P}_{\mathcal{C}} \quad \mathcal{P}_{\mathcal{A}} \quad \mathbf{0} \quad \mathcal{P}_{\mathcal{A}}^T \quad \mathcal{P}_{\mathcal{E}_2} \quad \mathbf{0} \quad \mathcal{P}_{\mathcal{P}} \quad \mathcal{P}_u \quad \mathcal{P}_{\Omega} \right] \cdot \mathbf{x} = \mathcal{P}_I^*, \quad (6.71)$$

where each element corresponds to the $N_{\mathcal{P}}$ pairs of elements in equation (6.68) and \mathcal{P}_I^* corresponds to the $N_{\mathcal{P}}$ pairs of $I_j(\mathbf{x}_0) + 4\pi\mu u_j^{P_1}(\mathbf{x}_0)$. Equation (6.71) is only included in the linear system when the particle is in the main channel. When the particle is in the branch channel we write the boundary integral equation (6.45) as

$$\begin{aligned} - \int_{\mathcal{A}} f_i^{D_1} G_{ij} \, ds(\mathbf{x}) + \int_{\mathcal{B}} f_i^{D_3} G_{ij} \, ds(\mathbf{x}) + \mu \int_{\mathcal{A}} u_i^{D_1} T_{ijk} n_k \, ds(\mathbf{x}) - \pi_3 \int_{\mathcal{E}_3} n_i G_{ij} \, ds(\mathbf{x}) \\ + \int_{\mathcal{P}} f_i G_{ij} \, ds(\mathbf{x}) + 4\pi\mu u_j(\mathbf{x}_0) = K_j(\mathbf{x}_0) + 4\pi\mu u_j^{P_3}(\mathbf{x}_0), \end{aligned} \quad (6.72)$$

for \mathbf{x}_0 on the particle boundary. Using $\mathbf{u}(\mathbf{x}_0) = \mathbf{V} + \Omega \mathbf{k} \wedge (\mathbf{x}_0 - \mathbf{x}_c)$, we discretise equation (6.72) to get

$$\begin{aligned} \left[\mathbf{0} \quad -\mathbf{I}_{\mathcal{A},j}^G(\mathbf{x}_0) \quad \mathbf{I}_{\mathcal{B},j}^G(\mathbf{x}_0) \quad \mu \mathbf{I}_{\mathcal{A},j}^T(\mathbf{x}_0) \quad 0 \quad -I_{\mathcal{E}_3,j}^G(\mathbf{x}_0) \quad \mathbf{I}_{\mathcal{P},j}^G(\mathbf{x}_0) \quad \mathbf{I}_{u,j} \quad I_{\Omega,j}(\mathbf{x}_0) \right] \cdot \mathbf{x} \\ = K_j(\mathbf{x}_0) + 4\pi\mu u_j^{P_3}(\mathbf{x}_0). \end{aligned} \quad (6.73)$$

Evaluation of (6.73) on each boundary element of \mathcal{P} leads to $N_{\mathcal{P}}$ pairs of equations which we write as

$$\left[\mathbf{0} \quad \mathcal{P}_{\mathcal{A}} \quad \mathcal{P}_{\mathcal{B}} \quad \mathcal{P}_{\mathcal{A}}^T \quad \mathbf{0} \quad \mathcal{P}_{\mathcal{E}_3} \quad \mathcal{P}_{\mathcal{P}} \quad \mathcal{P}_u \quad \mathcal{P}_{\Omega} \right] \cdot \mathbf{x} = \mathcal{P}_K^*, \quad (6.74)$$

where each element corresponds to the $N_{\mathcal{P}}$ pairs of elements in equation (6.73) and \mathcal{P}_K^* corresponds to the $N_{\mathcal{P}}$ pairs of $K_j(\mathbf{x}_0) + 4\pi\mu u_j^{P_3}(\mathbf{x}_0)$. Equation (6.74) is only included in the linear system when the particle is in the branch channel.

To complete the linear system we require the discretisation of the force and torque equations which ensure that the particle remains force and torque free. We may write

down the zero force condition with reference to equation (3.33), which is

$$\mathbf{L}_{\mathcal{P}} \cdot \mathbf{F}^P = \mathbf{0}, \quad (6.75)$$

where $\mathbf{L}_{\mathcal{P}}$ is defined in equation (3.76). The zero torque condition is stated by (3.34), which is

$$\mathbf{T}_{\mathcal{P}} \cdot \mathbf{F}^P = 0, \quad (6.76)$$

where $\mathbf{T}_{\mathcal{P}}$ is defined in equation (3.78).

From the discretisations of the boundary integral equations, the pressure equations and the force and torque equations we form the linear system,

$$\begin{bmatrix} \mathcal{C}_{\mathcal{C}} & \mathcal{C}_{\mathcal{A}} & 0 & \mathcal{C}_{\mathcal{A}}^T & \mathcal{C}_{\mathcal{E}_2} & 0 & \mathcal{C}_{\mathcal{P}} & 0 & 0 \\ \mathcal{A}_{\mathcal{C}} & \mathcal{A}_{\mathcal{A}}^m & 0 & \mathcal{A}_{\mathcal{A}}^{m,T} & \mathcal{A}_{\mathcal{E}_2} & 0 & \mathcal{A}_{\mathcal{P}}^m & 0 & 0 \\ 0 & \mathcal{B}_{\mathcal{A}} & \mathcal{B}_{\mathcal{B}} & \mathcal{B}_{\mathcal{A}}^T & 0 & \mathcal{B}_{\mathcal{E}_3} & 0 & 0 & 0 \\ 0 & \mathcal{A}_{\mathcal{A}}^b & \mathcal{A}_{\mathcal{B}} & \mathcal{A}_{\mathcal{A}}^{b,T} & 0 & \mathcal{A}_{\mathcal{E}_3} & 0 & 0 & 0 \\ 0 & U_{\mathcal{A}}^{P_1} & 0 & -\mathbf{F}_{\mathcal{A}}^{P_1} & Q_1 & 0 & U_{\mathcal{P}}^{P_1} & 0 & 0 \\ 0 & -U_{\mathcal{A}}^{P_3} & 0 & -\mathbf{F}_{\mathcal{A}}^{P_3} & 0 & Q_3 & 0 & 0 & 0 \\ \mathcal{P}_{\mathcal{C}} & \mathcal{P}_{\mathcal{A}} & 0 & \mathcal{P}_{\mathcal{A}}^T & \mathcal{P}_{\mathcal{E}_2} & 0 & \mathcal{P}_{\mathcal{P}} & \mathcal{P}_u & \mathcal{P}_{\Omega} \\ 0 & 0 & 0 & 0 & 0 & 0 & \mathbf{L}_{\mathcal{P}} & 0 & 0 \\ 0 & 0 & 0 & 0 & 0 & 0 & \mathbf{T}_{\mathcal{P}} & 0 & 0 \end{bmatrix} \cdot \mathbf{x} = \begin{bmatrix} \mathcal{C}_I \\ \mathcal{A}_I \\ \mathcal{B}_K \\ \mathcal{A}_K \\ 0 \\ \psi \\ \mathcal{P}_I^* \\ 0 \\ 0 \end{bmatrix}, \quad (6.77)$$

when the particle is in the main channel. When the particle is in the branch channel we have

$$\begin{bmatrix} \mathcal{C}_{\mathcal{C}} & \mathcal{C}_{\mathcal{A}} & 0 & \mathcal{C}_{\mathcal{A}}^T & \mathcal{C}_{\mathcal{E}_2} & 0 & 0 & 0 & 0 \\ \mathcal{A}_{\mathcal{C}} & \mathcal{A}_{\mathcal{A}}^m & 0 & \mathcal{A}_{\mathcal{A}}^{m,T} & \mathcal{A}_{\mathcal{E}_2} & 0 & 0 & 0 & 0 \\ 0 & \mathcal{B}_{\mathcal{A}} & \mathcal{B}_{\mathcal{B}} & \mathcal{B}_{\mathcal{A}}^T & 0 & \mathcal{B}_{\mathcal{E}_3} & \mathcal{B}_{\mathcal{P}} & 0 & 0 \\ 0 & \mathcal{A}_{\mathcal{A}}^b & \mathcal{A}_{\mathcal{B}} & \mathcal{A}_{\mathcal{A}}^{b,T} & 0 & \mathcal{A}_{\mathcal{E}_3} & \mathcal{A}_{\mathcal{P}}^b & 0 & 0 \\ 0 & U_{\mathcal{A}}^{P_1} & 0 & -\mathbf{F}_{\mathcal{A}}^{P_1} & Q_1 & 0 & 0 & 0 & 0 \\ 0 & -U_{\mathcal{A}}^{P_3} & 0 & -\mathbf{F}_{\mathcal{A}}^{P_3} & 0 & Q_3 & U_{\mathcal{P}}^{P_3} & 0 & 0 \\ 0 & \mathcal{P}_{\mathcal{A}} & \mathcal{P}_{\mathcal{B}} & \mathcal{P}_{\mathcal{A}}^T & 0 & \mathcal{P}_{\mathcal{E}_3} & \mathcal{P}_{\mathcal{P}} & \mathcal{P}_u & \mathcal{P}_{\Omega} \\ 0 & 0 & 0 & 0 & 0 & 0 & \mathbf{L}_{\mathcal{P}} & 0 & 0 \\ 0 & 0 & 0 & 0 & 0 & 0 & \mathbf{T}_{\mathcal{P}} & 0 & 0 \end{bmatrix} \cdot \mathbf{x} = \begin{bmatrix} \mathcal{C}_I \\ \mathcal{A}_I \\ \mathcal{B}_K \\ \mathcal{A}_K \\ 0 \\ \psi \\ \mathcal{P}_K^* \\ 0 \\ 0 \end{bmatrix}. \quad (6.78)$$

We recover the linear system given in equation (5.121) from equations (6.77) and (6.78) by omitting the last three columns of the matrix and the last three rows from the matrix and the column vectors.

Finally we must add the discretisation of the deflation term to the appropriate submatrix to obtain a unique solution. The discretisation of the deflation term is

$$\begin{aligned} n_j(\mathbf{x}_0) \int_{\mathcal{P}} n_i f_i \, ds(\mathbf{x}) &\approx n_j(\mathbf{x}_0) \sum_{r=1}^{N_{\mathcal{P}}} n_{i,r} f_{i,r} l_r \\ &= n_j(\mathbf{x}_0) \mathbf{D}_{\mathcal{P}} \cdot \mathbf{F}_{\mathcal{P}}, \end{aligned} \quad (6.79)$$

where

$$\mathbf{D}_{\mathcal{P}} = \begin{bmatrix} n_{x,1} & n_{y,1} & \cdots & n_{x,N_{\mathcal{P}}} & n_{y,N_{\mathcal{P}}} \end{bmatrix}. \quad (6.80)$$

We add $n_j(\mathbf{x}_0) \mathbf{D}_{\mathcal{P}}$ to $\mathcal{C}_{\mathcal{P}}$, $\mathcal{A}_{\mathcal{P}}^n$ and $\mathcal{P}_{\mathcal{P}}$ in (6.77), and to $\mathcal{B}_{\mathcal{P}}$, $\mathcal{A}_{\mathcal{P}}^b$ and $\mathcal{P}_{\mathcal{P}}$ in (6.78).

The size of the ‘influence’ matrix in equations (6.77) and (6.78) is $(4N_{\mathcal{A}} + 2N_{\mathcal{B}} + 2N_{\mathcal{C}} + 2N_{\mathcal{P}} + 5) \times (4N_{\mathcal{A}} + 2N_{\mathcal{B}} + 2N_{\mathcal{C}} + 2N_{\mathcal{P}} + 5)$. In our simulations we took $N_{\mathcal{A}} = 200$, $N_{\mathcal{B}} = 400$, $N_{\mathcal{C}} = 800$ and $N_{\mathcal{P}} = 316$ for a particle of radius $d/2$. When we changed the size of the particle we altered the number of boundary elements to maintain a constant element length. We found this number of boundary elements to be an acceptable compromise between accuracy and calculation time. For example, when the number of the boundary elements was doubled the pressures at the exits changed by no more than 0.07% for a particle of radius $0.5d$ located at $\mathbf{x}_c/d = (6, 0)$ in a branching channel with $\alpha = \pi/2$ and $Q = 0.5$. The translational velocity changed by less than 0.02% and the rotational velocity changed by 0.3%. Once we had calculated the influence matrix and the vector of known values we solved the system using GMRES (e.g. Saad 2003). We used an iterative solver due to the size of the influence matrix and the fast execution speed of the iterative method. The computation time of the solution to the linear system increased by just over 4 times when the number of boundary elements was doubled. Although this is a significant increase, it should be noted that the iterative scheme was around 10 times faster than Gaussian elimination. A further time saving was made by starting the next iteration with the solution to the previous iteration. We can then calculate the disturbance velocity using either equation (6.40) or (6.45) depending on the location of the point. Addition of the pertinent Poiseuille velocity provides the total velocity at the point.

We move the particle using the translational and rotational velocities from the solution of the linear system. Once the particle has been moved the master linear system is rebuilt and resolved. To move the capsule we integrated the kinematic equation,

$$\frac{d\mathbf{x}_r}{dt} = \mathbf{u}(\mathbf{x}_r), \quad (6.81)$$

where \mathbf{x}_r is the position vector of the r^{th} capsule node and the values of $\mathbf{u}(\mathbf{x}_r)$ are obtained from equation (6.24). We used the second order Runge-Kutta method (e.g. Atkinson 1978) to integrate (6.81) where we took an initial time step of $0.01 d/U_0$. We found that using a smaller time step caused no significant change in the path taken by the particle. In chapter 3 we showed that the disturbance velocity decayed to less than 1% of its maximum value at a distance of 3 particle radii. Therefore we did not allow the distance

between the particle and the entrance or the exits to become less than this distance.

6.3 Validation

For the validation and the presented results we truncated the channels so that $l = 12d$ and $L = l/2$. Once again we found this truncation length sufficient for the disturbance velocity to decay and for the disturbance tractions to attain a steady value. Although the mathematical model is derived for a particle with an arbitrary shape, we restrict our attention to a circle of radius a , which is placed with its centroid at $\mathbf{x}_c = (x_c, y_c)$. In chapter 3 we only required y_c to parameterise the position, however now that the particle is free to move into the branch channel we require both coordinates. From the previous chapter we saw that the important parameters are the ratio of channel heights, $\delta = D/d$, the branch angle, α and the flux ratio, Q . We use $U_0^{P_1}$ as our velocity scale, d as our length scale and $\mu U_0^{P_1}/d$ as the scale for pressure and traction. In summary our parameter space is,

$$\rho = \frac{a}{d}, \quad (6.82)$$

$$\mathbf{x}_c = (x_c, y_c), \quad (6.83)$$

$$\delta = \frac{D}{d}, \quad (6.84)$$

together with α and Q . In this section and the results we only consider $\alpha = \pi/2$ and $D = d$.

As a check on the numerical implementation, we confirmed that the discretised form of the integral identities (1.3.34) and (1.3.31) were satisfied to within an acceptable tolerance. Our next check on the validity of the numerical simulation was the introduction of a small particle with $\rho = 0.01$ at several different locations throughout the channels where the flux ratio, $Q = 0.5$. A particle of this size should hardly affect the flow and so the results can be checked against those in the previous chapter, where we should obtain exit pressures very close to those for a fluid-filled branching channel. The capsule velocity should also be extremely close to the local fluid velocity. These checks help to validate the numerical code for the branching channel when it contains a particle. We placed the small particle at a distance of $2d$ from the entrance and the exits and on the centreline of the respective channel. The centroid locations were $(2, 0)d$, $(10, 0)d$ and $(6, -5)d$. For a fluid-filled branching channel the exit pressures were $p(\mathcal{E}_2) = -17.294 \mu U_0^{P_1}/d$ and $p(\mathcal{E}_3) = -18.227 \mu U_0^{P_1}/d$. For each simulation involving the small particle, we found $p(\mathcal{E}_2) = -17.292 \mu U_0^{P_1}/d$ and $p(\mathcal{E}_3) = -18.223 \mu U_0^{P_1}/d$, which represent an error of 0.01% and 0.02% respectively. For each particle we found the translational velocity to be within 0.1% of its expected value. We checked the velocity error at the entrance and exits for each particle location and found that the error was no more than 0.1% at \mathcal{E}_1 , 0.05% at \mathcal{E}_2 and 0.2% at \mathcal{E}_3 . We also place a particle with $\rho = 0.01$ at $(6, 0)d$ and obtained identical results for the exit pressures and the velocity error at the ends.

Now that we have checked the model against the fluid-filled branching channel, we check our model against the straight channel geometry of chapter 3. In the previous chapter we showed that the disturbance due to the branch entrance decayed rapidly as we moved away from the branch. Therefore we expect that a particle placed sufficiently ‘far’ from the branch entrance will translate with the same velocity as in the straight channel case. We placed a particle of radius $\rho = 0.5$ at each of the locations $(2, 0)d$, $(10, 0)d$ and $(6, -5)d$, and calculated the translational velocity of the particle. When the particle was placed at $(2, 0)d$ it translated with velocity $0.889 U_0^{P_1} \mathbf{i}$, whereas in a straight channel the speed was $0.888 U_0^{P_1}$. Close to \mathcal{E}_2 we found that the particle’s velocity was $0.444 U_0^{P_1} \mathbf{i}$ which is the expected value since $Q = 0.5$. For the particle close to \mathcal{E}_3 we expect the translational velocity to be $-0.444 U_0^{P_1} \mathbf{j}$, where we computed $-0.445 U_0^{P_1} \mathbf{i}$. In each case the velocity error at the nearest entrance or exit was no more than 0.1%.

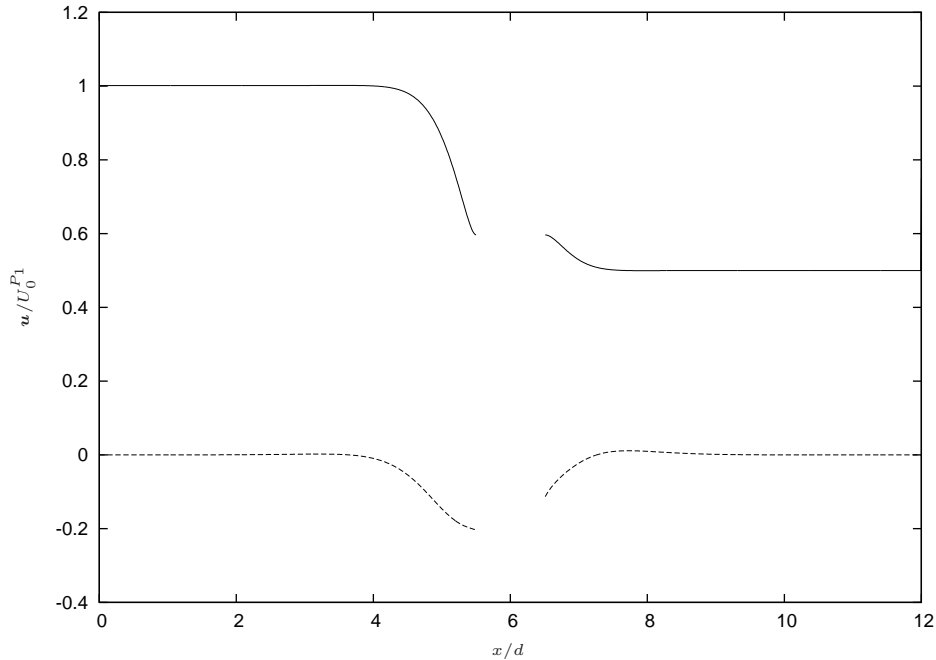
As in previous chapters we validated the numerical solution by comparing the solution obtained for a reference configuration with the solution for configurations with twice as many boundary elements and longer channels. The reference configuration had $l = 12d$, $L = l/2$, $\alpha = \pi/2$, $D = d$ and a particle of radius $d/2$ located at $(l/2, 0)d$. We found excellent agreement in all cases. For example, the velocities and exit pressures were all within 0.3% of the values for the reference configuration.

Finally to illustrate the decay of the velocity in the main and branch channels, we place a particle of radius $\rho = 0.5$ at $(6, 0)d$ and calculate the velocity along the centreline of the main channel. We also place a particle of the same size in the branch channel at $(6, -2)d$ and compute the velocity along the centreline of the branch channel. The velocity components are shown in figures 6.2 (a) and 6.2 (b). The gap in both profiles corresponds to the particle location where the velocity was not calculated. In both figures we can see the velocity disturbance decaying rapidly as we move away from the particle towards the entrance or the exits. The error in the velocity is no more than 0.2% at any one of \mathcal{E}_1 , \mathcal{E}_2 or \mathcal{E}_3 .

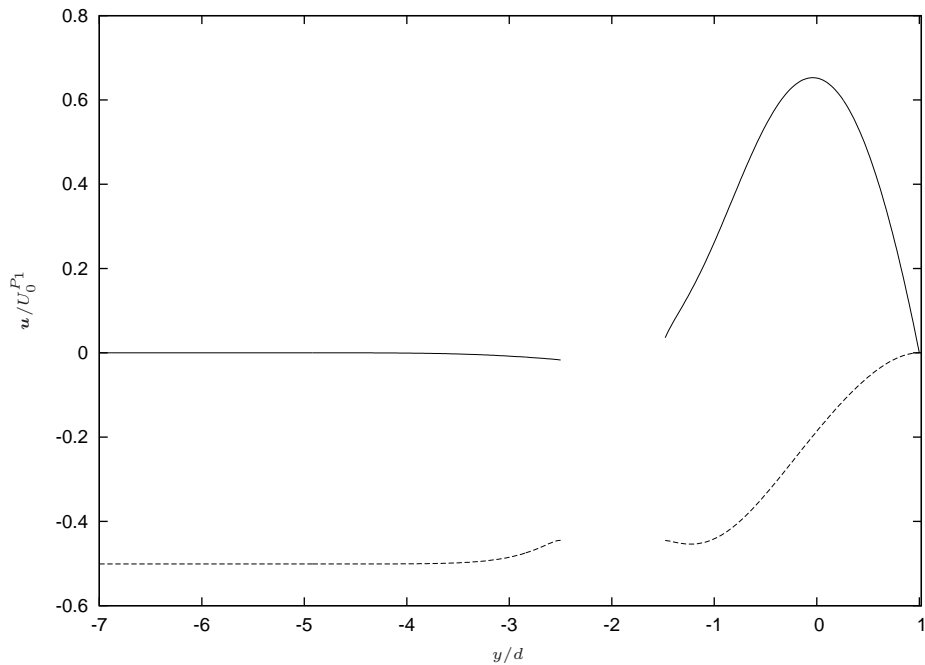
We have therefore satisfied ourselves that the numerical model for a rigid particle in a branching channel flow is performing as per our assumptions. However we have not discussed the motion of a particle, and in particular the deformation of \mathcal{A} when the particle migrates into the branch channel. In the next section we look at several configurations for the deformed notional boundary and select a method by which we will deform the notional boundary during a simulation.

6.4 Deformation of the notional boundary

When the particle moves from the main channel into the branch channel the shape of the notional boundary that separates the main channel from the branch channel is deformed to facilitate the transition. A straight dividing boundary is the default or reference configuration. When a particle translates along the channel and approaches \mathcal{A} , the notional boundary will deform. However we wish to deform \mathcal{A} in such a way that we maintain the accuracy of the numerical solution. We investigated four shapes for \mathcal{A} :



(a) x (—) and y (---) components of velocity along the main channel centreline containing a particle of radius $\rho = 0.5$ and with $\mathbf{x}_c/d = (6, 0)$.



(b) x (—) and y (---) components of velocity along the main channel centreline containing a particle of radius $\rho = 0.5$ and with $\mathbf{x}_c/d = (6, -2)$.

Figure 6.2 : Velocity profiles in a channel with $D = d$, $\alpha = \pi/2$ and $Q = 0.5$.

- i. A ‘goal’ shape with vertical straight lines going in the positive y -direction from the corners of the branch entrance to the centreline of the main channel, which were then connected by a horizontal straight line.
- ii. A ‘V’ shape with straight lines leaving the corners of the branch entrance and meeting at the intersection of the branch channel centreline and $y = -2d$.
- iii. Keeping \mathcal{A} in its reference configuration as much as possible and only deforming \mathcal{A} under the particle so that the shape of the deformed portion of \mathcal{A} traces the particle shape.
- iv. Keeping \mathcal{A} in its reference configuration as much as possible and deforming the boundary over the particle so that the shape of the deformed portion of \mathcal{A} traces the particle shape.

In the last two the minimum distance between \mathcal{A} and the particle is $0.1d$. We found that this distance provides sufficient separation between the boundaries of \mathcal{A} and \mathcal{P} such that the integral identities of Stokes flow given in equations (1.3.34) and (1.3.31) are satisfied to within a satisfactory numerical tolerance.

To quantify the differences between the configurations we placed a particle of radius $\rho = 0.2$ in a branching channel with $\alpha = \pi/2$ and $Q = 0.5$. To place the particle above, on and below the reference configuration we set $\mathbf{x}_c/d = (6.65, -0.795)$, $\mathbf{x}_c/d = (6.65, -1)$ and $\mathbf{x}_c/d = (6.65, -1.205)$ respectively. All of the configurations are shown in figures 6.3, 6.4 and 6.5 for the particle in the three locations. The only parameters which varied between the figures are the location of the centroid and the number of boundary elements on \mathcal{A} , where we increased the number of elements on the deformed \mathcal{A} to maintain a constant element length on \mathcal{A} .

We calculated the particle’s instantaneous translational velocity together with the exit pressures at \mathcal{E}_2 and \mathcal{E}_3 for each configuration. The calculated values are shown in table 6.1. The units of velocity and pressure are $U_0^{P_1}$ and $\mu U_0^{P_1}/d$ respectively. In the table ‘not applicable’ refers to the fact that \mathcal{A} would intersect the particle boundary. The velocity and the pressures should be identical for each of the particle positions, and any discrepancies should be due to inaccuracies in the numerical solution arising from the different shapes of \mathcal{A} . As we can see from the table, although there are differences between the particle’s velocity and the exit pressures for the different configurations, they are very minor.

In the case when the particle is above and close to either corner of the branch entrance the ‘goal’ shaped configuration may not be appropriate. Similarly the ‘V’ shaped boundary could become compromised for a particle travelling close to the wall of the branch channel. Therefore we choose to deform \mathcal{A} using shape (iii) as the particle draws near. If the particle moves further into the branch we will continue to deform \mathcal{A} around the particle such that no boundary element of \mathcal{A} is closer to the particle than our pre-defined minimum value. When the particle’s centroid crosses $y = -d$ we will flip \mathcal{A} so that the particle moves into the branch channel and the shape of \mathcal{A} matches that of shape (iv). As the particle moves further into the branch we will continue to deform \mathcal{A} until the particle

Particle centroid	Configuration of \mathcal{A}	Particle velocity	$p(\mathcal{E}_2)$	$p(\mathcal{E}_3)$
$(6.65, -0.795)d$	Straight	$(0.19819, -0.13913)$	-17.600	-18.513
	Shape (i)	$(0.19819, -0.13900)$	-17.596	-18.504
	Shape (ii)	$(0.19809, -0.13899)$	-17.597	-18.505
	Shape (iii)	$(0.19817, -0.13913)$	-17.600	-18.513
	Shape (iv)	$(0.19823, -0.13935)$	-17.604	-18.523
$(6.65, -1)d$	Straight	Not applicable		
	Shape (i)	$(0.06712, -0.18359)$	-17.605	-18.465
	Shape (ii)	$(0.06700, -0.18393)$	-17.615	-18.484
	Shape (iii)	$(0.06704, -0.18416)$	-17.619	-18.496
	Shape (iv)	$(0.06705, -0.18423)$	-17.620	-18.497
$(6.65, -1.205)d$	Straight	$(0.02184, -0.22889)$	-17.440	-18.455
	Shape (i)	$(0.02203, -0.22545)$	-17.364	-18.283
	Shape (ii)	Not applicable		
	Shape (iii)	$(0.02187, -0.22883)$	-17.439	-18.452
	Shape (iv)	$(0.02185, -0.22885)$	-17.440	-18.453

Table 6.1 : Particle velocity and exit pressures for different configurations of \mathcal{A} in a branching channel containing a particle with $\rho = 0.2$ positioned at three different locations.

is wholly below $y = -d$ (plus some tolerance) whereupon we will change \mathcal{A} back into its reference configuration. The evolution of the deformation of the notional boundary is shown in figure 6.6.

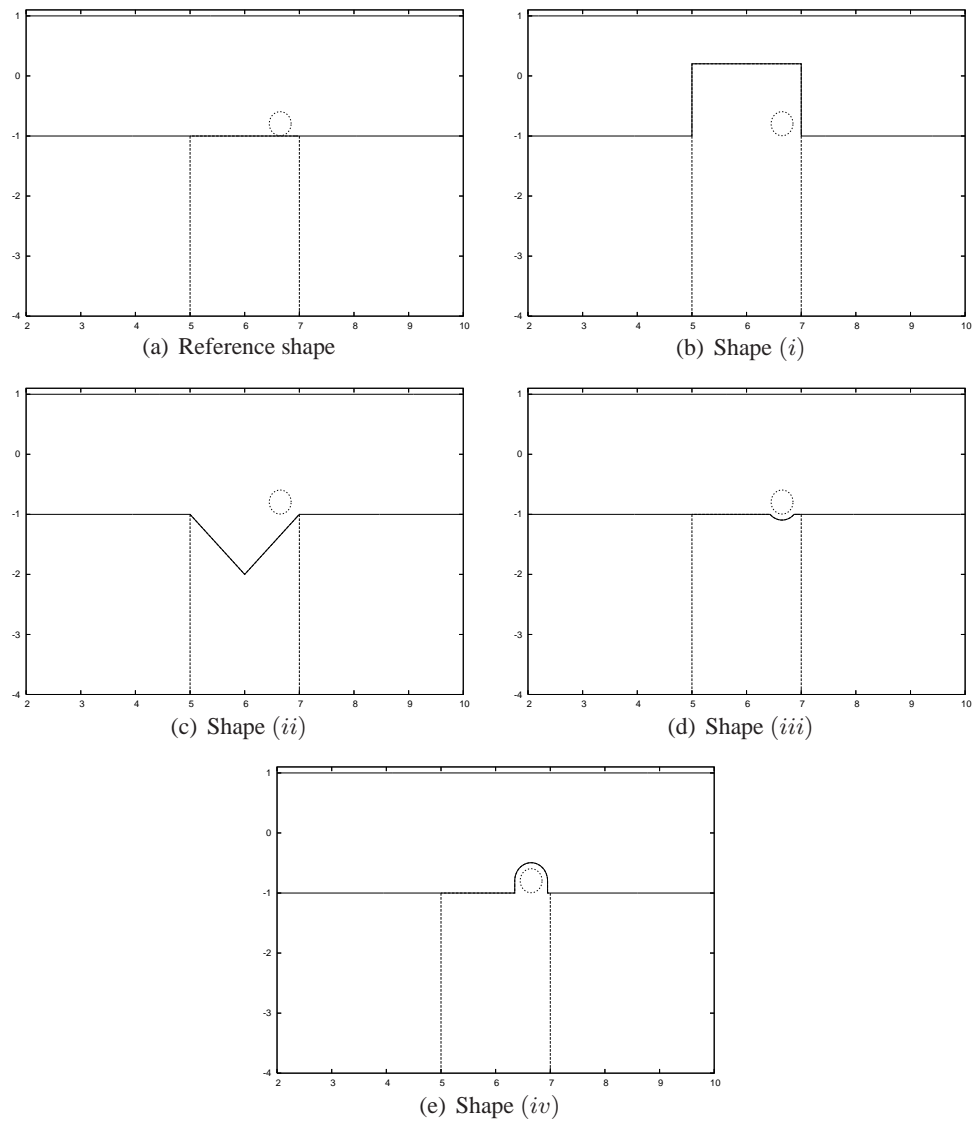


Figure 6.3 : Section of the flow domain showing the notional boundary configurations for a particle of radius $\rho = 0.2$ and centroid at $\mathbf{x}_c/d = (6.65, -0.795)$.

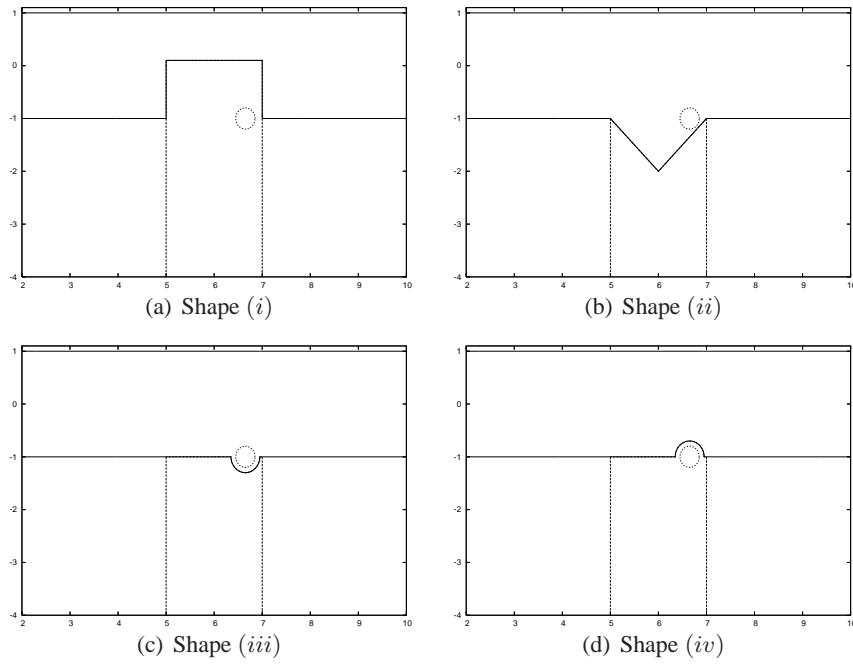


Figure 6.4 : Section of the flow domain showing the notional boundary configurations for a particle of radius $\rho = 0.2$ and centroid at $\mathbf{x}_c/d = (6.65, -1)$.

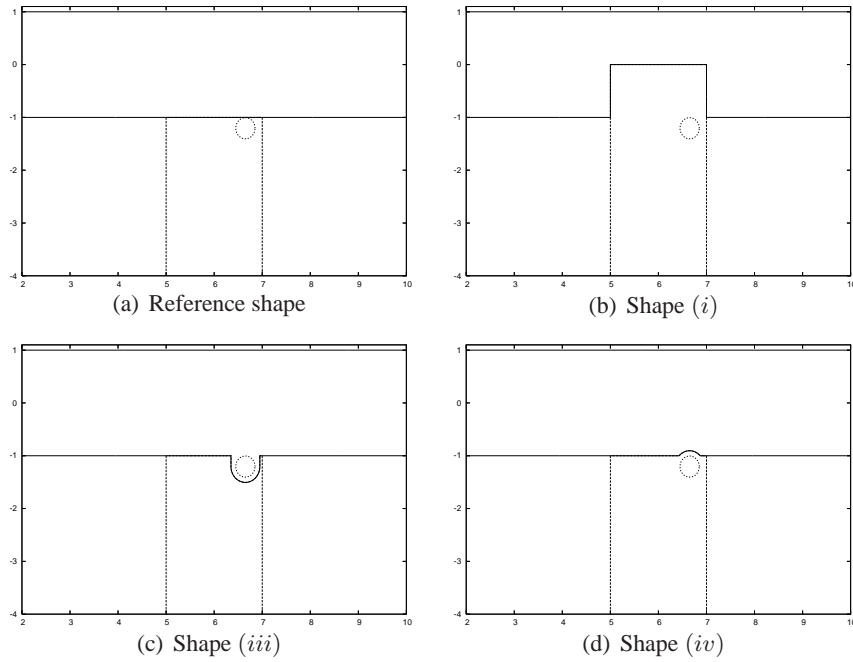


Figure 6.5 : Section of the flow domain showing the notional boundary configurations for a particle of radius $\rho = 0.2$ and centroid at $\mathbf{x}_c/d = (6.65, -1.205)$.

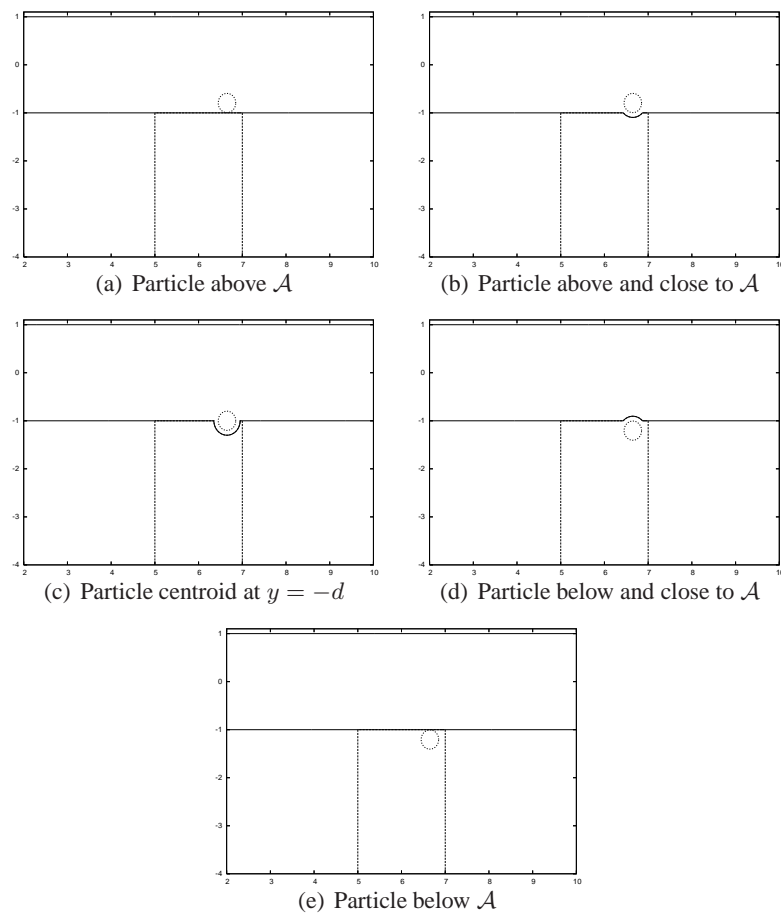


Figure 6.6 : Dividing boundary configurations during particle migration into the branch channel.

6.5 Results

In our results we restrict our attention to a particle of size $\rho = 0.5$ which is initially located at $\mathbf{x}_c/d = (2, 0)$ in a branching channel with $D = d$ and $\alpha = \pi/2$. We ran three simulations with $Q = 0.1, 0.5$ and 0.9 where we expect the particle in the $Q = 0.1$ simulation to pass into the branch channel thereby deforming the notional boundary in the way described in the previous section. We do not exhaustively test the parameter space here because our focus is on testing the algorithm by which we deform \mathcal{A} in preparation for the next chapter where we will more fully explore the effect of the parameters on a flexible capsule in a branching channel.

In figure 6.7 we plot the trajectories of the centroids of the capsules for the different flux ratios. When $Q = 0.1$ the particle migrates into the branch channel as expected and we can see that the particle only travels a short distance in the branch channel before it is travelling parallel to the walls. This is to be expected from the results of the previous chapter where we showed that the disturbance due to the branch entrance decayed within $2d$ of the branch entrance, as measured along the centreline. The particle then travels along the branch channel towards \mathcal{E}_3 slightly to the right of the branch channel's centreline. When we set the flux ratio to $Q = 0.5$, the particle travels towards the right-hand corner of the branch entrance. The simulations terminate when part of the particle boundary moves outside of the flow domain due to the constant time-step used in the numerical integration method employed to move the particle. Brenner (1961) showed that a three-dimensional particle settling towards an infinite plane only does so after an infinite time. It seems plausible that the same result applies in two-dimensions since the fluid can now only escape in two directions. However we must take the sharp corner of the right-hand entrance to the branch channel into consideration. Cawthorn and Balmforth (2010) consider the lubrication flow caused by a wedge falling under gravity towards a plane surface in a two-dimensional Stokes flow and find that contact occurs in finite time. In light of Cawthorn and Balmforth (2010) we may consider the particle to be a locally smooth surface and the corner of the branch entrance to be a wedge by changing the reference frame, and surmise that the particle may indeed touch the corner. When $Q = 0.9$ the particle travels towards the exit \mathcal{E}_2 and is dragged down towards the branch channel when it is above the branch entrance. Once the particle has passed the branch entrance it moves parallel to the walls of the main channel, slightly below the centreline due to the deflection experienced as it passed over the branch entrance.

In figure 6.8 we show the evolution of the normalised exit pressures at \mathcal{E}_2 and \mathcal{E}_3 as the particle travels along the channel. We normalise the pressure by dividing the varying pressure by the constant exit pressures obtained for the same configuration but without the particle, and label the normalised pressures as $\hat{p}(\mathcal{E}_2)$ and $\hat{p}(\mathcal{E}_3)$. The evolution of the normalised exit pressures for the $Q = 0.1$ case are shown in figure 6.8 (a). For reference, the pressures at \mathcal{E}_2 and \mathcal{E}_3 are $-12.70 \mu U_0^{P_1}/d$ and $-23.59 \mu U_0^{P_1}/d$ respectively. At the start of the simulation, when the particle is located at $\mathbf{x}_c/d = (2, 0)$, the magnitude of the pressures at \mathcal{E}_2 and \mathcal{E}_3 have increased by 2.5% and 1.3% respectively, over the pressures

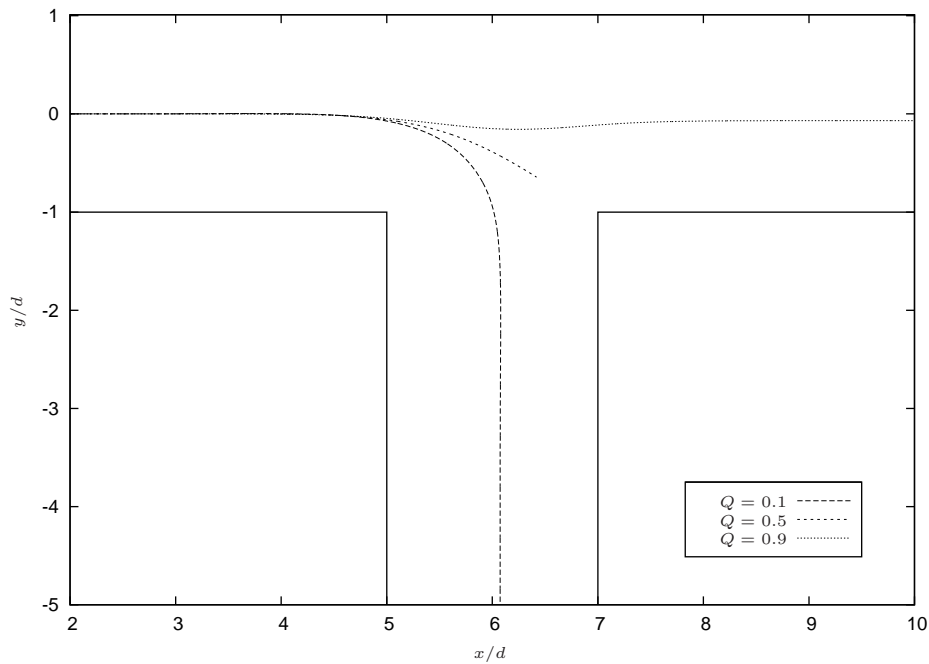


Figure 6.7 : A portion of the flow domain showing the centroid trajectories for a rigid particle with $\rho = 0.5$, $\alpha = \pi/2$ initially located at $\mathbf{x}_c/d = (2, 0)$ for $Q = 0.1, 0.5$ and 0.9 .

for a fluid-filled branching channel. The larger increase in the magnitude of the exit pressure at \mathcal{E}_2 is due to both pressures' magnitude increasing by approximately the same amount and the exit pressure at \mathcal{E}_3 being almost twice the pressure at \mathcal{E}_2 . The maximum increase in $\hat{p}(\mathcal{E}_2)$ is 7.3% which occurs at $t = 5.04 d/U_0^{P_1}$ when the particle's centroid is located at $\mathbf{x}_c/d = (5.98, -0.87)$ and just over 40% of the particle's area is below the branch entrance at $y/d = -1$. As the particle moves further into the branch channel the magnitude of the pressure at \mathcal{E}_2 reduces until it is slightly less than the pressure when a particle is not present, implying that the disturbance caused by the particle in the branch channel 'helps' the fluid in the main channel to maintain the flux rate at \mathcal{E}_2 . The maximum increase in $\hat{p}(\mathcal{E}_3)$ is 8.7% which occurs at the earlier time of $t = 4.35 d/U_0^{P_1}$ when the particle's centroid is located at $\mathbf{x}_c/d = (5.70, -0.41)$ and the particle is wholly in the main channel.

The normalised pressures for the $Q = 0.5$ simulation are shown in figure 6.8 (b). In a fluid-filled branching channel with the same parameters the exit pressures are equal to $-17.29 \mu U_0^{P_1}/d$ at \mathcal{E}_2 and $-18.23 \mu U_0^{P_1}/d$ at \mathcal{E}_3 . At the start of the simulation the magnitude of both of the exit pressures are 1.8% more than when the particle is absent. As the simulation progresses, the magnitude of the pressures increases until the simulation terminates when the particle is incident upon the right-hand corner of the branch entrance. The normalised pressure at \mathcal{E}_3 increases more rapidly after $t = 3 d/U_0^{P_1}$ but as the particle gets closer to the corner, the normalised pressure increases become almost equal.

The evolution of the normalised disturbance pressure for the case when $Q = 0.9$ is shown in figure 6.8 (c), where the particle travels to the exit of the main channel and is deflected slightly from its path as it passes close to the branch entrance. For a branching

channel without a particle the exit pressures are $-21.90 \mu U_0^{P_1}/d$ and $-12.86 \mu U_0^{P_1}/d$ at \mathcal{E}_2 and \mathcal{E}_3 respectively. The increase to the normalised exit pressure of the main channel remains between 1% and 2% for the duration of the simulation, with the increase at the start and end equal to 1.5%. The normalised exit pressure at \mathcal{E}_3 increases to a maximum of 4.7% at $t = 4.06 d/U_0^{P_1}$ when its centroid is at $\mathbf{x}_c/d = (5.56, -0.11)$, before decreasing to unity as the particle continues its journey to \mathcal{E}_2 .

Finally we will show the evolution of the particle's velocities for the three simulations. In figure 6.9 (a) we plot the magnitude of the translational velocity for the particle over the course of each simulation. The horizontal dotted line at $|\mathbf{u}| = 0.888 U_0^{P_1}$ corresponds to the translational velocity of a particle located on the centreline of a straight channel. For a particle offset by $0.07 d$ from the centreline, as in the final position for the $Q = 0.1$ and $Q = 0.9$ cases, the translational velocity in a straight channel is $0.883 U_0^{P_1}$. Therefore we also include a horizontal dotted line at 90% of this value, which is $0.795 U_0^{P_1}$, to indicate the expected velocity as the particle approaches \mathcal{E}_2 or \mathcal{E}_3 , where the 90% reflects the flux ratio. At the start of each simulation we can see that the magnitude of the particle's velocity matches the predicted value of $0.888 U_0^{P_1}$. When $Q = 0.1$ or $Q = 0.9$ the velocity is equal to the expected value of $0.795 U_0^{P_1}$ as the particle approaches the exit. It is interesting to note that the velocity attains a lower value in the $Q = 0.9$ case than in the $Q = 0.1$ case, and it also takes longer to achieve its downstream steady velocity. This may be explained by the distance each particle has to travel from the point where the centroid lies at approximately $(5, 0)d$. When $Q = 0.9$ the particle has to travel $2d$ to pass over the bifurcation. However, when $Q = 0.1$ the particle has to travel a shorter distance of approximately, $\pi d/2$, thereby allowing the particle to attain its unidirectional motion sooner. In all simulations the magnitude of the velocity falls below the lower of the predicted downstream steady velocities. Since the time-stepping method moved the particle out of the flow domain when $Q = 0.5$, we were unfortunately unable to compare the decrease in the particle's velocity with that predicted by lubrication theory. The rotational velocity of the particle is shown in figure 6.9 (b) for each of the simulations, where a positive value indicates anti-clockwise rotation. The rotational velocity in the $Q = 0.5$ and $Q = 0.9$ simulations fluctuates until either the simulation terminates as in the former, or it attains a constant rate of rotation as in the latter. In the simulation with $Q = 0.1$ the particle attains a maximum rotational speed of $-0.287 U_0^{P_1}/d$ at $t = 4.2 d/U_0^{P_1}$, which is close to the time where the disturbance pressure at \mathcal{E}_3 attains its maximum. From inspection of the exit pressure at \mathcal{E}_3 in figure 6.8 (a) and the rotational velocity in figure 6.9 (b) for the case $Q = 0.1$, we can see that the peak in the rotation velocity coincides with the peak in π_3 . However it is uncertain whether the peak in the disturbance pressure is caused by the relatively quick rotational velocity or the particle's location. The particle in the simulation with $Q = 0.5$ slows as it approaches the corner.

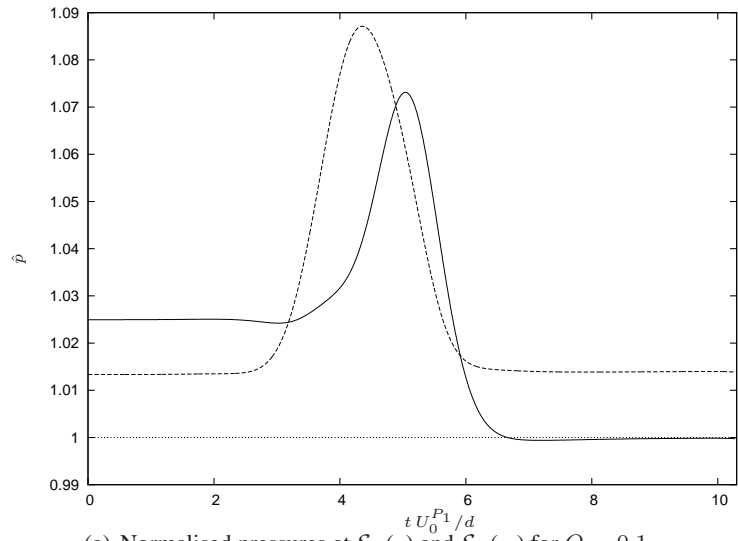
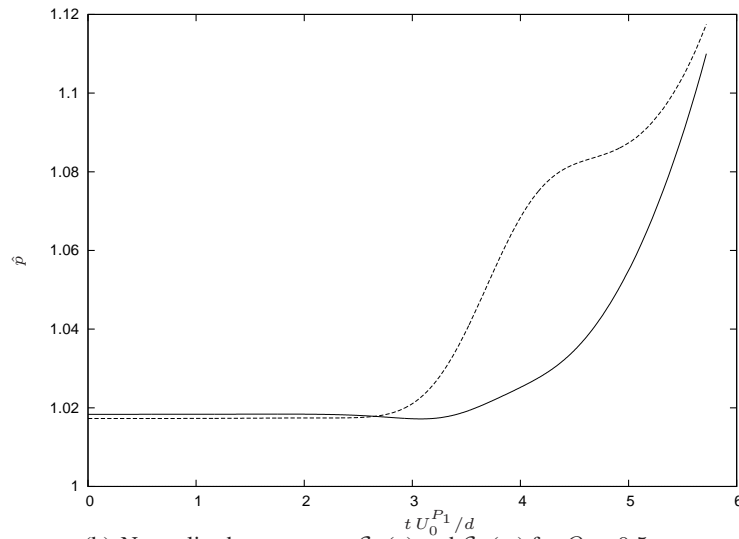
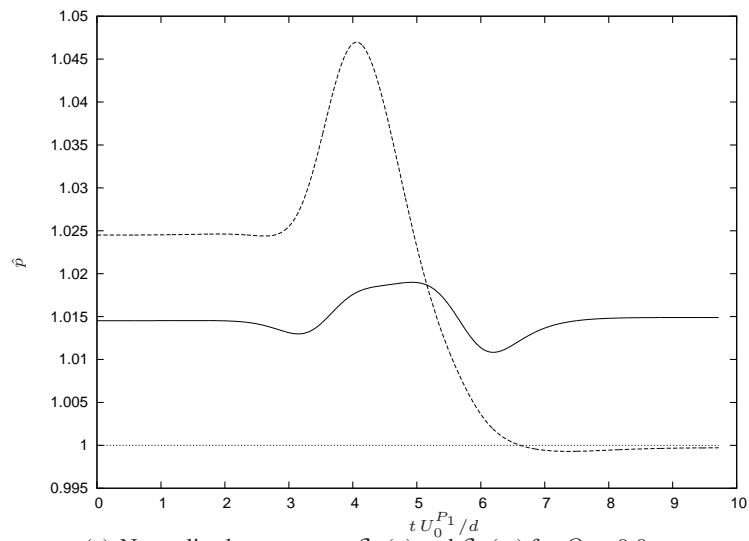
(a) Normalised pressures at \mathcal{E}_2 (—) and \mathcal{E}_3 (---) for $Q = 0.1$.(b) Normalised pressures at \mathcal{E}_2 (—) and \mathcal{E}_3 (---) for $Q = 0.5$.(c) Normalised pressures at \mathcal{E}_2 (—) and \mathcal{E}_3 (---) for $Q = 0.9$.

Figure 6.8 : Normalised pressures for a rigid particle with $\rho = 0.5$, $\alpha = \pi/2$ initially located at $\mathbf{x}_c/d = (2, 0)$ for $Q = 0.1, 0.5$ and 0.9 .

6.6 Discussion

In this chapter we have considered a pressure-driven flow in a channel with a side branch which contains a rigid neutrally buoyant particle. We prescribed the flux rates at the entrance and exits. We formulated the problem using the boundary integral method and found its solution numerically using the boundary element method. The solution provides the tractions on the particle boundary, the disturbance tractions on the channel walls and the pressure drops between the entrance and both exits.

We have tested the numerical model for a branching channel containing a rigid particle and obtained satisfactory accuracy. For a small particle we obtained the same results as for a fluid-filled branching channel. Far from the branch entrance we obtained results were in agreement with the results for a rigid particle in a straight channel, which confirms our

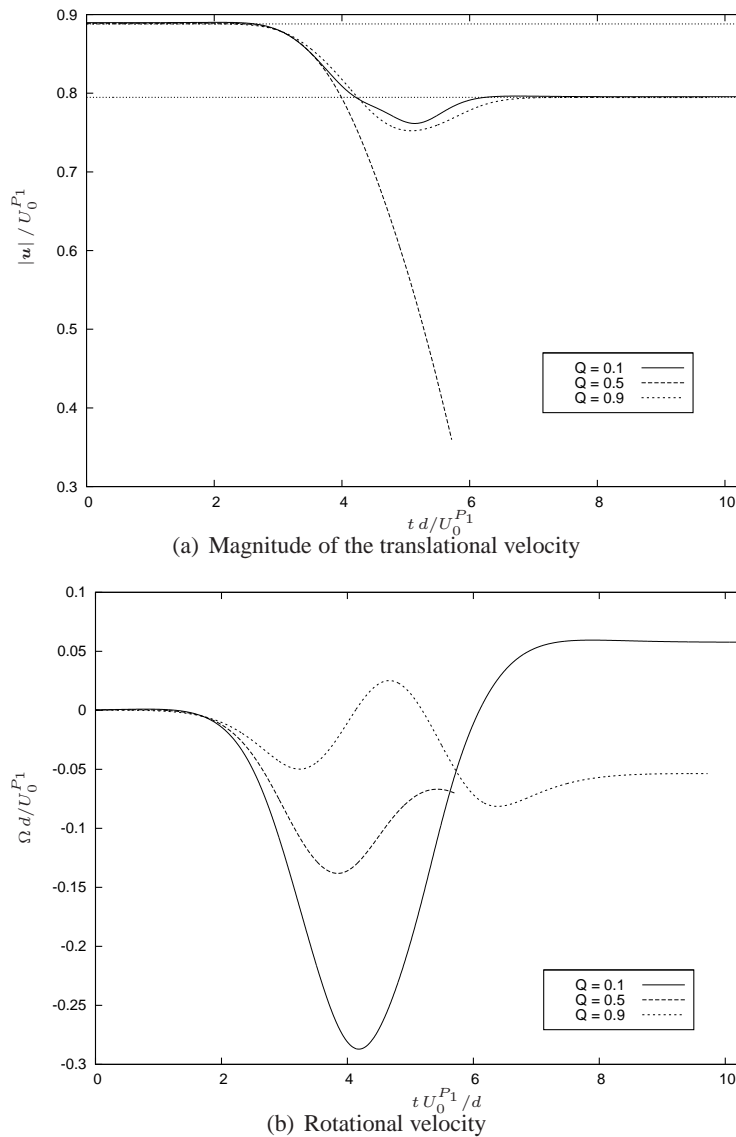


Figure 6.9 : Magnitude of the translational velocity and the rotational velocity for a particle with $\rho = 0.5$, $\alpha = \pi/2$ and initially located at $\mathbf{x}_c/d = (2, 0)$ for $Q = 0.1, 0.5$ and 0.9 .

assumption that the disturbance due to the branch entrance decays as we move towards the entrance or exits. We have discussed various methods of deforming the notional boundary to allow the particle to migrate into the branch channel, and showed that the pressures and particle velocities vary only slightly between the different configurations. To allow the particle to pass close to the corners of the branch entrance we chose to deform \mathcal{A} so that it remains mostly straight except in the vicinity of the particle where the notional boundary is deformed to closely fit the particle.

We performed simulations which allowed a particle to translate along the channel to both exits and showed that the results when the particle was close to the entrance or the exits match the straight channel model. We showed how the exit pressures fluctuate during the course of each simulation and found that the maximum pressure at \mathcal{E}_3 occurs at roughly the same time as the particle experiences the greatest angular velocity. We also found that the magnitude of the translational velocity falls below the entrance or exit speed when the particle is close to the branch entrance. Once the particle has passed the branch entrance, the particle speed increases until it attains the value predicted by the straight channel model. Therefore the disturbance effect of the branch entrance is such that it slows the particle and in the case when the particle moves into the branch considerably increases its angular velocity. When we set the flux ratio such that half the fluid enters each downstream channel, the particle moves onto the sharp right-hand corner of the branch entrance and the simulation terminates.

Chapter 7

The motion of a flexible capsule through a bifurcation

In the previous chapter we studied the motion of a rigid particle through a bifurcation. In this chapter we replace the rigid particle with an elastic capsule and examine the motion of the capsule and its deformation under various flow conditions. The derivation of the governing equations brings together the analysis in chapters 4 and 5 regarding the deformation of a flexible capsule in a straight channel and the fluid flow through a bifurcation respectively. The branch entrance and the capsule cause a disturbance to the upstream and downstream unidirectional flows which we describe mathematically using the boundary integral method. The governing equations describe the velocity field throughout the flow domain together with the velocity of the capsule boundary and the pressures at the exits to the computational domain. Application of the boundary element method to the governing equations yields a set of discretised equations which may be written as a linear matrix system and solved by standard methods.

7.1 Problem statement

We consider the motion of a fluid with viscosity μ in an infinite straight-walled channel of width $2d$. A branch channel of width $2D$ is attached to the lower wall of the channel at an angle α . A disturbance to the upstream and downstream flows is caused by the branch entrance and by the presence of a deformable capsule, which moves with the flow. The geometry is shown in figure 7.1 and comprises the walls of the main channel, \mathcal{C} , the walls of the branch channel, \mathcal{B} , the capsule \mathcal{P} and a notional boundary, \mathcal{A} , which separates the main channel from the branch channel. All unit normal vectors, \mathbf{n} , point into the fluid, and the unit normal on \mathcal{A} points into the fluid of the main channel. We assume that the disturbance caused by the capsule and the branch entrance decays upstream and downstream from the source of the disturbance so that the flow far from the disturbance is described by classical unidirectional Poiseuille flow. Since we will require channels of finite length in the numerical method, we truncate the channels so that the main channel has length l and the branch channel has length L , as measured along their centrelines and

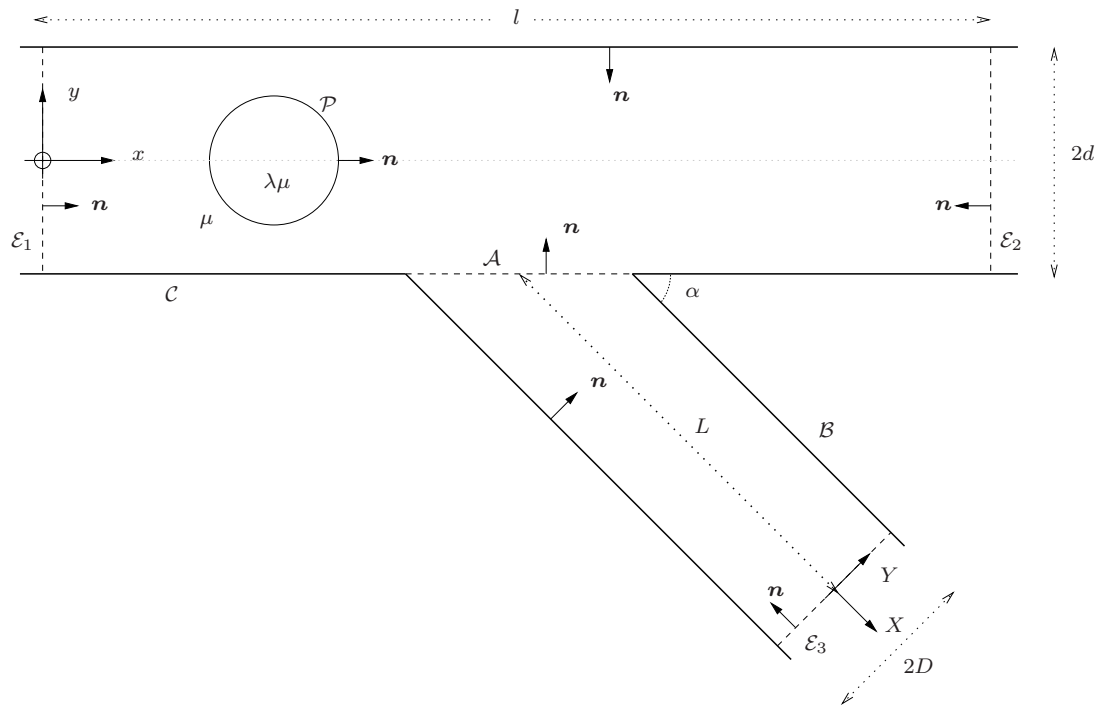


Figure 7.1 : A straight-walled branching channel which contains a fluid of viscosity μ and a deformable capsule containing a fluid of viscosity $\lambda\mu$.

illustrated in figure 7.1. We position the branch channel so that its centreline intersects the mid-point of the lower wall of the main channel, $(l/2, -d)$. We label the entrance of the main channel as \mathcal{E}_1 , the exit of the main channel as \mathcal{E}_2 and the exit of the branch channel as \mathcal{E}_3 . The entrance and exit in the main channel are located at $x = 0$ and $x = l$ respectively. In the branch channel we introduce local coordinates, (X, Y) , which have their origin on the centreline at \mathcal{E}_3 as indicated in figure 7.1. The mappings between the (x, y) coordinates of the main channel and the (X, Y) coordinates of the branch channel are given in equation (5.1) on page 114. The unit vectors in the main channel are i and j , which are mapped to their branch channel equivalents i' and j' using equation (5.3). The particle and the branch entrance disturb the flow but at \mathcal{E}_1 , \mathcal{E}_2 and \mathcal{E}_3 we assume that the disturbance has decayed and the flow has settled to Poiseuille flow, characterised by the streamwise flux rate at the pertinent entrance or exit. As in the previous two chapters we label the flux rate Q_r at each of \mathcal{E}_r where $r = 1, 2$ or 3 . The equations for the fluxes and the Poiseuille velocities are given in equations (5.4)–(5.11) of chapter 5. We label the ambient fluid in the channel as fluid 1 and the fluid inside the capsule as fluid 2.

Our aim is to compute the velocity field throughout the flow domain, the velocity field on the capsule boundary and the additional pressure drop between the entrance and both exits due to disturbance caused by the branch entrance and the capsule. To calculate the additional pressure drop due to the capsule we may compare the pressure drop calculated here with the value obtained in chapter 5 for a fluid-filled branching channel under the same flow parameters. We assume that the Reynolds number of the flow is very small so that the flow in the channels may be described using the linear equations of Stokes flow

given in equation (1.3.4). In the usual way, we decompose the velocity field, $\mathbf{u}^{(1)}$, and the traction field, $\mathbf{f}^{(1)}$, into background Poiseuille and disturbance components, which we identify using the superscripts P_r and D_r respectively, and where the r indicates to which of \mathcal{E}_r the quantity applies. The superscript (1) on the velocity and traction indicates that the quantity applies to the ambient fluid in the channel. The decompositions in the main and branch channels are given by,

$$\mathbf{u} = \mathbf{u}^{P_1} + \mathbf{u}^{D_1} = \mathbf{u}^{P_2} + \mathbf{u}^{D_2}, \quad (7.1)$$

$$\mathbf{f} = \mathbf{f}^{P_1} + \mathbf{f}^{D_1} = \mathbf{f}^{P_2} + \mathbf{f}^{D_2}, \quad (7.2)$$

$$\mathbf{u} = \mathbf{u}^{P_3} + \mathbf{u}^{D_3}, \quad (7.3)$$

$$\mathbf{f} = \mathbf{f}^{P_3} + \mathbf{f}^{D_3}, \quad (7.4)$$

where the first pair of equations apply in the main channel and the second pair apply in the branch channel. On the notional boundary, \mathcal{A} , we impose continuity of the velocity and traction fields such that

$$\mathbf{u} = \mathbf{u}^{P_1} + \mathbf{u}^{D_1} = \mathbf{u}^{P_2} + \mathbf{u}^{D_2} = \mathbf{u}^{P_3} + \mathbf{u}^{D_3} \quad (7.5)$$

$$\mathbf{f} = \mathbf{f}^{P_1} + \mathbf{f}^{D_1} = \mathbf{f}^{P_2} + \mathbf{f}^{D_2} = \mathbf{f}^{P_3} + \mathbf{f}^{D_3}, \quad (7.6)$$

where we define all tractions with reference to a unit normal vector which points into the main channel. On the channel walls we have $\mathbf{u} = \mathbf{0}$ by no-slip and no-penetration. On the walls of the main channel, \mathcal{C} , we have

$$\mathbf{u}^{P_1} = \mathbf{u}^{D_1} = \mathbf{u}^{P_2} = \mathbf{u}^{D_2} = \mathbf{0}, \quad (7.7)$$

and on the walls of the branch channel, \mathcal{B} , we have

$$\mathbf{u}^{P_3} = \mathbf{u}^{D_3} = \mathbf{0}. \quad (7.8)$$

In chapter 4 we discussed the decay of the disturbance velocity due to a flexible capsule in a straight channel. We cited the work of Sugihara-Seki (1993), Gaver and Kute (1998), Mortazavi and Tryggvason (2000) and Cortez (2002) and showed that the disturbance velocity in our calculations did indeed decay rapidly as we moved away from the capsule. Typically we found that the disturbance velocity had decayed to 1% of its maximum value at a distance of three capsule radii from the capsule centroid. The effect of the branch entrance was calculated in chapter 5 and we showed that the flow velocity is within 1% of its appropriate Poiseuille velocity at a distance of $3d$ from the branch entrance. Therefore based on the previously cited works, and the evidence in chapters 4 and 5, we assume

$$\mathbf{u}^{D_1} = \mathbf{0}, \text{ and } \mathbf{f}^{D_1} = -\pi_1 \mathbf{n} \text{ at } \mathcal{E}_1, \quad (7.9)$$

$$\mathbf{u}^{D_2} = \mathbf{0}, \text{ and } \mathbf{f}^{D_2} = -\pi_2 \mathbf{n} \text{ at } \mathcal{E}_2, \quad \text{and} \quad (7.10)$$

$$\mathbf{u}^{D_3} = \mathbf{0}, \text{ and } \mathbf{f}^{D_3} = -\pi_3 \mathbf{n} \text{ at } \mathcal{E}_3 \quad (7.11)$$

where π_1 , π_2 and π_3 are the constant disturbance pressures at the entrance, the exit to the main channel and the exit to the branch channel respectively. Since we are interested in the pressure drop between the entrance and the exits we set $\pi_1 = 0$ without loss of generality. To calculate the total pressure at the entrance or exits we add the disturbance pressure to the corresponding Poiseuille pressure. The Poiseuille pressures in the main channel are given by

$$p^{P_1}(x) = -G_1 x, \quad (7.12)$$

$$p^{P_2}(x) = -G_2 x, \quad (7.13)$$

where p^{P_1} is the Poiseuille pressure of the entrance Poiseuille flow with constant gradient $-G_1$, and p^{P_2} is the Poiseuille pressure of the Poiseuille flow defined with respect to the flux at \mathcal{E}_2 and with constant gradient $-G_2$. We have defined both Poiseuille pressures to be zero at \mathcal{E}_1 . The pressure gradient constants, G_1 and G_2 , are related to the Poiseuille centreline velocity and the flux rate by,

$$G_1 = 2 \frac{\mu U_0^{P_1}}{d^2} = \frac{3 \mu Q_1}{2 d^3} \quad (7.14)$$

$$G_2 = Q G_1, \quad (7.15)$$

where we have defined the flux ratio,

$$Q = \frac{Q_2}{Q_1}, \quad (7.16)$$

to measure the proportion of the fluid which enters the computational domain at \mathcal{E}_1 and exits from \mathcal{E}_2 . Equation (7.15) may be used to show,

$$\mathbf{u}^{P_2} = Q \mathbf{u}^{P_1}, \quad \mathbf{f}^{P_2} = Q \mathbf{f}^{P_1}, \quad \text{and} \quad p^{P_2} = Q p^{P_1}. \quad (7.17)$$

In the branch channel the Poiseuille pressure is

$$p^{P_3}(X) = -G_3 X \quad (7.18)$$

where $G_3 = 2 \mu U_0^{P_3}/D^2 = 3 \mu Q_3/2D^3$. When the constant pressure gradient $-G_3$ is applied to the branch channel the flux at \mathcal{E}_3 is Q_3 . In the main channel, the pressure difference between the entrance and the exit, Δp_2 , is given by

$$\begin{aligned} \Delta p_2 &= p(\mathcal{E}_1) - p(\mathcal{E}_2) \\ &= (p^{P_1}(\mathcal{E}_1) + \pi_1) - (p^{P_2}(\mathcal{E}_2) + \pi_2) \\ &= G_2 l - \pi_2, \end{aligned} \quad (7.19)$$

by equations (7.12) and (7.13), and between the entrance and the exit of the branch channel, Δp_3 , by

$$\begin{aligned}\Delta p_3 &= p(\mathcal{E}_1) - p(\mathcal{E}_3) \\ &= (p^{P_1}(\mathcal{E}_1) + \pi_1) - (p^{P_3}(\mathcal{E}_3) + \pi_3) \\ &= -\pi_3,\end{aligned}\tag{7.20}$$

by equations (7.12) and (7.18). The total pressures at the exits are

$$p(\mathcal{E}_2) = \pi_2 - G_2 l, \quad \text{and} \quad p(\mathcal{E}_3) = \pi_3.\tag{7.21}$$

On the capsule boundary we assume that the velocity on both sides of the boundary is equal, so that

$$\mathbf{u}^{(1)} = \mathbf{u}^{(2)}\tag{7.22}$$

on \mathcal{P} and where the (1) superscript indicates the ambient fluid in the channel and the (2) superscript indicates the fluid inside the capsule. We also introduce the interfacial traction jump,

$$\Delta \mathbf{f} = \mathbf{f}^{(1)} - \mathbf{f}^{(2)},\tag{7.23}$$

where once again the superscripts indicate to which fluid the traction applies. The constitutive equations which may be used to calculate $\Delta \mathbf{f}$ were introduced in section 4.2. Therefore on the capsule boundary we will seek to eliminate the disturbance velocity and traction in favour of the total velocity and traction.

In our discussion of the boundary conditions we have introduced unknown disturbance tractions, velocities and pressures. In the main channel we have the disturbance pressure, π_2 , and the disturbance tractions, \mathbf{f}^{D_1} , on the channel walls. In the branch channel we have π_3 and the \mathbf{f}^{D_3} on the channel walls. On the notional boundary we choose \mathbf{f}^{D_1} and \mathbf{u}^{D_1} for consistency with the main channel. On the particle boundary the interfacial traction jump is known from a suitable constitutive equation and the velocity is unknown.

To derive equations for the disturbance pressures π_2 and π_3 we bring together the analysis given in chapter 4 when discussing a flexible capsule in a straight channel, and the derivation of the disturbance pressures equations for a branching channel given in chapter 5. Firstly we will consider the capsule in the main channel, and apply the Lorentz reciprocal relation (1.3.22) to the \mathbf{u}^{P_1} and \mathbf{u}^{D_1} flows to get

$$\nabla \cdot (\mathbf{u}^{P_1} \cdot \boldsymbol{\sigma}^{D_1} - \mathbf{u}^{D_1} \cdot \boldsymbol{\sigma}^{P_1}) = 0,\tag{7.24}$$

which we integrate over the main channel's flow domain and apply the divergence theorem to get

$$\int_{\partial\Gamma_1} \mathbf{u}^{P_1} \cdot \mathbf{f}^{D_1} \, ds(\mathbf{x}) = \int_{\partial\Gamma_1} \mathbf{u}^{D_1} \cdot \mathbf{f}^{P_1} \, ds(\mathbf{x}),\tag{7.25}$$

where $\partial\Gamma_1 = \mathcal{E}_1 \cup \mathcal{E}_2 \cup \mathcal{A} \cup \mathcal{C} \cup \mathcal{P}$ is the boundary of the flow domain, and which can be

simplified to

$$\int_{\mathcal{E}_2} (\mathbf{u}^{P_1} \cdot \mathbf{f}^{D_1} - \mathbf{u}^{D_1} \cdot \mathbf{f}^{P_1}) \, ds(\mathbf{x}) = \int_{\mathcal{A}, \mathcal{P}} (\mathbf{u}^{D_1} \cdot \mathbf{f}^{P_1} - \mathbf{u}^{P_1} \cdot \mathbf{f}^{D_1}) \, ds(\mathbf{x}), \quad (7.26)$$

using equations (7.7) and (7.9). The left-hand side simplifies to $Q_1 \pi_2$ by equation (5.45) and the integral over \mathcal{P} is expressed in terms of the total velocity and traction thus,

$$\begin{aligned} \int_{\mathcal{P}} (\mathbf{u}^{D_1} \cdot \mathbf{f}^{P_1} - \mathbf{u}^{P_1} \cdot \mathbf{f}^{D_1}) \, ds(\mathbf{x}) &= \int_{\mathcal{P}} \left((\mathbf{u}^{(1)} - \mathbf{u}^{P_1}) \cdot \mathbf{f}^{P_1} - \mathbf{u}^{P_1} \cdot (\mathbf{f}^{(1)} - \mathbf{f}^{P_1}) \right) \, ds(\mathbf{x}) \\ &= \int_{\mathcal{P}} \left(\mathbf{u}^{(1)} \cdot \mathbf{f}^{P_1} - \mathbf{u}^{P_1} \cdot \mathbf{f}^{(1)} \right) \, ds(\mathbf{x}), \end{aligned} \quad (7.27)$$

using equations (7.1) and (7.2). Next we apply the Lorentz reciprocal relation to the Poiseuille flow, \mathbf{u}^{P_1} , and the capsule's internal flow in order to introduce the interfacial traction to our equation. Since the viscosity of the Poiseuille flow and the internal flow are different we use the Lorentz reciprocal relation applicable to two fluids which have different viscosities, which is

$$\nabla \cdot \left(\mu \mathbf{u}^{P_1} \cdot \mathbf{f}^{(2)} - \lambda \mu \mathbf{u}^{(2)} \cdot \mathbf{f}^{P_1} \right) = 0. \quad (7.28)$$

We divide this equation by μ and integrate only over the capsule's domain to get,

$$\begin{aligned} 0 &= \int_{\mathcal{P}} \left(\mathbf{u}^{P_1} \cdot \mathbf{f}^{(2)} - \lambda \mathbf{u}^{(2)} \cdot \mathbf{f}^{P_1} \right) \, ds(\mathbf{x}) \\ &= \int_{\mathcal{P}} \left(\mathbf{u}^{P_1} \cdot \mathbf{f}^{(2)} - \lambda \mathbf{u}^{(1)} \cdot \mathbf{f}^{P_1} \right) \, ds(\mathbf{x}), \end{aligned} \quad (7.29)$$

by equation (7.22). Adding equation (7.29) to equation (7.27) yields

$$\begin{aligned} \int_{\mathcal{P}} (\mathbf{u}^{D_1} \cdot \mathbf{f}^{P_1} - \mathbf{u}^{P_1} \cdot \mathbf{f}^{D_1}) \, ds(\mathbf{x}) &= - \int_{\mathcal{P}} \mathbf{u}^{P_1} \cdot \Delta \mathbf{f} \, ds(\mathbf{x}) \\ &\quad + (1 - \lambda) \int_{\mathcal{P}} \mathbf{u}^{(1)} \cdot \mathbf{f}^{P_1} \, ds(\mathbf{x}), \end{aligned} \quad (7.30)$$

which upon substitution into equation (7.26) gives,

$$\begin{aligned} \pi_2 &= \frac{1}{Q_1} \left(\int_{\mathcal{A}} (\mathbf{u}^{D_1} \cdot \mathbf{f}^{P_1} - \mathbf{u}^{P_1} \cdot \mathbf{f}^{D_1}) \, ds(\mathbf{x}) \right. \\ &\quad \left. - \int_{\mathcal{P}} \mathbf{u}^{P_1} \cdot \Delta \mathbf{f} \, ds(\mathbf{x}) + (1 - \lambda) \int_{\mathcal{P}} \mathbf{u}^{(1)} \cdot \mathbf{f}^{P_1} \, ds(\mathbf{x}) \right), \end{aligned} \quad (7.31)$$

for the disturbance pressure at \mathcal{E}_2 . If the branch were absent then the integral over \mathcal{A} would disappear from the equation and we would recover equation (4.19) for the disturbance

pressure in a straight channel. Therefore the disturbance pressure at \mathcal{E}_2 is dependent on the capsule's shape, the velocity of the capsule's perimeter and the disturbance velocity and traction on the notional boundary. It is interesting to note that when $\lambda = 1$ the velocities on \mathcal{P} are not included in equation (7.31). When the capsule is in the branch channel we omit the integrals over \mathcal{P} from the equation for π_2 .

To obtain an equation for π_3 we consider the branch channel when it contains the capsule, and apply the Lorentz reciprocal relation (1.3.22) as previously, but to the \mathbf{u}^{P_3} and \mathbf{u}^{D_3} flows, to get

$$\nabla \cdot (\mathbf{u}^{P_3} \cdot \boldsymbol{\sigma}^{D_3} - \mathbf{u}^{D_3} \cdot \boldsymbol{\sigma}^{P_3}) = 0, \quad (7.32)$$

which we integrate over the branch channel's flow domain and apply the divergence theorem to obtain

$$\int_{\partial\Gamma_2} \mathbf{u}^{P_3} \cdot \mathbf{f}^{D_3} \, ds(\mathbf{x}) = \int_{\partial\Gamma_2} \mathbf{u}^{D_3} \cdot \mathbf{f}^{P_3} \, ds(\mathbf{x}), \quad (7.33)$$

where $\partial\Gamma_2 = \mathcal{E}_3 \cup \mathcal{A} \cup \mathcal{B} \cup \mathcal{P}$ is the boundary of the flow domain. Expansion of $\partial\Gamma_2$ into its constituent boundaries yields,

$$\begin{aligned} \int_{\mathcal{E}_3} (\mathbf{u}^{P_3} \cdot \mathbf{f}^{D_3} - \mathbf{u}^{D_3} \cdot \mathbf{f}^{P_3}) \, ds(\mathbf{x}) &= - \int_{\mathcal{A}} (\mathbf{u}^{D_3} \cdot \mathbf{f}^{P_3} - \mathbf{u}^{P_3} \cdot \mathbf{f}^{D_3}) \, ds(\mathbf{x}) \\ &+ \int_{\mathcal{P}} (\mathbf{u}^{D_3} \cdot \mathbf{f}^{P_3} - \mathbf{u}^{P_3} \cdot \mathbf{f}^{D_3}) \, ds(\mathbf{x}), \end{aligned} \quad (7.34)$$

where we have used equations (7.8) and (7.11), and where the sign change on the integral over \mathcal{A} is due to the normal vector on \mathcal{A} pointing into the main channel. The left-hand side simplifies to $Q_3 \pi_3$ by equation (5.53). In the integral over \mathcal{A} we eliminate \mathbf{u}^{D_3} and \mathbf{f}^{D_3} in favour of \mathbf{u}^{D_1} and \mathbf{f}^{D_1} using the continuity of velocity and traction given in equations (7.5) and (7.6), to get

$$\int_{\mathcal{A}} (\mathbf{u}^{P_3} \cdot \mathbf{f}^{D_3} - \mathbf{u}^{D_3} \cdot \mathbf{f}^{P_3}) \, ds(\mathbf{x}) = \int_{\mathcal{A}} (\mathbf{u}^{P_3} \cdot \mathbf{f}^{D_1} - \mathbf{u}^{D_1} \cdot \mathbf{f}^{P_3}) \, ds(\mathbf{x}) + \psi \quad (7.35)$$

where

$$\psi = \int_{\mathcal{A}} (\mathbf{u}^{P_3} \cdot \mathbf{f}^{P_1} - \mathbf{u}^{P_1} \cdot \mathbf{f}^{P_3}) \, ds(\mathbf{x}), \quad (7.36)$$

which was first introduced in equation (5.56). When \mathcal{A} is straight ψ may be calculated exactly using equation (5.57). The integral over \mathcal{P} in equation (7.34) is expressed in terms of the total velocity and traction as

$$\begin{aligned} \int_{\mathcal{P}} (\mathbf{u}^{D_3} \cdot \mathbf{f}^{P_3} - \mathbf{u}^{P_3} \cdot \mathbf{f}^{D_3}) \, ds(\mathbf{x}) &= \int_{\mathcal{P}} \left((\mathbf{u}^{(1)} - \mathbf{u}^{P_3}) \cdot \mathbf{f}^{P_3} - \mathbf{u}^{P_3} \cdot (\mathbf{f}^{(1)} - \mathbf{f}^{P_3}) \right) \, ds(\mathbf{x}) \\ &= \int_{\mathcal{P}} \left(\mathbf{u}^{(1)} \cdot \mathbf{f}^{P_3} - \mathbf{u}^{P_3} \cdot \mathbf{f}^{(1)} \right) \, ds(\mathbf{x}), \end{aligned} \quad (7.37)$$

where we have used equations (7.3) and (7.4). In equation (7.30), had we applied the Lorentz reciprocal relation to \mathbf{u}^{P_3} instead of \mathbf{u}^{P_1} we would have obtained,

$$0 = \int_{\mathcal{P}} \left(\mathbf{u}^{P_3} \cdot \mathbf{f}^{(2)} - \lambda \mathbf{u}^{(1)} \cdot \mathbf{f}^{P_3} \right) ds(\mathbf{x}), \quad (7.38)$$

which we add to equation (7.37) to get,

$$\begin{aligned} \int_{\mathcal{P}} \left(\mathbf{u}^{D_3} \cdot \mathbf{f}^{P_3} - \mathbf{u}^{P_3} \cdot \mathbf{f}^{D_3} \right) ds(\mathbf{x}) &= - \int_{\mathcal{P}} \mathbf{u}^{P_3} \cdot \Delta \mathbf{f} ds(\mathbf{x}) \\ &+ (1 - \lambda) \int_{\mathcal{P}} \mathbf{u}^{(1)} \cdot \mathbf{f}^{P_3} ds(\mathbf{x}). \end{aligned} \quad (7.39)$$

Substitution of this equation into equation (7.34) gives,

$$\begin{aligned} \pi_3 = \frac{1}{Q_3} \left(\int_{\mathcal{A}} \left(\mathbf{u}^{P_3} \cdot \mathbf{f}^{D_1} - \mathbf{u}^{D_1} \cdot \mathbf{f}^{P_3} \right) ds(\mathbf{x}) + \psi \right. \\ \left. - \int_{\mathcal{P}} \mathbf{u}^{P_3} \cdot \Delta \mathbf{f} ds(\mathbf{x}) + (1 - \lambda) \int_{\mathcal{P}} \mathbf{u}^{(1)} \cdot \mathbf{f}^{P_3} ds(\mathbf{x}) \right), \end{aligned} \quad (7.40)$$

for the disturbance pressure at \mathcal{E}_3 . Once again, when $\lambda = 1$ the velocities on \mathcal{P} disappear from the equation. When the capsule is in the branch channel we omit the integrals over \mathcal{P} from equation (7.40), which as expected is identical to equation (5.54) for π_3 for a fluid-filled branching channel.

In order to write the disturbance pressure equations irrespective of the capsule location, we use the function, $\mathcal{H}_{\mathcal{P}}$, introduced in the previous chapter, and which is defined by

$$\mathcal{H}_{\mathcal{P}} = \begin{cases} 0 & \text{when the capsule is in the branch channel,} \\ 1 & \text{when the capsule is in the main channel,} \end{cases} \quad (7.41)$$

so that,

$$\begin{aligned} \pi_2 = \frac{1}{Q_1} \int_{\mathcal{A}} \left(\mathbf{u}^{D_1} \cdot \mathbf{f}^{P_1} - \mathbf{u}^{P_1} \cdot \mathbf{f}^{D_1} \right) ds(\mathbf{x}) \\ + \frac{\mathcal{H}_{\mathcal{P}}}{Q_1} \left(- \int_{\mathcal{P}} \mathbf{u}^{P_1} \cdot \Delta \mathbf{f} ds(\mathbf{x}) + (1 - \lambda) \int_{\mathcal{P}} \mathbf{u}^{(1)} \cdot \mathbf{f}^{P_1} ds(\mathbf{x}) \right), \end{aligned} \quad (7.42)$$

$$\begin{aligned} \pi_3 = \frac{1}{Q_3} \left(\int_{\mathcal{A}} \left(\mathbf{u}^{P_3} \cdot \mathbf{f}^{D_1} - \mathbf{u}^{D_1} \cdot \mathbf{f}^{P_3} \right) ds(\mathbf{x}) + \psi \right) \\ + \frac{1 - \mathcal{H}_{\mathcal{P}}}{Q_3} \left(- \int_{\mathcal{P}} \mathbf{u}^{P_3} \cdot \Delta \mathbf{f} ds(\mathbf{x}) + (1 - \lambda) \int_{\mathcal{P}} \mathbf{u}^{(1)} \cdot \mathbf{f}^{P_3} ds(\mathbf{x}) \right), \end{aligned} \quad (7.43)$$

for the disturbance pressures at the exits. The unknowns in equations (7.42) and (7.43) are

the disturbance pressures, the disturbance velocities and tractions on \mathcal{A} , and the velocity of the capsule boundary.

Our next goal is to derive a pair of boundary integral equations which describe the velocity field throughout the main channel and the branch channel. Once again we start by considering the main channel. In chapter 5 we derived equation (5.64) which may be used here provided the capsule boundary is also included in the boundary to the flow domain. Inclusion of \mathcal{P} in the derivation of equation (5.64) gives,

$$4\pi\mu u_j^{D1}(\mathbf{x}_0) = - \int_{\mathcal{A}, \mathcal{C}, \mathcal{P}} f_i^{D1} G_{ij} \, ds(\mathbf{x}) + \pi_2 \int_{\mathcal{E}_2} n_i G_{ij} \, ds(\mathbf{x}) + \mu \int_{\mathcal{A}, \mathcal{P}} u_i^{D1} T_{ijk} n_k \, ds(\mathbf{x}) + I_j(\mathbf{x}_0), \quad (7.44)$$

for \mathbf{x}_0 in the fluid of the main channel, and where $I(\mathbf{x}_0)$ is defined by equation (5.65). Application of the boundary integral equation (1.3.40) to the \mathbf{u}^{P1} flow over the particle boundary gives,

$$0 = - \int_{\mathcal{P}} f_i^{P1} G_{ij} \, ds(\mathbf{x}) + \mu \int_{\mathcal{P}} u_i^{P1} T_{ijk} n_k \, ds(\mathbf{x}), \quad (7.45)$$

for \mathbf{x}_0 in the fluid of the main channel. Adding this equation to equation (7.44) we obtain,

$$4\pi\mu u_j^{D1}(\mathbf{x}_0) = - \int_{\mathcal{A}, \mathcal{C}} f_i^{D1} G_{ij} \, ds(\mathbf{x}) - \int_{\mathcal{P}} f_i^{(1)} G_{ij} \, ds(\mathbf{x}) + \pi_2 \int_{\mathcal{E}_2} n_i G_{ij} \, ds(\mathbf{x}) + \mu \int_{\mathcal{A}} u_i^{D1} T_{ijk} n_k \, ds(\mathbf{x}) + I_j(\mathbf{x}_0) + \mu \int_{\mathcal{P}} u_i^{(1)} T_{ijk} n_k \, ds(\mathbf{x}). \quad (7.46)$$

The boundary integral equation for the $\mathbf{u}^{(2)}$ flow when \mathbf{x}_0 lies in the ambient fluid in the main channel is

$$0 = - \int_{\mathcal{P}} f^{(2)} G_{ij} \, ds(\mathbf{x}) + \lambda\mu \int_{\mathcal{P}} u^{(2)} T_{ijk} n_k \, ds(\mathbf{x}), \quad (7.47)$$

where we have only considered the capsule's boundary and where the left-hand side is zero because \mathbf{x}_0 lies outside of \mathcal{P} . Subtraction of this equation from equation (7.46) gives

$$4\pi\mu u_j^{D1}(\mathbf{x}_0) = - \int_{\mathcal{A}, \mathcal{C}} f_i^{D1} G_{ij} \, ds(\mathbf{x}) + \pi_2 \int_{\mathcal{E}_2} n_i G_{ij} \, ds(\mathbf{x}) + \mu \int_{\mathcal{A}} u_i^{D1} T_{ijk} n_k \, ds(\mathbf{x}) + I_j(\mathbf{x}_0) + \mathcal{H}_{\mathcal{P}} \left(- \int_{\mathcal{P}} \Delta f_i G_{ij} \, ds(\mathbf{x}) + \mu(1 - \lambda) \int_{\mathcal{P}} u_i^{(1)} T_{ijk} n_k \, ds(\mathbf{x}) \right), \quad (7.48)$$

where we have included the function $\mathcal{H}_{\mathcal{P}}$ to indicate when the integrals over \mathcal{P} appear in the equation. Equation (7.48) is valid for \mathbf{x}_0 located in fluid 1 in the main channel and may be used to calculate the disturbance velocity \mathbf{u}^{D1} in the main channel at any point

given π_2 , f^{D_1} on \mathcal{A} and \mathcal{C} , u^{D_1} on \mathcal{A} and the velocity of the capsule boundary. To obtain the total velocity, the calculated value of $u^{D_1}(\mathbf{x}_0)$ is added to $u^{P_1}(\mathbf{x}_0)$. When $\lambda = 1$ the velocities on \mathcal{P} disappear from the boundary integral equation in the same way as they did in the pressure equations. Equation (7.48) is also valid on the walls of the channel because the discontinuous double-layer potential is not evaluated over \mathcal{C} . Therefore when \mathbf{x}_0 lies on \mathcal{C} the left-hand side of equation (7.48) is zero by the no-slip boundary condition. When \mathbf{x}_0 lies on \mathcal{A} we follow the derivation of equation (5.68) and obtain,

$$2\pi\mu u_j^{D_1}(\mathbf{x}_0) = - \int_{\mathcal{A},\mathcal{C}} f_i^{D_1} G_{ij} \, ds(\mathbf{x}) + \pi_2 \int_{\mathcal{E}_2} n_i G_{ij} \, ds(\mathbf{x}) + \mu \int_{\mathcal{A}}^{PV} u_i^{D_1} T_{ijk} n_k \, ds(\mathbf{x}) \\ + I_j(\mathbf{x}_0) + \mathcal{H}_{\mathcal{P}} \left(- \int_{\mathcal{P}} \Delta f_i G_{ij} \, ds(\mathbf{x}) + \mu(1-\lambda) \int_{\mathcal{P}} u_i^{(1)} T_{ijk} n_k \, ds(\mathbf{x}) \right), \quad (7.49)$$

where PV indicates that we take the principal value of the integral of the double-layer potential over \mathcal{A} . When the capsule is in the main channel and \mathbf{x}_0 lies on \mathcal{P} , the double-layer potential integral over \mathcal{P} is present in equation (7.48) and in terms of its principal value is given by,

$$\int_{\mathcal{P}} u_i^{(1)} T_{ijk} n_k \, ds(\mathbf{x}) = 2\pi u_j^{(1)}(\mathbf{x}_0) + \int_{\mathcal{P}}^{PV} u_i^{(1)} T_{ijk} n_k \, ds(\mathbf{x}), \quad (7.50)$$

using equation (2.6.25) in Pozrikidis (1992). Substitution into (7.48) yields

$$2\pi\mu(1+\lambda)u_j^{(1)}(\mathbf{x}_0) = 4\pi\mu u_j^{P_1}(\mathbf{x}_0) - \int_{\mathcal{A},\mathcal{C}} f_i^{D_1} G_{ij} \, ds(\mathbf{x}) \\ + \pi_2 \int_{\mathcal{E}_2} n_i G_{ij} \, ds(\mathbf{x}) + \mu \int_{\mathcal{A}} u_i^{D_1} T_{ijk} n_k \, ds(\mathbf{x}) + I_j(\mathbf{x}_0) \\ - \int_{\mathcal{P}} \Delta f_i G_{ij} \, ds(\mathbf{x}) + \mu(1-\lambda) \int_{\mathcal{P}}^{PV} u_i^{(1)} T_{ijk} n_k \, ds(\mathbf{x}), \quad (7.51)$$

which is valid when \mathbf{x}_0 lies on the capsule boundary and where we have expressed the left-hand side in terms of the total velocity. The derivation of the boundary integral equation applicable to the branch channel proceeds in much the same way as for the main channel. We start by including the particle boundary in the branch channel boundary integral equation (5.72), to get

$$4\pi\mu u_j^{D_3}(\mathbf{x}_0) = \int_{\mathcal{A}} f_i^{D_1} G_{ij} \, ds(\mathbf{x}) - \int_{\mathcal{B},\mathcal{P}} f_i^{D_3} G_{ij} \, ds(\mathbf{x}) + \pi_3 \int_{\mathcal{E}_3} n_i G_{ij} \, ds(\mathbf{x}) \\ - \mu \int_{\mathcal{A}} u_i^{D_1} T_{ijk} n_k \, ds(\mathbf{x}) + \mu \int_{\mathcal{P}} u_i^{D_3} T_{ijk} n_k \, ds(\mathbf{x}) + K_j(\mathbf{x}_0), \quad (7.52)$$

for \mathbf{x}_0 located in the fluid of the branch channel, and where $\mathbf{K}(\mathbf{x}_0)$ is defined by (5.73). This time we apply the boundary integral equation (1.3.40) to the \mathbf{u}^{P_3} flow only over the particle boundary, and obtain

$$0 = - \int_{\mathcal{P}} f_i^{P_3} G_{ij} \, ds(\mathbf{x}) + \mu \int_{\mathcal{P}} u_i^{P_3} T_{ijk} n_k \, ds(\mathbf{x}), \quad (7.53)$$

for \mathbf{x}_0 in the fluid of the branch channel, which we add to equation (7.52) and rearrange to obtain

$$\begin{aligned} 4\pi\mu u_j^{D_3}(\mathbf{x}_0) &= \int_{\mathcal{A}} f_i^{D_1} G_{ij} \, ds(\mathbf{x}) - \int_{\mathcal{B}} f_i^{D_3} G_{ij} \, ds(\mathbf{x}) \\ &+ \pi_3 \int_{\mathcal{E}_3} n_i G_{ij} \, ds(\mathbf{x}) + \mu \int_{\mathcal{A}} u_i^{D_1} T_{ijk} n_k \, ds(\mathbf{x}) + K_j(\mathbf{x}_0) \\ &+ (1 - \mathcal{H}_{\mathcal{P}}) \left(- \int_{\mathcal{P}} \Delta f_i G_{ij} \, ds(\mathbf{x}) + \mu(1 - \lambda) \int_{\mathcal{P}} u_i^{(1)} T_{ijk} n_k \, ds(\mathbf{x}) \right), \end{aligned} \quad (7.54)$$

which is valid for \mathbf{x}_0 in fluid 1 in the branch channel. Equation (7.54) is valid for \mathbf{x}_0 located in fluid 1 in the branch channel and may be used to calculate the disturbance velocity \mathbf{u}^{D_3} at any point in the branch channel given π_3 , \mathbf{f}^{D_1} and \mathbf{u}^{D_1} on \mathcal{A} , \mathbf{f}^{D_3} on \mathcal{B} and the velocity of the capsule boundary. To obtain the total velocity, the calculated value of $\mathbf{u}^{D_3}(\mathbf{x}_0)$ is added to $\mathbf{u}^{P_3}(\mathbf{x}_0)$. When $\lambda = 1$ the velocities on \mathcal{P} disappear from the equation (7.54). Equation (7.54) is also valid on the walls of the branch channel because the discontinuous double-layer potential is not evaluated over \mathcal{B} . Therefore when \mathbf{x}_0 lies on \mathcal{B} the left-hand side of equation (7.54) is zero by the no-slip boundary condition. When \mathbf{x}_0 lies on \mathcal{A} we follow the derivation of equation (5.75) and obtain,

$$\begin{aligned} 2\pi\mu u_j^{D_3}(\mathbf{x}_0) &= \int_{\mathcal{A}} f_i^{D_1} G_{ij} \, ds(\mathbf{x}) - \int_{\mathcal{B}} f_i^{D_3} G_{ij} \, ds(\mathbf{x}) \\ &+ \pi_3 \int_{\mathcal{E}_3} n_i G_{ij} \, ds(\mathbf{x}) + \mu \int_{\mathcal{A}}^{PV} u_i^{D_1} T_{ijk} n_k \, ds(\mathbf{x}) + K_j^{PV}(\mathbf{x}_0) \\ &+ (1 - \mathcal{H}_{\mathcal{P}}) \left(- \int_{\mathcal{P}} \Delta f_i G_{ij} \, ds(\mathbf{x}) + \mu(1 - \lambda) \int_{\mathcal{P}} u_i^{(1)} T_{ijk} n_k \, ds(\mathbf{x}) \right), \end{aligned} \quad (7.55)$$

and we may eliminate \mathbf{u}^{D_3} on the left-hand side in favour of \mathbf{u}^{D_1} using equation (7.5). When the capsule is in the branch channel and \mathbf{x}_0 lies on \mathcal{P} , the double-layer potential integral over \mathcal{P} is expressed in terms of its principal value in equation (7.50), which upon

substitution into (7.54) yields

$$\begin{aligned}
2\pi\mu(1+\lambda)u_j^{(1)}(\mathbf{x}_0) &= 4\pi\mu u_j^{P_3}(\mathbf{x}_0) + \int_{\mathcal{A}} f_i^{D_1} G_{ij} \, ds(\mathbf{x}) - \int_{\mathcal{B}} f_i^{D_3} G_{ij} \, ds(\mathbf{x}) \\
&+ \pi_3 \int_{\mathcal{E}_3} n_i G_{ij} \, ds(\mathbf{x}) + \mu \int_{\mathcal{A}} u_i^{D_1} T_{ijk} n_k \, ds(\mathbf{x}) + K_j(\mathbf{x}_0) \\
&- \int_{\mathcal{P}} \Delta f_i G_{ij} \, ds(\mathbf{x}) + \mu(1-\lambda) \int_{\mathcal{P}}^{PV} u_i^{(1)} T_{ijk} n_k \, ds(\mathbf{x}), \tag{7.56}
\end{aligned}$$

which is valid when \mathbf{x}_0 lies on the capsule boundary and where we have expressed the left-hand side in terms of the total velocity.

We now have equations for the disturbance pressures and boundary integral equations for the velocity field in the main and branch channels. To obtain a linear system which represents the governing equations we employ the boundary element method (e.g. Pozrikidis 2002a). We discretise the boundaries into elements upon which we evaluate the boundary integral equations. We obtain a sufficient number of equations for the unknown tractions on \mathcal{C} and \mathcal{B} by evaluating equations (7.48) and (7.54) with \mathbf{x}_0 on each element of the respective boundary. Evaluation of the equations (7.49) and (7.55) with \mathbf{x}_0 on \mathcal{A} provides a sufficient number of equations for the disturbance tractions and velocities on the notional boundary. Depending on whether the particle is in the main channel or the branch channel, we evaluate equation (7.51) or (7.56) with \mathbf{x}_0 on each boundary element of the particle to obtain equations for the particle velocities. We have two equations for the disturbance pressures at the exits, namely equations (7.42) and (7.43). Therefore we have the same number of equations as unknowns and so our system is complete. We have completed our derivation of the governing equations for the flow of a flexible capsule through a bifurcation and now we move on to describe how the boundary element method is applied in order to find the numerical solution.

7.2 Numerical method

As in previous chapters our aim is to discretise the governing equations using the boundary element method and form the equations into the linear matrix system,

$$\mathbf{A} \cdot \mathbf{x} = \mathbf{b}, \tag{7.57}$$

where \mathbf{A} is the influence matrix containing the coefficients of the unknown disturbance pressures, tractions and velocities stored in the column-vector, \mathbf{x} , and \mathbf{b} is a column-vector containing known values. As before, when applying the boundary element method we discretise the notional boundary, the branch channel walls, the main channel walls, and the capsule's boundary into $N_{\mathcal{A}}$, $N_{\mathcal{B}}$, $N_{\mathcal{C}}$ and $N_{\mathcal{P}}$ equally-sized straight elements respectively. On each wall element we set the unknown disturbance traction to a constant 2-vector, which we label $\mathbf{f}_r^{D_1}$ on the r^{th} element of \mathcal{A} and \mathcal{C} , and $\mathbf{f}_r^{D_3}$ on the r^{th} element

of \mathcal{B} . On the r^{th} element of \mathcal{A} we set the disturbance velocity to \mathbf{u}_r^{D1} , and on \mathcal{P} we set the element midpoint velocity to \mathbf{u}_r . We specify the midpoint of the capsule boundary element because when we evaluate the boundary integral equation on the boundary elements of \mathcal{P} , we will place the pole at the midpoint of each element. When we come to move the capsule using the calculated boundary velocities, we will move the element endpoints, or nodes, and we will calculate the nodal velocities using a periodic cubic spline constructed from the midpoint velocities. We define the column-vector \mathbf{x} to be

$$\mathbf{x} = \left[\mathbf{F}_C^D \quad \mathbf{F}_A^D \quad \mathbf{F}_B^D \quad \mathbf{U}_A^D \quad \pi_2 \quad \pi_3 \quad \mathbf{U}_{\mathcal{P}}^{(1)} \right]^T \quad (7.58)$$

where the first four subvectors are described and defined in section 5.2, π_2 and π_3 are the disturbance pressures at \mathcal{E}_2 and \mathcal{E}_3 respectively, and the $\mathbf{U}_{\mathcal{P}}^{(1)}$ subvector houses the $2N_{\mathcal{P}}$ components of the velocity at the midpoint of each of the capsule boundary's elements. The subvector $\mathbf{U}_A^{(1)}$ is defined by

$$\mathbf{U}_{\mathcal{P}}^{(1)} = \left[u_{x,1}^{(1)} \quad u_{y,1}^{(1)} \quad \cdots \quad u_{x,N_{\mathcal{P}}}^{(1)} \quad u_{y,N_{\mathcal{P}}}^{(1)} \right]. \quad (7.59)$$

We will first discretise the disturbance pressure equations starting with equation (7.42) for π_2 , which we write as

$$\begin{aligned} Q_1 \pi_2 + \int_{\mathcal{A}} (\mathbf{u}^{P1} \cdot \mathbf{f}^{D1} - \mathbf{u}^{D1} \cdot \mathbf{f}^{P1}) \, ds(\mathbf{x}) \\ + \mathcal{H}_{\mathcal{P}} (\lambda - 1) \int_{\mathcal{P}} \mathbf{u}^{(1)} \cdot \mathbf{f}^{P1} \, ds(\mathbf{x}) = -\mathcal{H}_{\mathcal{P}} \int_{\mathcal{P}} \mathbf{u}^{P1} \cdot \Delta \mathbf{f} \, ds(\mathbf{x}), \end{aligned} \quad (7.60)$$

with the unknown disturbance pressure, disturbance tractions and capsule velocities on the left-hand side and the known value on the right-hand side. The integrals over \mathcal{P} are discretised as follows,

$$(\lambda - 1) \int_{\mathcal{P}} \mathbf{u}^{(1)} \cdot \mathbf{f}^{P1} \, ds(\mathbf{x}) \approx (\lambda - 1) \sum_{r=1}^{N_{\mathcal{P}}} \mathbf{u}_r^{(1)} \cdot \mathbf{f}_r^{P1}(\mathbf{x}_{m,r}) l_r = \mathbf{\Pi}_{\mathcal{P}}^{P1} \cdot \mathbf{U}_{\mathcal{P}}^{(1)}, \quad (7.61)$$

$$\int_{\mathcal{P}} \mathbf{u}^{P1} \cdot \Delta \mathbf{f} \, ds(\mathbf{x}) \approx \sum_{r=1}^{N_{\mathcal{P}}} \mathbf{u}^{P1}(\mathbf{x}_{m,r}) \cdot \Delta \mathbf{f}(\mathbf{x}_{m,r}) l_r = \mathbf{\Pi}_{\Delta}^{P1}, \quad (7.62)$$

where l_r and $\mathbf{x}_{m,r}$ are the element length and midpoint respectively, the calculation of $\Delta \mathbf{f}$ is discussed in section 4.3, and

$$\mathbf{\Pi}_{\mathcal{P}}^{P1} = (\lambda - 1) \left[f_{x,1}^{P1} l_1 \quad f_{y,1}^{P1} l_1 \quad \cdots \quad f_{x,N_{\mathcal{P}}}^{P1} l_{N_{\mathcal{P}}} \quad f_{y,N_{\mathcal{P}}}^{P1} l_{N_{\mathcal{P}}} \right]. \quad (7.63)$$

Combining equations (7.61) and (7.62) with the discretisation of the remaining terms given in equation (5.87), we may write the discretised analogue of equation (7.60) as

$$\left[\mathbf{0} \quad \mathbf{U}_A^{P1} \quad \mathbf{0} \quad -\mathbf{F}_A^{P1} \quad Q_1 \quad 0 \quad \mathcal{H}_{\mathcal{P}} \mathbf{\Pi}_{\mathcal{P}}^{P1} \right] \cdot \mathbf{x} = -\mathcal{H}_{\mathcal{P}} \mathbf{\Pi}_{\Delta}^{P1}, \quad (7.64)$$

where $\mathbf{U}_{\mathcal{A}}^{P_1}$ and $\mathbf{F}_{\mathcal{A}}^{P_1}$ are defined by equations (5.84) and (5.85) respectively. Performing a similar exercise for the π_3 disturbance pressure equation (7.43), we get

$$\begin{bmatrix} \mathbf{0} & -\mathbf{U}_{\mathcal{A}}^{P_3} & \mathbf{0} & -\mathbf{F}_{\mathcal{A}}^{P_3} & 0 & Q_3 & (1 - \mathcal{H}_{\mathcal{P}})\mathbf{\Pi}_{\mathcal{P}}^{P_3} \end{bmatrix} \cdot \mathbf{x} = \psi - (1 - \mathcal{H}_{\mathcal{P}})\mathbf{\Pi}_{\Delta}^{P_3}, \quad (7.65)$$

where $\mathbf{U}_{\mathcal{A}}^{P_3}$ is defined by equation (5.90), $\mathbf{F}_{\mathcal{A}}^{P_3}$ is defined by equation (5.91), and

$$\mathbf{\Pi}_{\Delta}^{P_3} = \sum_{r=1}^{N_{\mathcal{P}}} \mathbf{u}^{P_3}(\mathbf{x}_{m,r}) \cdot \Delta \mathbf{f}(\mathbf{x}_{m,r}) l_r, \quad (7.66)$$

$$\mathbf{\Pi}_{\mathcal{P}}^{P_3} = (\lambda - 1) \begin{bmatrix} f_{x,1}^{P_3} l_1 & f_{y,1}^{P_3} l_1 & \dots & f_{x,N_{\mathcal{P}}}^{P_3} l_{N_{\mathcal{P}}} & f_{y,N_{\mathcal{P}}}^{P_3} l_{N_{\mathcal{P}}} \end{bmatrix}. \quad (7.67)$$

Equations (7.64) and (7.65) represent the discretised versions of the disturbance pressure equations (7.42) and (7.43) respectively.

To discretise the boundary integral equations for the main and the branch channels derived in the previous section, we start by comparing them to the boundary integral equations derived for a fluid-filled branching channel in chapter 5. It is revealing to note that the main channel's boundary integral equation (7.48) may be obtained by adding

$$J_j(\mathbf{x}_0) = \mu(\lambda - 1) \int_{\mathcal{P}} u_i^{(1)} T_{ijk} n_k \, ds(\mathbf{x}) + \int_{\mathcal{P}} \Delta f_i G_{ij} \, ds(\mathbf{x}), \quad (7.68)$$

to the main channel equation (5.64) for a fluid-filled branching channel. Similarly, when the capsule is in the branch channel, we may obtain the boundary integral equation (7.54) by adding equation (7.68) to equation (5.72) for a fluid-filled branching channel. Therefore the discretisation of the boundary integral equations for the main and branch channels are obtained by adding the discretisations of equation (7.68) to the equations for a fluid-filled branching channel. The discretisation of the integrals in equation (7.68) are given in equations (4.74) and (4.76) of chapter 4, and are

$$\int_{\mathcal{P}} u_i^{(1)} T_{ijk} n_k \, ds(\mathbf{x}) \approx \mathbf{I}_{\mathcal{P},j}^T(\mathbf{x}_0) \cdot \left[\mathbf{U}_{\mathcal{P}}^{(1)} \right]^T, \quad (7.69)$$

$$\int_{\mathcal{P}} \Delta f_i G_{ij}(\mathbf{x}, \mathbf{x}_0) \, ds(\mathbf{x}) \approx \mathbf{\Pi}_{G,j}(\mathbf{x}_0), \quad (7.70)$$

where $\mathbf{I}_{\mathcal{P},j}^T$ is a row vector defined by equation (4.75), and where the full expansion of $\mathbf{\Pi}_{G,j}(\mathbf{x}_0)$ is given in equation (4.76). Therefore the discretisation of equation (7.68) is

$$J_j(\mathbf{x}_0) \approx \mu(\lambda - 1) \mathbf{I}_{\mathcal{P},j}^T(\mathbf{x}_0) \cdot \left[\mathbf{U}_{\mathcal{P}}^{(1)} \right]^T + \mathbf{\Pi}_{G,j}(\mathbf{x}_0). \quad (7.71)$$

When the capsule is in the main channel, we place \mathbf{x}_0 at the midpoint of each element of \mathcal{A} and \mathcal{C} , and evaluate equation (7.71). Following the placement of \mathbf{x}_0 on the elements of

\mathcal{C} we have $2N_{\mathcal{C}}$ equations which we write in matrix form as,

$$\mathbf{J}_{\mathcal{C}} = \mathcal{H}_{\mathcal{P}} \left(\mathbf{C}_{\mathcal{P}} \cdot \left[\mathbf{U}_{\mathcal{P}}^{(1)} \right]^T + \mathbf{C}_{\mathcal{II}} \right), \quad (7.72)$$

where we have included $\mathcal{H}_{\mathcal{P}}$ to indicate that the terms are only non-zero when the capsule is in the main channel, and where $\mathbf{C}_{\mathcal{P}}$ and $\mathbf{C}_{\mathcal{II}}$ house the $2N_{\mathcal{C}}$ components of $\mu(\lambda - 1)\mathbf{I}_{\mathcal{P},j}^T(\mathbf{x}_0)$, and $\Pi_{G,j}(\mathbf{x}_0)$ respectively. Following the same procedure for \mathcal{A} we obtain $N_{\mathcal{A}}$ pairs of equations which we write in matrix form as

$$\mathbf{J}_{\mathcal{A}}^m = \mathcal{H}_{\mathcal{P}} \left(\mathbf{A}_{\mathcal{P}} \cdot \left[\mathbf{U}_{\mathcal{P}}^{(1)} \right]^T + \mathbf{A}_{\mathcal{II}} \right), \quad (7.73)$$

where the m superscript indicates the main channel equation (7.49), and where $\mathbf{A}_{\mathcal{P}}$ and $\mathbf{A}_{\mathcal{II}}$ are similarly defined with respect to equation (7.71). When the capsule is in the branch channel we follow the same process and write

$$\mathbf{J}_{\mathcal{B}} = (1 - \mathcal{H}_{\mathcal{P}}) \left(\mathbf{B}_{\mathcal{P}} \cdot \left[\mathbf{U}_{\mathcal{P}}^{(1)} \right]^T + \mathbf{B}_{\mathcal{II}} \right), \quad (7.74)$$

when \mathbf{x}_0 is placed on \mathcal{B} , and where $(1 - \mathcal{H}_{\mathcal{P}})$ indicates that the terms are only non-zero when the capsule is in the branch channel, and where $\mathbf{B}_{\mathcal{P}}$ and $\mathbf{B}_{\mathcal{II}}$ house the $2N_{\mathcal{B}}$ components of $\mu(\lambda - 1)\mathbf{I}_{\mathcal{P},j}^T(\mathbf{x}_0)$, and $\Pi_{G,j}(\mathbf{x}_0)$ respectively. When \mathbf{x}_0 is placed on \mathcal{A} we have

$$\mathbf{J}_{\mathcal{A}}^b = (1 - \mathcal{H}_{\mathcal{P}}) \left(\mathbf{A}_{\mathcal{P}} \cdot \left[\mathbf{U}_{\mathcal{P}}^{(1)} \right]^T + \mathbf{A}_{\mathcal{II}} \right), \quad (7.75)$$

where the b superscript indicates the branch channel equation (7.55), and where $\mathbf{A}_{\mathcal{P}}$ and $\mathbf{A}_{\mathcal{II}}$ are the same as in equation (7.73). Putting together equations (7.72) – (7.75) we obtain,

$$\begin{bmatrix} \mathbf{J}_{\mathcal{C}} \\ \mathbf{J}_{\mathcal{A}}^m \\ \mathbf{J}_{\mathcal{B}} \\ \mathbf{J}_{\mathcal{A}}^b \end{bmatrix} = \begin{bmatrix} \mathcal{H}_{\mathcal{P}}\mathbf{C}_{\mathcal{P}} \\ \mathcal{H}_{\mathcal{P}}\mathbf{A}_{\mathcal{P}} \\ (1 - \mathcal{H}_{\mathcal{P}})\mathbf{B}_{\mathcal{P}} \\ (1 - \mathcal{H}_{\mathcal{P}})\mathbf{A}_{\mathcal{P}} \end{bmatrix} \cdot \left[\mathbf{U}_{\mathcal{P}}^{(1)} \right]^T + \begin{bmatrix} \mathcal{H}_{\mathcal{P}}\mathbf{C}_{\mathcal{II}} \\ \mathcal{H}_{\mathcal{P}}\mathbf{A}_{\mathcal{II}} \\ (1 - \mathcal{H}_{\mathcal{P}})\mathbf{B}_{\mathcal{II}} \\ (1 - \mathcal{H}_{\mathcal{P}})\mathbf{A}_{\mathcal{II}} \end{bmatrix}. \quad (7.76)$$

We will now consider the linear the linear system for the fluid-filled branching channel and show how it can be augmented to include equation (7.76). Writing the linear system for a fluid-filled branching channel given in equation (5.121) as

$$\begin{bmatrix} \mathbf{C}_{\mathcal{C}} & \mathbf{C}_{\mathcal{A}} & \mathbf{0} & \mathbf{C}_{\mathcal{A}}^T & \mathbf{C}_{\mathcal{E}_2} & \mathbf{0} & \mathbf{0} \\ \mathbf{A}_{\mathcal{C}} & \mathbf{A}_{\mathcal{A}}^m & \mathbf{0} & \mathbf{A}_{\mathcal{A}}^{m,T} & \mathbf{A}_{\mathcal{E}_2} & \mathbf{0} & \mathbf{0} \\ \mathbf{0} & \mathbf{B}_{\mathcal{A}} & \mathbf{B}_{\mathcal{B}} & \mathbf{B}_{\mathcal{A}}^T & \mathbf{0} & \mathbf{B}_{\mathcal{E}_3} & \mathbf{0} \\ \mathbf{0} & \mathbf{A}_{\mathcal{A}}^b & \mathbf{A}_{\mathcal{B}} & \mathbf{A}_{\mathcal{A}}^{b,T} & \mathbf{0} & \mathbf{A}_{\mathcal{E}_3} & \mathbf{0} \\ \mathbf{0} & \mathbf{U}_{\mathcal{A}}^{P_1} & \mathbf{0} & -\mathbf{F}_{\mathcal{A}}^{P_1} & Q_1 & \mathbf{0} & \mathbf{0} \\ \mathbf{0} & -\mathbf{U}_{\mathcal{A}}^{P_3} & \mathbf{0} & -\mathbf{F}_{\mathcal{A}}^{P_3} & \mathbf{0} & Q_3 & \mathbf{0} \end{bmatrix} \cdot \mathbf{x} \equiv \begin{bmatrix} \mathbf{C}_{FF} & \mathbf{0} \\ \mathbf{A}_{FF}^m & \mathbf{0} \\ \mathbf{B}_{FF} & \mathbf{0} \\ \mathbf{A}_{FF}^b & \mathbf{0} \\ \mathbf{\Pi}_{FF}^m & \mathbf{0} \\ \mathbf{\Pi}_{FF}^b & \mathbf{0} \end{bmatrix} \cdot \mathbf{x} = \begin{bmatrix} \mathcal{C}_I \\ \mathcal{A}_I \\ \mathcal{B}_K \\ \mathcal{A}_K \\ \mathbf{0} \\ \psi \end{bmatrix}, \quad (7.77)$$

where we have introduced a shorthand for the rows of the influence matrix, set the coefficients of $\mathbf{U}_{\mathcal{P}}^{(1)}$ to zero and where the subscript FF indicates a quantity defined in chapter

5 for a fluid-filled branching channel. The elements of the influence matrix and the vector of known values in the linear system (7.77) are mostly submatrices or subvectors. The first and second rows of the linear system correspond to the main channel's boundary integral equations with the first row generated when \mathbf{x}_0 was placed on the walls of the main channel and the second row when \mathbf{x}_0 was placed on the elements of \mathcal{A} . The third and fourth rows correspond to the branch channel's boundary integral equations where the third row corresponds to \mathbf{x}_0 on the walls of the branch channel and the fourth row to \mathbf{x}_0 lying on the notional boundary, \mathcal{A} . The fifth and sixth rows correspond to the pressure equations for π_2 and π_3 respectively. To incorporate the effect of the capsule we add the discretisation of the capsule integrals given in equation (7.76) to the linear system (7.77) and include the discretised pressure equations (7.64) and (7.65) to get,

$$\begin{bmatrix} \mathcal{C}_{FF} & \mathcal{H}_{\mathcal{P}}\mathcal{C}_{\mathcal{P}} \\ \mathcal{A}_{FF}^m & \mathcal{H}_{\mathcal{P}}\mathcal{A}_{\mathcal{P}} \\ \mathcal{B}_{FF} & (1 - \mathcal{H}_{\mathcal{P}})\mathcal{B}_{\mathcal{P}} \\ \mathcal{A}_{FF}^b & (1 - \mathcal{H}_{\mathcal{P}})\mathcal{A}_{\mathcal{P}} \\ \mathbf{\Pi}_{FF}^m & \mathcal{H}_{\mathcal{P}}\mathbf{\Pi}_{\mathcal{P}}^{P_1} \\ \mathbf{\Pi}_{FF}^b & (1 - \mathcal{H}_{\mathcal{P}})\mathbf{\Pi}_{\mathcal{P}}^{P_3} \end{bmatrix} \cdot \mathbf{x} = \begin{bmatrix} \mathcal{C}_I \\ \mathcal{A}_I \\ \mathcal{B}_K \\ \mathcal{A}_K \\ 0 \\ \psi \end{bmatrix} - \begin{bmatrix} \mathcal{H}_{\mathcal{P}}\mathcal{C}_{\Pi} \\ \mathcal{H}_{\mathcal{P}}\mathcal{A}_{\Pi} \\ (1 - \mathcal{H}_{\mathcal{P}})\mathcal{B}_{\Pi} \\ (1 - \mathcal{H}_{\mathcal{P}})\mathcal{A}_{\Pi} \\ \mathcal{H}_{\mathcal{P}}\mathbf{\Pi}_{\Delta}^{P_1} \\ (1 - \mathcal{H}_{\mathcal{P}})\mathbf{\Pi}_{\Delta}^{P_3} \end{bmatrix}, \quad (7.78)$$

as our linear system, and where the first column vector on the right-hand side corresponds to the vector of known values for a fluid-filled branching channel and the second corresponds to the capsule.

It remains to discretise the boundary integral equation for the case when \mathbf{x}_0 lies on the capsule boundary. Let us write equation (7.51) as

$$\begin{aligned} & \int_{\mathcal{A}, \mathcal{C}} f_i^{D_1} G_{ij} \, ds(\mathbf{x}) - \mu \int_{\mathcal{A}} u_i^{D_1} T_{ijk} n_k \, ds(\mathbf{x}) - \pi_2 \int_{\mathcal{E}_2} n_i G_{ij} \, ds(\mathbf{x}) \\ & + 2\pi\mu(1 + \lambda)u_j^{(1)}(\mathbf{x}_0) + \mu(\lambda - 1) \int_{\mathcal{P}}^{PV} u_i^{(1)} T_{ijk} n_k \, ds(\mathbf{x}) \\ & = I_j(\mathbf{x}_0) + 4\pi\mu u_j^{P_1}(\mathbf{x}_0) - \int_{\mathcal{P}} \Delta f_i G_{ij} \, ds(\mathbf{x}) \end{aligned} \quad (7.79)$$

which is valid for \mathbf{x}_0 on the capsule boundary when the capsule lies in the main channel.

The discretised analogues of the integrals over \mathcal{A} and the channel walls are given by

$$\int_{\mathcal{A}} f_i^{D1} G_{ij} \, ds(\mathbf{x}) \approx \mathbf{I}_{\mathcal{A},j}^G(\mathbf{x}_0) \cdot \mathbf{F}_{\mathcal{A}}^D, \quad (7.80)$$

$$\int_{\mathcal{B}} f_i^{D3} G_{ij} \, ds(\mathbf{x}) \approx \mathbf{I}_{\mathcal{B},j}^G(\mathbf{x}_0) \cdot \mathbf{F}_{\mathcal{B}}^D, \quad (7.81)$$

$$\int_{\mathcal{C}} f_i^{D1} G_{ij} \, ds(\mathbf{x}) \approx \mathbf{I}_{\mathcal{C},j}^G(\mathbf{x}_0) \cdot \mathbf{F}_{\mathcal{C}}^D, \quad (7.82)$$

$$\int_{\mathcal{A}} u_i^{D1} T_{ijk} n_k \, ds(\mathbf{x}) \approx \mathbf{I}_{\mathcal{A},j}^T(\mathbf{x}_0) \cdot \mathbf{U}_{\mathcal{A}}^D, \quad (7.83)$$

where each of $\mathbf{I}_{\mathcal{A},j}^G(\mathbf{x}_0)$, $\mathbf{I}_{\mathcal{B},j}^G(\mathbf{x}_0)$, $\mathbf{I}_{\mathcal{C},j}^G(\mathbf{x}_0)$ and $\mathbf{I}_{\mathcal{A},j}^T(\mathbf{x}_0)$ are defined in equations (5.101) – (5.104), and where we have also included the integral over \mathcal{B} because we will use it in the discretisation of equation (7.56) when the capsule lies in the branch channel. We label the integral over \mathcal{E}_2 by $\mathbf{I}_{\mathcal{E}_2,j}^G(\mathbf{x}_0)$ and its value may be calculated exactly using equations (2.44) and (2.45). Therefore we may approximate equation (7.79) by

$$\begin{aligned} & \mathbf{I}_{\mathcal{A},j}^G(\mathbf{x}_0) \cdot \mathbf{F}_{\mathcal{A}}^D + \mathbf{I}_{\mathcal{C},j}^G(\mathbf{x}_0) \cdot \mathbf{F}_{\mathcal{C}}^D - \mu \mathbf{I}_{\mathcal{A},j}^T(\mathbf{x}_0) \cdot \mathbf{U}_{\mathcal{A}}^D - \pi_2 \mathbf{I}_{\mathcal{E}_2,j}^G(\mathbf{x}_0) \\ & + 2\pi\mu(1+\lambda)u_j^{(1)}(\mathbf{x}_0) + \mu(\lambda-1) \int_{\mathcal{P}}^{PV} u_i^{(1)} T_{ijk} n_k \, ds(\mathbf{x}) \\ & = I_j(\mathbf{x}_0) + 4\pi\mu u_j^{P1}(\mathbf{x}_0) - \Pi_{G,j}(\mathbf{x}_0). \end{aligned} \quad (7.84)$$

To discretise the capsule integral and the velocity on the capsule boundary we define

$$P_j(\mathbf{x}_0^{(r)}) = 2\pi\mu(1+\lambda)u_j^{(1)}(\mathbf{x}_0^{(r)}) + \mu(\lambda-1) \int_{\mathcal{P}}^{PV} u_i^{(1)} T_{ijk} n_k \, ds(\mathbf{x}), \quad (7.85)$$

where $\mathbf{x}_0^{(r)}$ is the midpoint of the r^{th} element, and which we may approximate by

$$\begin{aligned} P_j(\mathbf{x}_0^{(r)}) & \approx \left(2\pi\mu(1+\lambda)\mathcal{P}_{u,j}(\mathbf{x}_0^{(r)}) + \mu(\lambda-1)\mathbf{I}_{\mathcal{P},j}^{T,PV}(\mathbf{x}_0^{(r)}) \right) \cdot \mathbf{U}_{\mathcal{P}}^{(1)} \\ & = \mathbf{I}_{\mathcal{P}}^{\mathcal{P}}(\mathbf{x}_0^{(r)}) \cdot \mathbf{U}_{\mathcal{P}}^{(1)}, \end{aligned} \quad (7.86)$$

and where

$$\mathcal{P}_{u,j}(\mathbf{x}_0^{(r)}) = \left[\delta_{r1}\delta_{xj} \quad \delta_{r1}\delta_{yj} \quad \cdots \quad \delta_{rN_{\mathcal{P}}}\delta_{xj} \quad \delta_{rN_{\mathcal{P}}}\delta_{yj} \right], \quad (7.87)$$

$$\mathbf{I}_{\mathcal{P},j}^{T,PV}(\mathbf{x}_0^{(r)}) = \left[\tilde{T}_{xj,1} \quad \tilde{T}_{yj,1} \quad \cdots \quad \tilde{T}_{xj,r}^{PV} \quad \tilde{T}_{yj,r}^{PV} \quad \cdots \quad \tilde{T}_{xj,N_{\mathcal{P}}} \quad \tilde{T}_{yj,N_{\mathcal{P}}} \right], \quad (7.88)$$

with the r^{th} pair of entries of $\mathbf{I}_{\mathcal{P},j}^{T,PV}(\mathbf{x}_0^{(r)})$ taking the principal value of the stress tensor integral because \mathbf{x}_0 lies on the r^{th} boundary element of \mathcal{P} . Substituting equation (7.86) into equation (7.84) and writing the resultant matrix equation in terms of the solution

vector \mathbf{x} we obtain,

$$\begin{aligned} & \left[\mathbf{I}_{\mathcal{C},j}^G(\mathbf{x}_0) \quad \mathbf{I}_{\mathcal{A},j}^G(\mathbf{x}_0) \quad \mathbf{0} \quad -\mu \mathbf{I}_{\mathcal{A},j}^T(\mathbf{x}_0) \quad -I_{\mathcal{E}_2,j}^G(\mathbf{x}_0) \quad 0 \quad \mathbf{I}_{\mathcal{P}}^{\mathcal{P}}(\mathbf{x}_0) \right] \cdot \mathbf{x} \\ & = I_j(\mathbf{x}_0) + 4\pi\mu u_j^{P_1}(\mathbf{x}_0) - \Pi_{G,j}(\mathbf{x}_0). \end{aligned} \quad (7.89)$$

Evaluation of this equation with \mathbf{x}_0 placed at the midpoint of each of the capsule's boundary elements results in $2N_{\mathcal{P}}$ equation which we write as

$$\left[\mathcal{P}_{\mathcal{C}}^m \quad \mathcal{P}_{\mathcal{A}}^m \quad \mathbf{0} \quad \mathcal{P}_{\mathcal{A}}^{m,T} \quad \mathcal{P}_{\mathcal{E}_2}^m \quad \mathbf{0} \quad \mathcal{P}_{\mathcal{P}}^m \right] \cdot \mathbf{x} = \mathcal{P}_{\Pi}^m, \quad (7.90)$$

where the m superscript indicates that the capsule is in the main channel and the elements of $\mathcal{P}_{\mathcal{C}}^m$, $\mathcal{P}_{\mathcal{A}}^m$, $\mathcal{P}_{\mathcal{A}}^{m,T}$, $\mathcal{P}_{\mathcal{E}_2}^m$ and $\mathcal{P}_{\mathcal{P}}^m$ house the $2N_{\mathcal{P}}$ values of $\mathbf{I}_{\mathcal{C},j}^G(\mathbf{x}_0)$, $\mathbf{I}_{\mathcal{A},j}^G(\mathbf{x}_0)$, $-\mu \mathbf{I}_{\mathcal{A},j}^T(\mathbf{x}_0)$, $-I_{\mathcal{E}_2,j}^G(\mathbf{x}_0)$ and $\mathbf{I}_{\mathcal{P}}^{\mathcal{P}}(\mathbf{x}_0)$ respectively, and \mathcal{P}_{Π}^m houses the $2N_{\mathcal{P}}$ values of $I_j(\mathbf{x}_0) + 4\pi\mu u_j^{P_1}(\mathbf{x}_0) - \Pi_{G,j}(\mathbf{x}_0)$. For convenience we write

$$\mathcal{P}^m = \left[\mathcal{P}_{\mathcal{C}}^m \quad \mathcal{P}_{\mathcal{A}}^m \quad \mathbf{0} \quad \mathcal{P}_{\mathcal{A}}^{m,T} \quad \mathcal{P}_{\mathcal{E}_2}^m \quad \mathbf{0} \right] \quad (7.91)$$

which enables us to write the linear system as

$$\begin{bmatrix} \mathcal{C}_{FF} & \mathcal{C}_{\mathcal{P}} \\ \mathcal{A}_{FF}^m & \mathcal{A}_{\mathcal{P}} \\ \mathcal{B}_{FF} & \mathbf{0} \\ \mathcal{A}_{FF}^b & \mathbf{0} \\ \Pi_{FF}^m & \Pi_{\mathcal{P}}^{P_1} \\ \Pi_{FF}^b & \mathbf{0} \\ \mathcal{P}^m & \mathcal{P}_{\mathcal{P}}^m \end{bmatrix} \cdot \mathbf{x} = \begin{bmatrix} \mathcal{C}_I \\ \mathcal{A}_I \\ \mathcal{B}_K \\ \mathcal{A}_K \\ 0 \\ \psi \\ \mathbf{0} \end{bmatrix} - \begin{bmatrix} \mathcal{C}_{\Pi} \\ \mathcal{A}_{\Pi} \\ \mathbf{0} \\ \mathbf{0} \\ \Pi_{\Delta}^{P_1} \\ 0 \\ -\mathcal{P}_{\Pi}^m \end{bmatrix}, \quad (7.92)$$

when the capsule is in the main channel.

Next we assume the capsule is in the branch channel and write the branch channel's boundary integral equation (7.56) as

$$\begin{aligned} & - \int_{\mathcal{A}} f_i^{D_1} G_{ij} \, ds(\mathbf{x}) + \int_{\mathcal{B}} f_i^{D_3} G_{ij} \, ds(\mathbf{x}) + \mu \int_{\mathcal{A}} u_i^{D_1} T_{ijk} n_k \, ds(\mathbf{x}) \\ & - \pi_3 \int_{\mathcal{E}_3} n_i G_{ij} \, ds(\mathbf{x}) + 2\pi\mu (1 + \lambda) u_j^{(1)}(\mathbf{x}_0) + \mu(\lambda - 1) \int_{\mathcal{P}}^{PV} u_i^{(1)} T_{ijk} n_k \, ds(\mathbf{x}) \\ & = K_j(\mathbf{x}_0) + 4\pi\mu u_j^{P_3}(\mathbf{x}_0) - \int_{\mathcal{P}} \Delta f_i G_{ij} \, ds(\mathbf{x}), \end{aligned} \quad (7.93)$$

for \mathbf{x}_0 on the capsule boundary. We approximate the equation by the matrix form,

$$\begin{aligned} & \left[\mathbf{0} \quad -\mathbf{I}_{\mathcal{A},j}^G(\mathbf{x}_0) \quad \mathbf{I}_{\mathcal{B},j}^G(\mathbf{x}_0) \quad \mu \mathbf{I}_{\mathcal{A},j}^T(\mathbf{x}_0) \quad 0 \quad -I_{\mathcal{E}_3,j}^G(\mathbf{x}_0) \quad \mathbf{I}_{\mathcal{P}}^{\mathcal{P}}(\mathbf{x}_0) \right] \cdot \mathbf{x} \\ & = K_j(\mathbf{x}_0) + 4\pi\mu u_j^{P_3}(\mathbf{x}_0) - \Pi_{G,j}(\mathbf{x}_0), \end{aligned} \quad (7.94)$$

where $\mathbf{I}_{B,j}^G(\mathbf{x}_0)$ is defined in equation (7.81). Evaluation of this equation with \mathbf{x}_0 placed at the midpoint of each of the capsule's boundary elements results in $2N_{\mathcal{P}}$ equation which we write as

$$\begin{bmatrix} \mathbf{0} & \mathcal{P}_{\mathcal{A}}^b & \mathcal{P}_{\mathcal{B}}^b & \mathcal{P}_{\mathcal{A}}^{b,T} & \mathbf{0} & \mathcal{P}_{\mathcal{E}_3}^b & \mathcal{P}_{\mathcal{P}}^b \end{bmatrix} \cdot \mathbf{x} = \mathcal{P}_{\Pi}^b, \quad (7.95)$$

where the b superscript indicates that the capsule is in the branch channel and the elements of $\mathcal{P}_{\mathcal{A}}^b$, $\mathcal{P}_{\mathcal{B}}^b$, $\mathcal{P}_{\mathcal{A}}^{b,T}$, $\mathcal{P}_{\mathcal{E}_3}^b$ and $\mathcal{P}_{\mathcal{P}}^b$ house the $2N_{\mathcal{P}}$ values of $-\mathbf{I}_{\mathcal{A},j}^G(\mathbf{x}_0)$, $\mathbf{I}_{\mathcal{B},j}^G(\mathbf{x}_0)$, $\mu \mathbf{I}_{\mathcal{A},j}^T(\mathbf{x}_0)$, $-\mathbf{I}_{\mathcal{E}_3,j}^G(\mathbf{x}_0)$ and $\mathbf{I}_{\mathcal{P}}^{\mathcal{P}}(\mathbf{x}_0)$ respectively, and \mathcal{P}_{Π}^b houses the $2N_{\mathcal{P}}$ values of $K_j(\mathbf{x}_0) + 4\pi\mu u_j^{P_3}(\mathbf{x}_0) - \Pi_{G,j}(\mathbf{x}_0)$. We write

$$\mathcal{P}^b = \begin{bmatrix} \mathbf{0} & \mathcal{P}_{\mathcal{A}}^b & \mathcal{P}_{\mathcal{B}}^b & \mathcal{P}_{\mathcal{A}}^{b,T} & \mathbf{0} & \mathcal{P}_{\mathcal{E}_3}^b \end{bmatrix} \quad (7.96)$$

which enables us to write the linear system as

$$\begin{bmatrix} \mathcal{C}_{FF} & \mathbf{0} \\ \mathcal{A}_{FF}^m & \mathbf{0} \\ \mathcal{B}_{FF} & \mathcal{B}_{\mathcal{P}} \\ \mathcal{A}_{FF}^b & \mathcal{A}_{\mathcal{P}} \\ \Pi_{FF}^m & \mathbf{0} \\ \Pi_{FF}^b & \Pi_{\mathcal{P}}^{P_3} \\ \mathcal{P}^b & \mathcal{P}_{\mathcal{P}}^b \end{bmatrix} \cdot \mathbf{x} = \begin{bmatrix} \mathcal{C}_I \\ \mathcal{A}_I \\ \mathcal{B}_K \\ \mathcal{A}_K \\ 0 \\ \psi \\ \mathbf{0} \end{bmatrix} - \begin{bmatrix} \mathbf{0} \\ \mathbf{0} \\ \mathcal{B}_{\Pi} \\ \mathcal{A}_{\Pi} \\ 0 \\ \Pi_{\Delta}^{P_3} \\ -\mathcal{P}_{\Pi}^b \end{bmatrix}, \quad (7.97)$$

when the capsule is in the branch channel. We are now in a position to construct the linear system using equation (7.92) when the capsule is in the main channel and using equation (7.97) when the capsule lies in the branch channel. It is important to note that the linear system simplifies significantly when the viscosity ratio is unity. We have seen in the governing disturbance pressure and velocity equations that when $\lambda = 1$ the capsule velocities disappear from the equations. Therefore we may reduce the linear system by omitting $\mathbf{U}_{\mathcal{P}}^{(1)}$ from \mathbf{x} which makes it equal to the vector of unknowns for a fluid-filled branching channel, which we will label \mathbf{x}_{FF} . The second column from the matrix in equations (7.92) and (7.97) may also be omitted. We also do not need to evaluate the relevant boundary integral equation on the boundary of the capsule in order to solve the linear system and so the last row in the aforementioned linear systems is also omitted. The resultant linear system is given by,

$$\begin{bmatrix} \mathcal{C}_{FF} \\ \mathcal{A}_{FF}^m \\ \mathcal{B}_{FF} \\ \mathcal{A}_{FF}^b \\ \Pi_{FF}^m \\ \Pi_{FF}^b \end{bmatrix} \cdot \mathbf{x}_{FF} = \begin{bmatrix} \mathcal{C}_I \\ \mathcal{A}_I \\ \mathcal{B}_K \\ \mathcal{A}_K \\ 0 \\ \psi \end{bmatrix} - \begin{bmatrix} \mathcal{H}_{\mathcal{P}} \mathcal{C}_{\Pi} \\ \mathcal{H}_{\mathcal{P}} \mathcal{A}_{\Pi} \\ (1 - \mathcal{H}_{\mathcal{P}}) \mathcal{B}_{\Pi} \\ (1 - \mathcal{H}_{\mathcal{P}}) \mathcal{A}_{\Pi} \\ \mathcal{H}_{\mathcal{P}} \Pi_{\Delta}^{P_1} \\ (1 - \mathcal{H}_{\mathcal{P}}) \Pi_{\Delta}^{P_3} \end{bmatrix}, \quad (7.98)$$

which is only different to the linear system for a fluid-filled branching channel by the second column vector on the right-hand side, which adds the disturbance caused by the

capsule's presence to the linear system. The matrix in equation (7.98), and more importantly its inverse, need only be computed once for a given configuration of the ends, \mathcal{A} , \mathcal{B} and \mathcal{C} . When the capsule is moved the vector on the right-hand side is updated and the solution to the linear system is obtained by multiplying by the matrix inverse.

The size of the 'influence' matrix on the left-hand side in equation (7.98) is $(4N_{\mathcal{A}} + 2N_{\mathcal{B}} + 2N_{\mathcal{C}} + 2) \times (4N_{\mathcal{A}} + 2N_{\mathcal{B}} + 2N_{\mathcal{C}} + 2)$. When $\lambda \neq 1$ the 'influence' matrix in equations (7.92) and (7.84) increases to $(4N_{\mathcal{A}} + 2N_{\mathcal{B}} + 2N_{\mathcal{C}} + 2N_{\mathcal{P}} + 2) \times (4N_{\mathcal{A}} + 2N_{\mathcal{B}} + 2N_{\mathcal{C}} + 2N_{\mathcal{P}} + 2)$. In our simulations we took $N_{\mathcal{A}} = 200$, $N_{\mathcal{B}} = 400$, $N_{\mathcal{C}} = 800$ and $N_{\mathcal{P}} = 316$ for a particle of radius $d/2$. When we changed the size of the particle we altered the number of boundary elements to preserve the element length. We found this number of boundary elements to be an acceptable compromise between accuracy and calculation time. Details on the validation of the numerical calculations are given in the next section.

Once we had calculated the influence matrix and the vector of known values we solved the system using GMRES (e.g. Saad 2003) when $\lambda \neq 1$ and by left-multiplication of the inverse of the 'influence' matrix when $\lambda = 1$. To obtain the nodal velocities of the capsule we evaluate the relevant boundary integral equation when $\lambda = 1$. When $\lambda \neq 1$ we construct a periodic cubic spline using the cumulative polygonal arc-length and use the spline to interpolate the nodal velocities. Once the nodal velocities are known we move the capsule, update the linear system and obtain the new solution. To move the capsule we integrated the kinematic equation,

$$\frac{d\mathbf{x}_r}{dt} = \mathbf{u}(\mathbf{x}_r), \quad (7.99)$$

where \mathbf{x}_r is the position vector of the r^{th} capsule node and the values of $\mathbf{u}(\mathbf{x}_r)$ are the velocities of the capsule nodes. To integrate (7.99) we used the adaptive time-stepping Runge-Kutta-Fehlberg method (e.g. Atkinson 1978) where we took an initial time step of $0.0005 d/U_0^{P_1}$ when we included bending moments and $0.005 d/U_0^{P_1}$ when bending moments were absent. Our small initial time step follows from the observations made by Pozrikidis (2001) on the effects of bending resistance on a capsule in a three-dimensional shear flow.

In chapter 3 we showed that the disturbance velocity decayed to less than 1% of its maximum value at a distance of 3 particle radii. Therefore we did not allow the distance between the particle and the entrance or the exits to become less than this distance.

7.3 Flow parameters

Except for where indicated, all of the validation and results to be presented in next two sections, were computed for the case when the main channel and the side branch are of equal width, $D/d = 1$. In all cases the main channel length is $l = 12d$ and the length of the branch is $L = 6d$. The dynamics depend on the viscosity ratio, λ , the initial

dimensionless capsule radius,

$$\rho = \frac{a}{d}, \quad (7.100)$$

where a is the radius of the unstressed circular shape, the initial shape of the capsule, the initial centroid location,

$$\mathbf{x}_c = (x_c, y_c), \quad (7.101)$$

the branch angle α , the ratio of the branch widths,

$$\delta = \frac{D}{d}, \quad (7.102)$$

the flux ratio, Q , and the two dimensionless parameters,

$$M = \frac{E_B}{\mu Q_1 d}, \quad W = \frac{k d}{\mu Q_1}, \quad (7.103)$$

where E_B is the bending modulus of the elastic membrane and k is the membrane stiffness. The M parameter describes the relative importance of bending moments in the elastic capsule membrane and W describes the relative importance of the membrane stiffness. We set $M = 0$ to model a capsule which does not resist bending and $M = 0.001$ for a capsule which does. The model was sensitive to the size of M with larger values causing instabilities to develop in the numerics. The small value of M is of a similar order to the analogous three-dimensional quantity used by Pozrikidis (2001). We also point out that in biological cells, such as red blood cells, the membrane's resistance to stretching is much stronger than its resistance to bending (e.g. Secomb et al. 2007), thereby providing further justification for our choice of values for M and W . The unstressed capsule shape is a circle, and in most of our presented results the capsule will also start each simulation as a circle. When the capsule is unstressed the interfacial traction jump, $\Delta \mathbf{f}$, will be zero. Therefore when the capsule starts as a circle and $\lambda = 1$, the disturbance pressures, π_2 and π_3 , and the unknown wall tractions and the tractions and velocities on \mathcal{A} will equal those obtained for a fluid-filled branching channel with the same parameters. We choose d , Q_1/d and d^2/Q_1 as our length, velocity and time scales.

7.4 Validation

We have already validated the numerical code for the elastic capsule in chapter 4 where we also satisfied ourselves that the disturbance velocity induced by the capsule's presence decayed rapidly as we approached the ends of the computational domain. In all of the results to be presented in the next section, the centreline disturbance velocities at \mathcal{E}_1 , \mathcal{E}_2 and \mathcal{E}_3 are all less than 1.5% of the respective Poiseuille velocities. We also confirmed that the tractions on the channel walls smoothly approach the appropriate values for Poiseuille flow as we approach the entrance or the exits.

To check the numerical solution we placed an unstressed capsule with $\lambda = 1$, $\rho = 0.5$, $W = 1$, $M = 0.001$ and $\mathbf{x}_c/d = (6, 0)$ in a branching channel flow with $l = 12d$,

$L = l/2$, $\alpha = \pi/2$, $Q = 0.5$ and $\delta = 1$. Since an unstressed capsule should have a negligible effect on the flow, the exit pressures should equal those for a fluid-filled branching channel with the same flow parameters. We found that the exit pressures did not change when the unstressed capsule was present. We removed the capsule and doubled the number of elements. The exit pressures changed by no more than 0.06%. We then reintroduced the stress-free capsule and once again found that the capsule's presence did not affect the exit pressures. Furthermore we increased the length of the channels so that $l = 24d$ while preserving the element length on the channel boundaries and compared the boundary tractions and velocities with those for the shorter channel. The values were in excellent agreement; the absolute error in the boundary tractions remained less than $0.05 \mu U_0^{P_1} / d$, and the absolute error in the velocities on \mathcal{A} were less than $0.005 U_0^{P_1}$.

Next we took the steady state capsule from a straight channel simulation with parameters $\lambda = 1$, $\rho = 0.5$, $W = 1$, $M = 0.001$ and placed it in a branching channel such that $\mathbf{x}_c/d = (6, 0)$, $\alpha = \pi/2$, $Q = 0.5$ and $\delta = 1$. When we doubled the number of boundary elements the disturbance pressures at the exits changed by no more than 0.05%.

To verify the numerical time integration method we compared the solution obtained from the Runge-Kutta-Fehlberg method with two separate simulations which used the second order Runge-Kutta method with constant time steps of $0.0005 d/U_0^{P_1}$ and $0.001 d/U_0^{P_1}$. The simulation parameters were $\lambda = 1$, $\rho = 0.5$, $W = 1$, $M = 0.001$, $\alpha = \pi/2$, $Q = 0.9$ and $\delta = 1$. The capsule was released with its centroid at $\mathbf{x}_c/d = (2, 0)$. There were no significant differences between the three simulations

Due to the incompressibility of the capsule fluid, the area inside the capsule should remain constant during a simulation. As a further check on our computations, we monitor the area contained inside the capsule boundary. For the results to be presented in the next section, it has been confirmed that the area changes by no more than 0.05% of its initial value for simulations with bending moments, $M \neq 0$, and by no more than 0.22% of its initial value for simulations for no bending moments, $M = 0$.

7.5 Results

We begin by examining the motion with a moderate sized capsule with $\rho = 0.5$ for different values of the flux ratio Q . We showed in chapter 4 that a flexible capsule in a straight channel required a distance of very many capsule diameters to achieve a steady-state configuration. However the capsule deforms into a parachute-like shape which qualitatively resembles the steady-state shape after only a few capsule diameters. Therefore in the simulations to be presented, the capsule was started sufficiently far upstream of the branch entrance for the parachute-like shape to emerge before the capsule reached the junction. Furthermore, in some applications there may be numerous branchings which occur over a relatively short distance and so it is questionable whether a capsule could achieve a steady-state between branchings. For example, capillaries in the microcirculation have numerous branchings. For this reason there is some justification in preferring near steady-state configurations to steady-state configurations when simulating a capsule entering a

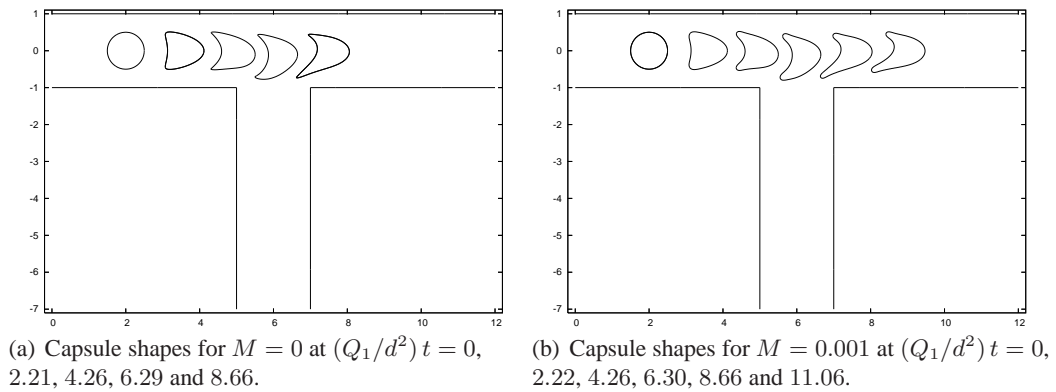


Figure 7.2 : Capsule journeys when $\lambda = 1$, $\rho = 0.5$, $W = 1$, $\alpha = \pi/2$ and $Q = 0.9$. At $t = 0$ the capsule centroid is at $\mathbf{x}_c/d = (2, 0)$.

branch. In the following simulations, the capsule is released at $t = 0$ in its unstressed circular configuration and with $\mathbf{x}_c/d = (2, 0)$, unless stated otherwise. It should be noted that a deformed capsule shape could be used as the initial shape, however the initial deformation must then be taken into account when interpreting the results, especially for capsules which begin their journey offset from the centreline.

We begin by discussing results for the case $\lambda = 1$ so that the viscosity of the ambient fluid equals that of the fluid contained in the capsule. In the first few cases we compare the results obtained with no bending resistance to those obtained in the absence of bending moments in a branching channel with $\delta = 1$ and $\alpha = \pi/2$. In figure 7.2 we show capsule journeys for a capsule with $\rho = 0.5$, $W = 1$ and $Q = 0.9$. The capsule in figure 7.2 (a) has $M = 0$ and so does not resist bending. In figure 7.2 (b) the capsule has a small resistance to bending with $M = 0.001$. When $Q = 0.9$ the capsule remains in the main channel, as can be observed in figures 7.2 (a) and 7.2 (a). The lower trailing tip becomes more deformed than the top trailing tip as it feels the effect of the fluid being drawn into the side branch. Once the capsule has passed over the entrance to the side branch, it begins to return to the symmetrical steady state shape seen in the straight channel simulations in chapter 4. As was remarked there, a distance of a considerable number of capsule radii is required to attain the steady shape and the present computational domain is too short to observe this. We can see that when $M = 0$ the capsule shape has noticeably more pointed tips than when $M = 0.001$. The simulation with $M = 0$ was terminated before the simulation for $M = 0.001$ because the numerical error became unacceptably large as the capsule travelled over the right-hand side of the branch entrance due to a steep rise in the curvature at the sharp lower trailing tip.

When $Q = 0.1$ the flow in the side branch is sufficiently strong to draw the capsule out of the main channel, as can be seen in figures 7.3 (a) and 7.3 (b) where $W = 1$ in both figures and $M = 0$ in the former and $M = 0.001$ in the latter. Again the sharp trailing tips are evident when bending resistance is absent. The initially circular capsule quickly deforms within two particle radii to the familiar parachute shape. As the capsule negotiates the corner into the side branch it undergoes considerable further deformation. The

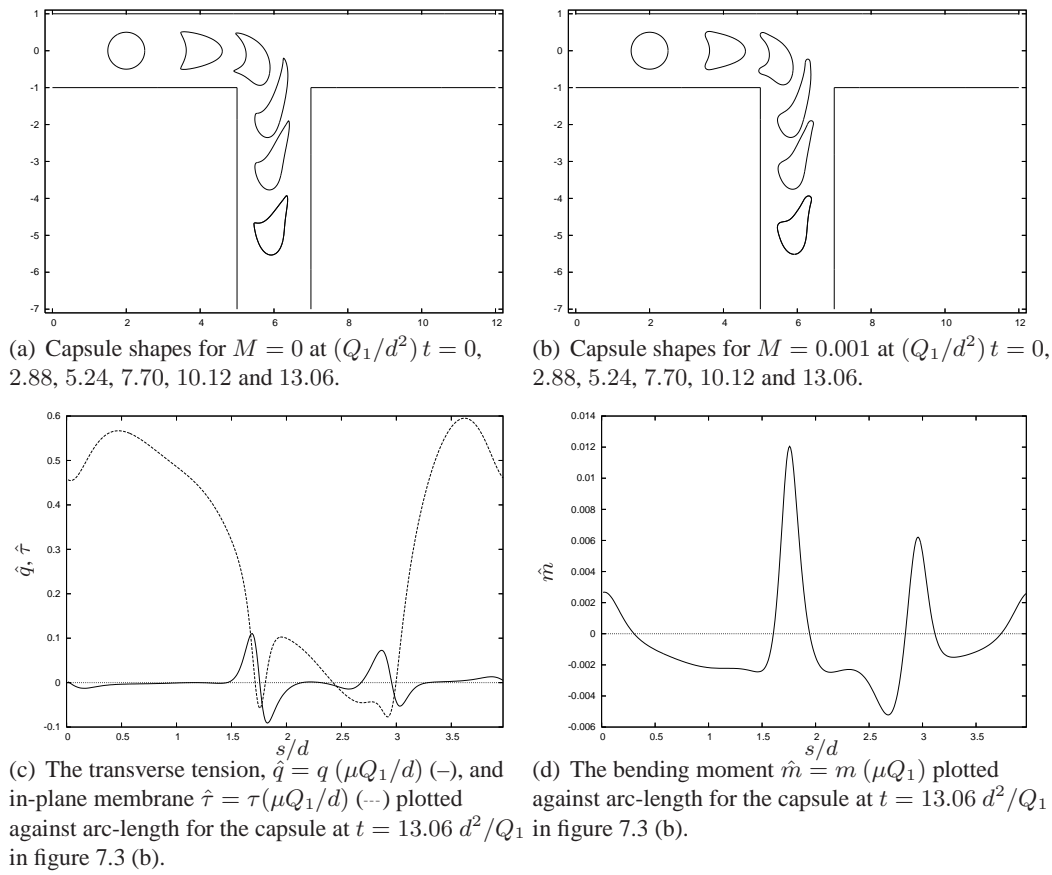


Figure 7.3 : Capsule journeys, membrane tensions and bending moments when $\lambda = 1$, $\rho = 0.5$, $W = 1$, $\alpha = \pi/2$ and $Q = 0.1$. At $t = 0$ the capsule centroid is at $\mathbf{x}_c/d = (2, 0)$. In (c) and (d) arc-length is measured anti-clockwise from zero at the lowermost point on the capsule as it appears in the final shape in figure 7.3 (b).

in-plane and transverse membrane tensions and the bending moment for the last capsule shown in figure 7.3 (b) at time $t = 13.06 d^2/Q_1$ are displayed in figures 7.3 (c) and 7.3 (d). In figure 7.4 we show the membrane tensions and bending moments for the steady-state shape of a capsule in a straight channel with the same flow parameters. The capsule shape is shown in figure 4.17 (a) of chapter 4. It is interesting to note that the peak values of the transverse and in-plane tensions in figure 7.3 (c) are slightly more than half of those for the steady-state solution in figure 7.4 (a), while the peak value of the bending moment in figure 7.3 (d) is about 70% of the peak value in figure 7.4 (b). The deformation seen in figure 7.3 (b) is sufficiently severe that the capsule retains the signature of the distortion suffered at the junction up to the point where the simulation was terminated. We expect that the capsule will slowly return to the steady-state shape as it moves further down the branch. According to the results from chapter 4, we may reasonably assume that the last capsule shape shown at $t = 13.06 d^2/Q_1$ is sufficiently far from the junction to consider it as being effectively carried in a unidirectional flow, aside from the disturbance due to the capsule itself. With this in mind, to estimate the recovery distance required for the capsule to attain a steady-state shape, we took the last capsule shape in figure 7.3 (b), which is shown at the time $t = 13.06 d^2/Q_1$, placed it into a straight channel flow with the same

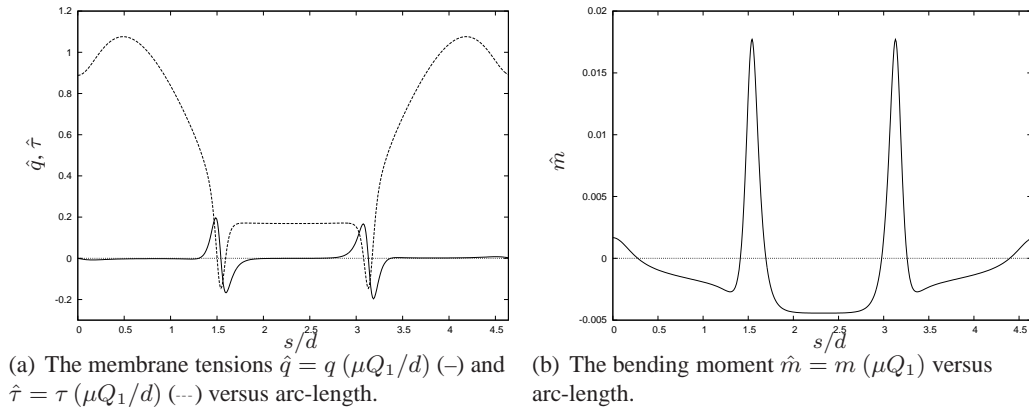


Figure 7.4 : The membrane tensions and the bending moment versus arc-length, for the steady-state shape of a capsule in a straight channel with $\lambda = 1$, $\rho = 0.5$, $W = 1$ and $M = 0.001$. The capsule shape is shown in figure 4.17 (a).

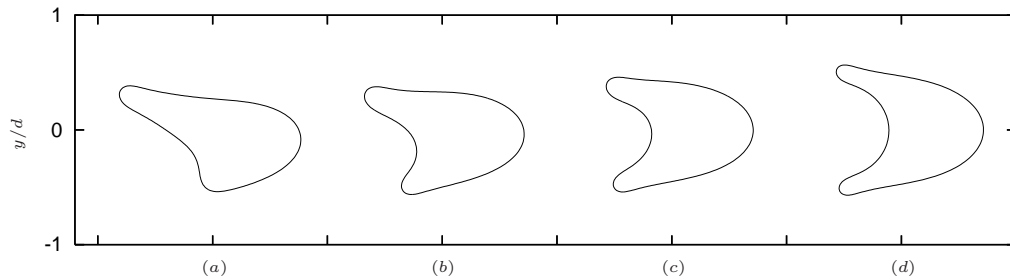


Figure 7.5 : Evolution of the final capsule shape from figure 7.3 (b) when $t = 13.06 d^2/Q_1$. Capsule shapes shown in (a), (b), (c) and (d) at $(Q_1/d^2)t = 0, 3.7, 9.0$ and 37.1 respectively. The final shape is the steady-state shape.

flux as that in the side branch. The evolution of the deformed capsule shape is shown in figure 7.5 . At $t = 0$ the deformed capsule is released and allowed to evolve. Shape (b) in the figure shows the capsule at $t = 3.7 d^2/Q_1$ when it has travelled 5.1 capsule radii along the channel. The capsule has developed the familiar parachute shape. At $t = 9.0 d^2/Q_1$ the capsule has moved 12.2 radii along the channel from its starting position. The capsule shape is shown as shape (c) in the figure and it closely resembles the steady-state shape which it finally attains at $t = 37.1 d^2/Q_1$ when the capsule has travelled a distance of 48.9 radii along the channel. A steady state was deemed to have been achieved when the normal component of the nodal velocity, $\mathbf{n} \cdot d\mathbf{X}_i/dt$, on the capsule boundary relative to the capsule centroid is less than $0.001 Q_1/d$ for all capsule nodes $i = 1, \dots, N_p$. This result indicates that the capsule retains the signature of the branch distortion for a recovery length of very many capsule radii after it has passed through the branch entrance. With regard to blood flow in the capillary network, for example, this suggests that although cells will tend to return to a shape resembling their equilibrium configuration for a straight tube over a fairly short distance, there is unlikely to be sufficient room for equilibrium to be fully established before the cell encounters a further branching.

Figure 7.6 displays the normalised exit pressures, \hat{p}_2 at \mathcal{E}_2 , and \hat{p}_3 at \mathcal{E}_3 , for the capsule journey shown in figure 7.3 (b). The normalised pressure is defined to be the pressure in

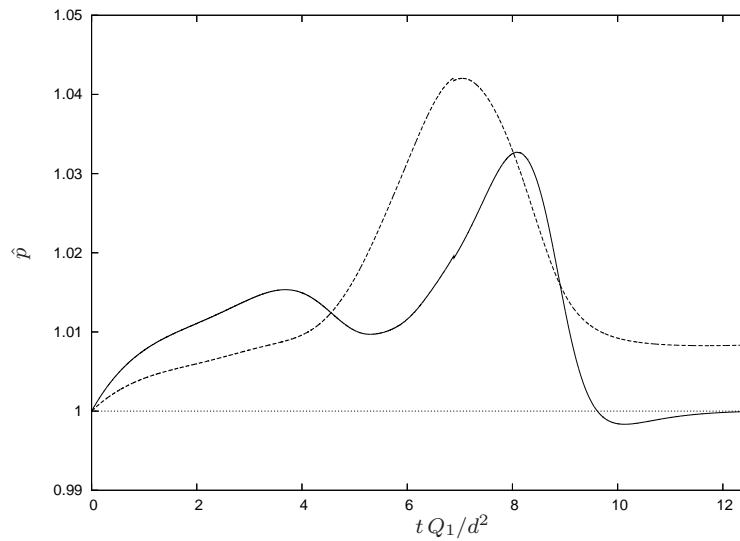


Figure 7.6 : Normalised pressures \hat{p}_2 (—) and \hat{p}_3 (---) against time for $\lambda = 1$, $\rho = 0.5$, $W = 1$, $M = 10^{-3}$, $\alpha = \pi/2$ and $Q = 0.1$. The capsule journey is shown in figure 7.3 (b).

the presence of the capsule divided by the constant pressure obtained under the same flow conditions but in the absence of the capsule. When $\hat{p}_2 = 1$ or $\hat{p}_3 = 1$ the pressure at the exit equals the fluid-filled channel exit pressure. At $t = 0$ the traction jump, $\Delta \mathbf{f}$, is zero and the flow behaves as if the capsule were absent, in which case \hat{p}_2 and \hat{p}_3 are both equal to one. Both of the normalised pressures, \hat{p}_2 and \hat{p}_3 increase in the early stages of the motion as stresses develop in the membrane. At $t \approx 4 d^2/Q_1$ the particle moves from the centreline of the main channel towards the branch and this is accompanied by an increase in the branch pressure, \hat{p}_3 , and a reduction in \hat{p}_2 . The maximum values of \hat{p}_2 and \hat{p}_3 occur at $t \approx 8 d^2/Q_1$ and $t \approx 7 d^2/Q_1$ respectively. At both of these times most of the capsule has passed into the branch. As the capsule travels further into the branch the normalised pressures decrease. At the end of the simulation, \hat{p}_2 returns to unity and \hat{p}_3 approaches 1.008, the increase over its initial value of unity being due to the presence of the capsule in the side branch.

When $Q = 0.5$, so that the flux at the exits are the same, a capsule released with its centroid on the channel centreline tends to get caught on the right-hand side of the branch entrance. This is illustrated in figure 7.7 (a) where $M = 0$ and in figure 7.7 (b) where $M = 0.001$. We can see once again that the trailing tips of the capsule when $M = 0$ are pointed rather than rounded. The trapped capsule is caught in what is effectively an extensional flow which stretches the capsule simultaneously into the branch and along the main channel. Manga (2006) found similar behaviour for a liquid drop caught at the apex of a bifurcating channel. Since the wall shear stress at a sharp corner is formally infinite in a Stokes flow (see Appendix E), it is interesting to look at the tensions which develop in the elastic membrane when the capsule is close to this point. In figure 7.7 (c) we plot the in-plane and transverse membrane tensions, $\hat{q} = q (\mu Q_1/d)$ and $\hat{\tau} = \tau (\mu Q_1/d)$, for the final capsule shape presented in figure 7.7 (b) at the time $t = 12.55 d^2/Q_1$. The capsule profile at this instant is shown in figure 7.7 (d). The transverse tension, \hat{q} , is rather

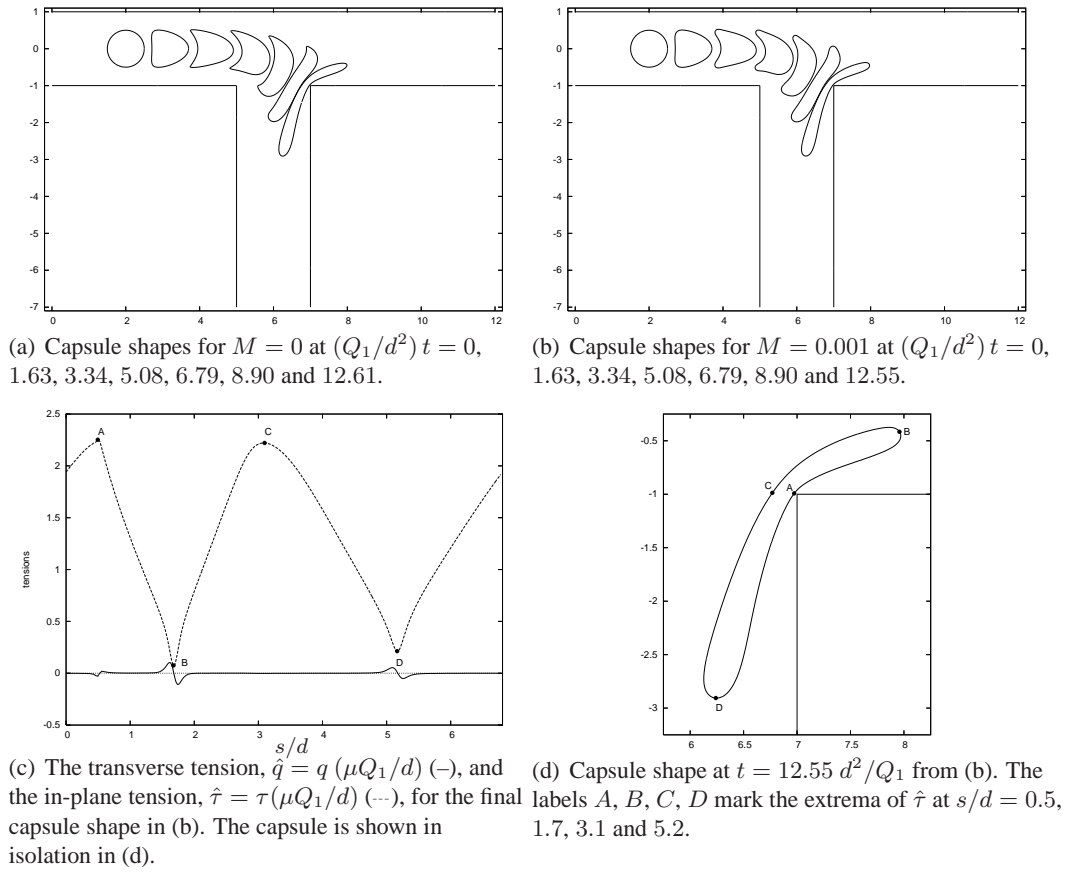


Figure 7.7 : Capsule journeys and membrane tensions when $\lambda = 1, \rho = 0.5, W = 1, \alpha = \pi/2$ and $Q = 0.5$. At $t = 0$ the capsule centroid is at $\mathbf{x}_c/d = (2, 0)$.

small around the capsule perimeter. The in-plane tension $\hat{\tau}$ remains positive around the capsule boundary, implying through the constitutive law (4.51), given in chapter 4, that the membrane is everywhere in extension from its circular reference configuration. Local minima of $\hat{\tau}$ occur at the tips of the capsule labelled B and D in the figure. The maxima of $\hat{\tau}$, which occur at the points marked A and C in the figure, is more than twice that for the steady-state capsule shown in figure 4.18 (a) of chapter 4. The occurrence of such large tensions on the capsule boundary close to the sharp corner suggests the possibility of bursting.

Capsules with a stronger membrane stiffness are expected to deform less during the motion. This is confirmed in figure 7.8 which shows the results of a calculation for $\lambda = 1, \rho = 0.5, W = 5, M = 0.001$ and $\alpha = \pi/2$. In figure 7.8 (a) we set $Q = 0.9$. The capsule experiences noticeably less deformation than that seen in figure 7.2 (b). Figure 7.8 (b) shows the capsule entering the branch when $Q = 0.1$. As expected the capsule becomes less deformed than that shown in figure 7.3 (b) when $W = 1$.

The effect of increasing the viscosity ratio is examined in figure 7.9 . Capsule journeys for the flux ratios $Q = 0.1$ and $Q = 0.9$ are shown for the case $\lambda = 5$ corresponding to a more viscous fluid inside the capsule, and where $\rho = 0.5, W = 1, M = 0.001$ and $\alpha = \pi/2$. The capsules in figure 7.9 (a) deform appreciably less than those seen in figure

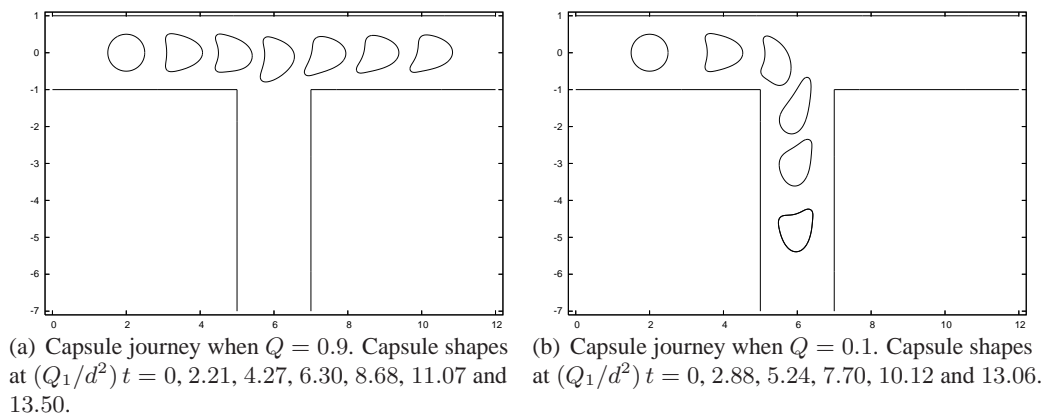


Figure 7.8 : Capsule journeys for $\lambda = 1$, $\rho = 0.5$, $W = 5$, $M = 0.001$ and $\alpha = \pi/2$. At $t = 0$ the capsule centroid is at $\mathbf{x}_c/d = (2, 0)$.

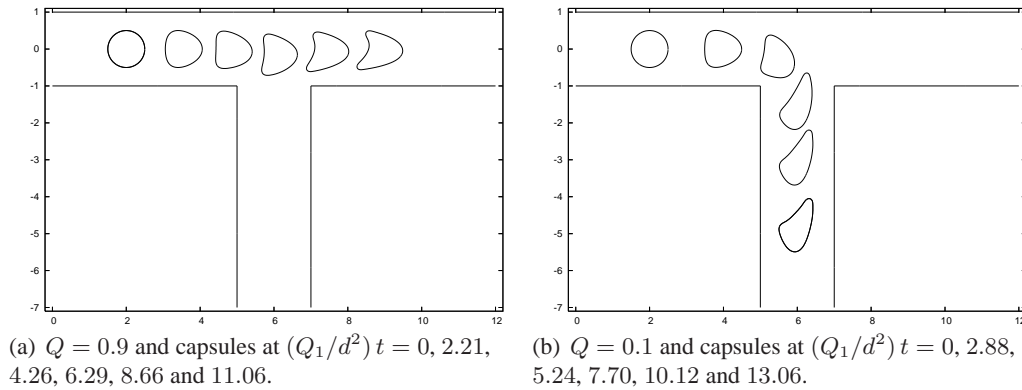


Figure 7.9 : Capsule journeys for $\lambda = 5$, $a = 0.5d$, $W = 1$ and $M = 10^{-3}$.

7.2 (b), which was computed for the same parameter values but with $\lambda = 1$. Comparison of figures 7.9 (b) and 7.3 (b) also reveals that the capsule suffers less deformation when λ takes the higher value. To observe the effect of the viscosity ratio on the trajectory of a capsule, a number of simulations were conducted for an initially circular capsule of radius $\rho = 0.5$ initially located at $\mathbf{x}_c/d = (2, 0)$ when $W = 1$, $M = 0.001$, $\alpha = \pi/2$ and $Q = 0.5$ for values of λ in the range 0.5 to 10. In all of the simulations, the capsule became trapped on the far corner of the branch entrance as in figure 7.7 (b). The trajectories of the capsule centroid are almost coincident over the range of quoted λ values, demonstrating that the viscosity ratio has little effect on the path taken by the capsule.

Figure 7.10 illustrates the motion for the larger capsule size $\rho = 0.75$ when $\lambda = 1$, $W = 1$, $M = 10^{-3}$, $\alpha = \pi/2$, $Q = 0.9$ and $Q = 0.1$. In both figure 7.10 (a) and 7.10 (b) the parachute-type shape is again evident but with much longer trailing tips than is found for the smaller particle. For $Q = 0.9$ the lower trailing tip extends more than the upper as the capsule passes over the entrance to the side branch. For $Q = 0.1$, the upper trailing tip extends more than the lower as the capsule turns the corner into the side branch.

In applications, an elastic capsule may be too large to fit through a channel or tube in its resting configuration and may need to deform in order to squeeze through. One example is that of a red blood cell squeezing through a narrow capillary. In figure 7.11

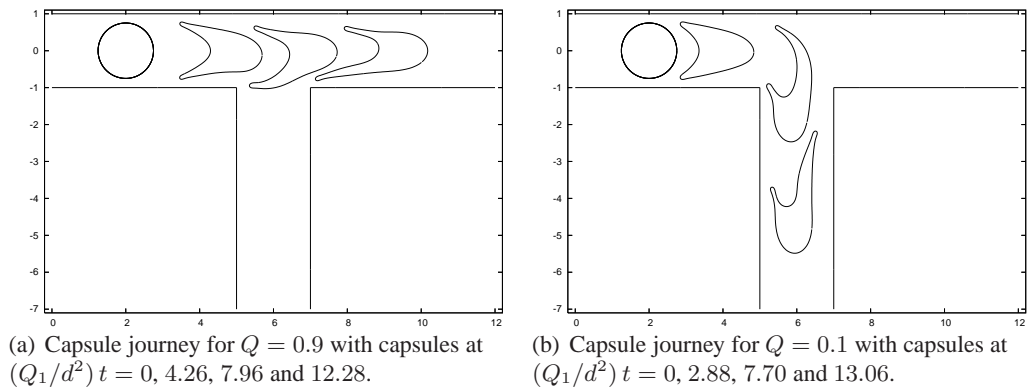


Figure 7.10 : Capsule journeys when $\lambda = 1$, $\rho = 0.75$, $W = 1$, $M = 10^{-3}$ and $\alpha = \pi/2$. At $t = 0$ the capsule centroid is at $\mathbf{x}_c/d = (2, 0)$.

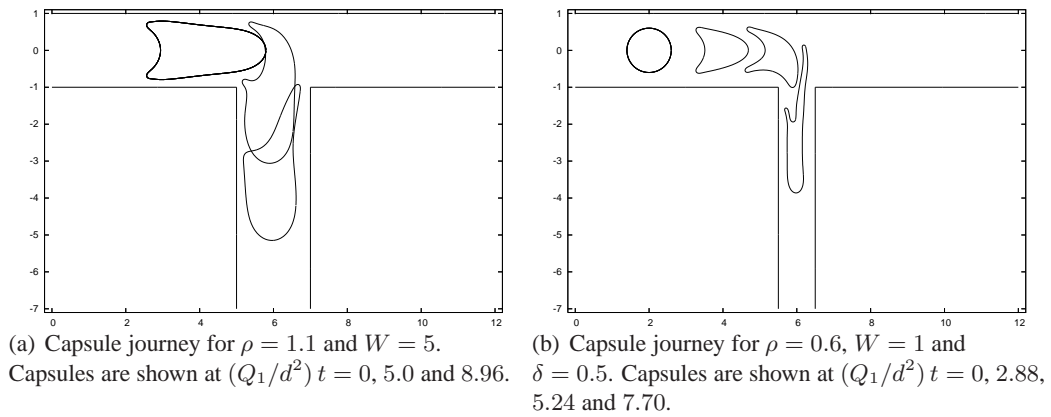


Figure 7.11 : Capsule journeys when $\lambda = 1$, $M = 10^{-3}$, $\alpha = \pi/2$ and $Q = 0.1$. At $t = 0$ the capsule centroid is at $\mathbf{x}_c/d = (2, 0)$.

(a) we show the results of a simulation for a capsule whose unstressed circular shape of radius $\rho = 1.1$ does not fit into the main channel. The initial configuration of the capsule shown at $t = 0$ in the figure was produced by first deforming the circular particle into an ellipse with semi-major axis $1.5125d$ and semi-minor axis $0.8d$, which has the same area as the undeformed circular capsule, and accounting for the strain incurred during the deformation. The ellipse was then placed into a straight channel flow with no side branch and allowed to evolve until it had developed a parachute-like shape. This shape was then taken as the starting configuration at $t = 0$ for the side-branch calculation shown in figure 7.11 (a). The membrane tensions, τ , q , and the bending moment, m , correct for the deformed capsule were set at the start of the simulation. The transit of the capsule from the main channel into the side branch is computed successfully. As in figures 7.3 (b) and 7.10 (b), the upper trailing tip of the capsule is extended more than the lower tip as the capsule turns the corner into the branch. The same calculation repeated for $W = 1$, and with the other parameters the same, shows more severe but qualitatively similar deformation of the capsule. In figure 7.11 (b) we illustrate the motion of a capsule which fits into the main channel but not into the side branch, with $\lambda = 1$, $\rho = 0.6$, $W = 1$, $M = 0.001$, $\alpha = \pi/2$ and $\delta = 0.5$. At the start of the simulation the capsule is inside

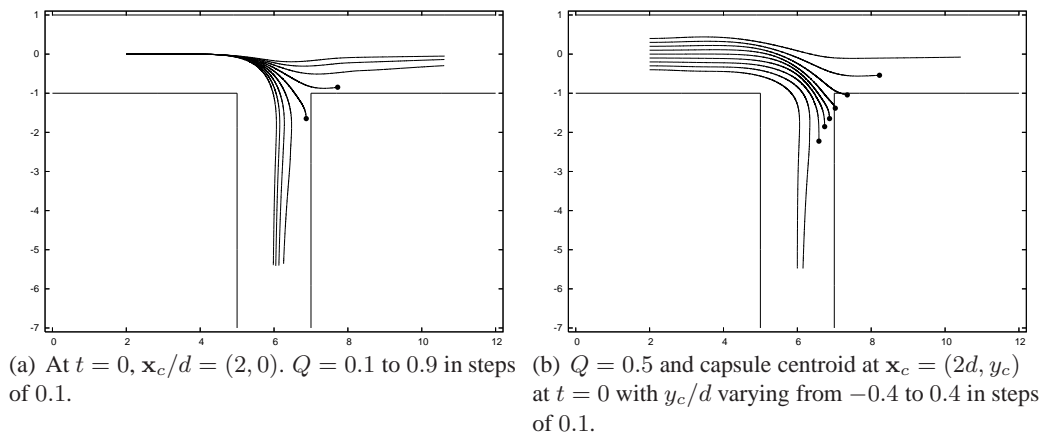


Figure 7.12 : Centroid paths for capsules with $\lambda = 1$, $\rho = 0.5$, $W = 1$, $M = 0.001$ and $\alpha = \pi/2$. In both figures trajectories terminating in a dot correspond to capsules which become trapped at the corner.

the main channel. The flux ratio $Q = 0.1$ is set so that the capsule is drawn out of the main channel and into the side branch. As the capsule squeezes into the branch, it rapidly undergoes severe deformation which is qualitatively similar to that seen in figures 7.3 (b) and 7.10 (b), but is much more strongly pronounced. In particular, the upper trailing tip forms an elongated tendril dragging behind the capsule.

In figure 7.12 (a) we plot the trajectories of the capsule centroid for numerous simulations carried out when $\lambda = 1$, $\rho = 0.5$, $W = 1$, and $M = 0.001$ and $\alpha = \pi/2$ for flux ratios equally-spaced between $Q = 0.1$ and $Q = 0.9$. At $t = 0$ the capsule centroid was at $\mathbf{x}_c/d = (2, 0)$. Those trajectories which terminate at a large dot correspond to capsules which have become trapped at the corner, as in figure 7.7 (b). For the other trajectories, the capsule migrates towards the centreline of the respective channel section after it has negotiated the branch region. The simulations were halted when the assumption of negligible disturbance velocities at either of the exits \mathcal{E}_2 or \mathcal{E}_3 is compromised due to the proximity of the capsule to the exits. In figure 7.12 (b) we plot the trajectories of the capsule centroid for $\lambda = 1$, $\rho = 0.5$, $W = 1$, $M = 0.001$, $\alpha = \pi/2$ and $Q = 0.5$, when the capsule is started with its centre at $\mathbf{x}_c/d = (2, y_c/d)$, where the offset y_c/d is taken from the set $\mathcal{S} = \{-0.4, -0.3, -0.2, -0.1, 0, 0.1, 0.2, 0.3, 0.4\}$. For $y_c/d \leq -0.3$ the capsule is drawn into the side branch. For $y_c/d = -0.2$ up to 0.3 inclusive the capsule is caught on the far corner of the side branch. Note that in two of the cases shown the capsule centroid ends up outside the channel. For $y_c/d = 0.4$ the capsule passes over the side branch and continues along the main channel. These results suggest that there is a capture zone, within which passing capsules will be carried into the side branch, which covers approximately the range $-1 < y/d < -0.3$.

In applications such as capillary flow, the corners at branchings will not be sharp, as here, but rounded. Although it is not straightforward to adapt the current method to cater for rounded corners due to complications with the deformation of the notional boundary \mathcal{A} , we can nonetheless make reasonable predictions of the capsule motion for non-sharp corners. By carefully scrutinising the near-corner capsule profiles, we can make a decision

as to the subsequent capsule path were the corner to become rounded-off. For example, in figure 7.7 (b), we can see that most of the capsule has moved into the branch by the time it has become trapped at the corner, and it seems likely that were it released, by rounding the corner for example, it would subsequently proceed into the branch. However, the tentative nature of such predictions should be emphasised. It is possible that a capsule which is extended some distance into the branch, and which appears to be moving in that direction, may recover and continue along the main channel. Therefore, one might hypothesise that the particular deformation experienced by a capsule may crucially affect the path taken. In fact, it may be the case that two capsules with different elastic properties, which are initially following identical trajectories, take different routes with one proceeding along the main channel, and the other being captured by the side branch. For the trajectories shown in figure 7.12 (b) we estimate that the capsules with the initial centroid locations $y_c/d = -0.2, -0.1, 0$ and 0.1 would proceed into the side branch on rounding the corner. Similarly, we estimate that the capsules with the initial centroid locations, $y_c/d = 0.2$ and 0.3 , would continue along the main channel. In the light of this, we may tentatively conclude that in a right-angled branching flow with equal flow rates through the exits, a mid-sized particle placed at a random position upstream in the main channel will migrate into the branch more than half of the time. We can also see this by examining the streamline figure 5.2 (a) in chapter 5 for a fluid-filled branching channel with the same parameters as above. The streamlines below the dividing streamline are more tightly packed than above, and so the fluid is flowing relatively faster in the region close to the left-hand side of the branch entrance. Since small particles should simply follow the streamlines we may anticipate that half of a distribution of small capsules travelling from upstream along the channel will enter the branch. Although a large capsule will distort the instantaneous streamline field, this nonetheless suggests that larger capsules approaching the branch entrance along the dividing streamline will tend to deform more at the bottom than at the top. Moreover, such a skewed distortion might favour a capsule moving into the branch rather than proceeding along the main channel. This slight bias favouring movement into the branch for $Q = 0.5$ suggests that, of a distribution of larger capsules travelling along the channel, slightly more than half will be drawn into the branch. This would tend to suggest that for multiple-particle flows, with a sufficient particle spacing for the present conclusions to hold, the particle fraction in the branch will be slightly higher than in the main channel.

The effect of changing the branch angle is examined in figure 7.13. Figure 7.13 (a) illustrates a capsule journey for an acute-angled branch with $\alpha = \pi/4$ for a capsule of size $\rho = 0.5$ when $\lambda = 1$, $W = 1$, $M = 0.001$ and $Q = 0.1$. Comparison of the final capsule shapes in figures 7.13 (a) and 7.3 (b) shows that when $\alpha = \pi/4$ the rear of the capsule is marginally more dimpled and therefore slightly closer to the limiting shape found for a straight channel. For moderate values of the flux ratio, Q , the capsule tends to snag on the rightmost corner of the branch opening; the range of Q values for which the capsule becomes trapped is wider than that for the right-angled branch discussed above. When Q is sufficiently large, so that most of the fluid proceeds along the main channel,

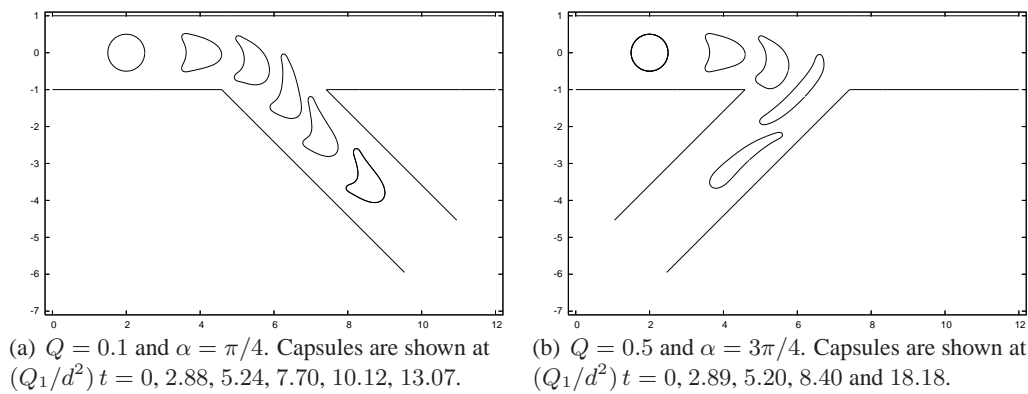


Figure 7.13 : Capsule journey when $\lambda = 1$, $\rho = 0.5$, $W = 1$ and $M = 10^{-3}$.

the capsule suffers minor deformation as it passes over the branch opening, similar to that observed in figure 7.2 (b). A calculation for a capsule entering a side branch at an obtuse angle is presented in figure 7.13 (b) for the case $\lambda = 1$, $\rho = 0.5$, $W = 1$ and $M = 0.001$, $\alpha = 3\pi/4$ and with $Q = 0.5$. Backward-pointing branches of this type may arise in microfluidic circuits (Roberts and Olbricht 2006). The journey and deformation experienced by the capsule is markedly different to that for a right-angled or acute-angled branch. For an obtuse angle, the capsule passes cleanly into the branch, and tends to elongate into a slender shape. This is in contrast to the behaviour found for $\alpha \leq \pi/2$, when the capsule tends to snag on the rightmost corner of the branch for mid-range values of Q . For the obtuse-angled branch, we carried out simulations for different particle sizes and for different viscosity ratios, and over a range of values of Q small enough to ensure the capsule enters the branch. In all cases, the results were similar to that seen in figure 7.13 (b). Under no circumstances did we find an example of the capsule snagging on the sharp leftmost corner of the branch.

To investigate the sensitivity of the capsule trajectory to its location in the oncoming flow for obtuse and acute branch angles, we performed a similar set of calculations to those shown in figure 7.12 (b). In figure 7.14 (a) we present results for simulations in which $\lambda = 1$, $\rho = 0.5$, $W = 1$, $M = 0.001$, $\alpha = \pi/4$, $Q = 0.5$ and the initial capsule centroid, $\mathbf{x}_c = (2d, y_c)$ with values of y_c/d taken from the set \mathcal{S} . For this acute angle all of the capsules become trapped at the rightmost corner of the branch entrance with the exception of those with initial centroid locations $y_c/d = 0.4$ and -0.4 , which continue along the main channel and enter the branch respectively. A careful consideration of the near-corner profiles for the capsules which become trapped, with the aim of deciding upon the subsequent path, is unfortunately inconclusive. Figure 7.14 (b) shows the centroid paths for the same parameters but with the branch angle $\alpha = 3\pi/4$. In all of the simulations the capsules either proceed along the main channel or enter the branch without becoming trapped. The capsules with $y_c/d = -0.4$ up to and including $y_c/d = 0.1$ enter the side branch, and the rest exit through \mathcal{E}_2 , so that more than half enter the side branch. It is likely that the exact proportion will depend on the deformability of the capsule. For example, for the simulation with $y_c = 0.2d$ when the capsule reaches the branch

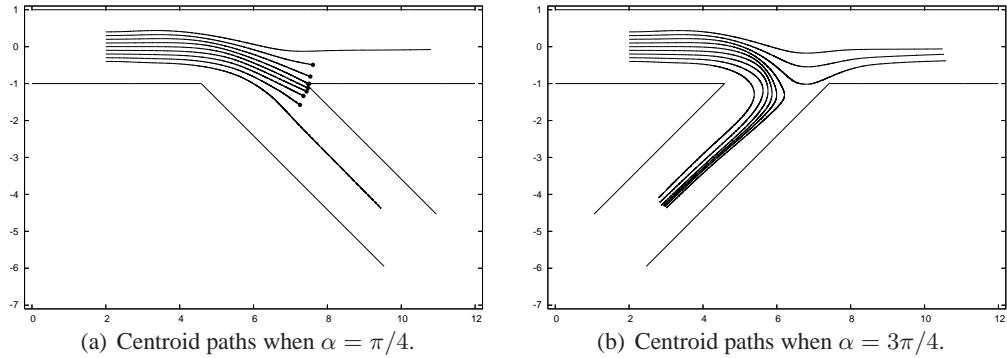


Figure 7.14 : Centroid paths for capsules with $\lambda = 1$, $\rho = 0.5$, $W = 1$, $M = 0.001$ and $Q = 0.5$. Capsule centroid at $t = 0$ is $\mathbf{x}_c = (2d, y_c)$ where y_c/d varies from -0.4 to 0.4 in steps of 0.1 . Trajectories terminating in a dot correspond to capsules which become trapped at the corner.

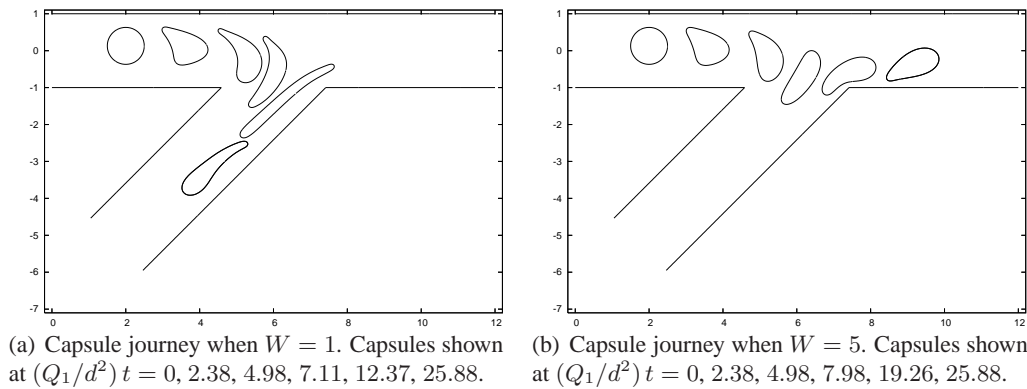


Figure 7.15 : Capsule journeys when $\lambda = 1$, $\rho = 0.5$, $M = 0.001$, $\alpha = 3\pi/4$ and $Q = 0.5$. The capsule centroid is initially located at $(2, 0.13)d$.

almost half of it becomes extended down into the branch before the capsule recovers and continues along the main channel. The very delicate balance between which of the two routes the capsule eventually takes could well be influenced by the elastic properties of the capsule.

The preceding remarks suggest that the route taken by a capsule may depend crucially on the extent to which it is able to deform. In figure 7.15 we give an example in which a capsule either proceeds along the main channel or else migrates into the side branch, depending on its elastic properties. The flow parameters for the two simulations are $\lambda = 1$, $\rho = 0.5$, $M = 0.001$, and $\alpha = 3\pi/4$ with $W = 1$ in figure 7.15 (a) and $W = 5$ in figure 7.15 (b). In both of the simulations the capsule is released with its centroid at $\mathbf{x}_c/d = (2, 0.13)$. The deformation is quite different in the two simulations and it ultimately determines the route taken by the capsule. When $W = 1$ the capsule is drawn into the branch, but when $W = 5$ it continues along the main channel. It is noteworthy that for both of the capsules it takes a time of $20.9 d^2/Q_1$ to negotiate the area of the junction and move down either into the branch or along the main channel (where the time is calculated from the difference between the third and the final capsule shapes). The long residence time of the capsule in the vicinity of the junction should be compared with those

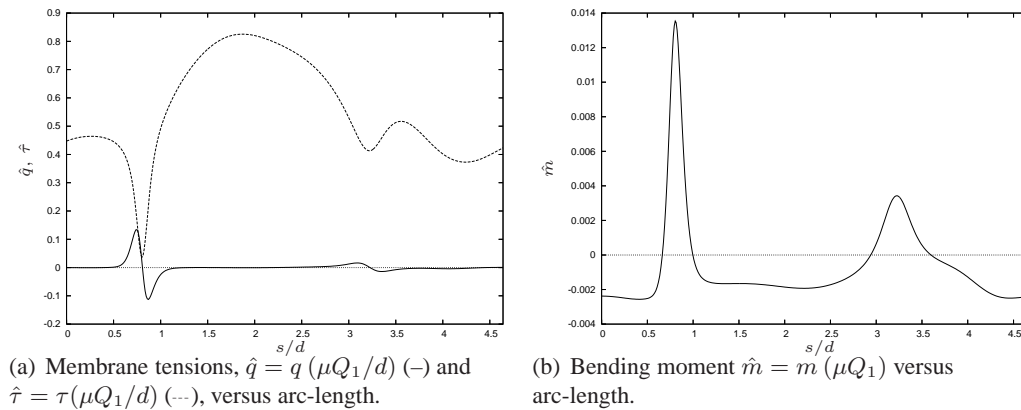


Figure 7.16 : Membrane tensions and bending moment for the final capsule shown in 7.15 (a) at $t = 25.88 d^2/Q_1$. Arc-lengths at the trailing and leading tips are $s/d = 0.80$ and $s/d = 3.23$ respectively, and is measured in an anti-clockwise direction.

for capsules which pass more readily into the side branch (see for example the simulations shown in figure 7.13 (a)). The longer residence times in the present calculations may to some extent be explained by reference to the streamline pattern shown in figure 5.8 (a) of chapter 5, which suggest an area of slow flow around the stagnation point where the dividing streamline connects with the side branch wall. We repeated the calculations for the same parameter values and for initial centroid positions in the range $(2, 0.12)d$ up to $(2, 0.16)d$. Again we found that the path taken by the capsule changed from the branch to the main channel when W was switched from 1 to 5. These calculations support the hypothesis put forward earlier that deformation may have an important influence on the route taken by a capsule at a junction. The strong deformation experienced by the capsule with $W = 1$ is sufficient to extend the capsule into the branch and draw it away from the main channel. The capsule with $W = 5$ suffers considerably less deformation and as a consequence follows the path of the main channel.

In figure 7.16 (a) we show the in-plane and transverse membrane tensions and the membrane bending moment for the last capsule shown in figure 7.15 (a) at $t = 25.88d^2/Q_1$. The maximum tensions are comparable in magnitude to those found for the steady-state capsule shape shown in figure 4.18 (a) in chapter 4. The same qualitative spike-like behaviour in the bending moment, which was observed for the steady-state capsule, is also observed in figure 7.16 (b) and the maximum overall bending moment is comparable between the two. We can therefore see that although a capsule entering an obtuse-angled branch is distorted into a quite different shape from the steady-state found in a straight channel, it suffers similar sized tensions and bending moments.

We performed similar calculations to those shown in figure 7.12 (b) but where we reduce the width of the side branch. Given the difficulties with capsules snagging on the rightmost corner of a right-angled or acute-angled branch, we confined our attention to an obtuse-angled branch, and conducted a suite of calculations taking $\lambda = 1$, $\rho = 0.5$, $W = 1$, $M = 0.001$, $\alpha = 3\pi/4$, and $\delta = 0.5$ so that the width of the side branch is half that of the main channel and is equal to the unstressed diameter of the capsule. In

the first case we set $Q = 0.5$ and set the capsule centroid so that at $t = 0$, $\mathbf{x}_c = (2d, y_c)$ with the values y_c/d are taken from the set \mathcal{S} . We found that all of the capsules except for the one started with its centroid at $(2, 0.4)d$ enter the branch and continue to \mathcal{E}_3 . The simulations were repeated for the same parameter values but with $W = 5$, so that the capsules have a stronger resistance to deformation, where again all but one capsule enter the branch channel. This at first may seem contrary to the phenomenon of plasma skimming (Krogh 1922) whereby the plasma layer close to the capillary walls is skimmed off into the daughter vessel. However the relative flux rates and fluid velocities play a key role in determining the haematocrit in the daughter capillaries. The experiments of Johnson (1971) concerning the flow of blood through a single capillary bifurcation demonstrated that the daughter capillary with the higher velocity tended to receive the greater haematocrit. Further confirmation was obtained experimentally by Yen and Fung (1978) using gelatin pellets to simulate red blood cells in a bifurcating capillary-sized tube. Slightly larger blood vessels were the focus of experiments by Pries et al. (1986) who studied a microvascular segment of a rat's mesentery. They showed that the haematocrit depends on the flux rates in the downstream channels as well as the ratio of the mean velocity of the ambient fluid to the mean capsule velocity. In our simulations we have $\delta = 0.5$ and $Q = 0.5$ so that the centreline velocities at \mathcal{E}_1 and \mathcal{E}_3 are equal, and the centreline velocity at \mathcal{E}_2 is half that at \mathcal{E}_1 . It seems that the higher centreline velocity is responsible for most of the capsules being drawn into the branch, even for equal flow rates at the exits. Capsules which start off the centreline of the main channel tend to drift toward the faster fluid in the middle and are then flushed through into the side branch. Therefore our two-dimensional simulations are in accord with the above mentioned experiments. Next we set $Q = 0.75$ so that most of the fluid exits through \mathcal{E}_2 and the centreline velocity at \mathcal{E}_2 is greater than that at \mathcal{E}_3 . The majority of the capsules, specifically those with y_c/d in the range -0.3 up to 0.4 inclusive, are carried along to \mathcal{E}_2 . The capsule which started with its centroid at $(2, -0.4)d$ enters the side branch. As predicted by experiment, we therefore see that the centreline velocities play an important role on the eventual course taken by the capsule.

Finally we set $Q = 2/3$ so that the centreline velocities at the exits \mathcal{E}_2 and \mathcal{E}_3 are equal. When $W = 1$ we found that the capsules with $y_c \geq 0.1$ travelled to \mathcal{E}_2 , and the capsules which started with $y_c \leq 0$ migrated into the branch. The journey of the capsule which started with $y_c = 0$ is shown in figure 7.17 (a) where we can see that the capsule became very stretched over the right-hand side entrance to the branch. The capsule did eventually move into the branch channel and travel to \mathcal{E}_3 . It is worth noting that the capsule started with $y_c = 0$ takes approximately twice as long to travel to the exit as the capsules started with $y_c = -0.4$ and $y_c = 0.4$. In figure 7.17 (b) we show the journey of a capsule started from $(2, 0)d$ but with $W = 5$ thus making it more resistant to stretching. When the capsule approaches the rightmost branch corner it deforms less than the previous case and does not get drawn into the branch channel. The area error was higher for these simulations. For instance, the final capsule shapes shown in figures 7.17 (a) and 7.17 (b) have area errors of 0.2% and 0.1% respectively. In summary, we see that

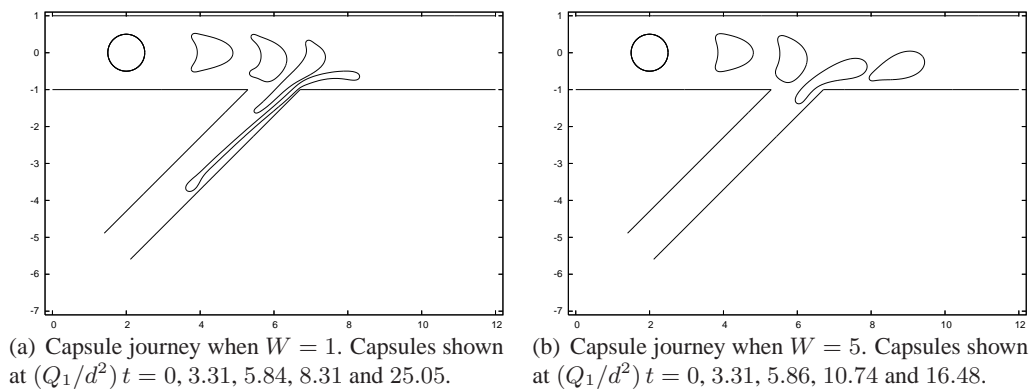


Figure 7.17 : Capsule journeys when $\lambda = 1$, $\rho = 0.5$, $M = 0.001$, $\alpha = 3\pi/4$, $\delta = 1/2$ and $Q = 2/3$. The capsule centroid is initially located at $(2, 0)d$.

the majority of capsules will migrate towards the exit which has the greatest centreline velocity. When the centreline velocities of the exits are equal then the elastic properties of the membrane may determine the capsule's trajectory, with more deformable capsules increasingly likely to enter the branch channel.

7.6 Deformation of the notional boundary

We have seen that when the capsule enters the branch it can undergo severe deformation. As the capsule passes into the branch the notional boundary, \mathcal{A} , is deformed to facilitate the transition from the main channel to the branch channel. As the notional boundary is deformed from its straight reference state boundary elements are added in order to preserve the original element length. When the capsule is in the region of the branch entrance and is bisected by the line $y = -d$ it is unclear in which channel the capsule resides. We define the capsule to be in the main channel when the capsule's centroid is such that $y_c \geq -d$ and the notional boundary is deformed around the underside of the capsule. This situation is depicted in figure 7.18 (a) where we take the capsule from the simulation shown in figure 7.3 (b) when the capsule's centroid is slightly above $y = -d$ and also show the notional boundary. We maintain the straight reference configuration for \mathcal{A} close to the left and right hand entrances to the branch channel and deform \mathcal{A} around the capsule while ensuring that the deformed notional boundary does not cross itself, \mathcal{P} or leave the flow domain. The notional boundary may be thought of as a cradle which will deform further as the capsule continues into the branch channel. In figure 7.18 (b) we show the capsule after its centroid has moved below $y = -d$ together with \mathcal{A} . We can see that the notional boundary has been flipped over so that the capsule now resides in the ambient fluid of the branch channel and beneath the notional boundary. Once again we only deform \mathcal{A} close to the capsule and maintain the straight reference configuration along $y = -d$ as much as possible. As the capsule moves further into the branch we modify the notional boundary so that it becomes less deformed. When the entire capsule lies below $y = -d$ (plus a small tolerance) the notional boundary is reset to its straight

reference configuration.

In the simulation shown in figure 7.7 (b) when $Q = 0.5$ the capsule became trapped on the right-hand side of the branch entrance. The final capsule shape from the simulation is shown in figure 7.18 (c) together with the notional boundary. In this case the notional boundary becomes extended around the top tip of the capsule and to the right of the right hand of the branch entrance.

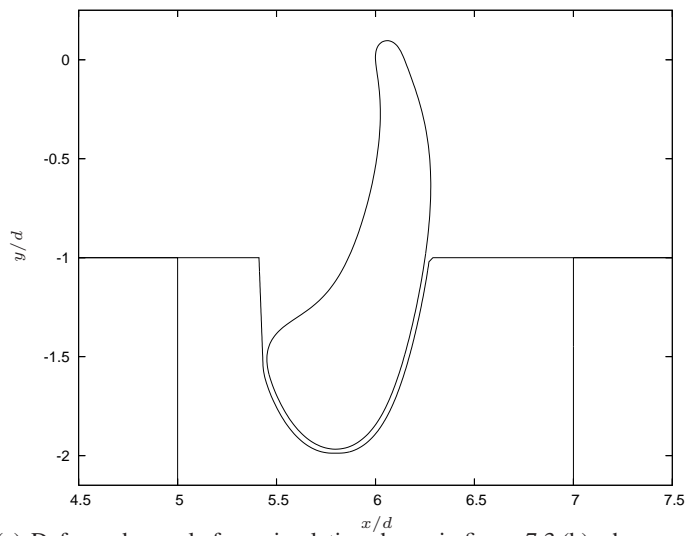
7.7 Discussion

We have considered the pressure-driven flow of an elastic capsule through a channel with a side branch. The capsule boundary was treated as a two-dimensional elastic membrane capable of resisting elastic stretching and bending. The capsule was carried in a pressure-driven ambient flow of fluid with generally different viscosity whose velocity profile approaches that corresponding to unidirectional Poiseuille flow with a prescribed flow rate far upstream and downstream in the main channel and downstream in the side branch. The Reynolds number was assumed to be sufficiently small for the flow to be described using the linear equations of Stokes flow.

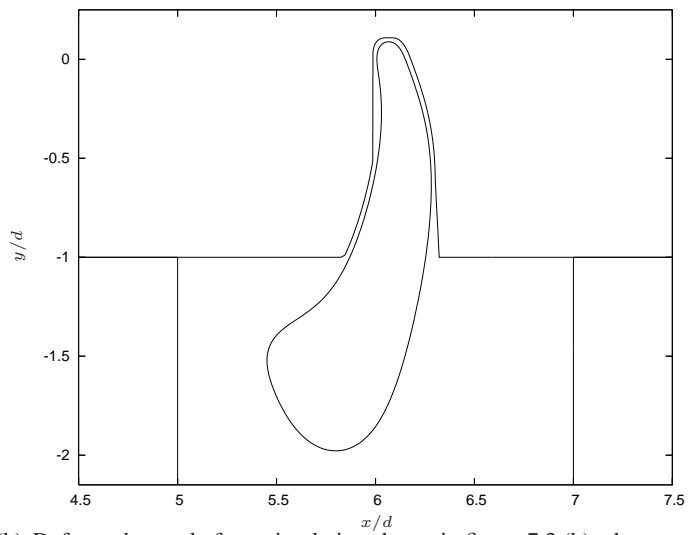
The problem was formulated and solved numerically using the boundary integral method. The computational domain was a truncated section of the branch geometry which allowed sufficient entry and exit lengths for the flow to return to its assumed unidirectional motion away from the junction. A domain decomposition-type approach was used which meant that it was only necessary to collocate the channel walls, the capsule boundary, and the notional boundary in order to solve for the velocity field and compute the motion of the capsule. Although the introduction of a notional boundary avoided the need to collocate the entrance and exits to the computational domain, care needed to be exercised when the capsule moved into the side branch, particularly for highly deformed capsules.

Previous workers have observed that a deformable elastic capsule will tend to drift toward the centreline in a tube flow, and this trend was confirmed for the present two-dimensional calculations in a straight channel with no side branch. We noted a tendency for the capsule to first move a little way toward the wall before heading toward the centreline, and this is in line with the three-dimensional calculations of Pozrikidis (2005c). Our two-dimensional calculations of the steady-state shapes computed in the presence of bending moments resemble those seen in experiments (e.g. Secomb et al. 2007) and in axisymmetric calculations (Quéguiner and Barthès-Biesel 1997, Secomb et al. 2001, Pozrikidis 2005a).

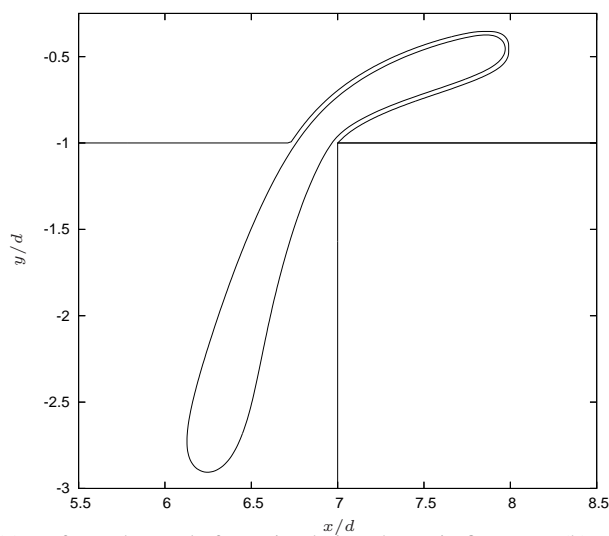
For a channel with a side branch, when the flow rate in the branch is sufficiently low, moderate-sized capsules approaching along the centreline of the main channel deviate downwards slightly from their path but do not enter the branch. As expected, when the flow rate in the branch is increased sufficiently, the capsule is drawn into the branch. Capsules which approach the branch junction along the main channel centreline may spend a considerable time negotiating the branch region. These capsules are naturally drawn



(a) Deformed capsule from simulation shown in figure 7.3 (b) when capsule centroid is above $y = -d$.



(b) Deformed capsule from simulation shown in figure 7.3 (b) when capsule centroid is below $y = -d$.



(c) Deformed capsule from simulation shown in figure 7.7 (b) when capsule centroid is below $y = -d$ and the capsule is extended over the right-hand corner of the branch entrance.

Figure 7.18 : Configurations of the deformed notional boundary.

toward an area of relatively slow-moving fluid at the point where the dividing streamline, which separates the fluid which enters the branch from that which proceeds along the main channel, makes contact with the wall. In the presently considered geometry, capsules entering a right-angled or acute-angled side branch may snag on the corner and become trapped. Capsules entering an obtuse-angled branch do not become trapped, but nevertheless may linger at the junction for some time undergoing significant deformation before continuing to one or other of the exits. Although the deformation in the region of the junction tends to be less pronounced for capsules which pass successfully into right-angled or acute-angled branch than an obtuse-angled branch, the elastic tensions and bending moments in the capsule membrane are comparable.

When the flow rates through the main channel exit and the side branch exit are the same, capsules will tend to follow the path where the velocity is greatest. Accordingly, they will tend to migrate into a side branch which is narrower than the main channel. When the two exits are of equal width, there is still an overall bias toward the side branch. However when the branch channel is narrower than the main channel and the centreline velocity at the branch exit is less than at the exit of the main channel we find that the majority of capsules remain in the main channel. This effect in the microcirculation is known as plasma skimming since the daughter channel may receive a relatively high proportion of the blood plasma.

When a capsule has entered the side branch, eventually it will migrate toward the centreline and relax to an equilibrium shape. Although it may quickly recover a shape resembling the final state, it may travel some considerable distance before fully achieving equilibrium. This suggests that in a complex tube network with frequent successive branches capsules might not have sufficient room to re-establish equilibrium before encountering another division. Consequently, the gross distortion which may result from turning through a significant branch angle into a side tube is likely to persist and be compounded at subsequent branches. In simulations, the distortion becomes less severe on increasing the elastic membrane stiffness or increasing the viscosity of the encapsulated fluid.

The route taken by a capsule at a branching may depend on the deformation experienced in the branch region, and consequently on the elastic properties of the capsule membrane. We have found that two capsules of different elastic stiffness, for example, which are started from the same position upstream of the branch under identical flow conditions may take different routes, with one continuing along the main channel and the other being drawn into the branch.

While the present work has considered the motion of a single capsule, in applications such as blood flow, for example, there may be many capsules present. If the capsules are widely spaced, then the present results may be applied. We have seen from simulations of capsules which start with different offsets from the centreline that the path taken by the capsule depends on the flux rate at the exit together with the ambient fluid velocity. By changing the centreline velocities at the exits by altering the flux ratio we were able to draw the majority of capsules along the main channel or have them migrate into the branch

channel thus altering the discharge haematocrit at the exits. These observations are in line with the observations on the flow of red blood cells (RBCs) in the microcirculation on p.59 of Popel and Johnson (2005) (and the references therein) who find that the different discharge haematocrits are due to daughter branches with higher flux rates drawing a disproportionate number of RBCs into the vessel.

For tightly-packed capsules, interactions between neighbours is expected to have an effect on the transit and deformation of each individual capsule. Although the addition of more capsules to the flow is theoretically simple within the framework presented here, there are practical computational difficulties associated with the deformation of the notional boundary \mathcal{A} when multiple capsules are present. Moreover, the computational domain will require a longer entrance and longer exits so as not to contravene the assumptions of the problem formulation, with a consequent increase in the demands placed on computer memory and CPU time.

7.8 Further work

In the numerical simulations presented in this chapter and in previous chapters we have found good agreement between the results of our calculations and published results for straight channels, pipes and branching channels. However we must stress that when comparing our results with three-dimensional calculations we can only perform qualitative comparisons. To extend our current model into three dimensions we must implement the notional boundary as a deformable surface, which is challenging computationally. We have also mentioned our desire to round the corners of the entrance to the branching channel in order to more accurately model the flow of red blood cells through a branching capillary. The rounding of the corners would also make it unclear where to join the notional boundary onto the channel walls. Furthermore, if we introduced an additional capsule into the branching channel flow we would have to deform the notional boundary around one or all of the capsules. We will now investigate whether we can avoid these implementational difficulties by omitting the notional boundary from the formulation.

We consider the same two-dimensional geometry as depicted in figure 7.1 but we remove the notional boundary \mathcal{A} . To derive a boundary integral equation for the flow we define the flow domain boundary, $\partial\Gamma = \mathcal{E}_1 \cup \mathcal{E}_2 \cup \mathcal{E}_3 \cup \mathcal{B} \cup \mathcal{C} \cup \mathcal{P}$, and apply the general boundary integral equation (1.3.40) to the total velocity and traction to get,

$$4\pi\mu u_j^{(1)}(\mathbf{x}_0) = - \int_{\partial\Gamma} f_i^{(1)} G_{ij} \, ds(\mathbf{x}) + \mu \int_{\partial\Gamma} u_i^{(1)} T_{ijk} n_k \, ds(\mathbf{x}) \quad (7.104)$$

for \mathbf{x}_0 in the ambient fluid. If the channel contained more than one capsule then \mathcal{P} is the boundary of all of the capsules. After applying the no-slip and no-penetration conditions on the channel walls and the boundary conditions at the entrance and exits given in

equations (7.9), (7.10) and (7.11) we obtain

$$\begin{aligned}
4\pi\mu u_j^{(1)}(\mathbf{x}_0) = & - \sum_{r=1}^3 \int_{\mathcal{E}_r} f_i^{P_r} G_{ij} \, ds(\mathbf{x}) + \sum_{r=2}^3 \pi_r \int_{\mathcal{E}_r} n_i G_{ij} \, ds(\mathbf{x}) \\
& - \int_{\mathcal{B}, \mathcal{C}, \mathcal{P}} f_i^{(1)} G_{ij} \, ds(\mathbf{x}) + \mu \sum_{r=1}^3 \int_{\mathcal{E}_r} u_i^{P_r} T_{ijk} n_k \, ds(\mathbf{x}) + \mu \int_{\mathcal{P}} u_i^{(1)} T_{ijk} n_k \, ds(\mathbf{x}).
\end{aligned} \tag{7.105}$$

All of the integrals over \mathcal{E}_1 , \mathcal{E}_2 and \mathcal{E}_3 may all be calculated analytically. We apply the boundary integral equation (1.3.40) to the total flow over the particle boundary to get

$$0 = - \int_{\mathcal{P}} f_i^{(2)} G_{ij} \, ds(\mathbf{x}) + \mu\lambda \int_{\mathcal{P}} u_i^{(2)} T_{ijk} n_k \, ds(\mathbf{x}), \tag{7.106}$$

for \mathbf{x}_0 in the fluid of the main channel, and subtract the equation from equation (7.105) to get

$$\begin{aligned}
4\pi\mu u_j^{(1)}(\mathbf{x}_0) = & - \sum_{r=1}^3 \int_{\mathcal{E}_r} f_i^{P_r} G_{ij} \, ds(\mathbf{x}) + \sum_{r=2}^3 \pi_r \int_{\mathcal{E}_r} n_i G_{ij} \, ds(\mathbf{x}) \\
& - \int_{\mathcal{B}, \mathcal{C}} f_i^{(1)} G_{ij} \, ds(\mathbf{x}) - \int_{\mathcal{P}} \Delta f_i G_{ij} \, ds(\mathbf{x}) + \mu \sum_{r=1}^3 \int_{\mathcal{E}_r} u_i^{P_r} G_{ij} \, ds(\mathbf{x}) \\
& + \mu(1 - \lambda) \int_{\mathcal{P}} u_i^{(1)} T_{ijk} n_k \, ds(\mathbf{x})
\end{aligned} \tag{7.107}$$

for \mathbf{x}_0 located in the fluid. Since the discontinuous double-layer potential over the channel walls is not present the equation is also valid for \mathbf{x}_0 located on the walls of the main channel or the branch channel, and where the velocity on the left-hand side is zero by no-slip. The unknowns in equation (7.107) are the disturbance pressures at \mathcal{E}_2 and \mathcal{E}_3 , the tractions on the channel walls and the velocities on the capsule boundary. Evaluation of equation (7.107) with \mathbf{x}_0 located on the walls will allow the calculation of the wall tractions. We may also evaluate the equation with \mathbf{x}_0 on the capsule boundary, while taking care to include the discontinuous jump in the double-layer potential, in order to calculate the velocities on the capsule boundary. However we still require equations for the disturbance pressures, π_2 and π_3 . Previously we have used the Lorentz reciprocal relation to derive equations for the disturbance pressures by applying the relation to a pair of flows. Now that we are treating the main channel and the branch channel as one, we would like apply the reciprocal relation to the total flow and one of the disturbance flows. However we do not have a natural choice for the disturbance flow. If we chose the \mathbf{u}^{D_1} flow then we would have to evaluate it in the branch channel. As an alternative we consider a simpler method. The flow throughout the branching channel satisfies the

Stokes equation,

$$\nabla \cdot \boldsymbol{\sigma}^{(1)} = \mathbf{0} \quad (7.108)$$

where $\boldsymbol{\sigma}^{(1)}$ is the stress field in fluid 1. Integrating this equation over the flow domain Γ gives

$$\mathbf{0} = \iint_{\Gamma} \nabla \cdot \boldsymbol{\sigma}^{(1)} \, dA(\mathbf{x}) = \int_{\partial\Gamma} \mathbf{f}^{(1)} \, ds(\mathbf{x}) \quad (7.109)$$

by the divergence theorem. After applying the boundary conditions at the entrance and exits we obtain

$$\sum_{r=1}^3 \int_{\mathcal{E}_r} \mathbf{f}^{Pr} \, ds(\mathbf{x}) + 2d \pi_2 \mathbf{i} + 2D \pi_3 \mathbf{i}' + \int_{B,C,\mathcal{P}} \mathbf{f}^{(1)} \, ds(\mathbf{x}) = \mathbf{0}, \quad (7.110)$$

where \mathbf{i}' is defined in equation (5.3). The fluid inside the capsule is governed by

$$\nabla \cdot \boldsymbol{\sigma}^{(2)} = \mathbf{0} \quad (7.111)$$

which when integrated over the capsule leads to

$$\mathbf{0} = \iint_{\mathcal{P}} \nabla \cdot \boldsymbol{\sigma}^{(2)} \, dA(\mathbf{x}) = \int_{\mathcal{P}} \mathbf{f}^{(2)} \, ds(\mathbf{x}) \quad (7.112)$$

by the divergence theorem. Subtracting this equation from equation (7.110) gives

$$\sum_{r=1}^3 \int_{\mathcal{E}_r} \mathbf{f}^{Pr} \, ds(\mathbf{x}) + 2d \pi_2 \mathbf{i} + 2D \pi_3 \mathbf{i}' + \int_{B,C} \mathbf{f}^{(1)} \, ds(\mathbf{x}) + \int_{\mathcal{P}} \Delta \mathbf{f} \, ds(\mathbf{x}) = \mathbf{0}. \quad (7.113)$$

From the definitions of the Poiseuille tractions we find that

$$\sum_{r=1}^3 \int_{\mathcal{E}_r} \mathbf{f}^{Pr} \, ds(\mathbf{x}) = -2dlQ G_1 \mathbf{i}, \quad (7.114)$$

which upon substitution into equation (7.113) gives

$$\int_{B,C} \mathbf{f}^{(1)} \, ds(\mathbf{x}) + 2d \pi_2 \mathbf{i} + 2D \pi_3 \mathbf{i}' = 2dlQ G_1 \mathbf{i} - \int_{\mathcal{P}} \Delta \mathbf{f} \, ds(\mathbf{x}), \quad (7.115)$$

where the terms on the left-hand side involve unknown quantities and the terms on the right-hand side are known functions. The two equations for the disturbance pressures are provided by the i and j components of this equation. We therefore have a sufficient number of equations to calculate the wall tractions and disturbance pressures at the exits. Since we make no assumptions about the geometry in equations (7.107) and (7.115) we may round the corners of the branch channel entrance. In fact there is almost no need to distinguish between the walls of the main and branch channels; we could just refer to the walls as one boundary.

Application of the boundary element method to the geometry, the boundary integral equation (7.107) and equation (7.115) will lead to set a discretised equations which can be formed into a linear system as we have demonstrated previously. The solution may then be used to compute the motion of the capsule or capsules using an appropriate time-integration method. It is also worth noting that when $\lambda = 1$ and the capsule boundary velocities disappear from equation (7.107) the inverse of the matrix in the linear system need only be calculated once, independent of the location of the capsule. Previously we had to recompute the matrix inverse when we changed the shape of the notional boundary.

We also wish to extend our two-dimensional model to three-dimensions to more accurately predict the motion of an elastic capsule along a branching tube. Two-dimensional simulations are able to capture some of the qualitative behaviour of three-dimensional capsules in straight tube flow, including some of the key features of the capsule profile and the tendency of capsules to migrate laterally to the tube centreline. However, two-dimensional studies are severely limited in their description of the elastic behaviour of the capsule membrane. For example, in-plane shear deformation occurs in three-dimensions but not in two-dimensions. Moreover some elastic capsules, red blood cells for example, show a strong resistance to change in the local surface area while maintaining the same interior cell volume. In the present two-dimensional work, the area inside a capsule is preserved but the capsule perimeter extends under deformation.

In summary, we have sketched out a method by which we could remove the notional boundary. We would therefore be able to extend the computational model to include the effects of rounded corners and the motion of multiple capsules. The removal of \mathcal{A} alone would facilitate a simpler transition from the current two-dimensional model to a three-dimensional model which calculates the passage of an elastic capsule through a branching tube.

Chapter 8

Conclusions

We started in chapter 1 by discussing the physical background of particle and capsule motion in a variety of situations. We mentioned the motion of the fluid-filled capsules, fluid drops and rigid particle in shear flows, channel flows and branching channel flows. This discussion provided a motivation to our research into the motion of a flexible capsule in a branching channel flow. We also provided the mathematical background to Stokes flow, Poiseuille flow and the boundary integral method which we used in each subsequent chapter. In chapters 2–7 we formulated a set of boundary integral equations which governed the motion. In each channel flow we considered a pressure-driven Stokes flow and prescribed the flux rate at the exit or exits to the computational domain. The pressure at each exit was therefore included as an unknown in each channel flow. Each problem was formulated and solved numerically using the boundary integral method. The computational domain was a truncated section of the channel geometry which allowed sufficient entry and exit lengths for the flow to return to its assumed unidirectional motion away from any disturbance, whether caused by the presence of a particle, capsule or a branch channel. We obtained equations for the pressure using the Lorentz reciprocal relation which avoided collocation of the channel ends which has been noted to cause numerical sensitivities (Pozrikidis 2005c). By setting the unknown tractions and velocities on the boundaries to constant vectors we applied the boundary element method to the channel geometry and the equations in order to obtain a set of algebraic equations which we solved by standard matrix methods. We showed that in each case the numerical solution was consistent with the underlying assumptions and we obtained good agreement with published results where possible. As we added complexity to the channel flow, by introducing a flexible capsule for example, we found that the boundary element formulation easily incorporated the increasingly diverse parameter space.

In chapter 2 we provided an introduction to the boundary integral method and its application to a simple but non-trivial fluid-filled straight channel flow which involved the placement on one of the walls of a small conveyor belt, which moved with a constant velocity. Despite the simplicity of the flow, a parallel may be drawn with cytoplasmic streaming in large plant cells (Verchot-Lubicz and Goldstein 2009). In the absence of a background Poiseuille flow we showed that an eddy is induced in the fluid when the

conveyor belt moves in either direction. The direction of the fluid in the eddy being determined by the direction of the conveyor belt's motion. When a background flow is introduced the fluid behaviour is dependent on the direction of the conveyor belt. When the belt moves in the opposite direction to the background flow then an eddy is created in the fluid and close to the belt for all values of the belt speed. The size of eddy, and the pressure drop between the entrance and exit, increased with the belt speed. When the conveyor belt moved in the same direction as the background flow then there is a critical belt speed below which the fluid is drawn towards the belt but then continues to the exit. However, when the belt speed reaches this critical value an eddy appears close to the top wall, and increases in size as the belt speed is increased. We found this critical belt speed to be the value which induced a zero wall shear stress at a point on the top wall. For all belt speeds the pressure drop between the ends decreases and the belt's motion may be interpreted as helping to maintain the flux rate in the channel. A larger conveyor belt induced a more rounded eddy while a smaller induced a triangular eddy.

In chapter 3 we dispensed with the conveyor belt and introduced a rigid particle of constant shape, in a first step towards a model for a flexible capsule in a channel flow. We repeated our application of the boundary integral and element methods in order to obtain a linear system from whose solution we obtained the boundary distribution of the tractions and the particle's velocity. We found that the particle did not move nearer to either wall which is in agreement with the reversibility property of Stokes flow. We also found that the particle's velocity was always less than the background flow, evaluated at the particle's centre, thus demonstrating that the particle 'slips' relative to the background flow, and showed excellent agreement with the results of Sugihara-Seki (1993). Of particular importance to our investigation was the rate of decay of the disturbance due to the particle as we moved away from it. We found that at a distance of three particle radii from the particle's centre the disturbance velocity was less than 1% of its maximum, and the velocity continued to fall with distance. When the particle lay on the centreline, we found that in a frame of reference moving with the particle there were six stagnation points present on the particle's perimeter. These points disappeared once the particle was moved away from the centreline, and instead a thin region of circulating fluid surrounded the particle and eddies appeared in the fluid. We found off-centre particles induced a greater pressure drop than centred ones, most likely due to asymmetry created in the flow and the presence of the eddies. Increasing the particle size while fixing its centre also created a larger pressure drop across the computational domain. When the gap width between the particle and one or both of the walls became small the pressure drop increases exponentially, due to the increased stress in the gap (Staben et al. 2003). We noted that Hasimoto and Sano (1980) had photographed eddies similar to the ones seen here.

In chapter 4 we removed the rigid particle and investigated the motion of a fluid drop in a straight channel, and the motion of a fluid-filled capsule in a straight channel. We found that a fluid drop reached a steady state after travelling many drop radii, and induced an additional pressure drop which was significantly less than that for a rigid particle of the same shape. Once again we found the disturbance velocity decayed rapidly as we moved

away from the drop, and in this case the disturbance velocity fell to less than 1% at a distance of 4 drop radii. We found that when a drop was started far enough away from the centreline it gradually moved towards the centreline, although we did find that when a drop was started only slightly off-centre, 2.5% of the channel width for example, the drop did not noticeably move laterally in the channel. We did find that drops started further from the centreline moved fastest towards to it but then slowed their approach. We found qualitative agreement with the published results of Mortazavi and Tryggvason (2000) and Zhou and Pozrikidis (1994). The differences between our results and those of Mortazavi and Tryggvason (2000) may be attributed to the fundamental assumptions about the flow. We are considering a Stokes flow whereas Mortazavi and Tryggvason (2000) consider a range of Reynolds numbers, the smallest of which was 0.25. We noted that the differences between our results and the results of Zhou and Pozrikidis (1994) were most likely due to the authors' use of a channel specific Green's function and an adaptive boundary element implementation.

We treated the elastic capsule as a two-dimensional elastic membrane capable of resisting elastic stretching and bending, and which contained a fluid of generally different viscosity to the ambient fluid. Before placing the elastic capsule into a channel, we checked the results of the elastic capsule module of our code against the results of Breyiannis and Pozrikidis (2000) for an elastic capsule in a linear shear flow, and found excellent agreement. We then replaced the fluid drop in the channel with an elastic capsule, a change which was easily incorporated into the boundary element formulation, and allowed the capsule to deform. We found that when bending resistance was omitted our numerical calculations failed to obtain a steady shape although such a shape has been shown to exist in two-dimensions by Breyiannis and Pozrikidis (2000). When we included a small resistance to bending we obtained a steady shape for the capsule after it had travelled many capsule radii. Our two-dimensional steady-state shape resembled that seen in experiments (e.g. Secomb et al. 2007) and in axisymmetric calculations (Quéguiner and Barthès-Biesel 1997, Secomb et al. 2001, Pozrikidis 2005a). The additional pressure drop for an elastic capsule was approximately the same as for a rigid particle of the same shape. Increasing the membrane stiffness led to a less deformed steady shape which was attained in a shorter time, translated along the channel faster, and induced a lower additional pressure drop. The viscosity of the encapsulated fluid was shown to have little effect on the eventual steady shape, although the time to reach the steady shape increased with the capsule's fluid viscosity, in line with comments in Quéguiner and Barthès-Biesel (1997) who studied the three-dimensional axisymmetric motion of an elastic capsule into a circular pore. Capsules which are initially displaced from the channel centreline migrate towards the centreline, which is in line with the three-dimensional work of Pozrikidis (2005c) with which we found good qualitative agreement. Larger capsules tend to steady shapes with elongated trailing tips. Additionally the larger capsules translate slower along the channel and induce a greater additional pressure drop. Finally we found that in all cases the disturbance velocity decayed rapidly and it had reduced to 1% of its maximum value at a typical distance of four capsule radii from the capsule's centroid.

In chapter 5 we considered the fluid motion in a branching channel in the absence of a particle or capsule, and with prescribed flux rates at the exits of the computational domain. We used the boundary integral method to calculate the fluid motion and validated the results by comparison with the results obtained from a finite difference code. The results were in excellent agreement for a variety of flow conditions. In the boundary integral formulation we introduced a notional dividing boundary between the main channel and the branch channel to facilitate the separate treatment of the flows in the distinct channels. We note also that the boundary integral formulation more easily includes the branch angle than the finite difference method which would have required significant amendment to include the effect of an arbitrary branch angle. In our boundary conditions we assumed that the flow disturbance induced by the branch decayed as we moved away from the branch entrance towards the entrance or either exit. We found that the boundary tractions did indeed decay to their expected values as we moved away from the branch and the velocity profile settled to the pertinent Poiseuille profile within 2 channel widths from the centre of the branch entrance. When we varied the flux ratio, thus determining the flux rate at the exits, we found that the pressure drop between entrance and exit was greatest at the exit which received the majority of the fluid. We found the pressure drop to be greatest at the exits, for a fixed value of the flux ratio, when the branch angle was $\pi/2$ and a minimum for an acute angle. By considering the shear stress on the walls close to the downstream corner of the branch entrance, we found that the location of the termination point of the streamline which divides the flow depends upon the ratio of the fluxes entering the downstream channels and the branch angle. When most of the fluid continues along the main channel the dividing streamline terminates on the branch channel wall, for acute and obtuse branch angles. As the branch angle becomes more obtuse the termination point moves further from the corner and into the branch channel. However, if the branch channel receives the majority of the fluid then the termination point lies on the main channel wall. Changing the branch angle in this case does not significantly move the dividing streamline's termination point.

Next we introduced a rigid particle into the branching channel. Before examining the particle motion we checked that the computed results were in agreement with those of a fluid-filled branching channel by comparing the wall tractions, disturbance velocities and pressures between those obtained in chapter 5 and those calculated with a small particle. We found consistent results for a variety of particle positions. When we released a small particle close to the entrance and among streamlines which all travelled to a particular exit the particle did indeed travel to that exit. A particle released with its centroid on the dividing streamline caused the numerical simulation to terminate when the particle touched the corner of the branch entrance, as expected. We found the minimum particle translational velocity to occur when the particle is in the vicinity of the branch entrance. When the particle is several particle radii from the branch entrance we found the velocity to match that predicted by the straight channel model considered in chapter 3, thus providing further evidence that the effect of the branch is limited to a region close to the branch entrance.

We discussed the method by which we would deform the notional boundary which separates the main channel from the branch channel. We found that different configurations did not greatly affect the numerical solution. We decided upon a method by which the notional boundary would remain in its original configuration as much as possible, and only be deformed in the region close to the particle, where we would change the shape of the notional boundary to closely follow the shape of the particle.

In chapter 7 we considered the pressure-driven flow of an elastic capsule through a channel with a side branch. We treated the capsule boundary as a two-dimensional elastic membrane which resisted elastic stretching and bending using simple constitutive relations. For simplicity, we used a circle as the unstressed state of the capsule and when released we allowed it to deform as it moved with the flow. When the deformed capsule was in the vicinity of the branch entrance care needed to be exercised when deforming the notional boundary around the capsule, particularly when the capsule was highly deformed.

After releasing the capsule we found that it adopted a parachute-like shape as observed in experiments (e.g. Secomb et al. 2007). When the capsule passes over the branch entrance on its way to the exit of the main channel, or migrates into the branch channel it suffers considerable deformation. However, since we expect the effect of the branch entrance to decay as we move away from it we found that the capsule will migrate towards the channel centreline and relax to a shape resembling its equilibrium state. We found that the capsule did not fully achieve its steady-state shape since a distance longer than that of our truncated computational domain was required. This does suggest however that in a complex network of channels with frequent branches, capsules are more likely to attain this semi-equilibrium state since the distance between branches may be relatively short. We found that the capsule deformation was less when we increased the elastic membrane stiffness or the viscosity of the encapsulated fluid.

Using the streamline calculations from the fluid-filled branching channel, we accurately predicted the direction which the capsule takes when it is released entirely within a region of streamlines which travel to a particular exit. A capsule which approaches the branch junction along the dividing streamline may spend a considerable time negotiating the branch region, since the fluid moves relatively slowly in this region especially close to the wall where we expect, in the absence of a capsule, the dividing streamline to terminate. We found that when a capsule approaches the downstream corner of the branch entrance and the branch angle was acute or a right-angle then the capsule becomes trapped on the corner. The capsule is then caught in an extensional flow which deforms the capsule along both channels simultaneously. For the case of an obtuse angled branch, we found that the capsule does not get caught on either corner of the branch entrance. When the capsule does migrate into the branch it could take a considerable length of time to navigate its way fully into the branch entrance, and tends to suffer considerably more deformation than a capsule which remains in the main channel or migrates into an acute-angled branch. However we found that when the capsules successfully travel to either exit the elastic tensions and bending moments in the capsule membrane are comparable for all branch angles. The greatest membrane tensions occur when the capsule becomes trapped

at the branch entrance corner. We found that there exists a region from which we could release the capsule and its path is determined by the elastic properties of the membrane. For instance, a capsule released with its centroid in this region which travelled into the branch channel could be made to remain in the main channel by increasing its membrane stiffness thereby making it more resistant to deformation.

When we narrowed the branch width, the capsule consistently travelled to the exit with the maximum centreline velocity. Putting this in the context of blood flow where red blood cells tend to congregate on the channel centreline, a portion of the ambient plasma is 'skimmed' from the main channel and enters the branch. Our results are consistent with this observed 'plasma skimming' effect in branching capillaries. When the downstream centreline velocities were equal we found a region close to the entrance and on the centreline from which it is possible to affect the exit to which the capsule travels. For example, a capsule started with its centroid on the centreline of the main channel and which travelled into the branch channel could be made to travel to the exit of the main channel by increasing the capsule's membrane stiffness. We therefore demonstrated that the direction in which the capsule travels may, in the marginal cases, be determined by the elastic properties of the membrane.

While we have considered the motion of a single capsule, in capsule-laden flows which arise in nature and industry there may be many capsules present. We can apply the current results provided the capsules are sufficiently spaced, although care must be exercised when a capsule becomes trapped at a corner since it could then be approached by another capsule and the capsule interaction must then be taken into account. For tightly-packed capsules, interactions between neighbours is expected to have an effect on the transit and deformation of each individual capsule. Although the addition of more capsules to the flow is theoretically simple within the framework presented here, there are practical computational difficulties associated with the deformation of the boundary which divides the main and branch channels when multiple capsules are present. Furthermore, we would require a longer computational domain so that the assumptions regarding the decay of the disturbance due to each capsule is not violated. To ameliorate this problem, we provided a sketch of a method by which we could remove the notional boundary entirely, and therefore easily include the motion of multiple capsules. Amendments to the channel geometry, round corners at the branch entrance for example, could also be included via this alternative method. Moreover, the path to a more realistic three-dimensional boundary integral implementation of an elastic capsule in a branching tube would be rendered more straightforward, since the necessity for a deformable dividing surface would be removed.

Finally we note that throughout our discussions we have assumed the channel walls to be straight. In flow domains, such as blood flow in the capillaries, this is evidently not the case. We do point out however that we have made this assumption in the interest of simplicity and irregularly shaped channel walls could easily be incorporated into the boundary element formulation, in two or three dimensions. For example Secomb et al. (2007) digitised a section of a rat's mesentery in order to provide a realistic domain for their finite-element calculations. This domain could be used by the boundary integral

formulation without amendment, and with the additional benefit of a cheaper computational cost since only the elements of the walls need to be discretised, as opposed to the entire flow domain when using the finite-element method. However the resulting matrix in the linear system will be much denser for the boundary element method than for the finite-element method. Repeatedly solving a linear system with a dense matrix may prove computationally expensive. Also we point out that the boundary integral method may only be applied to flows in which the Reynolds number is small, but it is in those flows where the boundary integral method provides an efficient, adaptable and accurate method of calculating the velocity field.

Appendices

Appendix A – Integration of the two-dimensional free-space Green's function

We used a quadrature to approximate the integral of the two-dimensional free space Green's function, or Stokeslet, over a straight element. The two-dimensional Stokeslet is defined by

$$G_{ij}(\mathbf{x}, \mathbf{x}_0) = -\delta_{ij} \ln(r) + \frac{(x_i - x_{0,i})(x_j - x_{0,j})}{r^2} \quad (\text{A.1})$$

where $r = |\mathbf{x} - \mathbf{x}_0|$, and the integral over element, E , is

$$\tilde{G}_{ij}(\mathbf{x}_0) = \int_E G_{ij}(\mathbf{x}, \mathbf{x}_0) \, ds(\mathbf{x}), \quad (\text{A.2})$$

where the element is taken to be a straight-line with start point, $\mathbf{x}_s = (x_s, y_s)$, and end point, $\mathbf{x}_e = (x_e, y_e)$. We use Gauss-Legendre quadrature to integrate the Stokeslet numerically along a line. Since the quadrature uses Legendre polynomials, which are defined on the domain $[-1, 1]$, we introduce a parameter $\xi \in [-1, 1]$, so that the line between \mathbf{x}_s and \mathbf{x}_e may be represented parametrically as

$$x(\xi) = \frac{1}{2}(x_e + x_s) + \frac{1}{2}(x_e - x_s)\xi, \quad (\text{A.3})$$

$$y(\xi) = \frac{1}{2}(y_e + y_s) + \frac{1}{2}(y_e - y_s)\xi. \quad (\text{A.4})$$

As ξ increases from -1 to 1 , the point \mathbf{x} moves from \mathbf{x}_s to \mathbf{x}_e . Expressing the integration variable in terms of ξ gives

$$\begin{aligned} ds(\xi) &= \sqrt{dx^2 + dy^2} \\ &= \sqrt{\left(\frac{1}{2}(x_e - x_s) \, d\xi\right)^2 + \left(\frac{1}{2}(y_e - y_s) \, d\xi\right)^2} \\ &= \frac{1}{2} \sqrt{(x_e - x_s)^2 + (y_e - y_s)^2} \, d\xi \\ &= h_\xi \, d\xi, \end{aligned} \quad (\text{A.5})$$

where h_ξ is the half-length of an element and defined by

$$h_\xi = \frac{1}{2} \sqrt{(x_e - x_s)^2 + (y_e - y_s)^2}. \quad (\text{A.6})$$

Therefore we can express \tilde{G}_{ij} in terms of ξ and approximate the integral using Gauss-Legendre quadrature to get,

$$\begin{aligned} \tilde{G}_{ij}(\mathbf{x}_0) &= \int_E G_{ij}(\mathbf{x}, \mathbf{x}_0) \, ds(\mathbf{x}) \\ &= h_\xi \int_{-1}^1 G_{ij}(\mathbf{x}(\xi), \mathbf{x}_0) \, d\xi \\ &\approx h_\xi \sum_{r=1}^{N_Q} G_{ij}(\mathbf{x}(\xi_r), \mathbf{x}_0) w_r, \end{aligned} \quad (\text{A.7})$$

where N_Q is the specified number of base points, ξ_r is the r^{th} root of the N_Q -degree Legendre polynomial and w_r is the integration weight for the r^{th} base point.

There are two cases to consider. In the first case the pole, \mathbf{x}_0 , does not lie on the element and so the Stokeslet is well defined and we can evaluate the integral using (A.7). When \mathbf{x}_0 lies on the element the Stokeslet is logarithmically singular. This is the second case and it occurs during the construction of the ‘influence’ matrix because \mathbf{x}_0 is placed at the midpoint of each of the boundary elements. In this case it is helpful to note that

$$\begin{aligned} r &= \sqrt{(x - x_0)^2 + (y - y_0)^2} \\ &= \sqrt{\left(\frac{1}{2}(x_e - x_s)\xi\right)^2 + \left(\frac{1}{2}(y_e - y_s)\xi\right)^2} \\ &= |h_\xi \xi|, \end{aligned} \quad (\text{A.8})$$

since $\mathbf{x} - \mathbf{x}_0 = \frac{1}{2}(\mathbf{x}_e - \mathbf{x}_s)\xi$, and so \tilde{G}_{ij} becomes

$$\begin{aligned} \tilde{G}_{ij}(\mathbf{x}_0) &= h_\xi \int_{-1}^1 \left(-\delta_{ij} \ln |h_\xi \xi| + \frac{(x_i - x_{0,i})(x_j - x_{0,j})}{(h_\xi \xi)^2} \right) d\xi \\ &= -h_\xi \delta_{ij} \left(2 \ln h_\xi + \int_{-1}^1 \ln |\xi| \, d\xi \right) + \frac{(x_{e,i} - x_{s,i})(x_{e,j} - x_{s,j})}{2 h_\xi}, \end{aligned} \quad (\text{A.9})$$

which contains an integrable logarithmic singularity at $\xi = 0$ when $i = j$. Taking the

principal value of the integral when the singularity is present gives

$$\tilde{G}_{xx}(\mathbf{x}_0) = 2h_\xi(1 - \ln h_\xi) + \frac{(x_e - x_s)^2}{2h_\xi}, \quad (\text{A.10})$$

$$\tilde{G}_{xy}(\mathbf{x}_0) = \tilde{G}_{yx}(\mathbf{x}_0) = \frac{(x_e - x_s)(y_e - y_s)}{2h_\xi}, \quad (\text{A.11})$$

$$\tilde{G}_{yy}(\mathbf{x}_0) = 2h_\xi(1 - \ln h_\xi) + \frac{(y_e - y_s)^2}{2h_\xi}, \quad (\text{A.12})$$

for the components of equation (A.9). More details on the quadrature method, together with the treatment of other kinds of boundary elements, may be found in Pozrikidis (1998).

Appendix B – Influence matrix deflation for a rigid particle

When a rigid solid particle travels along a straight channel the disturbance velocity, \mathbf{u}^D , caused by the particle is governed by the boundary integral equation,

$$4\pi\mu u_j^D(\mathbf{x}_0) = \pi_2 \int_{\mathcal{E}_2} n_i(\mathbf{x}) G_{ij}(\mathbf{x}, \mathbf{x}_0) ds(\mathbf{x}) - \int_{\mathcal{C}} f_i^D(\mathbf{x}) G_{ij}(\mathbf{x}, \mathbf{x}_0) ds(\mathbf{x}) - \int_{\mathcal{P}} f_i(\mathbf{x}) G_{ij}(\mathbf{x}, \mathbf{x}_0) ds(\mathbf{x}), \quad (\text{B.1})$$

derived in chapter 3, and where \mathcal{E}_2 is the exit to computational domain, π_2 is the disturbance pressure at \mathcal{E}_2 , \mathbf{n} is the normal vector which points into the fluid, $G_{ij}(\mathbf{x}, \mathbf{x}_0)$ is the free-space Green's function, s is arc-length, \mathbf{f}^D is the disturbance traction on the channel walls \mathcal{C} , and \mathbf{f} are the tractions on the particle boundary, \mathcal{P} . Unfortunately equation (B.1) does not have a unique solution. Let us define

$$\mathbf{f} = \hat{\mathbf{f}} + \chi \mathbf{n}, \quad (\text{B.2})$$

for the traction on the particle and where $\hat{\mathbf{f}}$ is the particular solution, χ is an arbitrary constant and \mathbf{n} is the normal vector which points out of the particle and into the fluid. Substituting equation (B.2) into equation (B.1) gives

$$\begin{aligned} 4\pi\mu u_j^D(\mathbf{x}_0) &= \pi_2 \int_{\mathcal{E}_2} n_i(\mathbf{x}) G_{ij}(\mathbf{x}, \mathbf{x}_0) ds(\mathbf{x}) - \int_{\mathcal{C}} f_i^D(\mathbf{x}) G_{ij}(\mathbf{x}, \mathbf{x}_0) ds(\mathbf{x}) \\ &\quad - \int_{\mathcal{P}} \hat{f}_i(\mathbf{x}) G_{ij}(\mathbf{x}, \mathbf{x}_0) ds(\mathbf{x}) - \chi \int_{\mathcal{P}} n_i(\mathbf{x}) G_{ij}(\mathbf{x}, \mathbf{x}_0) ds(\mathbf{x}) \\ &= \pi_2 \int_{\mathcal{E}_2} n_i(\mathbf{x}) G_{ij}(\mathbf{x}, \mathbf{x}_0) ds(\mathbf{x}) - \int_{\mathcal{C}} f_i^D(\mathbf{x}) G_{ij}(\mathbf{x}, \mathbf{x}_0) ds(\mathbf{x}) \\ &\quad - \int_{\mathcal{P}} \hat{f}_i(\mathbf{x}) G_{ij}(\mathbf{x}, \mathbf{x}_0) ds(\mathbf{x}) \end{aligned} \quad (\text{B.3})$$

because $\int_{\mathcal{P}} n_i(\mathbf{x}) G_{ij}(\mathbf{x}, \mathbf{x}_0) ds(\mathbf{x}) = 0$ by equation (1.3.34). Therefore an arbitrary multiple of the normal vector may be added to the particle traction without violating equation

(B.1). To ensure the uniqueness of the traction on the particle boundary an additional term, called the ‘deflation’ term, is added to the boundary integral equation (B.1). Since the lack of a unique solution stems from the tractions on the particle boundary we define the deflation term to be

$$D_j(\mathbf{x}_0) = n_j(\mathbf{x}_0) \int_P n_i(\mathbf{x}) f_i(\mathbf{x}) \, ds(\mathbf{x}), \quad (\text{B.4})$$

which is given in Pozrikidis (2005b). Substitution of equation (B.2) into equation (B.4) gives

$$D_j(\mathbf{x}_0) = n_j(\mathbf{x}_0) \int_P n_i(\mathbf{x}) \hat{f}_i(\mathbf{x}) \, ds(\mathbf{x}) + \chi n_j(\mathbf{x}_0) S_{\mathcal{P}}, \quad (\text{B.5})$$

which shows that an arbitrary multiple of the normal vector cannot be added to the particle traction in the deflation term, and where $S_{\mathcal{P}}$ is the total arc-length of the perimeter of \mathcal{P} . Therefore we can ensure that the tractions on the particle boundary are unique in equation (B.1) by adding the deflation term, $\mathbf{D}(\mathbf{x}_0)$, to the boundary integral equation. However we need to know how the presence of the deflation term will affect the solution to the boundary integral equation, and in particular will a solution to the ‘deflated’ boundary integral equation,

$$\begin{aligned} 4\pi\mu u_j^D(\mathbf{x}_0) + D_j(\mathbf{x}_0) &= \pi_2 \int_{\mathcal{E}_2} n_i(\mathbf{x}) G_{ij}(\mathbf{x}, \mathbf{x}_0) \, ds(\mathbf{x}) \\ &- \int_{\mathcal{C}} f_i^D(\mathbf{x}) G_{ij}(\mathbf{x}, \mathbf{x}_0) \, ds(\mathbf{x}) - \int_{\mathcal{P}} f_i(\mathbf{x}) G_{ij}(\mathbf{x}, \mathbf{x}_0) \, ds(\mathbf{x}), \end{aligned} \quad (\text{B.6})$$

be a solution to the original equation (B.1)? To calculate the deflation term’s value we multiply equation (B.6) by $n_j(\mathbf{x}_0)$ and integrate over \mathcal{P} with respect to $s(\mathbf{x}_0)$ to get

$$4\pi\mu I_1 + I_2 = \pi_2 I_3 - I_4 - I_5, \quad (\text{B.7})$$

where

$$I_1 = \int_{\mathcal{P}} u_j^D(\mathbf{x}_0) n_j(\mathbf{x}_0) \, ds(\mathbf{x}_0), \quad (\text{B.8})$$

$$I_2 = \int_{\mathcal{P}} D_j(\mathbf{x}_0) n_j(\mathbf{x}_0) \, ds(\mathbf{x}_0), \quad (\text{B.9})$$

$$I_3 = \int_{\mathcal{P}} \left(\int_{\mathcal{E}_2} n_i(\mathbf{x}) G_{ij}(\mathbf{x}, \mathbf{x}_0) \, ds(\mathbf{x}) \right) n_j(\mathbf{x}_0) \, ds(\mathbf{x}_0), \quad (\text{B.10})$$

$$I_4 = \int_{\mathcal{P}} \left(\int_{\mathcal{C}} f_i^D(\mathbf{x}) G_{ij}(\mathbf{x}, \mathbf{x}_0) \, ds(\mathbf{x}) \right) n_j(\mathbf{x}_0) \, ds(\mathbf{x}_0), \quad (\text{B.11})$$

and

$$I_5 = \int_{\mathcal{P}} \left(\int_{\mathcal{P}} f_i(\mathbf{x}) G_{ij}(\mathbf{x}, \mathbf{x}_0) \, ds(\mathbf{x}) \right) n_j(\mathbf{x}_0) \, ds(\mathbf{x}_0). \quad (\text{B.12})$$

To evaluate I_1 we cannot apply the divergence theorem because \mathbf{u}^D is undefined in the region bounded by \mathcal{P} . However we can write the velocity in terms of the total velocity and the Poiseuille velocity using $\mathbf{u}^D = \mathbf{u} - \mathbf{u}^P$, where \mathbf{u} is the total velocity and \mathbf{u}^P is the Poiseuille velocity. Therefore we have

$$\begin{aligned} I_1 &= \int_{\mathcal{P}} \mathbf{u}^D(\mathbf{x}) \cdot \mathbf{n}(\mathbf{x}) \, ds(\mathbf{x}) \\ &= \int_{\mathcal{P}} \mathbf{u}(\mathbf{x}) \cdot \mathbf{n}(\mathbf{x}) \, ds(\mathbf{x}) - \int_{\mathcal{P}} \mathbf{u}^P(\mathbf{x}) \cdot \mathbf{n}(\mathbf{x}) \, ds(\mathbf{x}), \end{aligned} \quad (\text{B.13})$$

where we have reverted to \mathbf{x} as the dependent variable. We may use the divergence theorem to transform the integral over \mathcal{P} involving the Poiseuille velocity to an integral over the region bounded by \mathcal{P} which we will label $A_{\mathcal{P}}$, to get

$$\begin{aligned} I_1 &= \int_{\mathcal{P}} \mathbf{u}(\mathbf{x}) \cdot \mathbf{n}(\mathbf{x}) \, ds(\mathbf{x}) - \int_{A_{\mathcal{P}}} \nabla \cdot \mathbf{u}^P(\mathbf{x}) \, dA(\mathbf{x}) \\ &= \int_{\mathcal{P}} \mathbf{u}(\mathbf{x}) \cdot \mathbf{n}(\mathbf{x}) \, ds(\mathbf{x}), \end{aligned} \quad (\text{B.14})$$

since $\nabla \cdot \mathbf{u}^P = 0$ because the Poiseuille flow is incompressible everywhere in the channel. On the particle boundary we may write the velocity in terms of the translational and rotational velocities, \mathbf{V} and $\Omega \mathbf{k}$, using

$$\mathbf{u}(\mathbf{x}) = \mathbf{V} + \Omega \mathbf{k} \wedge (\mathbf{x} - \mathbf{x}_c) \quad (\text{B.15})$$

to get

$$\begin{aligned} I_1 &= \int_{\mathcal{P}} \mathbf{u}(\mathbf{x}) \cdot \mathbf{n}(\mathbf{x}) \, ds(\mathbf{x}) \\ &= \mathbf{V} \cdot \int_{\mathcal{P}} \mathbf{n}(\mathbf{x}) \, ds(\mathbf{x}) + \Omega \int_{\mathcal{P}} (\mathbf{k} \wedge (\mathbf{x} - \mathbf{x}_c)) \cdot \mathbf{n}(\mathbf{x}) \, ds(\mathbf{x}) \\ &= \mathbf{V} \cdot \int_{\mathcal{P}} \mathbf{n}(\mathbf{x}) \, ds(\mathbf{x}) + \Omega \int_{A_{\mathcal{P}}} \nabla \cdot (\mathbf{k} \wedge (\mathbf{x} - \mathbf{x}_c)) \, dA(\mathbf{x}), \end{aligned} \quad (\text{B.16})$$

where we have used the divergence theorem to transform the second integral on the right-hand side. Since the normal vector in Cartesian coordinates is $\mathbf{n}(x, y) = (\frac{dy}{ds}, -\frac{dx}{ds})$, the

first integral on the right-hand side is

$$\int_{\mathcal{P}} \mathbf{n}(\mathbf{x}) \, ds(\mathbf{x}) = \int_{\mathcal{P}} \frac{dy}{ds} \mathbf{i} - \frac{dx}{ds} \mathbf{j} \, ds(\mathbf{x}) = \int_{\mathcal{P}} dy \mathbf{i} - \int_{\mathcal{P}} dx \mathbf{j} = \mathbf{0} \quad (\text{B.17})$$

by periodicity. Since the rigid particle is allowed to move with the flow, the centroid, $\mathbf{x}_c = (x_c, y_c)$, and the position vector, $\mathbf{x} = (x, y)$, will only depend on the time. Therefore the integrand of the second integral in equation (B.16) is

$$\nabla \cdot (\mathbf{k} \wedge (\mathbf{x}(t) - \mathbf{x}_c(t))) = \nabla \cdot (-(y(t) + y_c(t))\mathbf{i} + (x(t) + x_c(t))\mathbf{j}) = \mathbf{0}. \quad (\text{B.18})$$

Therefore substituting equations (B.17) and (B.18) into equation (B.16) shows that

$$I_1 = 0. \quad (\text{B.19})$$

The next term is I_2 which is

$$\begin{aligned} I_2 &= \int_{\mathcal{P}} D_j(\mathbf{x}_0) n_j(\mathbf{x}_0) \, ds(\mathbf{x}_0) \\ &= \int_{\mathcal{P}} \left(n_j(\mathbf{x}_0) \int_{\mathcal{P}} n_i(\mathbf{x}) f_i(\mathbf{x}) \, ds(\mathbf{x}) \right) n_j(\mathbf{x}_0) \, ds(\mathbf{x}_0) \\ &= \left(\int_{\mathcal{P}} n_j(\mathbf{x}_0) n_j(\mathbf{x}_0) \, ds(\mathbf{x}_0) \right) \left(\int_{\mathcal{P}} n_i(\mathbf{x}) f_i(\mathbf{x}) \, ds(\mathbf{x}) \right) \\ &= S_{\mathcal{P}} \int_{\mathcal{P}} n_i(\mathbf{x}) f_i(\mathbf{x}) \, ds(\mathbf{x}), \end{aligned} \quad (\text{B.20})$$

where $S_{\mathcal{P}}$ is the total arc-length of the particle. For I_3 , I_4 and I_5 we rearrange the order of integration to get

$$I_3 = \int_{\mathcal{E}_2} n_i(\mathbf{x}) \left(\int_{\mathcal{P}} n_j(\mathbf{x}_0) G_{ij}(\mathbf{x}, \mathbf{x}_0) \, ds(\mathbf{x}_0) \right) \, ds(\mathbf{x}), \quad (\text{B.21})$$

$$I_4 = \int_{\mathcal{C}} f_i^D(\mathbf{x}) \left(\int_{\mathcal{P}} n_j(\mathbf{x}_0) G_{ij}(\mathbf{x}, \mathbf{x}_0) \, ds(\mathbf{x}_0) \right) \, ds(\mathbf{x}), \quad (\text{B.22})$$

and

$$I_5 = \int_{\mathcal{P}} f_i(\mathbf{x}) \left(\int_{\mathcal{P}} n_j(\mathbf{x}_0) G_{ij}(\mathbf{x}, \mathbf{x}_0) \, ds(\mathbf{x}_0) \right) \, ds(\mathbf{x}), \quad (\text{B.23})$$

which all contain the common integral,

$$I_{6,i}(\mathbf{x}) = \int_{\mathcal{P}} n_j(\mathbf{x}_0) G_{ij}(\mathbf{x}, \mathbf{x}_0) \, ds(\mathbf{x}_0). \quad (\text{B.24})$$

Making use of the symmetry of the Green's function, $G_{ij}(\mathbf{x}, \mathbf{x}_0) = G_{ji}(\mathbf{x}_0, \mathbf{x})$, we write equation (B.24) as

$$I_{6,i}(\mathbf{x}) = \int_{\mathcal{P}} n_j(\mathbf{x}_0) G_{ji}(\mathbf{x}_0, \mathbf{x}) ds(\mathbf{x}_0). \quad (\text{B.25})$$

By swapping $i \leftrightarrow j$ and $\mathbf{x} \leftrightarrow \mathbf{x}_0$ in equation (B.25) we obtain

$$I_{6,j}(\mathbf{x}_0) = \int_{\mathcal{P}} n_i(\mathbf{x}) G_{ij}(\mathbf{x}, \mathbf{x}_0) ds(\mathbf{x}) \quad (\text{B.26})$$

which is zero by the continuity equation (1.3.34). Therefore we have

$$I_1 = I_3 = I_4 = I_5 = 0, \quad (\text{B.27})$$

and so equation (B.7) reduces to $I_2 = 0$, which implies

$$\int_P n_i(\mathbf{x}) f_i(\mathbf{x}) ds(\mathbf{x}) = 0 \quad (\text{B.28})$$

since the perimeter, $S_{\mathcal{P}}$, is non-zero. Therefore the deflation term,

$$D_j(\mathbf{x}_0) = n_j(\mathbf{x}_0) \int_P n_i(\mathbf{x}) f_i(\mathbf{x}) ds(\mathbf{x}) = 0, \quad (\text{B.29})$$

and the boundary integral equation (B.6) will be unaffected by its presence, and a solution of the deflated boundary integral equation will also be a solution of the non-deflated system.

The same process may be applied to the boundary integral equation for a branching channel containing a rigid particle to obtain the same result.

Appendix C – Calculation of $I(\mathbf{x}_0)$

When we consider a branching channel, the boundary integral equation for the main channel gives rise to the term,

$$I_j(\mathbf{x}_0) = (1 - Q) \int_{\mathcal{E}_2} \left(f_i^{P_1} G_{ij} - \mu u_i^{P_1} T_{ijk} n_k \right) ds(\mathbf{x}), \quad (\text{C.1})$$

which we may calculate exactly by substitution of the Poiseuille traction, \mathbf{f}^{P_1} , the Poiseuille velocity, \mathbf{u}^{P_1} , the Green's function and the stress tensor. At \mathcal{E}_2 we write the Poiseuille velocity and traction as

$$\mathbf{u}^{P_1} = \frac{G_1 d^2}{2\mu} \left(1 - \frac{y^2}{d^2} \right) \mathbf{i}, \quad \mathbf{f}^{P_1} = G_1 (-l \mathbf{i} + y \mathbf{j}), \quad (\text{C.2})$$

where $-G_1$ is the constant pressure gradient between \mathcal{E}_1 and \mathcal{E}_2 . We substitute the equations in (C.2) into equation (C.1) to get,

$$I_j(\mathbf{x}_0) = (1 - Q) G_1 \int_{\mathcal{E}_2} \left(-l G_{xj} + y G_{yj} + \frac{d^2}{2} T_{xjx} - \frac{1}{2} y^2 T_{xjx} \right) ds(\mathbf{x}). \quad (\text{C.3})$$

The Green's function and the stress tensor are defined in equations (1.3.29) and (1.3.30), from which we can see that both functions are written in terms of $\hat{\mathbf{x}}$, where $\hat{\mathbf{x}} = \mathbf{x} - \mathbf{x}_0$. At \mathcal{E}_2 , $\hat{x} = x - x_0 = l - x_0$ which is constant. Writing equation (C.3) in terms of $\hat{y} = y - y_0$ we obtain

$$I_j(\mathbf{x}_0) = (1 - Q) G_1 \int_{\mathcal{E}_2} \left(-l G_{xj} + y_0 G_{yj} + \hat{y} G_{yj} + \frac{d^2 - y_0^2}{2} T_{xjx} - y_0 \hat{y} T_{xjx} - \frac{1}{2} \hat{y}^2 T_{xjx} \right) d\hat{y}, \quad (\text{C.4})$$

where $ds = d\hat{y}$. Therefore to evaluate the integral (C.4) we must evaluate the integrals,

$$\int_{\mathcal{E}_2} G_{xj} d\hat{y}, \quad \int_{\mathcal{E}_2} G_{yj} d\hat{y}, \quad \int_{\mathcal{E}_2} \hat{y} G_{yj} d\hat{y}, \\ \int_{\mathcal{E}_2} T_{xjx} d\hat{y}, \quad \int_{\mathcal{E}_2} \hat{y} T_{xjx} d\hat{y}, \quad \text{and} \quad \int_{\mathcal{E}_2} \hat{y}^2 T_{xjx} d\hat{y}.$$

Calculation of the components of these integrals gives,

$$\int_{\mathcal{E}_2} G_{xx} d\hat{y} = [\hat{y}(1 - \ln r)]_{y=-d}^{y=d}, \quad (\text{C.5})$$

$$\int_{\mathcal{E}_2} G_{xy} d\hat{y} = \int_{\mathcal{E}_2} G_{yx} d\hat{y} = \hat{x} [\ln r]_{y=-d}^{y=d}, \quad (\text{C.6})$$

$$\int_{\mathcal{E}_2} G_{yy} d\hat{y} = [2\hat{y} - \hat{y} \ln r - 2\hat{x} \arctan(\hat{y}/\hat{x})]_{y=-d}^{y=d}, \quad (\text{C.7})$$

$$\int_{\mathcal{E}_2} \hat{y} G_{yx} d\hat{y} = \hat{x} [\hat{y} - \hat{x} \arctan(\hat{y}/\hat{x})]_{y=-d}^{y=d}, \quad (\text{C.8})$$

$$\int_{\mathcal{E}_2} \hat{y} G_{yy} d\hat{y} = \frac{1}{4} [3\hat{y}^2 - 2(r^2 + 2\hat{x}^2) \ln r]_{y=-d}^{y=d}, \quad (\text{C.9})$$

for the integrals involving the Green's function, where $\hat{y}(y = d) = d - y_0$, $\hat{y}(y = -d) = -d - y_0$ and $r = \sqrt{\hat{x}^2 + \hat{y}^2}$. The integrals involving the stress tensor are

$$\int_{\mathcal{E}_2} T_{xxx} d\hat{y} = -2 \left[\frac{\hat{x}\hat{y}}{r^2} + \arctan(\hat{y}/\hat{x}) \right]_{y=-d}^{y=d}, \quad (\text{C.10})$$

$$\int_{\mathcal{E}_2} T_{xyx} d\hat{y} = 2\hat{x}^2 \left[\frac{1}{r^2} \right]_{y=-d}^{y=d}, \quad (\text{C.11})$$

$$\int_{\mathcal{E}_2} \hat{y} T_{xxx} d\hat{y} = 2\hat{x}^3 \left[\frac{1}{r^2} \right]_{y=-d}^{y=d}, \quad (\text{C.12})$$

$$\int_{\mathcal{E}_2} \hat{y} T_{xyx} d\hat{y} = 2\hat{x} \left[\frac{\hat{x}\hat{y}}{r^2} - \arctan(\hat{y}/\hat{x}) \right]_{y=-d}^{y=d}, \quad (\text{C.13})$$

$$\int_{\mathcal{E}_2} \hat{y}^2 T_{xxx} d\hat{y} = 2\hat{x}^2 \left[\frac{\hat{x}\hat{y}}{r^2} - \arctan(\hat{y}/\hat{x}) \right]_{y=-d}^{y=d}, \quad (\text{C.14})$$

$$\int_{\mathcal{E}_2} \hat{y}^2 T_{xyx} d\hat{y} = -2\hat{x}^2 \left[\frac{\hat{x}^2}{r^2} + 2 \ln r \right]_{y=-d}^{y=d}. \quad (\text{C.15})$$

Substitution of equations (C.5)–(C.15) into equation (C.4) yields the x and y components of $I(\mathbf{x}_0)$ for a given \mathbf{x}_0 .

Appendix D – Finite difference model for a branching channel

The geometry for a two-dimensional branching channel where the branch is at right-angles to the main channel is shown in figure D.1. We take the top wall of the main channel to lie at $y = d$ and the bottom wall to lie at $y = -d$. The branch channel has the same width and joins on to the main channel such that the midpoint of the lower wall lies on the centreline of the branch channel. We take the main channel length to be $12d$ and the branch channel length to be $6d$. We may calculate the flow through the bifurcation using the finite-difference method by introducing the stream function, $\psi(\mathbf{x})$, which is constant along a streamline and satisfies the biharmonic equation,

$$\nabla^4\psi = 0, \quad (\text{D.1})$$

in an incompressible flow. The velocity, $\mathbf{u}(\mathbf{x}) = (u(\mathbf{x}), v(\mathbf{x}))$, is calculated from the stream-function by

$$u = \frac{\partial\psi}{\partial y} \quad \text{and} \quad v = -\frac{\partial\psi}{\partial x}. \quad (\text{D.2})$$

We introduce the vorticity component in the \mathbf{k} direction,

$$\zeta = \mathbf{k} \cdot (\nabla \wedge \mathbf{u}) = \frac{\partial v}{\partial x} - \frac{\partial u}{\partial y} = -\nabla^2\psi,$$

so that we may write the biharmonic equation for $\psi(\mathbf{x})$ as a pair of coupled partial differential equations,

$$\zeta = -\nabla^2\psi \quad \text{and} \quad \nabla^2\zeta = 0. \quad (\text{D.3})$$

For a two-dimensional flow we have

$$\zeta = -\psi_{xx} - \psi_{yy} \quad \text{and} \quad 0 = \zeta_{xx} + \zeta_{yy}, \quad (\text{D.4})$$

At the entrance and exits we assume that any disturbance caused by the branch channel has decayed and that the velocity is unidirectional Poiseuille flow characterised by the flux. At the entrance the flux is Q_1 and the Poiseuille velocity is \mathbf{u}^{P_1} , at the exit of the main channel the flux is Q_2 and the Poiseuille velocity is \mathbf{u}^{P_2} and at the exit of the branch channel the flux is Q_3 and the Poiseuille velocity is \mathbf{u}^{P_3} . We have $Q_1 = Q_2 + Q_3$ and all

5. Similarly we find that $\psi = Q_3$ on walls 3 and 4. In summary we have

$$\begin{aligned}\psi &= 0 && \text{on walls 1 and 2,} \\ \psi &= Q_1 && \text{on wall 5,} \\ \psi &= Q_3 && \text{on walls 3 and 4,}\end{aligned}\tag{D.13}$$

as the boundary conditions for ψ on the walls. To find $\psi(\mathbf{x})$ at the entrance and exits we integrate equation (D.2) for the pertinent Poiseuille velocity at \mathcal{E}_1 , \mathcal{E}_2 and \mathcal{E}_3 to get

$$\psi(y; \mathcal{E}_1) = U_0^{P_1} \left(y - \frac{y^3}{3d^2} + \frac{2}{3}d \right)\tag{D.14}$$

$$\psi(y; \mathcal{E}_2) = U_0^{P_2} \left(y - \frac{y^3}{3d^2} + \frac{2}{3}d \right) + Q_3\tag{D.15}$$

$$\psi(x; \mathcal{E}_3) = U_0^{P_3} \left(x - \frac{(x-6d)^3}{3d^2} - \frac{16}{3}d \right).\tag{D.16}$$

Therefore we know ψ on all the boundaries.

Our next step involves meshing the computational domain using $\Delta x d$ and $\Delta y d$ as the grid spacing in the x and y directions respectively. We use $\psi_{i,j}$ and $\zeta_{i,j}$ to denote the value of ψ and ζ at $x = i\Delta x$ and $y = j\Delta y$, and where $i = 0 \dots N (= 12d/\Delta x)$ and $j = 0 \dots M (= 8d/\Delta y)$. Using centred finite differences we approximate the equations in equation (D.4) using

$$\zeta_{i,j} = - \left(\frac{\psi_{i+1,j} - 2\psi_{i,j} + \psi_{i-1,j}}{\Delta x^2} + \frac{\psi_{i,j+1} - 2\psi_{i,j} + \psi_{i,j-1}}{\Delta y^2} \right)\tag{D.17}$$

$$0 = \frac{\zeta_{i+1,j} - 2\zeta_{i,j} + \zeta_{i-1,j}}{\Delta x^2} + \frac{\zeta_{i,j+1} - 2\zeta_{i,j} + \zeta_{i,j-1}}{\Delta y^2}.\tag{D.18}$$

To complete our boundary conditions we require equations for ζ at the entrance, exits and on the walls. The values of ζ at the entrance and exits are calculated using equation (D.3) and equations (D.5)–(D.7) to get

$$\zeta(y; \mathcal{E}_1) = \left(\frac{2U_0^{P_1}}{d^2} \right) y,\tag{D.19}$$

$$\zeta(y; \mathcal{E}_2) = \left(\frac{2U_0^{P_2}}{d^2} \right) y,\tag{D.20}$$

$$\zeta(x; \mathcal{E}_3) = \left(\frac{2U_0^{P_3}}{d^2} \right) (x - 6d).\tag{D.21}$$

To find ζ on the walls we consider wall 1 on which $\psi = 0$ and so $\psi_x = 0$ and $\psi_{xx} = 0$ which gives $\zeta = -\psi_{yy}$ and

$$\zeta_{i,j} = - \frac{\psi_{i,j+1} - 2\psi_{i,j} + \psi_{i,j-1}}{\Delta y^2},\tag{D.22}$$

with $j \neq 0$ and where $\zeta_{i,j}$ lies on the wall, $\zeta_{i,j+1}$ lies in the fluid in the main channel and

$\zeta_{i,j-1}$ is a ‘ghost’ point which lies outside of the computational domain. To eliminate the ‘ghost’ point we note that $u = 0$ on wall 1 so that

$$0 = u(x_i, y_j) = \frac{\partial \psi}{\partial y}(x_i, y_j) \approx \frac{\psi_{i,j+1} - \psi_{i,j-1}}{2 \Delta y} \quad (\text{D.23})$$

which gives $\psi_{i,j+1} = \psi_{i,j-1}$ and so

$$\zeta_{i,j} = 2 \frac{\psi_{i,j} - \psi_{i,j+1}}{\Delta y^2} = -2 \frac{\psi_{i,j+1}}{\Delta y^2}, \quad (\text{D.24})$$

on wall 1 since $\psi_{i,j}$ is on the wall and $\psi = 0$. Applying the same process to the remaining walls yields similar expressions. Therefore we can compute ζ exactly at the entrance and exits and use a finite difference approximation to calculate ζ on the walls. It remains to find expressions for $\zeta_{i,j}$ and $\psi_{i,j}$ which can be obtained from equations (D.17) and (D.18) to get

$$\zeta_{i,j} = \frac{\Delta x^2(\zeta_{i,j+1} + \zeta_{i,j-1}) + \Delta y^2(\zeta_{i+1,j} + \zeta_{i-1,j})}{2(\Delta x^2 + \Delta y^2)}, \quad (\text{D.25})$$

$$\psi_{i,j} = \frac{\Delta x^2(\psi_{i,j+1} + \psi_{i,j-1}) + \Delta x^2 \Delta y^2 \zeta_{i,j} + \Delta y^2(\psi_{i+1,j} + \psi_{i-1,j})}{2(\Delta x^2 + \Delta y^2)}. \quad (\text{D.26})$$

Using these equations we calculate $\zeta_{i,j}$ and $\psi_{i,j}$ at each node in the fluid domain. We continue iterating over the nodes which lie in the fluid domain and the walls on which we calculate $\zeta_{i,j}$ until the values of ψ in the fluid and ζ in the fluid and on the walls converge. Convergence is deemed to have occurred when the values of ψ and ζ at every node change by less than $10^{-9} Q_1$ and $10^{-9} Q_1/d^2$ in one iteration respectively. The flow streamlines are then plotted using the values of ψ . The velocity at a node in the fluid is calculated by

$$u(x_i, y_i) = \frac{\partial \psi}{\partial y} = \frac{\psi_{i,j+1} - \psi_{i,j-1}}{2 \Delta y}, \quad (\text{D.27})$$

$$v(x_i, y_i) = -\frac{\partial \psi}{\partial x} = \frac{\psi_{i-1,j} - \psi_{i+1,j}}{2 \Delta x}. \quad (\text{D.28})$$

The streamlines for $Q = 0.5$ are shown in figure D.2. Comparison with figure 5.2 (a) in chapter 5 shows an excellent agreement. The dividing streamline starts from the centre of the entrance on the left and terminates on the right-hand corner of the branch.

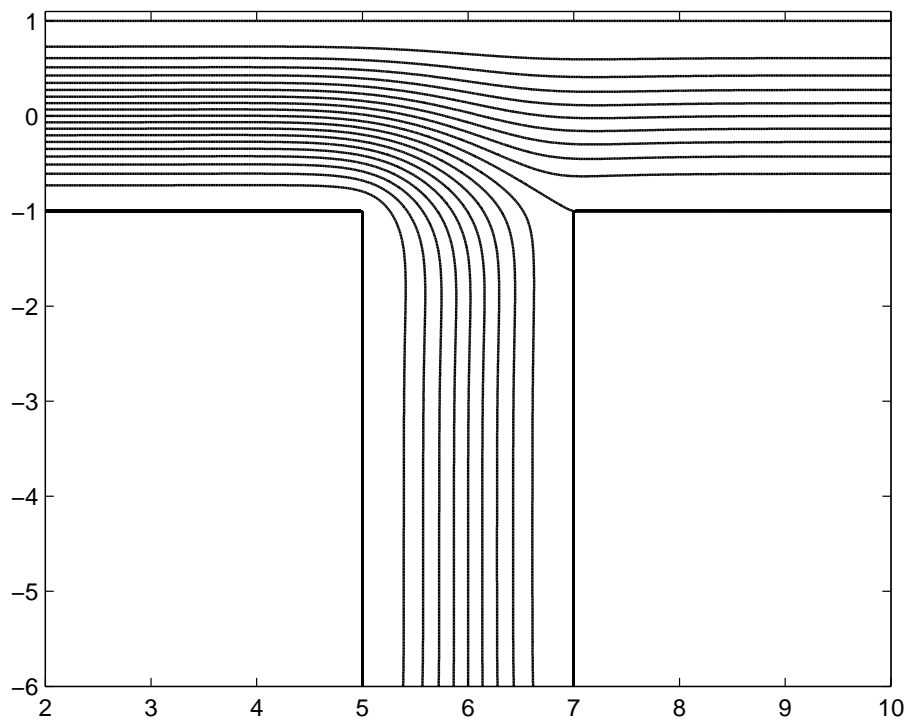


Figure D.2 : Streamlines for $Q = 0.5$ in a section of the branching channel computed by the finite difference method.

Appendix E – Stress at a corner in a branching channel

In figure E.1 we show a section of the branching channel which includes the right-hand branch entrance. We define local polar coordinates r and θ where r is the radial distance from the branch corner and θ is the angle. We set $\theta = 0$ on wall 1 and $\theta = \beta$ on wall 2 which extends into the branch channel. We introduce the local stream-function, $\psi(r, \theta)$, which satisfies the biharmonic equation,

$$\nabla^4 \psi = 0, \quad (\text{E.1})$$

in an incompressible flow. In terms of ψ , the r and θ components of velocity are

$$u_\theta(r, \theta) = -\frac{\partial \psi}{\partial r}, \quad u_r(r, \theta) = \frac{1}{r} \frac{\partial \psi}{\partial \theta}, \quad (\text{E.2})$$

where u_θ is the θ component of velocity and u_r is the r component. On the walls we choose

$$\psi(r, 0) = \psi(r, \beta) = 0, \quad (\text{E.3})$$

and impose the tangential flow condition so that

$$u_r(r, 0) = u_r(r, \beta) = 0, \quad (\text{E.4})$$

which may be written in terms of stream-function as

$$\left. \frac{1}{r} \frac{\partial \psi}{\partial \theta} \right|_{\theta=0} = \left. \frac{1}{r} \frac{\partial \psi}{\partial \theta} \right|_{\theta=\beta} = 0. \quad (\text{E.5})$$

In polar coordinates we write the biharmonic equation (E.1) as

$$\left(\frac{\partial^2}{\partial r^2} + \frac{1}{r} \frac{\partial}{\partial r} + \frac{1}{r^2} \frac{\partial^2}{\partial \theta^2} \right)^2 \psi = 0. \quad (\text{E.6})$$

Following the analysis given in chapter 7 of Acheson (1990) we postulate that the stream-function takes the form

$$\psi(r, \theta) = r^\gamma f(\theta), \quad (\text{E.7})$$

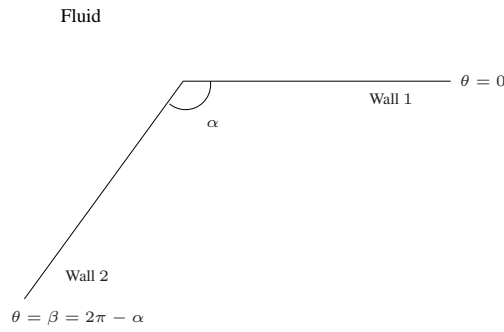


Figure E.1 : Local geometry at the right-hand corner of the branch entrance of the branching channel, with plane polar coordinates r and θ .

where γ is a constant. We substitute equation (E.7) into equation (E.6) and obtain

$$g'' + (\gamma - 2)^2 g = 0, \quad (\text{E.8})$$

where

$$g(\theta; \gamma) = f''(\theta) + \gamma^2 f(\theta) \quad (\text{E.9})$$

and a prime denotes differentiation with respect to θ . We have three special cases to consider:

Case i: $\gamma = 0$

When $\gamma = 0$ the stream-function is given by

$$\psi(\theta) = f(\theta) \quad (\text{E.10})$$

which represents a radial flow with a source or a sink at the origin. Since we are interested in flow around the corner we disregard this solution.

Case ii: $\gamma = 1$

The solution to equations (E.8) and (E.9) when $\gamma = 1$ is

$$f(\theta) = A \cos \theta + B \sin \theta + C\theta \cos \theta + D\theta \sin \theta. \quad (\text{E.11})$$

Applying the boundary conditions given in equations (E.3) and (E.4) on the wall at $\theta = 0$ we get

$$A = 0, \quad \text{and} \quad B + C = 0. \quad (\text{E.12})$$

On wall 2 where $\theta = \beta$ we find that β must satisfy

$$\sin^2 \beta = \beta^2 \quad (\text{E.13})$$

to avoid a trivial solution, and which is only satisfied when $\beta = 0$. Therefore we reject the solution.

Case iii: $\gamma = 2$

When $\gamma = 2$ we obtain

$$\psi(r, \theta) = r^2 (A + B\theta + C \sin(2\theta) + D \cos(2\theta)), \quad (\text{E.14})$$

for the stream-function. To satisfy the boundary conditions given in equations (E.3) and (E.4), the angle β must satisfy

$$\beta \sin(2\beta) + \cos(2\beta) - 1 = 0 \quad (\text{E.15})$$

to avoid a trivial solution. Equation (E.15) is satisfied when $\beta = 0, \pi, 2\pi$ and $\beta \approx 1.43\pi$ for $\beta \in [0, 2\pi]$. Since we are interested in the flow around a corner we reject the first three angles and set $\beta_0 = 1.43\pi$. The stream-function is given by

$$\psi(r, \theta) = A r^2 (1 - \cos(2\theta) + \chi (2\theta - \sin(2\theta))), \quad (\text{E.16})$$

where

$$\chi = \frac{\sin(2\beta_0)}{\cos(2\beta_0) - 1} \approx -0.223. \quad (\text{E.17})$$

The velocity components are

$$u_r = 2A r (\sin(2\theta) + \chi (1 - \cos(2\theta))), \quad (\text{E.18})$$

$$u_\theta = 2A r (1 - \cos(2\theta) + \chi (2\theta - \sin(2\theta))). \quad (\text{E.19})$$

The streamlines are shown in figure E.2 for a positive value of A , where we can see the presence of a stagnation point on the corner. The streamline direction is reversed when A is negative. If a 'far' field boundary condition were to be included then the value of A could be determined and we would have a unique solution. Now that we have calculated the velocity components we can compute the stress on the walls using the stress tensor,

$$\sigma_{ij} = -p \delta_{ij} + 2\mu e_{ij}, \quad (\text{E.20})$$

where p is the pressure and e_{ij} is the rate of strain tensor. Since we are only interested in the behaviour of the stress we will focus our attention on the rate of strain tensor. In polar coordinates we have

$$e_{rr} = \frac{\partial u_r}{\partial r} = 2A (\sin(2\theta) + \chi (1 - \cos(2\theta))), \quad (\text{E.21})$$

$$e_{\theta\theta} = \frac{1}{r} \frac{\partial u_\theta}{\partial \theta} + \frac{u_r}{r} = -e_{rr}, \quad (\text{E.22})$$

$$2e_{r\theta} = r \frac{\partial}{\partial r} \left(\frac{u_\theta}{r} \right) + \frac{1}{r} \frac{\partial u_r}{\partial \theta} = 4A (\cos(2\theta) + \chi \sin(2\theta)), \quad (\text{E.23})$$

all of which are independent of r and well defined with respect to θ . On the wall $\theta = 0$ we have

$$e_{rr} = -e_{\theta\theta} = 0, \quad \text{and} \quad e_{r\theta} = 2A, \quad (\text{E.24})$$

and

$$e_{rr} = -e_{\theta\theta} = 0, \quad \text{and} \quad e_{r\theta} = -2A, \quad (\text{E.25})$$

on $\theta = \beta$. We expect the sign to change on the $e_{r\theta}$ component because the unit vector in the θ direction points into the fluid on wall 1 and away from the fluid on wall 2. In summary, the stress is finite at the corner when $\gamma = 2$ and $\beta = \beta_0$ provided the pressure is finite.

We will now consider the general case when $\gamma \neq 0$, $\gamma \neq 1$ and $\gamma \neq 2$. The solution to equations (E.8) and (E.9) gives

$$\begin{aligned} \psi(r, \theta) &= r^\gamma f(\theta) \\ &= r^\gamma (A \cos(\gamma\theta) + B \sin(\gamma\theta) + C \cos((\gamma - 2)\theta) + D \sin((\gamma - 2)\theta)), \end{aligned} \quad (\text{E.26})$$

for the stream-function where A , B , C and D are constants. Applying the boundary conditions on wall 1 where $\theta = 0$ gives

$$C = -A, \quad (\text{E.27})$$

$$D = \frac{\gamma}{2 - \gamma} B. \quad (\text{E.28})$$

The conditions at $\theta = \beta$ only give a non-trivial solution for A and B when γ satisfies

$$\frac{\sin(\gamma\beta) \sin((\gamma - 2)\beta)}{1 - \cos(\gamma\beta) \cos((\gamma - 2)\beta)} = \frac{\gamma(\gamma - 2)}{\gamma^2 - 2\gamma + 2} \quad (\text{E.29})$$

for a given angle, β . Furthermore we find

$$B = A \left(\frac{-\gamma \sin(\gamma\beta) + (\gamma - 2) \sin((\gamma - 2)\beta)}{\gamma \cos(\gamma\beta) - \gamma \cos((\gamma - 2)\beta)} \right) = A \xi, \quad (\text{E.30})$$

where ξ is a known constant determined from γ and β . Therefore we are left with the constant, A , which could be calculated given a ‘far’ field boundary condition. The stream function is

$$\psi(r, \theta) = r^\gamma f(\theta) \quad (\text{E.31})$$

where

$$f(\theta) = A \left(\cos(\gamma\theta) + \xi \sin(\gamma\theta) - \cos((\gamma - 2)\theta) + \frac{\gamma \xi}{2 - \gamma} \sin((\gamma - 2)\theta) \right). \quad (\text{E.32})$$

The velocity components are given by

$$u_r(r, \theta) = r^{\gamma-1} \frac{df}{d\theta} \quad (\text{E.33})$$

$$u_\theta(r, \theta) = -\gamma r^{\gamma-1} f. \quad (\text{E.34})$$

To avoid a singularity in the velocity as $r \rightarrow 0$ we require $\gamma \geq 1$. In the chapters in which we consider a branching channel we set the angle α to $\pi/4$, $\pi/2$ and $3\pi/4$. The values of

γ computed using equation (E.29) for these branch angles are given in table E.1.

Branch angle (α)	$\beta = 2\pi - \alpha$	γ
$3\pi/4$	$5\pi/4$	1.67358343
$\pi/2$	$3\pi/2$	1.54448374
		1.90852919
$\pi/4$	$7\pi/4$	1.50500970
		1.65970163

Table E.1 : Values of the stream-function parameter, γ , for various branch angles.

Now that we have the exponent of r in the stream function, we will compute the e_{rr} component of the rate of strain tensor,

$$e_{rr} = \frac{\partial u_r}{\partial r} = (\gamma - 1) r^{\gamma-2} \frac{df}{d\theta}. \quad (\text{E.35})$$

Since $\gamma < 2$ for all three branch angles, $e_{rr} \sim r^{\gamma-2}$ as $r \rightarrow 0$ and the rate of strain tensor is singular and hence the stress is also singular at the corner. Therefore we have shown that the stress is singular at the corner in the cases considered in chapters 5–7.

In figure E.3 we plot the streamlines for $\alpha = 3\pi/4$ and $\gamma = 1.67358343$. The streamlines are directed around the corner with the direction determined from the sign of the constant A in equation (E.32). The stress on the walls is well-defined apart from at the corner where it is singular. Figure E.4 shows the streamlines for the two values of γ when $\alpha = \pi/2$. When $\gamma = 1.54448374$ the streamlines follow the shape of the corner, whereas when $\gamma = 1.90852919$ the flow exhibits a stagnation-point flow with both velocity components tending to zero as $r \rightarrow 0$. Finally, in figure E.5, we show the streamlines for an acute angled branch where $\alpha = \pi/4$. Once again there are two solutions for γ . When $\gamma = 1.50500970$ the flow traces the shape of the channel walls and flows around the corner. A stagnation flow is observed when $\gamma = 1.65970163$ with the streamlines dividing and travelling either to the right and above wall 1 or down and along wall 2.

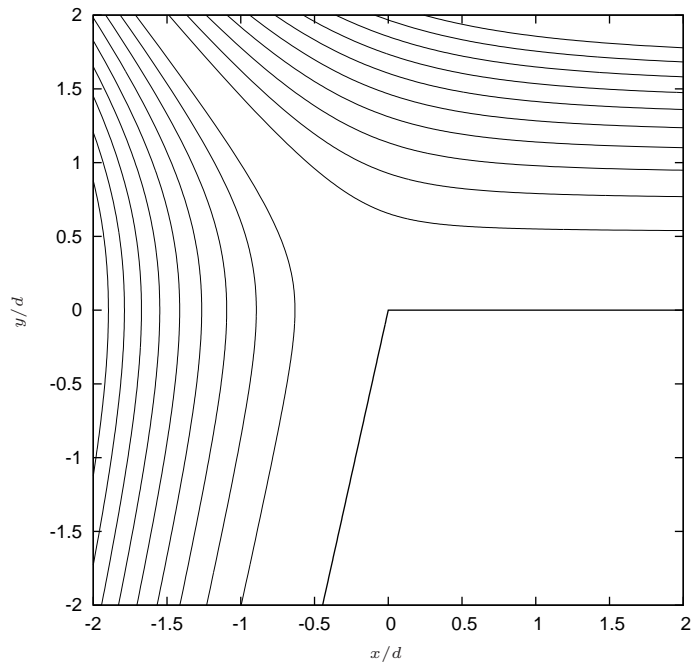


Figure E.2 : Streamlines close to a corner for $\alpha = 0.57\pi$ and $\gamma = 2$. The stress on the walls is well-defined in this case. When the constant A is positive in equation (E.16) the streamlines enter from the top-left.

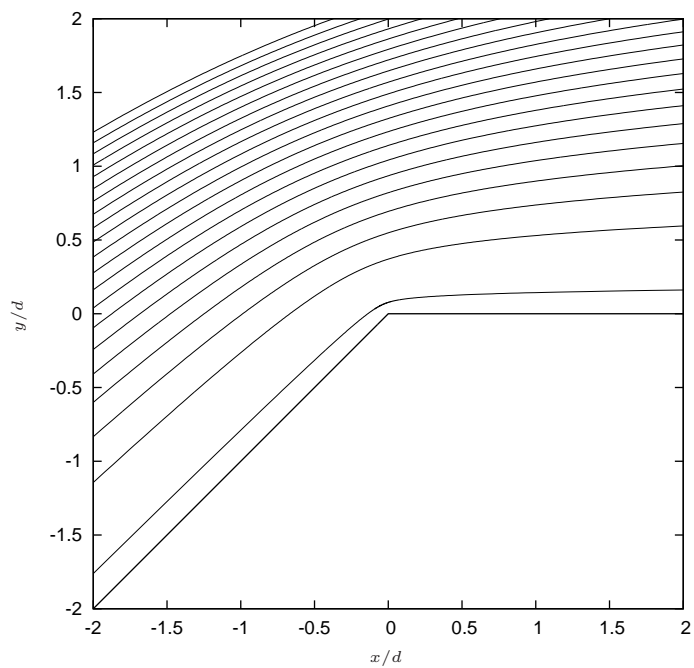


Figure E.3 : Streamlines close to a corner for $\alpha = 3\pi/4$ and $\gamma = 1.67358343$. The stress is singular at the corner.

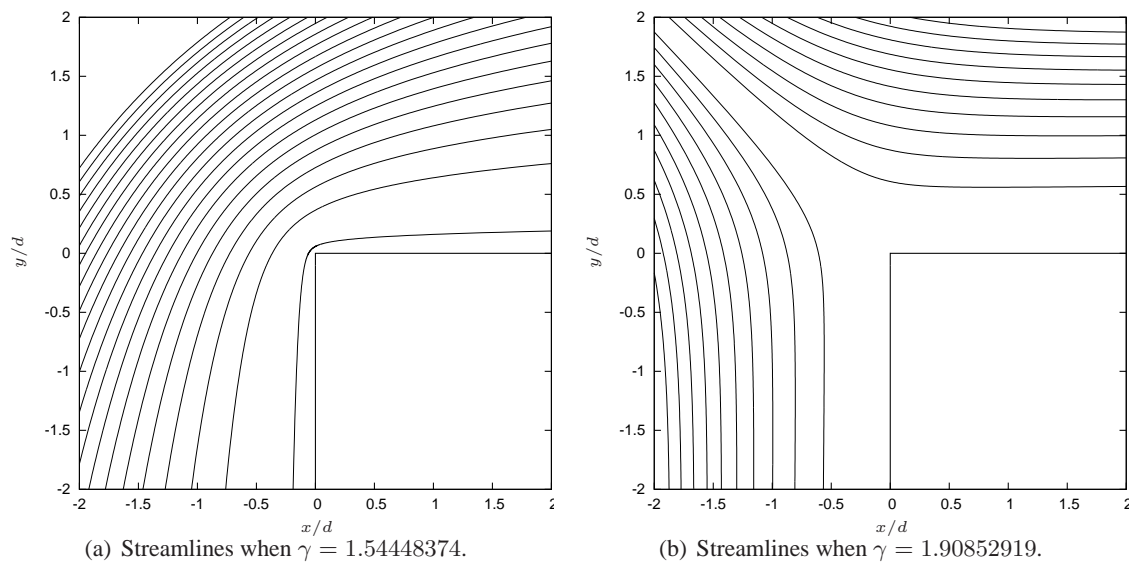


Figure E.4 : Streamlines close to a corner with $\alpha = \pi/2$ for the two values of γ . The stress is singular at the corner in both cases.

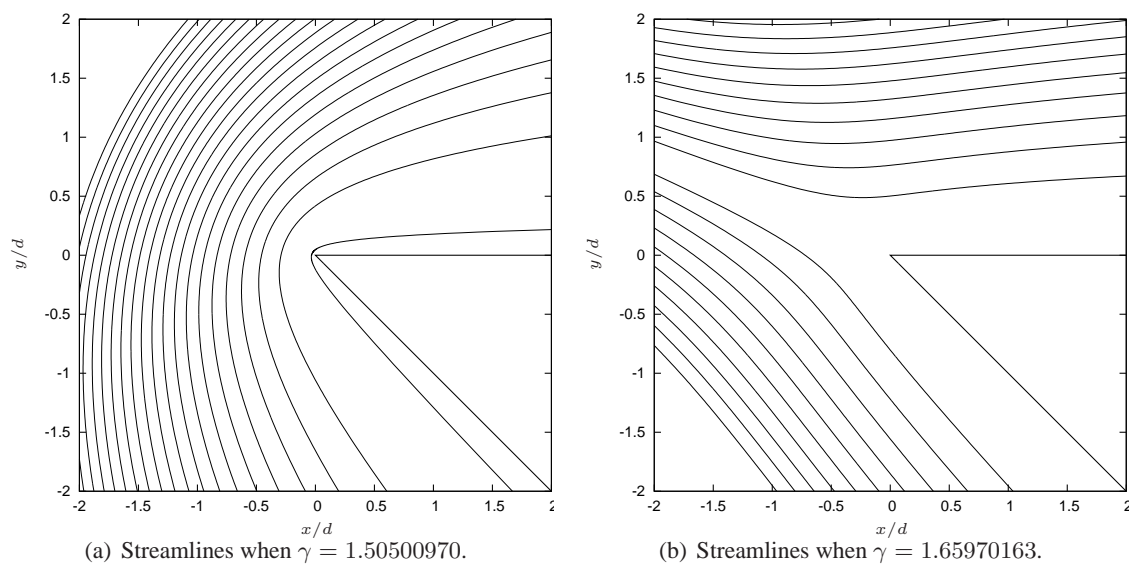


Figure E.5 : Streamlines close to a corner with $\alpha = \pi/4$ for the two values of γ . The stress is singular at the corner in both cases.

References

- D. J. Acheson. *Elementary Fluid Dynamics*. Oxford University Press, 1990.
- K. E. Atkinson. *An Introduction to Numerical Analysis*. John Wiley & Sons, New York, 1978.
- J. O. Barber, J. P. Alberding, J. M. Restrepo, and T. W. Secomb. Simulated Two-Dimensional Red Blood Cell Motion, Deformation, and Partitioning in Microvessel Bifurcations. *Annals Biomed. Eng.*, 36(10):1690–1698, 2008.
- D. Barthès-Biesel. Motion of a spherical microcapsule freely suspended in a linear shear flow. *J. Fluid Mech.*, 100:931–53, 1980.
- G. K. Batchelor. *An introduction to fluid dynamics*. Cambridge University Press, 1967.
- G. K. Batchelor. The stress system in a suspension of force-free particles. *J. Fluid Mech.*, 41(03):545–570, 1970.
- K. Benson. MCAT review. *Emory University*, 1999.
- H. Brenner. The slow motion of a sphere through a viscous fluid towards a plane surface. *Chem. Engng. Sci.*, 16(3-4):242–251, 1961.
- H. Brenner. Pressure drop due to the motion of neutrally buoyant particles in duct flows. *J. Fluid Mech.*, 43(04):641–660, 1970.
- H. Brenner. Pressure drop due to the motion of neutrally buoyant particles in duct flows. II. Spherical droplets and bubbles. *Industrial & Engineering Chemistry Fundamentals*, 10(4):537–543, 1971.
- G. Breyiannis and C. Pozrikidis. Simple shear flow of suspensions of elastic capsules. *Theoretical and Computational Fluid Dynamics*, 13(5):327–347, 2000.
- C. G. Caro, T. J. Pedley, R. C. Schroter, and W. A. Seed. *The Mechanics of the Circulation*. Oxford University Press, Oxford, 1978.
- C. J. Cawthorn and N. J. Balmforth. Contact in a viscous fluid. Part 1. A falling wedge. *J. Fluid Mech.*, 646(1):327–338, 2010.
- R. Cortez. The method of regularized Stokeslets. *SIAM Journal on Scientific Computing*, 23(4):1204–1225, 2002.

- C. Coulliette and C. Pozrikidis. Motion of an array of drops through a cylindrical tube. *J. Fluid Mech.*, 358:1–28, 1998.
- R. G. Cox and S. G. Mason. Suspended particles in fluid flow through tubes. *Annu. Rev. Fluid Mech.*, 3:291–316, 1971.
- J. F. Davidson, R. Clift, and D. Harrison. *Fluidization*. Academic Press, London, 1985.
- A. W. El-Kareh and T. W. Secomb. A model for red blood cell motion in bifurcating microvessels. *Int. J. Mult. Flow*, 26:1545–1564, 2000.
- Y. Fung. *Biomechanics: circulation*. Springer Verlag, 1997.
- Y. C. Fung. Stochastic flow in capillary blood vessels. *Microvascular Research*, 5(1): 34–48, 1973.
- D. P. Gaver and S. M. Kute. A theoretical model study of the influence of fluid stresses on a cell adhering to a microchannel wall. *Biophysical Journal*, 75(2):721–733, 1998.
- A. K. Gunstensen and D. H. Rothman. Lattice-Boltzmann studies of immiscible two-phase flow through porous media. *J. Geophys. Res.*, 98(B4):6431–6441, 1993.
- D. Halpern and T. W. Secomb. The squeezing of red blood cells through capillaries with near-minimal diameters. *J. Fluid Mech.*, 203:381–400, 2006.
- H. Hasimoto and O. Sano. Stokeslets and eddies in creeping flow. *Annu. Rev. Fluid Mech.*, 12(1):335–363, 1980.
- W. Hiller and T. A. Kowalewski. An experimental study of the lateral migration of a droplet in a creeping flow. *Experiments in Fluids*, 5(1):43–48, 1986.
- D. J. Jeffrey and Y. Onishi. The slow motion of a cylinder next to a plane wall. *Quart. J. Mech. Appl. Math.*, 34(2):129, 1981.
- M. J. Jensen, H. A. Stone, and H. Bruus. A numerical study of two-phase Stokes flow in an axisymmetric flow-focusing device. *Physics of Fluids*, 18:077103, 2006.
- P. C. Johnson. Red cell separation in the mesenteric capillary network. *Am. J. Physiol.*, 221(1):99, 1971.
- M. F. Kiani and G. R. Cokelet. Additional pressure drop at a bifurcation due to the passage of flexible disks in a large scale model. *J. Biomech. Eng.*, 116:497, 1994.
- A. Krogh. *The anatomy and physiology of capillaries*. Yale University Press, 1922.
- H. K. Kuiken. H. A. Lorentz: Sketches of his work on slow viscous flow and some other areas in fluid mechanics and the background against which it arose. *J. Engng. Math.*, 30(1), 1996.

- M. J. Lighthill. Pressure-forcing of tightly fitting pellets along fluid-filled elastic tubes. *J. Fluid Mech.*, 34:113–143, 1968.
- N. Liron and S. Mochon. Stokes flow for a Stokeslet between two parallel flat plates. *J. Eng. Math.*, 10(4):287–303, 1976.
- N. Liron and R. Shahar. Stokes flow due to a Stokeslet in a pipe. *J. Fluid Mech.*, 86(4):727–744, 1978.
- M. Loewenberg and E. J. Hinch. Numerical simulations of a concentrated emulsion in shear flow. *J. Fluid Mech.*, 321:395–419, 1996.
- M. S. Longuet-Higgins and E. D. Cokelet. The deformation of steep surface waves on water. I. A numerical method of computation. *Proceedings of the Royal Society of London. Series A, Mathematical and Physical Sciences*, pages 1–26, 1976.
- M. Manga. Dynamics of drops in branched tubes. *J. Fluid Mech.*, 315:105–117, 2006.
- S. Mortazavi and G. Tryggvason. A numerical study of the motion of drops in Poiseuille flow. Part 1. Lateral migration of one drop. *J. Fluid Mech.*, 411:325–350, 2000.
- A. S. Popel and P. C. Johnson. Microcirculation and Hemorheology. *Annu. Rev. Fluid Mech.*, 37:43–69, 2005.
- C. Pozrikidis. *Boundary Integral and Singularity Methods for Linearized Viscous Flow*. Cambridge University Press, Cambridge, 1992.
- C. Pozrikidis. *Numerical computation in science and engineering*. Oxford University Press, New York, 1998.
- C. Pozrikidis. Effect of membrane bending stiffness on the deformation of capsules in simple shear flow. *J. Fluid Mech.*, 440:269–291, 2001.
- C. Pozrikidis. *A Practical Guide to Boundary-Element Methods with the Software Library BEMLIB*. Chapman & Hall/CRC, 2002a.
- C. Pozrikidis. Buckling and collapse of open and closed cylindrical shells. *J. Engng. Math.*, 42(2):157–180, 2002b.
- C. Pozrikidis, editor. *Modeling and simulation of capsules and biological cells*. CRC Press, 2003.
- C. Pozrikidis. Axisymmetric motion of a file of red blood cells through capillaries. *Physics of fluids*, 17(3):031503, 2005a.
- C. Pozrikidis. Computation of Stokes Flow due to the Motion or Presence of a Particle in a Tube. *J. Eng. Math.*, 53:1–20, 2005b.
- C. Pozrikidis. Numerical simulation of cell motion in tube flow. *Annals Biomed. Eng.*, 33(2):165–178, 2005c.

- C. Pozrikidis. Numerical simulation of blood flow through microvascular capillary networks. *Bulletin of Mathematical Biology*, 71(6):1520–1541, 2009.
- A. R. Pries, K. Ley, and P. Gaehtgens. Generalization of the Fahraeus principle for microvessel networks. *Am. J. Physiol.*, 251(6):1324–1332, 1986.
- C. Quéguiner and D. Barthès-Biesel. Axisymmetric motion of capsules through cylindrical channels. *J. Fluid Mech.*, 348:349–376, 1997.
- S. Ramanujan and C. Pozrikidis. Deformation of liquid capsules enclosed by elastic membranes in simple shear flow: large deformations and the effect of fluid viscosities. *J. Fluid Mech.*, 361:117–143, 1998.
- P. R. Rao, G. I. Zahalak, and S. P. Sutera. Large deformations of elastic cylindrical capsules in shear flows. *J. Fluid Mech.*, 270:73–90, 1994.
- B. W. Roberts and W. L. Olbricht. The distribution of freely suspended particles at microfluidic bifurcations. *AIChE J.*, 52:199–206, 2006.
- Y. Saad. *Iterative methods for sparse linear systems*. Society for Industrial Mathematics, 2003.
- T. W. Secomb and R. Hsu. Motion of red blood cells in capillaries with variable cross-sections. *J. Biomech. Eng.*, 118:538–544, 1996.
- T. W. Secomb, R. Hsu, and A. R. Pries. Motion of red blood cells in a capillary with an endothelial surface layer: effect of flow velocity. *Am. J. Physiol.*, 281(2):H629, 2001.
- T. W. Secomb, B. Styp-Rekowska, and A. R. Pries. Two-dimensional simulation of red blood cell deformation and lateral migration in microvessels. *Annals Biomed. Eng.*, 35(5):755–765, 2007.
- M. E. Staben, A. Z. Zinchenko, and R. H. Davis. Motion of a particle between two parallel plane walls in low-Reynolds-number Poiseuille flow. *Physics of Fluids*, 15:1711, 2003.
- J. J. Stoker. *Differential Geometry*. John Wiley & Sons, New York, 1969.
- M. Sugihara-Seki. The motion of an elliptical cylinder in channel flow at low Reynolds numbers. *J. Fluid Mech.*, 257:575–575, 1993.
- M. Sugihara-Seki. The motion of an ellipsoid in tube flow at low Reynolds number. *J. Fluid Mech.*, 324:287–308, 1996.
- S. P. Sutera and R. Skalak. The history of Poiseuille’s law. *Annu. Rev. Fluid Mech.*, 25(1):1–20, 1993.
- H. Tözeren and R. Skalak. The steady flow of closely fitting incompressible elastic spheres in a tube. *J. Fluid Mech.*, 87(01):1–16, 1978.

- L. N. Trefethen and D. Bau. *Numerical linear algebra*. Society for Industrial Mathematics, 1997.
- J. Verchot-Lubicz and R. E. Goldstein. Cytoplasmic streaming enables the distribution of molecules and vesicles in large plant cells. *Protoplasma*, pages 1–9, 2009.
- Z-Y. Yan, A. Acrivos, and S. Weinbaum. Fluid skimming and particle entrainment into a small circular side pore. *J. Fluid Mech.*, 229:1–27, 1991.
- R. T. Yen and Y. C. Fung. Effect of velocity distribution on red cell distribution in capillary blood vessels. *Am. J. Physiol.*, 235(2):H251, 1978.
- G. I. Zahalak, P. R. Rao, and S. P. Sutera. Large deformations of a cylindrical liquid-filled membrane by a viscous shear flow. *J. Fluid Mech.*, 179:283–305, 1987.
- H. Zhou and C. Pozrikidis. The flow of suspensions in channels: Single files of drops. *Physics of Fluids*, 5:311, 1993.
- H. Zhou and C. Pozrikidis. Pressure-driven flow of suspensions of liquid drops. *Physics of Fluids*, 6:80, 1994.
- H. Zhou and C. Pozrikidis. Deformation of liquid capsules with incompressible interfaces in simple shear flow. *J. Fluid Mech.*, 283:175–200, 1995.